EXPERIMENTAL AND THEORETICAL INVESTIGATION ON CYCLIC LIQUEFACTION MECHANISMS AND ON THE EFFECTS OF SOME MITIGATION MEASURES

A thesis presented by

MELE Lucia

in partial fulfillment

of the requirements for the degree of

Doctor of Philosophy

In the field of

Civil Systems Engineering

Department of Civil, Architectural and Environmental Engineering

University of Napoli, Federico II

Napoli, Italy

April 2020

PhD Coordinator	Supervisors
Prof. Andrea Papola	Prof. Alessandro Flora Prof. Stefania Lirer

Some pages have been left blank voluntarily. Some of those results will be published soon.

Alla mia mamma e
al mio papà

In life,
what you really want
will never come easy.

SUMMARY

ABSTRACT

Earthquakes are one of the most destructive natural phenomena, that hit several places in the world. These ground motions are also dangerous because of possible soil liquefaction phenomena. Liquefaction is a phenomenon marked by a rapid loss of shear strength and stiffness, which may occur in loose, saturated sandy soil deposits. The consequences may be catastrophic as demonstrated in several case histories.

This thesis has been involved in the framework of LIQUEFACT project with the main purposes to better understand the mechanisms and the parameters that govern liquefaction phenomena and to study the possible mitigation techniques, providing guidelines and design tools for real applications in situ.

As well-known, ground improvement is currently considered to be the most appropriate mitigation technique to prevent soil liquefaction. In this research, the effectiveness of some techniques (densification, addition of fine contents and desaturation) has been verified via experimental evidences coming from laboratory testing. Pros and cons of the studied liquefaction countermeasures have widely been discussed.

Based on the experimental results performed on several sandy soils in different conditions, an insight on liquefaction mechanisms has been done. In particular, liquefaction phenomena have been widely studied starting from the trigger, passing from the parameters affecting liquefaction resistance, the behaviour of liquefied soils and concluding with the behaviour of re-consolidated soils, which experienced liquefaction.

Experimental tests have been processed according to an energetic approach. Such approach have been applied to saturated and non-saturated soils, although the most important findings have been obtained for non-saturated soils, for which the energetic approach can be used also for predicting the cyclic resistance curves and then used as a simple design tool in desaturation interventions as countermeasure against liquefaction. To do that, an innovative synthetic state parameter, the *specific volumetric energy to liquefaction* ($E_{v,liq}$), has been introduced. The role of $E_{v,liq}$, together with the *specific deviatoric energy to liquefaction* ($E_{s,liq}$) – which make up the *specific total energy to reach liquefaction* ($E_{tot,liq}$) – has been investigated.

In particular, the deviatoric component of specific energy to liquefaction has been used in the assessment of liquefaction potential of two case histories, whose results obtained according to the energetic-based approach have been compared with those of the stress-based approach.

Although further tests are necessary to validate the energetic models of interpretation of liquefaction phenomena for saturated and non-saturated soils, the preliminary results shown in this research work seem to be very promising.

CHAPTER 1

1. INTRODUCTION

Earthquakes are one of the most destructive natural phenomena, that hit several places in the world. These ground motions are dangerous not only because of inertial and kinematic stresses directly induced on the structure by shaking, but also because of possible soil liquefaction phenomena. Seismic shaking of sufficient strength and duration may transform saturated, loose sandy soils into a suspension of soil particles and water that behaves in a manner similar to a viscous fluid. This phenomenon is called liquefaction. As a consequence of that, excessive deformations of ground surface occur, causing loss of human lives and serious damage to civil engineering works and environment. However, the impact of Earthquake Induced Liquefaction Disasters (EILDs) on communities can be lessened if appropriate mitigation actions are taken.
This is one of the aspects on which the European project, LIQUEFACT focuses its attention. Funded by the EU within the Horizon2020 – DRS 2015 call (Research Innovation Action), it addresses the mitigation of risks to EILD events in European communities with a holistic approach (www.liquefact.eu). This project involves eleven partners, including University of Napoli, Federico II (Fig. 1.1).

Figure 1.1. Main Partners of LIQUEFACT project.

1.1 RESEARCH GOALS AND THESIS OUTLINE

This thesis has been developed in the framework of LIQUEFACT project with the main purposes to better understand the mechanisms and the parameters that govern liquefaction phenomena and to study the possible mitigation techniques, providing guidelines and design tools for real applications in situ.
It consists of two macro-parts: experimental activities and theoretical investigations.
The experimental activities have been carried out with the following aims:

- to contribute to site characterization of the field trial of LIQUEFACT project, located in Pieve di Cento (Bologna, Italy), which was affected by widespread liquefaction phenomena during the 2012 earthquake in Northern Italy. For this purpose, tests on reconstituted and undisturbed specimens have been carried out. This test site has been chosen by members of LIQUEFACT project to verify the effectiveness of some mitigation techniques (drainage and induced partial saturation).
- to improve the basic understanding of the mechanics of liquefaction behaviour of several sandy soils, performing tests in different state conditions and by means of different devices (triaxial and simple shear), with a particular insight on the behaviour of liquefied soils.
- to study three different mitigation techniques at a small scale (addition of fines, densification and desaturation).

Starting from the experimental evidences, several theoretical considerations have been made. Particular emphasis is placed on the interpretation from an energetic perspective of the results of cyclic tests in saturated and especially in unsaturated conditions, where promising and simple design tools in intervention of desaturation as liquefaction mitigation technique has been proposed. Further considerations have allowed to pass from small to field scale, using the proposed energetic approach to evaluate the susceptibility to liquefaction of a site through 1D site response analysis.
In Figure 1.2 a summary map of the present research work summarizes clearly the topics and themes treated in this thesis, which is organized as follows:

- Chapter 2 reviews some previous relevant research works. The fundamental understanding and concepts of soil liquefaction and some cases history are described, with special reference to the 2012 Northern Italy (Emilia-Romagna) earthquake. This is followed by a review on the behaviour of sandy soils under monotonic and cyclic loading and on the main factors which influence their behaviour. In the last part, the main mitigation techniques against soil liquefaction are described and their possible applications in situ are presented, with particular attention to the theoretical aspects of the desaturation.
- Chapter 3 describes the main features of the field trial located in Pieve di Cento (Bologna, Italy), where disturbed and undisturbed samples were retrieved and tested in laboratory.
- Chapter 4 presents the tested soil materials and the several devices used in the experimental activity, such as triaxial (for saturated and unsaturated tests) and simple shear apparatus. In this section, the ways of preparation of the reconstituted

specimens as well as the testing procedures are described. Particular attention is also focused on the "opening" of the undisturbed samples.

- Chapter 5 examines the first experimental results performed on several kinds of saturated and loose sands (indicated as "untreated" sands). In the first part, permeability, oedometric and monotonic tests are presented to characterize widely the soils, especially those retrieved from Pieve di Cento field trial. Further considerations are done on the concept of critical state in triaxial and simple shear tests. In the second part, the results of cyclic triaxial and simple shear tests are discussed and compared among them and with the results of the wide experimental program in cyclic simple shear apparatus that has been performed to show the effect of boundary conditions, non-sinusoidal loading, specimen preparation methods and initial static shear stress, on the liquefaction resistance. In the third and last part, the results from undisturbed specimens are shown, with a section dedicated to the effect of sampling.
- Chapter 6 is fully dedicated to analysis carried out on "treated" specimens. Three treatment techniques were studied: addition of plastic fines, densification and desaturation. Attention was focused on the effectiveness and the applicability of such technologies in situ. Further considerations are presented in this chapter on possible pros and cons of the aforementioned technologies.
- Chapter 7 can be considered as a useful insight of the behaviour of liquefied soil. In the first part of this section, the results shown in previous chapters are interpreted according to a "viscous key", based on the concept that the liquefied soils suffer from a changing phase. A new pore pressure model is proposed taking into account the effect of viscosity. In the second part, the effect of post-liquefaction on saturated and unsaturated soils is shown and discussed in detail.
- In Chapter 8 a new and promising energetic interpretation of liquefaction tests is presented for saturated and unsaturated soils. Attention is focused mainly on unsaturated soils, for which the introduction of an innovative synthetic state parameter, the *specific volumetric energy to liquefaction* ($E_{v,liq}$), is shown to be a key parameter in the interpretation of liquefaction tests. Moreover, further considerations are done on the possibility to predict the cyclic resistance curves of unsaturated sandy soils. Based on these observations, design tools for Induced Partial Saturation (IPS) as countermeasure against liquefaction are presented.
- In Chapter 9, based on the characterization of the studied field trial, achieved from laboratory tests, an analysis of liquefaction susceptibility assessment is performed using "traditional" models from literature. The results are then compared with those from the energetic approach proposed in this thesis, able to evaluate the excess of pore water pressure generated during a seismic event.
- Finally, in Chapter 10, a useful summary of the main findings of this research work is given and the main conclusions are provided and discussed. Possible future research works are also presented.

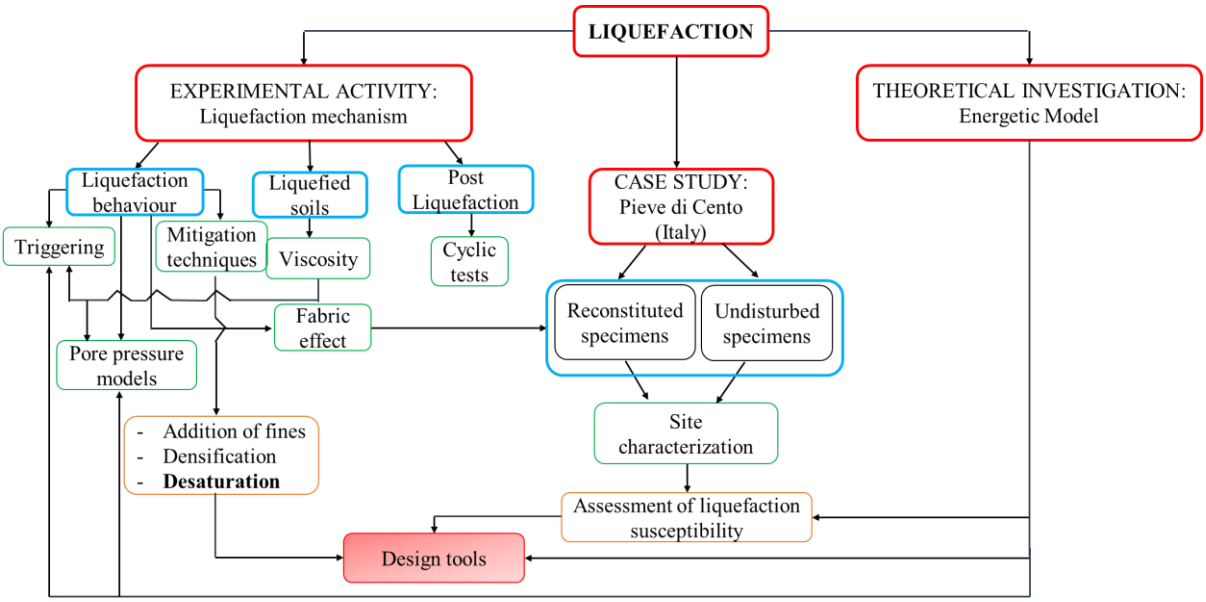

Figure 1.2. Summary map of the research work.

CHAPTER 2

2. LITERATURE REVIEW: SOIL LIQUEFACTION

In this chapter, the relevant literature regarding liquefaction is presented in several sections.

2.1 SOIL LIQUEFACTION AND CASE HISTORIES

2.1.1 DEFINITION AND MECHANISMS OF SOIL LIQUEFACTION

Marcuson (1978) defined liquefaction as "the transformation of a granular material from a solid to a liquefied state as a consequence of increased pore-water pressure and reduced effective stress". The term *effective stress* (σ') is used to describe the stress associated with the interparticle contact forces. As well known, according to Terzaghi's principle (Terzaghi, 1925) effective stress is defined, for saturated soils, as the difference between the external total stress (σ) and the internal pore water pressure (u). Moreover, the effective stress principle states that σ' governs the mechanical behaviour of the soils.
In saturated cohesionless soils (such as sandy or silty non-plastic soils), where the resistance is mobilized mainly by friction under the influence of confining stress (σ'), liquefaction phenomena may occur. In this case, soils reach a particular state of particle suspension resulting from release of contacts between particles of sands of deposits (σ'=0) (Ishihara, 1993).
This particular condition may be triggered by monotonic (static liquefaction) or cyclic loadings (dynamic liquefaction). In this work, only dynamic liquefaction will be discussed and studied in depth.
From a practical point of view, wind, traffic and especially earthquake are common sources of cyclic loading, which may trigger liquefaction phenomena. Although the permeability coefficient (k_w) of sandy soils is high enough to generally consider them in drained conditions, when the applied cyclic loading is faster than its capacity of drainage or they are confined by layers of low permeability - sandy soils may be in undrained conditions, as well. Under this condition, pore water pressure increases, reducing effective stresses until to get nihil (liquefaction).
Figure 2.1 may be useful to better understand what happens in saturated soils during this kind of phenomenon. Before an earthquake, for example, individual soil grains are held in place by frictional or adhesive contact forces, creating a solid soil structure with water filling the spaces between the grains (1). At the initiation of liquefaction, particle rearrangement with no change in volume causes the pore water pressure to increase; consequently, the particles lose their mutual contact and go into suspension: in this case soil behaviour switches from that of a solid to that of a fluid (2). After the earthquake, water flows out of the soil and the soil particles settle into a denser configuration (3).

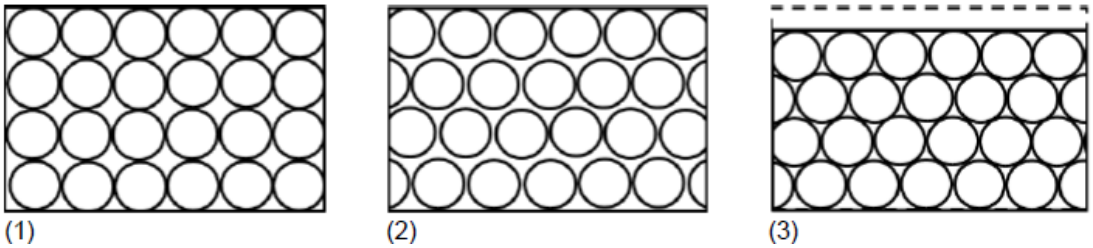

Figure 2.1. Scheme of liquefiable soils (National Academies of Sciences, Engineering and Medicine (2016)).

Since liquefaction is due to the development of excess pore water pressure under undrained conditions, liquefaction susceptibility is influenced by the variables that influence volume change behaviour in drained conditions. These variables include both effective confining pressure and soil characteristics as particle size, shape and gradation (Kramer, 1996).

Ishihara (1984; 1985) showed that rather than grain size alone, plasticity influences the liquefaction susceptibility of fine-grained soils. Ishihara and Koseki (1989) showed that plasticity index is one of the most important parameters influencing liquefaction resistance. Sands containing high plastic fines generally exhibit a higher resistance to liquefaction than clean sands.

Regarding gradation, well-graded soils are generally less susceptible to liquefaction than poorly graded soils (Kramer, 1996), as a matter of the fact that the filling of voids between larger particles by smaller particles in a well-graded soil results in lower potential under drained conditions and, consequently, lower excess pore water pressure under undrained conditions.

Moreover, soils with rounded particles shapes are known to densify more easily than soils with angular grains, it means that their liquefaction resistance is lower than angular-grained soils.

More generally, the term 'liquefaction' includes two different phenomena: flow liquefaction and cyclic mobility. The main difference between them is represented by the amplitude of the shear stress required in static conditions (*driving stress*) compared to the soil strength under the loading conditions. According to Kramer (1996), flow liquefaction "*can occur when the shear stress required for static equilibrium of a soil mass (the static shear stress) is greater than the shear strength of the soil in its liquefied state*", whereas cyclic mobility "*occurs when the static shear stress is less than the shear strength of the liquefied soil*". Practically, in flow liquefaction the pore water pressure increase, produced by monotonic or cyclic stresses, allows to reduce the soil shear strength inducing the soil failure. On the other hand, during cyclic mobility, that can only be triggered by cyclic loading, deformations develop incrementally, so the failure condition is governed by the soil strain rate. Cyclic liquefaction (also known as 'level ground liquefaction'), is a particular case of cyclic mobility characterized by the absence of driving stresses.

The consequences of flow liquefaction phenomena are often referred to as flow failures and may be catastrophic. Specifically, if the soil passes from a solid state to a liquid one, structures and infrastructures are literally swallowed by the liquefied soil, while the

underground structures are lifted at the ground surface, because of the upward buoyancy force generated by liquefaction.
The main effects connected to cyclic mobility are often referred to as lateral spreads, while one of the typical effects induced by cyclic liquefaction is the formation of sand boils. Based on current understanding, sand boils seem to occur when trapped pore water at elevated pressure bursts through weaknesses in overlying low-permeability layers and consequently, liquefied sand spilling over the ground surface.
Another important issue of damage induced by soil liquefaction are settlements. As shown in Figure 2.1, after liquefaction, pore water pressure dissipates and this phenomenon is accompanied by settlements of ground surface. The densification, and thus settlements of saturated sands is influenced by the maximum shear strain induced in the sand and by the amount of excess pore water pressure generated by the earthquake. Earthquake-induced settlement frequently causes damage to structure supported by shallow foundations, to utilities that serve pile-supported structures and to lifeline that are commonly buried at shallow depths (Kramer, 1996).

2.1.2 CASE HISTORIES

The consequences of soil liquefaction phenomena may be catastrophic. In literature, several well-documented cases of dramatic damage to structures and infrastructures have been reported.
In 1964, two strong motions caused liquefaction phenomena in two different parts of the world: Alaska (USA) on Good Friday, March 27 and Niigata (Japan) in June 16.
Alaska earthquake (M_w=9.2) caused ground failures, such as landslides, flow failures, lateral spread and ground settlement (Youd, 2014). Five large landslides within Anchorage disrupted major parts of the city causing losses of about $50 million (Hansen, 1966). The classical examples of liquefaction may be found in Valdez (Alaska), as reported by Coulter and Migliaccio (1966). Valdez is situated on the seaward edge of a large outwash delta composed of a thick section of saturated silty sand and gravel. The earthquake triggered a huge submarine flow slide, involving material that destroyed offshore harbour facilities and several near-shore installations. The disastrous flow failure at the water-front was caused by pore-water pressure rise in loose, contractive granular sediment cyclically deformed as shear and surface waves propagating though the sediment. As the pore pressures rose and reached a critical level, flow instability ensued. Because of the contractive behaviour, the residual strength of the stressed sediment became less than the static gravitational shear stress and flow deformation accelerated with a large mass of sediment flowing into deeper waters (Youd, 2014).
A few months later, another earthquake hit Japan, in particular the city of Niigata (M_w=7.6). Niigata city is located on the estuaries of the Shinano and Agano rivers. Extensive liquefaction phenomena caused severe damage to roads, buildings, railways and buried pipes (Yasuda and Harada, 2014). It is well documented by several photos (Fig. 2.2, Watanabe (1966)), taken after the strong motion. In Figure 2.2a apartment houses have been damaged in Kawagishi Town, while Figure 2.2b shows oil tanks settled

and tilted. The Showa bridge, which crosses the Shirano river, collapsed as reported in Figure 2.2c and finally in Figure 2.2d an uplifted sewage tanks is shown.
Ishihara and Koga (1981) carried out a soil investigation estimating that the sand layer from a depth of 3 to 13 m liquefied.

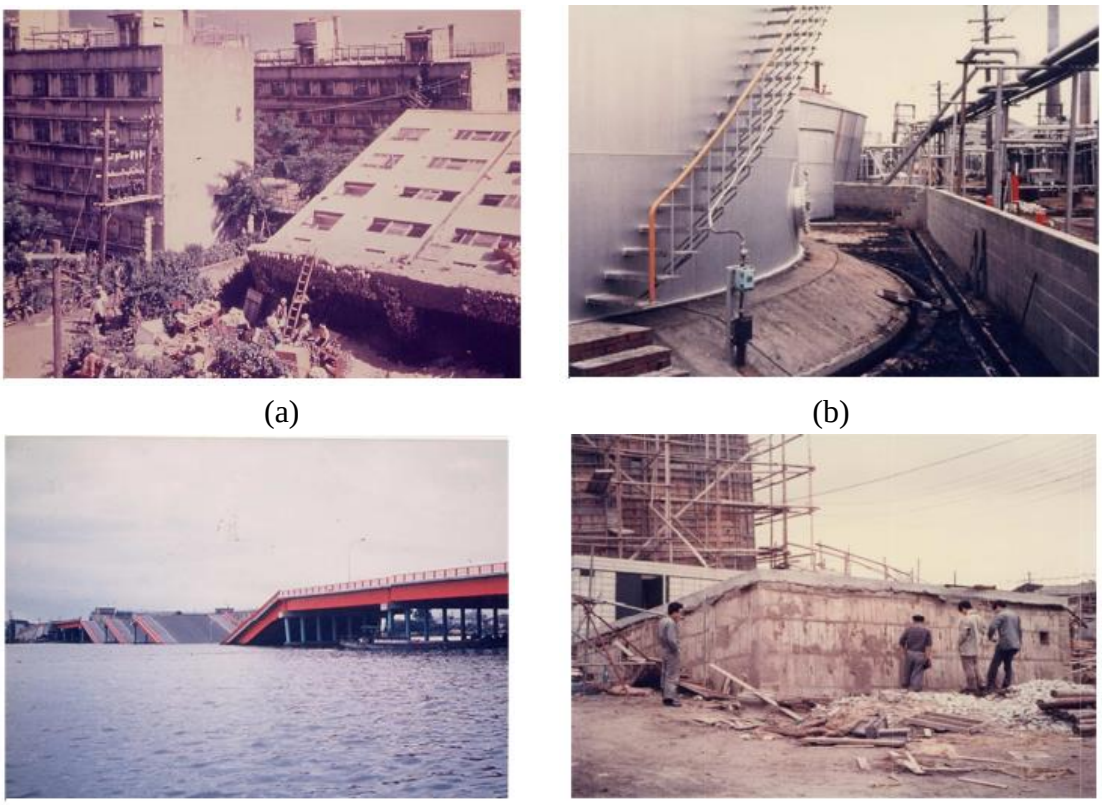

(a) (b)

(c) (d)

Figure 2.2. Soil liquefaction during 1964 Niigata earthquake (Photos by Watanabe (1966), adapted from Yasuda and Harada, 2014).

In 1995, extensive liquefaction phenomena occurred in Kobe (Japan). During the earthquake (M_w= 6.9) ports and harbour facilities were completely destroyed (Soga, 1998); in particular, two near-shore man made islands, Port Island and Rokko Island, in Kobe Port suffered from several damage. Even though the earthquake caused a total shutdown of the port facilities (Fig. 2.3), creating large economic loss for the city, soil liquefaction and lateral spreads were the major causes of the damage. The effects were ground settlements, lateral spreads, sand boils and pavement fissures, buildings and elevated roadways collapsed. In particular, lateral spreads of Port and Rokko Islands caused large seaward displacement of caisson walls.

Figure 2.3. Damage in Kobe after the 1995 Kobe earthquake.

Another important case history of liquefaction occurred in Kocaeli (Turkey) following the 17 August 1999 earthquake (M_w=7.4). Its epicentre was located close to the south east corner of the Izmit Bay, owing to that the most severe damage hit the marine structures (Boulanger et al., 2000). Sumer et al. (2002) summarized the effects of liquefaction during the above mentioned 1999 earthquake. Storage tanks near the shoreline tilted and structures settled, although, it is not quite clear if these settlements (and collapses) are caused by liquefaction or by other processes such as slope instability, surface rupture, or a combination of those processes (Sumer et al., 2002).

In the period between September 2010 and December 2011, Christchurch (New Zealand) and its surroundings were hit by a series of strong local earthquakes (the Canterbury Earthquake Sequence).

The most devastating earthquake was recorded on 22 February 2011 (M_w=6.2), causing heavy damage to the city and 185 fatalities. Many unreinforced masonry structures including the historic Christchurch Cathedral collapsed (Cubrinovski, 2013).

Rock falls and slope instabilities in the Port Hills affected significant number of residential properties in the south-eastern part of the city, but the most important geotechnical issue of the earthquakes was the extensive liquefaction phenomena in the eastern suburbs of Christchurch (Fig. 2.4). The liquefaction affected 60.000 residential buildings (properties), about 8.000 houses have been damaged beyond economic repair. The worst damage to residential houses was inflicted in areas where severe lateral spreading occurred. Buried pipe networks suffered from extensive liquefaction-induced damage. The wastewater system of Christchurch was hit particularly hard resulting in numerous failures and loss of service to large areas. Most of the damage to bridges was due to liquefaction in the foundation soils and lateral spreading of the river banks.

Figure 2.4. Damage induced by liquefaction in Christchurch (New Zealand), 2011.

Once again, Japan was hit in 2011 by liquefaction phenomena during the 11th March Tohoku earthquake (M_w=9), the largest earthquake ever recorded in Japan. According to the Japan Meteorological Association (JMA), the epicentre was located about 150 km offshore from Sendai (largest city in the Tohoku region) and at a depth of about 24 km. The most severe damages were recorded in Minami-Kurihashi, Kuki City, closed to the Pacific Coast of Tohoku Earthquake, with dramatic effects in terms of loss of life and damage to structures and infrastructures (Bhattacharya et al. 2011). More than half of the traditional-type wooden houses were damaged, while new-type wooden houses and steel or reinforced-concrete houses exhibited less damage ratio in terms of number of houses (Koseki et al., 2015). The main consequences of the earthquake were massive tsunami in many cities and towns along the coast with the crisis of the Fukushima Daiichi nuclear power plants and widespread liquefaction phenomena. As a matter of that fact, the classical evidences of liquefaction were recorded, such as sand boiling (Figs. 2.5; Koseki et al., 2015). In Tokyo, which is about 350–400 km far from the epicentre, an intense tremor was registered; as a consequence, liquefaction evidences were observed as well. In particular, Tokyo Disneyland was affected by liquefaction phenomena as reported by Bhattacharya et al. (2011) (Figure 2.6). Figure 2.6a shows the liquefaction occurred at the Takasu Park, while Figure 2.6b shows the liquefaction effects in the paved car park of the Disneyland amusement park. The liquefied and ejected soil consisted of different types of materials ranging from pure sand (brown colour) with small fines content to grey silty sand. The boiled material differed from place to place and was highly dependent on the specific gravity of the solid grains constituting the soil (Bhattacharya et al., 2011). Also light structures, such as traffic signal posts, lamp posts and electrical poles were struck by this kind of phenomenon (Figs. 2.6c – d; Bhattacharya et al., 2011).

As was generally observed in other earthquakes, many manholes popped out of the ground, causing damage to the water and sewerage pipelines. The reason can be explained as a combination of the settlement of the surrounding ground and the upward buoyancy force generated by liquefaction.

(a) (b)

Figure 2.5. Sand boiling in Minami-Kurihashi, Kuki City: private field (a); sport square (b) (Koseki et al., 2015).

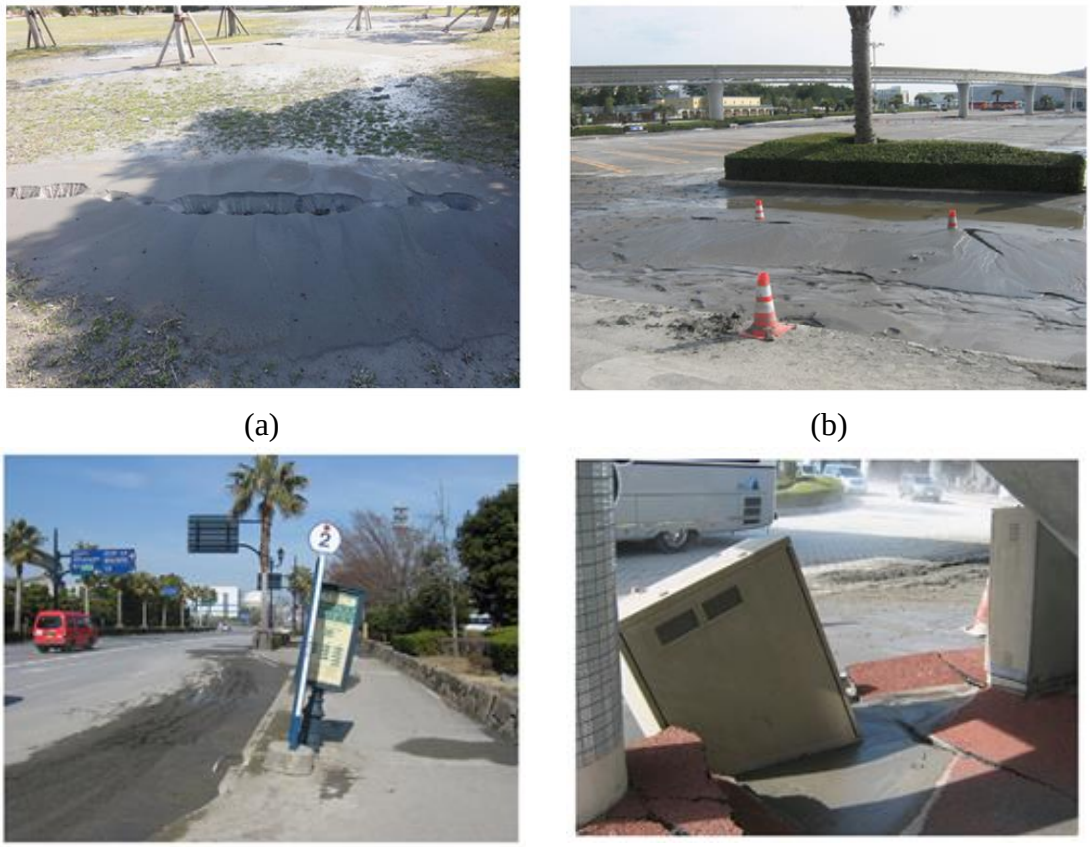

(a) (b)

(c) (d)

Figure 2.6. Liquefaction evidences: sand boiling in Takasu park (a) and Tokyo Disneyland (b); tilting of signal posts (c) and differential settlement of a transformer box near Maihama station (d) (Bhattacharya et al., 2011).

On May 2012, also Italy was struck by an important seismic sequence. The main shock occurred on 20 May 2012 (M_w=6.1) and caused extensive liquefaction phenomena. The

part of the country which was affected by these violent shakes was the area of the river Po Valley, in the foreland basin of two mountain chains constituted by the Alps and the northern Apennine, in the Emilia-Romagna Region (Northern-Italy). Since 19 May 2012, Emilia Romagna and surrounding parts of Veneto and Lombardia are hit by a long seismic sequence characterized by about two thousand of shakes. Many buildings collapsed and 27 victims were recorded. The epicenter of the 20 May event (44.89°N latitude and 11.23°E longitude) was located between the provinces of Modena and Ferrara, while the hypocenter was at a depth of 6.3 km, owing to that it is considered a shallow earthquake (Lai et al., 2015). This event was extremely interesting in Italian seismic literature. Firstly, it is due to the rarity of so extended soil liquefaction phenomena in Italy. Although Italy is a seismic country, liquefaction occurred only in restricted areas and owing to that the induced damage was generally limited. The most evident effects of liquefaction phenomena following the 2012 earthquake were found in San Carlo (Municipality of Sant'Agostino) and Mirabello, whose subsoil was characterized as an alluvial deposits of different depositional environment, which consists of alternated layers of silty-clayey deposits and sandy soils mainly constituting ancient rivers banks (Chiaradonna et al., 2018b).

To better understand the observed scenarios, an extensive investigation program, including geophysical surveys and geotechnical testing (soundings, cone penetration tests, seismic cone penetration tests, cross-hole and down-hole tests as well as many cyclic laboratory tests), was planned (Vannucchi et al., 2012).

The effects of liquefaction induced by the 2012 Northern Italy earthquake, have been immortalized and reported in several research works (Sciarra et al., 2012; Vannucchi et al., 2012; Lombardi and Bhattacharya, 2014; Lai et al., 2015). As an example, some photos have been reported in Figures 6.7 (Vannucchi et al., 2012), where the typical effects of liquefaction may be noted, such as sand boils, vents, sinkholes, craters, surface ruptures, extensional fissures. Many open spaces, as courtyards, gardens and roads, were completely covered by the ejected sand, mud and water.

Important information regarding the subsoil of the areas shaken by the 2012 May earthquake has been reported by Vannucchi et al. (2012). San Carlo and Mirabello villages lie on deep alluvial deposits of the Po Valley, a large basin of Quaternary sedimentation. The inferior Pleistocene sediments are characterized by sandy clays of marine origin, while superior Pleistocene alternates marine clay facies with continental sands. Holocene deposits have a continental origin and are represented by alternations of sandy clays, sands, silty sands and peats. The upper strata are constituted by fine graded cohesionless soils (sands and silts) of alluvial recent origin and are spatially heterogeneous. Regarding the water table depth, it is in general superficial as demonstrated by Severi and Staffilani (2012). According to them, the water table is about 80 and 130 cm below the ground surface during spring and during the seismic event the water table was at a season maximum.

(a) (b)

(c) (d)

Figure 2.7. Liquefaction evidences at San Carlo: main roads covered by grey silty sand ejected from the ground in San Carlo (a); garage (b); sand boils (c) and a private house (d) (Vannucchi et al., 2012).

Vannucchi et al. (2012) have inferred the subsoil stratigraphy of at San Carlo area, based on borehole 185130P132 included in the Regional database. It consists of a shallow silty layer (2 m thick) overlying a fine to medium sand stratum (5 m thick) which lies in turn on a cohesive thick layer of clay. A thick stratum of coarser sand (2 m) can be found at about 19 m. For the same site, a CPT profile was useful to identify the susceptibility to liquefaction. By applying the simplified procedure of Robertson and Wride (1998) the critical area extends from about 2 to 6 m. Vannucchi et al. (2012) showed the photo of a deep trench (Figure 2.8), excavated at San Carlo. It is worth noting that there is a shallower non liquefiable layer followed by the liquefiable sand stratum. The rising sand reached the surface and consequently, sand boils and volcanoes were formed at the ground surface. As confirmed by Lombardi and Bhattacharya (2014) the ejecta material consisted of grey silty sand with a significant amount of fine material.

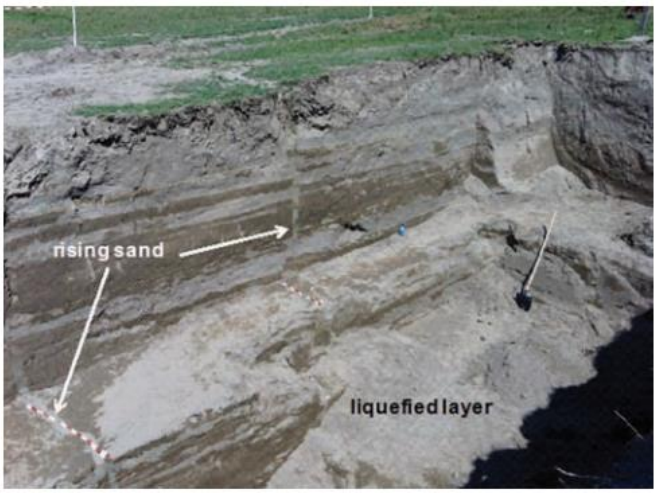

Figure 2.8. Deep trench (6 m depth) at San Carlo (Vannucchi et al., 2012).

The most recent earthquake which has been responsible of liquefaction phenomena was recorded in Indonesia, on the island of Sulawesi (M_w=7.5), on 28 September 2018. Sassa and Takagawa (2019) showed by means of field investigations that there was an occurrence of extensive liquefaction in coastal areas. Significant coastal liquefaction can result in a gravity flow of liquefied soil mass that can cause a tsunami. This seismic event was particularly disastrous: the whole Palu city was completely destroyed and swallowed by the mud. Also in this case the typical effects of liquefaction were noted, such as sand boils (Fig. 2.9).

Figure 2.9. Sand boils at a shelded area in Palu city (Indonesia) (Sassa and Takagawa, 2019).

2.2 LABORATORY TESTING ON POTENTIALLY LIQUEFIABLE SOIL

Laboratory tests can be carried out under monotonic and cyclic loading conditions in order to investigate the behaviour of potentially liquefiable soils.
To study the behaviour of soils under monotonic loading, tests by triaxial apparatus may be a good solution because of their simplicity. In triaxial tests (TX) a cylindrical specimen is subjected to an axial loading by means of a piston which can put forward in compression tests, while the radial stress (or cell pressure) is maintained constant. The vertical and horizontal stresses are principal stress directions during the whole test. Generally, this kind of tests are performed in strain-controlled condition. It means that a rate in terms of deformation has to be imposed. Although triaxial tests are very common, several experimental limits have to be highlighted. First of all, the end platens are not smooth, it implies that shear stresses can be developed at the bases of the specimen and thus, horizontal and vertical stresses cannot be considered principal stress directions. In this regard, studies were carried out by Kirkpatrick and Belshaw (1968) to investigate the strain field of dry sandy specimens by using X-ray technique. They noted that when the end platens are rough, rigid cones develop at the ends of the specimens. In other words, the platen friction produces non-uniform deformations. The result is a more pronounced peak – and then a softening - in stress-strain relationship than that of lubricated plates (Fig. 2.10; Drescher and Vardoulakis, 1982).

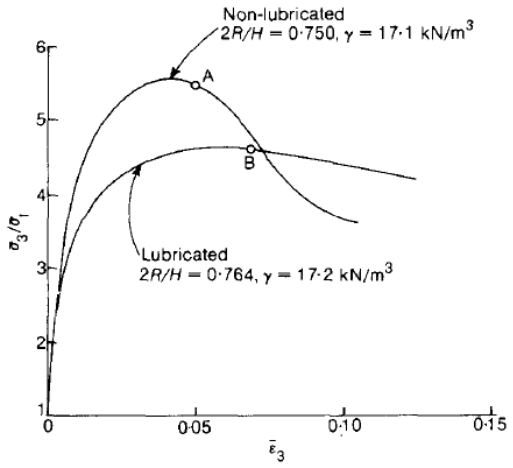

Figure 2.10. Stress ratio versus axial strain for dense sand in triaxial compression (Drescher and Vardoulakis, 1982).

Two solutions can be used to solve this problem: the first one is more traditional and it consists of preparing slender specimens (H=2D, where H is the height and D is the diameter of the specimen). For these specimens, the boarding effects may be considered negligible. The second solution is much more sophisticated, it consists of using smooth or lubricated ends.
The second experimental limit is related to non-uniformity of strains. In this case, a mobile pedestal can minimize the problem.

The third one is the error in the measurements of displacements because of a not perfect alignment of top cap with load cell or the more known 'bedding error'. These problems can be solved by using local displacements transducers or increasing the stiffness of the loading system.

As for the behaviour of soils under monotonic loading condition, also the behaviour under cyclic loading condition can be investigated through laboratory tests.

In 1966, Seed and Lee carried out undrained cyclic triaxial tests to study liquefaction behaviour of sandy soils. They consolidated samples of saturated sand under a confining stress and subjected them to a sequence of constant-amplitude cyclic axial stress in undrained conditions. During the tests excess pore water pressure builds-up and liquefaction may occur.

Generally, triaxial tests can be carried out in stress and strain controlled methods. As mentioned above, the strain controlled method is preferred in monotonic triaxial tests (TX); conversely, in cyclic tests (CTX), the stress controlled method is needed to impose the desired cyclic loading, by applying compression and extension loads (Fig. 2.11a, where q is the cyclic deviatoric stress). In this case, a frequency may be chosen (0.01 – 1 Hz) and axial and radial stress, σ_a and σ_r, respectively, may be controlled separately. The typical range of deformations which may be investigated is 0.01 – 10%. Generally, radial stress (σ_r) is maintained constant during the deviatoric phase, while the axial stress varies cyclically. In Figure 2.11b the stress state of the triaxial specimen is plotted according to Mohr's circles. It is worth noting that axial and radial stress are principal stress directions during the whole test and it is a strong limitation of this kind of tests because in situ, during an earthquake the continuous rotation of principal stresses direction occurs. It means that even though, cyclic triaxial tests are very easy to perform and for this very common, they are not enabled to reproduce in laboratory the complex cyclic simple shear stress path experienced by the soil during an earthquake. In other words, cyclic loading with continuous principal stress rotation is able to represent field loading conditions in which soil elements are subjected to simultaneous cyclic loading in the vertical and horizontal planes.

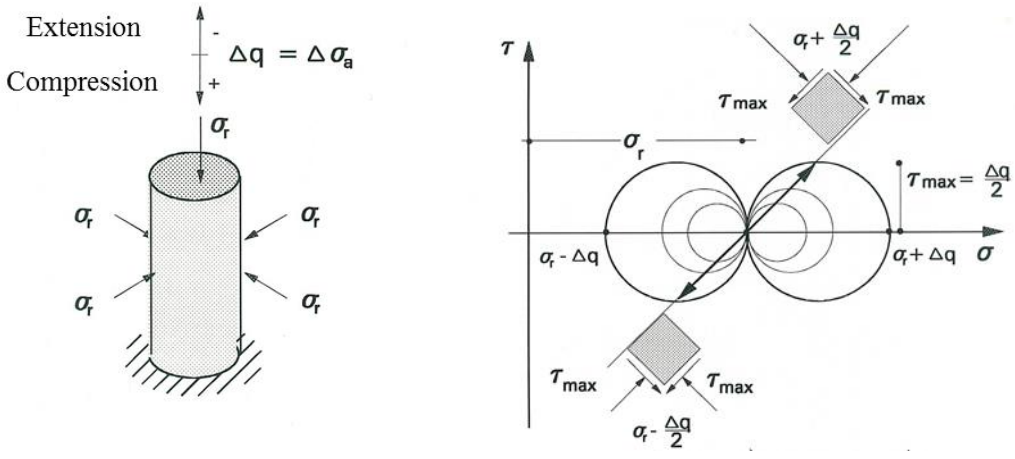

(a) (b)

Figure 2.11. Cyclic triaxial test: specimen during cyclic loading (a) and stress state according to Mohr's circles (b).

These limitations can be overcome by sophisticated testing devices, like the cyclic simple shear equipment (CSS), which allow to better simulate in situ stress conditions. As well known, a simple shear condition (k_0 condition) implies that the radial strains are equal to zero, it means that the diameter must be constant. An ideal simple shear deformation of a soil element at constant volume is achieved by: $\delta\varepsilon_{xx}= \delta\varepsilon_{yy}= \delta\varepsilon_{zz}= \delta\Upsilon_{yz}= \delta\Upsilon_{zx}=0$, $\delta\Upsilon_{xy}\neq 0$ with uniform deformation and stresses within the element (Fig. 2.12a).
According to the ASTM-D6528 (2007), "The specimen shall be constrained laterally such that the cross-sectional area at any location does not change by more than 0.1% during shear, the confinement must allow uniform shear deformation".
Concentric rings or reinforced membrane are the traditional ways to guarantee the aformentioned conditions. However, more modern devices consist of flexible boundaries, where the constant diameter can be maintened by means of sophisticated control systems. This configuration has the advantage to know the stress state of the specimen, completely. In fact as it can be easily understood, in configurations with rigid boundaries (concentric rings or reinforced membrane) not only the radial stress cannot be controlled but it is unknown. Conversely, using flexible boundary σ_r can be controlled, too. Few studies have been done to investigate and compare the effect of flexible or reinforced membrane (Sharma et al., 2017), therefore new tests could be useful to clarify this aspect in such kind of tests.
As for triaxial tests, monotonic and cyclic tests may be performed in simple shear conditions. However, the continuous rotation of principal stress directions makes difficult to interpret this kind of tests, especially in monotonic conditions. In particular, de Josselin de Jong (1971) postulated that the failure is associated with vertical rupture planes of maximum stress obliquity as shown in Figure 2.13a. On the other hand, Airey et al. (1985) showed that ruptures develop on horizontal axis, while Joer et al. (2011) proposed a new interpretation of simple shear tests. According to them, the "best-fit" linear failure plane is determined based on the actual failure plane observed in the specimen after completion of test (Fig. 2.13b). This interpretation shows a good agreement with the experimental results of triaxial tests. In Chapter 5 of this thesis, a short section will be dedicated to the interpretation of simple shear tests, with the main aim to contribute to a better understanding of this kind of tests.
Regarding the cyclic simple shear tests, they are performed by applying a cyclic tangential load on the boundaries of a short-height specimen (Fig. 2.12b), in a typical range of frequency of 0.01 – 1Hz.
The reason why short-height specimens are used in this kind of tests, is the inability to apply the complementary shear stress on the vertical boundaries of the specimen, resulting in complicated and non-uniform stress distributions during shearing. In undrained simple shear tests, the height of the specimen remains constant, which requires the vertical sides to elongate throughout the test. To allow this elongation in the apparatus, the complementary shear stress on the vertical sides cannot fully develop, and this is what leads to the non-uniform stress state (Acharya, 2017), as demonstrated by Airey and Wood (1987). This issue has not solved yet in traditional devices because complementary shear stresses at the vertical boundaries of the specimen cannot be applied. However, this

effect can be minimized by increasing the ratio between the diameter (D) and the height of the specimens.

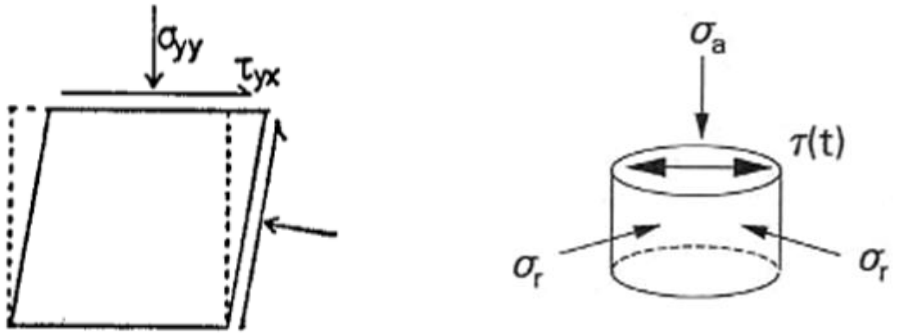

(a) (b)

Figure 2.12. Simple shear deformation (a) and scheme of a cyclic simple shear test (b).

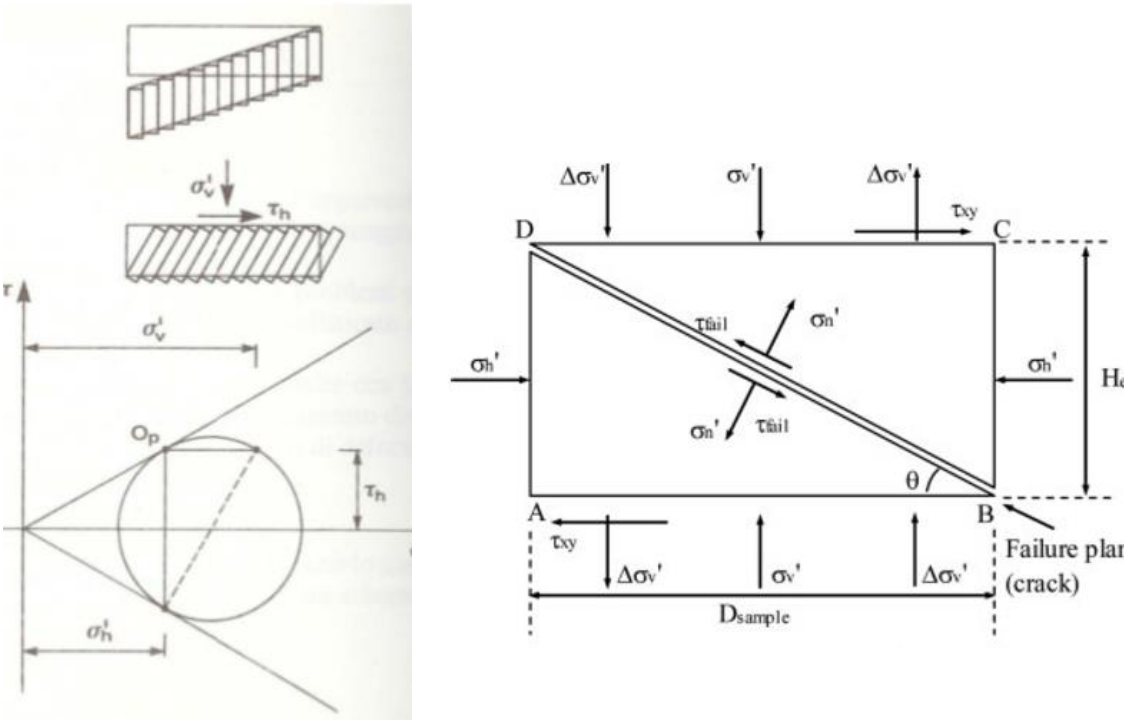

(a) (b)

Figure 2.13. Mohr's circle for failure with vertical rupture planes (de Josselin de Jong, 1971) and failure plane observed according to Joer et al. (2011).

Moreover, in laboratory tests the constant volume ideal simple shear can be imposed in drained and undrained conditions in different ways. For example, the vertical effective stress σ'_{yy} can be varied, with a constant height, to have a constant volume although it is free to drain (Fig. 2.14a); on the contrary, the total vertical stress σ_{yy} can be held constant

and in undrained conditions, pore pressures build up in order to change the effective stress (Fig. 2.14b) (Airey and Wood, 1986).

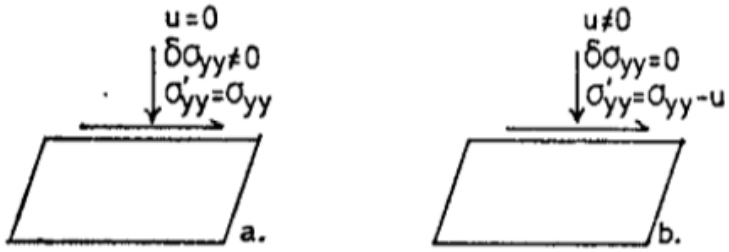

Figure 2.14. Drained constant volume simple shear (a) undrained simple shear (b) (Airey and Wood, 1986).

Airey and Wood (1986) demonstrated that the changes in vertical stress, measured in constant volume drained tests, should be identical to the changes in pore pressure, measured in undrained tests.
Owing to that, an equivalent excess pore pressure ratio has been calculated as the ratio between (σ_{v0}- σ_v) and σ_{v0}, where σ_{v0} is the initial vertical stress and σ_v is the current vertical stress (Bjerrum and Landva, 1966; Airey and Wood, 1986) in undrained cyclic simple shear tests.

On the other hand, torsional shear equipment for testing hollow (HCTS) or solid specimens (CTS) (Fig. 2.15) are also able to simulate the continuous rotation of principal stress directions, as happens in a real field subjected to seismic waves. These tests are performed by applying a cyclic torque to the upper base of a cylindrical specimen (Fig. 2.15). The possibility of using hollow cylinder specimens, and independently controlling inner and outer confining pressure (Fig. 2.15a) allows the application of triaxial consolidation prior to the application of shear loads. The torsional loads are generally applied by means of several kinds of devices, such as, electro-magnetic or electro-mechanical. During this phase, the frequency is constant (variable between 0.01 – 1 Hz), while the field of deformation that may be investigated is 0.001 – 1%.

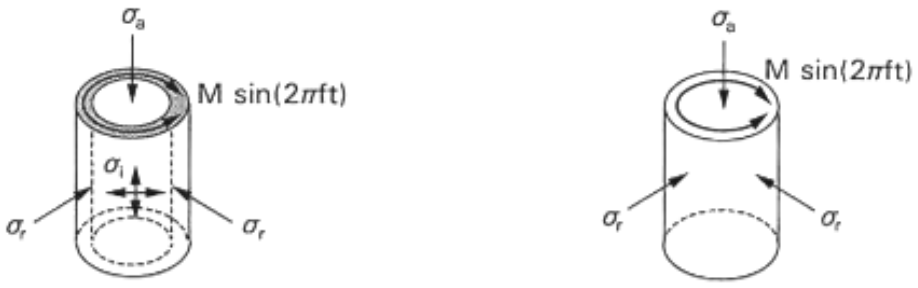

(a) (b)

Figure 2.15. Cyclic torsional shear test: hollow cylinder (a) and solid cylinder (b).

Dynamic tests, like resonant column tests (RC) are performed with the same electro-magnetic driving devices adopted for CTS tests. A constant amplitude torque with variable frequency is applied to a cylindrical specimen. The range of deformation that can be investigated is about 0.0001 – 0.1 %. Since RC tests are not suitable for large strains, they are not used to study soil liquefaction behaviour.

2.2.1 UNDRAINED BEHAVIOUR OF SANDS UNDER MONOTONIC AND CYCLIC LOADINGS

In order to better understand the undrained cyclic behaviour of sandy soils, a brief overview of some basic concepts of cohesionless soil behaviour is presented in this paragraph.

In 1936 Casagrande carried out drained stress-controlled triaxial tests on loose and dense sands. The results showed that, at a fixed confining pressure, loose and dense specimens approached the same void ratio. In other words, loose sands contracted or densified, while dense specimens first contracted and then, very quickly dilate. At large strains, under a constant shearing resistance, all specimens tend to reach the same void ratio, which was called critical void ratio (e_c). The state of the sand deforming continually, at a constant volume and under constant shear stress and confining pressure, is called the *steady state of deformation* (Castro, 1975; Castro and Poulos, 1977) or *critical state* (CS) because the basic concept is the same as the critical state for clayey soils (Schofield and Wroth, 1968). The locus of points describing the relationship between void ratio and effective confining pressure in the steady state of deformation is commonly called *critical state line* (CSL). The shear stress of sand mobilized at the steady state has been called *steady state strength* or *residual strength*.

Aside from critical state, sandy soils may go through other three states: the phase transformation state (PTS); the quasi-steady state (QSS) and the undrained instability state (UIS). Murthy et al. (2007) presented a useful simplification for the typical four states of a sand in undrained monotonic triaxial tests (Fig. 2.16).

The concept of *phase transformation* (PTS) was firstly introduced by Ishihara et al. (1975) to indicate the state at which the soil response changes from contractive to dilative. It is associated with a local minimum in the mean effective stress p' ($p'=(\sigma'_1+2\sigma'_3)/3$) (PTS in Fig. 2.16).

The quasi-steady state (QSS) is defined as the state at which the deviatoric stress q ($\sigma_1-\sigma_3$) reaches a local minimum in undrained shearing. It does not coincide with the PTS, in other words, the local minima in q and p' do not occur at the same axial strain (Fig. 2.16a). Monotonic loadings may be associated with the onset of liquefaction as well. This state is called *undrained instability state* (UIS). In this state q reaches a local and temporary maximum (Fig. 2.16). This latter state will be discussed in detail later.

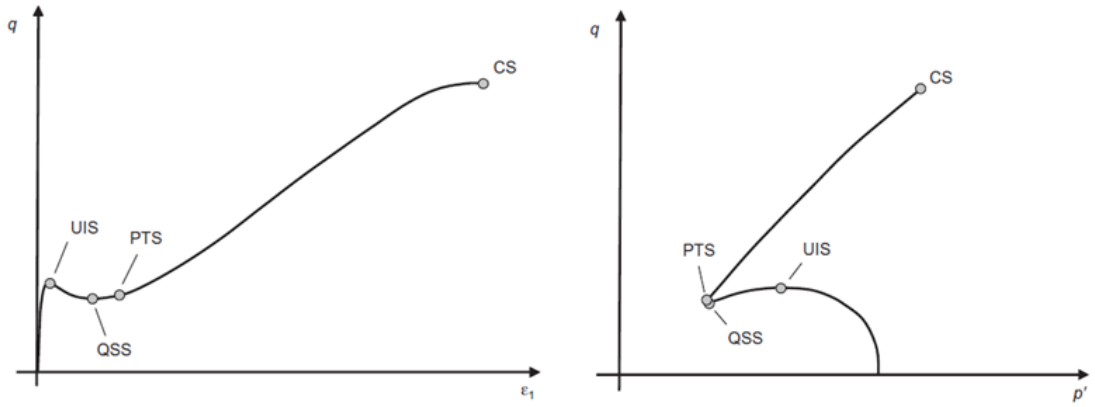

(a) (b)

Figure 2.16. Characteristic states of undrained shearing behaviour of sand in the plane ε_a-q (a) and in the plane p'-q (b) (Murthy et al., 2007).

As an example, the results of undrained monotonic triaxial tests performed by Ishihara (1993) have been reported in Figures 2.17. They are related to specimens of Toyoura sand at several confining pressures and relative densities, D_r (defined as $(e_{max}-e)/(e_{max}-e_{min})$, where e is the current void ratio).

In Figure 2.17a the results of a series of tests on loose samples of Toyoura sand (Dr=16%) have been shown in the plane ε_a-q. As reported by Ishihara (1993), the peak tends to decrease as the initial confining pressure decreases. On the contrary, to large strains ($\varepsilon_a >$ 25%), the specimens tend to exhibit almost identical behaviour. In these tests the critical state seems not to be reached. Sometimes, loose sand specimens show a slightly tendency of dilation even at large strains. However, it is possible to use extrapolation procedures, such as sigmoidal extrapolation (Murthy et al., 2007) to determinate the critical state condition. Figure 2.17b shows that the specimens with a lower confining pressure have a dilative behaviour right from beginning of the loading.

The same tendency is showed in Figures 2.17c-d for tests with a D_r of 38%, even though a critical state has been reached more clearly. Similar considerations can be done for dense sands (D_r=64%) reported in Figure 2.17e-f.

The general behaviour can be summarized as follows: if the relative density is high enough or the confining pressure is sufficiently low, the sand tends to exhibit dilative characteristics, where the shear stress rising with increasing shear strain until the critical state is reached at the end. At this state, the shear stress attains its maximum and this value is considered the strength of the sand. However, loose sands under high confining pressures, tend to deform at the beginning of the loading (contractive behaviour) and then starts to dilate, reaching the critical state at the end as shown in Figures 2.18 (Ishihara, 1993). In the test with the highest confining pressure (500kPa or 0.5 MPa) a temporary drop occurs at large strains, where the sand passes from a contractive to a dilative behaviour. In this case, the shear stress mobilized at this condition is smaller than the stress mobilized at the ultimate steady state at larger strains. It poses a technical problem as to which one should be considered the residual strength. It depends on circumstances encountered in practice, but most researchers consider the residual strength as the

minimum strength which is encountered, coinciding with the given definition of quasi-steady state.

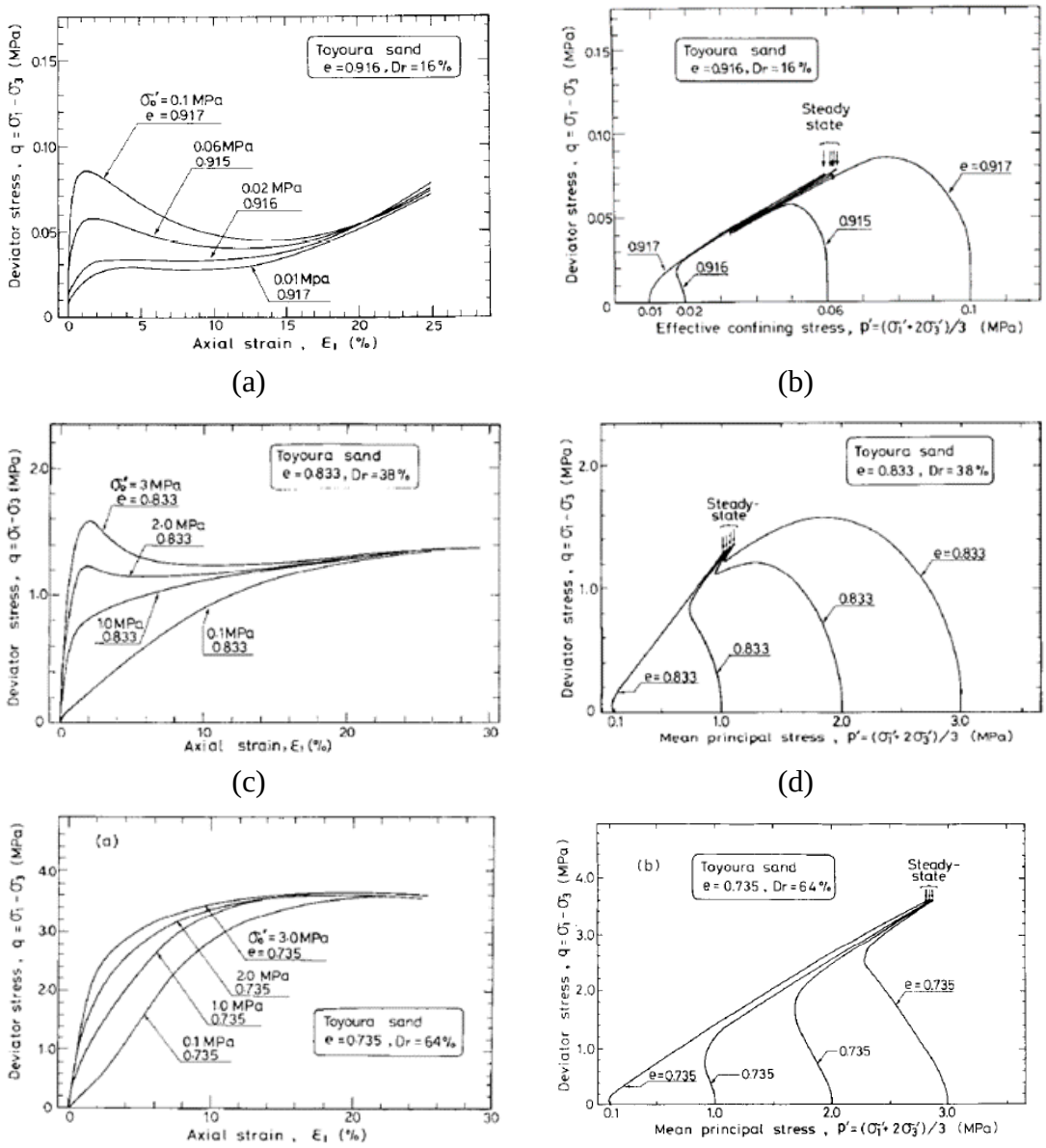

Figure 2.17. Undrained behaviour of Toyoura sand at several relative densities: Dr=16% in plane q-ε_a (a) and in the plane q-p' (b); Dr=38% in plane q-ε_a (c) and in the plane q-p' (d); Dr=64% in plane q-ε_a (e) and in the plane q-p' (f); (Ishihara, 1993).

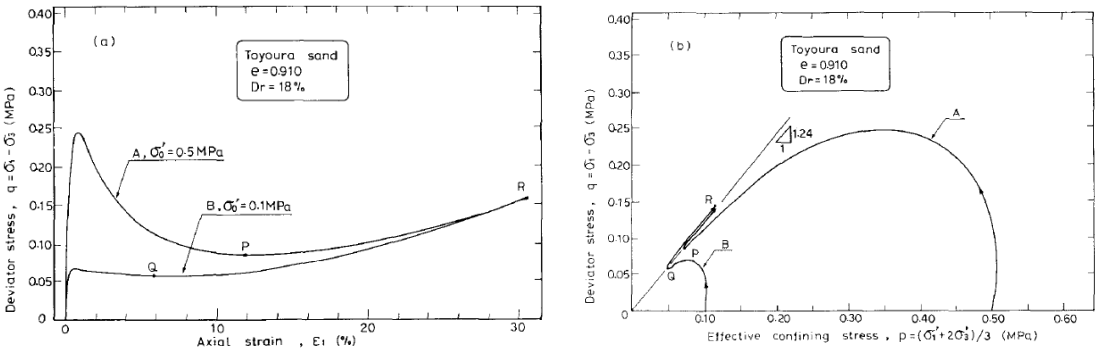

(a) (b)

Figure 2.18. Comparisons of two tests carried out on loose specimens of Toyoura sand in the plane ε_a-q (a) and in the plane p'-q (b) (Ishihara, 1993).

With the main aim to evaluate the effect of D_r on the undrained behaviour of sands, Figures 2.19 have been reported (Murthy et al., 2007). These tests have been carried out on Ottawa sand (clean sand) and consolidated at the same confining pressure: 650 kPa. As expected, the sand becomes less contractive with decreasing void ratio; moreover, unlike PTS, QSS and UIS vanish completely for dense specimens.

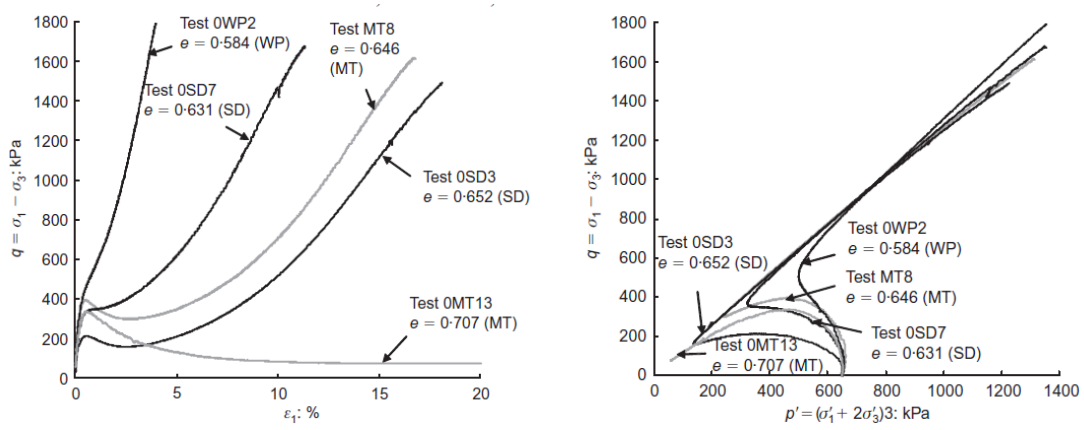

(a) (b)

Figure 2.19. Undrained monotonic response of Ottawa sand in the plane ε_a-q (a) and in the plane p'-q (b) (Murthy et al., 2007).

An interesting comparison between the soil behaviour in monotonic tests performed by triaxial and simple shear apparatus has been presented by Vaid and Sivathayalan (1996) and reported in Figure 2.20. The void ratio and the confining stresses are the same for all cases. The results from triaxial compression tests exhibits a hardening behaviour, while the test performed in simple shear apparatus seems to reach a steady condition. The authors attributed the smaller stiffness in shear mode partly to an isotropic initial stress state in triaxial test and in addition to the fact that initially the horizontal plane is not the plane of maximum shear stress, because it is 45° to the horizontal.

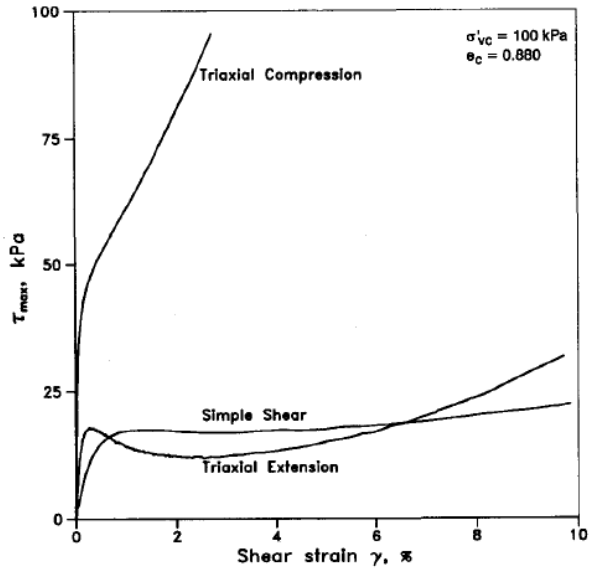

Figure 2.20. Comparison of simple shear, triaxial compression and extension behaviour (Vaid and Sivathayalan, 1996).

Before speaking about liquefaction again, a necessary insight should be presented about the critical state. CS is an effective and useful conceptual framework also in numerical modelling. The critical state line can be well represented by a power function of the form:

$$e_{cs} = \Gamma - \lambda \cdot \left(\frac{p'}{p_a}\right)^{\xi} \quad (2.1)$$

where p_a is a reference stress (typically taken as the atmospheric pressure), Γ, λ and ξ are fitting parameters (Li and Wang, 1998).
In the plane p'-q the critical state line is well represented by a straight line passing through the origin, whose equation is the following:

$$q = M_{cs} \cdot p' \quad (2.2)$$

where M_{cs} is a constant equal to the stress ratio at the critical state. The critical friction angle φ_{cs} is related to M_{cs} by the following equation:

$$\sin \varphi_{cs} = \frac{3 \cdot M_{cs}}{6 + M_{cs}} \quad (2.3)$$

Among different factors that can affect the critical state, Riemer and Seed (1997) included the drainage conditions and the stress path to which the sand is subjected during the shearing, in other words, the type of tests which is performed. The drainage conditions do not seem to significantly influence the position of CSL in the plane logp' -e, implying that both, drained and undrained tests can be put together to identify the critical state line. On the contrary, the stress-path can affect the position of the CSL as shown in Figure 2.21. It clearly, shows that the steady state strength in simple shear is lower than in triaxial tests. Although, the slope seems to be the same, the CSL in simple shear is shifted to the

left. The reason may lie in the fact that the mode of deformation, and then the strain orientations, can affect the effective stress conditions.

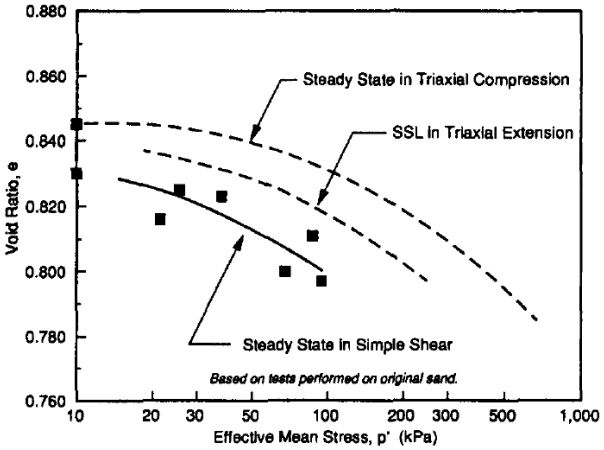

Figure 2.21. Comparison between CSL in undrained triaxial and simple shear tests (Riemer and Seed, 1997).

As mentioned before, the mechanical behaviour of sandy soils is influenced by the combined influence of density and confining stress. In 1985, Been and Jefferies introduced a state parameter (ψ) defined as:

$$\psi = e - e_{cs} \quad (2.4)$$

where e is the current void ratio and e_{cs} is the void ratio at the critical state corresponding to a given initial confining stress. According to them, ψ is the key factor influencing the behaviour of sand and it would be able to characterize uniquely the responses of different sands. In other words, for a fixed value of ψ the monotonic and the cyclic behaviour of sandy soils may be identified uniquely. More recent studies have shown that this assumption is not always reliable. It has been observed that when void ratio increases, the behaviour of sand becomes more sensitive to a small variation of void ratio.

The state parameter ψ can quantify the behaviour of medium and dense sands under high confining pressures, on the contrary, for loose sands under low confining pressure, the use of it seems not to be reliable (Ishihara, 1993).

After this useful overview of the undrained response of sands, it is possible to go back speaking about liquefaction.

In the first paragraph of this chapter, the definition of liquefaction has been given; however, the term liquefaction is used to describe a number of different phenomena. In 1996 Kramer distinguished liquefaction into two categories: flow liquefaction and cyclic mobility.

Flow liquefaction was widely studied by Castro (1969). He carried out undrained static and cyclic triaxial tests on isotropically and anisotropically consolidated specimens. Figure 2.22 summarizes the behaviour of sandy soils in different conditions in terms of relative density.

Specimen A is very loose and it exhibited a peak undrained strength at a small strains and then "collapsed", flowing rapidly to large strains. This behaviour was identified as "liquefaction" by Castro (1969) but now it is called more properly as "flow liquefaction" (Kramer, 1996).
Specimen B is dense and it initially contracts but then dilates. Specimen C is at an intermediate density, where the peak strength at low strains was followed by a strain-softening behaviour (limited liquefaction).
The effective stress conditions at the initiation of flow liquefaction can be described in stress-path space by a three-dimensional surface which will be called *flow liquefaction surface* (FLS). This condition may be reached under monotonic or cyclic loadings.

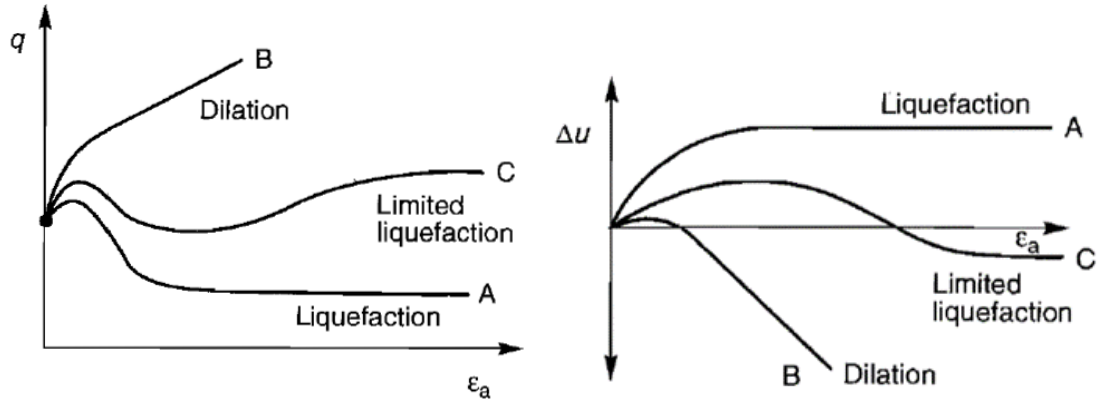

(a) (b)

Figure 2.22. Liquefaction, limited liquefaction and dilation in monotonic tests in the plane ε_a-q (a) and in the plane ε_a-Δu (b) (Kramer, 1996).

In monotonic tests, flow liquefaction may occur when the specimen generates positive pore water pressure and its resistance goes up until to reach a peak (the static shear strength) and then goes down toward the residual shear strength. Under these conditions, if the static shear stress required for equilibrium is greater than the residual shear strength the soil liquefies. Figure 2.23 (Kramer, 1996) is useful to better understand this kind of phenomenon. They are typical results of a test carried out on a loose, saturated sandy soils where flow liquefaction occurs. The shear stress at point B is the static shear stress required for equilibrium (undrained instability state (UIS) of Figure 2.16) and it is greater than shear strength (point C in Fig. 2.23). It is worth noting that beyond point C, the specimen reaches the steady-state of deformation (SSL in Fig. 2.23d) and the effective stress is not completely zero, but it is a small fraction of the initial effective confining pressure.

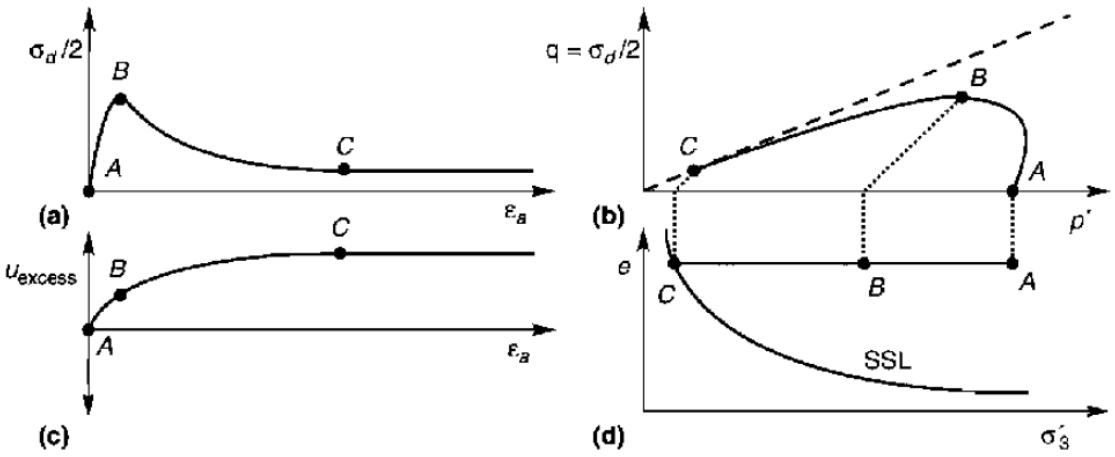

Figure 2.23. Response of isotropically consolidated loose, saturated specimens in the plane ε_a-q (a); p' – q (b); ε_a-Δu (c); σ'_3-e (d) (Kramer, 1996).

As for monotonic loading, also for cyclic loading flow liquefaction may occur. The conditions are the same described for static loading: when the static shear stress required for equilibrium is greater than its steady-state, flow liquefaction may be triggered.
On the other hand, when the static stress required for equilibrium is lower than the shear strength of the liquefied soil only cyclic mobility can occur. The development of cyclic mobility can be noted by the response of soil in cyclic tests. In this case, the effective stress path moves to the left until to reach the failure envelope. As a matter of the fact that the failure line cannot be crossed, additional loading cycles move up and down along the envelope. Three combinations of initial conditions and cyclic loading conditions can produce cyclic mobility (Fig. 2.24).
In Figure 2.24a, the static shear stress (τ_{st}) is greater than the amplitude of the cyclic shear stress (τ_{cyc}), but the steady-state strength is not exceeded. In these conditions *no reversal stress* occurs. As a matter of the fact that the stress-path cannot cross the drained failure envelope, the final cycles move up and down along the envelope.
As well as Figure 2.24a, no stress reversal occurs in Figure 2.24b, even though the steady state strength is exceeded at the end of the test. In this case, temporary instability occurs when the stress path touches the flow liquefaction surface and, generally, in this case significant strains develop.
In the last case, a *stress reversal* condition is presented (Fig. 2.24c) because $\tau_{st} < \tau_{cyc}$. In this condition the shear stress can change the versus, implying that each cycle includes compression and extension phase.
That said, the presence of a static shear stress (*driven shear stress*) can influence significantly the cyclic behaviour of sands. From a practical point of view, it is an interesting aspect, in the study of the seismic liquefaction hazard of slopes, earth dams or in case of structures that induce significant driven shear stresses in the subsoil.

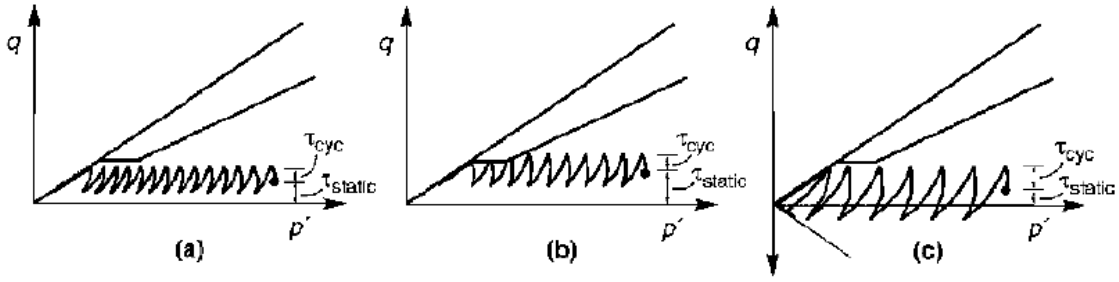

Figure 2.24. Particular cases of cyclic mobility (liquefaction): no stress reversal and no overcoming of steady-state strength (a); no stress reversal with momentary overcoming of steady-state strength (b); stress reversal with no overcoming of steady state strength (c) (Kramer, 1996).

To sum up, Figure 2.25 shows the zones of susceptibility to flow liquefaction and cyclic mobility. They can be triggered if the initial state of the specimen is in one of these two zones. As above, CSL is the critical state line, while FLS identifies the flow liquefaction.

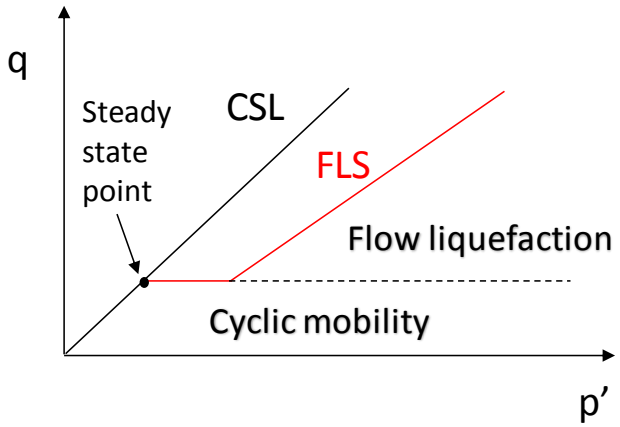

Figure 2.25. FLS and zone of susceptibility to flow liquefaction.

In this thesis, the attention will be focused on cyclic mobility, hereafter simply indicated as liquefaction.

To investigate the cyclic behaviour of saturated, cohesionless soils, Seed and Lee (1966) performed a number of undrained triaxial tests. The soil specimens were subjected to sinusoidal cyclic axial stress under a given confining stress. The ratio between the shear stress (τ_d) and the normal effective stress (σ'_{ref}) acting on the plane inclined at 45° on the horizontal plane is defined *cyclic stress ratio* or commonly, CSR:

$$CSR = \frac{\tau_d}{\sigma'_{ref}} = \frac{q_d}{2 \cdot \sigma'_{ref}} \qquad (2.5)$$

where q_d is the cyclic deviatoric stress, while σ'_{ref} is equal to:

$$\sigma'_{ref} = \frac{\sigma'_{1,c} + \sigma'_{3,c}}{2} \qquad (2.6)$$

Where $\sigma'_{1,c}$ and $\sigma'_{3,c}$ are, respectively, the maximum and the minimum principal effective stresses acting on the specimen at the end of the consolidation phase. In isotropically consolidated tests ($\sigma'_{1,c} = \sigma'_{3,c}$) σ'_{ref} is equal to the consolidation pressure.
Seed and Lee (1966) noted that in undrained conditions excess pore pressure grows up until to make zero the effective stress, causing liquefaction. Also strains increase their amplitude when number of cycles increases.
Ishihara (1985) reported some typical results of cyclic tests, carried out on Fuji sand specimens in different conditions in terms of relative density and CSR (Fig. 2.26). They were both consolidated at a confining pressure (σ'_0) of 98 kPa.

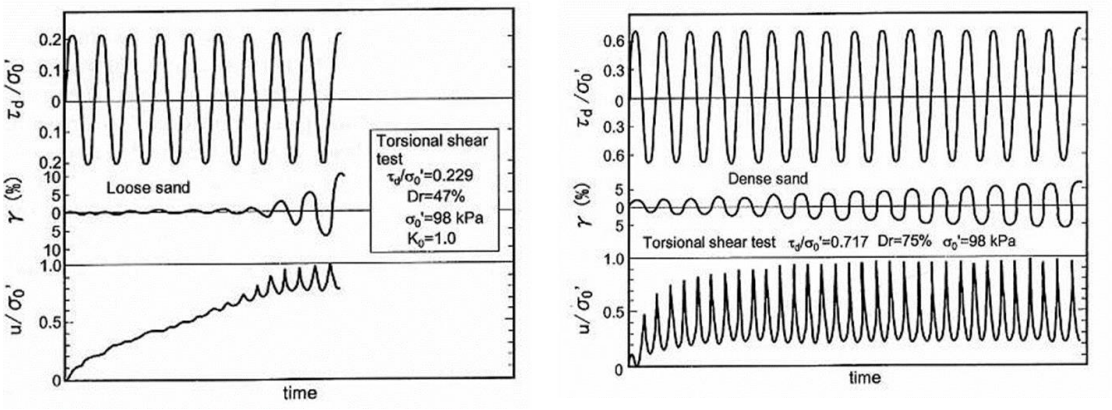

(a) (b)

Figure 2.26. Cyclic torsional shear tests on Fuji sand: loose specimen (a) and dense one (b) (Ishihara, 1985).

In loose specimen (Fig. 2.26a) shear strain hovers initially around 0 and increases suddenly after few cycles, while the ratio $\Delta u/\sigma'_0$, which is called *excess pore pressure ratio* or r_u grows up until to reach a value of 1, which means that effective stress is zero, according to Terzaghi's principle.
In dense sand (Fig. 2.26b) shear strain amplitude increase gradually, while r_u exhibits larger cycles without ever reaching the value of 1.
These results show the dependence of cyclic behaviour on void ratio (or relative density) of the specimen. As for monotonic tests, the cyclic behaviour is influenced by a combined effect of the initial confining pressure (σ'_0) and void ratio (or D_r), which could be summarized by the state parameter (ψ).

2.2.2 LIQUEFACTION TRIGGERING CRITERIA IN CYCLIC LABORATORY TESTS

Seed and Lee (1966) defined the term *initial liquefaction*, to describe the condition in which the excess pore pressures (Δu) that gradually developed under shear, reach the initial vertical effective stress (σ'_{v0}) for the first time, it means that the excess pore pressure ratio (r_u) is equal to 1.
One of the most important aspects in the study of liquefaction is when liquefaction really occurs. In other words, triggering criteria should be introduced, allowing to identity uniquely the attainment of liquefaction.
During the last centuries, several criteria have been provided, but the most famous and more used are two: stress and strain criteria.
The stress criterion is based on the measurements of excess pore water pressure (Δu). According to it, liquefaction occurs when r_u is equal to 1.0, as defined by Seed and Lee (1966). Some years later, in 1993, Ishihara suggested for soils containing some amount of fines (silty sands and sandy silts) using a threshold of r_u equal to about 0.90.
The strain criterion is based on the measurements of strains. Ishihara (1993) proposed to use a threshold of axial strain double amplitude (ε_{DA}) equal to 5% in cyclic triaxial tests and 3.75% double amplitude for shear strains (Υ_{DA}) in cyclic simple shear tests, which can be used for clean and sand with fines. Despite the fact that it is considered a typical value for liquefaction triggering, some researchers use different strain levels highlighting some limitations in the use of this criterion. Wu et al. (2004) showed that even though strain criterion may be fine for seismic performance of most earth structures, underground structures, pipeline and buildings, it has serious limitations. One of the issues is that the measurement of strains depends on deformation mode that the soil is subjected to, such as ε_{DA} in triaxial tests and shear strain Υ_{DA} in simple shear tests. Moreover, in loose sands the development of state of initial liquefaction ($r_u \approx 1$) is followed by accumulation of large strains, on the contrary in denser sands the attainment of initial liquefaction does not correspond to large strain owing to a strong dilatative behaviour. In this respect, Wu et al. (2004) showed as stress and strain criteria give the same result in terms of number of cycles for loose specimens, while their difference increases with D_r.
Starting from the definition of liquefaction: "the act or process of transforming any substance into a liquid" according to the Committee on Soil Dynamics of the Geotechnical Engineering Division of ASCE (1978), a new triggering criterion is developing, it is based on the rheological properties of fluids, as will be discussed in §2.2.2.3.

2.2.2.1 CYCLIC RESISTANCE CURVE

The liquefaction resistance of a sandy soil may be expressed graphically as a cyclic resistance curve. It can be plotted in the plane N_{liq}-CRR, where N_{liq} is the value of the cycle number N_{cyc} needed to reach liquefaction for a given value of CSR, defined according the a given triggering criterion, while CRR is the *cyclic resistance ratio*,

identified as the applied cyclic stress ratio for which $N_{cyc}=N_{liq}$. Based on what is highlighted in the previous paragraph, it is easier to understand that the choice of the liquefaction triggering criterion plays an important role in identification of the cyclic resistance curve.

The cyclic resistance curve of a soil in fixed conditions may be found by means of laboratory tests as cyclic triaxial tests, cyclic simple shear tests and cyclic torsional tests carried out on reconstituted specimens.

Several tests confirm that the liquefaction resistance depends on soil grain size distribution, state condition (void ratio and confining pressure) and soil fabric.

In fact, specimens prepared by different methods can show different resistance to liquefaction. Ishihara (1993) reported three main methods to prepare a reconstituted specimen in laboratory: moist tamping, dry deposition method and water sedimentation method, as shown in Figure 2.27.

Moist tamping consists of mixing five or six equal pre-weighed oven dried portions of sand with de-aired water to have a water content of about 5%. A membrane is stretched inside the split mould, attached to the base pedestal of the apparatus. Each portion of the slightly moist sand is strewn by hand to a predetermined height in five to six lifts. At each stage of the lifts, tamping is applied lightly with a small flat bottom tamper. This method is preferred when low D_r wanted to be reached. Owing to capillary effects between particles, the moist sand can be placed at a very loose structure, well in excess of the maximum void ratio of the dry sand. The D_r of the prepared specimen depends on the tamping energy. If a denser sample is to be prepared, a larger amount of energy needs to be applied, for example by increasing the number of tampings during compaction at each stage of the lift. One of the advantages of this method is that a wide range of void ratio can be obtained.

In *dry deposition method* oven dry sand is filled in a cone-shaped slender funnel with a nozzle about 12 mm in diameter. The sand is spread in the forming mould with zero height of fall at a constant speed until the mould becomes filled with the dry sand. Tapping energy is applied by hitting the side of the mould to obtain a desired density. Theoretically, any state of relative density may be obtained, by adjusting the tapping energy during the process of sample preparation. The specimen is generally denser than that prepared by the moist placement method. This method differs from what is generally called *air pluviation*, in which dry sand is discharged vertically in air from a small nozzle into the mould, without hitting the side of the mould. The air-pluviation method is known to produce samples that are always dilative.

Water sedimentation method consists of pouring dry sand through a l-2 mm diameter nozzle from just above water surface and allowed to sediment through a height of 2-3 cm under water. The sand is deposited continuously under water without causing appreciable segregation of the material. If a denser sample is to be prepared, compacting energy is applied by hitting the side of the mould stepwise during the process of sample placement.

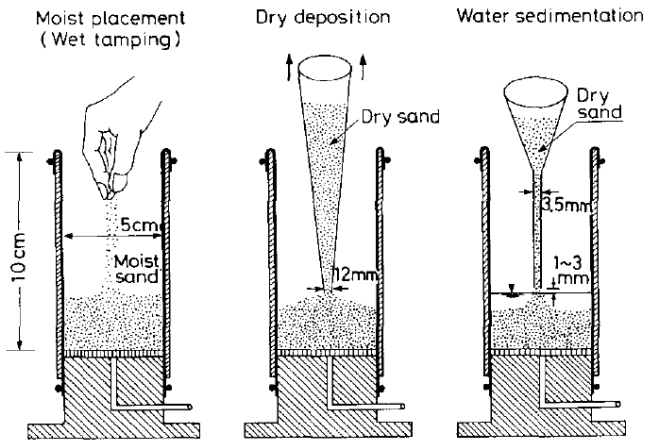

Figure 2.27. Methods of specimen preparation (Ishihara, 1993).

Mulilis et al. (1977) showed the effect of specimen preparation method on liquefaction resistance as reported in Figure 2.28. Several cyclic triaxial tests were carried out on specimens of Monterey sand prepared with two methods: air pluviation and moist tamping. Despite the fact that the specimens have been consolidated at the same confining pressure (σ'_0=54kPa) and relative density (D_r=50%) the results in terms of cyclic resistance curves are completely different (Fig. 2.28). In particular, the reconstituted specimens prepared by moist tamping exhibit a higher cyclic resistance to liquefaction than those prepared by air pluviation. Moreover, they showed that the methods of preparation influence also the slope of the curve. Such differences depend on the nature of fabric structure (orientation of the contacts between sand grains) created by different methods, therefore it is important to specify the method by which the specimens have been prepared.

Generally, the air pluviated specimens are the weakest, while the greater cyclic resistance is observed for moist tamping specimens. It is due to a different distribution of contacts that develops during the preparation. According to Mulilis et al. (1977), specimens having the highest distribution of interparticle contact planes orthogonal to the loading direction (normals) exhibit the higher cyclic resistance. In 1986, Tatsuoka et al. showed that it is certainly true in cyclic triaxial tests, but it cannot be considered as a general rule, because in torsional shear tests, the moist tamping specimens do not have the higher liquefaction resistance. In other words, the preparation methods may affect the cyclic undrained strength in different ways depending on whether triaxial or torsional shear stress.

It is worth noting that several researchers studied the effect of preparation technique in cyclic triaxial tests, while few studies have been done in cyclic simple shear tests. The reason lies in the fact that reconstituting uniformly loose specimens in simple shear setups is more challenging than in triaxial set-ups because of the larger cross-sectional area of simple shear specimens (Kwan and El Mohtar, 2018). For short and wide simple shear specimens, the deposition process requires going around the specimen area in circles while raising up the inverted volumetric flask, and therefore it is harder to maintain a constant drop height necessarily to provide uniformity. Moreover, the same authors

highlighted as the reconstitution methods are one of the most factors which affects liquefaction, especially for loose sands.
Due to the fact that reconstituted sand specimens prepared by different methods of preparation show a different liquefaction resistance, efforts should be done to recover undisturbed specimens from in situ deposits and test them under the representative conditions that they had in situ.

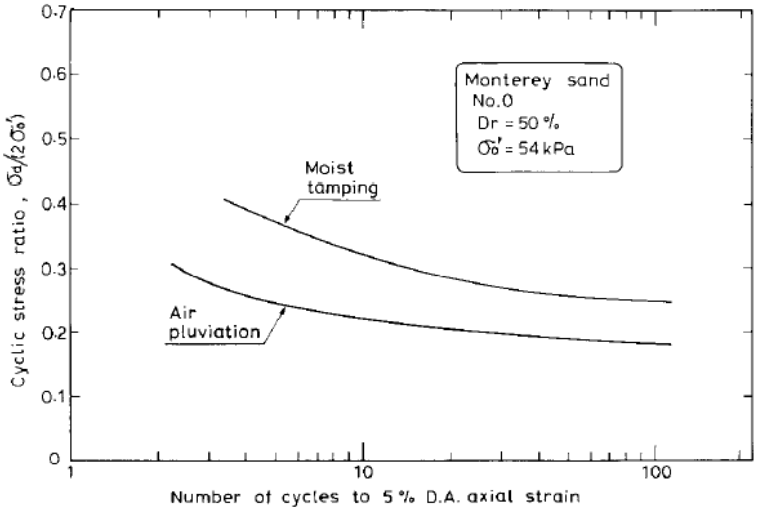

Figure 2.28. Effects of specimen preparation on liquefaction resistance (Mulilis et al., 1977).

Ishihara (1993) introduced two techniques to recover samples of sand from below the groundwater table: the tube-sampling and the ground freezing method. The former is useful to recover loose samples from sandy deposits, while the disturbance becomes more evident with the increase of Dr; the latter one has the advantage to recover also dense samples of sand. This technique was used to characterize the site of Niigata, after the earthquake. Yoshimi et al. (1989) carried out cyclic triaxial tests on frozen samples from Niigata, highlighting the effect of the ageing time.
The cyclic resistance of sandy soil is also influenced by the rotation of principal stresses as shown by Towata and Ishihara (1985b) and recently by Sivathayalan et al. (2014). Already in 2002, Sivathavalan and Vaid carried out hollow cylinder torsional shear tests, demonstrating that the drained and the undrained response are dependent on the direction of major principal stress during shear. Moreover, the gradual alignment of the direction of major principal stress along the weak horizontal bedding plane is responsible for the softening in undrained monotonic tests.
Sivathayalan et al. (2014) showed that the degree of stress rotation significantly affects the number of cycles to liquefaction as reported in Figure 2.29, where $\alpha_{\sigma,max}$ is the rotation of the principal stress to the vertical axis of the hollow cylinder specimen. The tests carried out with $\alpha_{\sigma,max}$=45° have the lower number of cycles at liquefaction. In these tests the plan of maximum shear stress coincides with the horizontal bedding plane, so the

lower liquefaction resistance can be attributed to the combination of high shear stress on the horizontal plane and the alignment of the plane of maximum shear stress with the bedding.

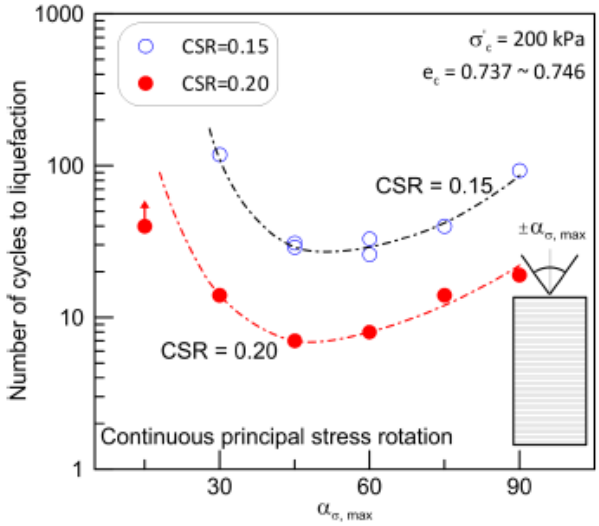

Figure 2.29. Influence of principal stress rotation on the number of cycles at liquefaction (Sivathayalan et al., 2014).

Although hollow cylinder torsional shear devices allow to control the principal stress directions and their rotation, they are not economical and practical to conduct tests for design purposes. Because of that, cyclic triaxial or simple shear tests are preferred, even though cyclic triaxial tests are not able to simulate the continuous rotations of principal stress directions (paragraph 2.2).
It is important to emphasize that cyclic triaxial and simple shear tests impose a different loading and their CSR are not equivalent. In 1975, Castro proposed a correction factor (c_r) to take into account the effects of different stress-path. Defining CSR_{ctx} the CSR in cyclic triaxial tests and CSR_{css} the CSR in cyclic simple shear tests, they can be linked through the following equation:

$$CSR_{css} = c_r \cdot CSR_{ctx} \quad (2.7)$$

The correction factor (c_r) is a function of the coefficient of earth pressure at rest, k_0, according to the following equation:

$$c_r = \frac{2 \cdot (1 + 2 \cdot k_0)}{3\sqrt{3}} \quad (2.8)$$

To use this formula, k_0 has to be known, but one of the problems is that it is not easy to find; therefore, Jacky's formula can be used, where k_0=(1-senφ), where φ is the peak friction angle.

2.2.2.2 PORE PRESSURE GENERATION MODELS

As well-known liquefaction is a phenomenon strongly linked to pore water pressure build-up. The simultaneous generation, dissipation, and redistribution of excess pore pressures within the layers of a soil deposit can significantly alter the stiffness and seismic response of the deposit. This is the reason why the pore pressure generation models play an important role in modelling the response of soil deposits. These kinds of models can be divided into three categories: stress-based, strain-based and energy-based models.
The first models were based on the results of cyclic stress-controlled tests, so that called stress-based. Lee and Albaisa (1974) observed that the generation of excess pore pressures in cyclic stress-controlled tests on saturated cohesionless soils falls in a narrow band defined by the excess pore pressure ratio, r_u and the ratio between the current number of loading cycles (N) and the number of cycles at liquefaction (N_{liq}). Later, De Alba et al. (1975) found that pore pressure ratio, r_u is related to number of loading cycles by:

$$r_u = \frac{1}{2} + \frac{1}{\pi} arcsen\left[2 \cdot \left(\frac{N}{N_{liq}}\right)^{\frac{1}{\alpha}} - 1\right] \quad (2.9)$$

where N_{liq} is the required number of cycles to produce initial liquefaction (r_u=1), while α is function of the soil properties and test conditions.
In the same year, Seed et al. (1975) developed an empirical expression for predicting r_u, which was simplified by Booker et al. (1976) as follow:

$$r_u = \frac{2}{\pi} \cdot arcsen\left(\frac{N}{N_{liq}}\right)^{\frac{1}{2\beta}} \quad (2.10)$$

where β is an empirical constant which depends on the soil type and test conditions and influences the shape of the curve N/N_{liq}-r_u (Fig. 2.30). This parameter can be calibrated from cyclic triaxial tests. Seed et al. (1975) recommend using a β equal to 0.7, especially for clean sands. Porcino and Diano (2017) showed that the experimental data of sands with a fines content (FC) lower than 20% fall inside the bounds suggested for clean sands ($0.6 < \beta < 1.0$), but for sands with FC > 20%, the experimental data fall outside the suggested upper bound, which seems to correspond to a value of β equal to 1.4. This is consistent with the experimental results of Polito et al. (2008), who carried out cyclic triaxial tests on reconstituted specimens of sands with a different non-plastic fines content (FC), relative densities (D_r) and cyclic stress ratio (CSR). They demonstrated that these factors influence the value of β according to the following equation:

$$\beta = c_1 \cdot FC + c_2 \cdot D_r + c_3 \cdot CSR + c_4 \quad (2.11)$$

where c_1, c_2, c_3 and c_4 are regression constants.

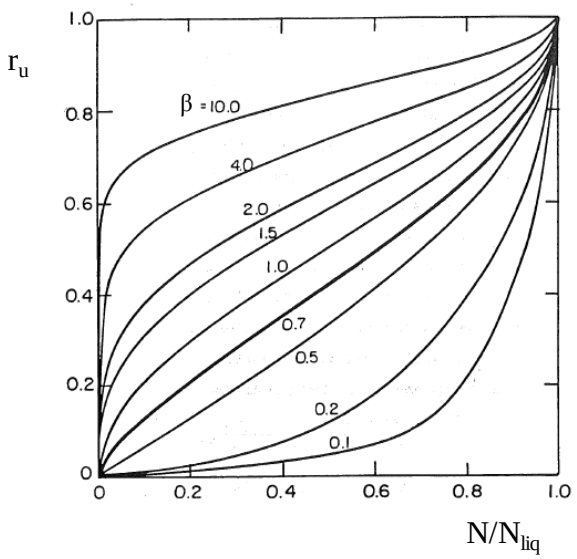

Figure 2.30. Influence of β on the shape of the curve N/N_{liq}-r_u (modified from Booker et al., 1976).

Recently, other pore pressure models have been developed, such as Baziar et al., (2011) and Chiaradonna et al. (2018a), that for sake of brevity will not be discussed in this thesis. After the stress-based methods, Dobry et al. (1985) proposed a strain-based model, where the pore pressure build-up is triggered only when a threshold shear strain is reached.
Although, stress and strain-based methods are simple forms, the application of those equations is difficult because the earthquake motion has to be converted to an equivalent number of uniform cycles.
This drawback can be overcome by energy-based methods (Green et al., 2000). In these models r_u is related to the energy dissipated per unit volume of soil. The dissipated energy per unit of volume or specific deviatoric energy (E_s), as it will be called in this thesis, can be calculated as the sum of the areas bounded by stress-strain (ε_s-q plane, where ε_s is the distorsional stress defined as $2/3(\varepsilon_a - \varepsilon_r)$) hysteresis loops ($D_{cyc}$ is the area of a cycle in the plane ε_s-q) as shown in Figure 2.31 for cyclic triaxial tests.

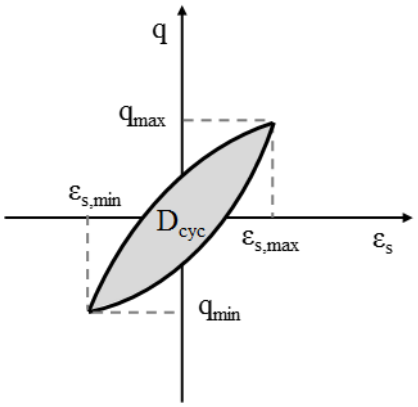

Figure 2.31. Cycle in q-ε_s plane to evaluate specific deviatoric energy from cyclic triaxial tests.

The specific deviatoric energy ($E_{s,i}$) at a generic cycle i (N_i), can be formally written through equation 2.12a for triaxial tests and 2.12b for cyclic simple shear tests:

$$E_{s,i} = \sum_{N_{cyc}=1}^{N_{cyc}=N_i} \iint_{D_{cyc}} dq \cdot d\varepsilon_s \qquad (2.12a)$$

$$E_{s,i} = \sum_{N_{cyc}=1}^{N_{cyc}=N_i} \iint_{D_{cyc}} d\tau \cdot d\Upsilon \qquad (2.12b)$$

The pioneers of these models were Nemat-Nasser and Shokooh (1979), who first of all found a correlation between the accumulated strain dissipated energy in a unite volume and the pore pressure build-up. Later, several laboratory tests were carried out by several researchers with the main aim to evaluate E_s from undrained cyclic triaxial, simple shear and torsional shear tests (Towata and Ishihara, 1985; Law et al., 1990; Figueroa et al., 1994; Liang et al., 1995; Dief and Figueroa, 2007; Baziar and Sharafi, 2011; Kokusho, 2013; Polito et al., 2013; Azeiteiro et al., 2017; Pan and Yang, 2017). The new findings were that the relationship r_u-Es seems to be unique, regardless of the device used to perform the tests. Moreover, some of the aforementioned researchers (Liang et al., 1995; Polito et al., 2013; Azeiteiro et al., 2017; Pan and Yang, 2017) performed tests also applying random and sinusoidal excitations to the specimens, highlighted once again the uniqueness of the relationship r_u-E_s. All of these experimental evidences have played an important role in the development of such energy-based models.
In particular, Berrill and Davis (1985) proposed a simple empirical formulation, which is reported below:

$$r_u = \alpha \cdot W_s^{\beta} \quad (2.13)$$

where Ws is the original form chosen by the authors to indicate the normalized energy dissipated per unit volume of the soil (E_s/σ'_0), while α and β have to be calibrated through cyclic laboratory tests.
GMP (Green, Mitchell and Polito, 2000) is one of the most important energy-based models. According to it, r_u can be written as:

$$r_u = \sqrt{\frac{W_s}{PEC}} \leq 1 \quad (2.14)$$

where PEC is a calibration parameter, which depends on fines content (FC) or relative density (Dr). PEC is determined from cyclic tests with sinusoidal loading, by plotting r_u versus the square root of W_s. The square root of PEC is the value on the horizontal axis corresponding to the intersection of a straight line drawn through the origin and the point

r_u=0.65, and a horizontal line drawn at r_u=1.0. The process to determine PEC is shown graphically in Figure 2.32 (Polito et al, 2013).

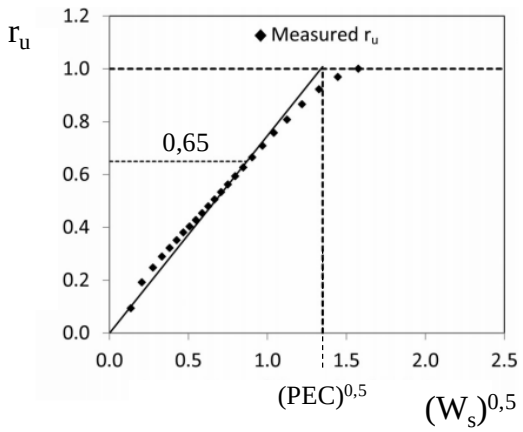

Figure 2.32. Graphic illustration to evaluate PEC from cyclic triaxial tests (modified from Polito at., 2013).

Numerically PEC can be found as:

$$PEC = \frac{W_{s,ru=0.65}}{(0.65)^2} = \frac{W_{s,ru=0.65}}{0.4225} \qquad (2.15)$$

where $W_{s,ru=0.65}$ is the value of W_s corresponding to r_u=0.65. The eq. (2.14) can be seen as a particular formulation of the eq. (2.13), where α is equal to $1/(PEC)^{0.5}$ and β is equal to 0.5.

The simplicity of their function forms makes easy their implementation into computer codes, like DEEPSOIL (Hashash, 2013). However, the calibration of their parameters from laboratory tests could not be easy.

2.2.2.3 BEHAVIOUR OF LIQUEFIED SOILS

As well known, liquefaction is characterized by a state change from solid to liquid. It poses a problem in modelling of liquefied soils. Some researchers treat them still as a solid but reducing stiffness and strength; on the other hand, other researchers study them like fluid (Aydan, 1995; Uzuoka et al., 1998; Hadush et al., 2000; Hwang et al., 2006; Chen and Liu 2011).

Hamada and Wakamatsu (1998) investigated the behaviour of liquefied soil during ground flow using several studies and experiments and concluded that liquefied soil behaves as a pseudoplastic fluid during ground movement, but after the earthquake motion ceases, the liquefied soil recovers its initial stiffness and returns to behave as a solid. As will be discussed later (§2.4.2: permeation grouting as mitigation techniques against liquefaction), in pseudo-plastic fluid, viscosity increases with the gradient of

velocity (Fig. 2.33). The relationship, which governs its rheological behaviour is given by the following equation:

$$\tau = \eta \cdot \left(\frac{dv}{dx}\right)^n \quad (2.16)$$

Where η is defined as an apparent viscosity, dv/dx is the gradient of velocity and n is a coefficient lower than 1.

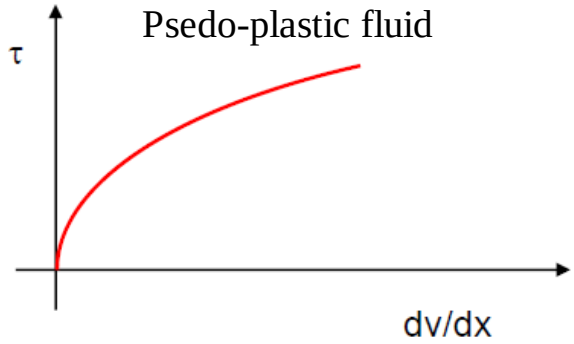

Figure 2.33. Pseudo-plastic behaviour in plane dv/dx versus τ.

Also Chen et al. (2006), analysing the main flow characteristics of liquefied sand through hollow torsion-shear tests, concluded that the behaviour of liquefied soil may be reproduced by a pseudo-plastic fluid. The flow constitutive model proposed by Chen et al. (2006) for a liquefied sand, in zero effective stress condition, is a relationship between the shear stress (τ) and the shear strain rate ($\dot{\gamma}$), which is given by the following equation:

$$\tau = k \cdot (\dot{\gamma})^n \quad (2.17)$$

where k and n are respectively the *fluid consistency coefficient* and *liquidity index* (n<1 for shear thinning non-Newtonian fluid; Zhou et al., 2014). The "viscosity of liquefied soil" can be expressed as:

$$\eta = \frac{\tau}{\dot{\gamma}} = k \cdot (\dot{\gamma})^{(n-1)} \quad (2.18)$$

The constitutive model parameters (k and n) must be calibrated on experimental results. In this framework, Chen et al. (2016), defined an “apparent viscosity” (η_i) at the cycle i as:

$$\eta_i = \frac{\tau_{i,max} - \tau_{i,min}}{\dot{\gamma}_{i,max} - \dot{\gamma}_{i,min}} \quad (2.19)$$

where τ_{max} and τ_{min} are the maximum and minimum values of the applied cyclic shear stress and $\dot{\gamma}_{max}$ and $\dot{\gamma}_{min}$ are the shear strain rates.

The apparent viscosity can be calculated also from cyclic triaxial tests results, easily converting the cyclic deviatoric stress (q) and the corresponding axial strain (ε_a) in the shear stress acting on the plane inclined at 45° on the horizontal plane (τ=q/2) and in the corresponding shear strain (γ=1.5ε). One of the most promising aspects of these models is the link with r_u. In fact, Chen et al. (2016) showed that a negative power-law function is suitable for describing the correlation between η and r_u. They also noted that the effective stress has a little influence on this correlation, but they did not investigate on the influence of other soil state parameters. This aspect will be studied in depth in this thesis. The original flow constitutive model proposed by Chen et al. (2006) was later implemented into the finite-difference algorithm FLAC3D to reproduce the flow deformation process induced by soil liquefaction. These flow constitutive models can be useful to predict liquefaction induced ground flow or lateral spreading.

2.2.3 POST LIQUEFACTION CYCLIC BEHAVIOUR

Commonly, re-liquefaction is thought to be unlikely due to an effect of densification after the first liquefaction, as explained clearly in Figure 2.34. The black dot represents the initial state of a soil in field condition. When a seismic event occurs in a liquefiable sandy soil, excess pore pressure increases until to vanish the effective vertical stress (blue dot). After the earthquake, a process of dissipation of the excess pore pressure develops (re-consolidation), leading to a densification of soil deposit.

Despite this densification effect, several cases reported in literature demonstrated that re-liquefaction phenomena occur very frequently, although a "weaker" motion is recorded, as reported by Yasuda and Tohno (1983), who studied the 1983 Nihonkai Chubu earthquake, or more recently by Lee et al (2015) for New Zealand earthquake (2010-2011) and Wakamatsu (2012) for Tohoku earthquake (2011). From a technical point of view, this topic is becoming extremely interesting, therefore an insight regarding the cyclic behaviour of soils after the first liquefaction is discussed in this research.

First of all, Finn et al. (1970) demonstrated the effect of previous strain amplitude (pre-shearing) history on the liquefaction resistance by tests performed in a cyclic simple shear apparatus. They showed that low strain amplitude (ε_{DA}=1%) of the first liquefaction tests increases the cyclic resistance of the soil, on the contrary, larger strain amplitude (ε_{DA}=4%) reduces the liquefaction resistance compared with that of the virgin soil, which has not experienced the seismic loading. Similar results have been presented by Seed et al. (1977), carrying out tests by using a shaking table, showing that a small cyclic pre-shearing improves the liquefaction resistance despite a small increase of D_r. More recently, Oda et al. (2001) performed undrained cyclic triaxial tests on dense specimens of Toyoura sand, reconstituted by air pluviation, and re-consolidated after being cycled, which reach different levels of axial strain in double amplitude (ε_{DA}). Consistently with the results of other authors, for small pre-shearing the cyclic resistance is higher or the

same as the virgin soil, by contrast it reduces for higher pre-shearing ($\varepsilon_{DA} \geq 2\%$), as shown in Figure 2.35.

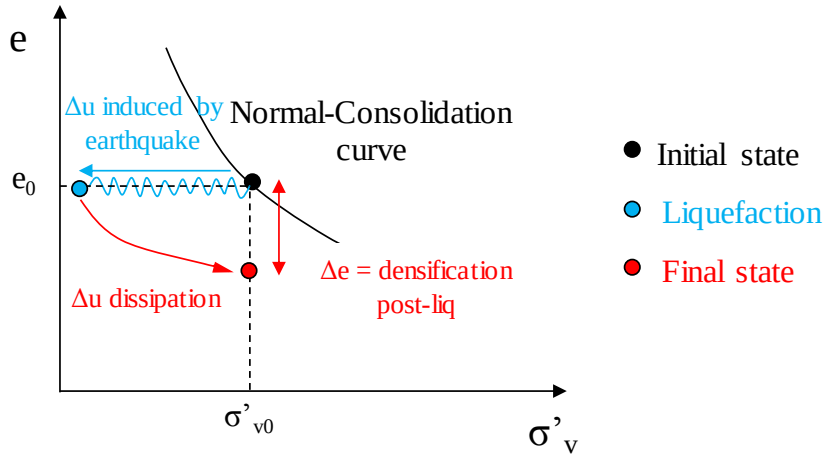

Figure 2.34. Densification due to a dissipation of excess pore pressure induced during an earthquake.

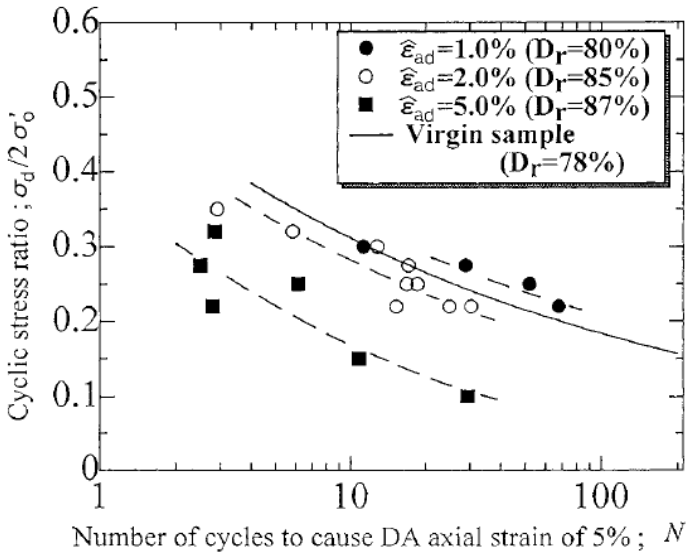

Figure 2.35. Change of re-liquefaction resistance due to an effect of pre-shearing (Oda et al., 2001).

Focusing on large pre-shearing, Emery et al. (1973) and Toki et al. (1981) attributed the effect of reduction of liquefaction resistance to a non-uniformity of the specimens after the first liquefaction. In particular, Emery et al. (1973) evaluated the uniformity of saturated sands at various stages in a cyclic loading test by solidifying them by a gelatin solution. They observed a loose layer on the top of the specimen after liquefaction, which is considered responsible of the significant reduction in the resistance to re-liquefaction.

On the other hand, Ishihara and Okada (1982) and Suzuki and Suzuki (1988) emphasized the effect of anisotropy, which is altered after liquefaction.
Oda et al. (2001) confirmed the anisotropy as a possible cause of change in liquefaction resistance of sandy soils by introducing a microstructural interpretation of re-liquefaction mechanism. According to them, if the cyclic strain is small, the microstructure remains essentially unchanged. The minor change only occurs through collapsing the unstable microstructure. On the other hand, if the cyclic strain is large enough, the microstructure is totally altered to induce an anisotropy. Even though, the overall void ratio does not change significantly, the sand particles form column-like structures, which are less stable when the specimen was stressed perpendicular to the elongation direction. The structure can withstand the increasing stress as long as the major stress direction (vertical) remains fixed. However, the connected voids are easily closed when the stress axes are rotated to be perpendicular to the elongation direction of the connected void. It means that the column-like structures are less stable under cyclic rotation of the principal stress direction. The connected voids between neighbouring columns are easily closed. In drained condition, such closure of the elongated voids causes the large volume contraction, while in undrained condition, a rapid increase of excess pore-water pressure occurs.
In other words, when liquefaction occurs, the fabric of the specimen changes, as a consequence the liquefaction resistance decreases.
Moreover, Ishihara and Okada (1982) showed that the resistance to a second liquefaction depends not only on the magnitude of the pre-shearing but more significantly on the direction of the applied pre-shear in the first cyclic loading.
All of these new findings derived from the analysis of the experimental results performed on saturated soils. In this research work, with the main aim to improve the basic understanding on the mechanics of post-cyclic undrained behaviour, tests on saturated and unsaturated soils have been performed and discussed in Chapter 7.

2.3 ASSESSMENT OF LIQUEFACTION POTENTIAL

It is extremely important to know if a seismic site is susceptible to liquefaction and several methods have been developed to evaluate the "liquefaction potential" in free field condition. It can be easily evaluated from the factor of safety (FS) that is defined as the ratio between the capacity of the soil and the demand of the earthquake. Demand is strongly linked to the earthquake, in other words it depends on its amplitude and duration, while Capacity is the demand which generates liquefaction. If FS is higher than 1, liquefaction will not occur, conversely if FS $\leq$1 it does not mean that liquefaction will occur certainly, but only that the site is potentially susceptible to liquefaction.
Liquefaction potential of a soil deposit may be evaluated by using several procedures, which can be summarized in three categories: stress-based, strain-based and energy-based procedures.

2.3.1 STRESS-BASED METHODS

The factor of safety (FS) in stress-based methods can be defined as:

$$FS = \frac{CRR}{CSR} \quad (2.20)$$

where CRR is the capacity and CSR is the demand.
The demand CSR can be evaluated through a simple formulation proposed by Seed and Idriss (1971). During the earthquake, shear waves propagate upwards and a soil column to a depth of z is assumed to move horizontally. Defining a_{max} as the peak horizontal acceleration on the ground surface, the maximum cyclic shear stress induced by the earthquake, τ_{max}, acting at the bottom of soil column, is given by:

$$\tau_{max} = r_d \cdot \frac{a_{max}}{g} \cdot \gamma z \quad (2.21)$$

Where r_d is a stress reduction coefficient to take into account the deformability of the soil column (r_d<1), g is the gravitational acceleration and γ is the unit weight of the soil.
The parameter r_d is a function of depth and it can be found graphically or by using empirical forms, such as (Idriss and Boulanger, 2004):

$$r_d = exp\left[\left(-1.012 - 1.126 \cdot sin\left(\frac{z}{11.73} + 5.133\right)\right) + \left(0.106 + 0.118 \cdot sin\left(\frac{z}{11.28} + 5.142\right)\right) M\right] \quad (2.22)$$

where M is the magnitude of the earthquake.
Known that γz is equal to σ_v and dividing both sides of the eq. (2.21) by the effective vertical stress (σ'_v), it becomes:

$$\frac{\tau_{max}}{\sigma'_v} = r_d \cdot \frac{a_{max}}{g} \cdot \frac{\sigma_v}{\sigma'_v} \quad (2.23)$$

As a matter of the fact that in situ the seismic solicitation is made of irregular cyclic loading and that the τ_{max} is reached only in few moments of the earthquake, CSR can be conventionally assumed as the 65% of τ_{max}/ σ'_v:

$$CSR = \frac{\tau_{ave}}{\sigma'_v} = 0.65 \cdot r_d \cdot \frac{a_{max}}{g} \cdot \frac{\sigma_v}{\sigma'_v} \quad (2.24)$$

The capacity CRR may be evaluated from laboratory or in situ tests.
Dealing with laboratory, as already mentioned, cyclic tests allow to determinate a cyclic resistance curve for a sandy soil in a fixed state condition (D_r and σ'_0). CSR should be compared to the value of CRR at a fixed number of cycles at liquefaction (N_{liq}). The latter

is chosen from the relationship (Fig. 2.36; Idriss, 1999) between the magnitude of the expected earthquake in situ and the number of equivalent cycles (N_{eq}).

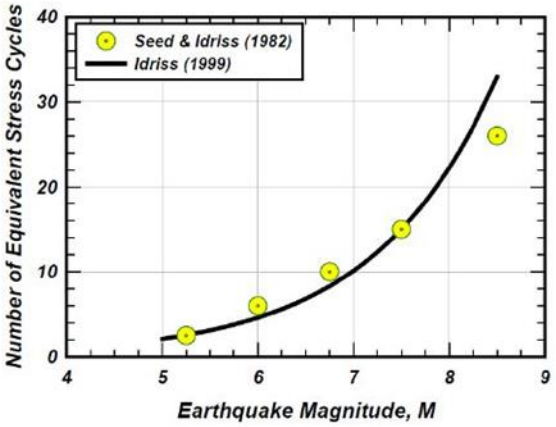

Figure 2.36. Relationship between the earthquake magnitude (M) with number of equivalent cycles (N_{eq}) (Idriss, 1999).

Once the Magnitude of the expected seismic event is known, N_{eq} can be determined and thus the corresponding CRR from the cyclic resistance curve. Therefore, the factor of safety can be evaluated.

The described procedure is easy to apply, but as mentioned in paragraph 2.2.2.1, undisturbed specimens should be tested in laboratory to evaluate precisely the cyclic behaviour of sandy soils and to estimate as correctly as possible the cyclic resistance to liquefaction. The problem is that not always it is possible to recover undisturbed samples, especially because of high costs of these operations.

To overcome this drawback, the capacity of the deposit can be evaluated from in situ tests, such as SPT or CPT. The factor of safety (FS) can be expressed as:

$$FS = \frac{CRR}{CSR} = \left(\frac{CRR_{M=7.5,\sigma'v=1}}{CSR}\right) \cdot MSF \cdot K_\sigma \cdot K_\alpha \quad (2.25)$$

Where the CSR is evaluated as described above (eq. (2.24)), while $CRR_{M=7.5,\ \sigma'v=1}$ is the liquefaction resistance referred to a magnitude M=7.5 and to σ'_v=103 kPa, MSF is the magnitude scaling factor, introduced to account for the effect of the duration of the seismic event, K_σ and K_α are correcting factors to account respectively for the effective overburden stress and for an initial static shear stress on the horizontal plane. The expressions of all the factors of equation (2.25) are not reported here for the sake of brevity, and can be easily found in literature (e.g., National Academies, 2016).

The capacity ($CRR_{M=7.5,\ \sigma'v=1}$) of soils can be evaluated by means of in situ tests, such as SPT or CPT. Among other, the following relationships can be used (Idriss and Boulanger, 2004):

$$CRR_{M=7.5,\sigma'v=1} = exp\left(\frac{N_{1,60cs}}{14.1} + \left(\frac{N_{1,60cs}}{126}\right)^2 - \left(\frac{N_{1,60cs}}{23.6}\right)^3 + \left(\frac{N_{1,60cs}}{25.4}\right)^4 - 2.8\right) \quad for\ SPT \quad (2.26)$$

$$CRR_{M=7.5,\sigma'v=1} = exp\left(\frac{q_{c1Ncs}}{113} + \left(\frac{q_{c1Ncs}}{1000}\right)^2 - \left(\frac{q_{c1Ncs}}{140}\right)^3 + \left(\frac{q_{c1Ncs}}{137}\right)^4 - 2.8\right) \quad for\ CPT \quad (2.27)$$

where $N_{1,60cs}$ and q_{c1Ncs} have been introduced to take into account the effect of fines content (FC) and they can be calculated from SPT or CPT results: number of blows (N_{60}) or tip resistance (q_c), respectively. Firstly, N_{60} and q_c, have to be normalized as $N_{1,60}$ and q_{c1N}, by using respectively, the factors C_N and C_q, as reported below:

$$N_{1,60} = C_N \cdot N_{60} \qquad C_N = \left(\frac{p_a}{\sigma'_{v0}}\right)^{0.5} \qquad for\ SPT \quad (2.28)$$

$$q_{c1N} = C_q \cdot q_c \qquad C_q = \left(\frac{p_a}{\sigma'_{v0}}\right)^{n} \qquad for\ CPT \quad (2.29)$$

where $0.5 \leq n \leq 1.0$.

$N_{1,60}$ and q_{c1N} can be used for clean sand, but for soils with a fines content (FC), $N_{1,60}$ and q_{c1N} have to be corrected as $N_{1,60cs}$ and q_{c1Ncs}, according the following equations (Idriss and Boulanger, 2004):

$$N_{1,60cs} = N_{1,60} + exp\left(1.63 + \frac{9.7}{FC} - \left(\frac{15.7}{FC}\right)^2\right) \quad for\ SPT \quad (2.30)$$

$$q_{c1Ncs} = q_{c1N} + \left(11.9 + \frac{q_{c1N}}{14.6}\right) \cdot exp\left(1.63 - \frac{9.7}{FC+2} - \left(\frac{15.7}{FC+2}\right)^2\right) \quad for\ CPT \quad (2.31)$$

Eqs. (2.26 and 2.27) have been obtained starting from experimental observations carried out in sites where liquefaction occurs and does not, known the results of SPT or CPT. The curves of Figure 2.37 split the plane into two parts, above the curves, liquefaction was recorded, while below no cases of liquefaction were observed. These charts are used to carry out a fast and a simplified liquefaction analysis of the tested site.

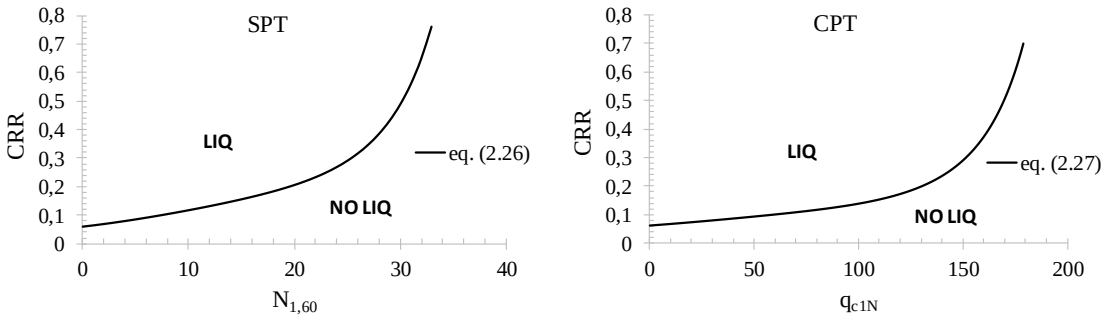

(a) (b)

Figure 2.37. Charts to evaluate the liquefaction resistance of sandy soil deposits for SPT (a) and CPT (b).

2.3.2 STRAIN-BASED METHODS

In strain-based methods, earthquake induced loading is expressed in terms of cyclic strains and the factor safety (FS) is defined as:

$$FS = \frac{\gamma_{th}}{\gamma_{cyc}} \quad (2.32)$$

where γ_{th} is the capacity and γ_{cyc} is the demand.
The capacity γ_{th} is defined as the shear strain amplitude required to cause sliding across grain-to-grain contact surfaces. Dobry et al. (1982), carried out several strain-controlled undrained cyclic tests and they noted that a threshold strain exists. Regardless of the specimen preparation technique, when shear strain is 0.01% excess pore pressure starts to increase. Therefore, this value is assumed as the capacity of the soil in these kinds of models.
The amplitude of the uniform cyclic strain (demand) can be evaluated from the following equation (Dobry et al., 1982):

$$\gamma_{cyc} = 0.65 \cdot r_d \cdot \frac{a_{max}}{g} \cdot \frac{\sigma_v}{G(\gamma_{cyc})} \quad (2.33)$$

where $G(\gamma_{cyc})$ is the shear modulus of the soil at $\gamma=\gamma_{cyc}$. It means that both sides of eq. (2.33) depends on γ_{cyc}, so $G(\gamma_{cyc})$ must be obtained iteratively from a measured G_{max} profile and appropriate modulus reduction curves.

2.3.3 ENERGY-BASED METHODS

Recently, new models are developing increasingly. They are based on the concept of energy, in particular the concept of dissipated energy, already described in paragraph 2.2.2.2. These models are based on the observation that the parameters used to quantify an earthquake are almost always linked to energetic concepts, first of all the magnitude, defined as the energy released during a seismic event.
Unlike stress and strain methods, the energy-based models do not need to convert the earthquake motion to an equivalent number of uniform cycles (N_{eq}), as a matter of the fact that the specific deviatoric energy does not depend on the shape of the cyclic loading. This is why several researchers have suggested the energy-based approach as an innovative and promising method for evaluating liquefaction potential in situ (Law et al., 1990; Desai, 2000; Kokusho, 2013; Kokusho, 2017).
In such models, the demand can be estimated from a large number of correlations based on the concept of magnitude or Arias intensity. For sake of brevity, the most important relationships will be described, while other correlations can be found in Green (2001).
One of the first and most important formulas was provided by Gutenberg and Richter (1956). According to them:

$$E_0 = 10^{1.5M+1.8} \quad (2.34)$$

where E_0 is the total radiated energy from the source (expressed in kJ), while M is the magnitude of the earthquake (Richter scale).
Later, Davis and Berrill (1982) modified the original formula of Gutenberg and Richter (1956) (eq. (2.34)), taking into account the distance from site to the center of energy release (r) and the initial effective overburden stress (σ'_{v0}):

$$E = \left(\frac{r^2 \cdot \sigma'^{1.5}_{v0}}{10^{1.5M}}\right)^{-1} \quad (2.35)$$

On the other hand, Kayen and Mitchell (1997) quantified the demand by using the Arias Intensity, while according to Kokusho (2013; 2017), the demand can be computed from the multiple reflection theory of SH waves, and finally Baziar and Jafarian (2007) used the recorded accelerations at ground surface and downhole arrays of Wildlife and Kobe earthquakes to assess average shear stress and strain history at several earthquake sites. The demand in this case was estimated from the area of stress-strain loops.
Regarding the capacity, it has been evaluated from different correlations based on the results of SPT, that for sake of brevity have not been reported. However, one of the first proposed expressions of the capacity, which was introduced by Gutenberg and Richter (1956), has been shown as an example:

$$Capacity = \left(\frac{450}{N_1^2}\right)^{-1} \quad (2.36)$$

where N_1 is the measured SPT N-value adjusted to 1 tsf (ton per square foot).In the previous equation no hammer-energy correction factors or fines correction were applied. After that, several modifications of this equation followed in literature.
Finally, the factor of safety by using energy-based methods can be assessed as the ratio of the capacity and the demand.
In this thesis, further considerations on these promising methods will be done (Chapters 8 and 9), where starting from the results of laboratory tests, a new and easy methodology will be proposed to assess the liquefaction potential in situ.

2.4 MITIGATION TECHNIQUES AGAINST LIQUEFACTION

Liquefaction is one of the major sources of damage to structures and infrastructures, generating not only economic losses but especially losses of human lives, as shown in paragraph 2.1.2.
When a site is susceptible to liquefaction (FS≤1) mitigation interventions should be realized to reduce the liquefaction potential.
Liquefaction risk can be mitigated through two approaches:

- Soil improvement to reduce the probability of liquefaction;

- Structural design to minimize damage during a seismic event.

In this thesis the attention will be focused on the geotechnical aspects of the mitigation; in other words, only the first point will be discussed and studied in depth.

Soil improvement techniques aim to increase the liquefaction resistance of liquefiable sandy deposits.

Ground improvement methods are widely used at many sites worldwide as a way of mitigating liquefaction damage. Nowadays, a very large number of literature contributions and site experiences exist. Such methods can be divided in four groups:

1) Densification of the liquefiable soil (to be achieved with any kind of compaction);
2) Stabilization of soil skeleton (to be achieved by different actions);
3) Desaturation of the liquefiable soil;
4) Dissipation of increased excess pore pressure (e.g. by improving drainage capacity).

It is worth noting that the first two technologies can be considered "indirect", because they are aimed to increase the capacity of soil resistance liquefaction (densification and stabilization of soil skeleton), while the others two are "direct" technologies, able to reduce the pore pressure changes that causes liquefaction.

In this thesis, three main techniques will be discussed in depth (densification, stabilization of soil skeleton and desaturation) because on them the attention will be focused in the experimental work of this research (Chapter 6).

2.4.1 DENSIFICATION

As well-known, dense sandy soils show a higher resistance to liquefaction than loose sands because of their dilative behaviour and then a lower tendency to generate excess pore pressure during cyclic loading. This is the concept on which the densification technique is based.

The effectiveness of densification can be verified in several research works (Ishihara 1985; Thevanayagam and Martin, 2002), where laboratory tests have been carried out on specimens with different relative density (D_r). Laboratory tests confirm that when D_r increases, liquefaction resistance increases as well.

Densification techniques can be divided in:

- Dynamic techniques;
- Compaction grouting.

Dynamic techniques are the most commonly used ground improvement techniques for liquefaction remediation at new construction sites. Several techniques belong to this group: vibro-compaction, vibro-replacement, dynamic compaction, deep blasting and sand compaction pile. While dynamic compaction is performed from the ground surface, the other ones have to be applied in depth.

Dynamic compaction consists of dropping a heavy weight repeatedly on the ground at regularly spaced intervals. The degree of compaction depends on the weight and the height from which it drops.

Vibro-compaction and vibro-replacement works by using a vibrator, which has to penetrate to a fixed depth. The energy of vibration reduces the void ratio of the sandy soils, and sometimes generates the liquefaction phenomenon locally. As shown in paragraph 2.2.3, the reconsolidation of soils generates a decreasing of void ratio and implies settlements, reason why the replacement of soils is needed.
In deep blasting tests, the ground is liquefied using explosives.
Sand compaction pile technology has been developed in Japan since the 1950s and has been widely applied to various structures on both clayey and sandy grounds (as liquefaction mitigation). In this technique, strong sand pile with consistent diameter are installed even with using top vibrator and vertical vibration sequence. The result is the same: relative density of the liquefiable soil sand consequently, their liquefaction resistance increases. The advantage of using them is that they are typically less expensive than other techniques (the costs of densification depend much more on the lateral extent of the improvement zone than on its depth) and the results in terms of D_r can be very effective, reaching value of about 80%, although it depends on fines content of the deposit. In fact, when the fines content is large, compaction is difficult.
In conclusion, soil densification is generally considered highly reliable, and the standard remedial measure against liquefaction. It reduces the void space of the soil, thereby decreasing the potential for volumetric change that would lead to liquefaction. Resistance to shear deformation also increases with increased density. Several sites improved by densification performed well during the 1964 Niigata, Japan, 1978 Miyagiken-oki, Japan, 1989 Loma Prieta, California, and 1994 Northridge, California, earthquakes (Watanabe, 1966; Ishihara et al., 1980; Mitchell and Wentz, 1991; Graf, 1992; Hayden and Baez, 1994).
Regarding the compaction grouting, it consists of the injection of a very stiff grout (normally a cement-water mixture) that does not permeate the native soil but results in the controlled growth of a grout bulb mass that displaces the surrounding soil. The compaction grout is injected through grout pipes (typically 5-10 cm in diameter) that are progressively inserted or withdrawn from a soil mass such that a grout column or series of bulbs is created over the treated depth interval. The sequences of this intervention have been described and shown in Figure 2.38 (Trevi spa). First, a grout pipe casing is driven into the ground to reach the susceptible soil. Then, as the pipe is withdrawn in stages, a stiff cement grout mixture is pumped through the pipe and is extruded from the tip at each stage to form expanding grout bulbs within the soil mass. The bulbs of grout displace the adjoining soil and densify the immediately surrounding zone. The grout bulbs inherently densify the loosest soil in the vicinity of the grout pipe and thus treat the material most susceptible of liquefaction.

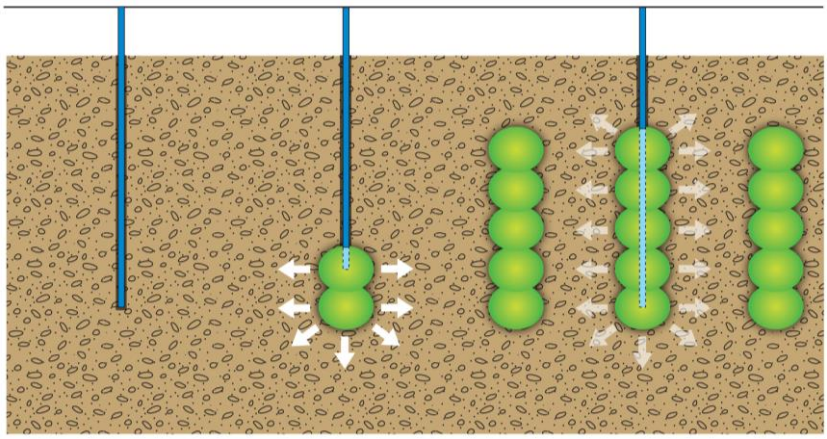

Figure 2.38. Sequences of the intervention of compaction grouting (Trevi spa).

One of the principal advantages of compaction grouting is that its maximum effect is in the weakest soil zone (Brown and Warner 1973). In addition, it is effective in fine-grained soils that were considered ungroutable (Brown and Warner 1973). Compaction grouting involves a set of complex parameters due to different possible soil conditions as well as grouting variables, e.g., grout hole spacing, grouting stage length, injection rate, limiting injection pressure, injection pipe diameter, and so forth. The application of the method, however, relied heavily on practical experience and empiricism.

2.4.2 STABILIZATION OF SOIL SKELETON

In the second group of mitigation techniques there are those able to stabilize the soil skeleton. Three of them play an important role: permeation grouting, jet grouting and soil replacement. The attention will be focused mainly on permeation grouting, which will be an important topic in the experimental part of this study (Chapter 6), while the other two techniques will be described briefly.

The term permeation grouting is used to indicate a low-pressure form of cement grouting that involves grout injection into voids, fissures and cavities in soil or rock formations in order to improve their properties, specifically to reduce their permeability, to increase their strength and durability or to decrease their deformability (Anagnostopoulos, 2005). It consists of the injection of mixtures within the soil pores without modify the soil structure.

While it may not be easy to define the exact range implied by “low-pressure”, it can be said that the pressures that can be generated by small pumps, that is, pressures less than 1.0 MPa, can be considered as low (Chang et al., 2005). For successful grouting, during the injection, the grout has to be in its fresh state with high penetrability. After that, it should be able to solidify, allowing the formation of a cement grouted granular soils, improving its original mechanical behaviour. The choice of the mixture to use is extremely important and their characteristics should be evaluated through laboratory tests (Mutman and Kayak, 2011).

The mixtures to inject into the soil can be a Newtonian and non-Newtonian fluids. A Newtonian fluid is viscous and its rheological behaviour is regulated by the following equation:

$$\tau = \mu \cdot \frac{dv}{dx} \quad (2.37)$$

where τ is the shear stress, μ is the coefficient of dynamic viscosity and dv/dx is the derivative velocity component hat is parallel to the direction of shear, relative to displacement in the perpendicular direction (Fig. 2.39).

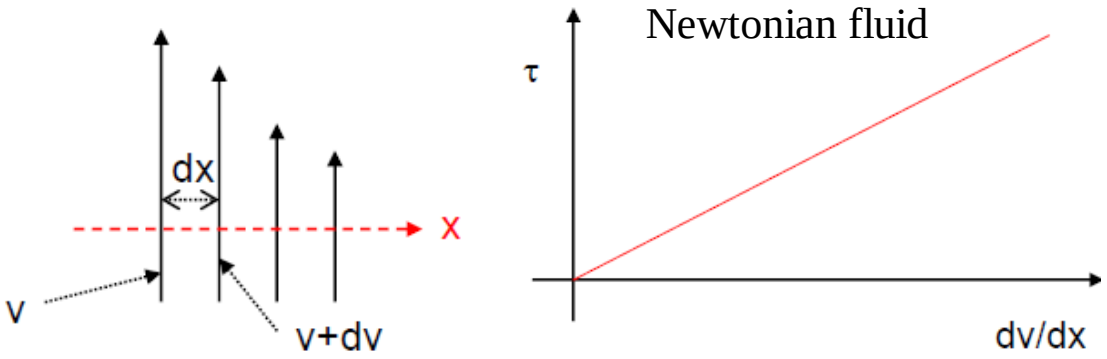

(a) (b)

Figure 2.39. Gradient of velocity (a) and Newtonian fluid (b).

In Non-Newtonian fluid, the relationship between τ and dv/dx is not linear. In these cases, the "shear-thinning" occurs, it means that the viscosity of the fluid decreases as the gradient of velocity increases. They can be divided in pseudo-plastic, dilatant and Bingham fluids.
The rheological behaviour of pseudo-plastic and dilatant fluids is governed by the same equation:

$$\tau = \mu^* \cdot \left(\frac{dv}{dx}\right)^n \quad (2.38)$$

where μ* is the coefficient of apparent viscosity, while n is a coefficient which is lower than 1 in pseudo-plastic fluids and higher than 1 in dilatant ones. Figure 2.40 shows their typical behaviour.

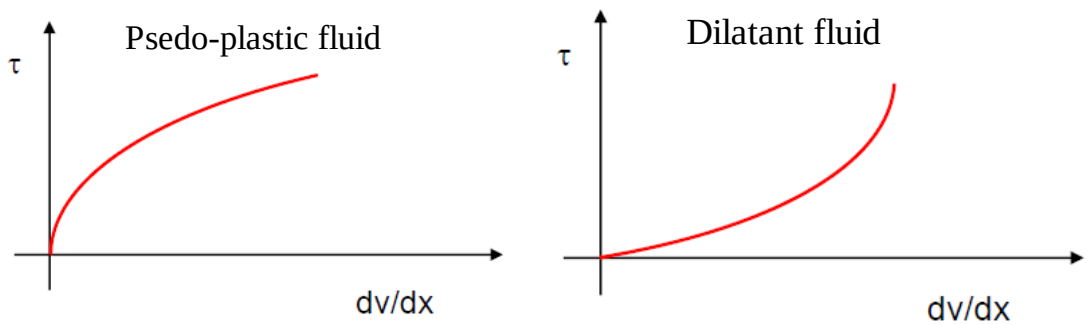

(a) (b)

Figure 2.40. Behaviour of Non-Newtonian fluids: Pseudo-plastic (a) and dilatant (b).

For pseudo-plastic and dilatant fluids, the equation (2.38) can be written as:

$$\tau = \mu^* \cdot \left(\frac{dv}{dx}\right)^{n-1} \cdot \left(\frac{dv}{dx}\right) \quad (2.39)$$

Introducing the coefficient of dynamic viscosity (μ) (eq.(2.37)), eq.(2.39) can be written as:

$$\mu = \mu^* \cdot \left(\frac{dv}{dx}\right)^{n-1} \quad (2.40)$$

This relationship expresses the dependence of the viscosity coefficient μ on the gradient of velocity through the coefficient n.
Bingham fluids behave like a Newtonian viscous fluid after that a critical value, τ_0 is exceeded (Fig. 2.41). The rheological equation is reported below:

$$\tau = \tau_0 + \mu \cdot \frac{dv}{dx} \quad (2.41)$$

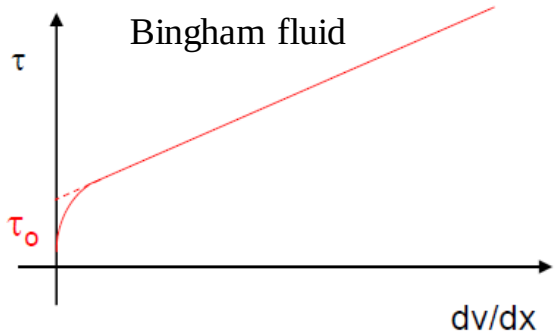

Figure 2.41. Behaviour of Bingham fluids.

Generally, the injected mixtures are suspensions or diluted solutions. Suspensions can be considered as Newtonian fluids, at least initially, while the diluted solutions behave like Bingham fluid.
As mentioned above, the permeation grouting consists of the injection of mixtures into the voids of the soil. This process is governed by Darcy's law:

$$v = k \cdot \frac{dh}{dL} \qquad (2.42)$$

where v is the velocity of the fluid in a porous medium, dh is the difference between final and initial head (h2-h1), dL is the length of flow path, and finally k is the permeability coefficient (absolute permeability), which can be expressed as:

$$k = \frac{\rho \cdot g}{\mu} \cdot K_0 \qquad (2.43)$$

where ρ is the density of the fluid, g is the gravity acceleration, μ is the viscosity of the fluid and K_0 is the absolute permeability. Eq. (2.43) shows that the permeability coefficient of a soil to a mixture is much higher as lower its viscosity is. From eq. (2.43), the term K_0 can be expressed as:

$$K_0 = k_i \cdot \frac{\mu_i}{\rho_i \cdot g} = k_w \cdot \frac{\mu_w}{\rho_w \cdot g} = k_m \cdot \frac{\mu_m}{\rho_m \cdot g} \qquad (2.44)$$

And then the permeability coefficient of the soil to the mixture (k_m) can be written as:

$$k_m = k_w \cdot \frac{\mu_w}{\mu_m} \cdot \frac{\gamma_m}{\gamma_w} \qquad (2.45)$$

Where:

- k_w is the permeability coefficient of the soil to water;
- μ_w is the viscosity of water (1cP);
- γ_w is the the specific weights of the water (9.8 kN/m^3);
- γ_m is the density of the mixture;
- μ_m is the viscosity of the mixture.

Figure 2.42 is extremely important to analyze the injectability of the mixture, strongly related to its initial viscosity (μ) and its variation over time μ (t). The chemical composition of the mixture must be calibrated (also by adding additives) in order to guarantee that the injection time is less than the gelling time (t_{gel}) of the mixture, because it marks a large increase in viscosity and hence a considerable slowing down of the permeation process. In other words, the injection time should be smaller than the gelling time.

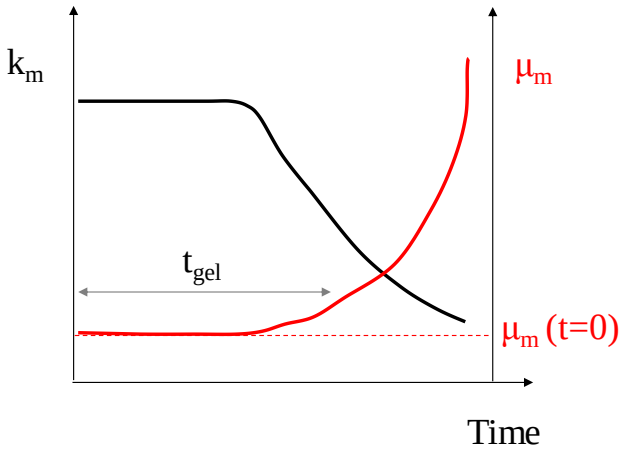

Figure 2.42. k_m and μ_m with time.

Traditionally, cement grouts have been used in permeation grouting intervention; however, more recently, researchers have been looking at silica-based gels (Gallagher 2000; Gallagher and Mitchell 2002; Gallagher et al. 2007), but innovative grouts may be used as well: such as employing urea-hydrolysing bacteria for biocementation of the soil (Dekuyer et al., 2012; Gao et al., 2019). Hydrolysis and denitrification induce calcite precipitation into soil, providing a cohesive strength and thus preventing soil particle movements (Yang and Cheng, 2013; Han et al., 2016). The problem for these kinds of techniques is that sometimes they are not environmental friendly, the research in this field is still ongoing.

Recently, some researchers proposed to inject plastic mixtures into the soil. Mixtures should be plastic enough to improve the response of the soil to liquefaction. Based on the experimental results of Ishihara and Koseki (1989) the resistance to liquefaction increases when the PI (plasticity index) increases. El Mohtar et al. (2012) proposed to inject bentonite suspensions to replace the water in the pore spaces of the desired site. The advantages of bentonite can be summarized as follows: its small size and high plasticity; wide availability; low cost; large experience base in geotechnical engineering; and lack of environmental contamination. Cyclic triaxial tests carried out on sand treated with bentonite, in two concentrations (3 and 5% by dry mass of sand), have been reported by El Mohtar et al. (2012). They confirm that the bentonite delays the generation of excess pore pressure. Taking into account the need to deliver the bentonite suspension in a sand deposit, the same authors studied the rheology of concentrated bentonite suspensions through the addition of sodium pyrophosphate (SPP), able to delay the gelling time of the suspensions.

Ochoa-Cornejo et al. (2016) proposed to use laponite instead of bentonite suspensions. Although the latter is natural and safe, its application in the field presents some problems, such as, the fact that bentonite suspensions cannot permeate into the soil without adding additive, like SPP; in fact, the inherent variability of this natural material, can lead to inconsistent results or difficulties in permeating finer deposits. Laponite is thus presented as a possible solution to overcome these challenges.

Laponite RD ($Na^{+\ 0.7}[(Si_8Mg_{5.5}Li_{0.3})\ O_{20}\ (OH)_{\ 4}]^{-0.7}$) is a synthetic nano-clay, which is used as a rheology modifier in a range of applications (e.g. cosmetics, inks, paints, surface coating, glazes). It is a 2:1 clay formed by a magnesium octahedral sheet sandwiched between two silica tetrahedral sheets (Fig. 2.43a). Isomorphic substitution of magnesium by lithium atoms generates negative charges on both faces, which are counterbalanced by interlayer cations, generally sodium. Single laponite particles have a disk-like shape approximately 25 nm in diameter and 1nm thickness (Fig. 2.43b) and specific gravity of 2.57 (Rockwood Additives Ltd. 2011); bentonite particles also have a fundamental thickness of 1nm but the diameter is much greater than laponite (200–1000nm). In dry form, laponite crystals form silt size stacks by sharing the inter layer sodium ions (Ochoa-Cornejo et al., 2016). The plasticity index PI is very high: 1100%, and for this reason it is called "super-plastic nanoparticle" (El Howayek 2011).

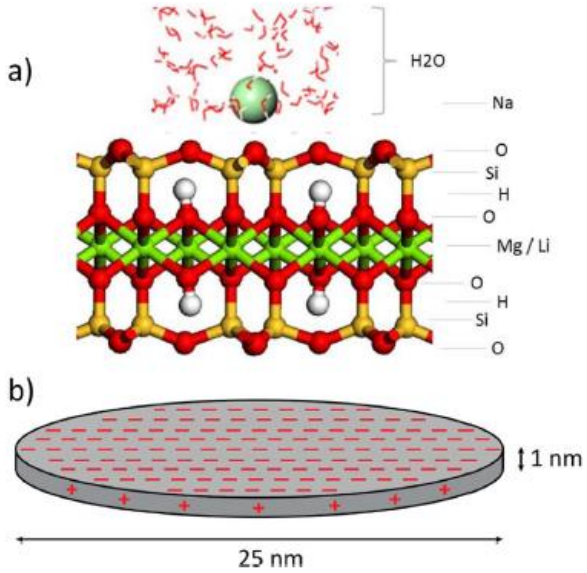

Figure 2.43. Structure of laponite (a) and geometry of individual laponite particle (b) (Ochoa-Cornejo et al., 2016).

In Figure 2.44 the phase diagram of laponite is shown (adapted from Santagata et al., 2014). It represents the ionic strength of the mixture (concentration of ions in solution in terms of molar concentration M) with the concentration of laponite in water, ϕ (ratio between the mass of laponite with the mass of water). When laponite is dissolved in water the phase of the mixture is Liquid (section A of Fig. 2.44) with a viscosity similar to that of water (1 cP). When laponite hydrates and swells the viscosity increases, forming a gel (Sol phase, section B in Fig. 2.44). The Sol phase (point B) represents the passage between a strongly aqueous solution and an Attractive gel (point C). If the percentage of laponite increases over time, for example in the case of drying, a solid phase similar to a vitrification process occurs, it is divided into Attractive and Repulsive Glass (D and E points respectively).

The concentration of laponite therefore regulates the state (liquid, gel or solid) of the mixture: during the permeation process, in which the aqueous mixture of laponite must

permeate without altering the soil structure, the mixture must be in a liquid phase. After the permeation process, a phase transition occurs and a new gel-like structure can be identified for the laponite mixture.

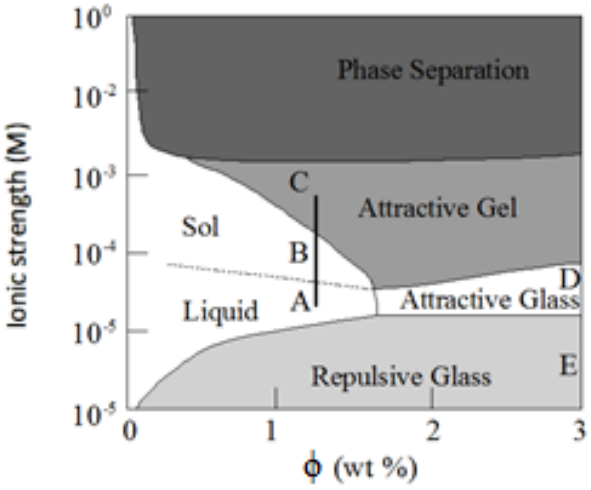

Figure 2.44. Phase diagram of laponite RD (adapted from Santagata et al., 2014): ionic strength versus the concentration of laponite in water ϕ.

Ochoa-Cornejo et al. (2016) performed several cyclic triaxial tests, 7 on clean sand (Ottawa sand) and 21 on sand treated with laponite in different concentrations (1, 3 and 5 by dry mass of the sand). The specimens were prepared by dry pluviation. This procedure was calibrated to achieve skeleton relative density (D_{rsk}) around 20%, where the skeleton relative density is calculated based on the skeleton void ratio (related to solid phase) and the limiting void ratio e_{max} and e_{min} of the clean sand. The specimens sand/laponite were prepared by placing sand and laponite, in the desired proportion in a sealed plastic contained. It is manually shaken for 20 minutes. A valve on the container, connecting to a copper pipe of 30 cm in length and 0.50 cm in diameter, was used to air-pluviate the mixture inside the triaxial split mould. The saturation of the specimen is performed in the triaxial cell to reach a B value of at least 0.95. The specimens were consolidated to an effective stress of 100 kPa. Clean sand specimens were sheared after 1 hour of the secondary consolidation, or aging, while for sand/laponite specimens, the aging stage was extended to 72 hours (based on the results of rheological tests). In Figure 2.45a the results of cyclic triaxial tests for clean and treated sand (1% of laponite) have been plotted in terms of cyclic resistance curves. On the other hand, in Figure 2.45b the number of cycles to liquefaction (N_{liq}) is plotted versus the aging time, for similar values of CSR (0.16-0.15). It shows that N_{liq} increases with aging duration and this relationship is described by an exponential function.

As indicated by Ochoa-Cornejo et al. (2016), the effectiveness of the treatment can be due to two mechanisms: the creation of "bridges" between sand grains due to the plastic nature of laponite, and the formation within the pores of a gel-like fluid that behaves as a material with a small distortion-stiffness (Huang et al. 2016; Ochoa-Cornejo et al. 2016).

Both mechanisms reduce the mobility of sand grains during loading cycles, improving the liquefaction resistance. The presence of "bridges" between the grains of sand has been confirmed by Santagata et al. (2014), as shown in cryo-SEM images of laponite in sand (Fig. 2.46).

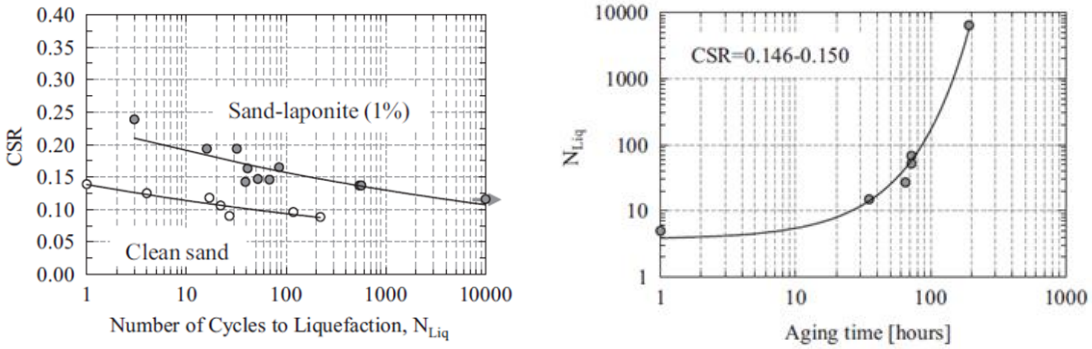

(a) (b)

Figure 2.45. Cyclic resistance of clean and treated sand with laponite (a) and increase in number of cycles to liquefaction with aging time for sand treated with 1% of laponite (b) (Ochoa-Cornejo et al., 2016).

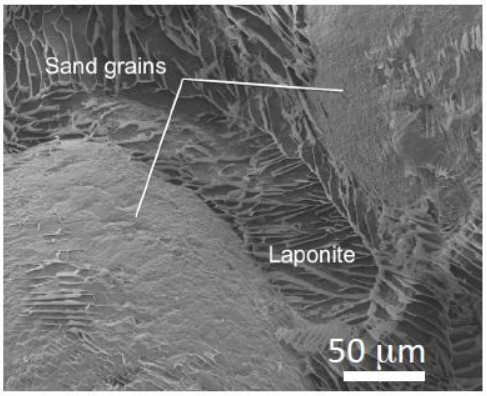

Figure 2.46. Cryo-SEM images of laponite permeated-sand (Santagata et al., 2014).

In conclusion, the permeation grouting is considered less invasive than other techniques, combining the need to reduce the risk of liquefaction and the protection of the integrity of the existing buildings or critical infrastructures. On the other hand, it is not suitable for soils with low permeability coefficient. Moreover, the volume and the homogeneity of the treated zone is uncertain.

Another way to stabilize the soil skeleton is the jet grouting. It consists of creating columns from fine to coarse. This technology is suited to consolidate loose soils, where large diameters can be obtained. Its effects are mainly two: firstly, the cement provides a cohesion, secondly, it can be adopted as rigid inclusions under the foundations.

Finally, soil replacement is often expensive and environmentally non-friendly methods. Nevertheless, in minor projects, local soil replacements may be used.

2.4.3 DESATURATION AND IPS

One of the most promising techniques against liquefaction is desaturation of the soil and in particular, the "induced partial saturation" or the so-called IPS, which consists of introducing a certain amount of air/gas into the voids (Fig. 2.47; Eseller-Bayat et al., 2012). This technology could be suitable especially when the goal is to protect existing buildings that may suffer from the use of more invasive methods.

The effectiveness of this technique has been demonstrated by means of laboratory tests carried out by several researchers (Chaney, 1978; Yoshimi et al., 1989; Ishihara et al., 2002; Yang et al., 2004; Yegian et al., 2007). They showed that even a small reduction in the degree of saturation (S_r) of an initially saturated sand can have a significant effect in terms of cyclic resistance to liquefaction. Martin et al. (1975) explained that a 1% reduction in the degree of saturation of a saturated sand specimen with 40% porosity can lead to 28% reduction in the pore water pressure increase per cycle. Chaney (1978) and Yoshimi et al. (1989) asserted that the resistance to liquefaction was about two times that of fully saturated samples when the degree of saturation is reduced to 90%.

In Figure 2.48, Zeybek (2017) collected and plotted some literature data, which highlight the influence of S_r on the liquefaction resistance to liquefaction. As expected, when the degree of saturation decreases, the liquefaction resistance increases.

To better understand why a soil with Sr<1 has a higher resistance to liquefaction than for S_r=1, some basic concepts on non-saturated soils have been provided.

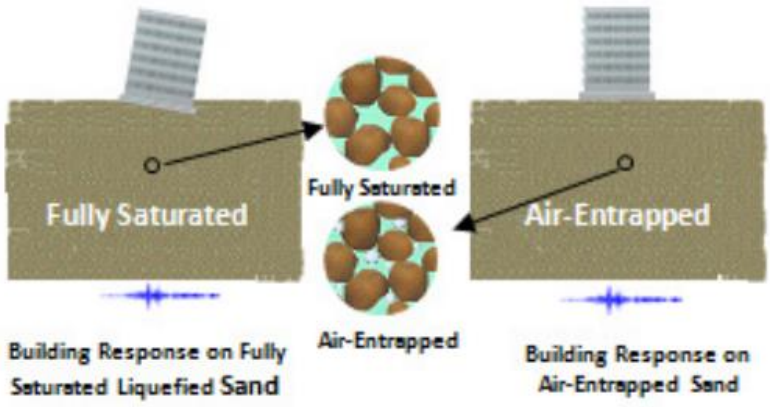

Figure 2.47. Concept of liquefaction mitigation using entrapped air (Eseller-Bayat et al., 2012).

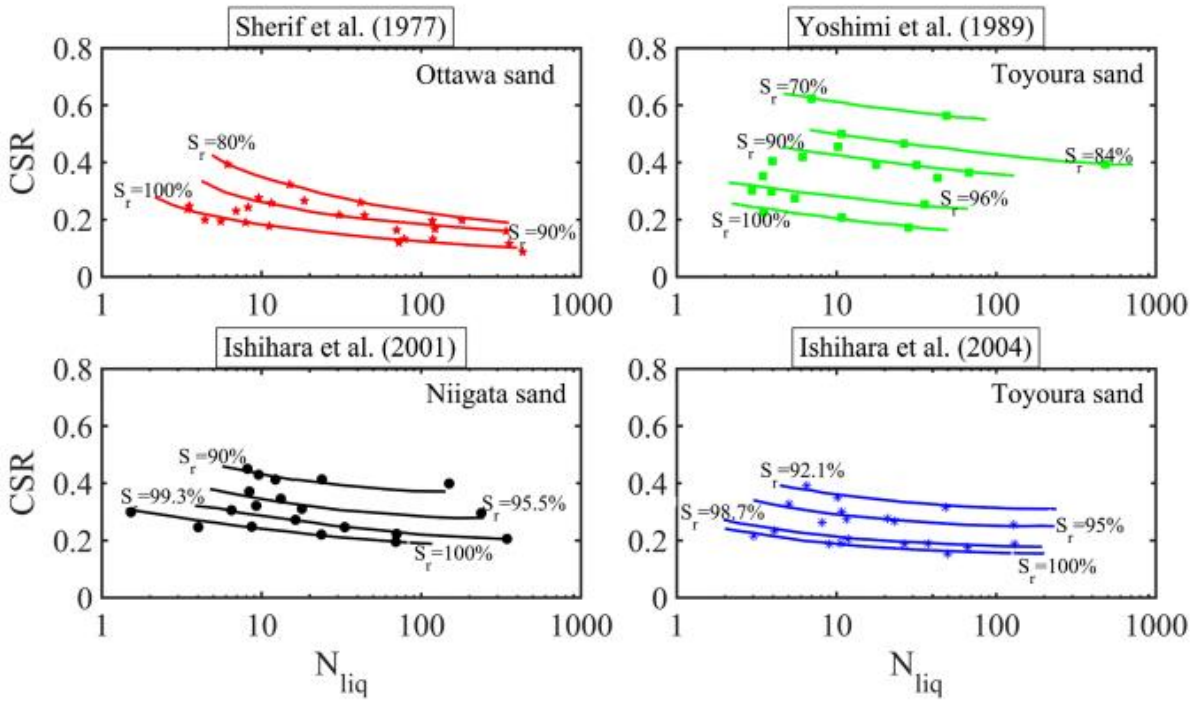

Figure 2.48. Influence of S_r on the liquefaction resistance of sandy soils (Zeybek 2017).

2.4.3.1 LIQUEFACTION IN NON-SATURATED SANDY SOILS

Unlike saturated soils (S_r=1) which are composed by two phases: soil skeleton and water, the soils with S_r<1 consists of three phases: soil skeleton, water and air. The distinction between unsaturated and saturated conditions was illustrated by Fredlund and Rahardjo (1993) and can be shown in Figure 2.49 (Tsukamoto et al., 2014), where the distinctions between "unsaturated", "partially saturated" and "fully-saturated" conditions is shown. Tsukamoto et al. (2014) reported the distributions of pore air and pore water pressure, u_a and u_w, respectively, with depth. The difference between pore air pressure and pore water pressure is called *matric suction* (s) and it depends on the surface tension and the radius of curvature of the meniscus. When the degree of saturation decreases, the matric suction increases because the meniscus retracts into small pore spaces where the radius of curvature of the meniscus is reduced. In Figure 2.49 the matric suction is also plotted with the degree of saturation (S_r); this chart is called soil water retention curve (SWRC). At a soil layer located well above a ground water table large matric suction comes into effect due to the surface tension developed at the pore air and pore water interfaces within soil structures. In this layer, the air phase is continuous. When the depth increases, the confining stress (σ_0) increases as well, together with pore air and pore water pressures. The rate of such increases is defined by the pore pressure coefficients: $B_a=du_a/d\sigma_0$ (for air) and $B_w=du_w/d\sigma_0$ (for water). They are lower than 1 because of surface tension. The pore water tends to increase faster than pore air pressure in response to the confining stress increase, so that the matric suction decreases gradually. With depth, the occluded

bubble becomes predominant, even though they do not interact with soil structure, they affect the compressibility of pore fluids. B_w is still lower than 1and it reaches a value equal to 1 only when the degree of saturation is equal to 1 (fully saturated soils). Moreover, Mihalanche and Buscarnera (2016) showed a useful and schematic representation of the phases in soils, when the degree of saturation increases (Fig. 2.50). In saturated soils, only two phases (soil and water) co-exist, while for high S_r, but lower than 1 (partially saturated soils), water has a continuous phase, while air presents occluded bubbles, trapped within the continuous water phase. Finally, for low S_r (unsaturated soils), air phase is prevalent than that of water.

In this thesis, the soils with a $S_r<1$ will be called generally, non-saturated soils. The terms unsaturated and partially saturated soils will be identified individually when necessary.

Moreover, the attention in this research will be focused on IPS technique that, as mentioned above, consists of introducing bubbles of gas into the void of the soil. In other words, this technology aims to achieve partially saturated soils (bubble occluded) to increase the resistance to liquefaction. Nevertheless, tests on unsaturated sandy soils have been performed as well because they were extremely useful to introduce a new interpretation of liquefaction for non-saturated sandy soils.

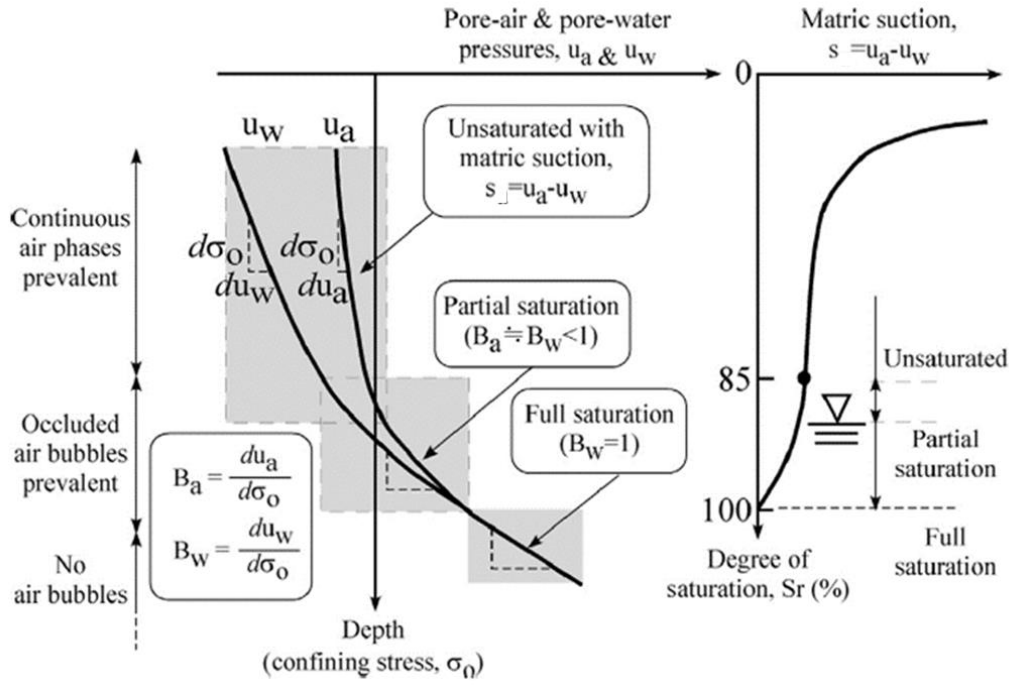

Figure 2.49. Schematic interpretation of fully, partially and unsaturated soil deposit (Tsukamoto et al., 2014).

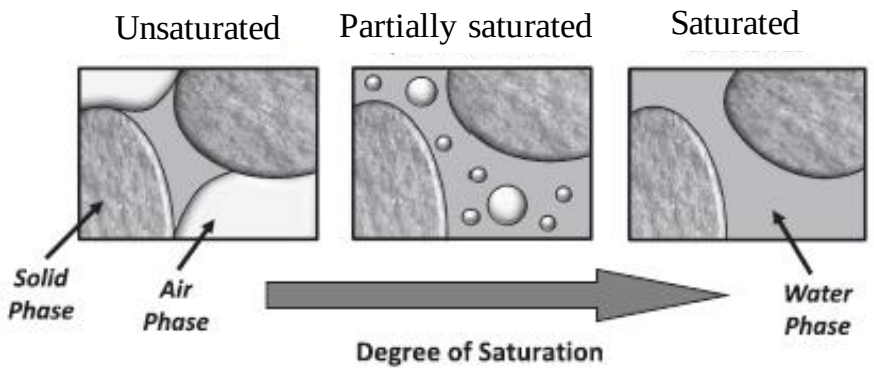

Figure 2.50. Schematic interpretation of fully, partially and unsaturated soils (Mihalache and Buscarnera, 2016).

As well-known in saturated soils the mechanical behaviour is regulated by Terzaghi's principle (Terzaghi, 1943) by means of effective stresses (σ'). In non-saturated soils it is still possible to define effective stress. The way to define such a stress depends on the degree of saturation, or better on the continuity of the air phase: for partially saturated soils, Terzaghi's definition could be used, whereas for unsaturated soils, the effect of matric suction has to be taken into account.
Among the different proposals, the one most used with this aim is probably that proposed by Bishop and Blight many years ago (Bishop and Blight, 1963):

$$\sigma'_{un} = (\sigma - u_a) + \chi \cdot (u_a - u_w) \quad (2.46)$$

where σ is the total stress; u_a, u_w and χ are, respectively, the pore air pressure, the pore water pressure and the material parameter accounting for the effect of the degree of saturation (Bishop's parameter). The term (σ-u_a) is called 'net stress', while (u_a-u_w) is the matric suction or more simply 'suction' (s). Several definitions of the parameter χ have been proposed by several researchers (e.g. Bishop and Blight, 1963; Vanapalli et al., 1996; Gallipoli et al., 2002); in this thesis, it will be assumed that χ = Sr (Gallipoli et al., 2003; Wheeler et al., 2003).
As indicated by Unno et al. (2008), even under non-saturated condition, soil can reach the liquefaction state. Based on the eq. (2.46), the complete liquefaction state can be achieved when both the pore air and water pressure are the same as the initial total confining pressure. The suction reaches zero when the specimens become liquefied and so the effective stress approach to zero, regardless of the parameter χ.
Because of the difficulties to evaluate effective stresses in non-saturated conditions (σ'_{un}) and the need to compare the results of tests carried out on saturated and non-saturated soils, the triggering criterion traditionally used to evaluate the attainment of liquefaction is the strain one. As for saturated soils, it can be assumed that liquefaction occurs when the strain in double amplitude is 5% in cyclic triaxial tests. Nevertheless, it is possible to define excess pore pressure ratio for non-saturated soils. In this case, r_u can be defined as the ratio between Δu and the initial confining stress (σ'_0), where Δu is the excess pore air

pressure for specimens with positive suction measurements, otherwise it is the excess pore water pressure (Wang et al., 2016).

Unlike saturated soils, in non-saturated soils subject to cyclic tests in undrained conditions, the volumetric strains are not equal to 0 and it depends on the compressibility of their fluid phase.

In the saturated soil specimens, the voids are filled with water and during cyclic loading, if the soil tends to contract, particle grains tend to re-arrange more closely together, but in undrained condition, water cannot be released and consequently pore pressure increases. In unsaturated soil, the voids are occupied by water and air that has the smallest compressibility. If the soil exhibits contractive behaviour, the application of cyclic loading also triggered an increase in pore water pressure, but it directly replaced the air void in order to dissipate an excessive energy. The phenomenon of increasing pore water pressure in unsaturated and saturated soil is clearly described in detail in Figure 2.51. It means that during undrained cyclic triaxial tests performed on partially saturated soils, the positive volumetric strains that rises, generate an increase of S_r. In other words, S_r changes during the tests.

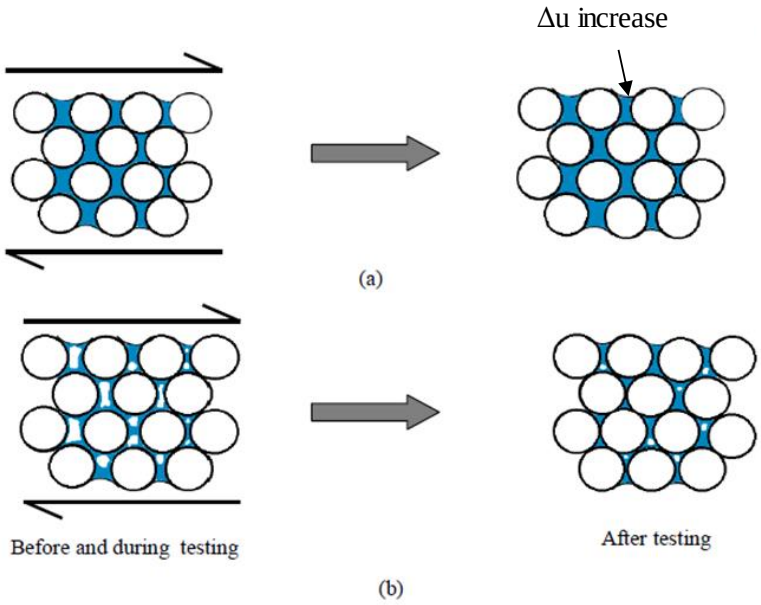

Figure 2.51. Particle configurations before and after testing in saturated (a) and unsaturated contractive soils (b) (modified from Kusumawardani et al., 2016).

From a qualitative point of view, also the presence of occluded bubbles can increase the compressibility of the fluid mixture (β_f), as shown by Mihalache and Buscarnera (2016):

$$\beta_f = \frac{1 - S_r}{u + p_a} + \beta_w S_r \quad (2.47)$$

where p_a is the atmospheric pressure, β_w is the compressibility of water ($4 \cdot 10^{-7}$ kPa^{-1}), while $u=u_a=u_w$, assuming that the pressure inside the gas bubbles and the surrounding liquid are identical.

Ultimately, during undrained cyclic loading, if the soil tends to contract, the volume of the gas phase decreases and consequently the pore pressure build-up is reduced. This is one of the reasons why a non-saturated sandy soil has a higher resistance to liquefaction than the saturated one. According to Okamura and Soga (2006), the presence of air in the voids increases the resistance against liquefaction in two ways: the first mechanism is connected to the very low volumetric stiffness of gases, because of which during undrained loading there is a volumetric reduction of the gas phase and therefore reduced excess pore pressures. This mechanism is the ruling one for high degrees of saturation (i.e. dispersed air bubbles). The second mechanism is due to the matric suction of unsaturated soils, which increases the stiffness and strength of soils (Bishop and Blight, 1963). This latter mechanism becomes relevant when the degree of saturation is low enough to have a continuous air phase.

Although it is well-known that non-saturated soils have a higher resistance to liquefaction than the saturated ones, the parameters governing the liquefaction resistance of non-saturated soils are not so clear. Yoshimi et al. (1989) proposed the degree of saturation (S_r) simply. In Figure 2.52, Okamura and Soga (2006) reported some literature results in form of relationship between S_r and the resistance of partially saturated soils (CRR_{15}, evaluated for N_{liq}=15) normalized with that of fully saturated soils or *Liquefaction Resistance Ratio* (LRR). As expected, liquefaction resistance increases when S_r decreases; however, the liquefaction resistance ratios were different for different sands tested at different conditions. It seems that S_r is not the predominant factor in liquefaction resistance of partially saturated soils. Yang et al. (2004) indicated the B-value as the key parameter in determining the increase of liquefaction resistance, B-value can be defined as:

$$B = \frac{1}{1 + n \cdot \frac{K_b}{K_w} + n \cdot \frac{K_b}{p_a} \cdot (1 - S_r)} \qquad (2.48)$$

where n is the porosity; p_a is the absolute fluid pressure; K_b is the bulk modulus of soil skeleton and K_w is the bulk modulus of pore water.

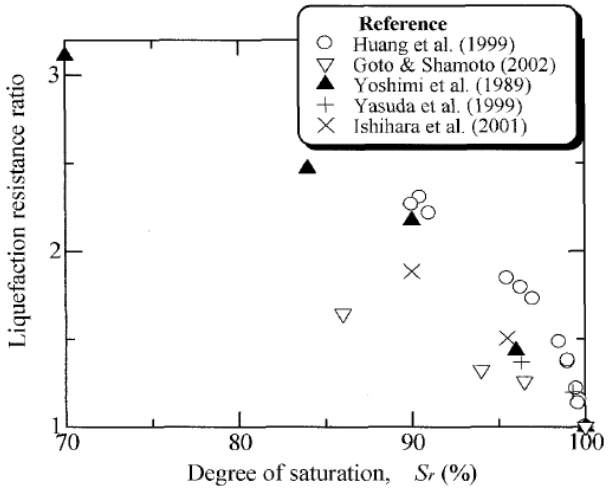

Figure 2.52. Effect of S_r on liquefaction resistance (Okamura and Soga, 2006).

Yang et al. (2004) also proposed the elastic wave velocity, and finally Okamura and Soga (2006) the potential volumetric strain (ε_v^*).
It can be determined easily from Boyle and Mariotte law, under the hypothesis of pore air as ideal gas and isothermal condition:

$$u_{a,0} \cdot V_{a,0} = u_{a,liq} \cdot V_{a,liq} \; = \; const \quad (2.49)$$

where $u_{a,0}$ and $u_{a,liq}$ are absolute pore air pressure at the beginning of the cyclic phase and at liquefaction, respectively, while $V_{a,0}$ and $V_{a,liq}$ are the initial volume of air and at liquefaction, respectively.
Known that $V_{a,0}$ can be written as:

$$V_{a,0} = V_{tot} \cdot [(1 - S_{r0}) \cdot n] \quad (2.50)$$

where V_{tot} is the total volume of the specimen, while S_{r0} is the initial degree of saturation and n is the porosity of the specimen, substituting eq. (2.50) in (2.49) gives:

$$u_{a,0} \cdot V_{tot} \cdot [(1 - S_{r0}) \cdot n] = u_{a,liq} \cdot \left(V_{a,0} - \Delta V\right) \quad (2.51)$$

where ΔV is the variation of volume induced by the compressibility of the fluid, assuming soil grains to be incompressible. Substituting again eq. (2.50) in (2.51) gives:

$$u_{a,0} \cdot V_{tot} \cdot [(1 - S_{r0}) \cdot n] = u_{a,liq} \cdot (V_{tot} \cdot [(1 - S_{r0}) \cdot n] - \Delta V) \quad (2.52)$$

Dividing both parts of the equation for V_{tot} and considering that liquefaction occurs according to its traditional definition: $u_{a,liq}=u_{w,liq}=\sigma$, where σ is the total stress, eq. (2.52) becomes:

$$u_{a,0} \cdot [(1 - S_{r0}) \cdot n] = \sigma \cdot [(1 - S_{r0}) \cdot n - \varepsilon_v] \quad (2.53)$$

where the definition of volumetric strain (ε_v) has been introduced ($\varepsilon_v=\Delta V/V$). Then, volumetric strain can be found:

$$\varepsilon_v = \frac{e_0}{1 + e_0} \cdot (1 - S_{r0}) \cdot \left(1 - \frac{u_{a,0}}{\sigma}\right) \quad (2.54)$$

where the porosity (n) has been replaced by its definition in terms of void ratio (e) as e/(1+e).
The same formula was achieved by Okamura and Soga (2006) by introducing the definitions of bulk moduli of air and water.
ε_v of eq. (2.54) is defined potential volumetric strain (ε_v^*) by Okamura and Soga (2006) and it is worth noting that even though it was obtained for $u_{a,liq}=u_{w,liq}=\sigma$, this formula can be also used to evaluate the volumetric strain expected at a fixed pore air pressure (u_a), replacing its value to σ. Moreover, one of the most findings is that the value of ε_v does not depend on the kind of soil.

Okamura and Soga (2006) plotted experimental results of already published papers in terms of potential volumetric strain versus liquefaction resistance ratio, showing a logarithmic fitting curve. Nevertheless, later, Wang et al. (2016) showed that this correlation was not in agreement with their experimental results for extremely loose specimens.

In this thesis a new innovative and promising state parameter ($E_{v,liq}$: specific volumetric energy to liquefaction) will be introduced in Chapter 8 as a key in interpreting the behaviour of non-saturated sandy soils and besides, it will be used in the proposed design tools for desaturation interventions against liquefaction.

The effectiveness of desaturation as a countermeasure against liquefaction is now known, but the problem is how to introduce bubbles into sand, or how to "desaturate" the soil. Several solutions have been proposed. These include: air injection (Okamura et al., 2010); water electrolysis (Yegian et al., 2006); sand compaction pile (Okamura et al., 2006) and the use of sodium perborate (Eseller-Bayat, 2009). In recent years, attempts have also been made to apply microbiology to geotechnical engineering.

Recently, some in-situ trial applications of this technology have been carried out to decrease the susceptibility of liquefiable soil deposits (e.g. Okamura et al., 2010; Nagao et al., 2015; Flora et al., 2019), confirming the beneficial effect of desaturation as countermeasure against liquefaction also a large scale.

2.4.4 DISSIPATION OF EXCESS PORE PRESSURE

The technologies able to dissipate the increased excess pore pressure, such as drainage and dewatering, have not been studied in this research; however, they will be presented briefly in this paragraph for sake of completeness.

Drains are one of the most common technologies used against liquefaction.

Shaking table tests (starting from the old but still actual work carried out by Sasaki and Taniguchi, 1982) indicate that gravel drains can accelerate the dissipation of excess pore water pressures, thereby limiting the loss of shear strength and reducing the uplift pressures acting on buried structures. At Cambridge, centrifuge modelling (Brennan and Madabhushi, 2006) has been carried out to investigate the mechanism by which drains affect the performance of a liquefiable site. It is generally agreed that the drains bring about a positive effect by relieving the excess pore pressures that are generated during an earthquake. Most of the past studies have been focused on the drainage characteristics of stone columns

Many kinds of technologies to realize a drainage system are available in the engineer practices.

Preformed drains or stone columns can be installed by vibro-replacement or auger-casing. In the vibro-replacement technique the potential for liquefaction is mitigated by increasing the density of soil surrounding drains, allowing drainage for the control of pore pressures, introducing stiff elements (stone columns) which can potentially carry higher stress levels causing reduction in stress levels in the surrounding soil (Priebe, 1989, 1991),

and providing a deformation restricting effect. The typical auger-casing system instead generally involves little or no densification.

Mitchell et al. (1995) and Hausler and Sitar (2001) document some of the sites where drains were used as a liquefaction mitigation measure. They report that, following moderate-sized earthquakes, these sites performed better than comparable unimproved sites. Design of drains in practice is guided by the seminal work carried out by Seed and Booker (1977), who developed design charts for the drain radius and drain spacing based on analytical methods.

Another technique to dissipate excess pore pressure is dewatering.

Lowering the ground water level by dewatering allows the locally increase of the effective stresses, which possibly eliminates the risk of liquefaction if the dewatering action is directly carried out in the liquefiable layer. Ground water lowering can be achieved, for instance, by natural gravity flow through embedded trenches or similar means. A further, very important effect of dewatering is the reduction of the degree of saturation, so that as mentioned in the previous paragraph, the pore water pressure build-up is reduced. This technology has been proposed as a countermeasure against liquefaction by Koseki et al. (2015) in Tohoku region (Japan), which was subjected to extensive liquefaction phenomena during the earthquake in 2011. However, dewatering technique is expensive.

REFERENCES

Acharya, B. (2017). Simple shear tests on clay. *PhD thesis, University of Sidney, Australia, Department of Civil Engineering.*

Airey, D. W. (1985). Some aspect of the behaviour of soils in simple shear. *Developments in Soil Mechanics and Foundation Engineering-2, Stress-strain Modeling of Soils*, 185-213.

Airey, D. W., and Wood, D. M. (1986). Pore pressures in simple shear. *Soils and foundations*, 26(2): 91-96.

Airey, D. W., and Wood, D. M. (1987). An evaluation of direct simple shear tests on clay. *Géotechnique*, *37*(1): 25-35.

Anagnostopoulos, C.A. (2005). Laboratory study of an injected granular soil with polymer grouts. *Tunnelling and Underground Space Technology*, 20: 525-533.

ASTM – D6528 (2007). Standard Test Method for Consolidated Undrained Direct Simple Shear Testing of Fine Grain Soils.

Aydan, O. (1995). Mechanical and numerical modelling of lateral spreading of liquefied soil. *Proc. 1st Int Conf on Earth-Geo Eng, Tokyo*. Vol. 881886.

Azeiteiro, R. J., Coelho, P. A., Taborda, D. M., and Grazina, J. C. (2017). Energy-based evaluation of liquefaction potential under non-uniform cyclic loading. *Soil Dynamics and Earthquake Engineering*, 92, 650-665.

Baziar, M. H., and Jafarian, Y. (2007). Assessment of liquefaction triggering using strain energy concept and ANN model: capacity energy. *Soil Dynamics and Earthquake Engineering*, 27(12): 1056-1072.

Baziar, M. H., Shahnazari, H., and Sharafi, H. (2011). A laboratory study on the pore pressure generation model for Firouzkooh silty sands using hollow torsional test. *Int J Civ Eng 9(2):126–134.*

Been, K. and Jefferies, M. G. (1985). A state parameter for sands. *Géotechnique,* 35 (2):99-l 12.

Berrill, J. B., and Davis, R. O. (1985). Energy Dissipation and Seismic Liquefaction of Sands: Revised Model. *Soils and Foundations*, 25: 106-118.

Bhattacharya, S., Hyodo, M., Goda, K., Tazoh, T., and Taylor, C. A. (2011). Liquefaction of soil in the Tokyo Bay area from the 2011 Tohoku (Japan) earthquake. *Soil Dynamics and Earthquake Engineering*, *31*(11): 1618-1628.

Bishop, A.W. and Blight, G. E. (1963). Some aspects of effective stress in saturated and partly saturated soils. *Géotechnique*, 13(3): 177–197, https://doi.org/10.1680/geot.1963.13.3.177.

Bjerrum, L. and Landva, A. (1966). Direct simple shear tests on a Norwegian quick cay. *Géotechnique*, 16, 1-20.

Booker, J. R., Rahman, M. S., and Seed, H. B. (1976). GADFLEA— A computer program for the analysis of pore pressure generation and dissipation during cyclic or earthquake loading. *Rep. No. EERC 76-24, Earthquake Engineering Research Center, Univ. of California at Berkeley, Berkeley, California.*

Boulanger, R., Iai, S., Ansal, A., Cetin, K.O., Idriss, I.M., Sunman, B., Sunman, K. (2000). Performance of Waterfront Structures. *Chapter 13, in 1999 Kocaeli, Turkey, Earthquake Reconnaissance Report, Supplement A to Earthquake Spectra, T.L. Youd, J.-P. Bardet, J.D. Bray, Eds*., 16: 295- 310.

Brennan, A.J., Madabhushi, S.P.G. (2006). Liquefaction remediation by vertical drains with varying penetration depths. *Soil Dynamics and Earthquake Engineering,* 26 (5): 469-475.

Brown, D.R. and Warner, J. (1973). Compaction grouting. *Journal of soil mechanics and foundation division (ASCE)* Vol.99 SM8 proceeding paper 9908: 589-601.

Casagrande, A. (1936). Characteristics of cohesionless soils affecting the stability of slopes and earth fills. *Journal of the Boston Society of Civil Engineers*, 23:13-32.

Castro, G. (1969). Liquefaction of sands. *ph. D. Thesis, Harvard Soil Mechanics.* Harvard University, Cambridge, Massachusetts.

Castro, G. (1975). Liquefaction and cyclic mobility of saturated sands. *Journal of Geotechnical and Geoenvironmental Engineering*, *101*(ASCE) GT6: 551 - 569.

Castro, G. and Poulos, S. J. (1977). Factors affecting liquefaction and cyclic mobility. *Journal of Geotechnical and Geoenvironmental Engineering*, *103*(ASCE) GT6: 501 - 516.

Chaney, R. (1978). Saturation effects on the cyclic strength of sands. In *Earthquake engineering and soil dynamics, pp. 342–358. New York, NY, USA: American Society of Civil Engineers*.

Chang, M., Mao, T.W., Wu, T.F., Shau, S.H., Yang, P.J., Hsieh, H.S. (2005). Treatment of liquefiable soils through low-pressure grouting: Field observations and testing. *Proceeding of international conference on problematic soils,* 967-974. N. Cyprus.

Chen, Y.M., Liu, H.L., Zhou, Y.D. (2006). Analysis on flow characteristics of liquefied and post-liquefied sand. *Chinese Journal of Geotechnical Engineering* 28(9): 1139-1143.

Chen, Y., and Liu, H. (2011). Simplified method of flow deformation induced by liquefied sands. In *Design, Construction, Rehabilitation, and Maintenance of Bridges* (pp. 160-167).

Chen G., Zhou E., Wang Z., Wang B., Li X. (2016). Experimental study on fluid characteristics of medium dense saturated fine sand in pre- and post-liquefaction. *Bulletin of Earthquake Engineering* 14(8): 2185-2212.

Chiaradonna A., Tropeano G., d'Onofrio A., Silvestri F. (2018a) Development of a simplified model for pore water pressure build-up induced by cyclic loading. *Bull Earthq Eng, BEE 16 (9):3627–3652, https://doi.org/10.1007/s10518-018-0354-4.*

Chiaradonna, A., Özcebe, A. G., Bozzoni, F., Fama, A., Zuccolo, E., Lai, C. G., Flora, A., Cosentini, M.R., d'Onofrio, A., Bilotta, E. and Silvestri11, F. (2018b). Numerical simulation of soil liquefaction during the 20 May 2012 M6. 1 Emilia Earthquake in Northern Italy: the case study of Pieve di Cento. In *Proceedings of the 16th European Conference on Earthquake Engineering, 16ECEE, Thessaloniki, Greece, 18-21 June 2018. Paper* (Vol. 11234).

Committee on Soil Dynamics of the Geotechnical Engineering Division (1978). Definition of terms related to liquefaction. *Journal of Geotechnical Engineering*, 104(GT9): 1197-1120.

Coulter, H. W., and Migliaccio, R. R. (1966). Effects of the earthquake of March 27, 1964, at Valdez, Alaska.

Cubrinovski, M. (2013). Liquefaction-Induced Damage in The2010-2011 Christchurch (New Zealand) Earthquakes. *Seventh International Conference on Case Histories in Geotechnical Engineering*, Chicago (USA), April-May 2013

Davis, R.O. and Berrill, J.B. (1982). Energy dissipation and seismic liquefaction of sands. *Earthquake Eng Struct Dyn* 1982; 10: 59 – 68.

DeAlba, P., Chan, C. K., and Seed, H. B. (1975). Determination of soil liquefaction characteristics by large-scale laboratory tests. *Rep. No. EERC 75-14, Earthquake Engineering Research Center, Univ. of California, Berkeley, California.*

de Josselin de Jong (1971). Discussion on stress-strain behaviour of soils. Proc. Roscoe Memorial Symposium, 258 – 261. Cambridge: Foulis.

Dekuyer, A., Cheng, L., Shahin, M. A., and Cord-Ruwisch, R. (2012). Calcium carbonate induced precipitation for soil improvement by urea hydrolysing bacteria. In *World Congress on Advances in Civil, Environmental and Materials Research* (pp. 2785-2793).

Desai, C. S. (2000). Evaluation of liquefaction using disturbed state and energy approaches. *Journal of geotechnical and geoenvironmental engineering*, 126(7): 618-631.

Dief, H. M., and Figueroa, J. L. (2007). Liquefaction assessment by the unit energy concept through centrifuge and torsional shear tests. *Canadian Geotechnical Journal*, 44(11): 1286-1297.

Dobry, R., Ladd, R. S., Yokel, F. Y., Chung, R. M., and Powell, D. (1982). Prediction of pore water pressure buildup and liquefaction of sands during earthquakes by the cyclic strain method *(Vol. 138). Gaithersburg, MD: National Bureau of Standards.*

Dobry R., Pierce, W.G., Dyvik R, Thomas, G.E., Ladd, R.S. (1985). Pore pressure model for cyclic straining of sand. *Civil Engineering Department, Rensselaer Polytechnic Institute, Troy.*

Drescher, A., and Vardoulakis, I. (1982). Geometric softening in triaxial tests on granular material. *Géotechnique,* 32(4): 291-303.

El Howayek A., (2011). Characterization, rheology and microstructure of laponite suspension. *MS Thesis*, School of Civil Eng., Purdue University.

El Mohtar, C. S., Bobet, A., Santagata, M. C., Drnevich, V. P., and Johnston, C. T. (2012). Liquefaction mitigation using bentonite suspensions. *Journal of Geotechnical and Geoenvironmental Engineering*, *139*(8): 1369-1380.

Emery, J. J., Finn,W. D., and Lee, K.W. (1973). Uniformity of saturated sand specimens. *ASTM STP 523,* West Conshohocken, Pa.

Eseller-Bayat, E. E. (2009). Seismic response and prevention of liquefaction failure of sands partially saturated through introduction of gas bubbles. *PhD thesis, Northeastern University, Boston*, MA, USA.

Eseller-Bayat E, Yegian MK, Alshawabkeh A, Gokyer S (2012). Prevention of liquefaction during earthquakes through induced partial saturation in sands. *Geotechnical engineering: new horizons.* Amsterdam: IOS Press; 188‑94.

Figueroa, J. L., Saada, A. S., Liang, L., & Dahisaria, N. M. (1994). Evaluation of soil liquefaction by energy principles. *Journal of Geotechnical Engineering, 120(9): 1554-1569.*

Finn, W. D., Bransby, P. L., and Pickering, D. J. (1970). Effect of strain history on liquefaction of sand. *Journal of Soil Mechanics & Foundations Div*, *96*(SM6).

Flora A., Chiaradonna A., Bilotta E., Fasano G., Mele L., Lirer S., Pingue L. (2019). Field tests to assess the effectiveness of ground improvement for liquefaction mitigation. *Invited lecture, 7th International Conference on Earthquake Geotechnical Engineering, 7ICEGE, Rome (Italy),* 17-20 June 2019.

Fredlund, D.G., and Rahardjo, H., (1993). Soil mechanics for unsaturated soils. *A Wiley-Interscience Publication, John Wiley & Sons, New York.*

Gallagher, P. (2000). Passive site remediation for mitigation of liquefaction risk. *Ph.D. dissertation, Virginia Tech, Blacksburg, VA.*

Gallagher, P. M., Conlee, C. T., and Rollins, K. M. (2007). Full-scale field testing of colloidal silica grouting for mitigation of liquefaction risk. *J. Geotech. Geoenviron. Eng.*, 133(2): 186–196.

Gallagher, P. M., and Mitchell, J. K. (2002). Influence of colloidal silica grout on liquefaction potential and cyclic undrained behavior of loose sand. *Soil Dynamics and Earthquake Engeneering*, 22(9-10): 1017–1026.

Gallipoli, D., Gens, A., Vanet, J. and Romero, E. (2002). Role of degree of saturation on the normally consolidated behavior of unsaturated soils. *In Unsaturated soils: proceedings of the third international conference on unsaturated soils, UNSAT 2002* (eds J. F. T. Juca, T. M. P. de Campos and F. A. M. Marinho), pp. 115–120. Abingdon, UK: Taylor & Francis Group.

Gallipoli, D., Gens, A., Sharma, R. and Vaunat, J. (2003). An elasto-plastic model for unsaturated soil incorporating the effects of suction and degree of saturation on mechanical behaviour. *Géotechnique* 53(1): 123–135, https://doi.org/10.1680/geot.2003.53.1.123.

Gao, Y., Hang, L., He, J., and Chu, J. (2019). Mechanical behaviour of biocemented sands at various treatment levels and relative densities. *Acta Geotechnica*, *14*(3): 697-707.

Graf, E. D. (1992). Compaction grout. *In Grouting, soil improvement and geosynthetics, ASCE Geotechnical Special Publication* No. 30(1): 275-287. Reston, VA: American Society of Civil Engineers.

Green, R.A., Mitchell, J.K., Polito, C.P. (2000). An energy-based pore pressure generation model for cohesionless soils. *In: John Booker memorial symposium developments in theoretical geomechanics, Rotterdam, The Netherlands, pp 383–390.*

Green, R.A. (2001). Energy-based evaluation and remediation of liquefiable soils. *Ph.D. thesis, Department of Civil Engineering, Virginia Polytechnic Institute and State University, Blacksburg, Va.*

Gutenberg, B., and Richter, C. F. (1956). Earthquake magnitude, intensity, energy, and acceleration: (Second paper). *Bulletin of the seismological society of America*, *46*(2): 105-145.

Hadush, S., A. Yashima, and R. Uzuoka. (2000). Importance of viscous fluid characteristics in liquefaction induced lateral spreading analysis. *Computers and Geotechnics 27(3):199-224.*

Hamada, M., and Wakamatsu, K. (1998). A study on ground displacement caused by soil liquefaction. *Proc. JpnSoc Civil Eng, 1998(596): 189-208.*

Han, Z., Cheng, X., and Ma, Q. (2016). An experimental study on dynamic response for MICP strengthening liquefiable sands. *Earthquake Engineering and Engineering Vibration*, *15*(4): 673-679.

Hansen, W. R. (1966). Effects of the earthquake of March 27, 1964, at Anchorage, Alaska. *US Government Printing Office.*

Hashash, Y. 2013. DEEPSOIL5.1. Available from http://deepsoil.cee.illinois.edu/

Hausler E.A. and Sitar N. (2001). Performance of soil improvement techniques in earthquakes. *Fourth International Conference on Recent Advances in Geotechnical Earthquake Engineering and Soil Dynamics*, Paper 10.15.

Hayden, P.F., and Baez, J.I. (1994). State of Practice for Liquefaction Mitigation in North America. *Proceeding, International Workshop on Remedial Treatment of Liquefiable Soils,* held in Tsukuba Science City, Japan, on 4-6 July.

Huang, Y. and Wang, L., (2016). Laboratory investigation of liquefaction mitigation in silty sand using laponite. *Engineering Geology*, 204, 23-32.

Hwang, J. I., Kim, C. Y., Chung, C. K., and Kim, M. M. (2006). Viscous fluid characteristics of liquefied soils and behavior of piles subjected to flow of liquefied soils. *Soil Dynamics and Earthquake Engineering*, *26*(2-4): 313-323.

Idriss, I.M., (1999). An update to the Seed-Idriss simplified procedure for evaluating liquefaction potential. *Proc., TRB Worshop New Approaches to Liq. Pubbl. n. FHWA-RD-99-165, Fed. Highw. Administation*.

Idriss, I. M., and Boulanger, R. W. (2004). Semi-empirical procedures for evaluating liquefaction potential during earthquakes, *in Proceedings, 11th International Conference on Soil Dynamics and 106 Earthquake Engineering, and 3rd International Conference on Earthquake Geotechnical Engineering, D. Doolin et al., eds., Stallion Press,* Vol. 1, pp. 32–56.

Ishihara, K. (1984). Post-earthquake failure of a tailings dam due to liquefaction of the pond Deposit. *Proceedings, International Conference on Case Histories in Geotechnical Engineering,* University of Missouri, St. Louis, 3: 1129-1143.

Ishihara, K. (1985). Stability of natural deposits during earthquakes. *Proceedings, 11th International Conference on Soil Mechanics and Foundation Engineering,* 1: 321-376.

Ishihara, K. (1993). Liquefaction and flow failure during earthquakes. *Géotechnique*, *43*(3): 351-451.

Ishihara, K. and Koga, Y (1981). Case studies of liquefaction in 1964 Niigata Earthquake. *Soils and Foundations,* 21 (3): 32-52.

Ishihara, K., Kawase, Y., and Nakajima, M (1980). Liquefaction Characteristics of Sand Deposits at an Oil Tank Site during the 1978 Miyagiken-Oki Earthquake, *Soils and Foundation, Japanese Society of Soil Mechanics and Foundation Engineering,* 20(2): 97-111.

Ishihara, K. and Koseki, J. (1989). Cyclic shear strength of fines-containing sands. *Proceeding 12th International Conference of Soil Mechanics, Rio de Janeiro*, 101-106.

Ishihara, K., and Okada, S. (1982). Effect of large preshearing on cyclic behavior of sand. *Soils and Found.*, Tokyo, 22(3): 109–125.

Ishihara, K., Tatsuoka, F. and Yasuda, S. (1975). Undrained deformation and liquefaction of sand under cyclic stress. *Soils and Foundations,* 15 (1): 29–44.

Ishihara, K., Tsukamoto, Y., Nakazawa, H., Kamada, K. and Huang, Y. (2002). Resistance of partly saturated sand to liquefaction with reference to longitudinal and shear wave velocities. *Soils and Foundations*. 42(6): 93–105.

Joer, H. A., Erbrich, C. T., and Sharma, S. S. (2011). *A new interpretation of the simple shear test* (pp. 353-358). London, UK: Taylor & Francis.

Kayen, R. E., and Mitchell, J. K. (1997). Assessment of liquefaction potential during earthquakes by Arias intensity. *Journal of Geotechnical and Geoenvironmental Engineering*, 123(12): 1162-1174.

Kirkpatrick, W. M. and Belshaw, D. J. (1968). On the interpretation of the triaxial test. *Géotechnique*, 18(*3): 336-350.*

Kokusho, T. (2013). Liquefaction potential evaluations: energy-based method versus stress-based method. *Canadian Geotechnical Journal,* 50(10): 1088-1099.

Kokusho, T. (2017). Liquefaction potential evaluations by energy-based method and stress-based method for various ground motions: *Supplement. Soil Dynamics and Earthquake Engineering*, 95, 40-47.

Koseki, J., Wakamatsu, K., Sawada, S., & Matsushita, K. (2015). Liquefaction-induced damage to houses and its countermeasures at Minami-Kurihashi in Kuki City during the 2011 Tohoku Earthquake, Japan. *Soil Dynamics and Earthquake Engineering, 79: 391-400*

Kramer, S. L. (1996). *Geotechnical earthquake engineering*. Prentice Hall, Upper Saddle River, NJ 07458.

Kusumawardani, R., Suryolelono, K. B., Suhendro, B., and Rifa'i, A. (2016). The dynamic response of unsaturated clean sand at a very low frequency. *International Journal of Technology, Jurnal Teknik Sipil dan Perencanaan, 1*.

Kwan, W. S., and El Mohtar, C. E. (2018). A review on sand sample reconstitution methods and procedures for undrained simple shear test. *International Journal of Geotechnical Engineering,* 1-9.

Lai, C. G., Bozzoni, F., Mangriotis, M. D., and Martinelli, M. (2015). Soil Liquefaction during the 20 May 2012 M5. 9 Emilia Earthquake, Northern Italy: Field Reconnaissance and Post-Event Assessment. *Earthquake Spectra*, *31*(4): 2351-2373.

Law, K. T., Cao, Y. L., & He, G. N. (1990). An energy approach for assessing seismic liquefaction potential. *Canadian Geotechnical Journal,* 27(3): 320-329.

Lee, K. L., and Albaisa, A. (1974). Earthquake induced settlements in saturated sands. *J. Geotech. Engrg. Div.*, 100(4): 387–406.

Lees J J, Ballagh R H, Orense R P, van Ballegooy S (2015). CPT-based analysis of liquefaction and re-liquefaction following the Canterbury earthquake sequence. *Soil Dynamics and Earthquake Engineering*, 79, 304-314.

Li, X. S. and Wang, Y. (1998). Linear representation of steady-state line for sand. *J. Geotech. Geoenviron. Engng ASCE*, 124 (12): 1215–1217.

Liang, L., Figueroa, J. L., and Saada, A. S. (1995). Liquefaction under random loading: unit energy approach. *Journal of Geotechnical Engineering*, 121(11): 776-781.

Lombardi, D., and Bhattacharya, S. (2014). Liquefaction of soil in the Emilia-Romagna region after the 2012 Northern Italy earthquake sequence. *Natural hazards*, *73*(3): 1749-1770.

Marcuson, W. F. (1978). Definition of terms related to liquefaction. *Journal of the Geotechnical engineering division*, *104*(9): 1197-1200.

Martin, G. R., Finn, W. L., and Seed, H. B. (1975). Fundementals of liquefaction under cyclic loading. *Journal of Geotechnical and Geoenvironmental Engineering*, *101*(ASCE) 11231 Proceeding).

Mihalache, C., and Buscarnera, G. (2016). Controllability criteria for soils saturated by a compressible fluid. *Journal of Engineering Mechanics*, *142*(10): 04016076.

Mitchell, J.K., and Wentz, F.J., (1991). Performance of improved ground during the Loma Prieta Earthquake. *University of California, Berkeley UCB/EERC* Report 91/12.

Mitchell, J. K., Baxter, C. D. P., and Munson, T. C. (1995). Performance of improved ground during earthquakes. *Soil improvement for earthquake hazard mitigation, ASCE Geotechnical Special Publication* No. 49, 423-438.

Mulilis, J. P., Arulanandan, K., Mitchell, J. K., Chan, C. K., and Seed, H. B. (1977). Effects of sample preparation on sand liquefaction. *Journal of the Geotechnical Engineering Division*, *103*(2): 91-108.

Murthy, T. G., Loukidis, D., Carraro, J. A. H., Prezzi, M., and Salgado, R. (2007). Undrained monotonic response of clean and silty sands. *Géotechnique*, *57*(3): 273-288.

Mutman, U., and Kavak, A. (2011). Improvement of granular soils by low pressure grouting. *International Journal of the Physical Sciences*, *6*(17): 4311-4322.

Nagao, K., Suemasa, N., Jinguuji, M., Nakazawa, H., (2015). In-situ applicability test of soil improvement for housing sites using Micro-Bubbles against soil liquefaction in URAYASU. *The twenty-fifth international ocean and polar engineering conference. International Society of Offshore and Polar Engineers*.

National Academies of Sciences, Engineering, and Medicine. (2016). State of the art and practice in the assessment of earthquake-induced soil liquefaction and its consequences. *Washington, DC: The National Academies Press. doi*, *1017226*, 23474.

Nemat-Nasser, S., and Shokooh, A. (1979). A unified approach to densification and liquefaction of cohesionless sand in cyclic shearing. *Canadian Geotechnical Journal*, *16(4): 659-678.*

Ochoa-Cornejo F., Bobet A., Johnston C. T., Santagata M., Sinfield J. V., (2016). Cyclic behaviour and pore pressure generation in sands with laponite, a super-plastic nanoparticle. *Soil Dynamics and Earthquake Engineering*, 88, 265-279.

Oda, M, Kawamoto K, Suzuki K, Fujimori H, Sato M (2001). Microstructural interpretation on reliquefaction of saturated granular soils under cyclic loading. *Journal of Geotechnical and Geoenvironmental Engineering ASCE*, 127 (5): 416-423.

Okamura M, Soga Y. (2006). Effects of pore fluid compressibility on liquefaction resistance of partially saturated sand. *Soils and Foundations*;46(5):695‑700.

Okamura, M., Ishihara, M. & Tamura, K. (2006). Degree of saturation and liquefaction resistances of sand improved with sand compaction pile. *J. Geotech. Geoenviron. Engng, ASCE* 132(2): 258-264.

Okamura M, Takebayashi M, Nishida K, Fujii N, Jinguji M, Imasato T, Yasuhara H, Nakagawa E. (2010). In-Situ desaturation test by air injection and its evaluation through field monitoring and multiphase flow simulation. *J. Geotech. Geoenviron. Engng ASCE*;137(7): 643‑52.

Pan, K., and Yang, Z. X. (2017). Evaluation of the liquefaction potential of sand under random loading conditions: Equivalent approach versus energy-based method. *Journal of Earthquake Engineering*, 1-25.

Polito, C. P., Green, R. A., and Lee, J. (2008). Pore pressure generation models for sands and silty soils subjected to cyclic loading. *Journal of Geotechnical and Geoenvironmental Engineering*, *134*(10): 1490-1500.

Polito, C., Green, R. A., Dillon, E., and Sohn, C. (2013). Effect of load shape on relationship between dissipated energy and residual excess pore pressure generation in cyclic triaxial tests. *Canadian Geotechnical Journal*, 50(11): 1118-1128.

Porcino, D. D., and Diano, V. (2017). The influence of non-plastic fines on pore water pressure generation and undrained shear strength of sand-silt mixtures. *Soil Dynamics and Earthquake Engineering*, *101*: 311-321.

Priebe, H.J., (1989). The prevention of liquefaction by vibro-replacement. *Proc., Earthquake Resistance Construction and Design*, Berlin, Germany.

Priebe, H.J., (1991). Vibro-replacement-design criteria and quality control. *In: Esrig, Bachus (Eds.), Deep Foundation Improvements: Design, Construction, and Testing, ASTM STP* 1089: 62- 72. Philadelphia.

Riemer, M. F., and Seed, R. B. (1997). Factors affecting apparent position of steady-state line. *Journal of geotechnical and geoenvironmental engineering*, *123*(3): 281-288.

Robertson, P.K. and Wride C.E. (1998). Evaluating cyclic liquefaction potential using the cone penetration test. *Can. Geotech. Journal, 35(3): 442-459.*

Rockwood Additives Ltd. (2011). Laponite performance additives. Specification sheet.

Santagata M., Bobet A., El Howayek A., Ochoa-Cornejo F., Sinfield J.V., Johnston C.T., (2014). Building a nanostructure in the pore fluid of granular soils. *In: Soga K., Kumar K., Biscontin G., Kuo M. (eds.) Geomechanics from Micro Macro*. 1377-1383.

Sasaki, Y,, and Taniguchi, E. (1982). Shaking Table Tests on Gravel Drains to Prevent Liquefaction of Sand Deposits, *Soils and Foundations, Japanese Society of Soil Mechanics and Foundation Engineering*, 22(3): 1-14.

Sassa, S., and Takagawa, T. (2019). Liquefied gravity flow-induced tsunami: first evidence and comparison from the 2018 Indonesia Sulawesi earthquake and tsunami disasters. *Landslides, 16*(1): 195-200.

Schofield, A., and Wroth, C. P. (1968). Critical state soil mechanics. *London: McGraw-Hill*.

Sciarra, A., Cantucci, B., Buttinelli, M., Galli, G., Nazzari, M., Pizzino, L., and Quattrocchi, F. (2012). Soil-gas survey of liquefaction and collapsed caves during the Emilia seismic sequence. *Annals of Geophysics, 55*(4).

Seed, H.B., and Booker, J.R., (1976). Stabilization of potentially liquefiable sand deposits using gravel drains. *ASCE, J. Geotech. Eng. Div*. https://doi.org/10.1017/CBO9781107415324.004.

Seed, H.B. and Idriss, I.M. (1971). Simplified Procedure for Evaluating Soil Liquefaction Potential. *Journal of the Soil Mechanics and Foundations Division ASCE* 97(SM9): 1249-1273.

Seed, H. B., and Lee, K. L. (1966). Liquefaction of saturated sands during cyclic loading. *Journal of the Soil Mechanics and Foundations Division*, 92(6):105-134.

Seed, H. B., Martin, P. P., and Lysmer, J. (1975). The generation and dissipation of pore water pressures during soil liquefaction. *Rep. No. EERC 75-26, Univ. of California, Berkeley, California.*

Seed, H. B., Mori, K., and Chan, C. K. (1977). Influence of seismic history on liquefaction of sands. *Journal of Geotechnical and Geoenvironmental Engineering, 103* (Proc. Paper 11318 Proceeding).

Severi, P. and Staffilani, F. (2012). Geologia ed Idrogeologia della pianura Ferrarese. *WARB Conference, Copparo Ferrara, Italy.*

Sharma, S. S., Ramsey, N., Lee, F. and Bhattarai B.N. (2017). Challenges in assessing the shear strength of offshore sediments using simple shear tests. *Proc., Geotechnical Frontiers 2017: Geotechnical Materials, Modelling and Testing, Orlando, Florida*, 327-336.

Sivathayalan, S., and Vaid, Y. P. (2002). Influence of generalized initial state and principal stress rotation on the undrained response of sands. *Canadian Geotechnical Journal, 39(1): 63-76.*

Sivathayalan, S., Logeswaran, P., and Manmatharajan, V. (2014). Cyclic resistance of a loose sand subjected to rotation of principal stresses. *Journal of Geotechnical and Geoenvironmental Engineering*, *141*(3): 04014113.

Soga, K. (1998). Soil liquefaction effects observed in the Kobe earthquake of 1995. *Proceedings Of The Institution Of Civil Engineers-Geotechnical Engineering*, 131(1), 34-51.

Sumer, B. M., Kaya, A., & Hansen, N. E. O. (2002). Impact of liquefaction on coastal structures in the 1999 Kocaeli, Turkey earthquake. In *The Twelfth International Offshore and Polar Engineering Conference*. International Society of Offshore and Polar Engineers.

Suzuki, T., and Suzuki, T. (1988). Effects of density and fabric change on reliquefaction resistance of saturated sand. *J. Japanese Geotech. Soc.*, Tokyo, 28(2): 187–195 (in Japanese).

Tatsuoka, F., Ochi, K., Fujii, S., and Okamoto, M. (1986). Cyclic undrained triaxial and torsional shear strength of sands for different sample preparation methods. *Soils and Foundations*, *26*(3): 23-41.

Terzaghi, K. (1925). Principles of soil mechanics. *Engineering News-Record*, *95*(19-27), 19-32.

Thevanayagam, S. and Martin, G.R. (2002). Liquefaction in silty soils screening and remediation issues. *Soil Dynamics and Earthquake Engineering*, 22: 1035–1042.

Toki, S., Miura, S., and Tanizawa, F. (1981). A few remarks on the relationship between relative density and strength characteristics of sand. *Proc., Symp. on Relative Density and Engrg. Characteristics of Sand*, 78–86 (in Japanese).

Towhata, I., and Ishihara, K. (1985a). Shear work and pore water pressure in undrained shear. *Soils and foundations*, 25(3), 73-84.

Towhata, I., & Ishihara, K. (1985b). Undrained strength of sand undergoing cyclic rotation of principal stress axes. *Soils and Foundations*, *25*(2), 135-147.

Tsukamoto, Y., Kawabe, S., Matsumoto, J., and Hagiwara, S. (2014). Cyclic resistance of two unsaturated silty sands against soil liquefaction. *Soils and Foundations*, *54*(6): 1094-1103.

Unno, T., Kazama, M., Uzuoka, R., and Sento, N. (2008). Liquefaction of unsaturated sand considering the pore air pressure and volume compressibility of the soil particle skeleton. *Soils and Foundations*, *48*(1): 87-99.

Uzuoka, R., Yashima, A., Kawakami, T., and Konrad, J. M. (1998). Fluid dynamics based prediction of liquefaction induced lateral spreading. *Computers and Geotechnics*, *22*(3-4): 243-282.

Vaid, Y. P., and Sivathayalan, S. (1996). Static and cyclic liquefaction potential of Fraser Delta sand in simple shear and triaxial tests. *Canadian Geotechnical Journal*, *33*(2): 281-289.

Vanapalli, S. K., Fredlund, D. G., Pufahl, D. E. and Clifton, A. W. (1996). Model for the prediction of shear strength with respect to soil suction. *Can. Geotech. J*. 33(3): 379–392.

Vannucchi, G., Crespellani, T., Facciorusso, J., Ghinelli, A., Madiai, C., Puliti, A., & Renzi, S. (2012). Soil liquefaction phenomena observed in recent seismic events in Emilia-Romagna Region, Italy. *International Journal of Earthquake Engineering*, *2*(3).

Wakamatsu, K (2012). Recurrent liquefaction induced by the 2011 Great East Japan earthquake compared with the 1987 earthquake. *The International Symposium on Engineering Lessons Learned from the 2011 Great East Japan Earthquake*, Tokyo, Japan.

Wang H, Koseki J, Sato T, Chiaro G, Tan Tian J (2016). Effect of saturation on liquefaction resistance of iron ore fines and two sandy soils. *Soils and Foundations*; 56(4):732‑44.

Watanabe, T. (1966). Damage to oil tank refinery plants and a building on compacted ground by the Niigata earthquake and their restoration. *Soils and Foundations*, 6 (2): 86-99.

Wheeler, S. J., Sharma, R. S. and Bulsson, M. S. R. (2003). Coupling of hydraulic hysteresis and stress–strain behaviour in unsaturated soils. *Géotechnique,* 53(1): 41–54, https://doi.org/10.1680/ geot.2003.53.1.41

Wu, J, Kammerer, A. M., Riemer, M. F., Seed, R. B., and Pestana, J. M. (2004). Laboratory study of liquefaction triggering criteria. In *13th world conference on earthquake engineering, Vancouver, BC, Canada, Paper* (No. 2580).

Yang, J., (2004). Evaluating liquefaction strength of partially saturated sand. *Journal of Geotechnical and Geoenvironmental Engineering, ASCE* 130 (9): 975–979.

Yang, Z., and Cheng, X. (2013). A performance study of high-strength microbial mortar produced by low pressure grouting for the reinforcement of deteriorated masonry structures. *Construction and Building Materials*, *41*, 505-515.

Yasuda, S., and Harada, K. (2014). Measures developed in Japan after the 1964 Niigata earthquake to counter the liquefaction of soil. *10NCEE, Paper No. 1778, Frontiers of Earthquake Engineering*, 21-25.

Yasuda, S., and Tohno, I. (1988). Sites of reliquefaction caused by the 1983 Nihonkai-Chubu earthquake. *Soils and Foundations, 28*(2): 61-72.

Yegian, M. K., Eseller-Bayat, E., Alshawabkeh, A. and Ali, S. (2007). Induced-partial saturation for liquefaction mitigation: experimental investigation. *J. Geotech. Geoenviron. Engng ASCE* 133(4): 372–380.

Yegian, M. K., Eseller, E. and Alshawabkeh, A. (2006). Preparation and cyclic testing of partially saturated sands. *Proc. 4th Int. Conf. on Unsaturated Soils (GSP 147),* Carefree, AZ, 508-518

Yoshimi, Y., Tokimatsu, K. and Hosaka, Y. (1989). Evaluation of liquefaction resistance of clean sands based on high-quality undisturbed samples. *Soils and Foundations,* 29(1): 93-104.

Youd, T. L. (2014). Ground failure investigations following the 1964 Alaska earthquake. *DOI: 10.4231/D3DN3ZW6P*.

Zeybek, A. (2017). Air Injection Technique to Mitigate Liquefaction beneath Shallow Foundations. *Ph.D. thesis, University of Cambridge*.

Zhou, E. Q., Lv, C., Wang, Z. H., and Chen, G. X. (2014). Fluid Characteristic of Saturated Sands under Cyclic Loading. *In Advances in Soil Dynamics and Foundation Engineering (pp. 178-186).*

CHAPTER 3

3. FIELD TRIAL IN PIEVE DI CENTO (BOLOGNA, ITALY)

Within the LIQUEFACT project, in order to assess the effectiveness of several mitigation measurements against liquefaction, a test-site was selected jointly with local authorities (i.e. Emilia Romagna Region and Municipality of Pieve di Cento). It was located in Pieve di Cento municipality (Fig. 3.1) (Bologna, Italy), in the Po valley, where extensive liquefaction phenomena occurred during the 2012 earthquake (M_w=6.1) (Fig. 3.2).

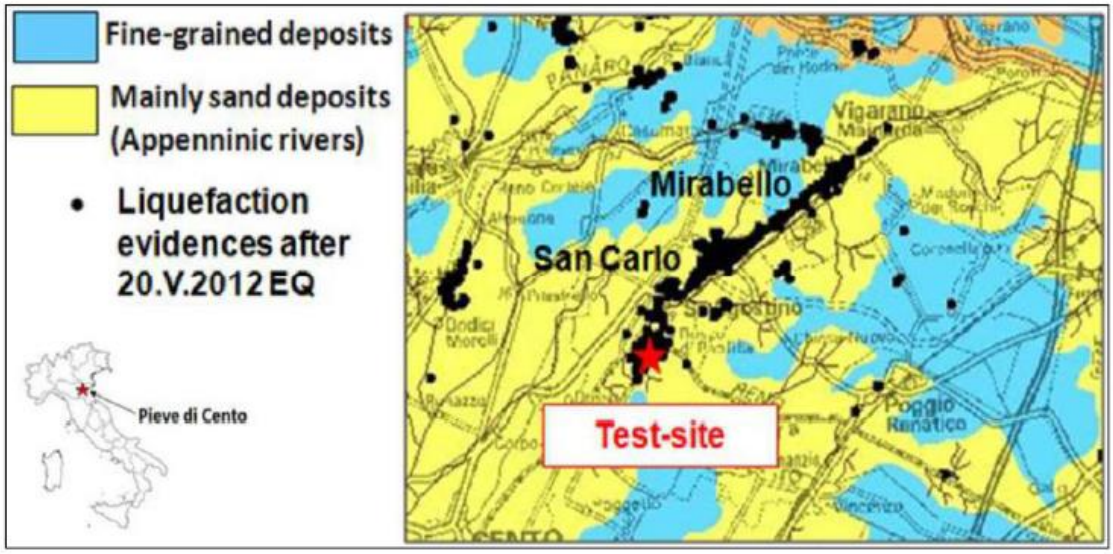

Figure 3.1. Location of the test site (Trevi spa).

(a) (b)

Figure 3.2. Liquefaction phenomena occurred in the test field area (Trevi spa).

In the Report of the LIQUEFACT project (D4.3), under the responsibility of Trevi spa, useful geological information has been reported and then collected and summarized in this thesis.

As shown in the Carta Geologica Italiana, Foglio n.75 MIRANDOLA (Fig. 3.3), Pieve di Cento is located in a bend of the current Reno River bed, in a paleochannel of the river. The subsoil is made of loose alluvial deposits which are extremely "young" from a geological point of view. The area is also characterized by the presence of Po river located just 18 km North, which runs roughly at the same elevation of Reno River in this area. Po and Reno rivers are connected by the so-called "Cavo Napoleonico"; it is an artificial channel which construction started in 1807, when the area was ruled by Napoleone Bonaparte.

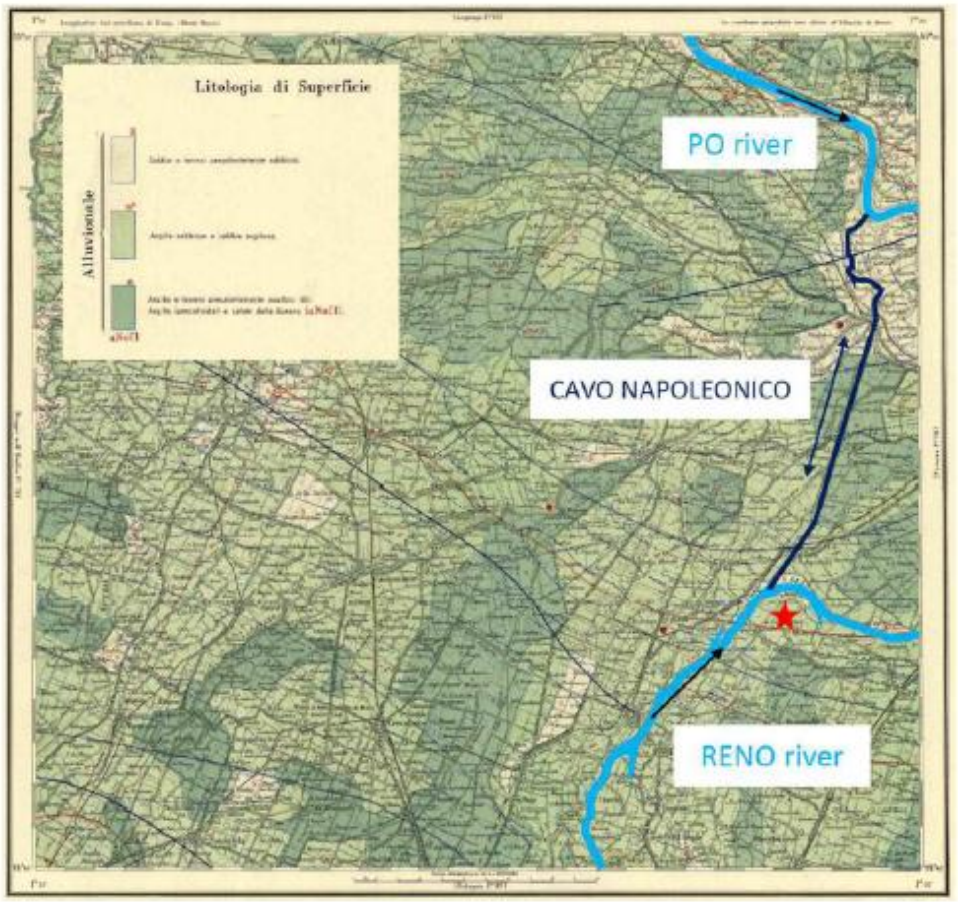

Figure 3.3. Italian Geologic Map, Foglio 75 Mirandola, test field location (red star) (Trevi spa).

3.1 DESCRIPTION OF THE FIELD TRIAL

With the main aim to define the mechanical behaviour of the soils before and after the liquefaction mitigation treatments, extensive in-situ and laboratory tests have been carried out.

Laboratory tests performed on Pieve di Cento soil samples make up one of the most important parts of this research and they will be shown in detail in Chapters 5 and 6.

Regarding in-situ tests, field investigation does not exceed 15 m from the ground surface, because, during the 2012 event, liquefaction involved only the shallowest layers.

Ground investigation was carried out aiming to define the soil stratigraphic sequence and to obtain information on the geotechnical properties of the different soil layers. It consisted of:

- Sand retrieved by a backhoe in the first 2 meters (trial pit);
- 5 boreholes reaching 10 m below the ground surface (CH1bis, CH2, CH3, CH4, CH5);
- 4 additional boreholes (CH2bis, CH3bis, CH4bis, CH5bis) performed only for retrieving undisturbed samples (with Osterberg and Gel Push samplers);
- 5 boreholes (BH1, CH1, BH2, BH3, BH4) up to 10 m from ground level used for seismic investigations (cross-holes tomographies).
- 5 penetration tests with piezocone (CPTU1, CPTU2, CPTU3, CPTU4 and CPTU5) up to a depth of 11 m from ground level;
- an Electrical Resistivity Tomography (ERT) performed at the surface along the longitudinal section covering both areas (HD and IPS).

In this research, the attention was focused on the first 3 points of the aforementioned list, but it is important to underline that all of them, together with laboratory tests, have allowed to characterize the test-site of this project.

In Figure 3.4a the plan view of the geotechnical campaign is reported, while in Figure 3.4b the position of the trial pit is highlighted.

Figure 3.5 shows the undisturbed samples retrieved in the field trial from different boreholes.

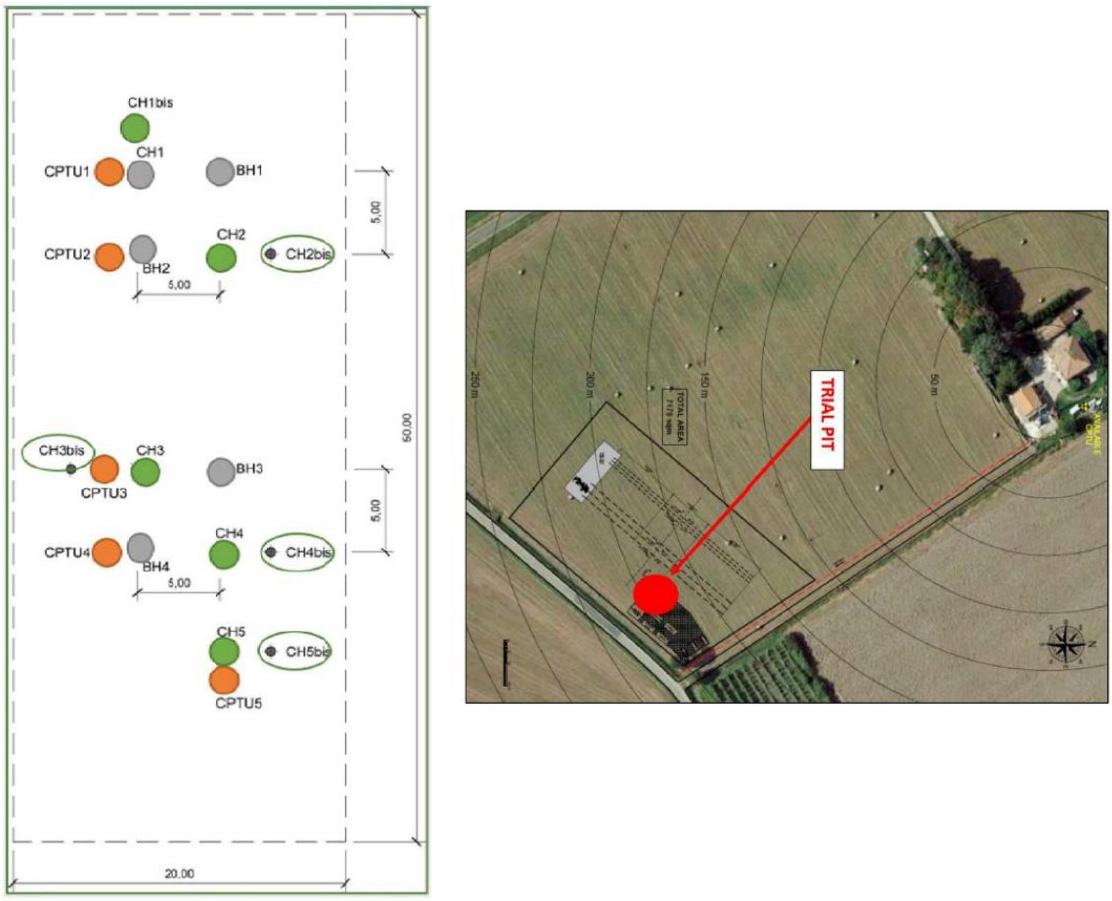

(a) (b)

Figure 3.4. Plan view of the investigated verticals (a) and of the trial pit (b) (Trevi spa).

Boreholes	date	Osterberg (m)	Gel Push (m)
CH1	04/09/2017		
CH1 BIS	08/09/2017	2,0-2,5	2,5-3,5
		3,5-4,0	
CH2	06/09/2017	3,0-3,5	4,5-5,5
		4,0-4,5	
CH3	06/09/2017	2,50-3,00	3,5-4,5
		4,50-5,00	
CH4	07/09/2017	2,00-2,50	5,0-6,0
		4,50-5,00	
CH5	11/09/2017	2,0-2,5	2,00-3,00
		3,5-4,0	

Figure 3.5. Undisturbed samples retrieved in the field trial (Trevi spa).

3.1.1 STRATIGRAPHY PROFILE

In the test-site of Pieve di Cento, sand was retrieved in the first 2 meters from a trial pit (Fig. 3.4b) by a backhoe. This sand has been widely characterized by means of laboratory tests, performed in the geotechnical laboratory of the University of Napoli Federico II (Chapters 5 and 6). It was characterized to have a brownish colour (Fig. 3.6a), owing to that it was called brown silty sand (BSS). Its grain size distribution curve is reported in Figure 3.6b, while the main physical properties are shown in Table 3.1. Moreover, mineralogical analysis on Pieve di Cento sand, where also carried out and the results can be found in Table 3.2.

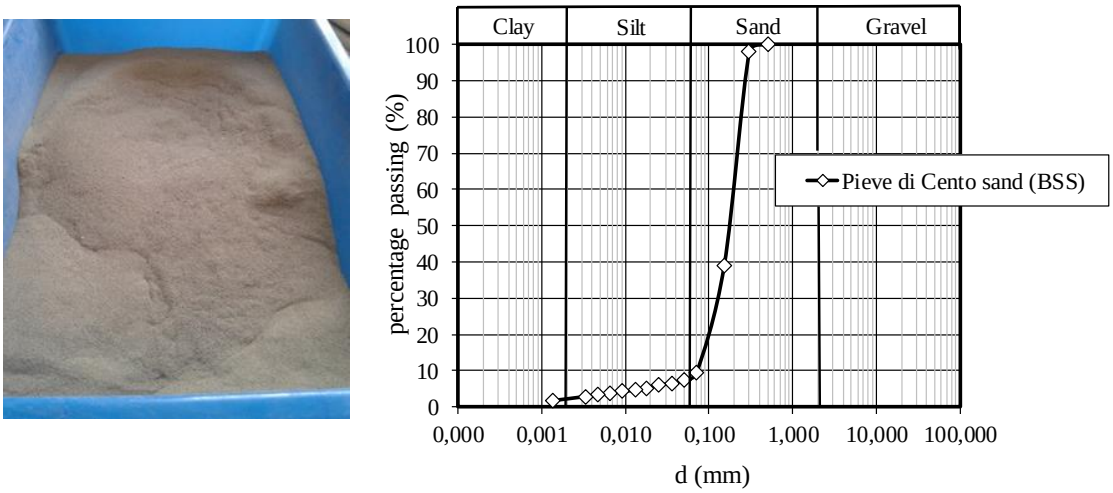

(a) (b)

Figure 3.6. Pieve di Cento sand (BSS), first 2 m from a pit trial: photos of dry sand (a) and grain size distribution curve (b).

Table 3.1. Pieve di Cento sand (BSS) properties.

	Pieve di Cento (BSS)
G_s	2.667
e_{max} - e_{min}	1.04 – 0.546
D_{50} (mm)	0.18
U_c	2.67
Fines content (%)	8

Table 3.2. Mineralogical analysis

Pieve di Cento Sand (BSS)	
Quartz	45 %
Calcite	20 %
Albite	15 %
Sanidiniti	7 %
Chlorinite	6 %
Mica	4 %
Kaolinite	3 %

Grain size analyses and Atterberg's limit tests (where possible) were carried out on soil samples retrieved from boreholes sampling (Fig. 3.7a). The grain size curves of samples from boreholes are plotted together in Figure 3.7b, compared to that of brown silty sand; while Table 3.3 shows the Atterberg's limits of finer materials. The Plasticity Index (PI) has been evaluated for each sample and it is plotted versus Liquid Limit (w_L) in Figure 3.8. It can be noted that the shallow finer soils (1.3 m < z < 2.8 m) are characterized by low plasticity, due to the fact that they contain a significant amount of sand and silt (Fig. 3.7b), while the deep finer soils (6.75 m < z < 8.3 m) are highly plastic, with value of PI between 37.5 and 56.9 % (Tab. 3.3).

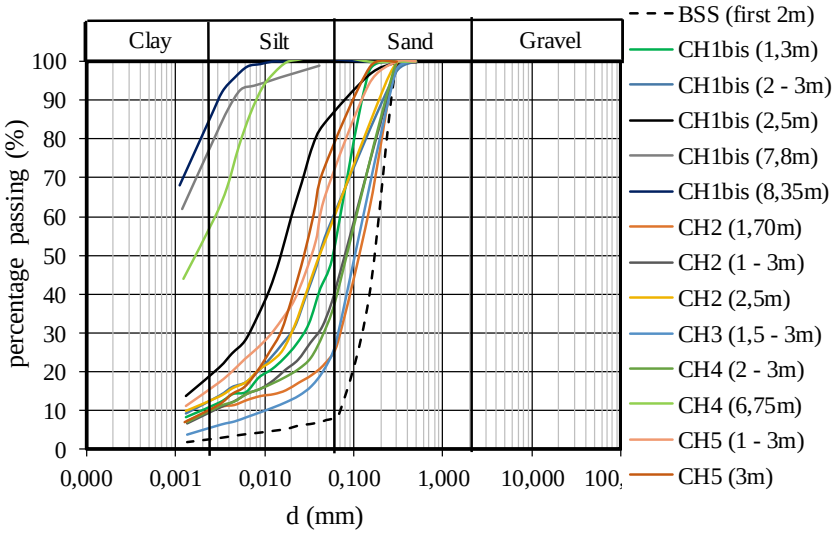

(a) (b)

Figure 3.7. Boreholes sampling (a) and grain size distribution curves of samples (b).

Table 3.3. Atterberg's limits.

Boreholes	z (m)	w_L (%)	w_P (%)	PI (%)
CH1bis	1.30	30.4	20.0	10.4
CH1bis	2.50	36.5	20.6	15.9
CH1bis	7.80	79.6	26.0	53.6
CH1bis	8.30	84.5	27.6	56.9
CH2	2.80	29.4	23.3	6.10
CH4	6.75	61.5	24.0	37.5

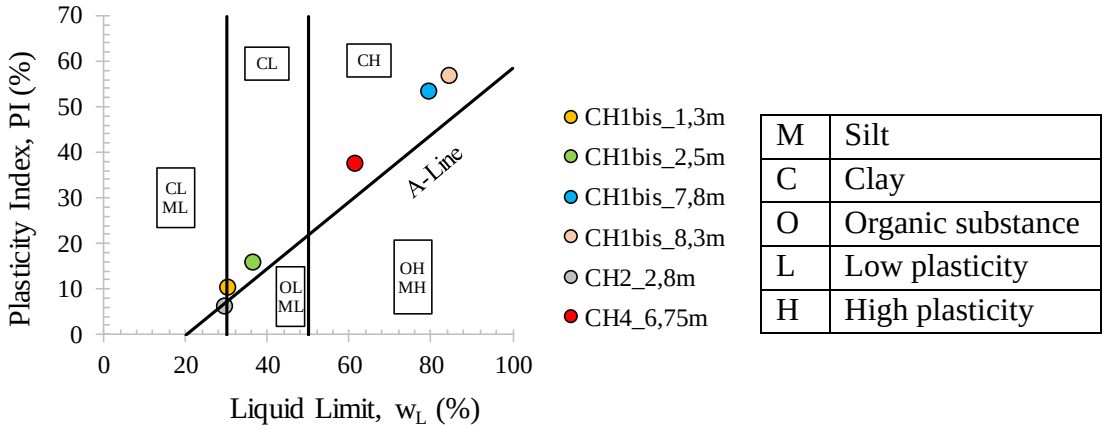

Figure 3.8. Plasticity chart of boreholes samples.

This information, together with the results of CPTu carried out at the test-site, but no reported in this research, have allowed to hypothesize the stratigraphy profile of Pieve di Cento till 10 m from ground surface as reported in Figure 3.9 (Chiaradonna et al., 2019). In the first 0.8 m below the ground surface, the presence of sandy silt can be noted, overlaying a layer of silty sand, which extends until 6 m, where a clayey layer goes on until 10 m and most likely over. A thin clayey layer was identified within the silty sand deposits between 4.4 and 4.7 m depth. The layer of silty sand is supposed to be the liquefiable layer. As pointed out by Vannucchi et al. (2012), for similar material and subsoil conditions identified at San Carlo site.

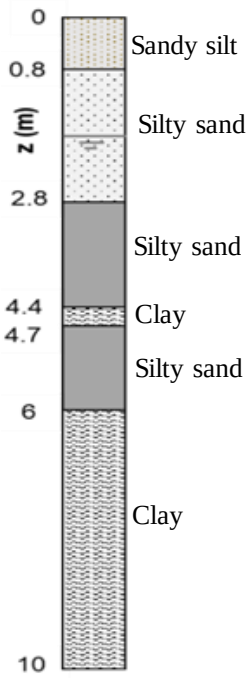

Figure 3.9. Stratigraphy profile of Pieve di Cento.

Due to the fact that the liquefiable layer is supposed to be the layer of silty sand below 2.8 m and even because interventions of mitigation are placed at a depth of 3 meters from the ground surface level, the sand samples were retrieved from the five boreholes at that depth, then mixed to achieve an "average sand", whose grain size distribution curve is plotted in Figure 3.10b, compared to that of brown silty sand. This 'average sand' has a greyish colour so that it is called grey silty sand (GSS) (Fig. 3.10a). The main physical properties of this material were determined and showed in Table 3.4, compared with those of BSS.

As already mentioned in paragraph 2.1.2, related to case histories and in particular to Emilia Romagna earthquake, Lombardi and Bhattacharya (2014) showed that the ejecta material consisted of grey silty sand with a significant amount of fine material, confirming the findings of this research.

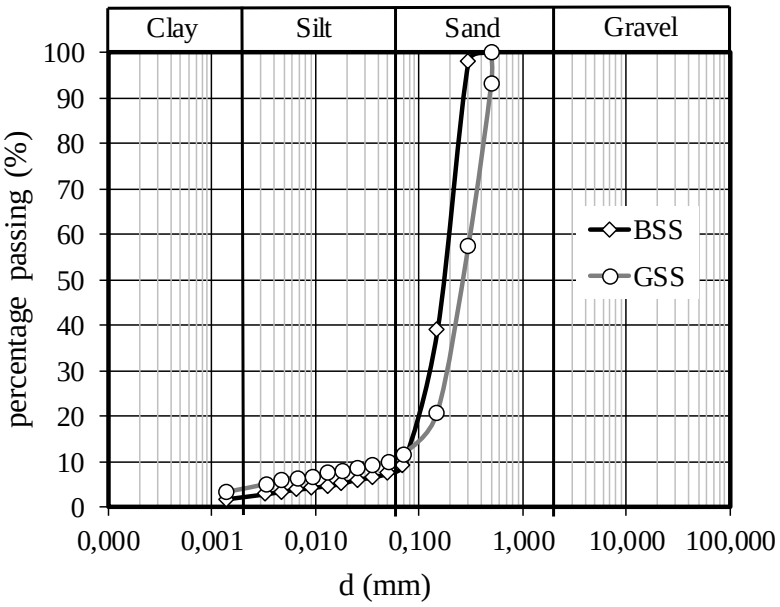

(a) (b)

Figure 3.10. Pieve di Cento sand: Grey Silty Sand (GSS): photo of dry sand (a) and grain size distribution curve (b).

Table 3.4. Pieve di Cento sand properties.

	Pieve di Cento (BSS)	Pieve di Cento (GSS)
G_s	2.667	2.655
e_{max} - e_{min}	1.04 – 0.546	0.884 – 0.442
D_{50} (mm)	0.18	0.28
U_c	2.67	5.00
Fines content (%)	8	11

3.2 UNDISTURBED SAMPLING

The undisturbed samples were collected by means of two different types of samplers: Osterberg piston sampler and a Gel Push sampler.

3.2.1 OSTERBERG SAMPLER

The Osterberg Sampler is a hydraulic sampler which is used to sample silty, clayey and fine granular soils. It consists of an external cylinder fitted on the sampler's head, an inner sliding sampling tube and a fixed piston at the centre of the pipe. Once the undisturbed soil is reached, the pressure of the water which fills the compression chamber above the sampling tube makes the latter start to embed into the soil. As the head of the sampling tube reaches the location of water's discharge lights, the pressure in the discharge chamber drops to zero, thus finalizing its embedment. Finally, the sampler is slightly rotated so as to cut the soil at the base of the sampling tube, which will contain an undisturbed sample of soil.

3.2.2 GEL-PUSHER SAMPLER

The Gel Push Sampler (GP-s) is a new sampling technology for sandy soils developed in Japan characterized by the use of a special polymer gel which, during sampling, is able of minimizing the friction between the soil sample and the sampler pipe. Such a sample is far less disturbed not only during the sampling but also during the extrusion phase in laboratory than a sample taken with Osterberg sampler. The application of the Gel Push Sampler for LIQUEFACT was the second one carried out in Italy and one of the first applications all over Europe. This sampler is made of three coaxial cylinders, the external one, named "outer tube", the "inner tube" and the sampler "stainless steel sampler"; the first one never moves, the other two, instead, move down the hole during sampling according to the three steps shown in Figure 3.11:

- Step (a) positioning phase: after drilling up to the sampling depth, rods are withdrawn and the internal chamber of the sampler is loaded with a special polymer slurry; then rods are set in place with the loaded sampler touching the bottom of the hole;
- Step (b) sampling phase: by applying a water pressure in a range between 2 and 5 MPa, the green piston is pushed down together with the inner tube and the stainless-steel sampler. The gel in the chamber is slowly replaced by water and it has two ways to go: mostly, it is discharged into soil through an upper no-return valve; a minor amount of gel moves down the anulus space between the sample and the inner tube, carrying out a double lubricating action. This gel helps the inner tube to move down into the soil creating, at the same time, a protective film between the sampler and the soil sample which nullifies lateral friction;

– Step (c) catching phase: once the gel in the chamber is fully replaced, water applies pressure between the green and the orange piston moving down, in that way, only the stainless-steel sampler. This phase allows the core-catcher to close making sure not to lose or weather material during extraction.

Soon after the collection, all the sample exposed surfaces were sealed with liquid paraffin and adhesive tape to guarantee proper conservation of its physical characteristics.

As will be shown in Chapter 5, Gel Pusher sampling seems to be a promising method to retrieve undisturbed sandy soil samples. They are extremely easy to extrude, because of gel (Fig. 3.12) and they preserve the relative density estimates in situ by means of the results of CPTu by using correlations proposed in literature.

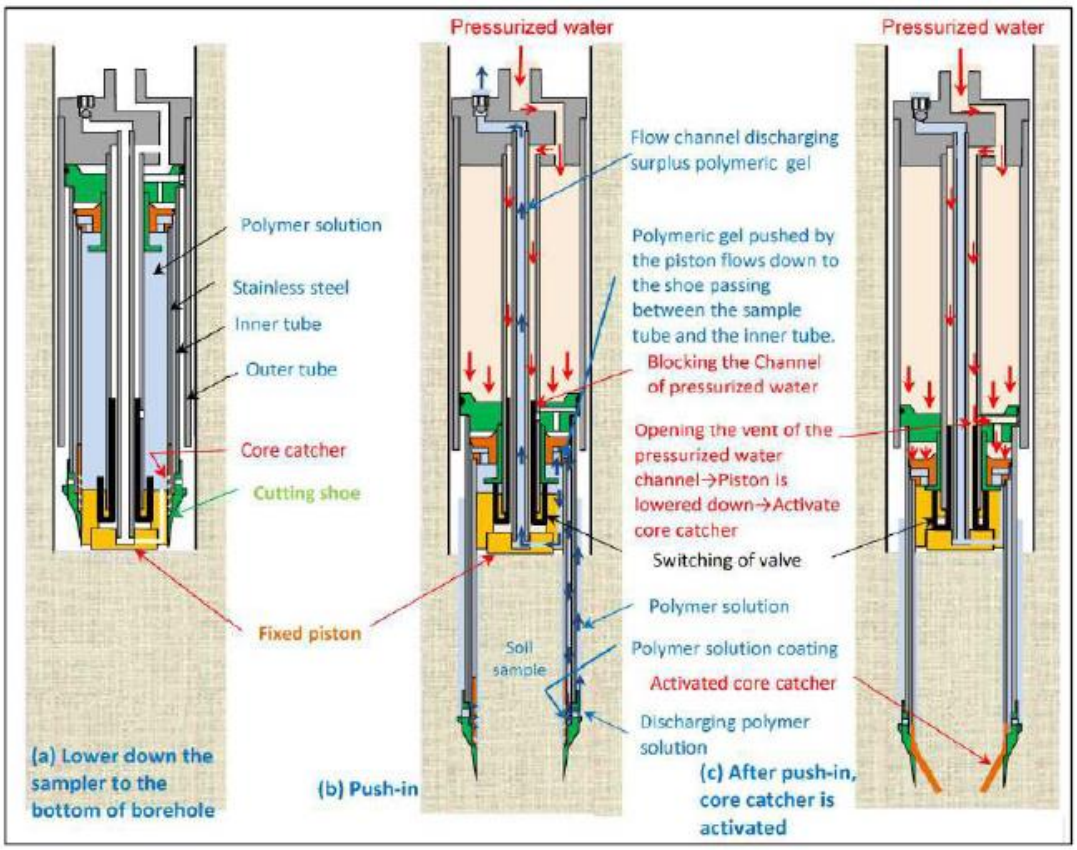

Figure 3.11. Gel Pusher sampler: positioning phase (a); sampling phase (b); catching phase (c) (Trevi spa).

Figure 3.12. Polimer gel around the sample (Trevi spa).

REFERENCES

Chiaradonna, A., Lirer, S., Flora, A. (2019). A damage-based liquefaction potential index for microzonation studies. *Engineering Geology* (Under review).

LIQUEFACT deliverable 4.3. Field trials at the selected case study pilot testing site. Trevi spa.

Lombardi, D., and Bhattacharya, S. (2014). Liquefaction of soil in the Emilia-Romagna region after the 2012 Northern Italy earthquake sequence. *Natural hazards*, *73*(3): 1749-1770.

Vannucchi, G., Crespellani, T., Facciorusso, J., Ghinelli, A., Madiai, C., Puliti, A., and Renzi, S. (2012). Soil liquefaction phenomena observed in recent seismic events in Emilia-Romagna Region, Italy. *International Journal of Earthquake Engineering*, *2*(3).

CHAPTER 4

4. EXPERIMENTAL ACTIVITY: MATERIALS AND LABORATORY DEVICES

Several laboratory tests were performed in this research on different materials and by means of different laboratory devices, as described in this chapter.

4.1 MATERIALS

In this section the materials tested in this research, are presented. Standard sands, well characterized by other researchers were tested, such as Leighton Buzzard (fraction E), Ticino, Silica (No. 5) and Inagi sands, which is an inland weathered sand widely found in the Tama district in the west of Tokyo, Japan. In addition, some Italian sands were studied, coming from Emilia Romagna region, which was affected by extensive liquefaction phenomena during the 2012 earthquake. In particular, two localities have been considered: Sant'Agostino and Pieve di Cento. The latter one is the site chosen by the members of the European project LIQUEFACT to test the effectiveness of some mitigation techniques against liquefaction, as already discussed in Chapter 3 of this thesis. Sant'Agostino (Ferrara, Italy) is located 13 km far from Pieve di Cento; there is here the sand was retrieved at a depth of 6.8 – 8m from ground surface. In addition, materials from mines have been tested such as bauxite, an aluminium ore (the main source of aluminium), characterized to have a red colour, for the presence of iron. Two types of bauxite have been studied, a coarser and a finer one. The coarser was obtained from Australia through a Japanese company, while the finer one comes from a Spanish mine (San Ciprian) in Northern Spain.
For greater clarity, the grain size distribution curves have been plotted separately, according the following subdivision: standard sands (Leighton Buzzard, Ticino, Inagi and Silica (No. 5) sands) in Figure 4.1a; Italian sands (Sant'Agostino and Pieve di Cento sands) in Figure 4.2a and mine's soils (bauxite, finer and coarser) in Figure 4.3a. Furthermore, the main physical properties of those materials have been reported in Table 4.1.
As for Pieve di Cento sand (BSS) (Chapter 3), a mineralogical analysis of Sant'Agostino sand has been carried out through X-ray diffraction testing. That sand is composed mainly by quartz, along with feldspar and calcite. The optical microscopic image is also reported in Figure 4.2.

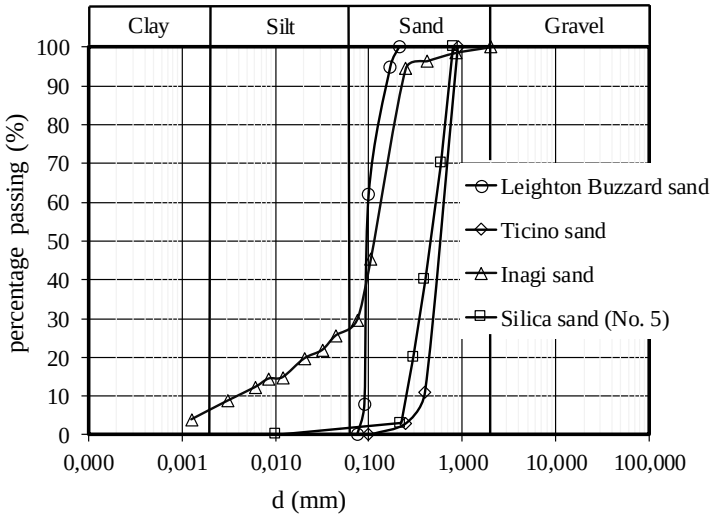

(a)

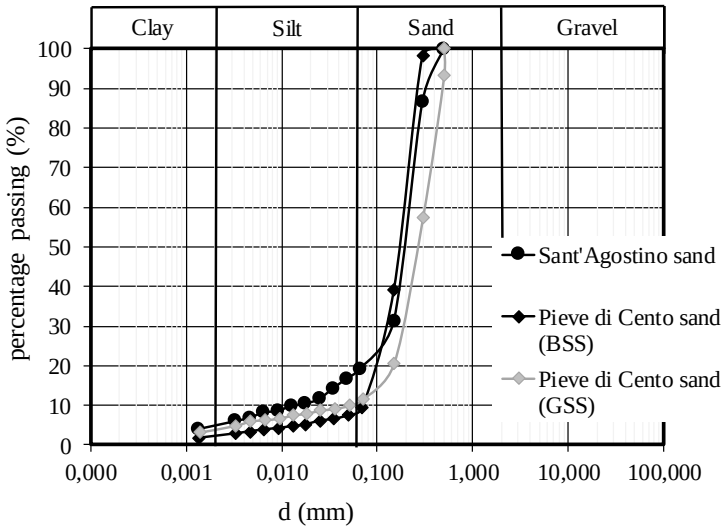

(b)

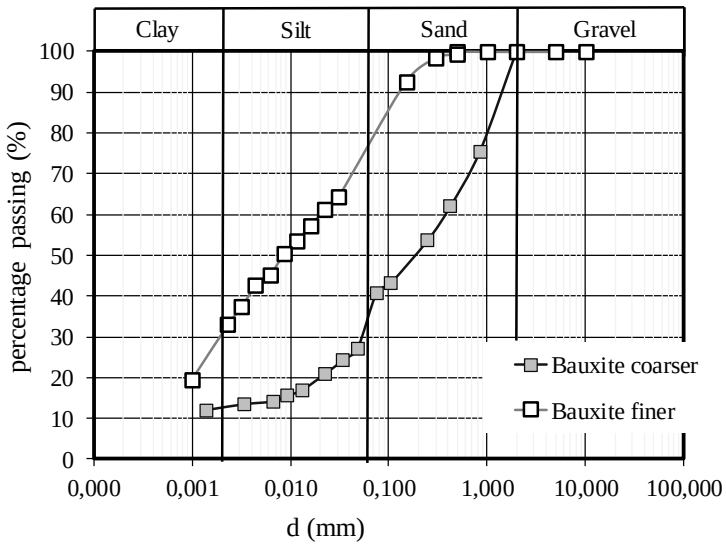

(c)

Figure 4.1. Soils tested in this research: standard sands (a); Italian sands (b) and mine's soils (c).

Table 4.1. Main physical properties of the tested materials.

Material	Specific gravity, G_s	e_{max}-e_{min}	D_{50} (mm)	Uniformity coefficient, U_c	Fines content, FC (%)
Leighton Buzzard*	2.65	1.01 – 0.613	0.100	1	0.0
Ticino**	2.68	0.923 – 0.574	0.530	1	0.0
Inagi***	2.66	1.64 – 0.907	0.115	30	29.5
Silica No.5****	2.64	1.11 – 0.695	0.471	1.9	0.0
Sant'Agostino	2.67	1.01 – 0.370	0.200	16.7	20.0
Pieve di Cento (BSS)	2.67	1.04 – 0.546	0.180	2.67	8.0
Pieve di Cento (GSS)	2.65	0.884 – 0.442	0.300	5.0	12.0
Bauxite coarser***	2.64	-	0.200	400	40.6
Bauxite finer	3.58	-	0.009	>20	80.0

*Visone (2008); **Fioravante and Giretti (2016); ***Tan Tian (2019); ****Lin et al. (2017; 2018).

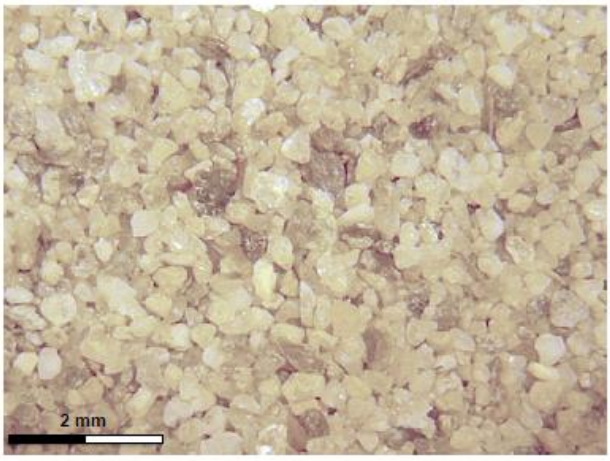

Figure 4.2. Microscopic image of Sant'Agostino sand.

The value of e_{max} and e_{min} for the tested materials have been evaluated according the standard ASTM D4253 and ASTM D4254. Because of the high percentage of fine content in bauxite materials, those values could not be determined and in particular for the coarser bauxite, the degree of compaction (D_c) was considered instead of the relative density (D_r). The degree of compaction is defined as the ratio between the dry density of the specimen (ρ_d) and the maximum dry density (ρ_{dmax}), which is 1.70 g/cm^3 for the coarser bauxite. Regarding the finer bauxite, it is worth noting that the presence of iron is confirmed by the high value of G_s (3.58; Tab. 4.1).

To investigate the plasticity of that material, Atterberg's limits have been evaluated and reported below:

$$w_L = 31.7\% \; w_P = 30.0\% \text{ and then, } PI = w_L - w_P = 1.7\%$$

and plotted in the plasticity chart in Figure 4.3. It is possible to note that despite the high fines content (80%), the plasticity index (PI) is extremely low.

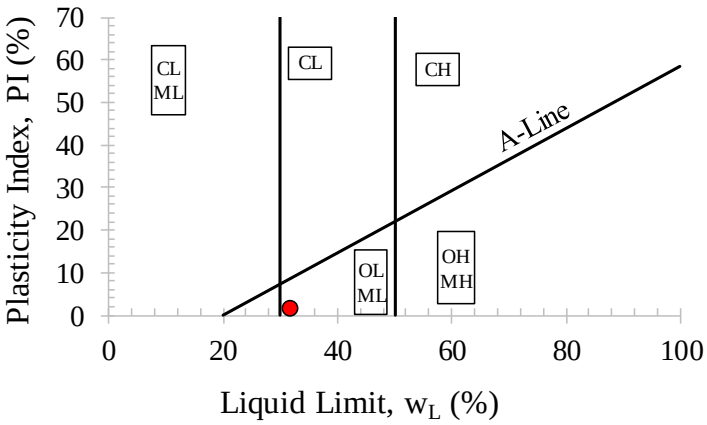

M	Silt
C	Clay
O	Organic substance
L	Low plasticity
H	High plasticity

Figure 4.3. Plasticity chart for finer bauxite.

4.2 LABORATORY DEVICES

As already mentioned, the experimental activity played an important role in this research. Monotonic and cyclic (triaxial and simple shear) tests have been performed by means of several laboratory devices, which will be described briefly in the following paragraphs.

4.2.1 TRIAXIAL CELL BISHOP&WESLEY (UNIVERSITY OF NAPOLI, FEDERICO II)

A triaxial cell Bishop & Wesley (Fig. 4.4), available at University of Napoli Federico II, has been used with the main aim to characterize the soils under monotonic and cyclic loading.
It is possible through a double configuration, which allows to work in stress and strain controlled conditions.
The hydraulic stress-path cell allows to control independently three pressures: axial, radial and back pressure, by means of a Watson regulator. The air pressure is transferred to the water in the cell and in the lower chamber of the ram by means of air/water interfaces, while a volume gauge is also used to measure the volume of water which goes in or out from the specimen. The cell is also provided of several transducers to measure cell pressure, pore pressure, an LVDT (Linear Vertical Displacement Transducer) to evaluate the settlements of the specimens and a load cell which can measure until 3 kN.
In such apparatus, the deviatoric stress q, is related to the pressure σ_r in the chamber at the base of the ram and the pressure σ_c in the cell by the simple vertical equilibrium equation (Bishop and Wesley, 1975):

$$q = \frac{1}{A_s} \cdot (\sigma_r \cdot A_l - \sigma_c \cdot A_u - W) \quad (4.1)$$

where W is the weight of the ram, A_s is the cross section of the specimen, and A_l and A_u are, respectively, the area of the cross section of the lower and the upper flexible rollseal diaphragms. This seal is indicated as bellofram in Fig. 4.4a.
Furthermore, a suction cup allows to perform cyclic triaxial and monotonic tests (extension), keeping the top of the specimen fixed at the load cell by means of a vacuum system.
In strain conditions the ram is driven by a stepper motor, where the deformation rate can be chosen by operator. The acquisition system is based on and A/D card located in a personal computer.

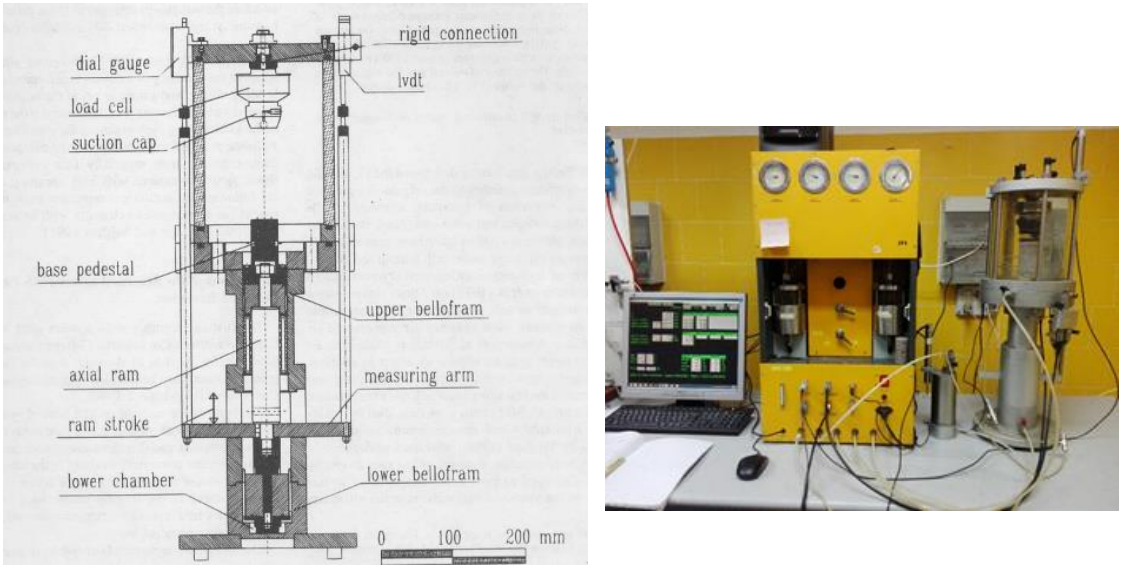

(a) (b)

Figure 4.4. Bishop & Wesley triaxial cell (University of Napoli, Federico II): cross section scheme (Aversa and Vinale, 1995) (a) and photo in the geotechnical laboratory of Federico II University of Napoli (b).

4.2.1.1 SPECIMEN'S PREPARATION AND TEST METHODOLOGY

The specimens have been prepared by water sedimentation technique. According to it, dry sand is pluviated in a steel mould, containing water (Fig. 4.5a), whose dimensions are d=38 mm and h=76 mm. Thereafter, they are frozen (Fig. 4.5b).

(a) (b)

Figure 4.5. Preparation of a specimen for a triaxial test in a Bishop & Wesley apparatus (a) and frozen specimen (b).

The testing phases can be summarized in the following points:

- Thawing in drained condition;
- Saturation;

- Consolidation;
- Deviatoric (monotonic or cyclic) loading.

In some cyclic tests two more phases have been performed:

- Re-consolidation;
- Re-loading (second liquefaction).

The first phase of the test was thawing in drained condition imposing a low isotropic confining effective pressure of 10 kPa. This phase is followed by saturation, which allows to reach a degree of saturation (S_r) approximately equal to 1, which corresponds to a B value or Skempton coefficient larger than 0.98.

After the specimen was saturated (B>0.98), an isotropic confining stress was applied, and then the deviatoric phase can start, imposing a monotonic or a cyclic loading.

In monotonic tests, the velocity of strain can be imposed. In this research 0.5 %/h and 1.0 %/h have been chosen for drained and undrained tests, respectively.

In cyclic test a frequency of 0.008 Hz has been imposed. The choice of this low value allows to avoid backlash phenomena.

To test the post-liquefaction behaviour, the specimens were re-consolidated and then a new cyclic phase was imposed, with the same methodology already described.

4.2.2 TRIAXIAL CELL "MATRIX" (UNIVERSITY OF NAPOLI, FEDERICO II)

Some drained and undrained monotonic tests have been performed in a MaTrix triaxial cell at the University of Napoli, Federico II. It was designated at the University of Tokyo (Tatsuoka et al., 1994, Santucci de Magistris et al., 1999), where it is very common.
The basic components of MaTRIX are: a triaxial cell, a unique mechanical axial loading system and several transducers, connected through A/D and D/A converters to a microcomputer that controls the tests and records the data (Tatsuoka 1988). The operating scheme of this device is shown in Figure 4.6a, while a picture is reported in Figure 4.6b.
The specimen is placed in a triaxial chamber, put inside an iron frame, which supports the motor and contrasts the advancement of the ram in its application of the deviator stress. The pressure cell is made of Plexiglas and reinforced with aluminium bands at its ends. In order to reduce the disturbance of the soil specimen, its design allows to work with the cell open. The specimen can be placed on the pedestal by hand, guaranteeing a correct alignment between the loading piston, the specimen cap, and the specimen. Moreover, the pedestal is smooth, avoiding shear stress at the base of the specimen and then a perfect triaxial stress state. Owing to that, the drainage is on the lateral surface of the pedestal.
Furthermore, the base pedestal can move avoiding the non-uniformity of strains. A detail of the base pedestal is shown in Figure 4.7.

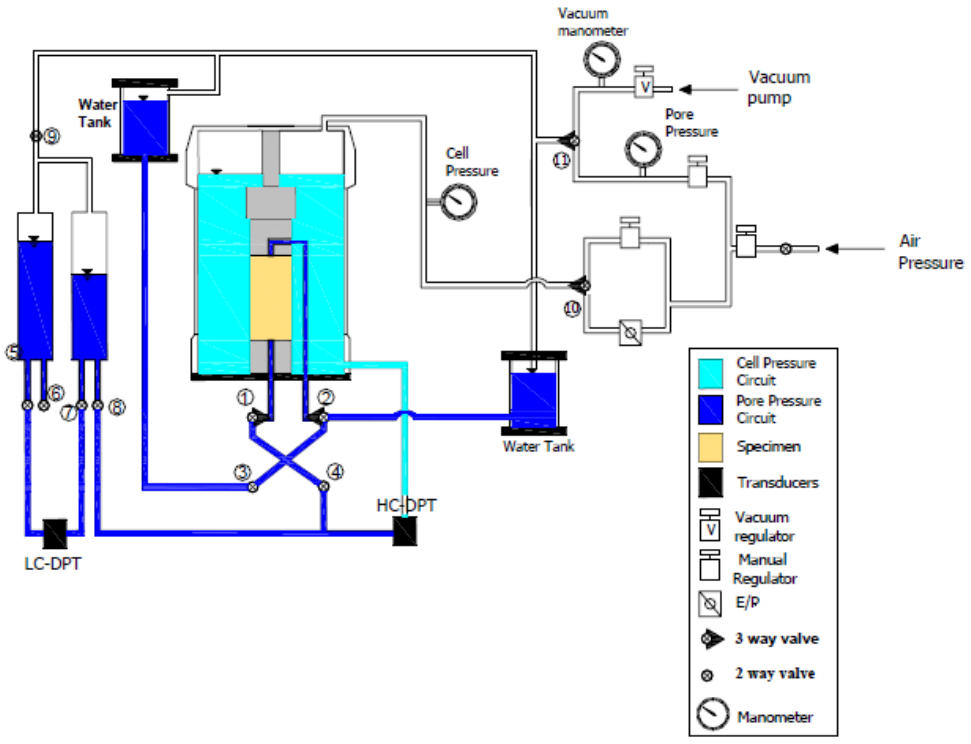

(a)

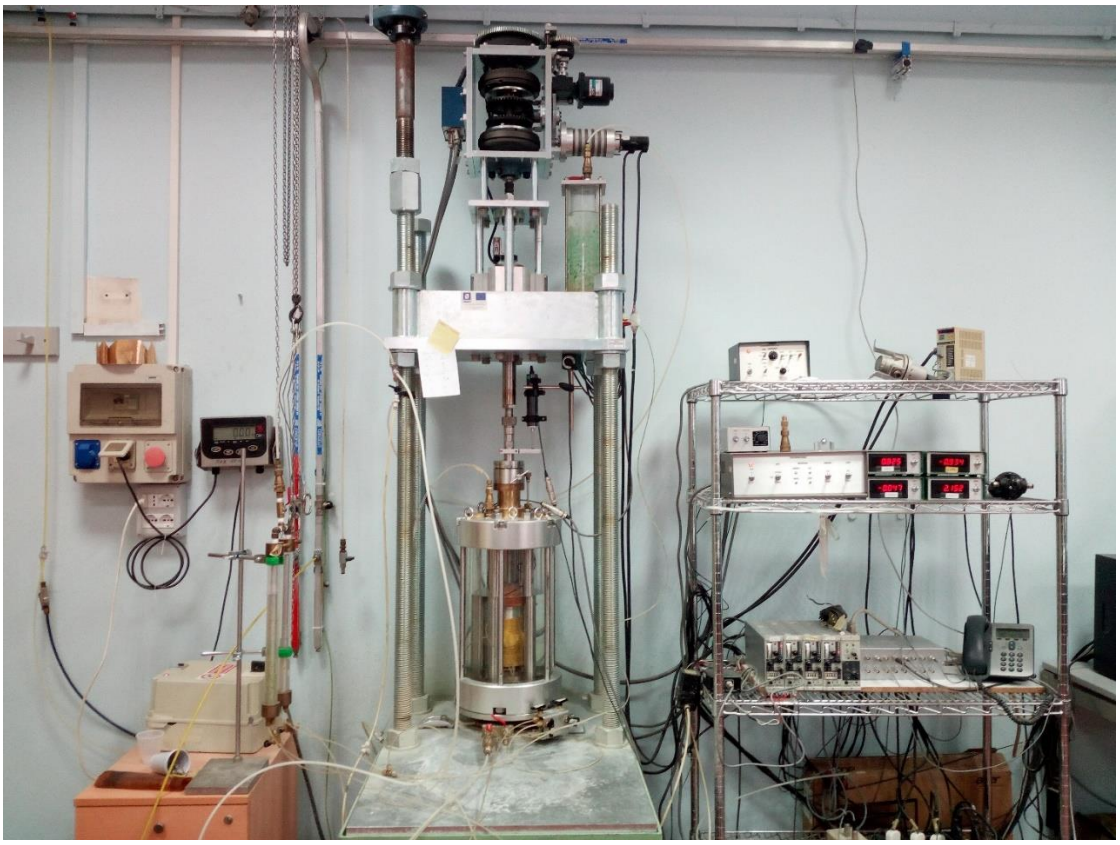

(b)

Figure 4.6. MaTRIX triaxial cell (University of Napoli, Federico II): functioning scheme (a), cell of geotechnical laboratory of University of Napoli Federico II (b).

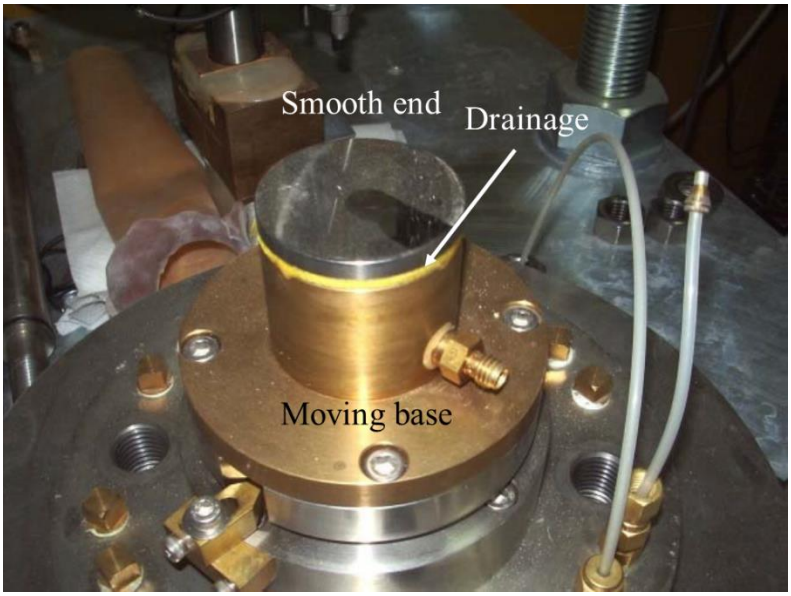

Figure 4.7. Detail of the base pedestal of MaTRIX triaxial cell (University of Napoli, Federico II).

The stress path can be controlled by an advanced axial loading device and an electro-pneumatic transducer. The axial load application system allows to maintain a constant strain rate and to apply very small unload-reload cycles with an axial strain amplitude of the order of 0.001% or less, without a noticeable time lag when reversing the loading direction.
The loading device was designed to automatically switch the motor on and off and select the upward and downward loading shaft direction through a personal computer and a D/A converter.
The cell pressure is regulated by an electro-pneumatic transducer (Fujikura Transducer Mod. RT: E/P) that receives the commanding signal from a computer. Alternatively, cell pressure can be controlled by a manual regulator (Fairchild). By now, the pore pressure is controlled only through a manual regulator.
The load cell used in the present study, designed at the University of Tokyo is pressure-insensitive; i.e., the reading (output voltage) from the load cell does not change with changes in the cell pressure. Moreover, to eliminate the effects of piston friction, it is placed inside the triaxial cell.
This load cell (Fig. 4.8) is made of a very stiff material (i.e., phosphor bronze) and is essentially non-compressible when subjected to changes in the cell pressure σ_c within the range used in the present study (i.e., σ_c=0~600kPa), which is negligible compared to the compressive strength of the load cell material. Forces applied on the load cell induce deformation in the top weakened part of the transducer, to which four electrical resistance (ER) strain gauges in a full Wheatstone bridge are attached. Thus the load cell deformation is directly connected both to the output voltage and to the axial force.

Figure 4.8. Load cell of MaTRIX triaxial cell (University of Napoli, Federico II).

The effective confining pressure is measured accurately and directly through a liquid-liquid High Capacity Differential Pressure Transducer (HC-DPT) produced by Fuji Electric (FCX-A type FCH/I). The two channels of HC-DPT are connected respectively to the pore pressure water and to the cell pressure water (Fig. 4.9).
The generalized equation for the evaluation of the effective confining pressure acting at every level in a saturated sample is given by:

$$\sigma'_r = p_h - u + \Delta\sigma_{rm} \quad (4.2)$$

Where p_h is the liquid pressure applied on the high pressure face of the HC-DPT and evaluated as:

$$p_h = \sigma_c + (h_{cl} + h_{DP}) \cdot \gamma_w \quad (4.3)$$

With σ_c cell air pressure; h_{cl} height of cell water from the sample bottom, h_{DP} distance of HC_DPT down from the specimen bottom, γ_w unit weight of water.
The term u in eq. (4.2) is the pore water pressure applied on the low pressure face of the HC-DPT. u is given by:

$$u = \sigma_{bp} + (h_{cl} + h_{DP}) \cdot \gamma_w \quad (4.4)$$

where σ_{bp} is back air pressure, while h_{cl} is the height of burette water surface from the sample bottom.
Finally, the last term in eq. (4.2): $\Delta\sigma_{rm}$ is the stress correction for membrane force.
Also the volume change measurement method adopted is illustrated in Figure 4.9. It utilizes a low capacity differential pressure transducer (LC-DPT) from Fuji Electic (FCX-A type FHC/I). This instrument is directly connected to a double burette system: a very useful trick to compensate for water evaporation assuming that the rate of water evaporation is probably the same in the two burettes.
One burette is used to give a reference level for the reading of LC-DPT, the other one is directly connected with the specimen pore water. A back pressure is applied to water inside burettes. The pressure helps dissolving air (if present) in the pore water fluid, thus improving the quality of the measure, and helps reducing the evaporation phenomenon.

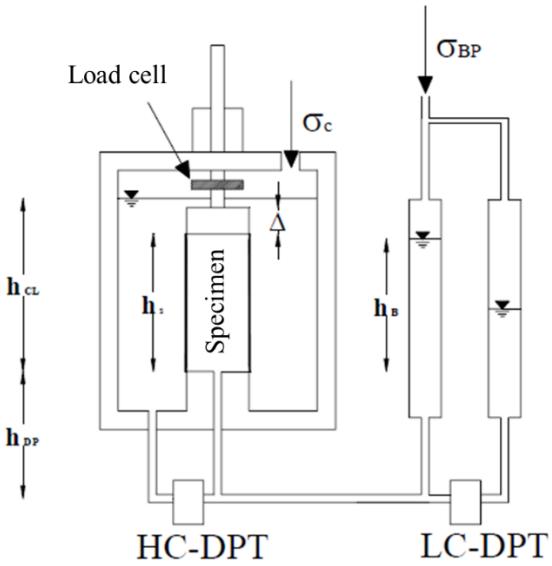

Figure 4.9. HCDPT and LCDPT of MaTRIX triaxial cell (University of Napoli, Federico II).

Regarding to axial strains, two different devices can be used: an LVDT and a gap sensor. The former is produced by Kanetec, it has a maximum measuring range of 40 mm, while its output voltage is ± 5 Volt.
On the other hand, the gap sensor is a proximity transducer AEC-5509 (Applied Elettronics Corporation) placed in opposition with a steel target integrated with the top cap. The electromagnetic field produced by the instrument changes with the changing in its distance from the target. Its maximum measuring range is 2 mm.

4.2.2.1 SPECIMEN'S PREPARATION AND TEST METHODOLOGY

The monotonic tests carried out in the MaTrix triaxial cell have been performed on specimens prepared by 1D- compression technique. It consists of mixing dry sand with a fixed amount of water to have the desired degree of saturation (S_r), in this case 50%. The moisture is then poured in a mould and compacted to have the following dimensions: d=50mm and h=100mm (Fig. 4.10a). Before starting a test, the specimen is covered by filter paper (Fig. 4.10b) to improve the drainage of water toward the pedestal drainage (Fig. 4.7).
As traditional triaxial test, the testing phases can be divided in:

- Saturation;
- Consolidation;
- Application of the deviatoric load.

(a) (b)

Figure 4.10. Preparation of a specimen for a MaTrix triaxial test in a mould (a) and specimen covered with filter paper (b).

The saturation occurs by means of a percolation into the specimen due to a hydraulic gradient imposed between the bottom and the top of the specimen. Measurement of B Skempton coefficient is necessary to establish if the specimen is saturated that is if, the saturation phase can be concluded. The next step is the isotropic consolidation, where cell and back pressure are imposed to reach a given effective stress. When the volume strains tend to a constant value, deviatoric stress is applied by means of a drive able to push forward at a speed chosen by the operator. In this research, a velocity of 0.5 mm/h and 1.0 mm/h has been applied respectively for drained and undrained tests.

4.2.3 CYCLIC TRIAXIAL JAPANESE CELL (UNIVERSITY OF TOKYO)

The cyclic triaxial Japanese cell (stress controlled), available at the University of Tokyo, can work in saturated and unsaturated conditions, where the Linkage Double Cell System was used (Wang et al. 2016) as shown in Figure 4.11a-b. A vertical sinusoidal cyclic loading was applied by a double action cylinder controlled by a function generator and an E/P regulator converting electric signal to pneumatic signal to maintain the total mean principal stress (p) constant. By using double function generator, σ_c can be simultaneously adjusted following the vertical cyclic loading applied by the vertical stress control system (Tsukamoto et al., 2002).

A double action cylinder was installed to apply cyclic loading. Two sides of the double action cylinder were connected to two pressure regulators, respectively. The pressure at the bottom of the cylinder is kept constant and the pressure at the top of the cylinder is controlled by the E/P regulator. The LVDT allows to measure axial strain and its maximum displacement capacity is 20 mm. Furthermore, two types of DPT has been used: a high capacity range, called HCDPT and the Low Capacity Differential Pressure Transducer (LCDPT).

HCDPT was used to measure the pressure difference in water levels between the burette (i.e. the amount of water sucked/expelled from the specimen) and the cell. It has a capacity range of 0 to 320 kPa. LCDPT measures the difference in water levels between the inner and outer cell (i.e., volume change of the specimen) and has a capacity range of 0 to 6 kPa.

To reduce the duration of the tests, membrane filter was used to the pedestal instead of the traditional ceramic disk for unsaturated specimens (Nishimura et al., 2012) as can be seen in Figure 4.11b. The pore water pressure (u_w) can be measured by a pressure transducer. The pore air pressure (u_a) is measured by another pressure transducer connected to the top cap, on which a hydrophobic filter is glued (Fig. 4.11b). The suction can be computed as the difference between u_a-u_w. Volume change of the unsaturated specimens is monitored by the inner cell system. The inner cell and a reference tube which were filled with de-aired water were connected to a DPT. Volume change of a specimen was obtained by considering change of water level in the inner cell and movement of the top cap.

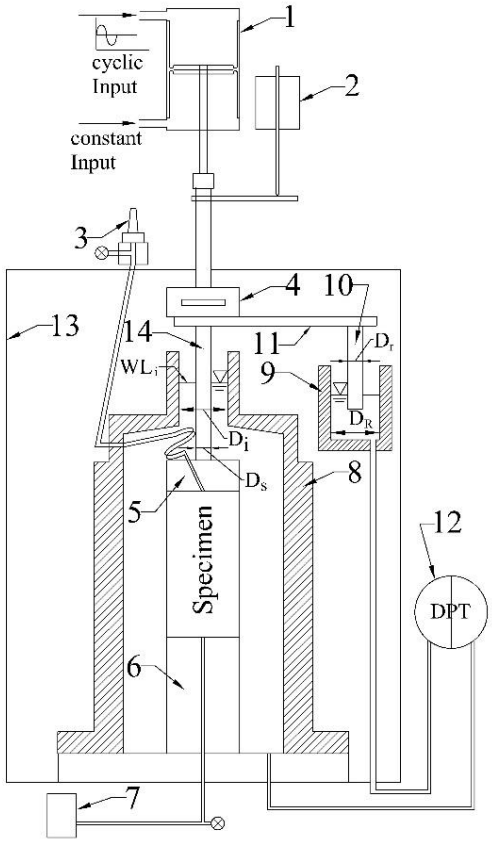

1. Double action cylinder
2. VDT
3. Pore air pressure transducer
4. Load cell
5. Top cap
6. Pedestal
7. Pore water pressure transducer
8. Inner cell
9. Reference tube
10. Linkage acrylic rod
11. Aluminum plate
12. DPT
13. Pressure cell
14. Stainless steel loading shaft

D_s :Diameter of loading shaft
D_r :Diameter of linkage rod
D_R : Inner diameter of reference tube
D_i : Inner diameter of upper part of inner cell
$D_s = D_r$; $D_R = D_i$
WL_i: Water level in the inner cell

(a)

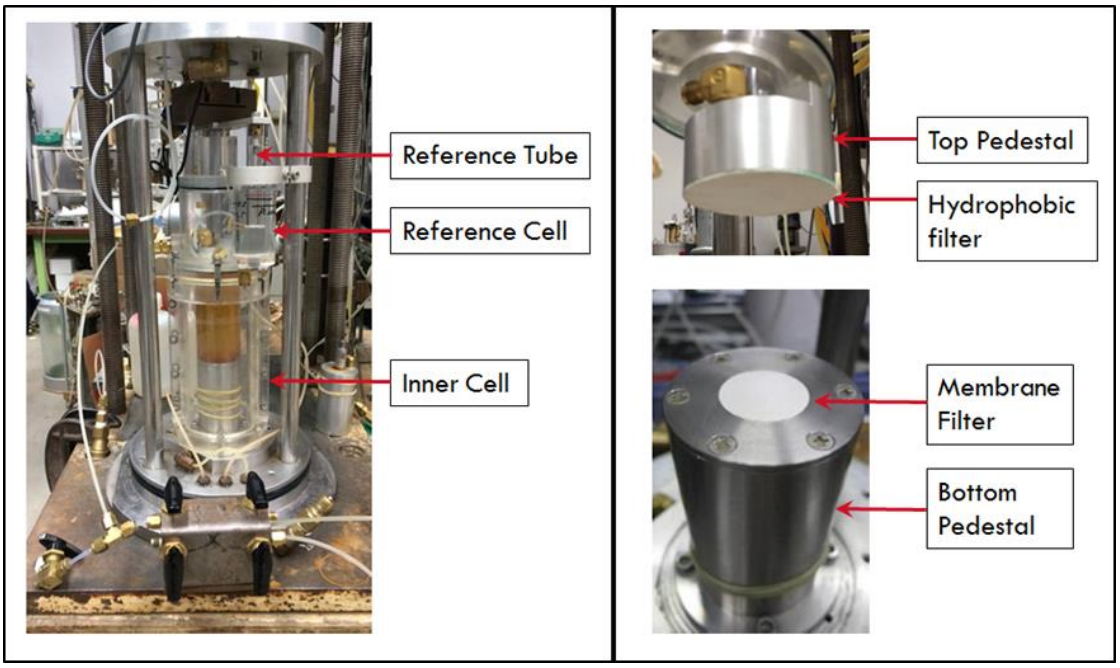

(b)

Figure 4.11. Cyclic Japanese triaxial cell (University of Tokyo) (Wang et al., 2016) and photo of the Linkage Double Cell System (L) and Top Cap and Bottom Pedestal (R) (Tan Tian, 2019) (b).

4.2.3.1 SPECIMEN'S PREPARATION AND TEST METHODOLOGY

As for MaTrix cell, the specimens (d=50 mm and h=100 mm) have been prepared by 1D-Compression method as already explained in paragraph 4.2.2.1. As an example, some photos of the prepared specimens have been shown in Figure 4.12.

(a) (b)

Figure 4.12. Photos of 1D-Compression specimens: bauxite (a) and silica sand N°5 (b).

After the preparation, the specimen is transferred from the mould on top of the saturated membrane filter on the bottom pedestal. In this phase, the pore water pressure should record negative value, since air is exposed to the atmosphere. The specimen, is then consolidated, increasing the confining pressure up to the desired or target maximum confining pressure. When the secondary settlement is attained the desired Cyclic Stress Ratio (CSR) can be applied with a frequency of 0.1 Hz. Even though this frequency is higher than the one adopted in the Bishop & Wesley cell, it is still low enough to ensure the equalization of the air and water pressures, as shown by Nishimura et al. (2012).
However, it should be emphasized that the triaxial device of University of Tokyo is able to work with low degrees of saturation, so for higher values of S_r, before being consolidated, the specimens have been subjected to a saturation phase through a burette. This saturation phase has the main aim to increase the water content of the specimen to reach the desired S_r. This phase is followed by consolidation and then by the application of a CSR as mentioned above. For these specimens, the pore air pressure u_a was not measured. However, in such conditions it is reasonable to consider that the air phase is not continuous (i.e. air bubbles are dispersed into water), and therefore for thermodynamic equilibrium the air pressure is equal to the pore water pressure. For the specimens having a lower degree of saturation, in which on the contrary the air phase is likely to be continuous, the air pore pressure was measured.
As for saturated cyclic tests, also for unsaturated tests the post-liquefaction behaviour has been studied for some tests. In this case, after liquefaction, the specimens are re-consolidated at the same confining stress of the first consolidation, to dissipate the excess pore pressure raised during the first cyclic phase and after that a new cyclic phase is imposed.

4.2.4 SIMPLE SHEAR APPARATUS (UNIVERSITY OF NAPOLI, FEDERICO II)

As explained in Chapter 2, the loading conditions in the field, imposed by a seismic event, can experience continuous rotation of the directions of principal stresses. Simple shear tests are plane strain tests which allow smooth and continuous rotation of the direction of principal axes of stress during shearing resembling many types of field loading conditions.

Through LIQUEFACT funds a simple shear apparatus, able to perform monotonic and cyclic tests, has been purchased by the University of Napoli, Federico II.

As well known, a simple shear condition implies that the diameter of the specimen (or more in general, the transversal section) is maintained constant. Generally, it can be performed by means of concentric rings or reinforced membrane, while the apparatus of the University of Napoli is much more sophisticated because it is able to work according two different configurations: the first one obtained acting on the confining pressure (flexible boundary), the second one is realized by means of confining rings (rigid boundary). In both cases, the simple shear state should be guaranteed (see for instance § 5.1.3.2).

The apparatus consists of a dynamic servo-controller (DSC), able to control 2 electro-mechanical dynamic actuators for applying the vertical and horizontal loads to the specimen. The vertical and horizontal displacements are measured by Encoders which are part of the servo motors. The maximum range of travel in each axis is protected by a limit switch and each strain rate is easily set from the computer.

Vertical and horizontal loads are measured by using two load cells, both submersible (important in configuration with confining pressure), with a maximum measure of 5kN.

The configuration with rings differs from those with confining pressure because of the presence of the cell, as can be easily noted looking at Figure 4.13.

In configuration with confining pressure a simple shear condition can be obtained by means of a sophisticated control system of the software Clisp Studio. The controlling software enables all stages of a test (Saturation, Consolidation (Isotropic, Anisotropic or K_0), Static Loading, Cyclic Shear (Stress or Strain) and Liquefaction). In consolidation phase (K_0 condition) the apparatus can adjust the vertical load to maintain a constant diameter, known the water that is going out from the specimen and the vertical displacements. In this case, a latex membrane is used to confine the specimen, while the pressurized water allows to apply a given pressure by means of an air/water interface device, reported in Figure 4.14 together with the other basic components of that system. The Hydraulic Automatic Pressure Controller (HAPC) is connected to the base of the specimen and allows to impose a back-pressure and measure the volume of water that goes in or out from the specimen by means of a volume gauge.

In other words, the cyclic simple shear apparatus can control the confining cell pressure, vertical load, horizontal load and back pressure independently.

The configuration with a confining pressure can be used to perform:

- Simple Shear test with the height of the sample kept constant using Active height control (undrained);

- Cyclic Shear test with a cyclic horizontal force applied to the specimen whilst the Vertical stress on the specimen is maintained (drained);
- Cyclic Shear test with a cyclic horizontal force applied to the specimen whilst the height of the specimen is maintained (undrained);
- Cyclic Shear test with a cyclic horizontal displacement applied to the specimen whilst the Vertical stress on the specimen is maintained (drained);
- Cyclic Shear test with a cyclic horizontal displacement applied to the specimen whilst the height of the specimen is maintained (undrained);
- Cyclic Shear test to study liquefaction.

The total vertical stress (σ_v) is defined by Clisp Studio as:

$$\sigma_v = \frac{F_v}{A} + (\sigma_c - bp) \quad (4.5)$$

where F_v is the force measured by vertical load cell, A is the area of the specimen, σ_c is the cell pressure and bp is the back pressure at the start of this stage. During the liquefaction phase, the cell pressure can be adjusted to maintain a constant σ_v. The reason why, σ_v should be kept constant is to simulate the field stress path which occurs in many geotechnical loading situations. It can be achieved by increasing σ_h during the shearing phase. Obviously, the height of the specimen is constant.

(a) (b)

Figure 4.13. Cyclic simple shear cell with confining pressure (a) and confining rings (b) (University of Napoli, Federico II).

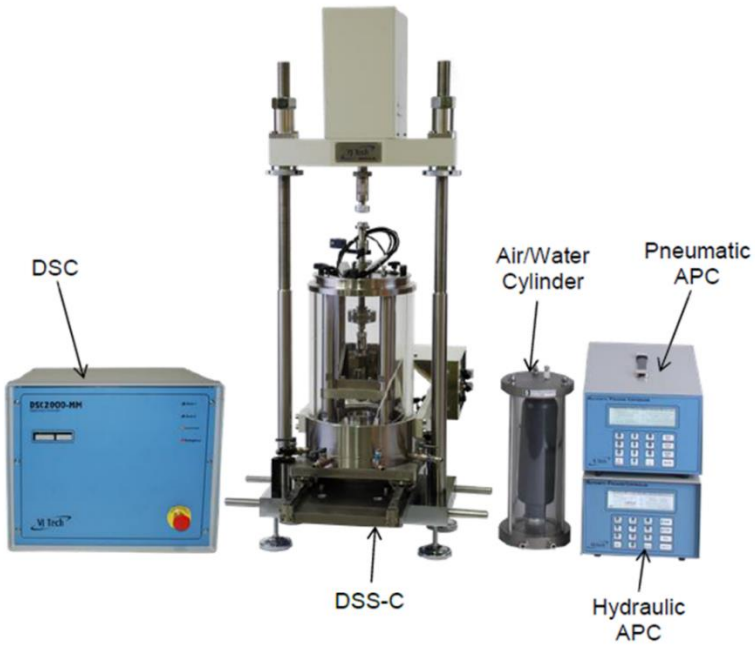

Figure 4.14. Basic system components of Cyclic Simple Shear (CSS) apparatus with confining pressure.

The configuration with rings consists of a series of concentric rings used to confine the specimen, guaranteeing a simple shear condition. Obviously, the cell pressure cannot be controlled and during the liquefaction tests (undrained conditions), the height of the specimen is maintained constant. Moreover, using this configuration, the excess pore water pressure cannot be recorded during the cyclic phase.
In Figure 4.15 the specimens with flexible and rigid boundary are shown.

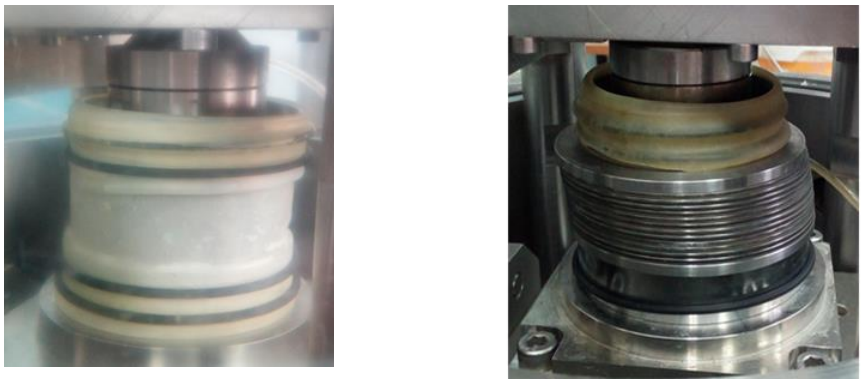

(a) (b)

Figure 4.15. Specimens with flexible (a) and rigid (b) boundaries.

4.2.4.1 SPECIMEN'S PREPARATION AND TEST METHODOLOGY

In order to evaluate the effect of preparation techniques on the liquefaction resistance, three different preparation techniques have been used for specimens tested by cyclic simple shear (CSS) apparatus: 1D-Compression, moist tamping and air pluviation.

The water sedimentation procedure (WS) has not been tested because of the high amount of fines content in the tested sands. Although this preparation technique has been recognized as one of the most reliable methods to reconstitute a specimen because it is able to simulate the natural deposition process of soils, it generates the separation of the fine content particles of the soil from the granular part. In other words, WS method is more reliable for clean sand or sand with a negligible amount of fines content. 1D-Compression has been already described in paragraph 4.2.2.1. Regarding the moist tamping technique, it is very similar, consisting of disposing five equal pre-weighed oven-dried portions of soil, mixed with de-aired water at a desired water content (5% was used in this study). Each portion of the soil is strewn by hand to a predetermined height. At each stage of the lifts, tamping is applied lightly with a small flat bottom tamper.
In air pluviation, the dry sand is discharged vertically in air from a nozzle of a funnel. However, as well known, the obtained relative density of the reconstituted specimens depends both on the height of fall during the preparation and on the nozzle's dimensions. Owing to that, the densities obtained by fall tests for different height and two different nozzles (d= 4mm and d=15mm) have been evaluated as shown in Figure 4.16 for Pieve di Cento (GSS) sand.

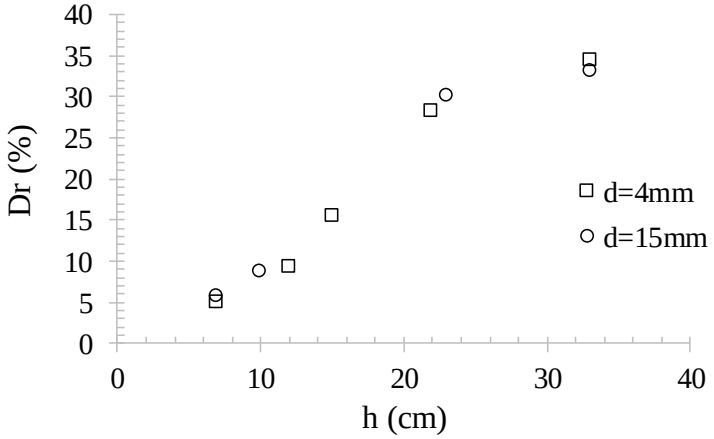

Figure 4.16. Relative density versus height of fall for Pieve di Cento (GSS) sand.

The dimension of nozzle seems not to influence the D_r of the specimens, on the contrary, when the height of fall increases, the D_r increases as well. The air pluviation specimens have been prepared with a height of fall of 40 cm, to reach D_r of about 40%.
However, the used methods present pros and cons. All of them are very simple to prepare and are suitable for sandy specimens with a significant amount of fines content because they avoid the separation of smaller particles. Furthermore, 1D-compression and moist tamping allow to achieve a wide range of relative density, while the air pluviation has the disadvantage to reach lower and uncontrolled D_r, achieved after the flushing. Moreover, it is extremely sensitive to drop height especially for simple shear specimens (large diameter). On the other hand, 1D compression and moist tamping can be subjected to high stresses, during the compaction, that can be higher than the confining stress in the performed tests (Frost and Park, 2003). In addition, the formation of layers can create

discontinuity into the specimens. However, in §5.1.5.3 the effect of specimen preparation techniques will be shown and discussed.
Regarding the testing procedures by CSS apparatus, it should be emphasized that, even though the phases of a test are the same (saturation, consolidation, deviatoric), a distinction should be done between the configuration with rings and with confining pressure.
In configuration with confining pressure, the specimens (d=70 mm and h=26 mm) were saturated by increasing both cell and back pressure to have an effective stress of 10 kPa.
In configuration with rings, the specimens (d=70 mm and h=26 mm) were saturated by using flushing. The saturation of the specimens was checked by B-value through a B-test in the configuration with 'flexible boundary', while it was not possible in configuration with rings because cell pressure cannot be controlled. For B higher than 0.95, the specimens were considered saturated. Thereafter, the specimens were consolidated. As mentioned above, in the configuration with flexible boundary a k_0 consolidation can be applied, adjusting the vertical load to have a constant diameter, known the water volume goes out during consolidation and the vertical settlements. In this case, the horizontal stress is imposed, while in rigid configuration the total vertical stress is chosen by the experimenter. After the consolidation phase, different amplitude Cyclic Stress Ratio (CSR) were applied, where CSR is the ratio between the shear stress (τ) and the initial vertical effective stress (σ'_v). Several wave forms (sinusoidal, triangular, rectangular and sawtooth) were used with a frequency of 0.05 Hz as it will be described in §5.1.5.2.

4.2.4.2 UNDISTURBED SPECIMENS: EXTRUSION AND TEST METHODOLOGY

Undisturbed specimens were tested in cyclic simple shear apparatus to identify the cyclic resistance curve of Pieve di Cento sand as it will be described in the next Chapter.
It has been already mentioned that two types of sampler have been used to recover undisturbed sample: Osterberg and Gel-Pusher (§3.2.1; §3.2.2).
For Osterberg sampler the extrusion can be done by means of an extruder (Fig. 4.17a), while for a Gel-Pusher sampler, the presence of gel makes easier the extrusion without the extruder (Fig. 4.17b). In fact, the sample can slide from the sampler for gravity. It means that the sample retrieved from a Gel-Pusher is really "undisturbed", while an effect of densification could occur during the extrusion of Osterberg sample, as it will be confirmed in the next Chapter (§5.2.3).
The sampler cutter allows to have specimens with d=70 mm and h=26 mm (Fig. 4.18a). All of them have been tested by using a flexible boundary, following the procedures described in paragraphs 4.2.4 and 4.2.4.1.

(a) (b)

Figure 4.17. Extrusion of undisturbed samples, from Osterberg (a) and Gel-Pusher (b) samplers.

(a) (b)

Figure 4.18. Undisturbed specimens for a cyclic simple shear test (a) and specimens recovered with a membrane (b).

REFERENCES

ASTM – D4253-54 (2006). Standard test methods for maximum index density and unit weight of soils using a vibratory table.

Aversa, S. E., and Vinale, F. (1995). Improvements to a stress-path triaxial cell. *Geotechnical Testing Journal*, *18*(1): 116-120.

Bishop, A. W., & Wesley, L. D. (1975). A hydraulic triaxial apparatus for controlled stress path testing. *Geotechnique*, *25*(4). 657-670.

Fioravante, V., and Giretti, D. (2016). Unidirectional cyclic resistance of Ticino and Toyoura sands from centrifuge cone penetration tests. *Acta Geotechnica*, *11*(4): 953-968.

Frost, J. D., and J. Y. Park. (2003). A Critical Assessment of the Moist Tamping Technique. G*eotechnical Testing Journal* 26 (1): 57–70.

Joer, H. A., Erbrich, C. T., and Sharma, S. S. (2011). A new interpretation of the simple shear test. *London, UK: Taylor & Francis.* (pp. 353-358).

Lin, W., Mao, W., and Koseki, J. (2017). Acoustic Emission Technology to Investigate Internal Micro-Structure Behaviour of Shear Banding in Sands. *In Advances in Laboratory Testing and Modelling of Soils and Shales*, (207-214). Springer, Cham. https://doi.org/10.1007/978-3-319-52773-4_23.

Lin, W., Mao W., Koseki J., and Liu A. (2018). Frequency response of acoustic emission to characterize particle dislocations in sandy soil. In *GeoShanghai International Conference*, (689-697). Springer, Singapore. https://doi.org/10.1007/978-981-13-0125-4_77.

Nishimura, T., Koseki, J., Fredlund, D. G. & Rahardjo, H. (2012). Micro-porous membrane technology for measurement of soil-water characteristic curve. *Geotechnical Testing Journal*. 35 (1): 201–208.

Santucci de Magistris, F., Koseki, J, Amaya, M, Hamaya, S, Sato, T, Tatsuoka, F (1999). Triaxial testing system to evaluate stress-strain behaviour of soils for wide range of strain and strain rate. *ASTM Geotechnical Testing Journal*, 22(1): 44-60.

Tan Tian J. (2019). Characterization of Liquefaction and Seepage Properties under Different Saturation Conditions of Bauxite During Maritime Transport. *PhD thesis*. University of Tokyo.

Tatsuoka, F. (1988). Some recent developments in triaxial testing systems for cohesionless soils, *Keynote lecture, ASTM special Technical Publication* No.977, pp.7-67.

Tatsuoka, F, Sato, T, Park, CS, Kim, YS, Mukabi, JN, Kohata, Y (1994). Measurements of elastic properties of geomaterials in laboratory compression tests. *ASTM Geotechnical Testing Journal*, 17(1): 80-94.

Tsukamoto, Y., Kawabe, S., Matsumoto, J. and Hagiwara, S. (2014). Cyclic resistance of two unsaturated silty sands against soil liquefaction. *Soils and Foundations.* 54 (6): 1094–1103

Wang, H., Sato, T., Koseki, J., Chiaro, G. and Tan Tian, J. (2016). A system to measure volume change of unsaturated soils in undrained cyclic triaxial tests. *Geotechnical Testing Journal*, 39 (4): 532–542.

Visone C., (2008). Performance-based approach in seismic design of embedded retaining walls. *PhD Thesis*, University of Napoli Federico II, Napoli, Italy.

CHAPTER 5

5. EXPERIMENTAL ACTIVITY: UNTREATED SPECIMENS

An extensive testing program has been performed, in order to characterize the sandy soils presented in Chapter 4 and investigate their mechanical behaviour in static and dynamic conditions.
In this section the results of "untreated" soils will be shown and discussed. The term "untreated" has been used in this research work to indicate loose saturated sands ($35<D_r(\%)<50$) consolidated with low confining pressures ($25<\sigma'_c(kPa)<100$), which traditionally represent the natural conditions of the liquefiable soils. Such a term has been used to distinguish the specimens in the aforementioned state from those in different conditions in terms of relative density (D_r) and degree of saturation (S_r). Tests performed on such specimens, called "treated", will be presented and discussed in Chapter 6.
Finally, with the main aim to characterize Pieve di Cento field trial, within the European project LIQUEFACT, undisturbed specimens have been tested (Chapter 3). The experimental results will be compared with those of reconstituted specimens to evaluate the fabric effect.

5.1 RECONSTITUTED SPECIMENS

In this paragraph the results of untreated and reconstituted specimens will be shown.

5.1.1 PERMEABILITY TESTS

Six permeability tests have been performed on Leighton Buzzard and Pieve di Cento (both BSS and GSS obtained as described in §3.1.1) sands, whose results are shown in Figure 5.1, where the values of permeability coefficient to water (k_w) versus time have been plotted. Additionally, for greater clarity, the k_w values of the performed tests, have been summarized in Table 5.1.

Table 5.1. Permeability tests.

Test	Material	FC (%)	e_0	D_{r0} (%)	k_w (m/s)
PW_LB	Leighton Buzzard	-	0.854	39.3	$2.20\cdot10^{-4}$
PW_BSS30FC	PdC_BSS	8.0	0.892	30.0	$1.00\cdot10^{-4}$
PW_BSS60FC	PdC_BSS	8.0	0.744	60.0	$8.70\cdot10^{-5}$
PW_BSS30	PdC_BSS	-	0.958	30.0	$2.00\cdot10^{-4}$
PW_BSS60	PdC_BSS	-	0.831	60.0	$1.48\cdot10^{-4}$
PW_GSS40FC	PdC_GSS	11.0	0.707	40.0	$1.84\cdot10^{-5}$

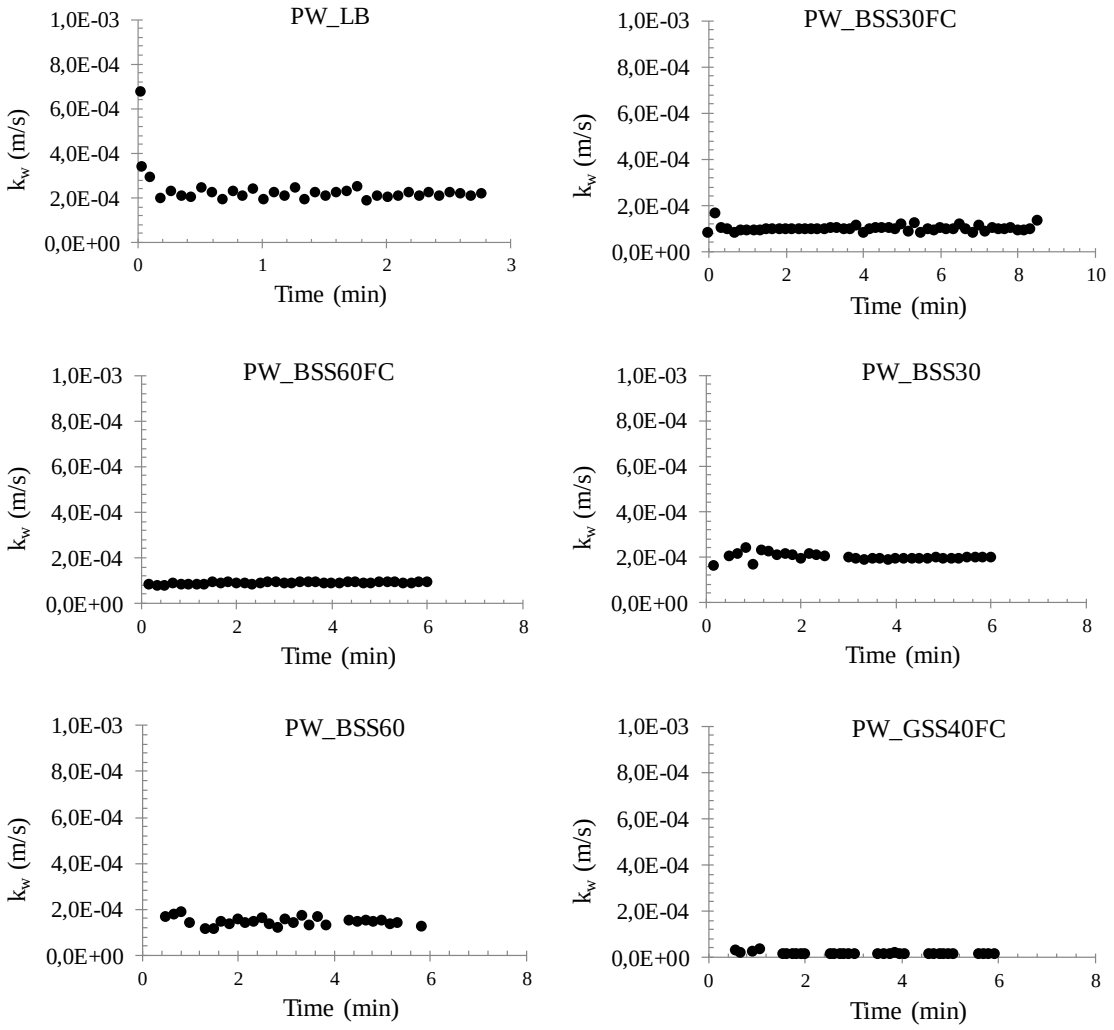

Figure 5.1. Results of permeability tests.

It can be noted that the permeability coefficient to water of Leighton Buzzard sand (D_r 40%) is $2.20 \cdot 10^{-4}$m/s, while it is lower for Pieve di Cento sands (both BSS and GSS). As well-known, the value of k_w depends on D_r as confirmed by looking at Table 5.1. k_w for PW_BSS30FC test (D_r=30%) is $1.00 \cdot 10^{-4}$m/s, while it is $8.70 \cdot 10^{-5}$m/s for PW_BSS60FC test, where the D_r is higher (60%). In addition, it can be noted that the fines content reduces the value of k_w, in fact for the material obtained removing the particles passing No 0.075mm sieve (PW_BSS30 and PW_BSS60 tests) the values of k_w are higher than that for natural sands (PW_BSS30FC and PW_BSS60FC tests).
Finally, k_w for GSS with a D_r=40% results lower than that for BSS, even if permeability tests on brown silty sand have been carried out with different D_r. It could be explained taking into account the value of D_{10}, on which k_w depends. D_{10} is higher for BSS than for GSS (Fig. 4.1) and consequently, k_w for BSS results higher than that of GSS.

5.1.2 OEDOMETRIC TESTS

With the main aim to contribute to the definition of a geotechnical model at Pieve di Cento test site, oedometric tests have been carried out on reconstituted specimens of Pieve di Cento soils, retrieved from the first two meters in depth of the field trial (BSS) or from boreholes sampler. Their grain size distribution curves have been already shown in Figure 3.7. Oedometric specimens had a diameter of 56 mm and a height of 20 mm and the tests are summarized in Table 5.2. Sandy specimens have been prepared by water sedimentation technique, while the clayey ones have been retrieved from boreholes samples at known depths by means of a sample cutter. The results of the oedometric tests are shown in Figures 5.2 (clay) and 5.3a (sandy soils). As well known, the yielding stress, corresponding to the maximum curvature of the experimental curves, is lower for clayey soils than for sandy ones. The tests start from similar void ratios (Tab. 5.2) but thereafter, void ratios decrease in a different way. In particular, the sand from borehole CH2 (Oe_CH2_Sand test) is more compressible than the other two sands. It is due to a higher fines content (FC>40%) as can be observed in Figure 5.3b, where for sake of completeness the grain distribution curves of sandy soils tested in oedometer device have been plotted together.
Finally, in Figures 5.4 the photos of Oe_CH2_Sand and Oe_CH3_Sand specimens, at the end of the test, are shown. It is evident the greyish sand in Oe_CH3_Sand specimen, while Oe_CH2_Sand specimen appears brown, due to a high percentage of fines (Fig. 5.3b).

Table 5.2. Oedometric tests on Pieve di Cento soils.

Test	Material	Boreholes	Depth (m)	e_0
Oe_BSS	BSS	-	First 2 m	0.964
Oe_CH1_Clay	Clay	CH1-Box2	8,30 – 8.40	1.042
Oe_CH4_Clay	Clay	CH4-Box2	6.75	0.999
Oe_CH2_Sand	Sandy soil	CH2	1.00 – 3.00	0.998
Oe_CH3_Sand	Sandy soil	CH3	1.50 – 3.00	0.951

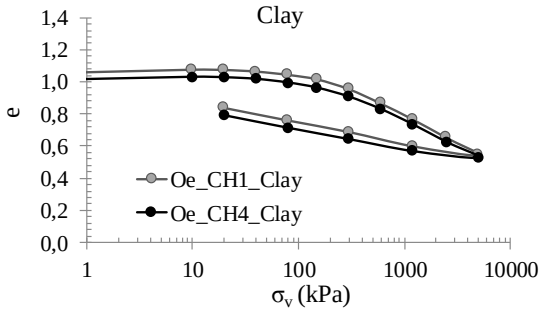

Figure 5.2. Results of oedometric tests on clay specimens.

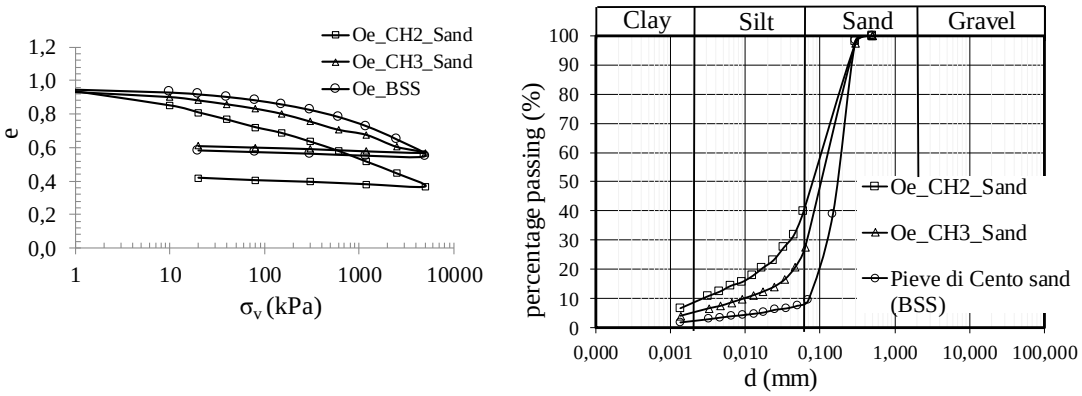

(a) (b)

Figure 5.3. Comparisons between oedometric tests on sandy soils (a) and relative grain size distribution curves (b).

(a) Oe_CH2_Sand (b) Oe_CH3_Sand

Figure 5.4. Specimens at the end of oedometric tests: Oe_CH2_Sand (a) and Oe_CH3_Sand (b).

5.1.3 MONOTONIC TESTS

The static behaviour of Italian sands (Sant'Agostino and Pieve di Cento sands) (Fig. 4.1b – Tab. 4.1)) in drained and undrained conditions, has been investigated through triaxial (TX) and simple shear tests (SS). The TX tests have been carried out in the Bishop & Wesley apparatus (§4.2.1) and compared with those performed in the MaTrix cell (§4.2.2), while the SS tests have been carried out in the simple shear apparatus by using the configuration with flexible boundary (§4.2.4).

The results of triaxial tests performed by means of a Bishop & Wesley apparatus on the three kinds of sands will be discussed first (Tab. 5.8).

For Sant'Agostino sand (SAS): 8 tests have been performed (Tab. 5.8): 7 in compression (TX_SAS1 to TX_SAS7) and 1 in extension. The extension test (TX_SAS8) was carried out in drained condition, according to a p' constant stress-path; on the other hand, the 7 compression tests have been carried out in undrained and drained conditions. Two of the

latter have been performed according to p' constant stress-path. The tests have been carried out on specimens with different void ratios and then D_r, ranging from 39.1% to 65.2%, and by applying different confining stresses ($25<\sigma'_c$ (kPa)<300).
For Pieve di Cento sands, 10 tests on BSS (3 of which undrained) and 10 on GSS (2 in undrained conditions) have been performed (Tab. 5.3). The tests on BSS have been carried out with several values of confining stresses, which range between 10 – 250 kPa, while the D_r varies between 35.8 – 66.4 %. For GSS, the specimens have been consolidated to σ'_c varying between 30 and 200 kPa, while the specimens have been prepared with a D_r ranging between 34.8 and 59.3 %.

Table 5.3. Experimental program of triaxial tests on Italian sands (Bishop & Wesley apparatus).

Test	Sand	σ'_c (kPa)	Stress path	e_0*	D_{r0}* (%)
TX_SAS1					
TX_SAS2					
TX_SAS3					
TX_SAS4					
TX_SAS5					
TX_SAS6					
TX_SAS7					
TX_SAS8					
TX_BSS1	PdC_BSS	50	C_CIU	0.765	55.7
TX_BSS2	PdC_BSS	100	C_CIU	0.784	51.8
TX_BSS3	PdC_BSS	200	C_CIU	0.773	54.0
TX_BSS4	PdC_BSS	20	C_CID(p')	0.830	42.5
TX_BSS5	PdC_BSS	30	C_CID(p')	0.712	66.4
TX_BSS6	PdC_BSS	10	C_CID	0.795	49.6
TX_BSS7	PdC_BSS	75	C_CID	0.863	35.8
TX_BSS8	PdC_BSS	100	C_CID	0.761	56.5
TX_BSS9	PdC_BSS	200	C_CID	0.719	65.0
TX_BSS10	PdC_BSS	250	C_CID	0.784	51.8
TX_GSS1	PdC_GSS	50	C_CIU	0.658	51.1
TX_GSS2	PdC_GSS	100	C_CIU	0.649	53.2
TX_GSS3	PdC_GSS	30	C_CID	0.656	51.6
TX_GSS4	PdC_GSS	50	C_CID	0.622	59.3
TX_GSS5	PdC_GSS	70	C_CID	0.681	45.9
TX_GSS6	PdC_GSS	100	C_CID	0.720	37.1
TX_GSS7	PdC_GSS	150	C_CID	0.695	42.8
TX_GSS8	PdC_GSS	150	C_CID	0.730	34.8
TX_GSS9	PdC_GSS	100	C_CID(p')	0.650	52.9
TX_GSS10	PdC_GSS	200	C_CID(p')	0.726	35.7

*at the end of consolidation phase. CID=consolidate isotropically drained; CIU= consolidate isotropically undrained; CID(p')= consolidate isotropically drained with p' constant; C=compression; E=extension.

In Figures 5.5, 5.6 and 5.7 the results of undrained tests on SAS, BSS and GSS, have been plotted, respectively, in the typical planes: ε_a-q (a); p'-q (b); ε_a- Δu (c); ε_a-q/p' (d).
In undrained tests, all specimens of Italian sands exhibit, at the beginning of the shear phase a contractive behaviour and then a dilative one. It could be due to the fact that, even though the specimens are loose, they have been consolidated at relatively low confining stresses (25 – 200 kPa). It suggests that these tests start from states below the Critical State Line (CSL). Apart from three tests on Sant'Agostino sand and one test on Pieve di Cento sand (TX_BSS3), the excess pore pressure decreases below its initial value.
Looking at the response of soils in the plane ε_a-q it can be noted that Pieve di Cento sands (BSS and GSS) show a more stable behaviour than Sant'Agostino sand, furthermore, the results of the tests plotted in the plane ε_a- Δu show that the critical state is almost always reached.
Apart from TX_SAS3, the quasi-steady state (QSS) and the undrained instability state (UIS), already defined in Chapter 2, vanish completely in these tests. Once again, it means that the initial state of deviatoric phase for these tests is below the CSL.
Furthermore, the tests plotted in the plane ε_a-q/p' may identify a unique curve except for TX_SAS1 test, which exhibits a higher ratio q/p' versus ε_a.

Figure 5.5. Results of undrained triaxial tests on Sant'Agostino sand in the planes ε_a-q (a); p'-q (b); ε_a- Δu (c); ε_a-q/p' (d).

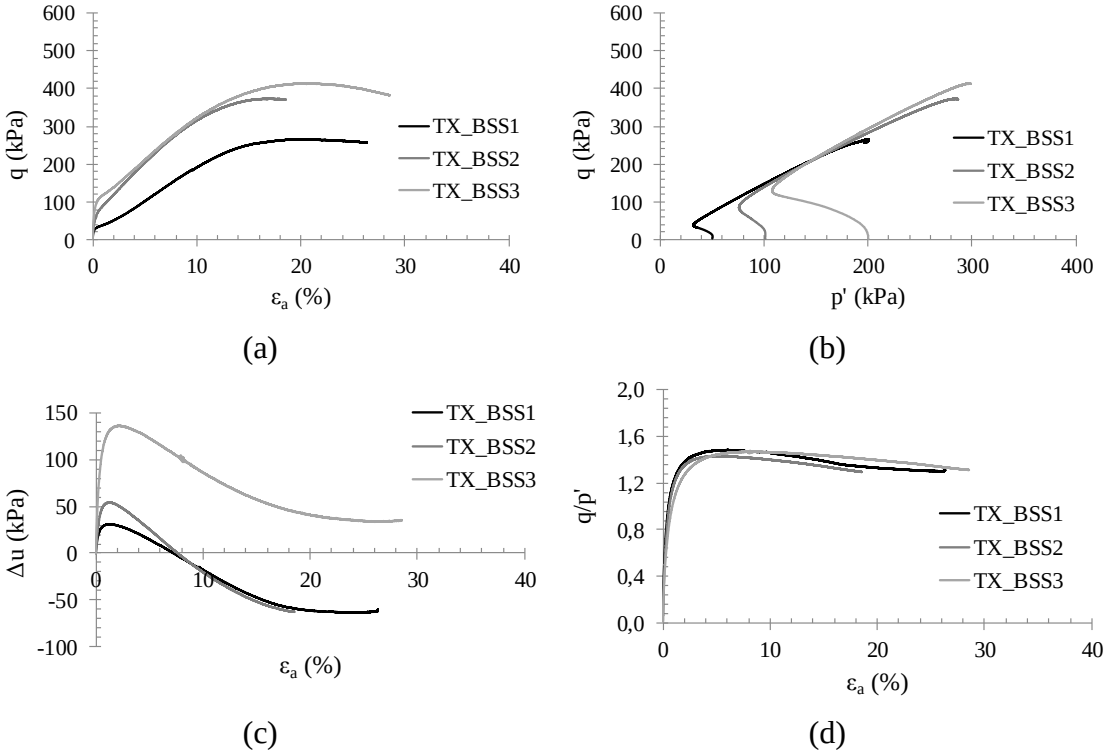

Figure 5.6. Results of undrained triaxial tests on Pieve di Cento (BSS) sand in the planes ε_a-q (a); p'-q (b); ε_a- Δu (c); ε_a-q/p' (d).

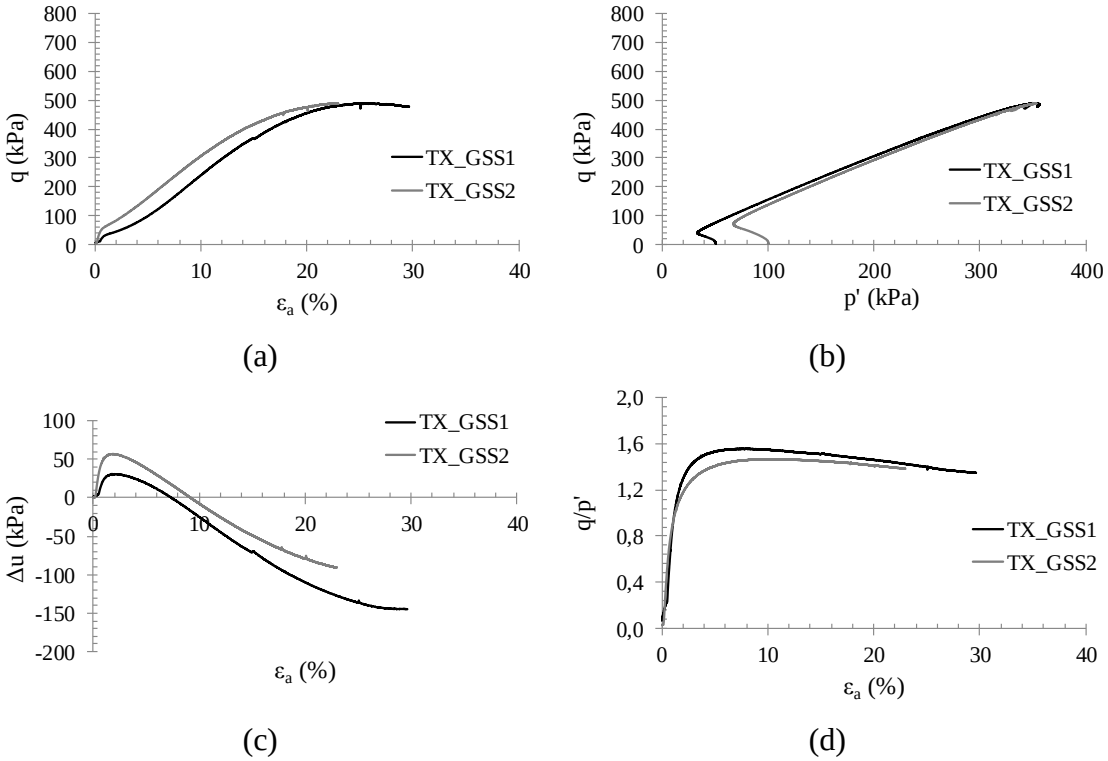

Figure 5.7. Results of undrained triaxial tests on Pieve di Cento (GSS) sand in the planes ε_a-q (a); p'-q (b); ε_a- Δu (c); ε_a-q/p' (d).

In Figures 5.8, 5.9 and 5.10 the results of drained tests have been plotted in the typical planes: ε_a-q (a), p'-q (b); ε_a- ε_v (c); ε_a-q/p' (d). Regardless of the sand, the response of soils in the plane ε_a-q is stable. On the other hand, the results in the plane ε_a- ε_v. show that the behaviour of the soil is contractive at the beginning of the shear phase and then almost always they dilate.

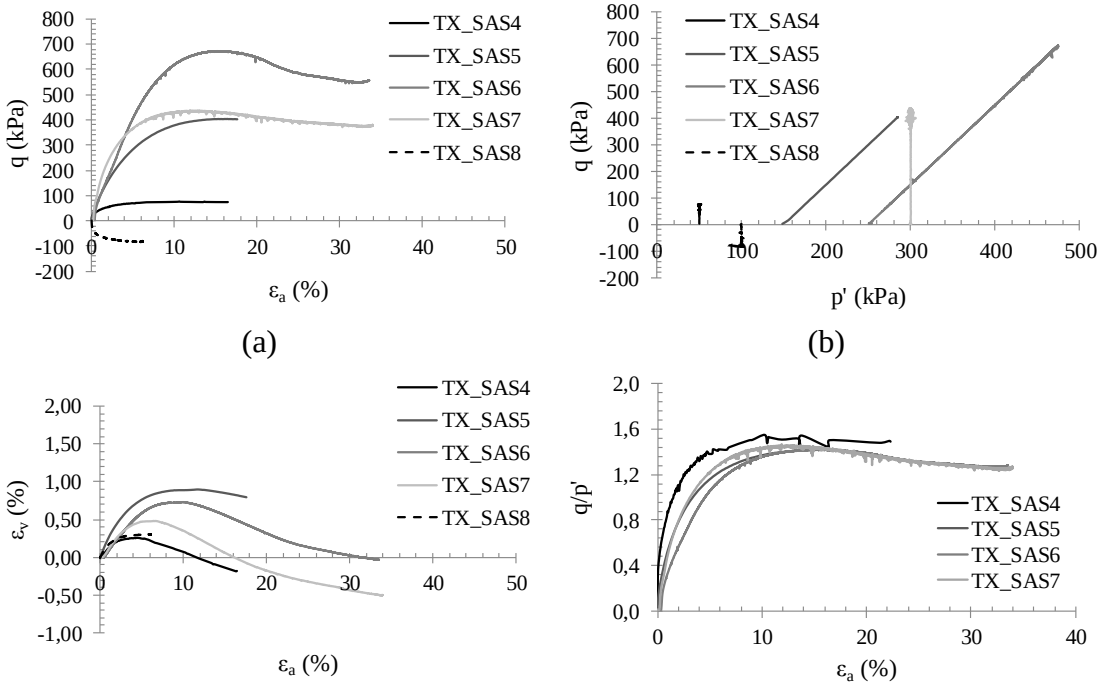

Figure 5.8. Results of drained triaxial tests on Sant'Agostino sand in the typical planes: ε_a-q (a); p'-q (b); ε_a- ε_v (c); ε_a-q/p' (d).

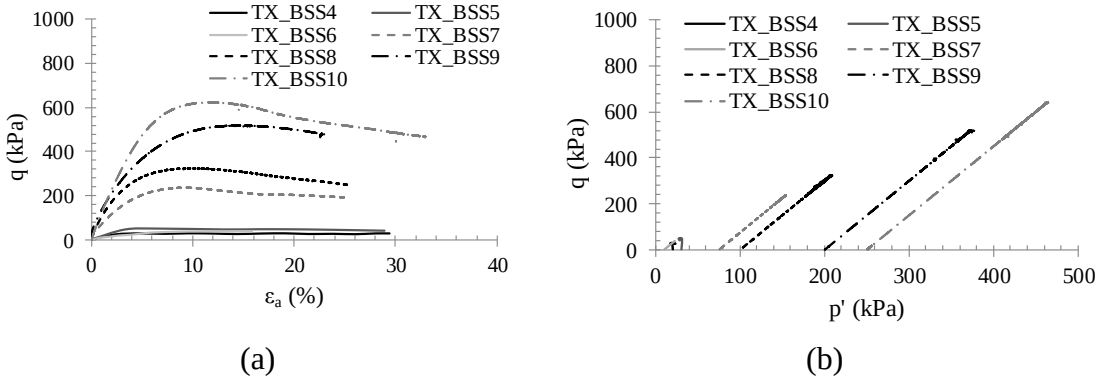

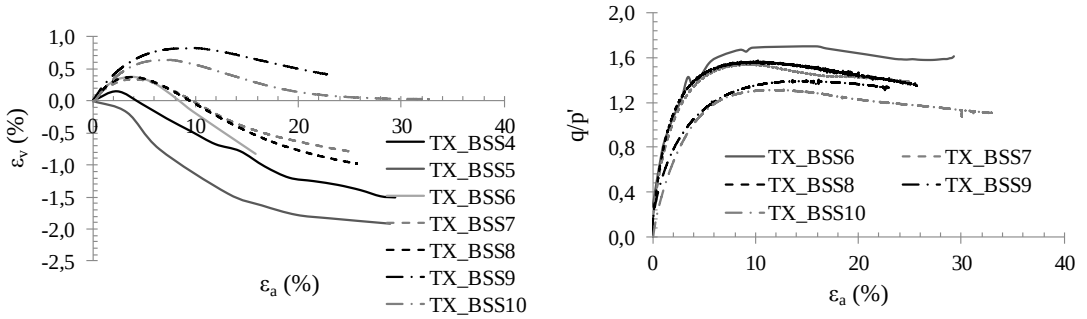

(c) (d)

Figure 5.9. Results of drained triaxial tests on Pieve di Cento (BSS) sand in the typical planes: ε_a-q (a); p'-q (b); ε_a- ε_v (c); ε_a-q/p' (d).

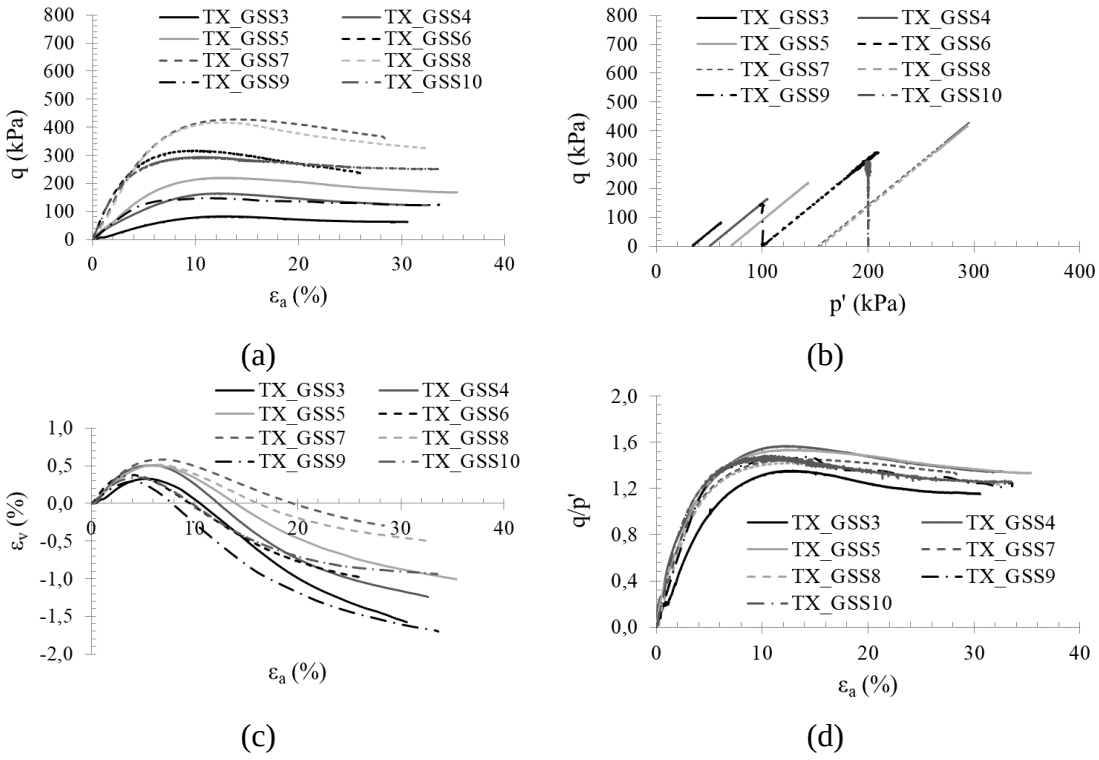

(a) (b)

(c) (d)

Figure 5.10. Results of drained triaxial tests on Pieve di Cento (GSS) sand in the typical planes: ε_a-q (a); p'-q (b); ε_a- ε_v (c); ε_a-q/p' (d).

As well-known the identification of the critical state line is a crucial element for the development and the use of constitutive models for sands, but it should be specified that the critical state condition for sands is difficult to define. It is due to two experimental problems: the first is that usually, at the end of drained triaxial tests, volumetric strains have not stopped yet; the second is that strain localization tends to make the measurements of volume changes or pore pressure in drained and undrained tests, respectively, less accurate and representative of the true soil behaviour at critical state. Moreover, it takes no sense to reach axial deformations larger than 20-25% in laboratory because the hypothesis of cylindrical shape and homogeneity of the specimen cannot hold

anymore, so uncertainties arise on stress and strain evaluations. In almost all tests, the critical state is not reached, so that the CSL and the critical state friction angle (φ_{cv}) for Italian sands, can be evaluated by extrapolation of the experimental results, through the best fitting of the data with a sigmoidal function. The details of this procedure are shown in Appendix A.

Putting together the results of drained and undrained compression tests in the plane e-logp', the critical state line of each tested sand can be identified as a power function, whose form has been reported in eq. (2.1). The parameters Γ, λ and ξ have been calibrated for Sant'Agostino and Pieve di Cento sands to have the best fitting with the experimental results (Fig. 5.11a-c-e). In the plane p' – q, the CSL can be represented as a straight line passing through the origin (eq. (2.2)), the slope of the line is M_{cs} (Fig. 5.11b-d-f). Moreover, solving eq. (2.3) the critical state angle φ_{cs} can also be achieved. In Table 5.4 void ratio and effective stress in critical state conditions, e_{cs} and p'_{cs} respectively, are reported, while in Table 5.5, the fundamental parameters in critical state condition (Γ, λ, ξ, M_{cs} and φ_{cs}) for the three kinds of tested sands are compared.

In Figure 5.11a-c-e, a good agreement in CSL for both drained and undrained tests can be observed. Nevertheless, the general trend of drained tests presents a scatter which is more significant than that shown in undrained tests and it is in agreement with the experimental data of Vergulto and Ishihara (1996). It seems to suggest that the results of undrained tests are preferable to identify the CSL. On the contrary, the drainage conditions (drained or undrained) seem not to influence the friction angle in critical state condition (φ_{cs}).

The same eqs. (2.2-2.3) can be used to evaluate the state of phase transformation. In Figure 5.13 the experimental results of Italian sands have been plotted in the plane p' – q. As for the critical state, the value of M_{TP} can be obtained. In Table 5.6 the friction angles of phase transformation (φ_{PT}) are summarized for the tested sands.

It is worth noting that the friction angles of phase transformation (φ_{PT}) and those of critical state (φ_{cs}) obtained by the experimental data are very similar (Tabs. 5.5 – 5.6) with φ_{PT} slightly lower than φ_{cs}.

Table 5.4. Results of monotonic triaxial tests in terms of critical state conditions (Bishop & Wesley apparatus).

Test	Sand	σ'_c (kPa)	Stress path	e_0*	D_{r0}* (%)	e_{cs}	p'_{cs} (kPa)
TX_SAS1							
TX_SAS2							
TX_SAS3							
TX_SAS4							
TX_SAS5							
TX_SAS6							
TX_SAS7							
TX_SAS8							
TX_BSS1	PdC_BSS	50	C_CIU	0.765	55.7	0.705	201.1
TX_BSS2	PdC_BSS	100	C_CIU	0.784	51.8	0.784	286.0
TX_BSS3	PdC_BSS	200	C_CIU	0.773	54.0	0.773	302.1
TX_BSS4	PdC_BSS	20	C_CID(p')	0.830	42.5	0.858	20.0
TX_BSS5	PdC_BSS	30	C_CID(p')	0.712	66.4	0.746	30.0
TX_BSS6	PdC_BSS	10	C_CID	0.795	49.6	0.825	21.1
TX_BSS7	PdC_BSS	75	C_CID	0.863	35.8	0.875	143.0
TX_BSS8	PdC_BSS	100	C_CID	0.761	56.5	0.779	183.1
TX_BSS9	PdC_BSS	200	C_CID	0.719	65.0	0.714	357.9
TX_BSS10	PdC_BSS	250	C_CID	0.784	51.8	0.780	412.4
TX_GSS1	PdC_GSS	50	C_CIU	0.658	51.1	0.658	364.2
TX_GSS2	PdC_GSS	100	C_CIU	0.649	53.2	0.649	360.7
TX_GSS3	PdC_GSS	30	C_CID	0.656	51.6	0.687	54.3
TX_GSS4	PdC_GSS	50	C_CID	0.622	59.3	0.646	92.2
TX_GSS5	PdC_GSS	70	C_CID	0.684	45.2	0.706	132.1
TX_GSS6	PdC_GSS	100	C_CID	0.720	37.1	0.721	189.2
TX_GSS7	PdC_GSS	150	C_CID	0.695	42.8	0.701	273.2
TX_GSS8	PdC_GSS	150	C_CID	0.730	34.8	0.739	277.7
TX_GSS9	PdC_GSS	100	C_CID(p')	0.650	52.9	0.695	100.0
TX_GSS10	PdC_GSS	200	C_CID(p')	0.726	35.7	0.743	200.0

*at the end of consolidation phase. CID=consolidate isotropically drained; CIU= consolidate isotropically undrained; CID(p')= consolidate isotropically drained with p' constant; C=compression; E=extension.

Figure 5.11. Critical state lines in the plane logp' - e (a-c-e) and p' – q (b-d-f) for Sant'Agostino and Pieve di Cento sand (BSS and GSS), respectively.

Table 5.5. Critical state parameters obtained to have the best fitting with the experimental results of triaxial tests.

Sand	Γ	λ	ξ	M_{cs}	φ_{cs} (°)
Sant'Agostino					
Pieve di Cento (BSS)					
Pieve di Cento (GSS)					

Figure 5.12. Critical state lines for Italian sands in the plane logp' – e.

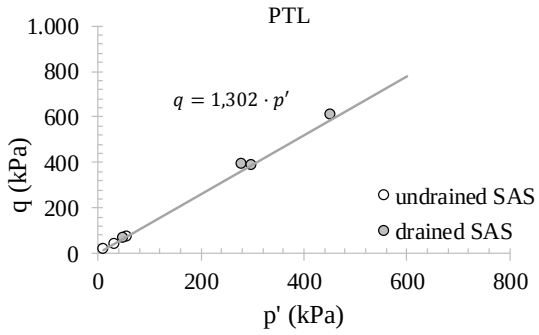

(a) SAS

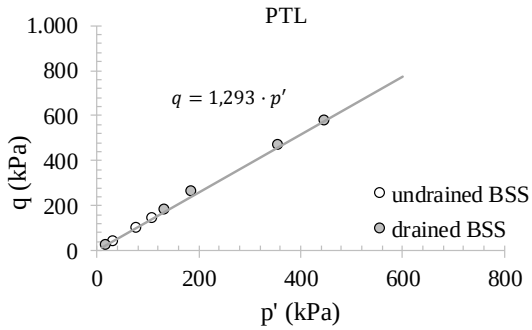

(b) BSS

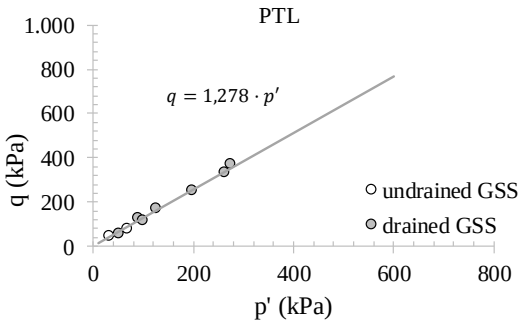

(c) GSS

Figure 5.13. Phase transformation state line in the plane p' – q for SAS (a), BSS (b) and GSS (c).

Table 5.6. Phase transformation state parameters.

Sand	M_{PT}	φ_{PT} (°)
Sant'Agostino		
Pieve di Cento (BSS)		
Pieve di Cento (GSS)		

5.1.3.1 THE EFFECTS OF END CONDITIONS

In order to evaluate the effect of the used device and in particular, the effects of end conditions on the results of triaxial tests, further monotonic tests (drained and undrained) on GSS have been carried out by using MaTrix cell (§ 4.2.2). In Table 5.7 the performed tests have been summarized.
As already mentioned, one of the most important characteristics of this device consists of smooth plates, that have been used to minimize non-homogeneities in the strain distribution and to avoid the development of shear bands. Moreover, one test (JTX_GSS5_free) has been performed with a free moving plate (bottom), limiting the experimental problem of non-uniform strains.

Table 5.7. Experimental program of triaxial tests performed in a MaTrix cell.

Test	Sand	σ'_c (kPa)	Stress path	e_0*	D_{r0}* (%)
JTX_GSS1	PdC_GSS				
JTX_GSS2	PdC_GSS				
JTX_GSS3	PdC_GSS				
JTX_GSS4	PdC_GSS				
JTX_GSS5_free	PdC_GSS				
JTX_GSS6	PdC_GSS				
JTX_GSS7	PdC_GSS				
JTX_GSS8	PdC_GSS				
JTX_GSS9	PdC_GSS				
JTX_GSS10	PdC_GSS				

*at the end of consolidation phase. CID=consolidate isotropically drained; CIU= consolidate isotropically undrained; C=compression.

In Figure 5.14 the results of the undrained tests have been plotted in the traditional planes: ε_a – q (a); p' – q (b), ε_a – Δu (c) and ε_a-q/p' (d). The tests have been carried out with similar values of relative densities ($D_r \approx 38.3\%$) and different confining stresses: 50, 100 and 150 kPa. A stable response of soil can be noted in stress-strain relationship, while a contractive, followed by a dilative behaviour is shown in the plane ε_a – Δu, it is much more pronounced for the lowest confining stresses.

Figure 5.14. Results of undrained tests in MaTrix cell plotted in the plane ε_a-q (a); p' -q (b), ε_a-Δu (c) and ε_a-q/p' (d).

In addition, the results of seven drained tests have plotted together in the planes: ε_a – q; p' – q; ε_a – ε_v and ε_a – q/p' respectively in Figure 5.15a-b -c-d.

Plotting together the results of drained tests in the plane ε_a – q/p' (Fig. 5.15d), it can be noted that they overlap to each other.

Figure 5.15. Results of drained tests in MaTrix cell plotted in the plane ε_a-q (a); p' -q (b); ε_a- ε_v (c); ε_a-q/p' (d).

With the main aim to evaluate the effects of end conditions on the behaviour of sandy soils, the results of triaxial tests obtained from the Bishop & Wesley Triaxial cell were compared to those from the MaTrix cell. It should be specified that even though the specimens have been prepared with similar relative densities, two different preparation techniques have been adopted (frozen specimens for Bishop & Wesley and 1D compression for MaTrix cell).

In Figures 5.16 and 5.17 undrained test results have been plotted for confining stresses of 50 and 100 kPa, respectively. For σ'_c of 50kPa the value of maximum deviatoric stress is roughly the same, even if it is reached at different values of axial strain: 10% in MaTrix cell and beyond 20% in Bishop & Wesley cell (Fig. 5.16a). For specimens consolidated at 100kPa, the maximum deviatoric stress of Bishop & Wesley is higher than that recorded in MaTrix cell (Fig. 5.17a), where a more stable behaviour is exhibited. Moreover, in both cases, lower excess pore pressure develops in MaTrix cell even though the maximum positive values of excess pore pressure reached in tests consolidated at 100kPa are identical (Fig. 5.17c).

Looking at the comparisons between the results from the two types of device used in this research, one of the most evident differences is the stiffness of the specimens, evaluating through the Young's modulus in undrained conditions (E_0), defined as the ratio between q and ε_a. The stiffness is smaller in Bishop & Wesley as shown in Figures 5.16d – 5.17d and it can be considered as an effect of a better uniformity of strains into the specimens. However, it should be specified that ε_a at small levels of strain have been measured by means of a Gap Sensor (GS), which is placed on the top cap of the specimen, inside the

cell. It allows to have more precise measures of the displacements of the specimen, without taking into account the stiffness of the loading system.

Figure 5.16. Comparisons between the results of undrained tests in Bishop & Wesley (TX_GSS1) and MaTrix (JTX_GSS1) cell with a confining stress of 50kPa.

Figure 5.17. Comparisons between the results of undrained tests in Bishop & Wesley (TX_GSS2) and MaTrix (JTX_GSS2) cell with a confining stress of 100kPa.

Similar considerations can be done for drained tests. As for undrained tests, the drained tests have been grouped based on the same value of the confining stress. In Figures 5.18 -19 -20 the results for 50, 100 and 150 kPa are shown, respectively. In all cases, as for undrained tests, the stiffness in drained conditions (Young modulus, E) is lower for the specimens tested in Bishop & Wesley apparatus than for those tested in the MaTrix cell. Overall, the mechanical response of Pieve di Cento (GSS) sand achieved in Bishop & Wesley and MaTrix cells are very different. In particular, specimens consolidated to 150kPa, with similar values of D_r, show a completely different behaviour (Fig. 5.20c): specimens tested in the MaTrix cell are contractive, while those tested in the Bishop & Wesley show a dilative response. It suggests that different CSLs are expected.

Figure 5.18. Comparisons between the results of drained tests in Bishop & Wesley (TX_GSS4) and MaTrix cell (JTX_GSS4 and JTX_GSS5_free) with a confining stress of 50kPa.

Figure 5.19. Comparisons between the results of drained tests in Bishop & Wesley (TX_GSS6) and MaTrix (JTX_GSS6 and JTX_GSS7) cell with a confining stress of 100kPa.

Figure 5.20. Comparisons between the results of drained tests in Bishop & Wesley (TX_GSS7 and TX_GSS8) and MaTrix (JTX_GSS8 and JTX_GSS9) cell with a confining stress of 150kPa.

Unlike the results of tests performed in the Bishop & Wesley triaxial cell, all specimens of MaTrix cell attain a steady condition, apart from JTX_GSS6 test which was stopped at ε_a of 13% because of an experimental problem, it implies that no need to extrapolate the data in critical state conditions. It can be considered as an effect of lubricated ends, enable to avoid localization phenomena of strains into the specimens. The results of triaxial tests performed in a MaTrix cell have been summarized in Table 5.8 in terms of void ratio and mean effective stress in critical state conditions (e_{cs} and p'_{cs}, respectively).

Table 5.8. Results of monotonic triaxial tests in terms of critical state conditions (MaTrix cell).

Test	Sand	σ'_c (kPa)	Stress path	e_0*	D_{r0}* (%)	e_{cs}	p'_{cs} (kPa)
JTX_GSS1	PdC_GSS						
JTX_GSS2	PdC_GSS						
JTX_GSS3	PdC_GSS						
JTX_GSS4	PdC_GSS						
JTX_GSS5_free	PdC_GSS						
JTX_GSS6	PdC_GSS						
JTX_GSS7	PdC_GSS						
JTX_GSS8	PdC_GSS						
JTX_GSS9	PdC_GSS						
JTX_GSS10	PdC_GSS						

*at the end of consolidation phase. CID=consolidate isotropically drained; CIU= consolidate isotropically undrained; C=compression.

The CSL is obtained in the plane logp' - e by the best fitting with the experimental results (Fig. 5.21a), while the friction angle in critical state condition (φ_{cs}) can be estimated plotting the experimental data in the plane p' – q (Fig. 5.21b) and then applying eq (2.3). The critical state parameters have been summarized in Table 5.9. A useful comparison between the CSL from Bishop & Wesley and MaTrix cell results is reported in Figure 5.21c-d. The CSL from MaTrix data is above that obtained from Bishop & Wesley cell data, even though the difference is not so significant (Tab. 5.9). On the contrary, an important difference can be observed in terms of φ_{cs} (Fig. 5.21d; Tab. 5.9): the friction angle in critical state conditions is 36.7° for tests performed in MaTrix cell and 32.9° in Bishop & Wesley apparatus. These results are in agreement with those reported in literature. In fact, even though a peak of strength should occur in tests performed with rough plates, it is followed by a softening (non-uniformity of strains), which is responsible of an underestimation of the φ_{cs}.

In conclusion, it can be observed that the difference between the results of tests performed by the two different triaxial cells (Bishop & Wesley and MaTrix) at the critical state should be attributed to the effect of ends conditions, since the preparation technique does not play an important role in identification of critical state parameters.

Figure 5.21. Critical state lines in the plane logp' - e (a) and p' – q (b) for Pieve di Cento sand (GSS), evaluated through a MaTrix cell; while a comparison with the results obtained in Bishop&Wesley cell in the plane logp' - e (c) and p' – q (d) have been reported, as well .

Table 5.9. Critical state parameters obtained by triaxial tests for GSS sand.

Apparatus	Γ	λ	ξ	M_{cs}	φ_{cs} (°)
Bishop&Wesley					
MaTrix					

5.1.3.2 INTERPRETATION OF UNDRAINED SIMPLE SHEAR TESTS AND COMPARISONS WITH TRIAXIAL TESTS

In order to compare the results of monotonic tests performed in triaxial and simple shear devices, further tests, summarized in Table 5.10, have been carried out in a simple shear apparatus.

Undrained simple shear tests on Pieve di Cento (GSS) sand were performed with flexible boundary because this configuration allows to control the value of horizontal stress. The specimens have been prepared with two average relative density (D_r): 41 and 70% to compare the monotonic response of loose and dense specimens. They have been prepared by 1D-compression method, except for SS_GSS4, which has been reconstituted by moist tamping, so that also the effect of specimen's preparation will be shown and discussed

below. Specimens were saturated and consolidated at different confining stresses (Tab. 5.10). As already explained in paragraph 4.2.4, the consolidation is performed by means of a sophisticated control system which allows to maintain a constant diameter and thus to guarantee a simple shear stress condition.

Table 5.10. Undrained simple shear tests on Pieve di Cento sand (GSS).

Test	Sand	Prep. Tech	σ'_h (kPa)	σ'_v (kPa)	e_0*	D_{r0}* (%)	Stress-path
SS_GSS1	GSS	1D-C					
SS_GSS2	GSS	1D-C					
SS_GSS3	GSS	1D-C					
SS_GSS4	GSS	MT					
SS_GSS5	GSS	1D-C					

However, the control system needed to impose a simple shear condition, introduces unavoidable oscillations of the diameter's measure around the target value. Quantifying these oscillations is extremely important to understand if a truly simple shear condition occurs. In other words, the radial strains (ε_r) should be small enough to remain in elastic field; on the contrary, plastic deformations could be induced, changing the diameter permanently (Lirer et al., 2011). In this framework, the radial strains have been computed during the k_0-consolidation phase. As an example, in Figures 5.22 ε_r has been plotted versus time for a loose (SS_GSS1; a) and a dense (SS_GSS3; b) specimen.
In both cases, the radial strains have an order of magnitude of 10^{-3}% that can be considered low enough to assume the deformations belong to the elastic field (the elastic threshold is generally indicated with the value of 10^{-3}%).

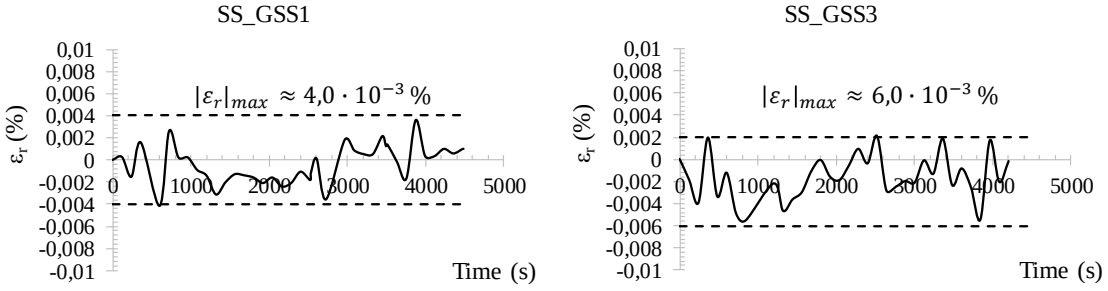

(a) (b)

Figure 5.22. Radial strain with time during k_0-consolidation for a loose specimen (a) and a dense one (b).

Established that the radial strains are not significant, and consequently a simple shear condition can be guarantee, the results of monotonic tests have been reported and discussed as follows. The shear stress has been imposed with a rate of 0.001 mm/min in undrained conditions. In Figures 5.23 and 5.24 the results have been reported in the typical planes: γ-τ (a); $\sigma'_v - \tau$ (b); γ-Δu (c), for loose and dense specimens, respectively.

As expected, the denser specimens (Fig. 5.24) exhibit a strain hardening type response. Even though the tests were conducted under different initial vertical stresses and void ratios, the stress path show a similar pattern of behaviour. Moreover, the effect of specimen's preparation seems not to be relevant as demonstrated by comparing SS_GSS3 and SS_GSS4 tests performed under similar conditions but reconstituted by different preparation methods: 1D-compression and moist tamping, respectively. Although, it should be emphasized that such techniques are very similar as it will be discussed in paragraph 5.1.5.3.

Regarding the critical state, apart from SS_GSS1 and SS_GSS4, the steady state is not reached for shear strains of 15 or 20%. Therefore, as for triaxial tests, the extrapolation is needed. Further details have been reported in Appendix A.

Figure 5.23. Results of simple shear tests for loose specimens in the planes: γ-τ (a); σ'_v – τ (b); γ-Δu (c).

Figure 5.24. Results of simple shear tests for dense specimens in the planes: γ-τ (a); σ'_v – τ (b); γ-Δu (c).

As already discussed in Chapter 2, the interpretation of simple shear tests is not very easy and still today this topic is widely discussed in literature. With the main aim to contribute at improving the interpretation of this kind of tests, further considerations have been done on the results of undrained simple shear tests. First of all, it should be reminded that unlike triaxial tests, in simple shear tests a continuous rotation of principal stress directions occurs: it means that the vertical and horizontal stresses are not principal anymore, as in triaxial tests.

This interpretation has been used to evaluate the friction angle in critical state condition (φ_{cv}), which is equal to 35.8°, consistent with the value achieved from triaxial tests in MaTrix cell (36.7°) and higher than that obtained from triaxial tests in Bishop & Wesley cell (32.9°).

Figure 5.25. Interpretation of undrained simple shear tests for loose and dense specimens by means of Mohr's circle (a and b) and rotation of vertical principal stress direction (c and d).

A comparison between the results of undrained simple shear and triaxial tests in the plane γ- τ is reported in Figure 5.26. Such tests have similar initial conditions, and the comparison is possible considering the shear strain (γ) as 1.5 times the axial strains (ε_a) and the shear stress as q/2. In triaxial test higher shear stress can be observed probably due mainly to a difference in consolidation phase: isotropic for triaxial and anisotropic (k_0 condition) in simple shear. However, further tests are needed to better understand such interesting aspect.

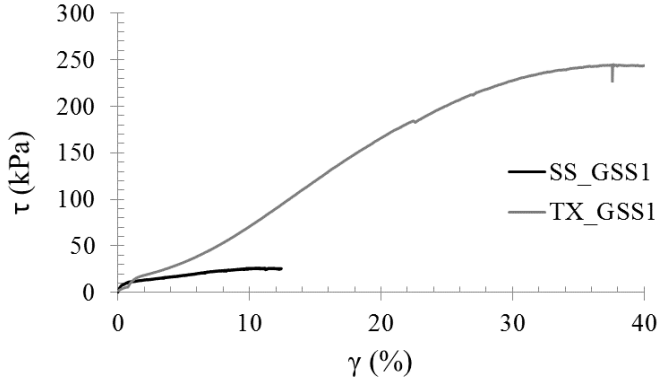

Figure 5.26. Comparison of simple shear (SS_GSS1) and triaxial test results (TX_GSS1) in the plane γ-τ.

Finally, further considerations have been done to identify the critical state line (CSL) in the plane logp' - e. In Table 5.11 the results are summarized, while in Figure 5.27 the results of undrained simple shear (SS) tests are plotted in the plane logp' - e to identify a critical state line (CSL), which is compared with that achieved from triaxial (TX) test results.

Consistently with Riemer and Seed (1997), the CSL from SS tests is below that from TX tests (Bishop & Wesley and MaTrix cell), even though the slope is the same and the scatter of the experimental data is much more evident. Further tests are needed to confirm the found curve.

Table 5.11. Undrained simple shear tests on Pieve di Cento sand (GSS).

Test	Sand	Prep. Tech	σ'_h (kPa)	σ'_v (kPa)	e_0*	D_{r0}* (%)	Stress-path	e_{cs}	p'_{cs} (kPa)
SS_GSS1	GSS	1D-C							
SS_GSS2	GSS	1D-C							
SS_GSS3	GSS	1D-C							
SS_GSS4	GSS	MT							
SS_GSS5	GSS	1D-C							

*at the end of consolidation phase.

Figure 5.27. Critical state lines achieved for undrained SS tests in the plane logp' – e, compared with those evaluated for TX tests.

Table 5.12. Critical state parameters obtained by monotonic tests for GSS sand.

Apparatus	Γ	λ	ξ
TX_Bishop&Wesley			
TX_MaTrix			
Simple Shear			

5.1.4 CYCLIC TRIAXIAL TESTS

With the main aim to evaluate the cyclic behaviour and consequently, the cyclic resistance curves of the tested sands, undrained cyclic triaxial and simple shear tests have been performed on several sands (Fig. 4.1 and Tab. 4.1) as reported in Table 5.13. The results of cyclic triaxial tests have been discussed as follows.

Cyclic triaxial tests on untreated specimens have been performed in a Bishop & Wesley apparatus (§4.2.1). The tests have been carried out on specimens with a D_r, ranging between 37.2 and 54.9 %. The confining stress investigated is generally 50 kPa, except for Leighton Buzzard specimens that have been consolidated also at 25 and 100 kPa. These conditions are similar to the natural conditions in situ of the liquefiable sandy soils. The cyclic stress ratio (CSR) was imposed in the range 0.080 – 0.300, as shown in Table 5.13.

Table 5.13. Cyclic triaxial tests on untreated sandy soils.

Test	Sand	σ'_c (kPa)	e_0*	D_{r0} * (%)	CSR
CTX_LB1	Leighton Buzzard	25	0.825	46.6	0.115
CTX_LB2	Leighton Buzzard	50	0.835	44.1	0.179
CTX_LB3	Leighton Buzzard	50	0.794	54.4	0.128
CTX_LB4	Leighton Buzzard	50	0.824	46.9	0.109
CTX_LB5	Leighton Buzzard	50	0.812	49.9	0.080
CTX_LB6	Leighton Buzzard	50	0.805	51.6	0.097
CTX_LB7	Leighton Buzzard	50	0.792	54.9	0.147
CTX_LB8	Leighton Buzzard	100	0.837	43.6	0.099
CTX_LB9	Leighton Buzzard	100	0.832	44.8	0.147
CTX_T1	Ticino				
CTX_T2	Ticino				
CTX_T3	Ticino				
CTX_SAS1	Sant'Agostino	50	0.707	47.3	0.147
CTX_SAS2	Sant'Agostino	50	0.738	42.5	0.128
CTX_SAS3	Sant'Agostino	50	0.719	45.5	0.098
CTX_SAS4	Sant'Agostino	50	0.713	46.4	0.087
CTX_BSS1	PdC_BSS	50	0.808	47.0	0.210
CTX_BSS2	PdC_BSS	56	0.828	42.9	0.160
CTX_BSS3	PdC_BSS	50	0.769	54.9	0.180
CTX_GSS1	PdC_GSS	50	0.723	36.4	0.200
CTX_GSS2	PdC_GSS	50	0.699	41.9	0.180
CTX_GSS3	PdC_GSS	50	0.705	40.5	0.170
CTX_GSS4	PdC_GSS	50	0.704	40.7	0.150
CTX_GSS5	PdC_GSS	50	0.697	42.3	0.120

*at the end of consolidation phase.

As an example, the typical results of undrained cyclic triaxial tests have been reported in the following planes: ε_a – q; p' – q; N_{cyc} – CSR; N_{cyc} – r_u – ε_a, as shown in Figures 5.28 to 5.32 for Leighton Buzzard, Ticino, Sant'Agostino and Pieve di Cento (BSS and GSS) sands, respectively.

In Figure 5.28 the results of some tests carried out on Leighton Buzzard sand are shown. In the plane ε_a – q the area of each cycle increase with number of loading cycles, while the imposed deviatoric stress (q) is controlled during the tests, even though when liquefaction occurs (r_u=0.90 or $\varepsilon_{DA} \geq$5%) the load is not maintained (see for instance Figure 5.28g -m). In the plane p'-q the critical state line is also plotted as a grey dashed line in compression and in extension, according to the characterization of Visone (2008). The static characterization is consistent with the cyclic results of this research. As well-known, the stress-path moves toward the CSL, reducing effective mean stress as a consequence of pore pressure build-up. In Figure 5.28d-h-n both r_u, and axial strains (ε_a) are plotted versus the number of loading cycles. Regardless of confining stress, ε_a are extremely small during the first cycles and then suddenly increase until to reach the critical value of axial strains in double amplitude (ε_{DA}) of 5%. Similar considerations can be done for r_u with N_{cyc}. When it reaches a value of about 0.70, it increases quickly, attaining the critical value of 0.90.

Similar considerations can be done for Ticino sand (Fig. 5.29), even though in the performed tests on this material, both ε_a and r_u increase more gradually.

As regards of Italian sands, as for Leighton Buzzard, the static characterization performed in this research is consistent with the results of cyclic triaxial tests as shown in the plane p'-q (Figs. 5.30b-f-l; 5.31b-f-l; 5.32b-f-l). Moreover, it should be noted that even though just one test has been carried out in extension (TX_SAS8) for Sant'Agostino sand, the value of M_{ext} (q/p' = -0.888) has been considered to trace the critical state line for q lower than 0. The same CSL in extension has been assumed for Pieve di Cento sands (Figs. 5.31-5.32). In all tests, the supposed CSL in extension seems to be in good agreement with the results of cyclic triaxial tests. Furthermore, for Pieve di Cento sands (BSS and GSS), the cyclic stress-path has been plotted together with the corresponding undrained monotonic triaxial test: TX_BSS1 and TX_GSS1 consolidated at 50 kPa (Tab. 5.3). In both cases, at the beginning of cyclic phase the stress path follows that of monotonic test (Fig. 5.31b-c).

As already explained in Chapter 2, the liquefaction resistance of a soil in a known state, can be graphically identified in the plane N_{liq}- CRR through a cyclic resistance curve.

As already mentioned, it is assumed in this study that liquefaction is triggered at 5% double strain amplitude (ε_{DA}), according to strain criterion or at r_u=0.90, being $r_u=\Delta u/\sigma'_c$ (stress criterion), where Δu is the excess of pore water pressure for the specimen. As well known, for loose saturated soils stress and strain criteria give the same result in term of N_{liq}. It is confirmed by the results of this research, summarized in Table 5.14. The maximum scatter is 2 cycles for CTX_BSS3 test.

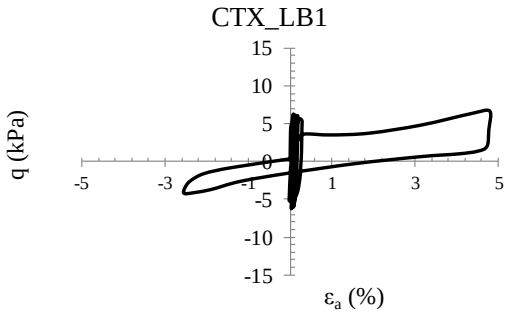

(a) σ'_c=25kPa

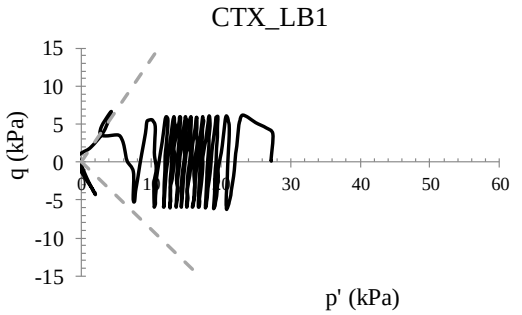

(b) σ'_c=25kPa

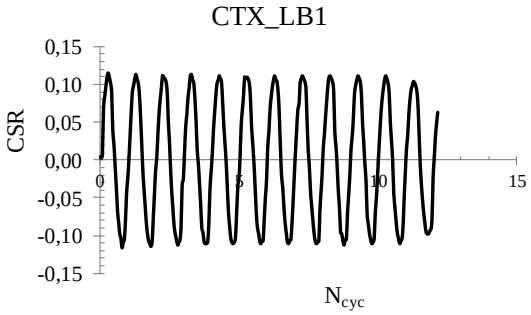

(c) σ'_c=25kPa

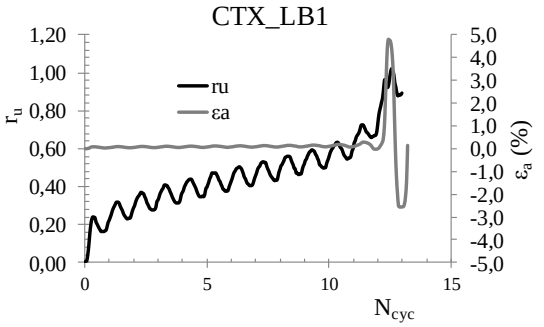

(d) σ'_c=25kPa

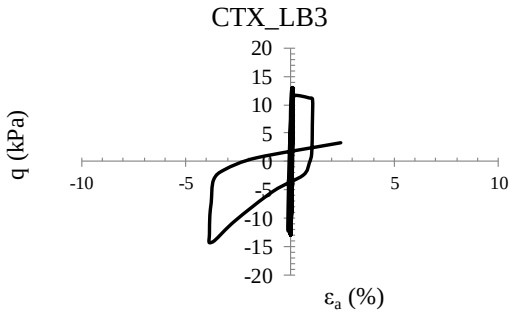

(e) σ'_c=50kPa

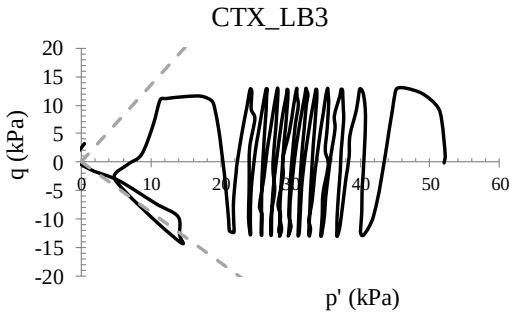

(f) σ'_c=50kPa

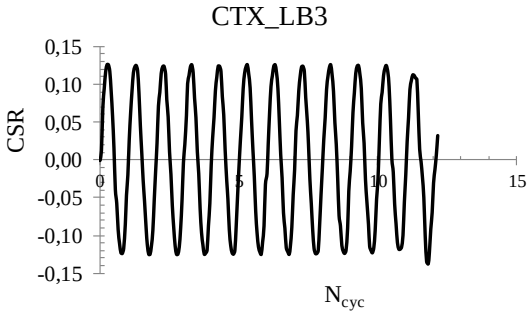

(g) σ'_c=50kPa

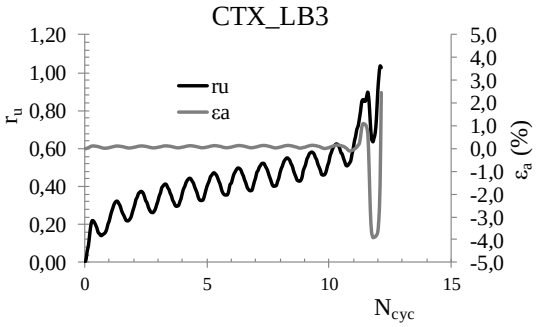

(h) σ'_c=50kPa

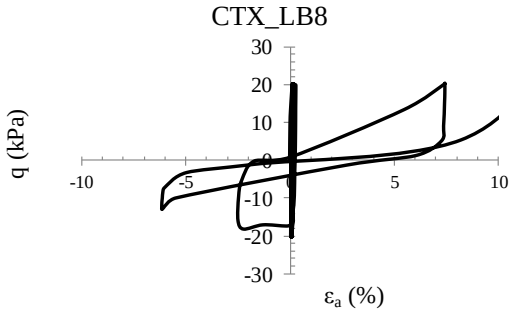

(i) σ'_c=100kPa

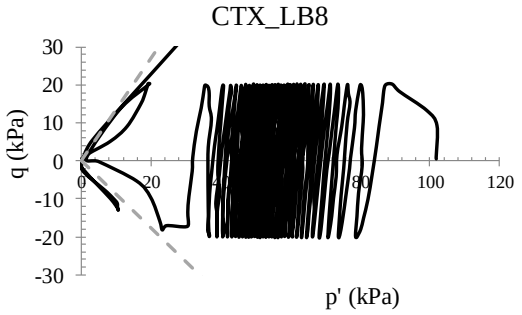

(l) σ'_c=100kPa

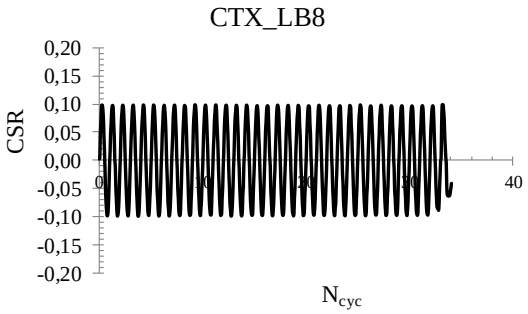

(m) σ'$_c$=100kPa

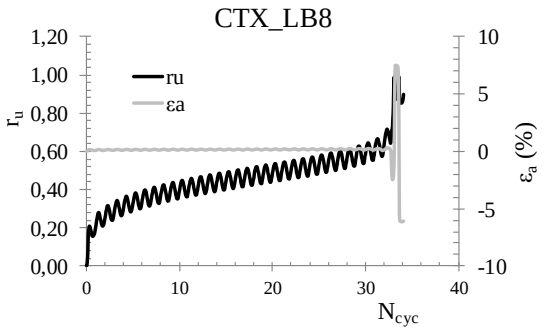

(n) σ'$_c$=100kPa

Figure 5.28. Results of cyclic triaxial tests on Leighton Buzzard sand in the planes: ε_a – q (a-e-i); p' – q (b-f-l); N_{cyc} – CSR (c-g-m); N_{cyc} – r_u – ε_a (d-h-n).

Figure 5.29. Results of cyclic triaxial tests on Ticino sand in the planes: ε_a – q (a-e); p' – q (b-f); N_{cyc} – CSR (c-g); N_{cyc} – r_u – ε_a (d-h).

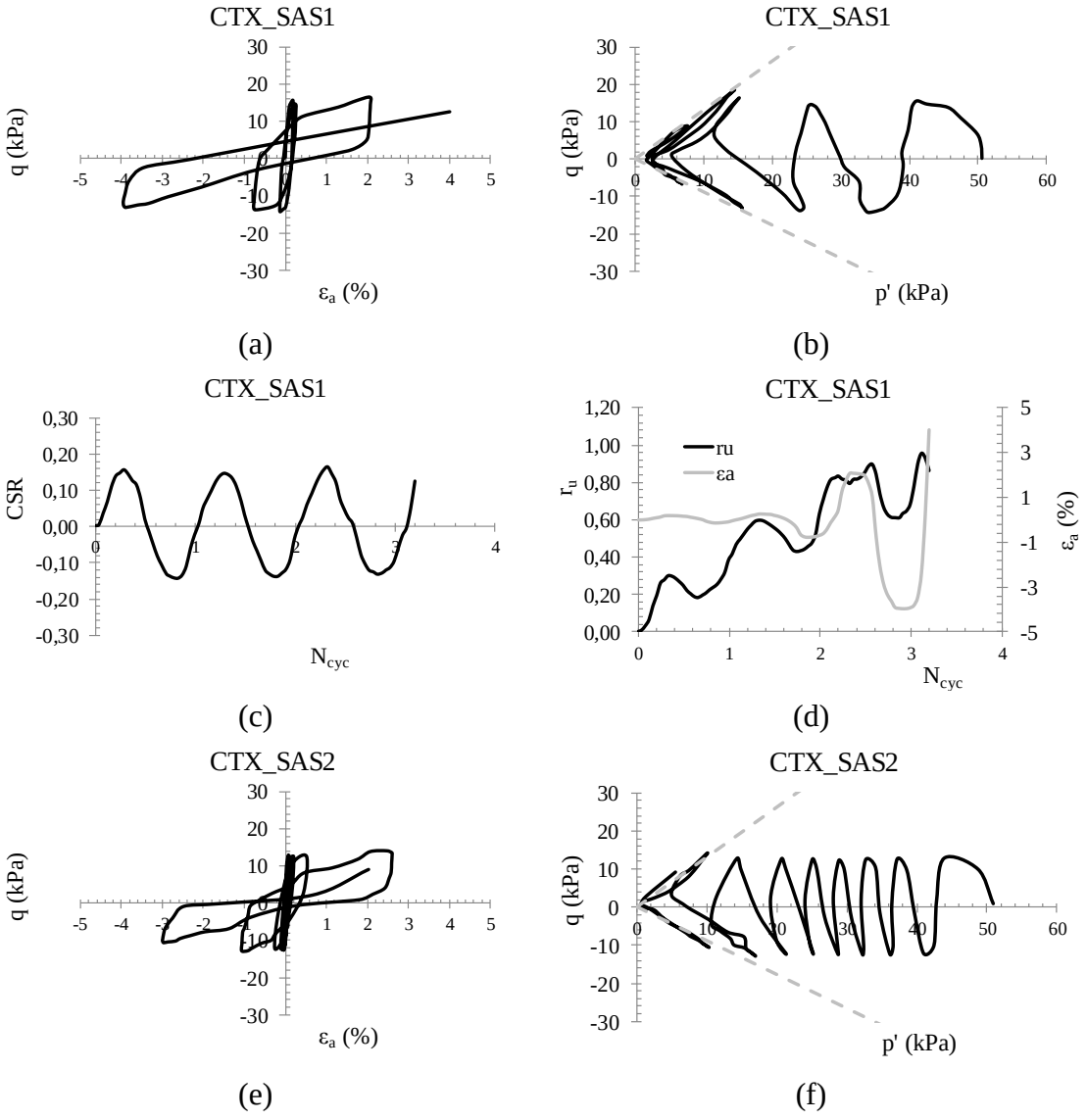

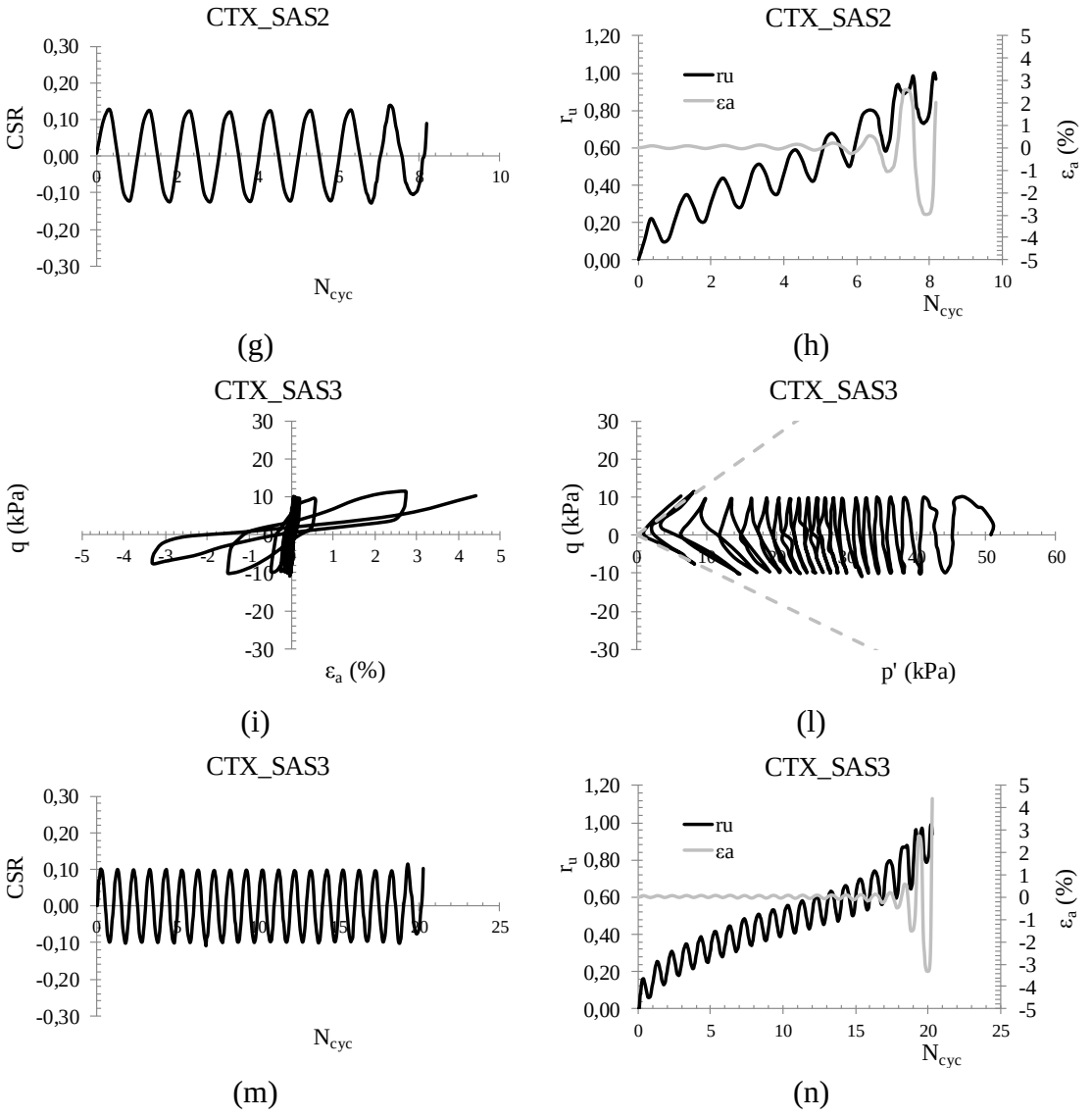

Figure 5.30. Results of cyclic triaxial tests on Sant'Agostino sand in the planes: ε_a – q (a-e-i); p' – q (b-f-l); N_{cyc} – CSR (c-g-m); N_{cyc} – r_u – ε_a (d-h-n).

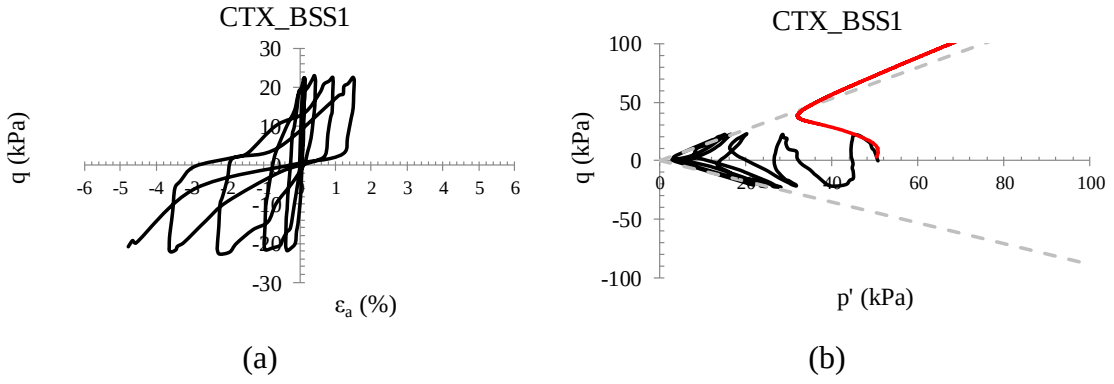

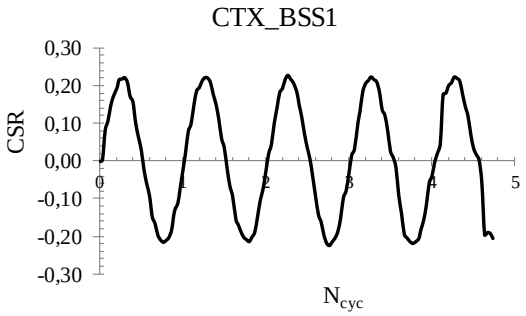
CTX_BSS1
CSR
N_cyc

(c)

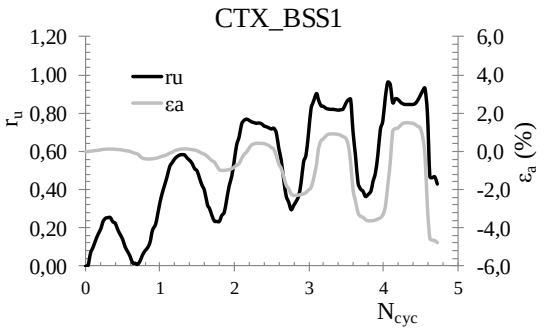
CTX_BSS1
ru
εa
r_u
ε_a (%)
N_cyc

(d)

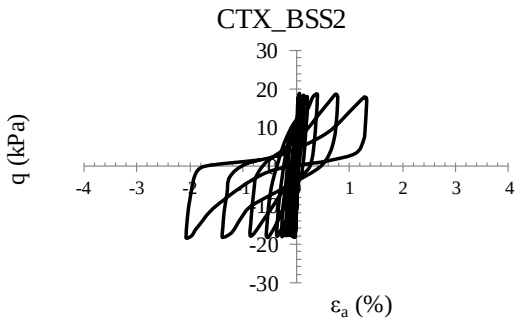
CTX_BSS2
q (kPa)
ε_a (%)

(e)

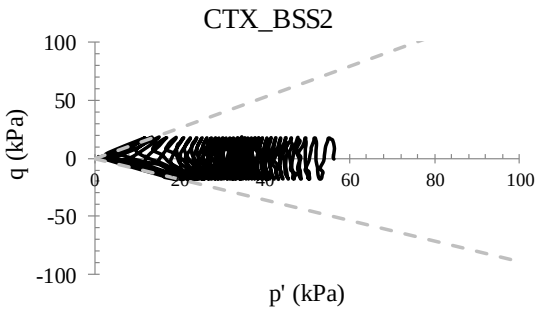
CTX_BSS2
q (kPa)
p' (kPa)

(f)

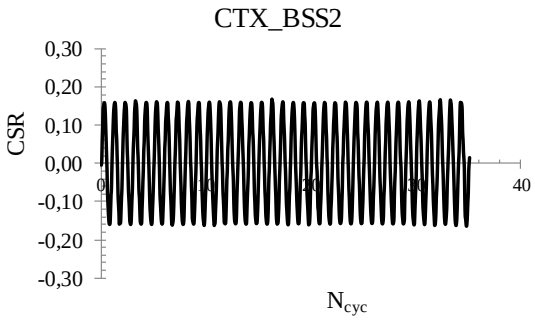
CTX_BSS2
CSR
N_cyc

(g)

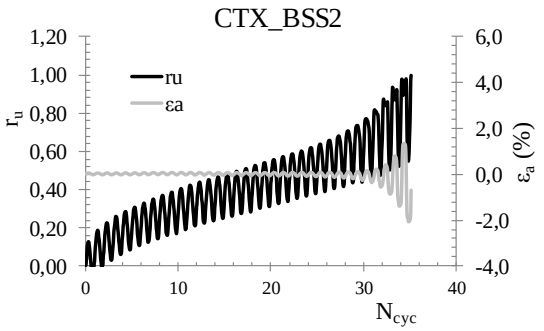
CTX_BSS2
ru
εa
r_u
ε_a (%)
N_cyc

(h)

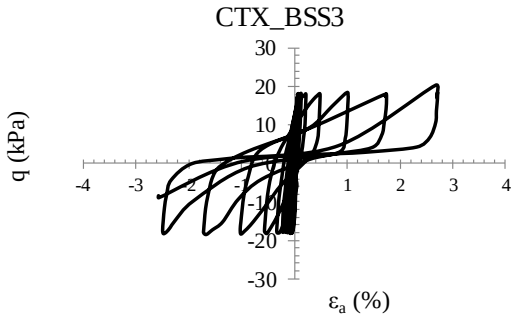
CTX_BSS3
q (kPa)
ε_a (%)

(i)

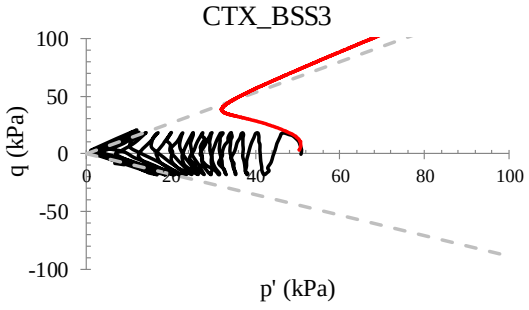
CTX_BSS3
q (kPa)
p' (kPa)

(l)

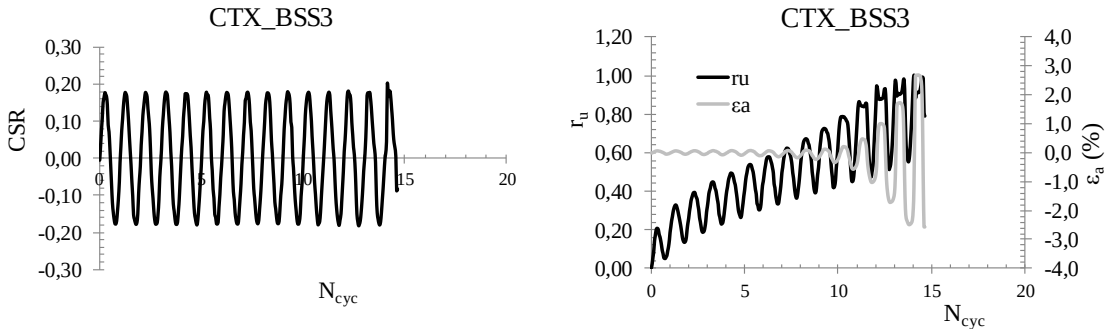

(m) (n)

Figure 5.31. Results of cyclic triaxial tests on Pieve di Cento (BSS) sand in the planes: ε_a – q (a-e-i); p' – q (b-f-l); N_{cyc} – CSR (c-g-m); N_{cyc} – r_u – ε_a (d-h-n).

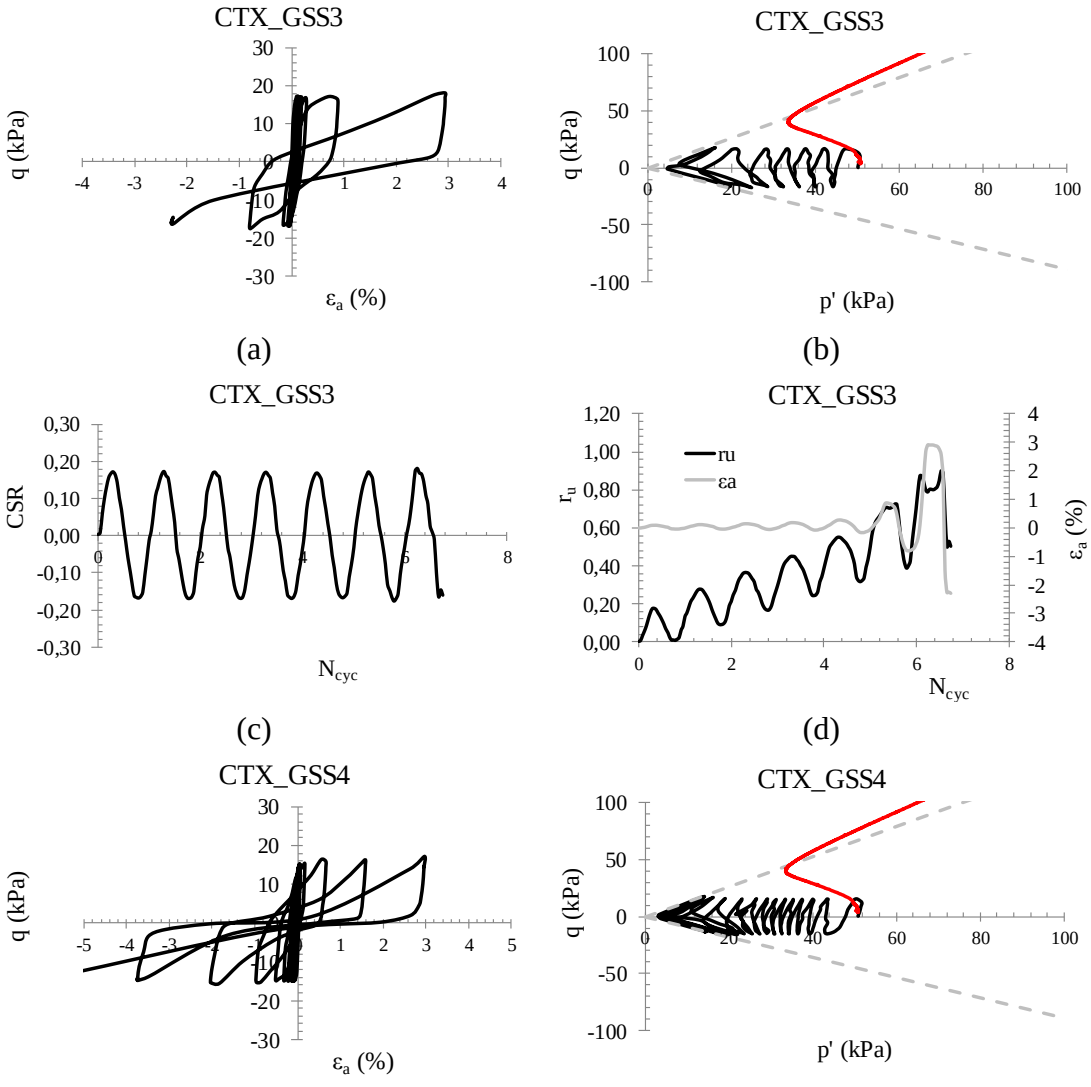

(a) (b)

(c) (d)

(e) (f)

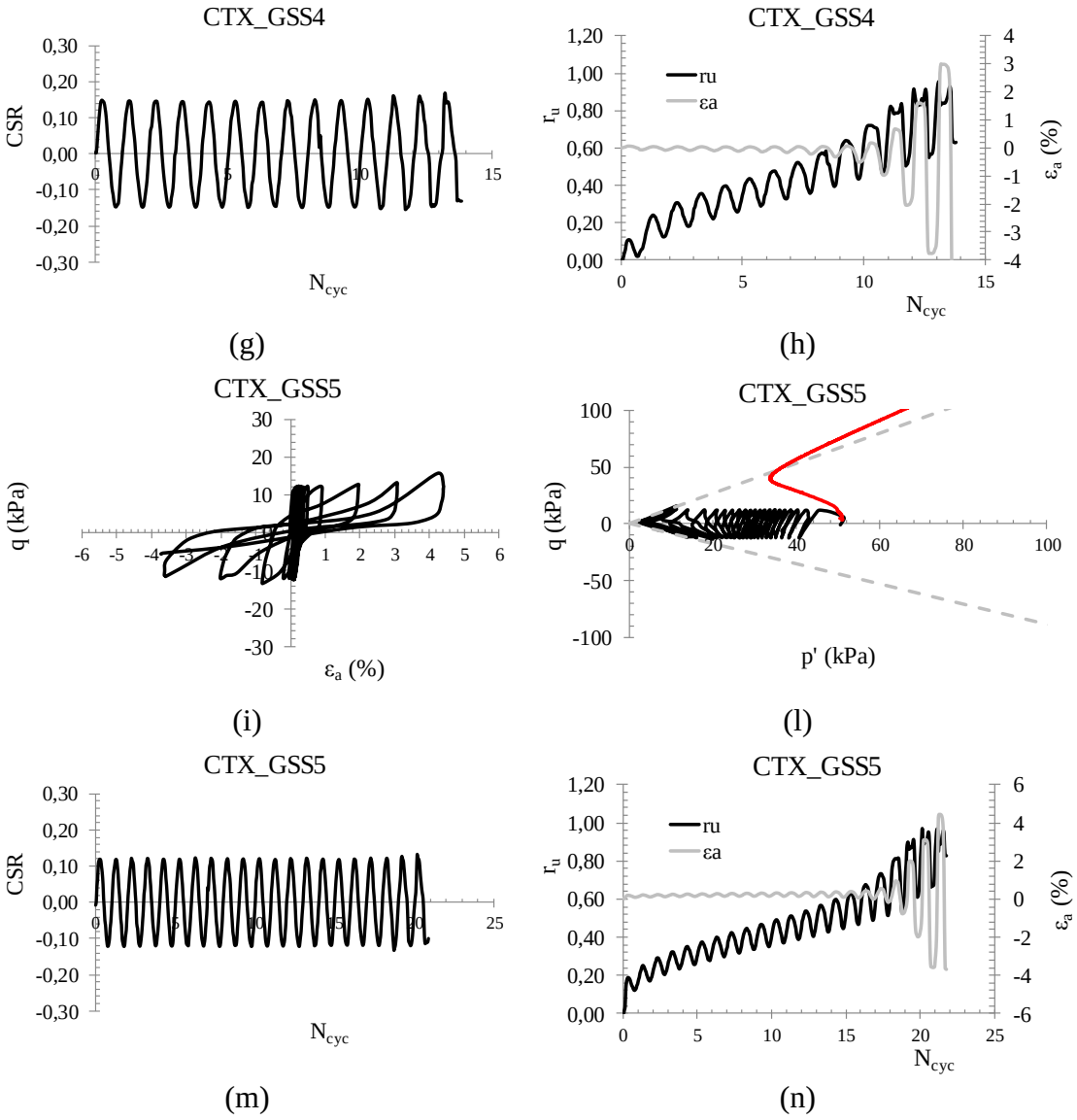

Figure 5.32. Results of cyclic triaxial tests on Pieve di Cento (GSS) sand in the planes: ε_a – q (a-e-i); p' – q (b-f-l); N_{cyc} – CSR (c-g-m); N_{cyc} – r_u – ε_a (d-h-n).

In Figure 5.33, the results of tests reported in Table 5.14 are plotted in the plane N_{liq}-CRR.

Apart from tests carried out on Leighton Buzzard sand, where three different values of confining stress have been imposed (25; 50 and 100 kPa), all specimens have been consolidated at a confining stress of 50 kPa (56 kPa for CTX_BSS2).

Despite the difference of confining stress, for Leighton Buzzard sand a unique liquefaction resistance curve may be defined. It would seem to confirm that the state parameter (ψ) introduced by Jefferies & Been (2006) might be used as a synthetic parameter, which expresses the resistance to liquefaction, taking into account the void ratio and the stress state of the specimens (eq. 2.4). The interpretation of cyclic triaxial tests through the state parameter will be discussed in the next paragraph (§5.1.4.1).

Table 5.14. Results of cyclic triaxial tests on sandy soils.

Test	Sand	σ'_c (kPa)	e_0*	D_{r0} *(%)	CSR	N_{liq} r_u=0.90	N_{liq} ε_{DA}=5%
CTX_LB1	Leighton Buzzard	25	0.825	46.6	0.115	12.3	12.0
CTX_LB2	Leighton Buzzard	50	0.835	44.1	0.179	1.2	1.0
CTX_LB3	Leighton Buzzard	50	0.794	54.4	0.128	12.0	12.0
CTX_LB4	Leighton Buzzard	50	0.824	46.9	0.109	14.2	14.0
CTX_LB5	Leighton Buzzard	50	0.812	49.9	0.080	No	No
CTX_LB6	Leighton Buzzard	50	0.805	51.6	0.097	No	No
CTX_LB7	Leighton Buzzard	50	0.792	54.9	0.147	4.0	4.0
CTX_LB8	Leighton Buzzard	100	0.837	43.6	0.099	33.0	33.0
CTX_LB9	Leighton Buzzard	100	0.832	44.8	0.147	1.1	1.0
CTX_T1	Ticino						
CTX_T2	Ticino						
CTX_T3	Ticino						
CTX_SAS1	Sant'Agostino	50	0.707	47.3	0.147	3.0	2.7
CTX_SAS2	Sant'Agostino	50	0.738	42.5	0.128	7.0	7.5
CTX_SAS3	Sant'Agostino	50	0.719	45.5	0.098	19.0	19.0
CTX_SAS4	Sant'Agostino	50	0.713	46.4	0.087	No	No
CTX_BSS1	PdC_BSS	50	0.808	47.0	0.210	4.0	4.6
CTX_BSS2	PdC_BSS	56	0.828	42.9	0.160	33.0	>34
CTX_BSS3	PdC_BSS	50	0.769	54.9	0.180	12.0	14.0
CTX_GSS1	PdC_GSS	50	0.723	36.4	0.200	1.0	1.0
CTX_GSS2	PdC_GSS	50	0.699	41.9	0.180	1.5	1.5
CTX_GSS3	PdC_GSS	50	0.705	40.5	0.170	6.5	7.0
CTX_GSS4	PdC_GSS	50	0.704	40.7	0.150	12.1	12.5
CTX_GSS5	PdC_GSS	50	0.697	42.3	0.120	19.5	20.0

*at the end of consolidation phase.

The cyclic resistance of Sant'Agostino sand is lower than that of Pieve di Cento sand and it could be due to the fact that Sant'Agostino sand has a higher fines content - probably characterized by low plasticity - than Pieve di Cento sand (see Tab. 4.1). Regarding the comparison between the two kinds of Pieve di Cento sand (BSS and GSS), it could be noted that BSS has a higher resistance to liquefaction than BSS, but it might be due to a difference in term of D_r, 48 and 40%, respectively for BSS and GSS.

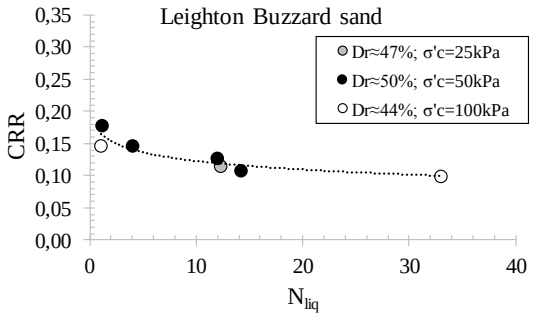

(a) (b)

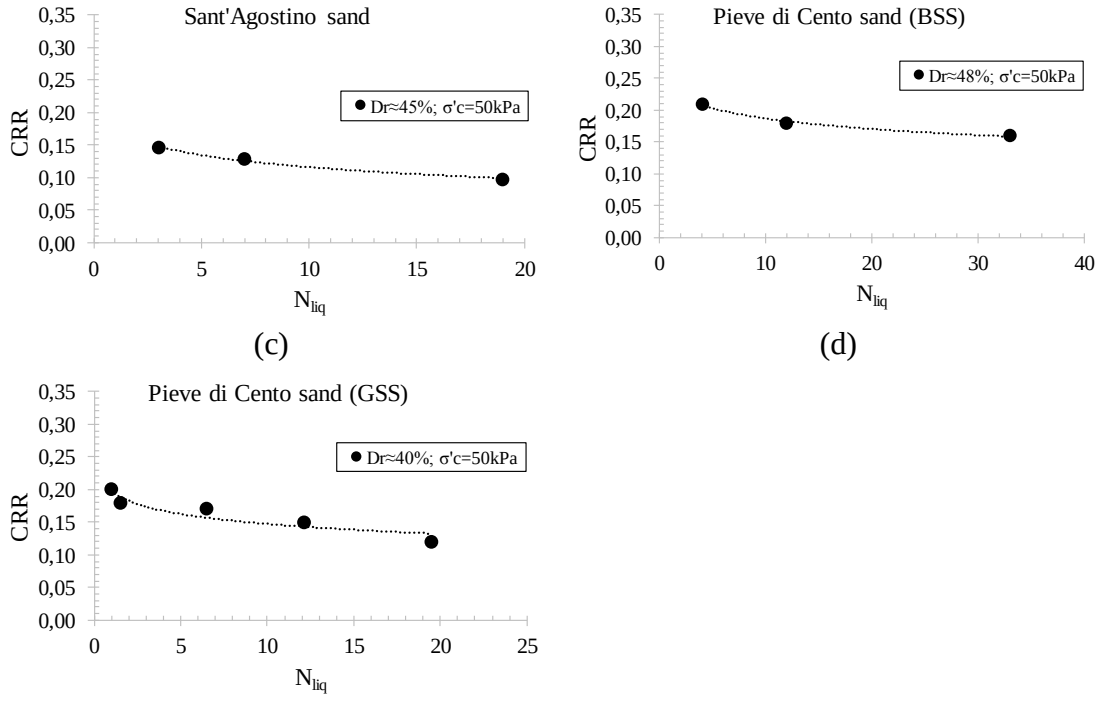

Figure 5.33. Cyclic resistance curves of tested soils: Leighton Buzzard (a); Ticino (b); Sant'Agostino (c) and Pieve di Cento (BSS and GSS) (d – e, respectively) sands.

5.1.4.1 INTERPRETATION OF CYCLIC TRIAXIAL TESTS THROUGH THE STATE PARAMETER (ψ)

The results of cyclic triaxial tests, which were performed on soils of which the CSL is known, have been interpreted through the state parameter (ψ) defined by eq. 2.4. For Italian sands, the critical state line has been identified from triaxial tests as reported in §5.1.3, while for Leighton Buzzard and Ticino sands the results of Visone (2008) and Fioravante and Giretti (2016) have been considered, respectively. In Table 5.15, the computed values of ψ are shown, while in Figure 5.34 the experimental results of this research for N_{liq} ranging between 12 and 19 are plotted together with the experimental results of Jefferies and Been (2006), performed on 13 different sands in the plane state parameter (ψ) versus CRR_{15}, which is the cyclic resistance ratio evaluated for N_{liq} equal to 15. It is worth noting that the red point, relating CTX_SAS3 reaches liquefaction after 19 cycles, so the $CRR_{,15}$ would tend to be higher, consistently with the other experimental results presented in this research. Nevertheless, the data presented in this thesis are in agreement with those already published, showing the reliability of the proposed relationship by Jefferies and Been (2006).

However, it should be noted that two tests on Leighton Buzzard, consolidated at 100 kPa (CTX_LB8 and CTX_LB9), which are above the CSL as confirmed by positive ψ (Tab. 5.15), seem to belong to the same cyclic resistance curve identified by tests consolidated at 50 kPa (Fig. 5.33a). It could be explained by looking at Figure 5.34. For state parameter

higher than 0 (contractive behaviour), the relationship ψ versus CRR_{15} tends to reach a horizontal asymptote, implying that even though ψ increases, the CRR_{15} does not change so much.

Table 5.15. Results of cyclic triaxial tests on sandy soils in terms of state parameter (ψ).

Test	Sand	σ'_c (kPa)	e_0*	e_{cs}	ψ	CSR	N_{liq} r_u=0.90	N_{liq} ε_{DA}=5%
CTX_LB1	LB	25	0.825	0.873	-0.0481	0.115	12.3	12.0
CTX_LB2	LB	50	0.835	0.851	-0.0156	0.179	1.2	1.0
CTX_LB3	LB	50	0.794	0.851	-0.0566	0.128	12.0	12.0
CTX_LB4	LB	50	0.824	0.851	-0.0266	0.109	14.2	14.0
CTX_LB5	LB	50	0.812	0.851	-0.0386	0.080	No	No
CTX_LB6	LB	50	0.805	0.851	-0.0456	0.097	No	No
CTX_LB7	LB	50	0.792	0.851	-0.0586	0.147	4.0	4.0
CTX_LB8	LB	100	0.837	0.851	0.00881	0.099	33.0	33.0
CTX_LB9	LB	100	0.832	0.851	0.00381	0.147	1.1	1.0
CTX_T1	Ticino							
CTX_T2	Ticino							
CTX_T3	Ticino							
CTX_SAS1	SAS							
CTX_SAS2	SAS							
CTX_SAS3	SAS							
CTX_SAS4	SAS							
CTX_BSS1	PdC_BSS							
CTX_BSS2	PdC_BSS							
CTX_BSS3	PdC_BSS							
CTX_GSS1	PdC_GSS							
CTX_GSS2	PdC_GSS							
CTX_GSS3	PdC_GSS							
CTX_GSS4	PdC_GSS							
CTX_GSS5	PdC_GSS							

*at the end of consolidation phase.

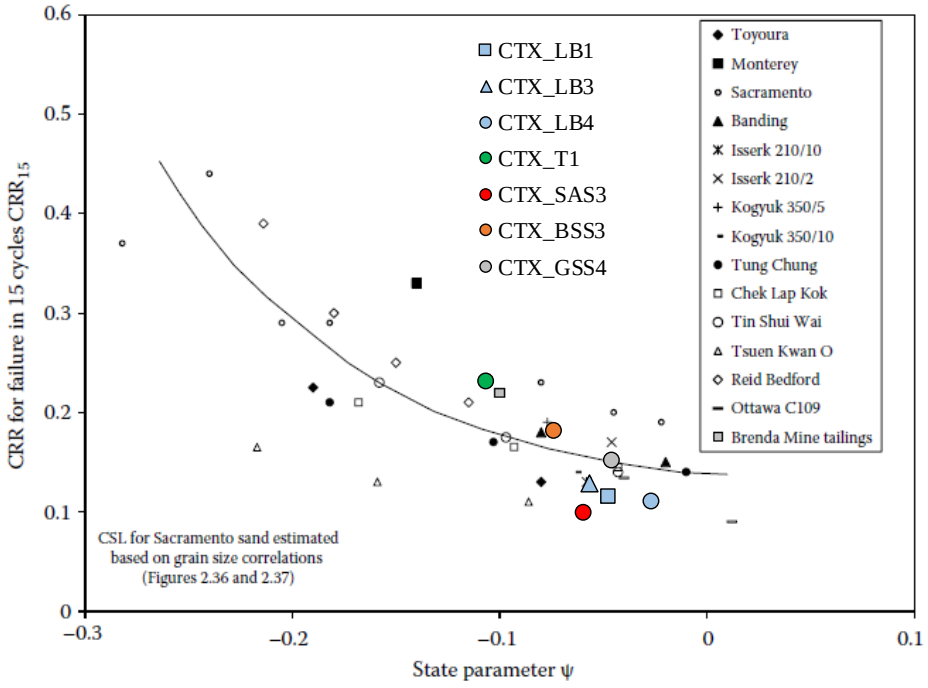

Figure 5.34. Comparison between the experimental data of this research ($12<N_{liq}<19$) with those reported by Jefferies and Been (2006) in the plane ψ versus CRR_{15}.

5.1.4.2 EXCESS PORE PRESSURE BUILD-UP

In saturated sands the excess pore pressure is widely recognized as the key parameter in understanding the liquefaction failure development. Because of that, an insight of the pore pressure generation has been done for the tested (loose) sands (§5.1.4). The excess pore pressure ratio (r_u) for each test has been plotted with N_{cyc}/N_{liq}, where N_{liq} is the number of cycles in fully liquefaction condition (r_u=1.0) (Fig. 5.35). For each material, the curves overlap each other, regardless of the applied CSR.

They have been interpreted by using the correlation of Booker et al. (1976) (eq. (2.10)), where the parameter β has been calibrated to have the best fitting with the experimental results and then reported in Table 5.16. It can be noted that despite similar conditions in term of D_r, the achieved values of β are very different, ranging between 0.6 (Ticino sand) and 1.1 (Leighton Buzzard). Such results confirm the dependence on the soil type. In particular, the value of β seems to depend on D_{60}, rather than the FC as reported by Polito et al. (2008) (eq. (2.11)). In Figure 5.36, the found relationship between β and D_{60} has been shown. It is a power function, whose equation, which is also reported in the same Figure, is the following:

$$\beta = 0.490 \cdot D_{60}^{-0.355} \quad (5.1)$$

Further tests on different materials are needed to confirm such finding.

Figure 5.35. Excess pore pressure ratio versus N_{cyc}/N_{liq} for Leighton Buzzard (a); Ticino (b); Sant'Agostino (c); Pieve di Cento (BSS) (d) and Pieve di Cento (GSS) (e) sands.

Table 5.5.16. Calibration of β for tested sands.

Sand	β
Leighton Buzzard	1.1
Ticino	0.6
Sant'Agostino	1.0
Pieve di Cento (BSS)	0.8
Pieve di Cento (GSS)	0.7

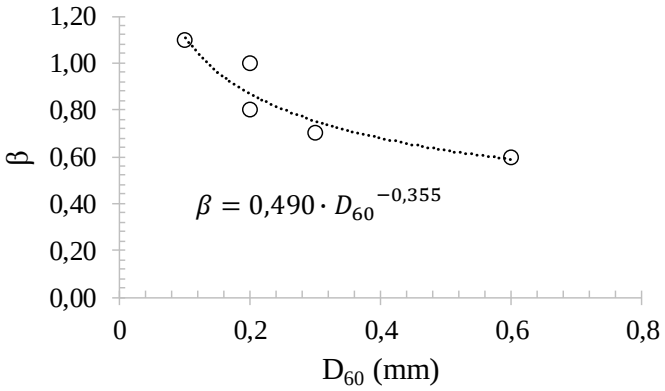

Figure 5.36. Relationship between D_{60} and β.

5.1.5 CYCLIC SIMPLE SHEAR TESTS

Undrained cyclic simple shear tests using Pieve di Cento sands were performed with flexible and rigid boundary, on loose and fully saturated specimens prepared by three different specimen preparation techniques: one-dimensional compression (1D-compression), moist tamping (MT) and air pluviation (AP), already described in paragraph 4.2.4.1 (Tab. 5.17). They have been prepared to have an average relative density (D_r) of 45% and consolidated at different values of vertical effective stresses (σ'_v), ranging between 49.5 and 214 kPa. After consolidation, several loading waveforms (sinusoidal, triangular, rectangular and sawtooth) have been used to analyse the effect that the loading shape has on the cyclic resistance. The void ratios and the relative densities of the specimens at the end of the consolidation phase have been reported in Table 5.17.
As for cyclic triaxial tests, in cyclic simple shear tests the attainment of liquefaction was identified according to stress (r_u=0.90) and strain criteria ($\gamma_{DA} \geq 3.75\%$).
In the following paragraphs some effects have been analysed, such as those of the boundaries (confinement), the waveform applied on the specimen, the preparation techniques and the non-symmetrical cyclic loading for the presence of an initial static shear stress. In Table 5.17, the value of the normalized initial static shear stress (α) is also reported, it is defined as follows:

$$\alpha = \frac{\tau_{st}}{\sigma'_{v0}} \quad (5.2)$$

where σ'_{v0} is the vertical effective consolidation stress; τ_{st} is the initial static shear stress applied on the horizontal plane of the specimen before sharing.

Table 5.17. Cyclic simple shear tests on untreated sandy soils.

Test	Sand	Prep. Tech	Boundary	σ'_h (kPa)	σ'_v (kPa)	e_0*	D_{r0}* (%)	Wave form	CSR	α
CSS_BSS1F										
CSS_BSS2F										
CSS_BSS3F										
CSS_BSS1R										
CSS_BSS2R										
CSS_BSS3R										
CSS_GSS1F										
CSS_GSS2F										
CSS_GSS3F										
CSS_GSS4F										
CSS_GSS5F										
CSS_GSS6F										
CSS_GSS7F										
CSS_GSS1MT										
CSS_GSS2MT										
CSS_GSS3MT										
CSS_GSS4MT										
CSS_GSS5MT										
CSS_GSS6MT										
CSS_GSS7MT										
CSS_GSS8MT										
CSS_GSS1AP										
CSS_GSS2AP										
CSS_GSS3AP										
CSS_GSS4AP										
CSS_GSS5AP										
CSS_GSS1tri										
CSS_GSS2tri										
CSS_GSS3tri										
CSS_GSS1rect										
CSS_GSS2rect										
CSS_GSS3rect										
CSS_GSS1st										
CSS_GSS2st										
CSS_GSS3st										
CSS_GSS1R										
CSS_GSS2R										
CSS_GSS3R										

*at the end of consolidation phase.

5.1.5.1 THE EFFECT OF BOUNDARY CONDITIONS AND THE ROTATION OF PRINCIPAL STRESS DIRECTIONS

In order to evaluate the effect of confinement, cyclic simple shear tests have been performed by using flexible and rigid boundaries, at the same conditions in terms of preparation technique (1D-Compression), wave form (sinusoidal) and physical state (D_r and σ'_v).

Six tests (3 for BSS and 3 for GSS) have been performed with rigid boundary; and other ten with flexible boundary (3 for BSS and 7 for GSS), by applying different CSR (Tab. 5.17).

As an example, the results of CSS_BSS2R and CSS_GSS2R tests, performed with rigid boundary, are shown in Figures 5.37 and 5.38. The cycles $\tau - \gamma$ have been reported in Figures 5.37a and 5.38a, while in Figures 5.37b and 5.38b the trend of shear strain and the sinusoidal CSR are plotted with N_{cyc}. It has to be emphasized that the configuration with rings of the cyclic simple shear apparatus does not allow to measure and record the pore pressure during the undrained cyclic phase. Because of that, an equivalent excess pore pressure ratio has been calculated as the ratio between (σ_{v0}- σ_v) and σ_{v0}, where σ_{v0} is the initial vertical stress, while σ_v is the current vertical stress (Bjerrum and Landva, 1966; Airey and Wood, 1986). In Figures 5.37c and 5.38c the evaluated excess pore pressure is plotted with N_{cyc}. It can be observed that also for CSS tests, the stress and strain criteria give the same results for loose sands, in fact N_{liq} is 10 for CSS_BSS2R test and 8 for CSS_GSS2R test. It confirms that r_u has been evaluated correctly.

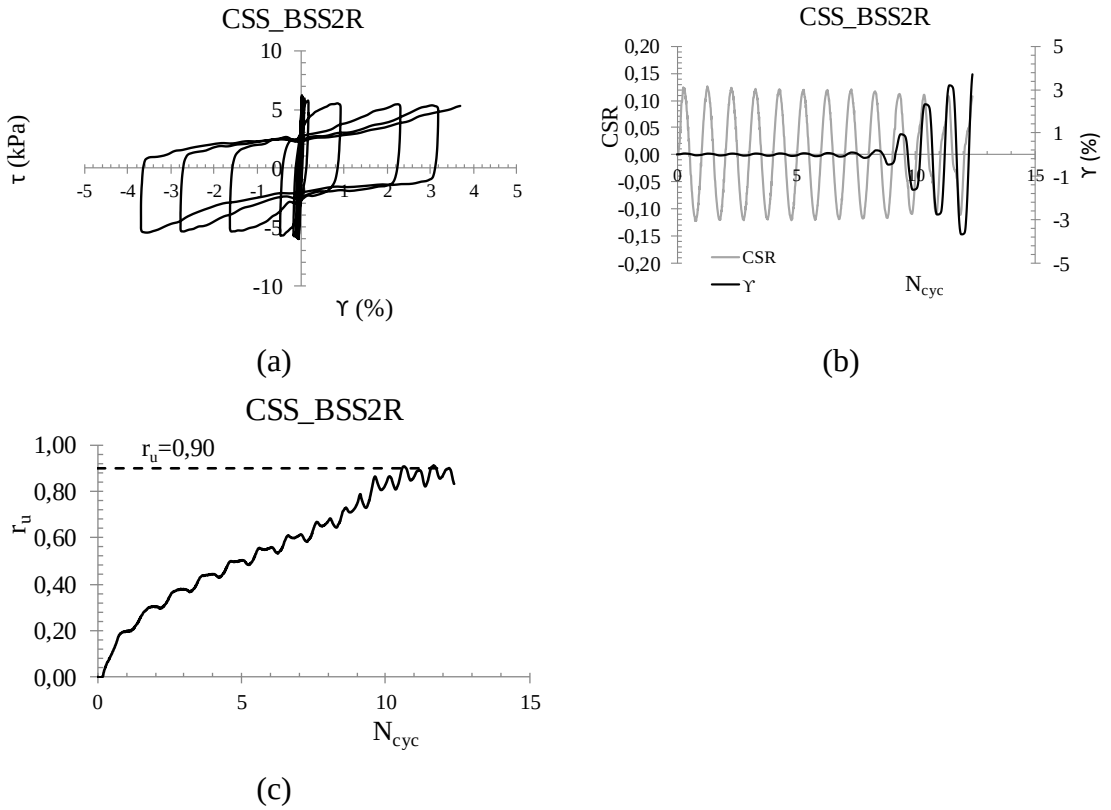

Figure 5.37. Results of cyclic simple shear tests with rigid boundary on Pieve di Cento (BSS) sand in the plane: τ-γ (a); N_{cyc}-CSR-γ (b) and N_{cyc} – r_u (c).

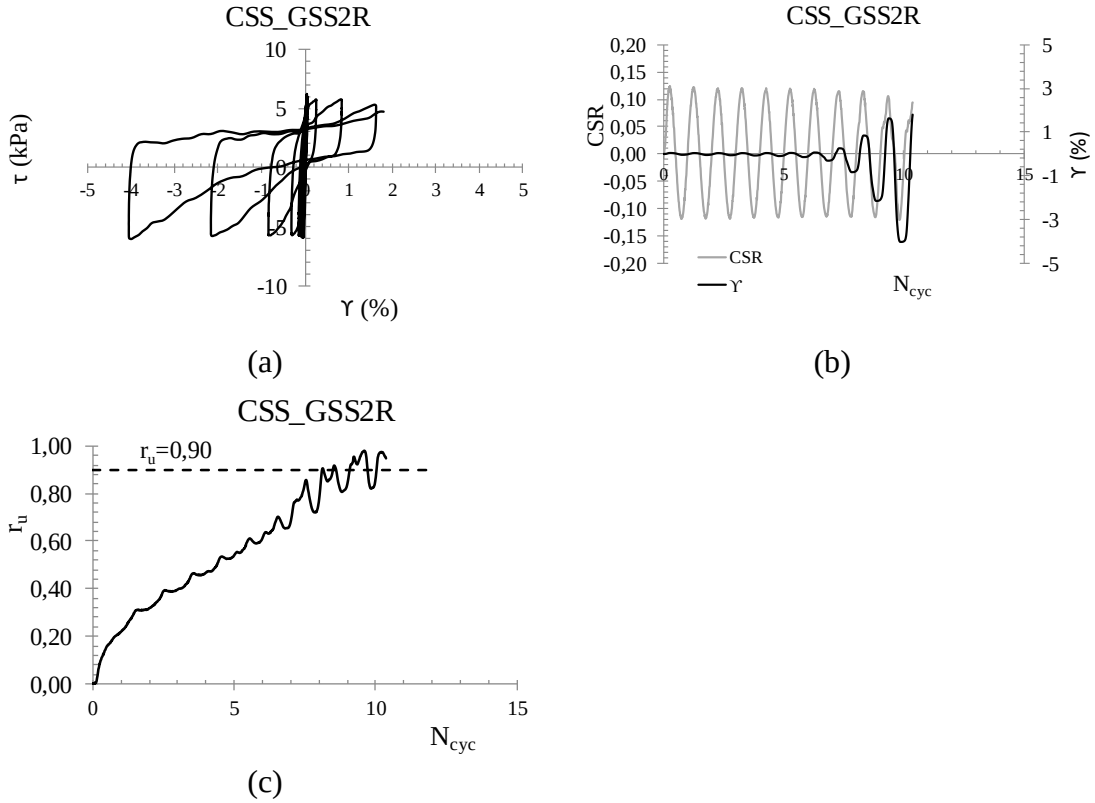

Figure 5.38. Results of cyclic simple shear tests with rigid boundary on Pieve di Cento (GSS) sand in the plane: τ-γ (a); N_{cyc}-CSR-γ (b) and N_{cyc} – r_u (c).

In Figures 5.39 and 5.40 the results of CSS_BSS2F and CSS_GSS2F tests, performed with flexible boundary, are shown in the following planes: τ-γ (Figs. 5.39a-5.40a); τ- σ' (Figs. 5.39b-5.40b); CSR - N_{cyc} (Figs. 5.39c-5.40c); N_{cyc} – r_u – γ (Figs. 5.39d-5.40d). Obviously, in both cases, during the shaking phase, the area of cycle in the plan τ-γ increases and, as for triaxial tests, when liquefaction occurs the load decreases because the control system is not able to maintain the imposed CSR. Figures 5.39b and 5.40b show the stress path of the test and the CSL is reported as well, confirming a good agreement with the results of monotonic tests. It should be specified that, since monotonic tests have not been performed on BSS, the same CSL of GSS has been assumed.
Furthermore, excess pore pressure ratio and shear strains increase gradually until to reach the thresholds, respectively of 0.90 and 3.75%. As can be observed, also in this case, the two criteria give the same results in terms of N_{liq} (N_{liq}=17 for CSS_BSS2F and N_{liq}=9 for CSS_GSS2F).

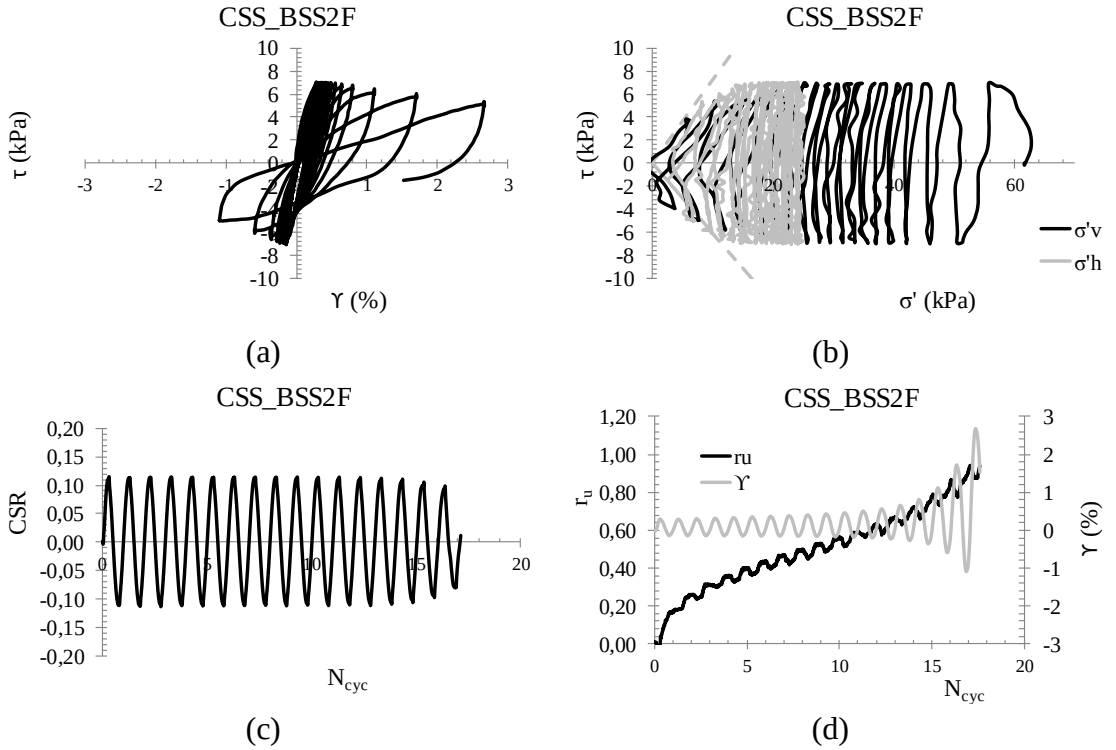

Figure 5.39. Results of a cyclic simple shear test with flexible boundary (CSS_BSS2F): τ-γ (a); τ- σ' (b); CSR - N_{cyc} (c); N_{cyc} – r_u- γ (d).

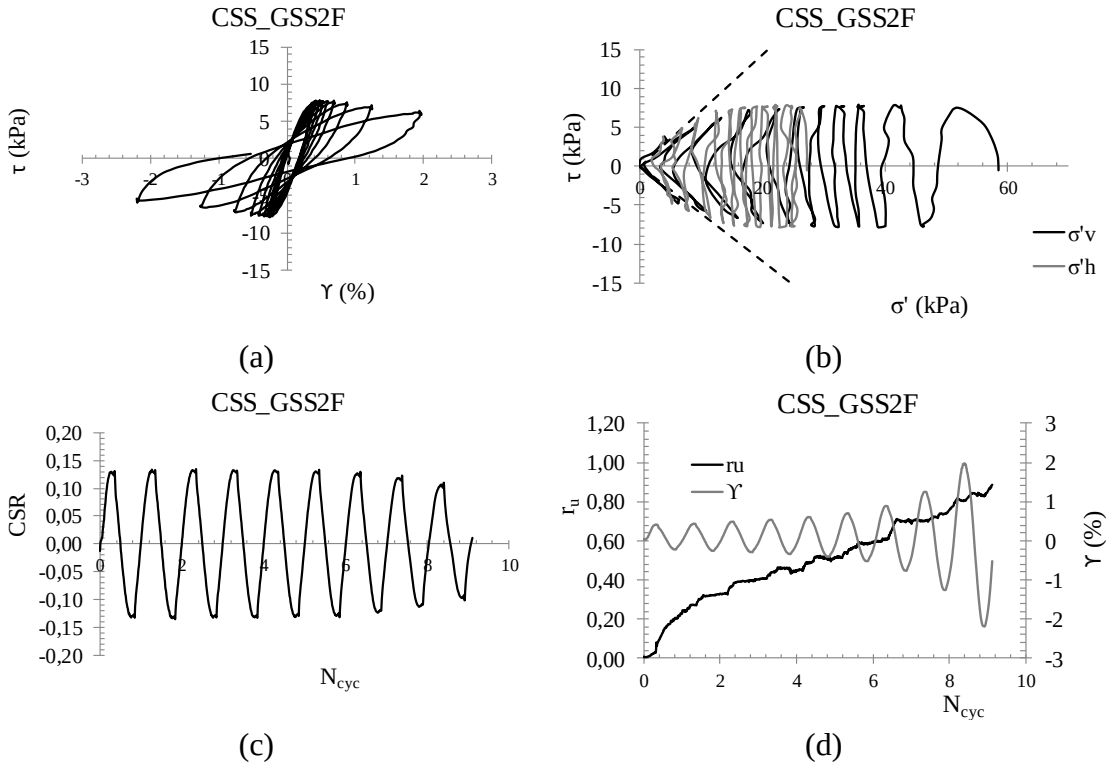

Figure 5.40. Results of a cyclic simple shear test with flexible boundary (CSS_GSS2F): τ-γ (a); τ- σ' (b); CSR - N_{cyc} (c); N_{cyc} – r_u- γ (d).

In order to study in depth the effects of different boundary conditions in cyclic tests, the results of some tests have been compared. Results from BSS, CSS_BSS2F and CSS_BSS3R, are presented together in Figure 5.41, even though the CSR values are slightly different: 0.115 and 0.110, respectively. On the other hand, for GSS, two tests with the same CSR (0.130) have been chosen: CSS_GSS2F and CSS_BSS1R. The comparisons are plotted in Figure 5.42.

Regardless of the type of sand, it can be observed that the responses of tested soil with two different boundary conditions are different. Looking at Figures 5.41a and 5.42a, the area of the cycles τ- γ seems to be higher for tests with rigid boundary; moreover, isolating the first cycles in the plane γ-CSR (Figs. 5.41b – 5.42b) it can be observed clearly a softer stress – strain response in the first cycle for flexible boundary and then an increased rate of shear strain accumulation with N_{cyc}.

For BSS, the shear modulus (G) in the first cycles in tests with rigid boundary seems to be much higher than that of flexible boundary, consequently, the accumulation of shear strain with N_{cyc} is much more pronounced for tests performed with a flexible boundary condition (Fig. 5.41c). On the other hand, for GSS it can be noted that after the first cycle (Fig. 5.42b), the secant shear modulus of CSS_GSS1R test is similar to that of CSS_GSS2F and then a sudden increase of shear strain can be noted (Fig. 5.42c).

Furthermore, comparing the results of tests of GSS with the same CSR (CSS_GSS2F and CSS_BSS1R) in terms of shear strain and excess pore pressure (Fig. 5.42c -d) it is worth noting that CSS_GSS1R attains liquefaction at a small number of cycles than CSS_GSS2F test. Nevertheless, the trend of r_u with N_{cyc} is the same with rigid and flexible boundary, for both BSS and GSS, as confirmed by looking at Figures 5.41e and 5.42e, plotting N_{cyc}/N_{liq} versus r_u.

Plotting the results in the plane CRR-N_{liq} (Fig. 5.43), a unique cyclic resistance curve can be identified.

Nevertheless, it is worth noting that the experimental data of GSS with rigid boundary lie below the corresponding curve with flexible boundary, while this difference is not evident for BSS. Sharma et al. (2017) showed different curves for different boundary conditions, where those with rigid boundary are generally below those with flexible one. For BSS such difference could not be noted because the cyclic resistance curve is very flat. Further tests on different sands could be useful to clarify this interesting aspect.

However, even though the cyclic resistance curve can be assumed unique, the different response of sands due to different boundary conditions can be explained with a different strain distribution. According to the results of Sharma et al. (2017), confining rings impose a relatively uniform deformation. Effects of strain localizations for tests with a confining pressure may lead to higher cyclic resistance.

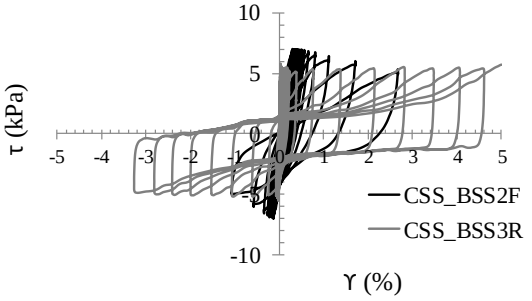

(a)

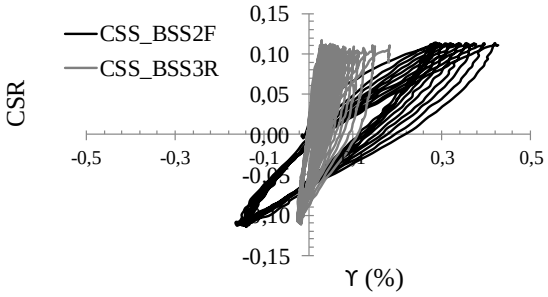

(b)

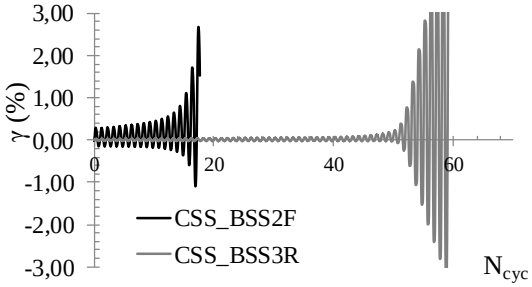

(c)

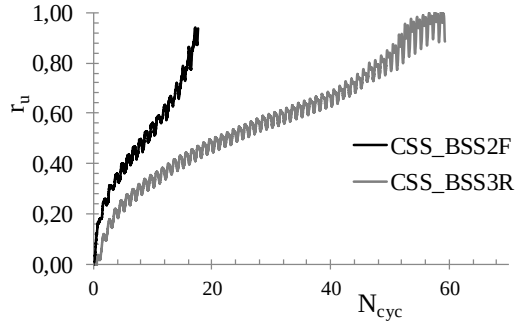

(d)

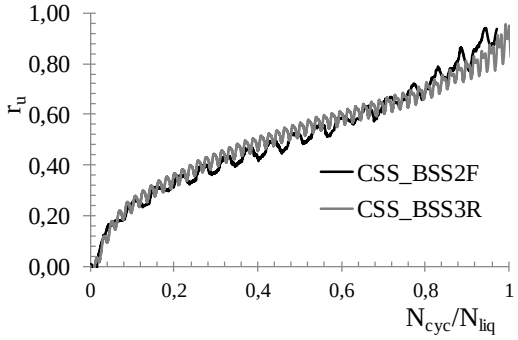

(e)

Figure 5.41. Comparisons of tests performed with different boundary conditions for BSS in the planes: τ-γ (a); first cycles in CSR-γ (b); N_{cyc} –γ (c); N_{cyc} - r_u (d); N_{cyc}/N_{liq} – r_u (e).

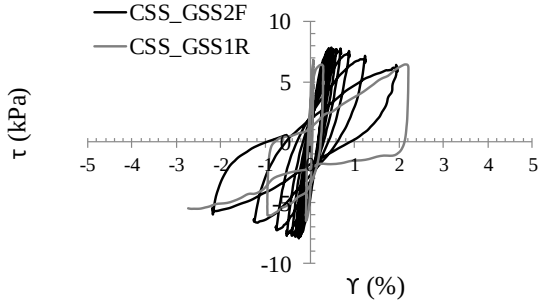

(a)

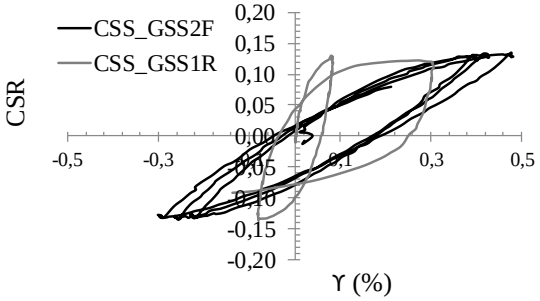

(b)

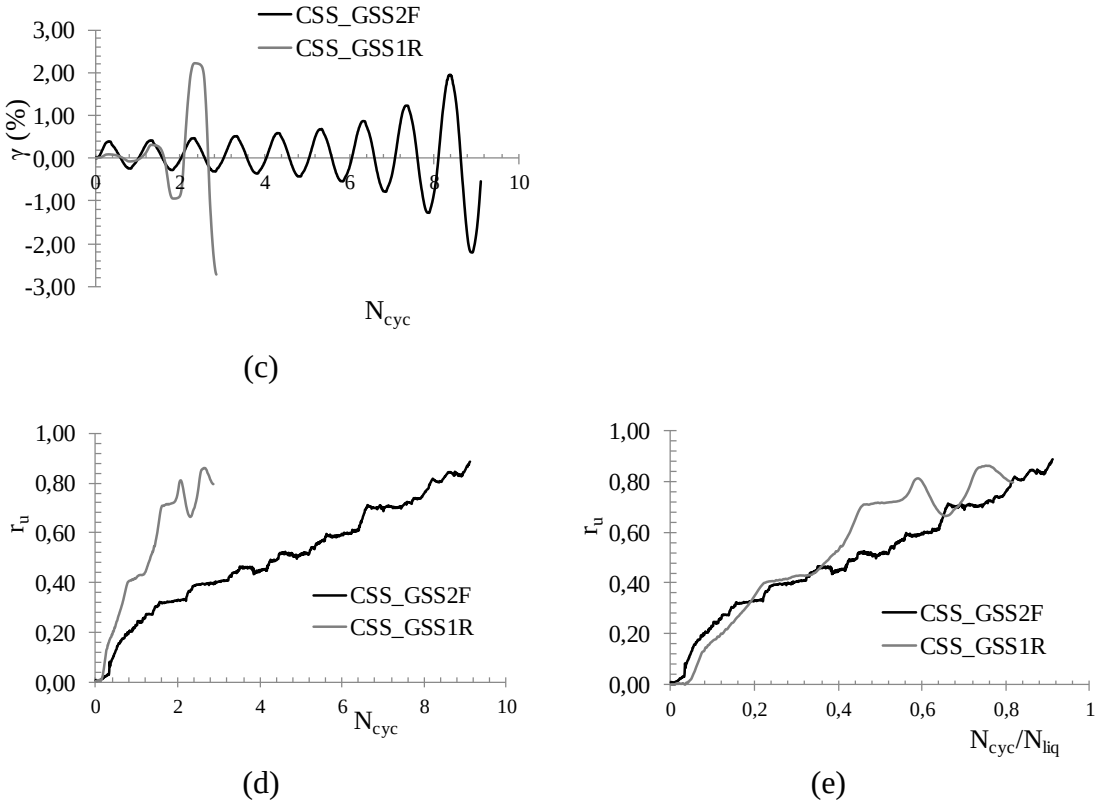

Figure 5.42. Comparisons of tests performed with different boundary conditions for GSS in the planes: τ-γ (a); first cycles in CSR-γ (b); N_{cyc} –γ (c); N_{cyc} - r_u (d); N_{cyc}/N_{liq} – r_u (e).

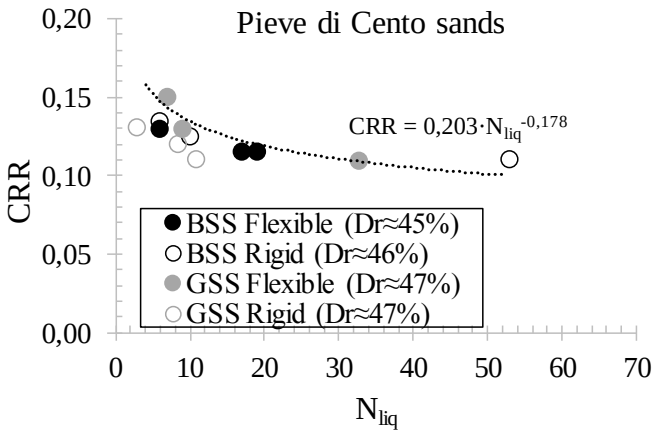

Figure 5.43. Cyclic resistance curve for Pieve di Cento sands.

A uniform field deformation, in addition to the fact that the diameter is surely constant because of rigid confining rings, would make the use of rigid boundary extremely advantageous. Nevertheless, as a matter of the fact that horizontal (or radial) stress cannot be controlled, the stress state of the specimen is not completely known. On the contrary,

tests performed with flexible boundary allow to control horizontal stresses and consequently the stress state can be represented by Mohr's circles.

In Figure 5.44a-c the effective vertical and horizontal stresses (σ'_v and σ'_h) have been plotted with N_{cyc} for CSS_BSS2F and CSS_GSS2F tests. The effective vertical (σ'_v) and horizontal (σ'_h) stresses start from their respective initial value, reached at the end of the consolidation phase, and both decrease during the loading cycles. First of all, it should be noted that the values of k_0 (0.39 and 0.46 respectively for CSS_BSS2F and CSS_GSS2F test) are consistent with the value of k_0 obtained via Jaky's equation (k_0=1-senφ). At the end of the consolidation phase, horizontal and vertical stresses are principal stress directions, it means that the difference between σ'_v and σ'_h is the diameter of Mohr's circle at the beginning of the shearing phase (red circle in Fig. 5.44b-d). During the loading cycles, when a shear stress acts on the specimen, according to a sinusoidal waveform, the principal stress directions rotate in a continuous way, simulating what happens in situ during an earthquake. At every half cycle, when τ is equal to 0, vertical and horizontal are once again principal stresses. Their difference and thus, the diameter of Mohr's circle decreases (Fig. 5.44) until to reach an isotropic state, where the Mohr's circle collapses in a point.

Figure 5.44. Effective vertical and horizontal stresses with N_{cyc} (a-c) and Mohr's circles for τ=0 (b- d).

During the cycles, the Mohr's circle pulses and at the same way its pole, which moves along the circumference.

Liquefaction is attained when $\alpha = \beta = 45°$, such a value is critical as indicated by Sivathayalan et al. (2014), because under these conditions the alignment of the plane of maximum shear stress with the bedding plane occurs.

Figure 5.45. Rotation of principal stress directions for $\tau=\tau_{max}$ in CSS_BSS2F (a) and CSS_GSS2F (b) tests.

In conclusion, comparing the results of cyclic simple shear tests performed with two different boundary conditions some considerations can be drawn up.
The configuration with rigid boundary ensures nil radial strains, guaranteeing a perfect simple shear stress state. On the contrary, flexible boundary to maintain a constant diameter introduces unavoidable oscillations of the diameter's measure around the target value. Nevertheless, such a value has been computed and considered low enough to assume a simple shear stress state. In addition, flexible boundary has the advantage to allow the complete knowledge of the stress state of the specimens.
Furthermore, even though the cyclic resistance curve seems to be roughly unique, the stress-strain response of the soil is different. A slightly lower cyclic resistance of tests carried out with rigid boundary could be due to a more uniform deformations than those obtained in the other configuration. However, it should be specified that normalizing N_{cyc} with N_{liq}, r_u follows the same trend for tests performed with different boundary conditions.

5.1.5.2 THE EFFECT OF WAVEFORMS ON LIQUEFACTION RESISTANCE

In order to evaluate the effect of waveforms on liquefaction resistance, nine cyclic simple shear tests have been carried out by applying non-sinusoidal waveforms on GSS. In particular, three different shape of loading have been used: triangular, rectangular and sawtooth (Tab. 5.17). The specimens have been prepared with 1D-Compression and performed with flexible boundary. The different waveforms are plotted in Figure 5.46.

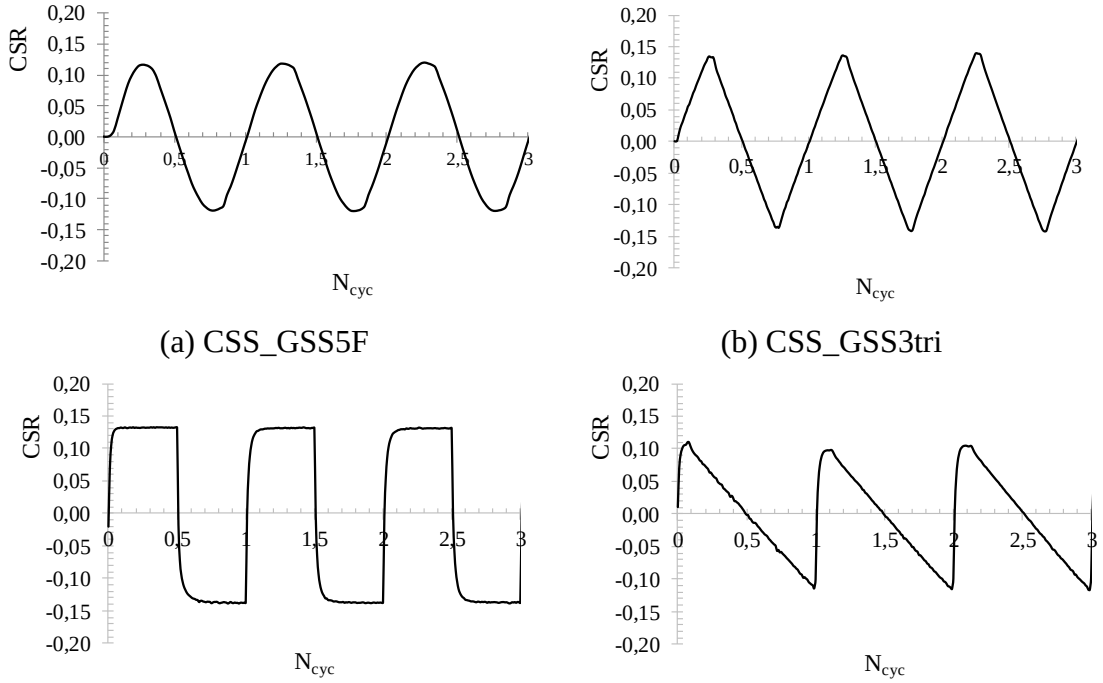

(a) CSS_GSS5F (b) CSS_GSS3tri

(c) CSS_GSS2rect (d) CSS_GSS2st

Figure 5.46. Waveforms for cyclic loading: sinusoidal (a); triangular (b); rectangular (c) and sawtooth (d).

As for sinusoidal loading, liquefaction was identified according to stress or strain criteria, which give similar results in terms of N_{liq}.

Plotting the results in the plane N_{liq}-CRR (Fig. 5.47), it can be observed that an effect of different waveforms on the cyclic resistance curve exists clearly. In particular, triangular and rectangular load shapes require higher amplitudes of loading at a fixed N_{liq} than those subjected to sinusoidal loading. Moreover, the curve of triangular shape seems to be very flat. On the contrary, the experimental dots of sawtooth load shape seem to identify a curve, which intersect that of sinusoidal tests, identified a very pending curve.

Figure 5.47. Results of different loading waveforms in the plane N_{liq}-CRR.

The results confirm the findings of Polito et al. (2013), according to which triangular and rectangular load shapes give higher liquefaction resistance than that of sinusoidal load shape.
The higher liquefaction resistance for triangular load shape than that for rectangular or sinusoidal load can be justified as an effect of the instantaneous change of velocity.

5.1.5.3 THE EFFECT OF PREPARATION TECHNIQUES

In order to evaluate the effect of the preparation technique on the liquefaction resistance, three preparation techniques have been used: 1D-Compression, moist tamping and air pluviation, as described in §4.2.4.1.
Typical results of cyclic simple shear tests on specimens prepared by 1D-compression technique have previously been shown (Figs. 5.39-5.40). As an example, tests prepared by moist tamping and air pluviation are reported in Figure 5.48 in the planes γ-τ (a-c) and N_{cyc}-γ -r_u (b-d).

Figure 5.48. Results of tests prepared with different methods in the plane γ -τ (a-c) and N_{cyc}- r_u- γ (b-d).

Figure 5.49. Results of different preparation techniques in the plane N_{liq}-CRR.

As expected, the two methods of preparation: 1D-C and MT give the same resistance curve. It should be specified that these two methods are very similar. In 1D-compression the specimen is compacted at the top, it means that it is not perfectly uniform, with looser parts at the bottom. On the contrary, the traditional moist tamping technique should allow a better uniformity in terms of relative density into the specimen. In spite of this, the cyclic behaviour of loose sands seems not to be affected by this aspect, as confirmed by Figure 5.50a, where the cycles τ-γ have been compared.

Figure 5.50. Comparison of two specimen preparation techniques (1D-compression and Moist Tamping) in the plane γ– τ (a) and a detail of the first cycles (b).

Despite a small difference in terms of CSR (0.130 and 0.132, respectively for CSS_GSS2F and CSS_GSS3MT), the cyclic behaviour seems to be the same even in the first cycles (Fig. 5.50b).

It is worth noting that, despite the fact that CSS_GSS5MT test has been performed at a vertical effective stress of 214.1 kPa (Tab. 5.17), the experimental result in the plane N_{liq}-CRR is in agreement with those of tests performed at lower effective vertical stresses (about 50kPa). The reason may lie in the fact that the CSL is very flat at low stresses and

then the state parameter (ψ) for CSS_GSS5MT is roughly the same as the other tests. However, further details regarding the interpretation of cyclic tests with the state parameter will be shown in the Chapter 6, where these tests will be analysed and discussed together with those of denser specimens.

Figure 5.51. Excess pore pressure versus N_{cyc}/N_{liq} for different preparation techniques: 1D-compression (a); Moist Tamping (b) and Air Pluviation (c).

Table 5.18. Calibrated values of β for different preparation techniques.

Preparation techniques	β
1D compression	1.1
Moist Tamping	1.0
Air Pluviation	1.1

5.1.5.4 THE EFFECT OF NON-SYMMETRICAL CYCLIC LOADING

From a practical point of view, the presence of a static shear stress can influence significantly the liquefaction resistance of sands. It is an interesting aspect, involving slopes, earth dams, river levees, soil foundation of heavy structures subjected to a seismic loading.

To take into account the effect of a static shear stress and thus, of a non-symmetrical cyclic loading, a τ_{st} has been applied, and thus $\alpha \neq 0$ (Tab. 5.17). Moreover, the combined effects of non-symmetrical cyclic loading and preparation techniques have been analysed.

In symmetrical tests ($\tau_{st}=0$), shear stresses cycle around 0 symmetrically, while shear strains accumulate slowly at the beginning of loading and then increase, always cycling around 0 (Figs. 5.37 to 5.42). A quite different behaviour is observed in non-symmetrical tests. Such response depends on whether the cyclic stress (τ_{cyc}) exceeds or not the static one (τ_{st}), as studied by several researchers in triaxial, simple shear and torsional shear devices (e.g. Vaid and Chern, 1983; Hyodo et al., 1994; Porcino et al., 2008; Chiaro et al., 2012).

When $\tau_{cyc} \leq \tau_{st}$ a *non-reversal condition* is observed. In this case, failure results from the accumulation of excessive permanent shear strains (drift).

Conversely, in the *shear stress reversal* ($\tau_{cyc} > \tau_{st}$) the shear strains accumulate in the direction of the driving shear force. It was defined "ratcheting" by Seed et al. (2003).

As an example, in test CSS_GSS5F, the imposed static shear stress is 6.15 kPa, while the cyclic shear stress is 5.80 kPa (Fig. 5.52a). It means that a no reversal condition ($\tau_{cyc} < \tau_{st}$) occurs, as can be clearly shown by looking at Figure 5.52c, where the stress-path of such test is plotted. As mentioned above, excessive permanent shear strains have been accumulated (Fig. 5.52b).

On the contrary, a stress reversal condition occurs in the other tests (CSS_GSS4F; CSS_GSS6F; CSS_GSS7F). In particular, two of them (CSS_GSS4F, CSS_GSS7F) have been shown in Figure 5.52d – 5.52g. In both cases, a progressive accumulation of shear strains can be observed, but an important difference lies in the direction of γ. In CSS_GSS4F test, γ moves toward positive strains, while follows negative strains in CSS_GSS7F test. Such different response is due to a direction of driving shear force, positive in CSS_GSS4F (Fig. 5.52f) and negative in CSS_GSS7F test (Fig. 5.52i).

Furthermore, Figure 5.52i seems to suggest that the critical state friction angle in extension should be lower than that assumed in this research as the symmetrical angle of φ_{cv}. Further tests should be performed to identify the CSL in extension.

With the main aim to analyse the effect of a small static shear stress on the cyclic resistance curve, the results of symmetrical and non-symmetrical tests have been plotted together in the plane N_{liq}-CRR (Fig. 5.53), divided for the different specimen's preparation methods.

Figure 5.52. Results of cyclic simple shear tests in no stress reversal (a-b), stress reversal with a positive driving shear force (c-d) and stress reversal with a negative driving shear force (e-f).

In the analysed tests, regardless of the preparation method to reconstitute the specimens, the presence of a small static shear stress (positive or negative) does not influence the cyclic resistance of sand. The reason can lie in the fact that the imposed τ_{st} is very small, with a value of α ranging between -0.02 and 0.12. Higher static shear stress should be applied to have a more evident decrease of the liquefaction resistance.

Figure 5.53. Effect of initial static shear stress on cyclic resistance for specimens prepared with different methods: 1D-compression (a); Moist Tamping (b) and Air Pluviation (c).

Although, as shown in Figure 5.52, the stress-strain response is very influenced by a static shear stress, it seems not to affect the cyclic resistance to liquefaction significantly. This aspect has been deepened by studying the trend of excess pore pressure versus the normalized number of cycles, as shown in Figures 5.54, 5.55 and 5.56 respectively for 1D-compression, moist tamping and air pluviation specimens. Once again, the equation of Booker et al. (1976) (eq. (2.10)) was fitted to the experimental results. For each group of tests, in symmetrical and non-symmetrical conditions, a unique expression of pore pressure generation can be identified, calibrating the parameter β to have the best fitting to the experimental results. In other words, r_u follows the same trend for tests prepared with the same method and in the same condition in terms of static shear stress, as can be shown in Figure 5.54b and 5.55b.

In Table 5.19 the values of β are summarized. It should be noted that a difference always exists between β calibrated with and without a static shear stress, even though it is small for moist tamping specimens, while it is more significant for 1D-compression specimens. As shown in Figure 5.54, the shape of the curve, and thus β, is different, in fact for $\tau_{st}=0$, the more traditional S-shape can be observed, while for $\tau_{st} \neq 0$ the double curvature is less evident. Moreover, at the beginning of shearing, r_u raises up faster than tests with symmetrical cyclic loading, the reason should lie in the presence of a τ_{st}, where an abrupt increase of pore water pressures is expected due to the fact that the stress-path starts closer to CSL than that in symmetrical cyclic loading condition. Similar considerations can be done for air pluviation specimens (Fig. 5.56). On the contrary, the presence of a static shear stress for moist tamping specimens seems not to be significant in pore pressure generation models. A possible explanation could be the fact that the moist tamping preparation is the method which guarantees more uniform specimens. The effect of a static shear stress could be redistributed among sand grains more uniformly in such specimens. Moreover, τ_{st} is applied at the bottom of the specimen, where looser layers are expected in 1D-compression methods, as described in the previous paragraph. It could be the reason why the most significant difference in β for $\tau_s t=0$ and $\tau_{st} \neq 0$ is observed for 1D-compression specimens.

Table 5.19. Calibrated values of β for different preparation techniques.

	β	
Preparation	$\tau_{st}=0$	$\tau_{st}\neq0$
1D-C	1.1	1.5
MT	1.0	1.1
AP	1.1	1.3

In conclusion, although the presence of the imposed static shear stress does not influence the cyclic resistance curve, the excess pore pressure generation is much more sensitive to an applied static shear stress, albeit small. Moreover, the methods of specimen's preparation influence in different way the effect on pore pressure increase of an acting τ_{st}.

Figure 5.54. Excess pore pressure versus N_{cyc}/N_{liq} for symmetrical cyclic loading (a) and non-symmetrical cyclic loading (b) in 1D-Compression specimens.

Figure 5.55. Excess pore pressure versus N_{cyc}/N_{liq} for symmetrical cyclic loading (a) and non-symmetrical cyclic loading (b) in Moist Tamping specimens.

Figure 5.56. Excess pore pressure versus N_{cyc}/N_{liq} for symmetrical cyclic loading (a) and non-symmetrical cyclic loading (b) in Air Pluviation specimens.

5.1.6 CYCLIC RESISTANCE CURVE: CYCLIC TRIAXIAL VS CYCLIC SIMPLE SHEAR TESTS

In this paragraph, the results of cyclic triaxial (CTX) and simple shear (CSS) tests performed on the same sands (Pieve di Cento) in similar conditions, have been compared in terms of liquefaction resistance. The correlation proposed by Castro (1975) (eq. (2.7)) has been used to make CTX and CSS data comparable.

To sum up, k_0 deriving from the results of laboratory tests seems to be more reliable than that computed via Jacky's formula. It is a further confirm of the reliability of the control system of CSS tests with flexible boundary.

Figure 5.57. Comparisons between CTX and CSS tests in the plane N_{liq}-CRR for BSS (a) and GSS (b) by using Jacky's formula to estimate k_0.

Figure 5.58. Comparisons between CTX and CSS tests in the plane N_{liq}-CRR for BSS (a) and GSS (b) by using k_0 achieved from CSS tests performed with flexible boundary.

Table 5.5.20. Data to use Castro's correlation (eq. (2.7)).

	BSS	GSS
φ_p (°)		
k_0_Jacky		
cr_Jacky		
k_0_Lab		
cr_Lab		

Further considerations have been done on the excess pore pressure generations. In Figure 5.59a - b, r_u versus N_{cyc}/N_{liq} are plotted for BSS in triaxial and simple shear conditions (for specimens prepared by 1D-compression methods), respectively, while in Figure 5.60a - b the results for GSS are compared. In both cases, the excess pore pressure model of Booker et al. (1976) has been considered, and once again the parameter β has been calibrated to have the best fitting with the experimental results. Such values are summarized in Table 5.21.

As expected, BSS and GSS show a similar behaviour in CSS tests, with a β equal to 1.0 and 1.1, respectively.
Comparing the results of CTX and CSS tests, it can be observed higher r_u increases in CSS than in CTX tests at the beginning of shearing; consequently, higher values of β have been obtained (Tab. 5.21).

Figure 5.59. Excess pore pressure generation models for BSS sand in cyclic triaxial (a) and simple shear (b) tests.

Figure 5.60. Excess pore pressure generation models for GSS sand in cyclic triaxial (a) and simple shear (b) tests.

Table 5.21. Values of β calibrated for CTX and CSS tests for Pieve di Cento sands.

	β	
	CTX	CSS
BSS	0.8	1.0
GSS	0.7	1.1

5.2 UNDISTURBED SPECIMENS

Within the European project LIQUEFACT, with the main aim to define a more realistic as possible geotechnical model, undisturbed samples have been retrieved in the field trial of Pieve di Cento. As well known, the results from reconstituted sandy specimens should always be treated with great care because they cannot perfectly reflect the natural fabric of a sand deposit, owing to that it is extremely important to perform tests on undisturbed specimens.
As already discussed in Chapter 3, two different soil samplers have been used: Osterberg and Gel-Pusher samplers (Fig. 3.5). In Table 5.22 the tests performed on undisturbed specimens are summarized. Boreholes, type of samplers (Osterberg and Gel-Pusher), depth and kind of performed test are specified.

Table 5.22. Tests carried out on undisturbed soils.

Boreholes	Sampler	Depth (m)	Test
CH1bis	Gel-Pusher	3.3	GSDC; e
CH1bis	Gel-Pusher	3.0	CSS; GSDC; e
CH1bis	Gel-Pusher	3.1	CSS; GSDC; e
CH1bis	Osterberg	3.6	CSS; GSDC; e
CH1bis	Osterberg	3.8	CSS; GSDC; e
CH1bis	Osterberg	4.0	CSS; GSDC; e
CH1bis	Osterberg	4.0	CSS; GSDC; e
CH1bis	Osterberg	2.0 – 2.5	GSDC
CH2	Gel-Pusher	5.0	CSS; GSDC; e
CH2	Gel-Pusher	5.0	CSS; GSDC; e
CH2	Gel-Pusher	5.0	Oed; GSDC; e
CH3	Osterberg	4.8	CSS; GSDC; e
CH3	Osterberg	5.0	CSS; GSDC; e
CH3	Gel-Pusher	3.5	GSDC
CH3	Gel-Pusher	4.5	GSDC
CH3	Gel-Pusher	4.0	TS*; Dr
CH5	Gel-Pusher	3.0	CSS; GSDC; e
CH5	Gel-Pusher	3.0	CSS; GSDC; e
CH5	Osterberg	2.5	GSDC; e
CH5	Osterberg	2.5	CSS; GSDC; e
CH5	Osterberg	2.2	CSS; GSDC; e
CH5	Osterberg	2.0	GSDC
CH5	Osterberg	2.3	GSDC

*Chiaradonna et al., 2019

Oedometric (Oed), cyclic simple shear (CSS) and torsional shear (TS; Chiaradonna et al., 2019) tests have been performed. Grain size distribution curve (GSDC) and void ratio (e) have been evaluated after each test. The grain size distribution curves of the undisturbed

specimens are plotted together in Figure 5.61 and compared with the curve of BSS (from first 2m). It is worth noting that the achieved curve has been essential to create a reliable stratigraphy profile of Pieve di Cento site (Chapter 3). The results of the performed tests on the undisturbed samples from Pieve di Cento test site have been reported in the following paragraphs.

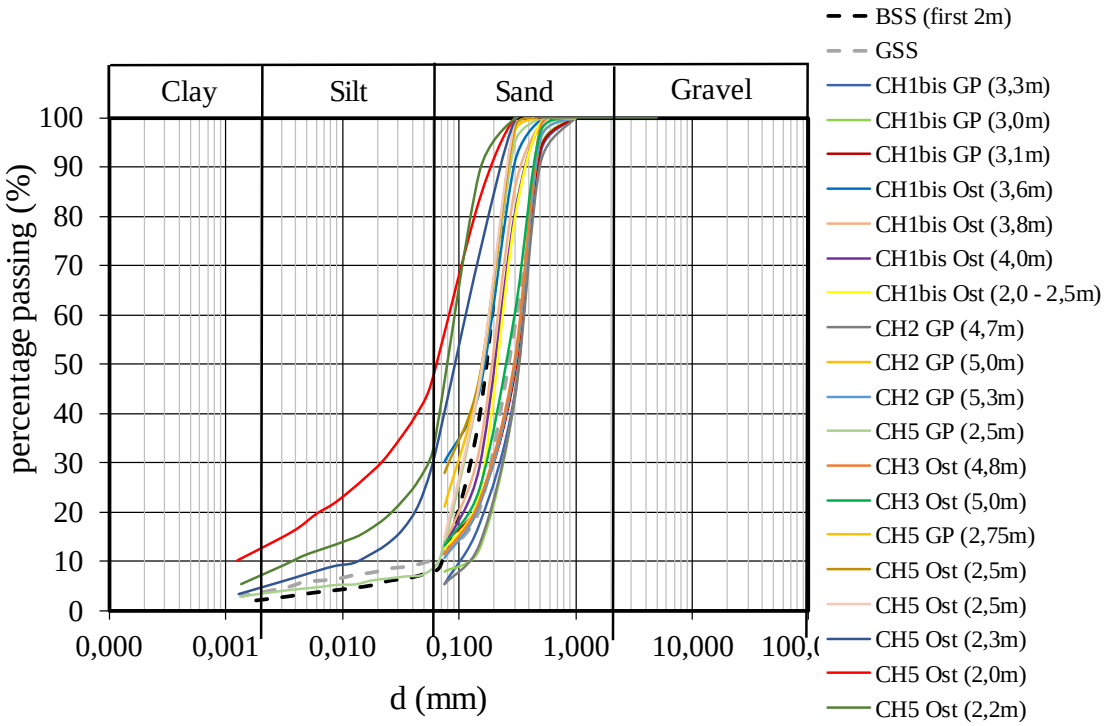

Figure 5.61. Grain size distribution curves of undisturbed specimens of Pieve di Cento.

5.2.1 OEDOMETRIC TEST

One test has been performed on a specimen, retrieved from a Gel Pusher sampler at a depth of 5.00m (Tab. 5.23). The result has been plotted in the traditional plane logσ'-e in Figure 5.62a, while in Figure 5.62b, for sake of completeness, the grain size distribution curve of the undisturbed specimen, evaluated after the test, is plotted with those of reconstituted sandy soil specimens on which oedometric tests have been performed as well (§5.1.2).

From Figure 5.62a, it can be observed that the initial void ratio (e_0) of the undisturbed specimen is smaller than those of the reconstituted specimens. The undisturbed one seems to be less compressible than the other specimens, likely due to a different grain size distribution (Fig. 5.62b).

Moreover, the yielding stress, corresponding to the maximum curvature of the experimental curves, is about 500 kPa, higher than that for reconstituted specimens.

Table 5.23. Oedometric test on Pieve di Cento undisturbed soils.

Test	Material	Undisturbed sampler	Depth (m)	e_0
Oe_CH2_GP	Sandy Soil	Gel Pusher CH2	5.00	0.727

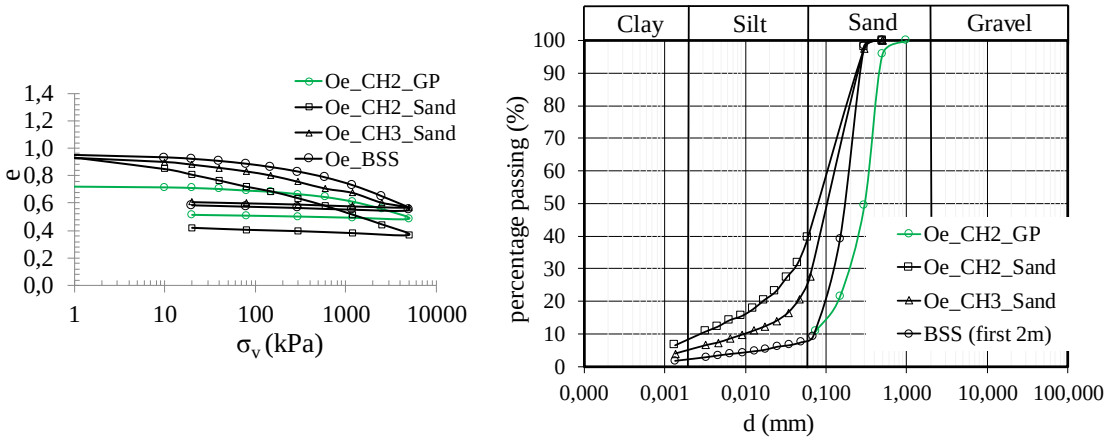

(a) (b)

Figure 5.62. Result of Oe_CH2_GP test (a) and relative grain size distribution curve (b).

5.2.2 CYCLIC SIMPLE SHEAR TESTS

Thirteen cyclic simple shear tests have been performed on undisturbed specimens, whose testing program is summarized in Table 5.24. All of them has been tested in flexible boundary conditions to know the stress state completely.

The results of some tests have been represented in the traditional planes γ-τ and N_{cyc}- r_u – γ (Fig. 5.63). The same considerations, done for reconstituted specimens, can be extended to undisturbed specimens, although an interesting difference seems to emerge. Unlike reconstituted specimens, the correspondence between stress and strain triggering criteria for liquefaction is not verified as reported in Table 5.25 or observed in Figure 5.63.

The attainment of liquefaction for r_u equal to 0.90 occurs always before that the critical value of shear strain (3.75%) is reached. It could be due to lower values of void ratio, which implies that the stress and strain criteria give different results in terms of N_{liq}. To confirm this, the scatter between two criteria is significant especially for Osterberg samples where the effect of the sampling has negative implications on the natural density of the samples as it will be discussed in the following paragraph (§5.2.3).

Table 5.24. Cyclic simple shear tests on Pieve di Cento undisturbed soils.

Test	Borehole	Sampler	Depth (m)	e_0	σ'_h (kPa)	σ'_v (kPa)	e_c*	CSR
CSS_CH1_O1	CH1bis	Osterberg	3.6	0.680	23.6	76.1	0.653	0.100
CSS_CH1_O2	CH1bis	Osterberg	3.8	0.622	19.6	51.3	0.613	0.130
CSS_CH1_O3	CH1bis	Osterberg	4.0	0.603	19.2	51.2	0.593	0.140
CSS_CH1_O4	CH1bis	Osterberg	4.0	0.682	20.0	51.0	0.675	0.140
CSS_CH5_GP1	CH5	Gel-Pusher	3.0	0.654	12.7	44.3	0.648	0.095
CSS_CH5_GP2	CH5	Gel-Pusher	3.0	0.714	13.8	32.8	0.692	0.165
CSS_CH5_O1	CH5	Osterberg	2.5	0.949	11.9	28.5	0.908	0.170
CSS_CH5_O2	CH5	Osterberg	2.0	0.877	20.5	41.1	0.855	0.150
CSS_CH2_GP1	CH2	Gel-Pusher	5.0	0.668	23.3	60.4	0.655	0.120
CSS_CH1_GP1	CH1bis	Gel-Pusher	3.0	0.697	13.6	40.5	0.692	0.110
CSS_CH1_GP2	CH1bis	Gel-Pusher	3.1	0.631	13.9	41.4	0.623	0.120
CSS_CH3_O1	CH3	Osterberg	4.8	0.546	24.1	61.0	0.533	0.120
CSS_CH3_O2	CH3	Osterberg	5.0	0.658	24.2	61.8	0.650	0.140

*at the end of consolidation phase.

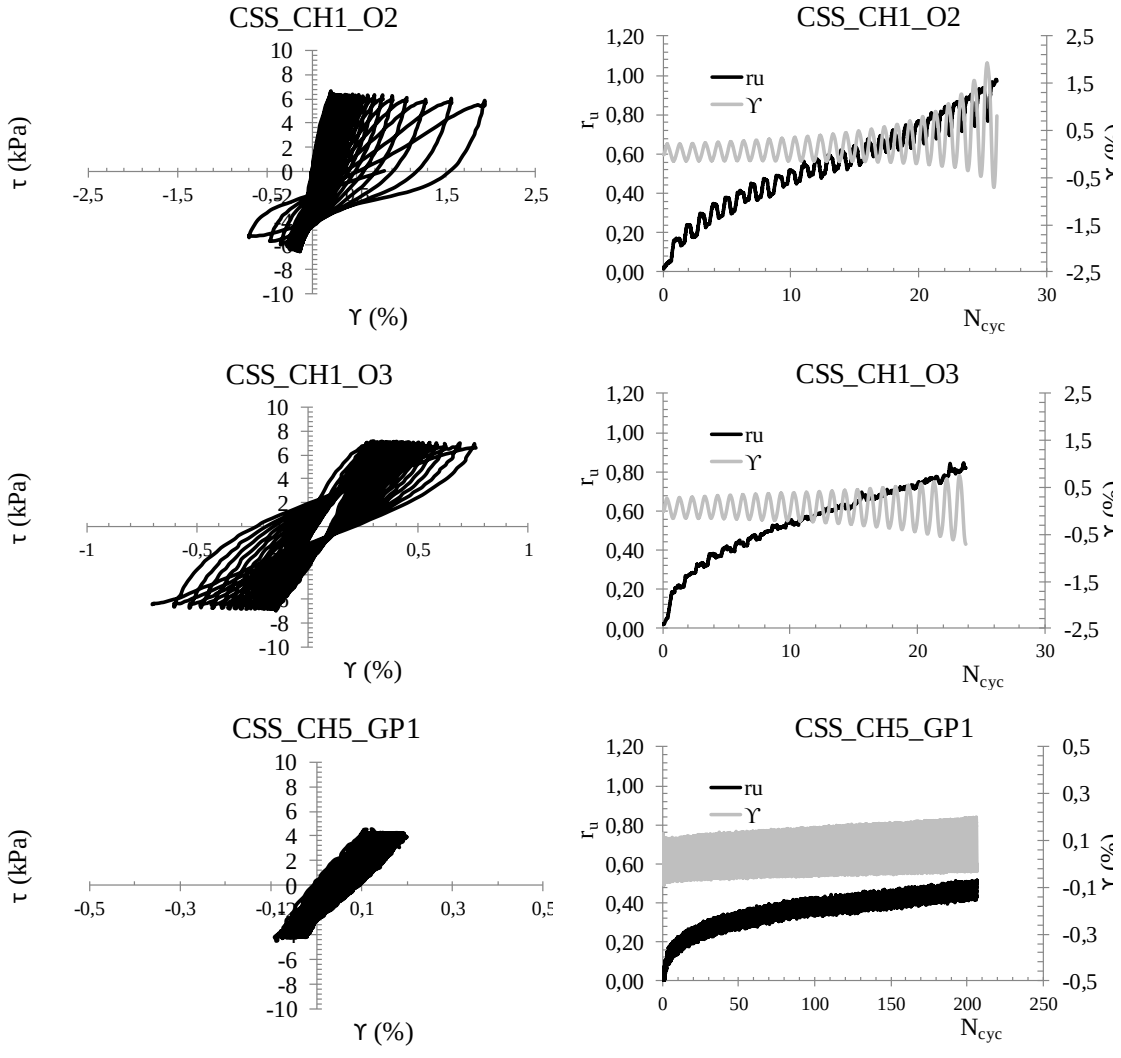

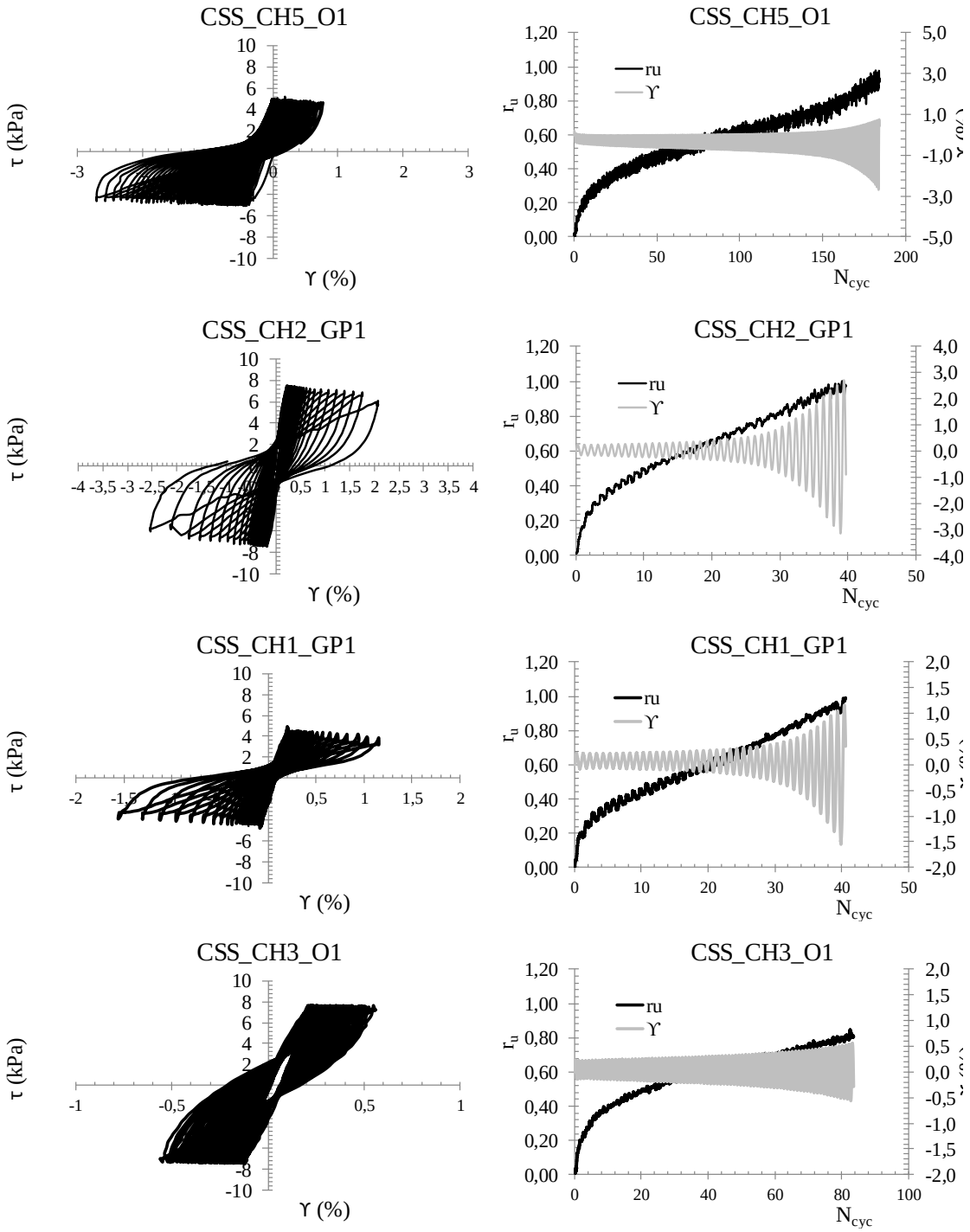

Figure 5.63. Results of cyclic simple shear tests on undisturbed specimens.

As a matter of the fact that the two liquefaction triggering criteria give different results in terms of N_{liq} and because the attainment of r_u equal to 0.90 occurs before than the attainment of γ_{DA} equal to 3.75%, the stress criterion has been chosen to identify liquefaction. The results in the plane N_{liq}-CRR are plotted taking into account the stress criterion (r_u=0.90) (Fig. 5.64). The achieved experimental data are plotted together with the results of reconstituted specimens (BSS and GSS) prepared by using different methods. The square dots have been used for Osterberg samples, while the triangular ones

for Gel Pusher samples. The semi-logarithmic scale has allowed to see the experimental points which reach liquefaction at higher number of cycles.

Table 5.25. Results of cyclic simple shear tests on undisturbed specimens of Pieve di Cento.

Test	Borehole	Sampler	Depth (m)	e_0	σ'_h (kPa)	σ'_v (kPa)	e_c*	CSR	N_{liq} (r_u)	N_{liq} (γ)
CSS_CH1_O1	CH1bis	Ost	3.6	0.680	23.6	76.1	0.653	0.100	320	260
CSS_CH1_O2	CH1bis	Ost	3.8	0.622	19.6	51.3	0.613	0.130	24	>26
CSS_CH1_O3	CH1bis	Ost	4.0	0.603	19.2	51.2	0.593	0.140	26	>28
CSS_CH1_O4	CH1bis	Ost	4.0	0.682	20.0	51.0	0.675	0.140	68.6	>70
CSS_CH5_GP1	CH5	GP	3.0	0.654	12.7	44.3	0.648	0.095	No	No
CSS_CH5_GP2	CH5	GP	3.0	0.714	13.8	32.8	0.692	0.165	9	7
CSS_CH5_O1	CH5	Ost	2.5	0.949	11.9	28.5	0.908	0.170	175	180
CSS_CH5_O2	CH5	Ost	2.0	0.877	20.5	41.1	0.855	0.150	188	>190
CSS_CH2_GP1	CH2	GP	5.0	0.668	23.3	60.4	0.655	0.120	33	34
CSS_CH1_GP1	CH1bis	GP	3.0	0.697	13.6	40.5	0.692	0.110	36	>40
CSS_CH1_GP2	CH1bis	GP	3.1	0.631	13.9	41.4	0.623	0.120	12	>12
CSS_CH3_O1	CH3	Ost	4.8	0.546	24.1	61.0	0.533	0.120	>80	>80
CSS_CH3_O2	CH3	Ost	5.0	0.658	24.2	61.8	0.650	0.140	53	>53

*at the end of consolidation phase.

Figure 5.64. Results of cyclic simple shear tests on undisturbed specimens.

Looking at Figure 5.64, it can be noted that the experimental points relative to Gel-Pusher samplers exhibit lower liquefaction resistance than those from Osterberg sampler and it is certainly due to the effect of sampling. In addition to the void ratio, the grain size distribution plays an important role, as well. For instance, the experimental points of CH5-Ost (z=2.0 – 2.5m) show a high cyclic resistance, which can be explained looking at their grain size distributions (Fig. 5.61). The fines content, probably plastic, is 30 – 40%, much higher than the other ones. Both of specimens retrieved from CH3 Ostreberg

(CH3-Ost (z=5.0m)) have very similar grain distribution curves than GSS, on the other hand, CH1-bis Ost (z=3.5 – 4.0m) specimens are comparable with BSS.
Regarding Gel-Pusher specimens, apart from CH5-GP (z=3.0m), the grain distribution curves are similar to GSS.
The scatter of the experimental data points can be obviously explained by an effect of variability, due to the fact that natural soils have been tested.

5.2.2.1 COMPARISONS BETWEEN RECONTITUTED AND UNDISTURBED SPECIMENS: THE FABRIC EFFECT

Figure 5.65, clearly shows as the specimens from CH1bis and CH2 Gel Pusher samples, taken respectively at a depth of 3 and 5 m, exhibit the same resistance to liquefaction as the reconstituted ones by 1D-compression or moist tamping. Generally speaking, it means that the fabric effect may be considered negligible and additionally, that the 1D-compression and moist tamping preparation methods are more suited to replicate the natural behaviour of undisturbed material than the air pluviation.
To study in depth if the fabric plays a role on the stress-strain response of soil, two tests have been compared: CSS_GSS3F and CSS_CH1_GP1. The results of the two tests, in the planes γ-CSR, N_{cyc}- γ and N_{cyc} – r_u, are plotted respectively in Figure 5.65a, b and c.
It is shown clearly in Figure 5.65b that at the beginning of the shearing phase, the shear strains are exactly the same, but after 20 cycles the reconstituted specimen starts showing higher γ, mainly towards the positive strains.
By contrast, the trend of r_u seems to be different from the beginning of the shearing phase where higher r_u can be observed for the undisturbed specimen (CSS_CH1_GP1) than for the reconstituted one, but with increased number of cycles the curves tend to intersect each other, even if with different fluctuation in amplitude.

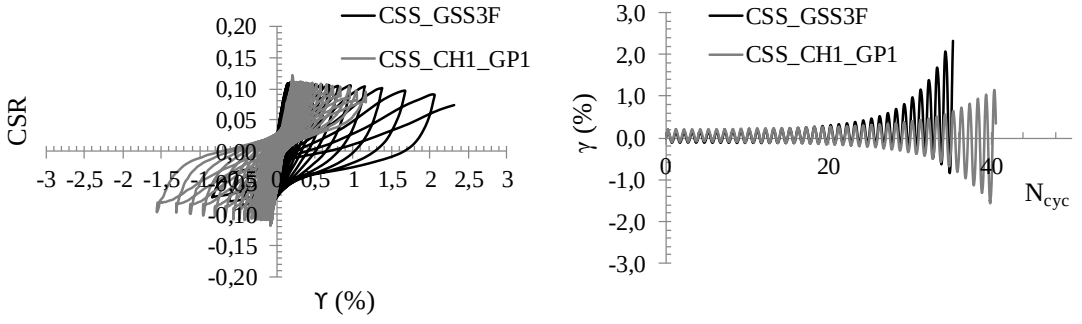

(a) (b)

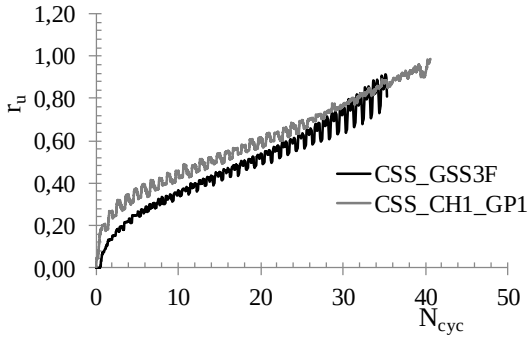

(c)

Figure 5.65. Comparisons between reconstituted and undisturbed specimens in the planes: γ - CSR (a) and N_{cyc}-γ (b); N_{cyc}-ru (c).

This aspect can be deepened by interpreting the results of the undisturbed specimens by the pore pressure generation model of Booker et al. (1976). The tests performed on undisturbed specimens, where a fully liquefaction (r_u=1.0) has been reached, have been plotted in the plane N_{cyc}/N_{liq} versus r_u, with the main aim to evaluate the pore pressure generation law and compare it with that of reconstituted specimens. Apart from the test CSS_CH5_GP2, the curves overlap each other, perfectly (Fig. 5.66).

Figure 5.66. Pore pressure generation for undisturbed specimens.

As for reconstituted specimens, β has been calibrated to have the best fitting to the experimental results. The found value is 1.4 that is higher than those obtained for reconstituted specimens (1.1 and 1.0 for 1D-compression and moist tamping, respectively).

These findings suggest that even though the cyclic resistance curve is the same, the evolution of pore pressure during loading is different, because undisturbed specimens exhibit higher r_u at the beginning than that of specimens reconstituted by 1D-compression or moist tamping methods.

Once again, it should be emphasized that the results of reconstituted specimens should be treated with great care because none of the preparation methods is able to perfectly reflect the natural fabric of a sand deposit. Therefore, if possible, specimens with the least possible degree of disturbance should be tested to characterize a site in the best way.

5.2.3 EFFECT OF SAMPLING ON UNDISTURBED SPECIMENS

The difference in sampling carried out by means of both Osterberg and Gel Pusher samplers, already described in §3.2.1 and 3.2.2 may be better investigated in laboratory. In Figure 5.61 the grain size distribution curves of undisturbed specimens have been shown. Some of them are very different from BSS and GSS, especially in term of amount of fines content (FC). Owing to that it can be supposed that the values of e_{max} and e_{min} will be significantly different from BSS and GSS, the values of D_r in Table 5.24 are not reported. Despite this aspect, it can be noted that the Gel Pusher specimens have lower void ratios than those of Osterberg specimens. In particular, the specimen of test CSS_CH1_GP1 has a grain distribution curve similar to that of GSS, so that the same values of e_{max} and e_{min} could be considered (Tab. 4.1) and then, the value of D_r could be assumed roughly equal to 42%. At the same way, the D_r of specimen of oedometric test (Oe_CH2_GP) may be evaluated and it is equal to 35.5%. Based on this estimate, the Gel Pusher samplers seems to be able to retrieve real "undisturbed samples". In fact the calculated values of D_r are very similar to those that have been evaluated in site from CPTU tests by other authors. In contrast, Osterberg samplers create a higher disturb of the specimens as can be easily understand from the lower values of void ratio, which lead to higher resistance to liquefaction.

REFERENCES

Airey, D. W. and Wood, D. M. (1986). Pore pressures in simple shear. *Soils and Foundations*, 26, 91-96.

Bjerrum, L. and Landva, A. (1966). Direct simple shear tests on a Norwegian quick cay. *Géotechnique*, 16, 1-20.

Chiaro, G., Koseki, J., and Sato, T. (2012). Effects of initial static shear on liquefaction and large deformation properties of loose saturated Toyoura sand in undrained cyclic torsional shear tests. *Soils and Foundations*, *52*(3): 498-510.

Drescher, A., and Vardoulakis, I. (1982). Geometric softening in triaxial tests on granular material. *Géotechnique,* 32(4): 291-303.

Fioravante, V., and Giretti, D. (2016). Unidirectional cyclic resistance of Ticino and Toyoura sands from centrifuge cone penetration tests. *Acta Geotechnica*, *11*(4): 953-968.

Hyodo, M., Tanimizu, H., Yasufuku, N., Murata, H., (1994). Undrainedcyclic and monotonic triaxial behavior of saturated loose sand. *Soils and Foundations* 34 (1): 19–32.

Ishihara, K. (1993). Liquefaction and flow failure during earthquakes. *Géotechnique*, *43*(3): 351-451.

Jefferies, M., and Been, K. (2006). *Soil liquefaction: a critical state approach*. Taylor and Francis Group.

Lirer, S., Flora, A., & Nicotera, M. V. (2011). Some remarks on the coefficient of earth pressure at rest in compacted sandy gravel. *Acta Geotechnica*, *6*(1): 1-12.

Mele, L., Flora, A., Lirer, S., d'Onofrio, A., & Bilotta, E. (2018a*). Experimental Study of the Injectability and Effectiveness of Laponite Mixtures as Liquefaction Mitigation Technique.* In *Geotechnical Earthquake Engineering and Soil Dynamics V* (pp. 267-275). Reston, VA: American Society of Civil Engineers.

Mele, L., Tian, J. T., Lirer, S., Flora, A., and Koseki, J. (2018b). Liquefaction resistance of unsaturated sands: experimental evidence and theoretical interpretation. *Géotechnique*, DOI: 10.1680/jgeot.18.p.042.

Mele L., Lirer S., Flora A. (2019a). The effect of confinement in liquefaction tests carried out in a cyclic simple shear apparatus. *7th International Symposium on Deformation Characteristics of Geomaterials*, Glasgow (Scotland), June 2019.

Mele L., Lirer S., Flora A. (2019b). The effect of densification on Pieve di Cento sands in cyclic simple shear tests. *7th Convegno Nazionale Ricercatori Ingegneria Geotecnica*, Lecco (Italy), July 2019.

Mulilis, J. P., Arulanandan, K., Mitchell, J. K., Chan, C. K., and Seed, H. B. (1977). Effects of sample preparation on sand liquefaction. *Journal of the Geotechnical Engineering Division*, *103*(2): 91-108.

Murthy, T. G., Loukidis, D., Carraro, J. A. H., Prezzi, M., and Salgado, R. (2007). Undrained monotonic response of clean and silty sands. *Géotechnique*, *57*(3): 273-288.

Polito, C., Green, R. A., Dillon, E., and Sohn, C. (2013). Effect of load shape on relationship between dissipated energy and residual excess pore pressure generation in cyclic triaxial tests. *Canadian Geotechnical Journal*, *50*(11): 1118-1128.

Porcino, D., Caridi, G., and Ghionna, V. N. (2008). Undrained monotonic and cyclic simple shear behaviour of carbonate sand. *Géotechnique*, 58(*8):* 635-644.

Seed, R. B., Cetin, K. O., Moss, R. E., Kammerer, A. M., Wu, J., Pestana, J. M., Riemer M.F., Sancio R.B., Bray R.E., Kayen, R.E. and Faris, A. (2003). Recent advances in soil liquefaction engineering: a unified and consistent framework. In *Proceedings of the 26th Annual ASCE Los Angeles Geotechnical Spring Seminar: Long Beach, CA*.

Sharma S.S., Ramsey, N., Lee, F., and Bhattarai, B.N. (2017). Challenges in assessing the shear strength of offshore sediments using simple shear tests. *Proc., Geotechnical Frontiers 2017: Geotechnical Materials, Modelling and Testing*, Orlando, Florida, 327-336.

Vaid, Y. P., and Chern, J. C. (1983). Effect of static shear on resistance to liquefaction. *Soils and foundations*, *23*(1): 47-60.

Verdugo, R. (1992). Characterization of sandy soil behavior under large deformation. *Doctoral Thesis, Department of Civil Engineering*, University of Tokyo, Japan.

Verdugo, R., and Ishihara, K. (1996). The steady state of sandy soils. *Soils and foundations*, 36(2): 81-91.

Visone C., (2008). Performance-based approach in seismic design of embedded retaining walls. *PhD Thesis*, University of Napoli Federico II, Napoli, Italy.

CHAPTER 6

6. EXPERIMENTAL ACTIVITY: MITIGATION TECHNIQUES

Within the European project LIQUEFACT, the most promising and innovative liquefaction mitigation techniques have been studied: addition of fines, densification and desaturation.
In this section an insight is proposed on the study of the aforementioned technologies at laboratory scale. It aims at verifying the effectiveness and the applicability of the above mentioned liquefaction countermeasures. At the end of the chapter a useful discussion on the three proposed techniques have been reported, evaluating positive and negative aspects of each technology.

6.1 ADDITION OF PLASTIC FINES

As already mentioned in Chapter 2 (§2.4.2), adding plastic fines to the soil may contribute to increase its resistance to liquefaction. In this study, it has been verified by adding to the sandy specimens a superplastic nanoparticle: the laponite. In particular, laponite RD ($Na^{+0.7}[(Si_8Mg_{5.5}Li_{0.3})O_{20}(OH)_4]^{-0.7}$) was adopted, with a specific gravity G_s =2.57 (Rockwood Additives Ltd. 2011) and a very high plasticity index (PI), equal to 1100%, so that called "super-plastic nanoparticle" (El Howayek 2011).
To investigate the effectiveness of this mitigation technique, cyclic triaxial tests on untreated sand and sand treated with laponite were carried out, whereas to study the applicability of this countermeasure against liquefaction, permeability and viscosity tests were performed on the mixture water/laponite (Mele et al., 2018a). In order to better analyse the effects of laponite on cyclic resistance, a clean uniform sand (Leighton Buzzard, fraction E; Fig. 1a; Tab. 1) has been chosen to be tested.

6.1.1 CYCLIC TRIAXIAL TESTS

Two cyclic triaxial tests have been carried out on treated sand. The sand-laponite specimens have been made by manually mixing sand and dry laponite: the amount of laponite added in the specimen is 1% of dry weight of sand. The sand/laponite mixture was subsequently pluviated (the corresponding concentration of laponite in water is ϕ= 3% by weight) in a steel cylinder with water and then frozen. The testing procedure is the same as the untreated specimens, even though for sand/laponite specimen an aging time of 110 hours was waited to ensure the complete gelification of laponite within the pores. Thereafter, different values of CSR have been applied (Tab.6.1). The results of the two tests are plotted in Figures 6.1 and 6.2 in the traditional planes: ε_a -q (a); p' – q (b); N_{cyc} – CSR (c) and $N_{cyc} – r_u – \varepsilon_a$ (d). As can be observed, the area of cycles ε_a -q increases with

N_{cyc}, while the stress paths move to the origin of the axes, due to an increase of pore pressure (Figs. 6.1d – 6.2d).

Table 6.1. Cyclic triaxial tests on Leighton Buzzard sand treated with laponite.

Test	Lap (%)	σ'$_c$ (kPa)	Aging (h)	e_0	D_{r0} (%)	CSR
T_CTX_LB1	1	50	110	0.783	57.2	0.162
T_CTX_LB2	1	50	110	0.799	53.1	0.135

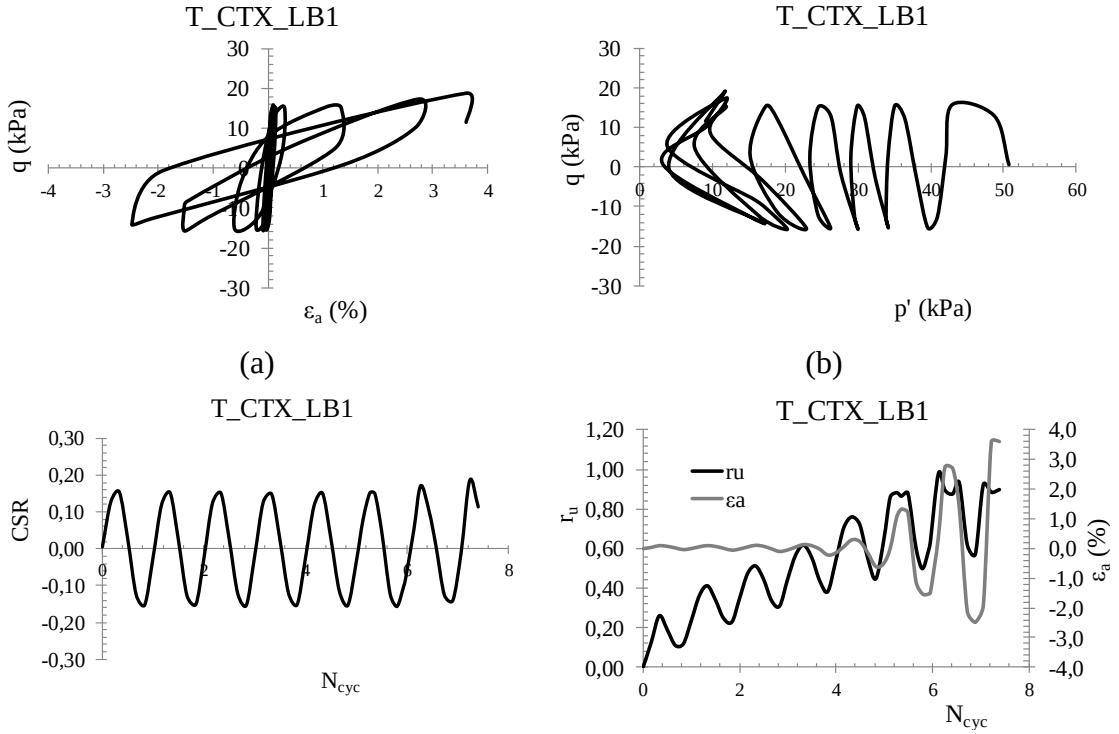

Figure 6.1. Results of cyclic triaxial tests of sand treated with laponite (T_CTX_LB1) in the planes: ε_a -q (a); p' – q (b); N_{cyc} – CSR (c) and N_{cyc} – r_u – ε_a (d).

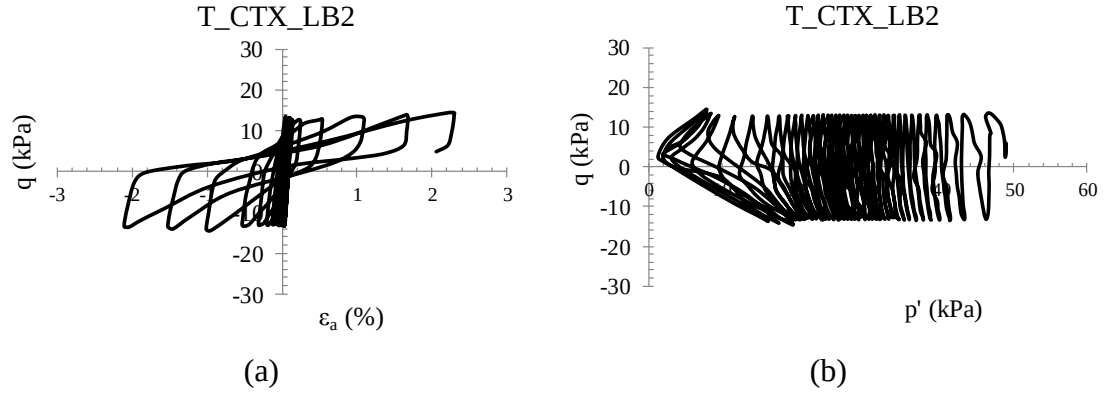

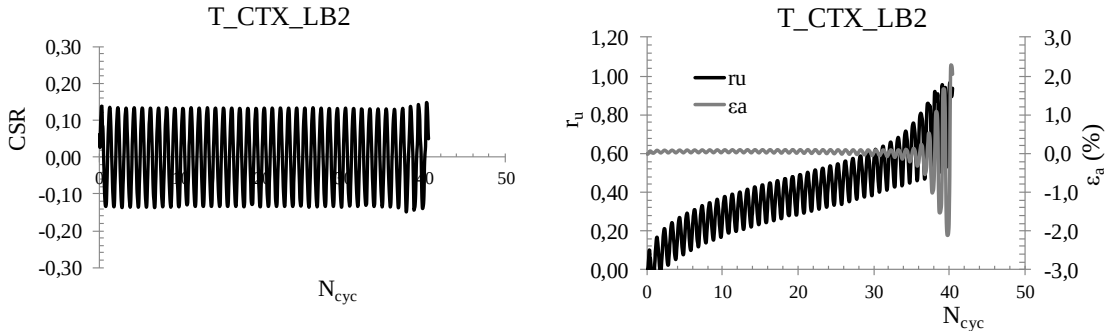

(c) (d)

Figure 6.2. Results of cyclic triaxial tests of sand treated with laponite (T_CTX_LB2) in the planes: ε_a -q (a); p' – q (b); N_{cyc} – CSR (c) and N_{cyc} – r_u – ε_a (d).

It should be specified that one of the most important experimental problems in these kinds of tests is the measure of pore pressure. In fact, the presence of gel could distort the measure at the transducer, but the small concentrations of laponite (3% in water) allow to avoid that issue, so that the value of pore pressure recorded can be considered reliable.
To better understand the effect of laponite in cyclic resistance, two tests have been compared: CTX_LB3 (clean sand) and T_CTX_LB2 (sand-laponite) (Fig. 6.3). Although the CSR value is slightly different (CSR=0.128 for CTX_LB3 and CSR= 0.135 for T_CTX_LB2; see Tab. 6.1), the delay in the build-up of pore pressure (Fig. 6.3a) and in the attainment of ε_{DA} equal to 5% for treated specimens (Fig. 6.3b) is clearly evident. The presence of 1% of laponite extends the number of cycles to reach liquefaction according to stress (r_u=0.90) and strain ($\varepsilon_{DA}\geq$5%) criteria. For both of the treated specimens N_{liq} is independent from the chosen failure criterion, as reported in Table 6.2 and confirmed by Ochoa-Cornejo et al. (2016).

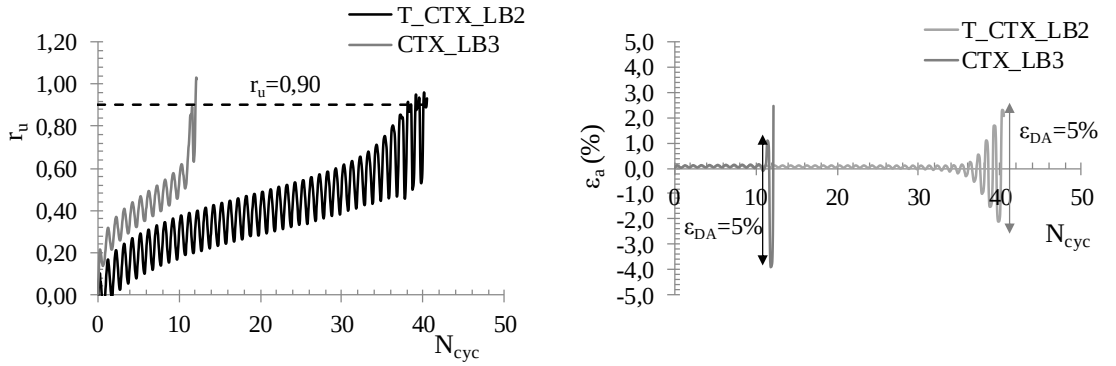

(a) (b)

Figure 6.3. Comparisons of treated and untreated cyclic behaviour in terms of r_u (a) and ε_a (b).

Table 6.2. Results of cyclic triaxial tests on Leighton Buzzard sand treated with laponite.

Test	Lap (%)	σ'_c (kPa)	Aging (h)	e_0	D_{r0} (%)	CSR	N_{liq} r_u 0.90	N_{liq} ε_{DA}5%
T_CTX_LB1	1	50	110	0.783	57.2	0.162	6.1	7
T_CTX_LB2	1	50	110	0.799	53.1	0.135	38	40

The stress criterion has been then used to identify the attainment of liquefaction and build the cyclic resistance curve (Fig. 6.4). Even though just two tests were carried out on treated specimens, the improvement of liquefaction resistance, adding laponite is evident. Small amount of laponite (1% of dry weight of sand) can increase the soil liquefaction strength: the presence of a laponite gel within the pores contributes to create bridge between the particles of sand, limiting the mobility of sand and thus delays the triggering of the liquefaction process. This seems more evident for higher N_{liq}. Further tests could be useful to better understand the liquefaction behaviour of treated sands at small N_{liq} and then higher CSR.

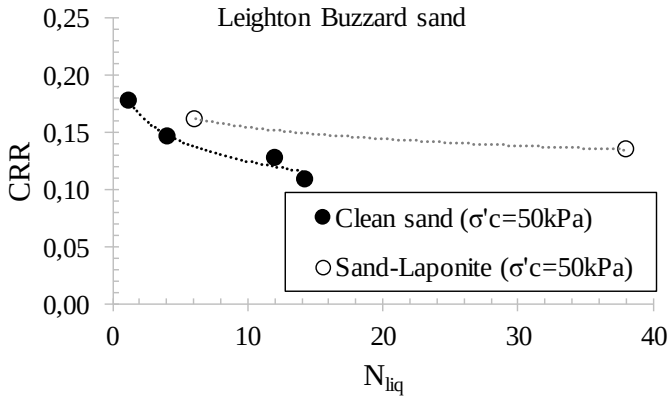

Figure 6.4. Cyclic resistance curves of clean and treated sand.

6.1.1.1 EXCESS PORE PRESSURE BUILD-UP

Figure 6.3a suggests that even though the sand treated with laponite presents a higher liquefaction resistance, the trend of the curve N_{cyc}-r_u for treated and untreated sand is very similar. In order to compare their behavior, the relationship $N_{cyc}/N_{liq} – r_u$ has been plotted in Figure 6.5. It can be observed that the curves of treated soil overlap those of clean sand. Moreover, the relationship of Booker et al. (1976) has been calibrated on the experimental data (Fig. 6.5). The best fitting for the results of laboratory tests can be achieved adopting β=0.70. This important observation implies that for treated sands (with low laponite concentration) the same pore pressure generation model of Booker et al. (1976) can be used as for untreated soils.

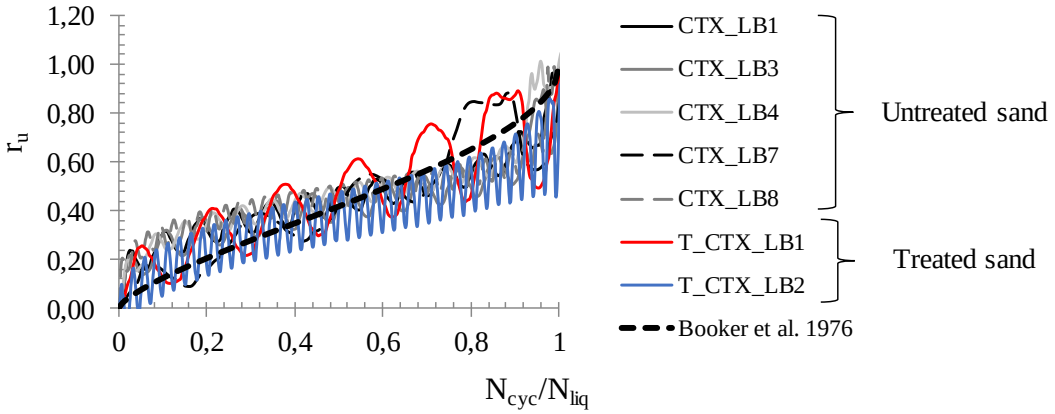

Figure 6.5. Experimental results for treated and untreated specimens in the plane N_{cyc}/N_{liq} - r_u.

Although the presence of laponite plays an important role in the improvement of liquefaction resistance, the evolution of pore pressure versus N_{cyc}/N_{liq} follows the same trend of untreated specimens. It is probably due to the fact that the concentration of laponite is high enough to increase resistance to liquefaction, but low enough not to alter the trend of excess pore pressure. A concentration of 1% of laponite keeps together the grains of sand, forming "localized bridges" and not a continuous and homogeneous matrix of gel into the pore spaces, that can be created only increasing the concentrations of laponite, reaching for instance a value of 5%, as confirmed by Ochoa-Cornejo (2016). Therefore, the excess pore pressure models used for clean sand can be used for sand treated with laponite when the concentrations are low (<5%).

6.1.2 VISCOSITY AND PERMEABILITY TESTS

The experimental results, showed in the previous paragraph (§6.1.1), have highlighted the effectiveness of the treatment by laponite as countermeasure against liquefaction because of the capacity of that material to change its state from liquid to gel into the pores of the soil, reducing the mobility of sand grains. On the other hand, this same important rheological aspect may lead to problems regarding the applicability in situ. In this respect, the injectability of mixture water-laponite has to be studied in depth.

The injectability of a mixture within the pores of a soil (Lirer et al. 2006) is related to the size of the suspended particles, the initial viscosity of the mixture (μ_0), and its gelling time (t_{gel}). These rheological parameters can be measured by means of viscosity tests with a Marsh cone (Fig. 6.6a): the tests were carried out on water/laponite mixtures prepared with two different concentrations ϕ (ϕ = 1.5 – 3.0%, Tab. 6.3; Mele et al., 2018a).

In two tests (PV3 and PV4), an additive (SPP = sodium pyrophosphate) was also added to the water/laponite mixture in order to test its influence on rheological mixture properties. Actually, SPP should delay the gelling time, for easing the permeation into the soil. The tested mixtures have been prepared by mixing dry laponite (and SPP in PV3 and PV4) with water, always ensuring a complete solubilization of the components.

Constant load permeability tests (Tab.6.3) have been carried out in a permeameter (diameter d= 35.3 mm and a height h=72 mm) with the aim to measure the permeability of the sand specimens (D_{r0} = 40%) to the water/laponite mixture and to the water/laponite/SPP mixtures (Fig. 6.6b).

Table 6.3. Viscosity and permeability tests on mixture water/laponite.

	Test	Fluid	ϕ_{lap} (%)	ϕ_{SPP} (%)
Viscosity tests	PV1	wat+lap	1.5	-
	PV2	wat+lap	3.0	-
	PV3	wat+lap+SPP	3.0	0.06
	PV4	wat+lap+SPP	3.0	0.03
Permeability tests	PL_LB1	wat+lap	1.5	-
	PL LB2	wat+lap	3.0	-
	PL_LB3	wat+lap+SPP	3.0	0.06
	PL_LB4	wat+lap+SPP	3.0	0.03

(a) (b)

Figure 6.6. Test devices: Marsh cone (a) and permeameter (b).

The results of the viscosity tests, summarized in Table 6.4 and plotted in Figure 6.7a, show that the initial value of the viscosity (μ_0) of the tested mixtures is very low and similar to that of the water (μ_w=1cP), except for the test PV2, and it is certainly due to its higher concentration of laponite and the lack of SPP. The results indicate that the initial viscosity and the gelling time (t_{gel}) of the mixtures without additives (PV1 and PV2) are obviously a function of the concentration of laponite. As expected, the additive (SPP) ensures low viscosity of the mixture even for high laponite concentration (ϕ_{lap}= 3%), and delays the gelification process of the mixture, by making easier the in situ mixture injection.

Regarding permeability tests, it can be noted, from Table 6.5, that there is no permeation into the specimen to the mixture water/laponite (PL_LB1 and PL_LB2), regardless of

concentration of nanoparticle in water. Owing to that SPP has been added and, as shown in Fig. 6.7b (PL_LB3 and PL_LB4), permeation occurs. Moreover, in the same Figure the black dashed line indicates the value of permeability coefficient to water of PW_LB test (k_w=2.1·10^{-4} m/s; Tab. 5.1; Fig. 5.1). It is worth noting that the presence of SPP not only improves the permeability into the specimen but contributes to make the permeability coefficient to the mixture (k_m) very similar to that of water.

Table 6.4. Viscosity tests on mixture water/laponite.

	Test	Fluid	ϕ_{lap} (%)	ϕ_{SPP} (%)	μ_0 (cP)
Viscosity tests	PV1	wat+lap	1.5	-	1.44
	PV2	wat+lap	3.0	-	4.50
	PV3	wat+lap+SPP	3.0	0.06	1.70
	PV4	wat+lap+SPP	3.0	0.03	1.97

Table 6.5. Permeability tests on mixture water/laponite.

	Test	Fluid	ϕ_{lap} (%)	ϕ_{SPP} (%)	k_m (m/s)
Permeability tests	PL_LB1	wat+lap	1.5	-	No
	PL_LB2	wat+lap	3.0	-	No
	PL_LB3	wat+lap+SPP	3.0	0.06	1.90·10^{-4}
	PL_LB4	wat+lap+SPP	3.0	0.03	1.84·10^{-4}

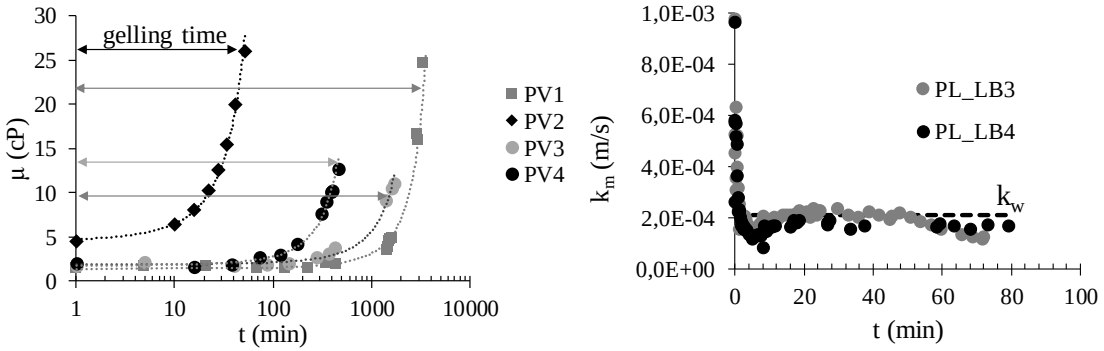

Figure 6.7. Results of viscosity tests for water/laponite mixture (a) and permeability tests to water laponite mixture (b).

During the permeability tests the permeated mixture has been collected to evaluate – through the evaporation of water at 105°C - the concentration of laponite in water. The results of PL_LB3 and PL_LB4 tests were plotted in Figure 6.8. In both cases, ϕ is null at the beginning of the permeation because of the pore water going out from the specimen, after that ϕ increases until to reach a value of 3%, which corresponds to the initial concentration of laponite for the prepared mixture (Tab. 6.5).

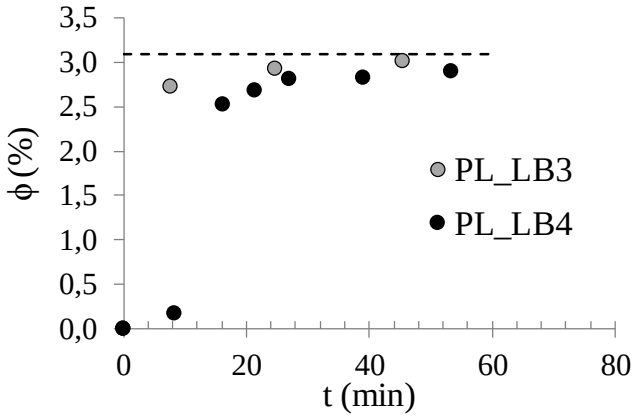

Figure 6.8. Concentration of laponite in the permeated mixture measured during the tests PL_LB3 and PL_LB4.

Finally, eq. (2.45) has been validated for the laboratory tests performed in this research. From the results of viscosity tests, the permeability coefficient to the mixture water-laponite (k_m) has been achieved per via eq. (2.45) and compared with the experimental values obtained from the permeability tests (Fig. 6.9). The good agreement of the estimated values with those achieved experimentally by means of permeability tests, for two different concentrations of SPP, allows to confirm the importance on the eq. (2.45) in permeation treatment of plastic particles.

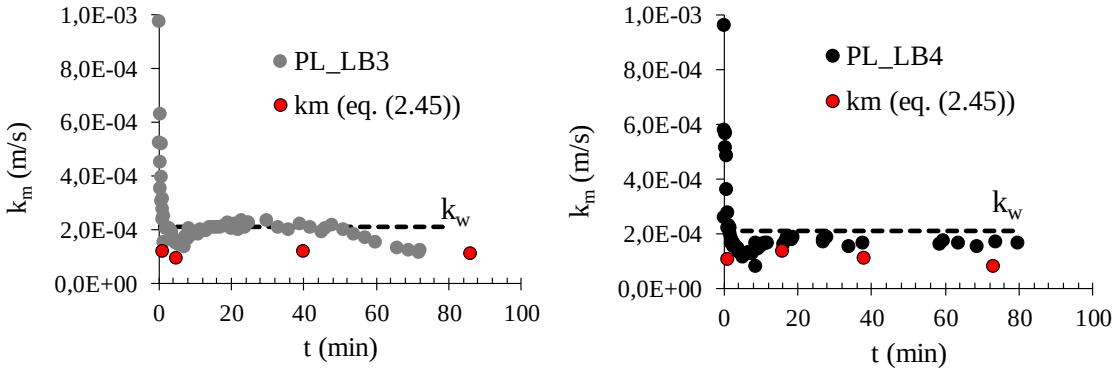

(a) (b)

Figure 6.9. Comparisons between the measured values of permeability coefficient and the estimated valued per via eq. (2.45) for concentrations of SPP of 0.06 % (a) and 0.03% (b).

6.2 DENSIFICATION

Since the dilatative tendency of dense sands, they present a higher liquefaction resistance to liquefaction than loose sandy soils. To verify the effectiveness of densification as liquefaction mitigation technique, cyclic triaxial and simple shear tests have been carried out.

6.2.1 CYCLIC TRIAXIAL TESTS

Cyclic triaxial tests have been carried out on Sant'Agostino (Mele et al., 2018b; Lirer & Mele, 2019) and GSS Pieve di Cento sands as reported in Table 6.6.
For triaxial tests, the specimens have been prepared as the loose ones, as previously mentioned in the paragraph 4.2.1.1. Sant'Agostino specimens have been consolidated at 50 kPa, while one GSS specimen has been consolidated at σ'_c equal to 25 kPa (Tab. 6.6).

Table 6.6. Cyclic triaxial tests on dense specimens.

Test	Sand	σ'_c (kPa)	e_0*	D_{r0}*(%)	CSR
CTX_SAS5	Sant'Agostino	50	0.604	63.4	0.179
CTX_SAS6	Sant'Agostino	50	0.636	58.4	0.147
CTX_SAS7	Sant'Agostino	50	0.652	55.9	0.128
CTX_SAS8	Sant'Agostino	50	0.536	74.1	0.198
CTX_SAS9	Sant'Agostino	50	0.524	75.9	0.179
CTX_SAS10	Sant'Agostino	50	0.542	73.1	0.164
CTX_GSS6	PdC GSS				
CTX_GSS7	PdC GSS				
CTX_GSS8	PdC GSS				
CTX_GSS9	PdC GSS				
CTX_GSS10	PdC GSS				
CTX_GSS11	PdC GSS				
CTX_GSS12	PdC GSS				
CTX_GSS13	PdC GSS				
CTX_GSS14	PdC GSS				

*at the end of consolidation phase.

The results of some tests in the planes: $\varepsilon_a - q$; $p' - q$; $N_{cyc} - CSR$; $N_{cyc} - r_u - \varepsilon_a$, are shown in Figures 6.10 (SAS) and 6.11 (GSS). As for loose sands, the results of cyclic tests are consistent with those of monotonic tests, from which the CSL has been identified (Chapter 5). The stress-path moves towards the CSL, implying an increase of pore pressure. Unlike liquefaction tests performed on loose sands, for dense sands the triggering liquefaction criteria (stress and strain) do not give the same results in terms of N_{liq} as shown in Table 6.7. As an example, it can be clearly observed in Figure 6.11h for CTX_GSS11, that r_u equal to 0.90 is attained after 11.5 cycles, when ε_{DA} is only 2%.

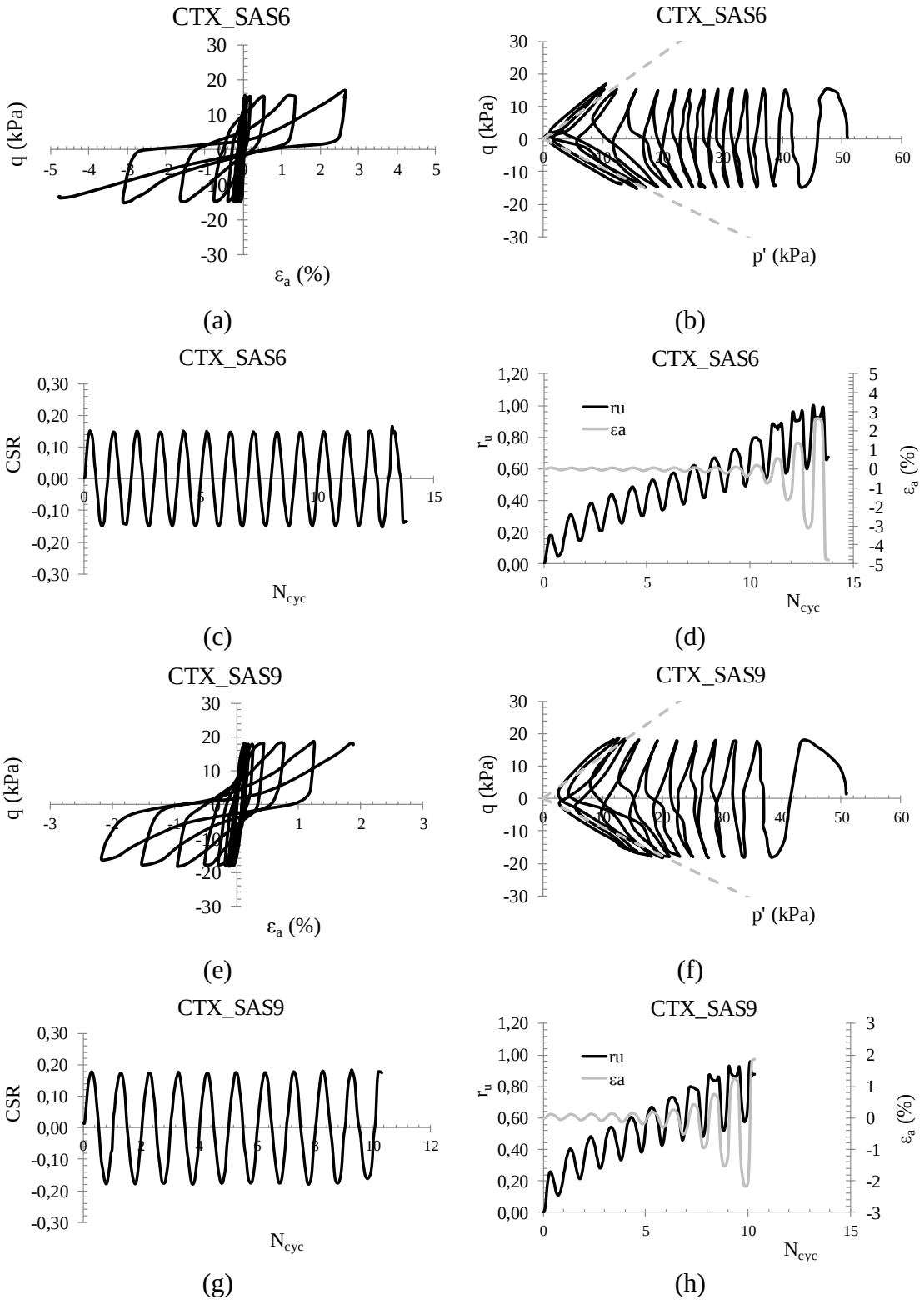

Figure 6.10. Results of cyclic triaxial tests on Sant'Agostino sand in the planes: ε_a – q (a-e); p' – q (b-f); N_{cyc} – CSR (c-g); N_{cyc} – r_u – ε_a (d-h).

Figure 6.11. Results of cyclic triaxial tests on Pieve di Cento (GSS) sand in the planes: ε_a – q (a-e); p' – q (b-f); N_{cyc} – CSR (c-g); N_{cyc} – r_u – ε_a (d-h).

Table 6.7. Results of cyclic triaxial tests on dense specimens.

Test	Sand	σ'_c (kPa)	e_0*	D_{r0}* (%)	CSR	N_{liq} r_u=0.90	N_{liq} ε_{DA}=5%
CTX_SAS5	Sant'Agostino	50	0.604	63.4	0.179	3.0	3.0
CTX_SAS6	Sant'Agostino	50	0.636	58.4	0.147	11.5	13.0
CTX_SAS7	Sant'Agostino	50	0.652	55.9	0.128	14.0	15.5
CTX_SAS8	Sant'Agostino	50	0.536	74.1	0.198	4.0	8.0
CTX_SAS9	Sant'Agostino	50	0.524	75.9	0.179	9.0	-
CTX_SAS10	Sant'Agostino	50	0.542	73.1	0.164	28.0	41.0
CTX_GSS6	PdC GSS						
CTX_GSS7	PdC GSS						
CTX_GSS8	PdC GSS						
CTX_GSS9	PdC GSS						
CTX_GSS10	PdC GSS						
CTX_GSS11	PdC GSS						
CTX_GSS12	PdC GSS						
CTX_GSS13	PdC GSS						
CTX_GSS14	PdC GSS						

*at the end of consolidation phase.

Moreover, the results of the tests on Sant'Agostino and Pieve di Cento (GSS) sands are plotted in the plane N_{liq} – CRR, where N_{liq} has been evaluated according to stress criterion (r_u=0.90). As expected, regardless of the tested soil, higher D_r lead to higher liquefaction resistance.

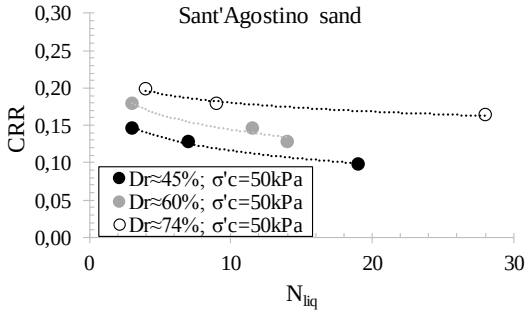

(a) (b)

Figure 6.12. Cyclic resistance curves with different D_r for Sant'Agostino (a) and Pieve di Cento (GSS) sands (b).

It is worth noting that the test CTX_GSS14, which has been consolidated at 25kPa, seems to fit well the experimental curve found for tests performed with a confining stress of 50kPa. It could be explained through the concept of state parameter (ψ). In Table 6.8 the state parameter has been reported for the performed tests. It can be noted that ψ of CTX_GSS14 test is -0.195, comparable with those of the other tests (CTX_GSS11, 12

and 13) performed with similar D_r and different confining stress (50 kPa), whose average value is -0.199.
However, the curve from Sant'Agostino sand (D_r≈74%) match that from Pieve di Cento (GSS) sand (D_r≈54%), nevertheless the average value of ψ are -0.309 and -0.149, respectively, so very different. It would confirm what reported by Ishihara (1993), according to which the state parameter could be not reliable to quantify the behaviour of different sands under low confining stresses.

Table 6.8. Results of cyclic triaxial tests on dense specimens.

Test	Sand	σ'_c (kPa)	e_0*	ψ	CSR	N_{liq} r_u=0.90	N_{liq} ε_{DA}=5%
CTX_SAS5	Sant'Agostino	50	0.604	-0.238	0.179	3.0	3.0
CTX_SAS6	Sant'Agostino	50	0.636	-0.206	0.147	11.5	13.0
CTX_SAS7	Sant'Agostino	50	0.652	-0.190	0.128	14.0	15.5
CTX_SAS8	Sant'Agostino	50	0.536	-0.307	0.198	4.0	8.0
CTX_SAS9	Sant'Agostino	50	0.524	-0.319	0.179	9.0	-
CTX_SAS10	Sant'Agostino	50	0.542	-0.301	0.164	28.0	41.0
CTX_GSS6	PdC GSS						
CTX_GSS7	PdC GSS						
CTX_GSS8	PdC GSS						
CTX_GSS9	PdC GSS						
CTX_GSS10	PdC GSS						
CTX_GSS11	PdC GSS						
CTX_GSS12	PdC GSS						
CTX_GSS13	PdC GSS						
CTX_GSS14	PdC GSS						

*at the end of consolidation phase.

6.2.1.1 EXCESS PORE PRESSURE BUILD-UP

For each D_r, the tests have been plotted in terms of excess pore pressure (r_u) versus N_{cyc}/N_{liq} (Figs. 6.13 and 6.14) and interpreted using the model of Booker et al. (1976), reported in Chapter 2 (eq. (2.10)). The value of β has been calibrated to have the best fitting for the experimental results and summarized in Table 6.9.
It shows that the value of D_r, in the investigated range, does not influence significantly the shape of excess pore pressure variation law and thus β. On the contrary, the type of the soil, and in particular D_{60}, plays an important role in pore pressure generation, confirming the findings shown in §5.1.4.2 (Fig. 5.36).

Figure 6.13. Excess pore pressure (ru) versus N_{cyc}/N_{liq} for Sant'Agostino sand with different D_r: 45% (a); 60% (b) and 74% (c).

Figure 6.14. Excess pore pressure (r_u) versus N_{cyc}/N_{liq} for Pieve di Cento (GSS) sand with different D_r: 40% (a); 54% (b) and 65% (c).

Table 6.9. Calibration of β for loose and dense Sant'Agostino and Pieve di Cento (GSS) sands.

SAS_ D_r (%)	β	GSS_ D_r (%)	β
45	1.0	40	0.7
60	1.0	54	0.7
74	1.1	65	0.7

6.2.2 CYCLIC SIMPLE SHEAR TESTS

The beneficial effect of densification was also studied performing cyclic simple shear tests on Pieve di Cento sands (BSS and GSS) (Mele et al. 2019a). The tests carried out are summarized in Table 6.10. All tests have been performed in flexible boundary conditions and preparing the specimens by 1D-Compression technique. Additionally, one test (CSS_GSS11F) has been performed by applying a static shear stress; thus, an α (τ_{st}/σ'_v) value has been also calculated (Tab. 6.10).

In Figures 6.15 and 6.16 the results of some cyclic simple shear tests on dense sands, BSS and GSS respectively, have been plotted in the planes: γ–τ (a); σ'_v– σ'_h- τ (b); N_{cyc} – CSR (c); N_{cyc} – r_u –γ (d).

Similar considerations, already done for loose specimens can be done for denser sands. In Figure 6.17 the test CSS_GSS11F is shown, where a static shear stress (τ_{st}) of 4.89 kPa has been applied, as is clearly noted in Figure 6.17b, where the stress-path of effective vertical stress is shown.

As well known, the positive shear stress generates a shift of shear strain towards positive direction (Fig. 6.17d).

Table 6.10. Cyclic simple shear tests on dense specimens (Pieve di Cento sands).

Test	Sand	Preparation Technique	σ'_h (kPa)	σ'_v (kPa)	e_0*	D_{r0}* (%)	CSR	α
CSS_BSS4F	PdC_BSS	1D-Compr	44.8	60.0	0.659	77.1	0.155	-
CSS_BSS5F	PdC_BSS	1D-Compr	28.9	59.5	0.653	78.3	0.135	-
CSS_BSS6F	PdC_BSS	1D-Compr	34.5	60.6	0.656	77.7	0.160	-
CSS_GSS8F	PdC_GSS	1D-Compr	24.0	49.0	0.581	68.6	0.150	-
CSS_GSS9F	PdC_GSS	1D-Compr	24.8	43.9	0.598	64.7	0.130	-
CSS_GSS10F	PdC_GSS	1D-Compr	25.2	49.7	0.574	70.1	0.165	-
CSS_GSS11F	PdC_GSS	1D-Compr	23.8	51.5	0.587	67.2	0.159	0.095

*at the end of consolidation phase.

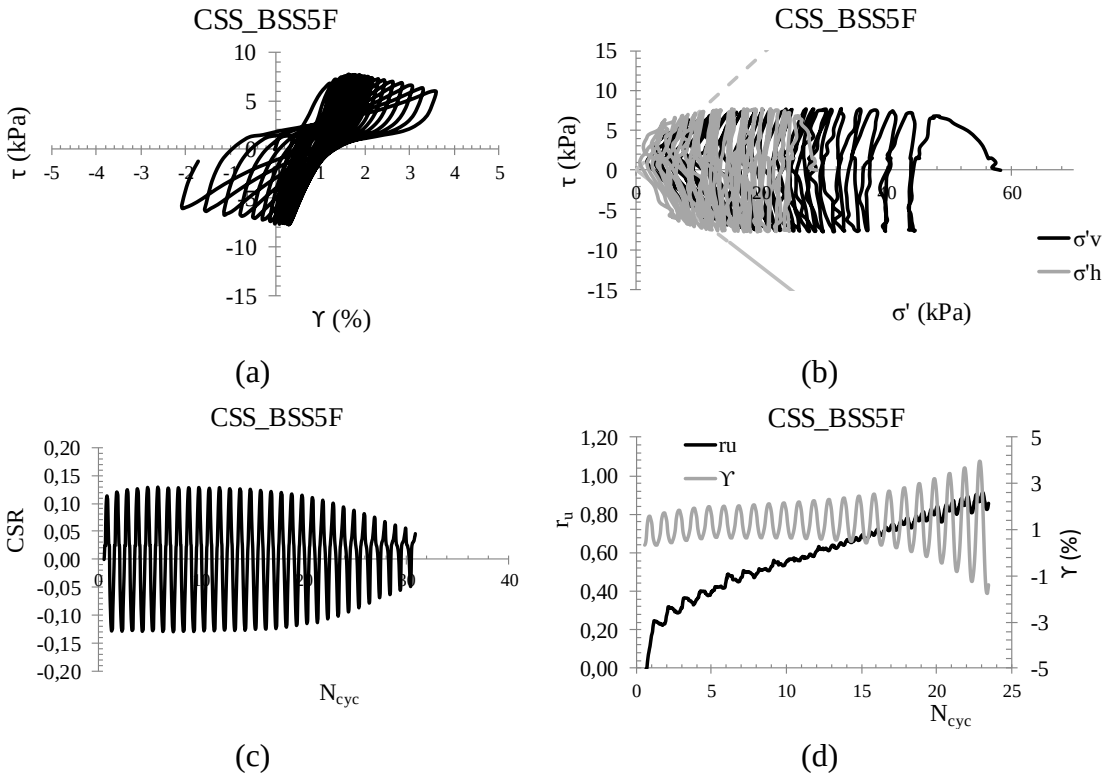

Figure 6.15. Results of cyclic simple shear test on Pieve di Cento (BSS) sand in the planes: γ–τ (a); σ'$_v$– σ'$_h$- τ (b); N_{cyc} – CSR (c); N_{cyc} – r_u –γ (d).

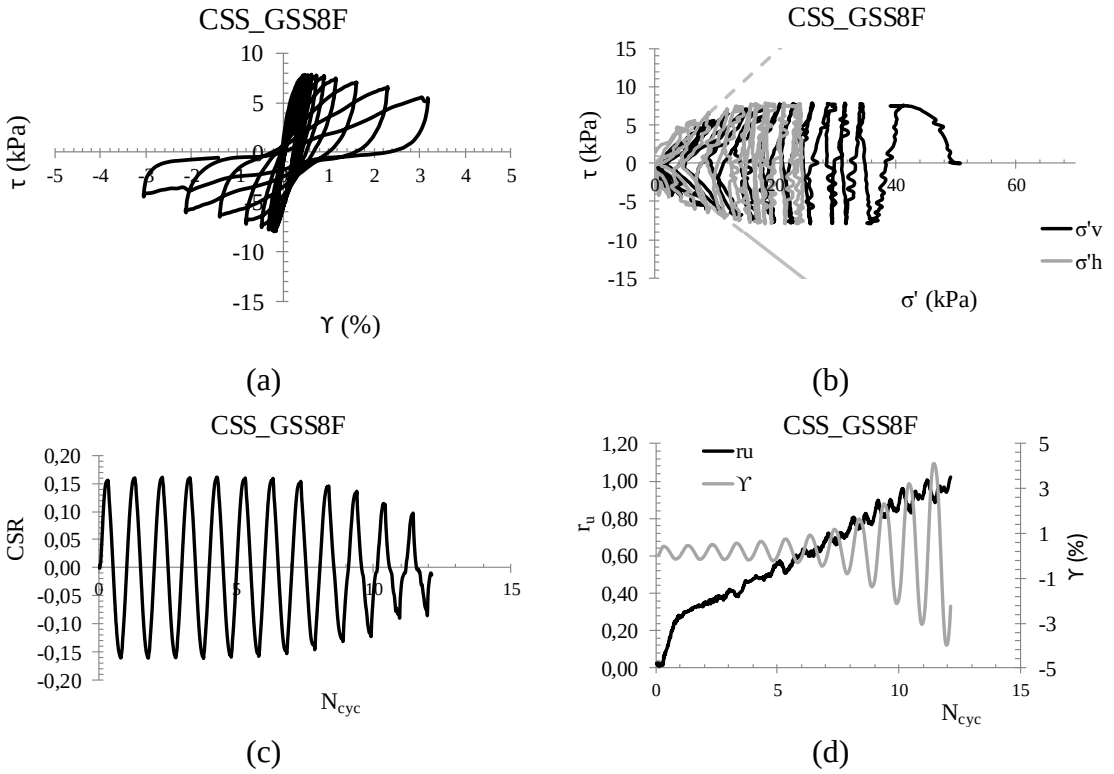

Figure 6.16. Results of cyclic simple shear tests on Pieve di Cento (GSS) sand in the planes: γ –τ (a-e); σ'$_v$– σ'$_h$- τ (b-f); N_{cyc} – CSR (c-g); N_{cyc} – r_u –γ (d-h).

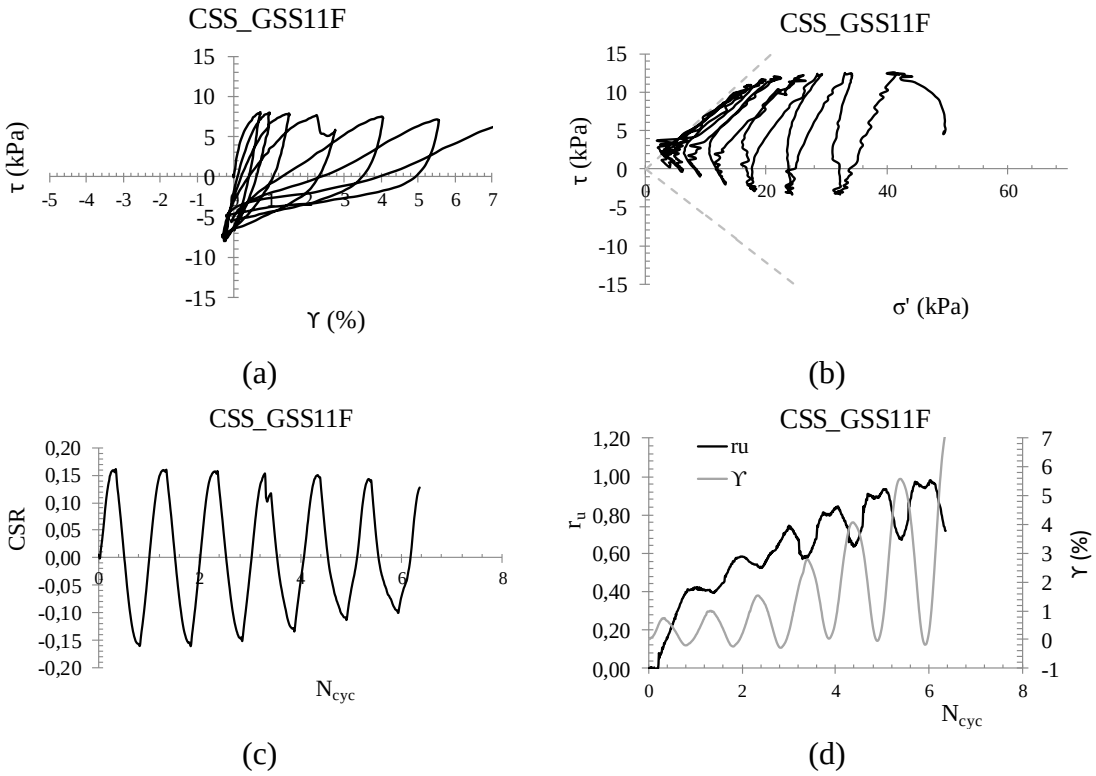

Figure 6.17. Results of cyclic simple shear test with a static shear stress applied, in the planes: γ–τ (a); σ'$_v$–τ (b); N_{cyc} – CSR (c); N_{cyc} – r_u – γ (d).

In Table 6.11 the results of cyclic simple shear tests are reported in terms of N_{liq} evaluated according to stress and strain criteria. Unlike triaxial tests, N_{liq}\(Υ_{DA} 3.75%) is lower than N_{liq}\(r_u 0.90).

However, the effectiveness of densification as countermeasure against liquefaction is clearly shown in Figure 6.18a.

In addition, in Figure 6.18b the effect of non-symmetrical cyclic loading has been shown. As expected, even though only one test has been performed under this condition, the presence of a static shear stress seems to decrease the liquefaction resistance, as a matter of the fact that the stress-path starts from a point closer to CSL (Fig. 6.17b).

Table 6.11. Results of cyclic simple shear tests on dense specimens (Pieve di Cento sands).

Test	Sand	Prep. Techn	σ'$_h$ (kPa)	σ'$_v$ (kPa)	e_0*	D_{r0}* (%)	CSR	α	N_{liq} r_u0.90	N_{liq} Υ_{DA}3.75%
CSS_BSS4F	PdC_BSS	1D-C	44.8	60.0	0.659	77.1	0.155	-	3.5	1.5
CSS_BSS5F	PdC_BSS	1D-C	28.9	59.5	0.653	78.3	0.135	-	23.0	20.0
CSS_BSS6F	PdC_BSS	1D-C	34.5	60.6	0.656	77.7	0.160	-	13.0	13.0
CSS_GSS8F	PdC_GSS	1D-C	24.0	49.0	0.581	68.6	0.150	-	11.0	9.0
CSS_GSS9F	PdC_GSS	1D-C	24.8	43.9	0.598	64.7	0.130	-	74.0	70.0
CSS_GSS10F	PdC_GSS	1D-C	25.2	49.7	0.574	70.1	0.165	-	10.0	9.0
CSS_GSS11F	PdC_GSS	1D-C	23.8	51.5	0.587	67.2	0.159	0.095	5.0	4.0

*at the end of consolidation phase.

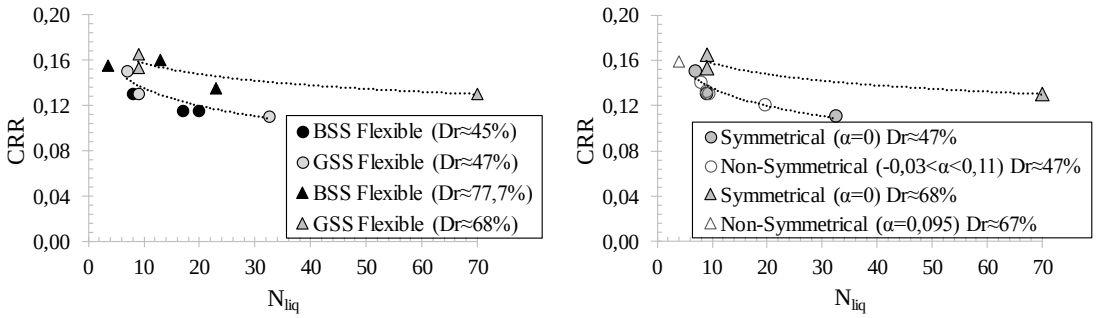

(a) (b)

Figure 6.18. Effect of densification for BSS and GSS (a); effect of non-symmetrical cyclic loading (b).

6.2.2.1 EXCESS PORE PRESSURE BUILD-UP

To better understand the effect of a static shear stress in the generation of pore pressure, CSS_GSS11F has been compared with CSS_GSS8F test in terms of r_u versus N_{cyc}/N_{liq} (Fig. 6.19). For the other tests, it was not possible to plot the results in that plane because the condition of fully liquefaction has not reached yet when the tests were stopped. As for loose sands (§5.1.5.4), the parameter β of the correlation of Booker et al. (1976) has been calibrated. The values are summarized in Table 6.12. It is worth noting that β increases passing from loose (1.1) to dense specimens (1.3) for symmetric cyclic loading, while no change occurs when a static shear stress is applied.

Unlike cyclic triaxial tests, where D_r seems to have an insignificant effect on the parameter β, in cyclic simple shear tests dense specimens show higher β. In other words, the pore pressure generation in CSS tests is more affected by an increase of D_r.

Furthermore, a higher value of β for dense specimens (Tab. 6.12) suggests a higher accumulation of r_u in the first cycles, thereafter, a lower increase of r_u occurs, reaching the threshold (r_u=0.90) after more cycles.

Figure 6.19. Excess pore pressure (r_u) versus N_{cyc}/N_{liq} for symmetrical (CSS_GSS8F) (a) and non-symmetrical (CSS_GSS11F) cyclic loading (b).

Table 6.12. Calibrated values of β for different preparation techniques.

	β	
	$\tau_{st}=0$	$\tau_{st}\neq0$
Loose	1.1	1.5
Dense	1.3	1.5

6.2.2.2 COMPARISON BETWEEN CYCLIC TRIAXIAL AND CYCLIC SIMPLE SHEAR TESTS

As for loose sands, the results in terms of liquefaction resistance from cyclic simple shear and triaxial tests have been compared by using Castro's correlation (eq. (2.7)), where k_0 has been evaluated from the results of cyclic simple tests as the ratio between σ'_h and σ'_v. The average value for tests on GSS is 0.521, obviously higher than that evaluated for loose sand (0.500).

In Figure 6.20, the results of cyclic triaxial and cyclic simple shear tests are compared in the plane N_{liq}-CRR. As can be clearly noted, the cyclic resistance curve is unique.

This result confirms once again, that Castro's correlation is fine to transform the data of cyclic triaxial tests in those of cyclic simple shear tests, showing additionally the reliability of the performed tests.

Figure 6.20. Comparison between CTX and CSS test results in the plane N_{liq}-CRR for GSS.

6.3 DESATURATION

In order to evaluate the effectiveness of desaturation as a mitigation technique against liquefaction, cyclic triaxial tests have been carried out in non-saturated conditions (UCTX) (§2.4.3.1). The triaxial Japanese cell (University of Tokyo) was used for this purpose (§4.2.3). The testing program of this kind of tests has been shown in Table 6.13. Three kinds of sand have been tested: Sant'Agostino (Mele et al., 2018b), Pieve di Cento (GSS) and Silica (N°5) sands. They have been tested in several conditions in terms of S_r, D_r and confining stress (σ'_{un}); this latter has been evaluated according to Bishop notation (eq.(2.46)), assuming the material parameter (χ) equal to S_r.

Table 6.13. Cyclic triaxial tests on non-saturated specimens.

Test	Sand	σ'_{un} (kPa)	S_{r0}* (%)	e_0*	D_{r0}* (%)	CSR
UCTX_SAS1	Sant'Agostino	49.5	53.0	0.707	47.3	0.370
UCTX_SAS2	Sant'Agostino	50.5	54.0	0.672	52.8	0.348
UCTX_SAS3	Sant'Agostino	48.9	56.0	0.667	53.6	0.307
UCTX_SAS4	Sant'Agostino	50.5	90.0	0611	62.3	0.160
UCTX_SAS5	Sant'Agostino	49.8	81.5	0.602	63.8	0.222
UCTX_SAS6	Sant'Agostino	49.8	87.2	0.590	65.6	0.254
UCTX_SAS7	Sant'Agostino	49.9	86.7	0.583	66.7	0.223
UCTX_SAS8	Sant'Agostino	48.8	87.6	0.591	65.5	0.258
UCTX_SAS9	Sant'Agostino	50.4	88.5	0.613	62.0	0.297
UCTX_GSS1	PdC_GSS					
UCTX_GSS2	PdC_GSS					
UCTX_GSS3	PdC_GSS					
UCTX_GSS4	PdC_GSS					
UCTX_GSS5	PdC_GSS					
UCTX_GSS6	PdC_GSS					
UCTX_GSS7	PdC_GSS					
UCTX_GSS8	PdC_GSS					
UCTX_GSS9	PdC_GSS					
UCTX_GSS10	PdC_GSS					
UCTX_GSS11	PdC_GSS					
UCTX_GSS12	PdC_GSS					
UCTX_GSS13	PdC_GSS					
UCTX_GSS14	PdC_GSS					
UCTX_GSS15	PdC_GSS					
UCTX_GSS16	PdC_GSS					
UCTX_SS1	SS5					
UCTX_SS2	SS5					
UCTX_SS3	SS5					

*at the end of consolidation phase

Typical results of some non-saturated tests on Sant'Agostino, Pieve di Cento (GSS) and Silica (N°5) sands, are plotted in Figures 6.21 – 6.22 – 6.23, respectively, in four planes: q - ε_a; q - (p-u_a) for unsaturated tests and q - (p-u_w) for partially saturated tests; u_a, u_w and s versus N_{cyc} for unsaturated tests and u_w and versus N_{cyc} for partially saturated tests (as already mentioned in §2.4.3.1., the pore air pressure u_a was not measured for partially saturated soils) and finally ε_a versus N_{cyc}.

As for saturated conditions, the behaviour of non-saturated soils describes cycles in the plane q - ε_a, whose area increases during the cyclic loading. Nevertheless, it should be noted that the deviatoric stress is perfectly maintained also after liquefaction, which is traditionally defined for non-saturated soils according to strain criterion (ε_{DA}=5%).

Moreover, the stress-path (Figs. 6.21b-f, 6.22b-f-l and 6.23b) moves toward the origin of axes, implying an increase of pore air (unsaturated soils) and pore water (partially saturated soils) pressures as shown in Figures 6.21c-g, 6.22c-g-m and 6.23c. In particular, for unsaturated soils, also the suction (s) has been plotted versus the number of cycles.

It can be noted that the suction is always extremely low, cycling around a value similar to the initial one (at the end of consolidation phase), and very close to zero. Accordingly, u_w and u_a increase together.

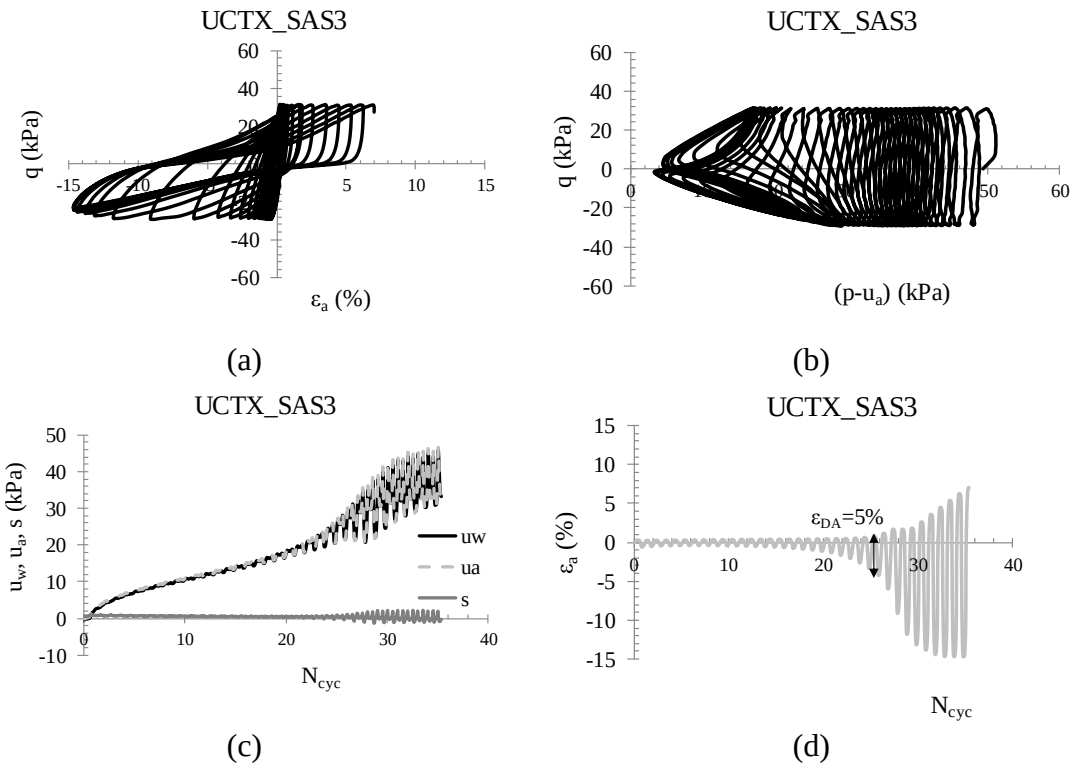

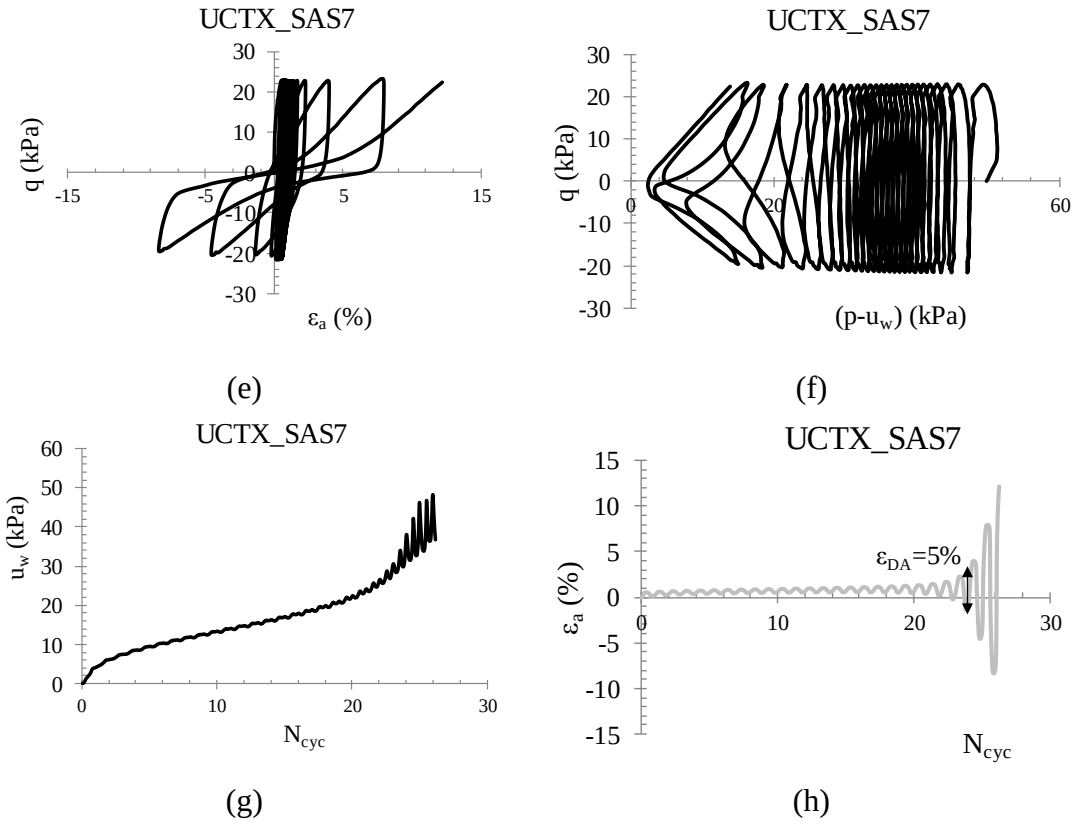

Figure 6.21. Results of cyclic triaxial test performed on non-saturated specimen of Sant'Agostino sand, in the planes: ε_a- q (a); q - (p-u_a/u_w) (b); u_a, u_w and s - N_{cyc} (c), and ε_a –N_{cyc} (d).

Figure 6.22. Results of cyclic triaxial test performed on unsaturated specimen of Pieve di Cento (GSS) sand, in the planes: ε_a- q (a); q - (p-u_a/u_w) (b); u_a, u_w and s - N_{cyc} (c), and $\varepsilon_a - \varepsilon_v$ - N_{cyc} (d).

Figure 6.23. Results of cyclic triaxial test performed on non-saturated specimen of Silica N°5 sand, in the planes: ε_a- q (a); q - (p-u_w) (b); u_w - N_{cyc} (c), and ε_a – ε_v - N_{cyc} (d).

Table 6.14 summarizes the results of non-saturated tests in terms of N_{liq}. As for saturated soils, N_{liq} identified according to strain and stress criteria have been compared, where for stress criteria, r_u is defined as the ratio between Δu_a (unsaturated soils) or Δu_w (partially-saturated soils) and the confining stress expressed according to Bishop's notation. For tests where r_u does not attain the critical value (0.90), only N_{liq} evaluated for ε_{DA}=5% has been reported.

As for dense saturated sands, the two criteria do not give the same results in terms of N_{liq}, especially for unsaturated soils. Instead, for the partially saturated ones, the difference tends to decrease; in other words, stress and strain criteria tends to give the same result when Sr increases, as clearly shown in Table 6.14. It means that, when ε_{DA}=5%, r_u will be lower than 0.90, and then the value of effective stress at liquefaction (ε_{DA}=5%), or so called $\sigma'_{un,liq}$ will not be nil. Mele and Flora (2019) proposed the following relationship between $\sigma'_{un,liq}/\sigma'_{un,0}$ and the initial degree of saturation (S_{r0}):

$$\frac{\sigma'_{un,liq}}{\sigma'_{un,0}} = -2 \cdot 10^{-4} \cdot S_{r0}^2 + 2 \cdot 10^{-2} \cdot S_{r0} + 0.10 \qquad (6.1a)$$

obtained to have the best fitting for the experimental results presented by Mele et al. (2018b). It can be easily noted that for S_{r0}=100%, $\sigma'_{un,liq}/\sigma'_{un,0}$ is 0.10, consistently with the definition of liquefaction according to strain criterion (r_u=0.90), because for saturated sandy soils the stress and strain criteria give the same results in term of N_{liq}.

Table 6.14. Results of cyclic triaxial tests on non-saturated specimens.

Test	Sand	σ'_{un} (kPa)	S_{r0}* (%)	e_0*	D_{r0}* (%)	CSR	N_{liq} r_u=0.90	N_{liq} ε_{DA}=5%
UCTX_SAS1	Sant'Agostino	49.5	53.0	0.707	47.3	0.370	11.2	3.6
UCTX_SAS2	Sant'Agostino	50.5	54.0	0.672	52.8	0.348	18.0	6.1
UCTX_SAS3	Sant'Agostino	48.9	56.0	0.667	53.6	0.307	34.0	26.0
UCTX_SAS4	Sant'Agostino	50.5	90.0	0611	62.3	0.160	202.0	201.0
UCTX_SAS5	Sant'Agostino	49.8	81.5	0.602	63.8	0.222	36.0	35.3
UCTX_SAS6	Sant'Agostino	49.8	87.2	0.590	65.6	0.254	-	11.3
UCTX_SAS7	Sant'Agostino	49.9	86.7	0.583	66.7	0.223	25.0	24.4
UCTX_SAS8	Sant'Agostino	48.8	87.6	0.591	65.5	0.258	10.5	9.6
UCTX_SAS9	Sant'Agostino	50.4	88.5	0.613	62.0	0.297	3.0	2.1
UCTX_GSS1	PdC_GSS							
UCTX_GSS2	PdC_GSS							
UCTX_GSS3	PdC_GSS							
UCTX_GSS4	PdC_GSS							
UCTX_GSS5	PdC_GSS							
UCTX_GSS6	PdC_GSS							
UCTX_GSS7	PdC_GSS							
UCTX_GSS8	PdC_GSS							
UCTX_GSS9	PdC_GSS							
UCTX_GSS10	PdC_GSS							
UCTX_GSS11	PdC_GSS							
UCTX_GSS12	PdC_GSS							
UCTX_GSS13	PdC_GSS							
UCTX_GSS14	PdC_GSS							
UCTX_GSS15	PdC_GSS							
UCTX_GSS16	PdC_GSS							
UCTX_SS1	SS5							
UCTX_SS2	SS5							
UCTX_SS3	SS5							

*at the end of consolidation phase

In order to verify the reliability of eq. (6.1a), the average values of $\sigma'_{un,liq}/\sigma'_{un,0}$ for each S_{r0}, of Pieve di Cento (GSS) and silica (N°5) sands, have been plotted in Figure 6.24 together with the experimental results already published.

It can be noted that the relationship proposed by Mele and Flora (2019) seems to be confirmed by the experimental results of GSS and SS5. It should be emphasized that such results are related to several grains distributions (Fig. 4.1 and Tab. 4.1) and state conditions in terms of D_r (from 29.4 to 67.2%) and confining stresses (from and 25 kPa for some tests on Pieve di Cento sand, see Table 6.13, to 60 kPa for Inagi sand). It is believed that, obviously, D_r influences the trend of r_u and then the value of $\sigma'_{un,liq}$;

however, such dependence seems to be negligible if compared with the effect of S_r, which plays a most important role in liquefaction resistance of non-saturated soils.
Moreover, eq. (6.1a) is extremely important for non-saturated soils, where the attained r_u at liquefaction (ε_{DA}=5%), lower than 0.90 for what has already been said, can be easily computed as (1- $\sigma'_{un,liq}/\sigma'_{un,0}$).
In particular, the value of r_u at liquefaction (ε_{DA}=5%) can be defined as follows:

$$r_u(\varepsilon_{DA} = 5\%) = 2 \cdot 10^{-4} \cdot S_{r0}^2 - 2 \cdot 10^{-2} \cdot S_{r0} + 0.90 \quad (6.1b)$$

Such equation is plotted in Figure 6.25 together with the experimental results of this research and those already published by Mele et al. (2018b).

Figure 6.24. Experimental values of $\sigma'_{un,liq}/\sigma'_{un,0}$ versus S_{r0} along with the best fitting curve proposed by Mele and Flora (2019).

Figure 6.25. Experimental values of $r_u(\varepsilon_{DA}=5\%)$ versus S_{r0} along with the best fitting curve.

The effectiveness of desaturation as a liquefaction mitigation technique can be clearly noted in Figure 6.26, where the cyclic resistance curves of non-saturated sands have been

compared with those of saturated sands. It should be specified that the cyclic resistance curves have been plotted according to strain criterion.

As expected, regardless of the kind of soil, when the degree of saturation increases the resistance to liquefaction decreases. It is clearly shown in Figure 6.27, where the Liquefaction Resistance Ratio for N_{liq}=15 ($LRR_{,15}$= $CRR_{un,15}/CRR_{s,15}$; where $CRR_{un,15}$ is the resistance of partially saturated soils and $CRR_{s,15}$ is that of fully saturated soils evaluated for N_{liq}=15) has been plotted with S_r. The results of this research have been compared with those from Bauxite and Inagi sand samples (Fig. 4.1 and Tab. 4.1) already published by Mele et al. (2018b). The scatter of the experimental results of Pieve di Cento (GSS) sand is evident for both high and low S_r (48 and 91%), suggesting a strong dependence on the grain distribution of the tested soils as already pointed out by Okamura and Soga (2006).

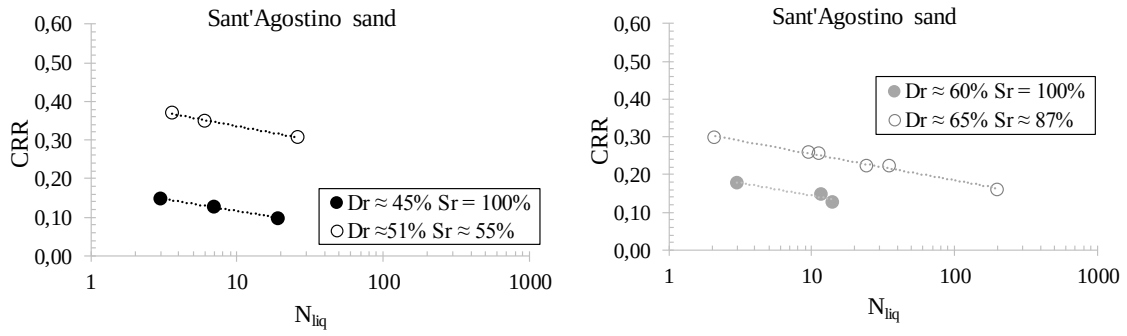

(a) (b)

Figure 6.26. Effect of desaturation for Sant'Agostino (a-b) and Pieve di Cento (GSS) (c-d-e) sands.

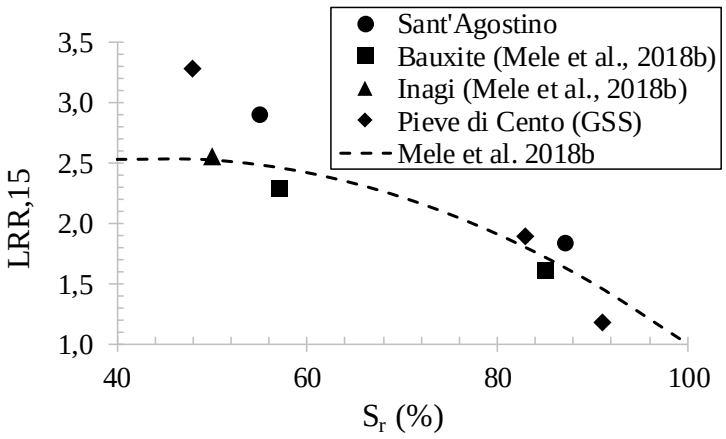

Figure 6.27. Liquefaction Resistance Ratio for N_{liq}=15 ($LRR_{,15}$) versus S_r.

6.3.1 EXPERIMENTAL EVIDENCES

As already described in §2.4.3.1, because of the Double Cell System in the used triaxial apparatus, the volumetric strains ε_v can be measured during the tests performed on non-saturated specimens.

An example of these measurements is plotted in Figure 6.28 for the UCTX_SAS2 test (see Table 6.13): during the cycles, ε_v increases with a rate similar to that of the pore pressure (Figure 6.28a-c-e) or the effective stress decrements (Figure 6.28b-d-f). This may mean that the increase of ε_v with the number of cycles due to the compressibility of air (because of the undrained condition), delaying the pore pressure build-up is at least one of the reasons of the increase of liquefaction resistance.

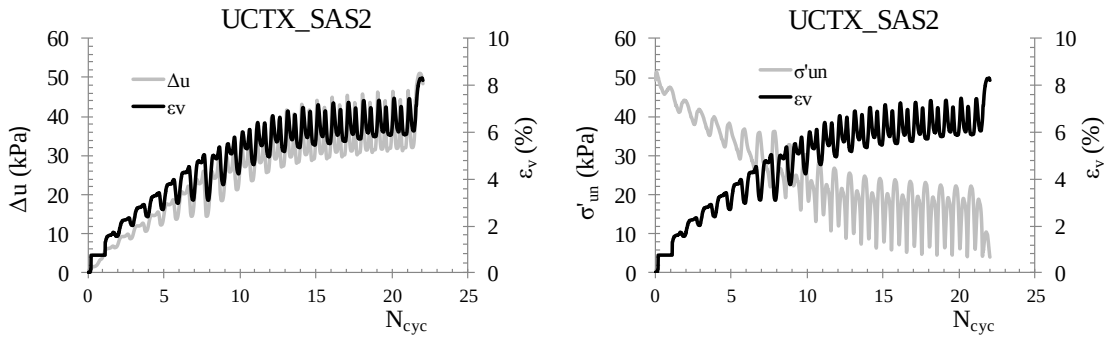

Figure 6.28. Excess pore pressure and volumetric strain plotted against number of cycles (a-c-e); effective stress and volumetric strain with number of cycles (b-d-f).

The volumetric strains measured in non-saturated tests for SAS, Pieve di Cento (GSS) and silica (N°5) sands are plotted versus the number of cycles in Figure 6.29, except for the unsaturated tests of GSS (Sr≈48%), because they are stopped before reaching r_u equal to 0.90.

It can be noted that increasing the number of cycles, ε_v increases to a final value $\varepsilon_{v,fin}$ which, depends on the values of S_{r0}, D_r (or e) and confining pressure (σ'_{un}). Therefore, a unique final value of $\varepsilon_{v,fin}$ exists for each set of S_r, D_r (or e) and σ'_{un}.

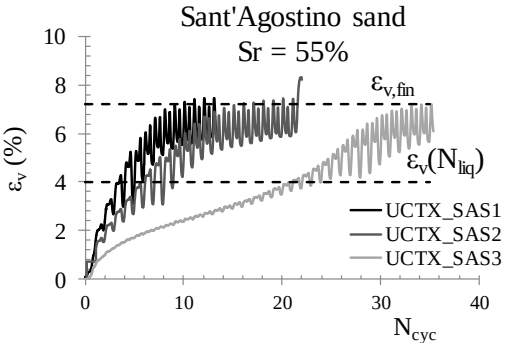

(a) σ'_{un}=50kPa

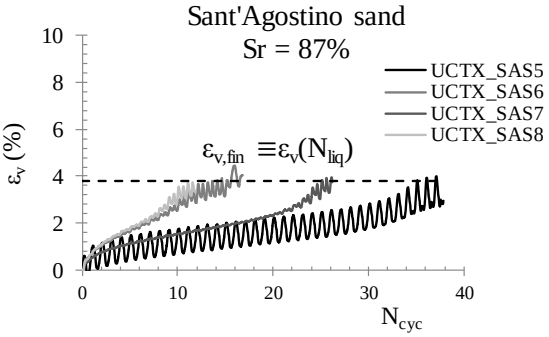

(b) σ'_{un}=50kPa

Figure 6.29. Volumetric strain plotted against number of cycles for SAS, Pieve di Cento (GSS) and Silica N°5 sands for different Sr.

Consistently with what has previously been observed, it can be noted that for lower degree of saturation (Fig. 6.29a-f), the final value of the volumetric strains does not correspond with the value of ε_v attained at liquefaction ($\varepsilon_{v,liq}$) evaluated according to strain approach, while for the higher degree of saturation (Figure 6.29b-c-d-e) it does (i.e. $\varepsilon_{v,fin}= \varepsilon_{v,liq}$).
In particular, the tests with S_r equal to 55% of Sant'Agostino sand, reach $\varepsilon_{v,fin}\approx7\%$, while $\varepsilon_{v,liq}$ is about 4%. Similar considerations for silica sand, where $\varepsilon_{v,fin}$ and $\varepsilon_{v,liq}$ are not equal and about 4 and 2.7%, respectively. On the other hand, the tests with higher S_r (partially saturated soils) reach smaller values of the final volumetric strain. Tests performed on Sant'Agostino sand, with $S_r\approx87\%$, reached a $\varepsilon_{v,fin,}$ value coincident with that of $\varepsilon_{v,liq}$ and equal to 3.5%. For Pieve di Cento (GSS) sand, for S_r equal to 83 and 91% consolidated at 50 kPa, $\varepsilon_{v,liq,}$ is about 4%, while for the two tests performed at 25 kPa ($S_r\approx93\%$), $\varepsilon_{v,liq}$ is lower and equal to 2%, highlighting the dependence of $\varepsilon_{v,fin}$ on the confining stress.
It is possible to write a theoretical relation between the final volumetric deformation and the initial degree of saturation applying Boyle and Mariotte law (Okamura and Soga, 2006). In order to do so, it must be first recalled that in all tests, regardless of the initial value of S_r, the pore air pressure is always almost equal to the pore water pressure (i.e. the suction can be considered always as being nihil). Then, the complete attainment of liquefaction must correspond to a condition in which both these pressures are equal to the total confining pressure ($u_a=u_w= \sigma$), which means that the net stress is zero. The two conditions of net stress and suction being zero (that combination indicates that the effective stress in the Bishop notation, Equation 2.46, must be zero) imply the attainment of liquefaction phenomenon. Based on these considerations, Boyle and Mariotte law allows to write the eq. 2.53, that, for the sake of convenience, is reported below:

$$\varepsilon_{v,fin} = \frac{e_0}{1+e_0} \cdot (1 - S_{r0}) \cdot \left(1 - \frac{u_{a,0}}{\sigma}\right) \quad (6.2)$$

Equation 6.2 indicates that for a given value of D_r (and e_0), σ and S_{r0}, there is a unique value of $\varepsilon_{v,fin}$. This is consistent with the experimental results previously described and plotted in Figure 6.29. Obviously, for S_r=100%, the volumetric strain is zero.

In Figure 6.30 the experimental data are plotted versus the initial degree of saturation S_{r0}: it can be observed that Equation 6.2 (plotted using the average value of e_0) underestimates the experimental values of $\varepsilon_{v,fin}$, for both Sant'Agostino and Pieve di Cento (GSS) sands, on the contrary it is consistent with the experimental data of silica sand.
The scatter between the observed values of $\varepsilon_{v,fin}$ and the theoretical values computed by eq. (6.2), evident mainly for Italian sands, could be explained as a matter of the fact that eq. (6.2) is based on the hypothesis of considering the pore air into the soil as an ideal gas, which is as true as the pressure is low and the temperature is high. The particles of an ideal gas should interact with the container walls only through elastic collisions, but as well known, it is not possible especially for higher Sr, where occluded bubbles exist in a fluid mixture.
According to what has been said, eq. (6.2) should be more reliable to predict the final volumetric strains for the lower S_r values than for the higher ones.

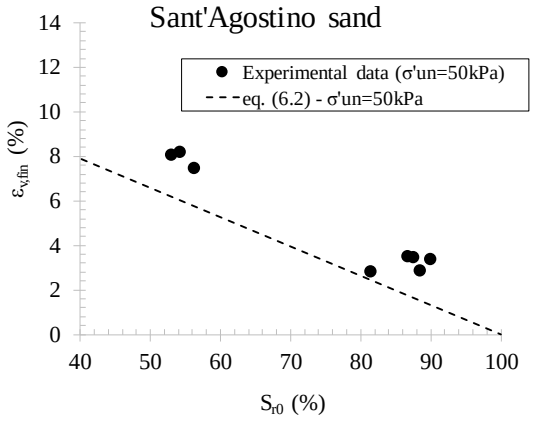

(a)

Figure 6.30. Final volumetric strain as a function of the initial degree of saturation: experimental data and theoretical correlations (equation (6.2)) for Sant'Agostino (a), Pieve di Cento (GSS) (b) and Silica (N°5) sands (c).

As already discussed in Chapter 2 (§2.4.3.1), Okamura and Soga (2006) defined the highest value of ε_v for the soil achieved when $u_a = u_w = \sigma$ as potential volumetric strain (ε_v*), which can be evaluated from eq. (6.2), which is coincident with $\varepsilon_{v,fin}$, as called above. The same authors identified ε_v* as the possible key parameter in liquefaction resistance, connecting it to $LRR_{,15}$. In order to verify that statement, the experimental results of this research in terms of ε_v* and those reported by Mele et al., (2018b) (Bauxite and Inagi sand), have been plotted with $LRR_{,15}$, together with the results of already published test results shown by the same authors (Fig. 6.31). Especially for lower ε_v*, the logarithmic relationship proposed by Okamura and Soga (2006), and reported in Figure 6.31, overestimates the $LRR_{,15}$, consistently with what was observed by Wang et al. (2016). It means that the proposed relationship cannot be considered as a general rule in liquefaction. In fact, ε_v* cannot be considered as a key parameter in the study of liquefaction of unsaturated sandy soils, even because, according to this approach, liquefaction should be evaluated by means of the stress criterion, but, as mentioned several times, in non-saturated tests the strain criterion is generally used, thus, avoiding the problem to define the effective stresses.
Despite such limitations, ε_v* (or $\varepsilon_{v,fin}$) seems to play an important role in liquefaction of unsaturated tests. Owing to that, such parameter has been studied in depth in this research, making further considerations.

Figure 6.31. Comparison between the experimental data of this research and the hypothetical relationship proposed by Okamura and Soga (2006).

For each non-saturated test, the effective stress was plotted versus the volumetric strain (Figure 6.32). It can be noted (Figure 6.32a-c-e) that test results related to the same S_r overlap.
Once again, it can be noted as the final volumetric strain, attained when the effective stress, σ'_{un}, is equal to 0 kPa, depends mainly on S_r.
In addition, in Figure 6.32b-d-f the average curves for different average degrees of saturation for Sant'Agostino, Pieve di Cento and silica (N°5) sands are plotted.

Such figures will be used in the following to simplify the computation of the energy components (see Chapter 8).

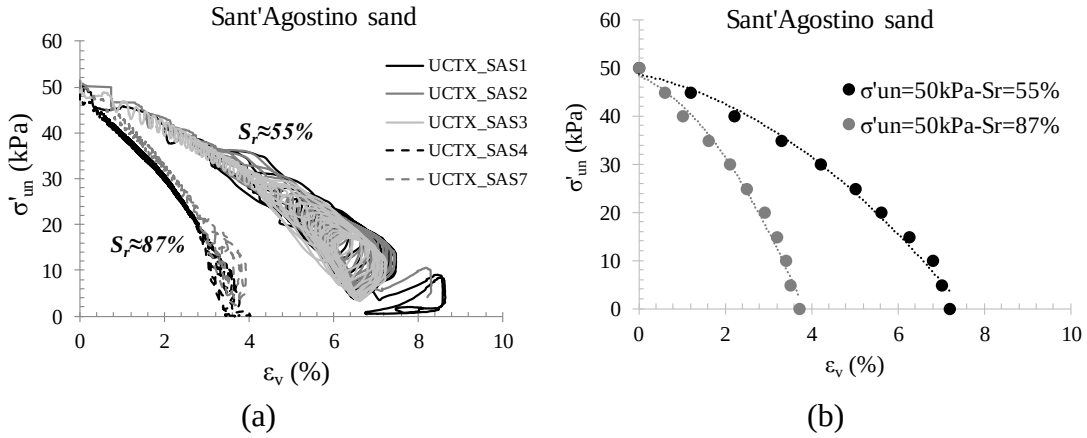

Figure 6.32. Volumetric strain plotted against effective stress for different degrees of saturation (a-c-e) and average curves (b-d-f).

In the following, therefore, it will be considered as a general law, having the following expression, as already reported by Mele et al. (2018b):

$$\frac{\sigma'_{un}}{\sigma'_{un,0}} = 1 - \left(\frac{\varepsilon_v}{\varepsilon_{v,fin}}\right)^{1.7} \quad (6.3)$$

where ε_v is the volumetric strains, which is obviously different from 0, because of the higher compressibility of air than that of water.
Even though it is expected that some differences may appear at much higher confining stresses because of the increased gas solubility, it must be highlighted that on site liquefaction is a critical mechanism for the possible effects on structures at ground level only when it takes place in shallow layers (i.e. at low confining stresses, say for $\sigma'_{un} \leq$ 100 kPa). Therefore, from a practical point of view and with this limitation, it is suggested that it is reasonable to consider eq. (6.3) as a general law, valid for all possible intrinsic and state properties of different soils at low confining stresses.

Figure 6.33. Dimensionless effective stress ($\sigma'_{un}/\sigma'_{un,0}$) plotted against dimensionless volumetric strain ($\varepsilon_v/\varepsilon_{v,fin}$).

During the cyclic loading in undrained conditions the lower compressibility of gaseous phase generates a decrease of volume and thus positive volumetric strains, which implies an increase of the degree of saturation. Starting from the measurements of volumetric strains, the degree of saturation can be computed, easily.
As an example, some results of Sant'Agostino sand are plotted in Figure 6.34, in terms of S_r versus N_{cyc}. In the lower part of the graph, represented by continuous lines, the unsaturated test results are shown. The average initial degree of saturation is equal to 55% and during the tests, as expected, S_r increases without reaching the fully saturation condition (S_r=1). It is obviously due to the fact that the maximum volumetric strain, that

can be generated for the giving void ratio and confining stress (eq. (6.2)), is low, not allowing to reach S_r=1.

Studying the liquefaction resistance of soils which have reached the fully saturation condition after liquefaction could be very important from a technical point of view. This problem is strongly connected with the post liquefaction behaviour of soils in non-saturated conditions, which will be discussed in the next Chapter.

Figure 6.34. Degree of saturation versus N_{cyc} for Sant'Agostino sand.

6.3.2 EXCESS PORE PRESSURE GENERATION MODEL FOR NON-SATURATED SANDY SOILS

In Chapter 2, the most important and famous excess pore pressure generation models for saturated specimens have been presented. Moreover, the model of Booker et al. (1976) has been used to simulate the pore pressure build-up for saturated tests performed in this research work, where the parameter β has been calibrated to have the best fitting for the experimental results.

In this research, an initial effort has been done to develop an excess pore pressure generation model for non-saturated soils, based on the experimental data presented in this Chapter.

One of the biggest problems in the prediction of pore pressure build-up for non-saturated soils is due to the fact that the attainment of liquefaction is traditionally defined according to a strain criterion (ε_{DA}=5%) and thus, at N_{liq} does not correspond r_u=0.90.

The proposed model has been developed starting from the model of Booker et al. (1976), whose reliability has already been proved for saturated soils. The challenge has been to generalize eq. (2.10) for saturated and non-saturated soils, taking into account the fact that for non-saturated soils, liquefaction is assumed to occur when ε_{DA} reaches the threshold of 5%.

To this purpose, in Figure 6.35 some comparisons between the pore pressure build-up for saturated and non-saturated soils (Sant'Agostino and Pieve di Cento (GSS) sands), which attain liquefaction at the same, or similar number of cycles, have been shown. In particular, for Sant'Agostino sand, in Figure 6.35a, CTX_SAS9 and UCTX_SAS8 tests, which liquefy at the same N_{cyc} (about 9) have been compared, while in Figure 6.35b the results from CTX_SAS2 and UCTX_SAS2 tests have been shown. In these latter tests, liquefaction is reached at similar N_{cyc} values, 7 and 6.1, respectively. On the other hand, for Pieve di Cento (GSS), CTX_GSS4 and UCTX_GSS5 tests, where sand liquefy at the same N_{cyc} (12) have been compared in Figure 6.35c, while in Figure 6.35d CTX_GSS8 and UCTX_GSS8 test results have been shown, reaching liquefaction at a similar N_{cyc}, 6.1 and 7.7, respectively.

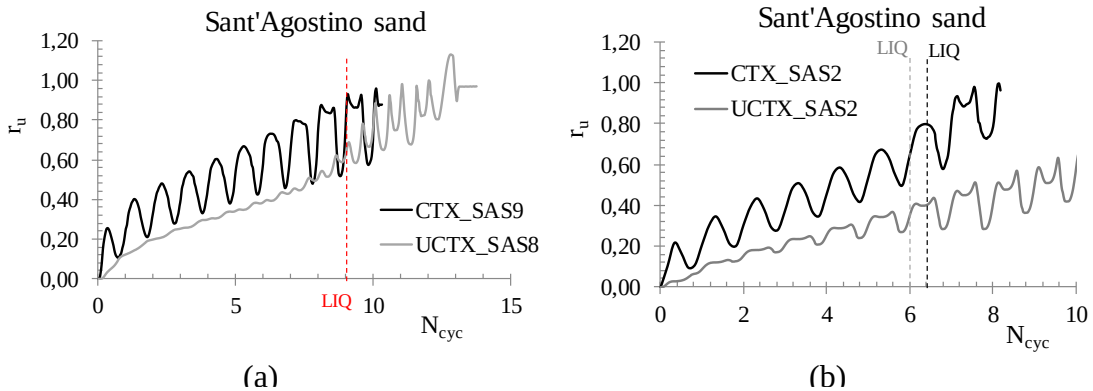

(c) (d)

Figure 6.35. Comparisons between the excess pore pressure build-up of saturated and non-saturated soils, which attend liquefaction at the same (a-c) or similar (b-d) number of cycles for Sant'Agostino and Pieve di Cento (GSS) sands.

As expected, saturated specimens exhibit a more evident increase of excess pore pressure ratio with N_{cyc}, and furthermore, even though saturated and non-saturated tests attain liquefaction at the same (or similar) N_{cyc}, non-saturated specimens reach lower r_u,

corresponding to $r_u(\varepsilon_{DA}=5\%)$ (eq. (6.1b); Fig. 6.25), being liquefaction defined according to strain criterion, as mentioned several times in this Chapter.
However, the trend of saturated and non-saturated soil curves seems on average to be the same, as confirmed by plotting $r_u/r_{u,liq}$ versus N_{cyc}/N_{liq} (Fig. 6.36), for the same tests shown in Figure 6.35, where $r_{u,liq}$ is 0.90 for saturated soils and $r_u(\varepsilon_{DA}=5\%)$ for non-saturated soils, and N_{liq} is evaluated according to strain criterion for non-saturated specimens ($\varepsilon_{DA}=5\%$).

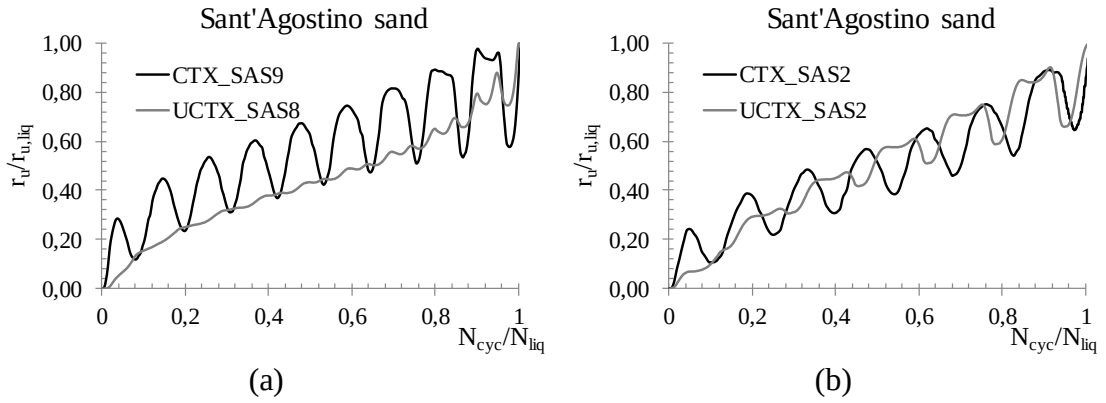

Figure 6.36. Comparisons between the excess pore pressure build-up of saturated and non-saturated soils (Sant'Agostino sand, a-b; Pieve di Cento (GSS) sand, c-d), in the plane N_{cyc}/N_{liq}-$r_u/r_{u,liq}$.

The similar average trends observed in Figure 6.36, seem to suggest that the ratio between r_u of saturated and non-saturated specimens with N_{cyc} is constant. It can be formally written as follow:

$$\left|\frac{r_{u,ns}}{r_{u,s}}\right|_{Ncyc} = \left|\frac{r_{u,ns}}{r_{u,s}}\right|_{Nliq} = \frac{r_{u,ns,liq}}{r_{u,s,liq}} = \frac{r_u(\varepsilon_{DA}=5\%)}{0.90} \qquad (6.4)$$

At a generical cycle N_{cyc}, the ratio $r_{u,ns}$ (non-saturated specimens) and $r_{u,s}$ (saturated specimens) is constant, and then is equal to the ratio $r_{u,ns}/r_{u,s}$ when liquefaction occurs. Moreover, it is known that $r_{u,ns,liq}$ is given by $r_u(\varepsilon_{DA}=5\%)$ and computed via eq. (6.1b), while $r_{u,s,liq}$ is 0.90 for saturated soils (stress criterion for liquefaction triggering). In other

words, known the excess pore pressure build-up for a given saturated soil, which attends liquefaction after N_{liq} cycles, the excess pore pressure build-up for the soil in non-saturated conditions, which liquefy after the same N_{liq} cycles, can be obtained by scaling the saturated curve of a factor given by eq. (6.4), as reported below:

$$r_{u,ns} = r_{u,s} \cdot \frac{r_u(\varepsilon_{DA} = 5\%)}{0.90} \qquad (6.5)$$

To confirm the reliability of eq. (6.5), the excess pore pressure build-up of tests UCTX_SAS8, UCTX_SAS2, UCTX_GSS5 and UCTX_GSS8 (already shown in Figures 6.35 and 6.36) have been simulated, scaling the saturated curves. The results can be observed in Figure 6.37.

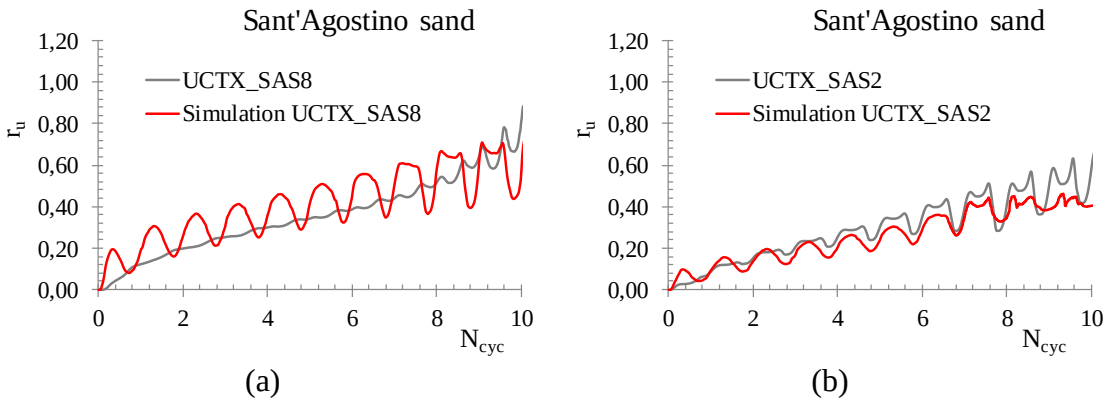

Figure 6.37. Comparisons between the experimental and simulated (eq. (6.5)) excess pore pressure build-up of non-saturated tests on Sant'Agostino (a-b) and Pieve di Cento (GSS) (c-d) sands.

The good agreement between the prediction of excess pore pressure build-up, achieved via eq. (6.5) and the experimental results highlight the reliability of the eq. (6.5). However, it needs to know the pore pressure generation trend of the saturated soil, which reaches liquefaction after the same number of cycles as the non-saturated soil, whose pore pressure generation trend want to be predicted.

With the main aim to make more general such procedure of prediction of pore pressure build-up for non-saturated soils, the expression of Booker et al. (1976) (eq. (2.10)) has been used.

(6.6)

Obviously, for saturated soils eq. (6.6) is exactly the traditional formula of Booker et al., (1976), being the $r_u(\varepsilon_{DA}=5\%)$ equal to 0.90.
Generally speaking, eq. (6.6) can be considered as a general excess pore pressure model (stress-based), that can be used for saturated and non-saturated soils, just knowing the degree of saturation (eq. (6.1b)). In order to verify eq. (6.6), the excess pore pressure in tests on non-saturated specimens have been simulated, assuming β equal to the values calibrated for the corresponding saturated tests and already shown in this thesis.
In Figures 6.38 – 6.39 and 6.40, the results for some tests on non-saturated specimens of Sant'Agostino, Pieve di Cento (GSS) and silica (N°5) sands are shown.
It should be specified that in case of silica sand (N°5), for which tests on saturated specimens have not been performed, the parameter β of eq. (2.10) has been estimated through the correlation proposed in Figure 5.36, where β is linked to D_{60}. By applying such correlation, β is equal to 0.63 and this value has been used in eq. (6.6).
The prediction of excess pore pressure build-up for non-saturated soils observed in Figures 6.38 to 6.40 seems to satisfactorily agree with the experimental data to which it has been compared. Some differences between experimental and simulated accumulation of r_u with N_{cyc} is mainly found when liquefaction occurs at a small N_{liq} ($N_{liq}<5$), as can be noted in Figure 6.39d and 6.40b. In these cases, as for saturated soils, the shape of the curve is not well defined since liquefaction is attained in few cycles.
Furthermore, the simulations cannot go beyond N_{liq} ($\varepsilon_{DA}=5\%$), because the domain of eq. (6.6) is $0 < N_{cyc}/N_{liq} < 1$.
The results presented in this section can be considered as a preliminary study on the generation of pore pressure in non-saturated soils. However, such approach appears very promising, and therefore, it deserves further insights.
Additionally, it is worth noting that the good agreement between the prediction and the experimental pore pressure build-up in non-saturated soils, confirms the reliability of the experimental results and the correlations proposed (see, for instance eq. (6.1) and Fig. 5.36), on which the pore pressure generation model is based.

Figure 6.38. Comparisons between the experimental and simulated (eq. (6.6)) excess pore pressure build-up of non-saturated tests on Sant'Agostino sand.

Figure 6.39. Comparisons between the experimental and simulated (eq. (6.6)) excess pore pressure build-up of non-saturated tests on Pieve di Cento (GSS) sand.

Figure 6.40. Comparisons between the experimental and simulated (eq. (6.6)) excess pore pressure build-up of non-saturated tests on silica sand N°5.

6.4 PROS AND CONS OF THE STUDIED MITIGATION TECHNIQUES

In this Chapter the main results of laboratory tests on sandy soil specimens treated by using three liquefaction mitigation techniques (addition of fines, densification and desaturation) have been presented and discussed.
All of them can be considered effective, increasing the resistance to liquefaction with respect to that of "untreated" specimens. However, it is worth noting that each of them has pros and cons that will be discussed in this paragraph.
Regarding the addition of fines, laponite has been used. Its superplastic nature is able to create bridges among the particles of sand, decreasing the mobility of them during an earthquake, that an increase of resistance to liquefaction. Permeability tests carried out on a mixture water/laponite have highlighted that the permeation occurs, adding opportunely sodium pyrophosphate (SPP), which can delay the gelling time of the mixture. It implies that this technique is not only effective but also applicable because it can be easily injected into the soil. Moreover, laponite is not so expensive and then, it should be used in little quantities, so that this countermeasure is considered convenient also from an economic point of view. Despite these positive aspects, it is also important to consider the negative ones. Firstly, the environmental aspects. This technique, in fact consists of introducing a plastic material into the soil, that even if it is not polluting, it is a mixture which will become a gel and could obstruct the natural flow of groundwater. Another important point is the duration of this countermeasure, further tests are needed to clarify this aspect and finally, from a technical point of view, the treated volume is unknown. It is impossible to know which is the area that this intervention will recover.
The second technique which has been studied is densification. It is one of the most known technologies used against liquefaction in the world. It reduces the void space of the soil, thereby decreasing the potential for volumetric change that would lead to liquefaction. It is simple and there are several ways to apply it in situ (dynamic compaction, vibro compaction, the use of stone columns or compaction grouting) as already mentioned in

§2.4.1, moreover it lasts over time. However, also this technique has negative aspects which have to be considered. This countermeasure changes the stress state of the soil and it is not recommended close to existing buildings.

Desaturation seems to be one of the most innovative and promising techniques against liquefaction. The effectiveness has been tested in laboratory and unlike addition of fines, it does not have environmental problems, even though it might be difficult to apply. Nevertheless, several researches are carrying out tests to introduce simple way to apply desaturation in situ, such as air injection, water electrolysis, sand compaction pile and use of sodium perborate. Another technical issue is that the degree of saturation cannot be controlled in situ.

The pros and cons of the three countermeasures have been summarized In Table 6.15.

In conclusion, although these techniques are all effective as countermeasure against liquefaction, as demonstrated by laboratory tests, the choice of one or the other has to be made carefully, taking into account the characteristic of the site and the pros and cons of the different techniques which may be applied.

Table 6.15. Pros and cons of the liquefaction countermeasures studied in this thesis.

Countermeasures	Pros	Cons
Addition of plastic fine (Laponite)	- Effectiveness - Injectable (adding SPP); - Not so expensive.	- Environmental aspects; - Uncertainty on duration; - Uncertainty on the treated volume.
Densification	- Simple to apply; - Several possible applications; - Well-known and studied for long time; - Durable.	- Stress state change; - To avoid close to existing buildings.
Desaturation	- Effective even with higher S_r; - Innovative and promising; - No environmental problems.	- Difficult to apply (air, bacteria); - Control of S_r; - Uncertainty on duration.

REFERENCES

El Howayek A., (2011). Characterization, rheology and microstructure of laponite suspension. *MS Thesis*, School of Civil Eng., Purdue University.

Ishihara, K. (1993). Liquefaction and flow failure during earthquakes. *Géotechnique*, *43*(3): 351-451.

Lirer S., Flora A., Verdolotti L., Lavorgna M., Iannace S., (2006). Permeation grouting of fine grained pyroclastic soils and rocks. *Ground Improvement,* 10: 135-177.

Lirer S. and Mele L. (2019). On the apparent viscosity of granular soils during liquefaction tests. *Bulletin and Earthquake Engineering*. DOI: 10.1007/s10518-019-00706-0.

Mele, L., and Flora, A. (2019). On the prediction of liquefaction resistance of unsaturated sands. *Soil Dynamics and Earthquake Engineering*. DOI: 10.1016/j.soildyn.2019.05.028.

Mele, L., Flora, A., Lirer, S., d'Onofrio, A., and Bilotta, E. (2018a). Experimental Study of the Injectability and Effectiveness of Laponite Mixtures as Liquefaction Mitigation Technique. In *Geotechnical Earthquake Engineering and Soil Dynamics V: Slope Stability and Landslides, Laboratory Testing, and In Situ Testing* (pp. 267-275). Reston, VA: American Society of Civil Engineers.

Mele L., Tan Tian J., Lirer S., Flora A., Koseki J. (2018b). Liquefaction resistance of unsaturated sands: experimental evidence and theoretical interpretation. *Géotechnique*. DOI: 10.1680/jgeot.18.p.042.

Mele, L., Lirer, S., and Flora, A. (2019a). The Effect of Densification on Pieve di Cento Sands in Cyclic Simple Shear Tests. In *National Conference of the Researchers of Geotechnical Engineering* (pp. 446-453), Springer, Cham. DOI: 10.1007/978-3-030-21359-6_47

Ochoa-Cornejo, F., Bobet, A., Johnston, C. T., Santagata, M., and Sinfield, J. V. (2016). Cyclic behavior and pore pressure generation in sands with laponite, a super-plastic nanoparticle. *Soil Dynamics and Earthquake Engineering*, 88, 265-279.

Okamura M, Soga Y. (2006). Effects of pore fluid compressibility on liquefaction resistance of partially saturated sand. *Soils and Foundations*;46(5):695‑700.

Rockwood Additives Ltd. (2011). Laponite performance additives. Specification sheet.

Wang H, Koseki J, Sato T, Chiaro G, Tan Tian J (2016). Effect of saturation on liquefaction resistance of iron ore fines and two sandy soils. *Soils and Foundations*; 56(4):732‑44.

CHAPTER 7

7. LIQUEFIED SANDS AND POST-LIQUEFACTION BEHAVIOUR

In this Chapter, further considerations about the results of treated and untreated soils have been made. The attention will be focused on the behaviour of liquefied sands and on the post-liquefaction behaviour soils in saturated and unsaturated conditions.

7.1 BEHAVIOUR OF LIQUEFIED SOILS

As described in §2.2.2.3, several experimental researches concluded that liquefied soil behaves as a fluid during the seismic sharing, but after the earthquake motion ceases, due to the dissipation of excess pore water pressure, the liquefied soil recovers its initial stiffness and returns to behave as a solid. Such a change of state can be analysed by considering the soil as an equivalent pseudo-plastic material, characterized by an apparent viscosity (η) that changes during the cyclic loading and that can be evaluated via eq. (2.19).
Following this approach, the results of untreated and treated soils, presented in the previous Chapters -5 and 6, respectively- have been interpreted according to a "viscous key".

7.1.1 APPARENT VISCOSITY MEASUREMENTS

Although the definition of apparent viscosity has been given as a function of τ and γ, it can be calculated also from cyclic triaxial tests results, easily converting the cyclic deviatoric stress (q) and the corresponding axial strain (ε_a) in the shear stress acting on the plane inclined at 45° on the horizontal plane ($\tau = q/2$) and in the corresponding shear strain ($\varepsilon = 1.5 \cdot \gamma$).
In Figure 7.1 the experimental relationships between the shear stress (τ) and the shear strain rates ($\dot{\gamma}$) of some cyclic triaxial tests (Tab. 5.13) have been shown.

Figure 7.1. Shear stress (τ) versus shear strain rates ($\dot{\gamma}$).

The values of the deviatoric strain rate ($\dot{\gamma}$) (max and min) increase with N_{cyc} and, as a consequence, the enclosed area of the stress-strain rate loop gradually increases, and then the energy dissipation rate increases gradually with N_{cyc}.

For each stress-strain rate loop (Fig.7.1), a single value of the apparent viscosity, the diagonal line slope of $\tau - \dot{\gamma}$, can be computed via eq. (2.19).

Figure 7.2 sketches the expected trend of η with the number of cycles (N_{cyc}): during the first cycles, pore pressures start to develop and therefore the effective stress decreases; the soil is behaving under cyclic loading as a solid, but η (Eq. (2.19)), which starts from an initial value called η_0, slightly decreases because soil stiffness is decreasing. When a change of phase, from solid to liquid, starts to take place (for $\eta=\eta_{trans}$), a sharp decrease of the apparent viscosity is expected. Theoretically, this should be a sudden, complete drop to a minimum value. However, it must be expected that a transition phase with a high rate of reduction of η is needed to fully reach the fluid state. When this is fully attained, a minimum value η_{fluid} is reached (Figure 7.2) as reported by Mele et al. (2018). In this phase ($\eta=\eta_{fluid}$), a rapid loss of the soil strength and stiffness occurs and the liquefied soil behaves as a pseudo-plastic fluid.

For each saturated cyclic triaxial test (loose and dense specimens, see Tabs. 5.13 and 6.6) the apparent viscosity was plotted with N_{cyc} (Figure 7.3 (a-c-e-g-i)). The same results have been also plotted in semi-logarithmic plane in Figure 7.3 (b-d-f-h-l), in order to make clearer the minimun value reached by η at the end of the tests, when fully liquefaction was attained (η_{fluid}).

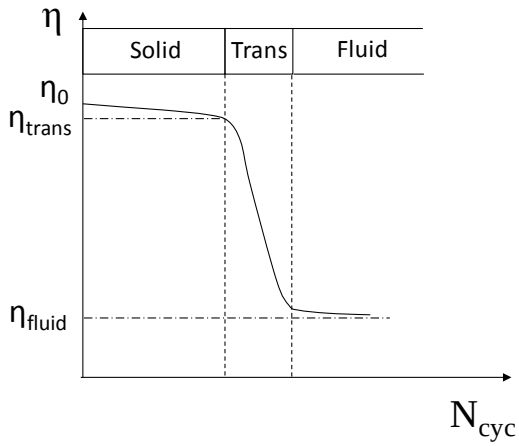

Figure 7.2. Sketch of the expected trend of the apparent viscosity η with the number of cycles, N_{cyc}.

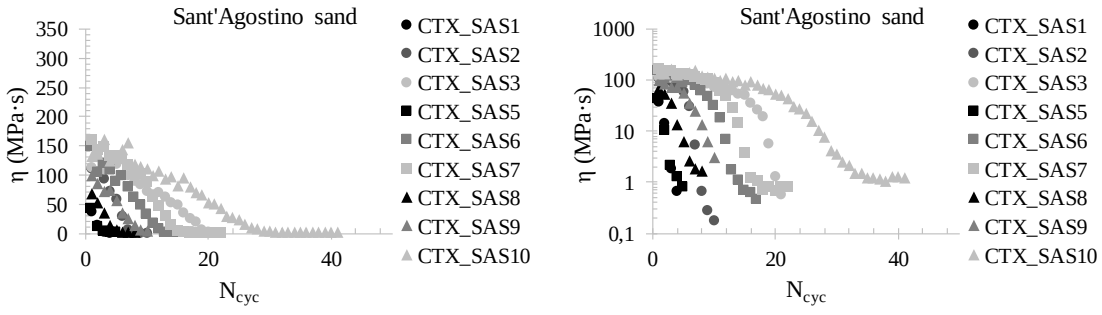

(e) (f)

Figure 7.3. The apparent viscosity decay law for different tested soils (a-c-e-g-h) and in semi-logarithmic scale (b-d-f-h-l) achieved by cyclic triaxial tests.

The shape of the experimental curves in Figure 7.3 is similar to the one sketched in Figure 7.2, where the apparent viscosity decreases as the number of cycles N_{cyc} increases.
The trend of the "decay law" (η-N_{cyc}) is clearer for tests where the liquefaction is attained in many cycles (N_{liq}>10): in these cases, it can be noted that in the first part of the loading process, the apparent viscosity slightly decreases.

Moreover, interpreting the tests performed on undisturbed (frozen) specimens of Messina gravel by Flora et al., (2012), according to the concept of apparent viscosity, Lirer and Mele (2019) showed a strong dependence of η_0 on grain size, and in particular on the parameter D_{50}, as shown in Figure 7.5.

η_0 increases with D_{50} according to a power function, whose expression is reported in Figure 7.5, where the arrows indicate the dispersion of the experimental data. It can be noted that such relationship is confirmed by the experimental results presented in this research. In fact, for all the tested sands with a D_{50} ranging from 0.10 to 0.53 mm (see, Fig. 4.1 and Tab. 4.1), η_0 seems to assume an average value of 150 MPa·s. It is worth noting that the dependence of η_0 on the grain size of the soil starts becoming important for coarser sands and gravels.

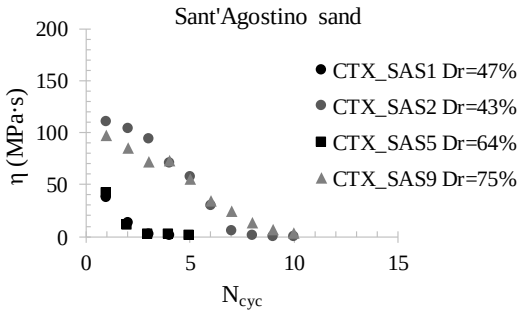

(a) (b)

Figure 7.4. The effect of relative density on the apparent viscosity decay law for Sant'Agostino (a) and Pieve di Cento (GSS) (b) sands.

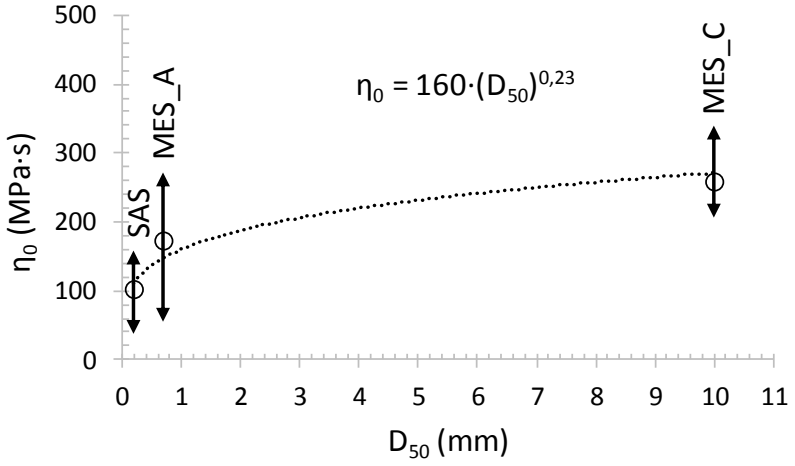

Figure 7.5. Initial apparent viscosity (η_0) with D_{50} of Sant'Agostino sand and Messina gravel (MES_A and MES_C) (Lirer and Mele, 2019).

Regarding the final value (η_{fluid}), it depends on D_r, as shown in Figure 7.3f-l.

For Sant'Agostino sand the final value of η can be assumed equal to 0.3, 0.6 and 2MPa·s for average D_r of 46, 60 and 74%, respectively. The confining pressure seems to affect less the value of η_{fluid}, although Lirer and Mele (2019) showed a strong dependence of η_{fluid} on σ'_c. In fact, η_{fluid} is 8MPa·s for tests with σ'_c equal to 200kPa and 20 MPa·s for tests performed at 400 kPa. Probably, this dependence becomes important for high σ'_c, while it is negligible in the studied range: 25 – 100 kPa. Moreover, as expected, η_{fluid} is not affected by the applied CSR: when liquefaction is fully attained the soil behaves like a liquid and its properties are linked to properties of soil, regardless of the cyclic loading that bring it to attain liquefaction.

Regarding the non-saturated sandy soils, the apparent viscosity can be defined as well via eq. (2.19). As for saturated soils, three different field of behaviour (solid, transition and fluid) can be clearly identified as reported in Figure 7.6, where the results are also plotted in a semilogarithmic scale (Fig. 7.6 b-d-f-h-j-l) to better identify the value of η_{fluid}.

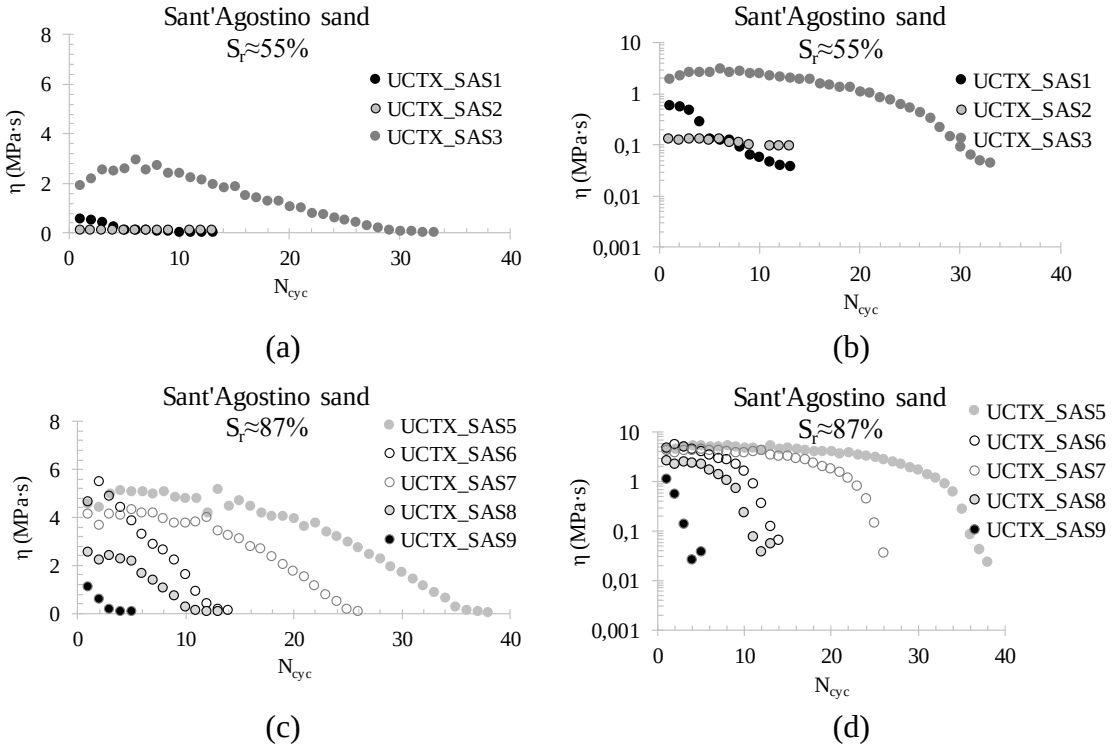

Figure 7.6. The apparent viscosity decay laws for non-saturated soils (a-c-e-g-i-k) and in semi-logarithmic scale (b-d-f-h-j-l) achieved by cyclic triaxial tests.

Firstly, such results (Fig. 7.6) should be compared with those of saturated soils (Fig. 7.3). It is clearly evident the quantitative difference of the computed values of the apparent viscosity, in particular η of non-saturated tests is about one order of magnitude lower than those of saturated cyclic triaxial tests. Such a difference may be due to higher strain rate in non-saturated tests than that in saturated ones, because of a different frequency imposed during the tests (see, for instance §4.2.1.1 and 4.2.3.1). In other words, the adopted frequency is an important parameter in apparent viscosity decay law, influencing not only η_0 but also η_{fluid} as well. However, further cyclic triaxial tests, performed with the same frequency should be carried out, to better understand how the frequency influences the values of the apparent viscosity.

As regards the degree of saturation, it seems not to affect η_0, which is more or less the same for all performed tests, regardless of the kind of soil and confining stress (see for instance Fig. 7.6 i-j, where UCTX_GSS13 and UCTX_GSS14 tests have been

consolidated at 25 kPa). On the contrary, the value of η_{fluid} is not constant, likely depending on S_r (Fig. 7.6 b-d-f-h-j-l). In particular, the tests with a lower value of S_r show a higher value of η_{fluid}. It is congruent to the fact that the presence of a higher amount of air contributes to increase the viscosity. Furthermore, the slope of the curve η-N_{cyc} in the transition phase seems to depend on the CSR and S_r.
Moreover, as reported by Mele et al. (2018), who carried out tests on unsaturated specimens of Bauxite and Inagi sand (Tab. 4.1), η_{trans} ranges in a limited interval, which means that it can be considered independent on Sr, although an interesting dependence seems to exist on the uniformity coefficient (U_c). For lower values of the coefficient of uniformity (i.e. less graded materials) η_{trans} decreases.
The decay laws $\eta - N_{cyc}$ achieved from cyclic triaxial tests have been compared with those from cyclic simple shear tests carried out on loose and dense sands (Tabs. 5.17 and 6.9). In particular, in Figure 7.7a-c the tests on Pieve di Cento sands prepared by 1D-compression method and performed by means of a flexible boundary have been plotted.

Figure 7.7. The apparent viscosity decay laws of Pieve di Cento sands (a-b) and in semi-logarithmic scale (b-d) achieved by cyclic simple shear tests.

As for non-saturated cyclic triaxial tests, the values of the apparent viscosity computed in cyclic simple shear tests are one order of magnitude lower than those of saturated cyclic triaxial tests. Once again, such a difference could be due to a difference in terms of imposed frequency (see, for instance §4.2.1.1 and 4.2.4.1), which would make incomparable CTX and CSS tests.

However, apart from a quantitative difference between the results of cyclic triaxial and simple shear tests, similar considerations can be done qualitatively, such as the fact that η_{fluid} depends on Dr but not on CSR.
In Chapter 5 (§5.1.5.2), the effect of shape loading on the cyclic resistance has been evaluated. With the main aim to evaluate the effect of waveforms on apparent viscosity decay law, η for each cycle has been evaluated for tests performed with non-sinusoidal cyclic loading (triangular, rectangular and sawtooth, see Tab. 5.17). The results have been plotted in Figure 7.8.

Moreover, the waveform seems to play an important role in the shape of apparent viscosity decay law, in particular, for triangular cyclic loading the scatter of the data is significant, on the contrary, for sawtooth waveform the typical shape observed for sinusoidal cyclic loading can be noted (Fig. 7.8c).
Finally, η_{fluid} seems to depend on the shape of cyclic loading, as well.

Figure 7.8. The apparent viscosity decay law of Pieve di Cento (GSS) sand for different waveforms: triangular (a); rectangular (b) and sawtooth (c).

The effect of the preparation techniques on the apparent viscosity decay law has been evaluated as well. In particular, in Figure 7.9 the apparent viscosity decay laws for Pieve di Cento (GSS) specimens prepared by Moist Tamping (a) and Air Pluviation (b) are plotted. Looking at the experimental evidences, shown in Figure 7.9, η_0 seems not to be

influenced by the adopted preparation technique, while, once again the effect of confining stress is confirmed by looking at Figure 7.9a, where CSS_GSS5MT specimen exhibit a higher η_0 than all the other specimens as a matter of the fact that such specimen has been consolidated at 200 kPa of effective vertical stress against 50 kPa of the other ones (Tab. 5.17).

The independence of the specimen preparation technique on the apparent viscosity decay law is much more evident plotting together three tests (CSS_GSS1F, CSS_GSS3MT and CSS_GSS1AP) performed in similar conditions (Ta. 5.17), which attend liquefaction after a similar N_{liq} (about 6), as reported in Figure 7.10. Despite the fact that CSS_GSS1AP exhibits a value of η_0 slightly higher than those computed for Moist Tamping and 1D-Compression techniques, the three decay laws are very similar; in other words, the methodology chosen to prepare the specimen does not influence the trend of apparent viscosity with number of cycles.

Figure 7.9. The apparent viscosity decay law of Pieve di Cento (GSS) specimens prepared by Moist Tamping (a) and Air Pluviation (b).

Figure 7.10. The effect of preparation technique on the apparent viscosity decay law of Pieve di Cento (GSS).

7.1.1.1 LIQUEFACTION TRIGGERING CRITERION

As already discussed in §2.2.2, liquefaction is historically identified according to stress or strain criteria. However, the experimental results presented in Chapter 5 and 6 have shown as for untreated specimens the two criteria give similar results in terms of N_{liq}; on the contrary, for dense and non-saturated specimens, the two criteria give often different results in terms of N_{liq}. The choice of one criterion rather than other is extremely important because on it depends the cyclic resistance curve. Moreover, several strain threshold have been proposed in literature, making "subjective" the attainment of liquefaction.
This paragraph develops with the main aim to clarify the attainment of liquefaction (physically intended as a change of state), starting from the concept of apparent viscosity. Defining liquefaction as a change of state from solid to liquid, it is reasonable to assume that the apparent viscosity could be adopted as a liquefaction triggering criterion too. In order to verify this hypothesis, the results of some cyclic triaxial tests have been plotted in the planes η-N_{cyc}-r_u and η-N_{cyc}-ε_a. In particular, the results from untreated soils in the aforementioned planes are plotted from Figure 7.11 to 7.15 for Leighton Buzzard, Ticino, Sant'Agostino, and Pieve di Cento (BSS and GSS) sands, respectively. The results show a strong correlation between the apparent viscosity decay laws and the pore pressure generation or the accumulation of axial strains. In particular, looking at the plane η-N_{cyc}-r_u, it can be noted that the value of η decreases as the pore water pressure r_u increases and the maximum gradient of the curvature (the elbow of the curve η-$N_{cyc,}$ close to the η_{fluid} value) is attained approximately at the pore pressure ratio threshold (r_u=0.90) or in correspondence of ε_{DA}=5% (in the plane η-N_{cyc}-ε_a), being the two criteria coincident for untreated soils. Thus, the elbow of the apparent viscosity decay law, which comes before η_{fluid} (fully liquefaction), can be considered as the triggering of liquefaction.
It can be expressed more clearly plotting the gradient of the curvature ($\Delta\eta/\eta$) versus N_{cyc} (Fig. 7.16), where $\Delta\eta/\eta$ is evaluated as $(\eta_i-\eta_{i+1})/\eta_i$. The relationship may be described by a sort of bell-shaped curve, whose maximum represents the drop of the apparent viscosity and then the change of state, from solid to liquid. In the same Figure, for each test, for sake of simplicity, N_{liq} evaluated according to the two approaches have been reported too. It is easy to note that the maximum of the curve is attained exactly, in correspondence of N_{liq}.

Figure 7.11. Results of cyclic triaxial tests on Leighton Buzzard sand in terms of η-N_{cyc}-r_u (a-c-e) and η-N_{cyc}-ε_a (b-d-f).

Figure 7.12. Results of cyclic triaxial tests on Ticino sand in terms of η-N_{cyc}-r_u (a) and η-N_{cyc}-ε_a (b).

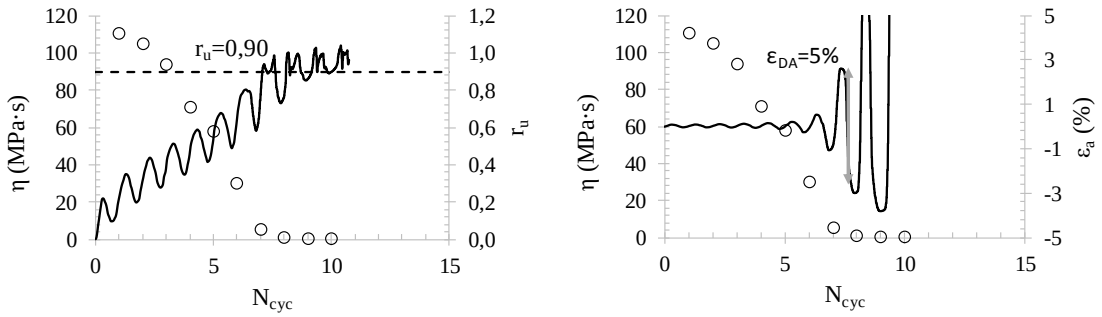

(a) CTX_SAS2 (b) CTX_SAS2

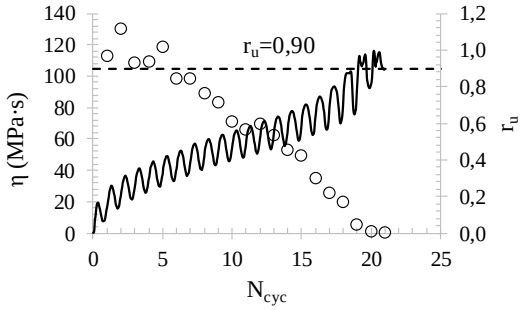

(c) CTX_SAS3

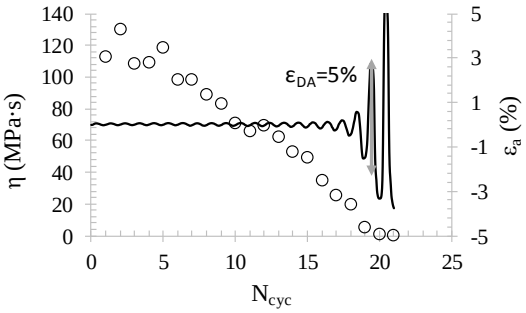

(d) CTX_SAS3

Figure 7.13. Results of cyclic triaxial tests on Sant'Agostino sand in terms of η-N_{cyc}-r_u (a-c) and η-N_{cyc}-ε_a (b-d).

Figure 7.14. Results of cyclic triaxial tests on Pieve di Cento (BSS) sand in terms of η-N_{cyc}-r_u (a) and η-N_{cyc}-ε_a (b).

Figure 7.15. Results of cyclic triaxial tests on Pieve di Cento (GSS) sand in terms of η-N_{cyc}-r_u (a-c) and η-N_{cyc}-ε_a (b-d).

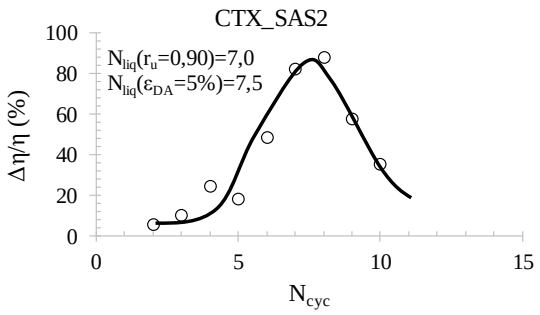
CTX_SAS2
$N_{liq}(r_u=0,90)=7,0$
$N_{liq}(\varepsilon_{DA}=5\%)=7,5$
Δη/η (%)
N_{cyc}
0
20
40
60
80
100
0
5
10
15

(e)

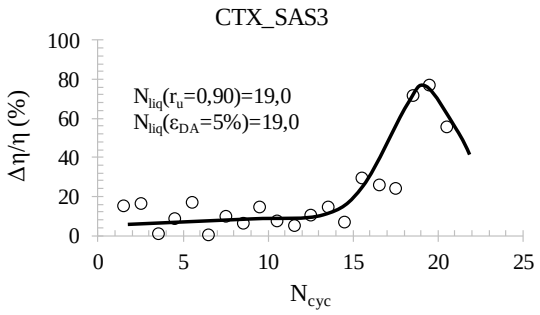
CTX_SAS3
$N_{liq}(r_u=0,90)=19,0$
$N_{liq}(\varepsilon_{DA}=5\%)=19,0$
Δη/η (%)
N_{cyc}
0
20
40
60
80
100
0
5
10
15
20
25

(f)

Figure 7.16. Results of cyclic triaxial tests in terms of $\Delta\eta/\eta$ versus N_{cyc} for different sandy soils.

Starting from these experimental evidences and thus considering the elbow of the apparent viscosity decay law as the physical attainment of liquefaction, the results of treated specimens have been plotted in the same planes (η-N_{cyc}-r_u and η-N_{cyc}-ε_a) in order to identify the exact N_{liq} to which liquefaction occurs, since, in such cases, the traditional criteria give different values in terms of N_{liq}.

First of all, the tests treated with laponite have been shown in Figure 7.17, where η and r_u (or ε_a) has been plotted together versus N_{cyc}.

Despite the presence of laponite, the trend of η with N_{cyc} follows the same pattern described in §7.1.1 for untreated sand. The apparent viscosity decreases as the number of cycles N_{cyc} increases. The value of η_0 of T_CTX_LB2 test (about 200 MPa·s) is two times higher than that of T_CTX_LB1 (90 MPa·s) and it is probably an effect of the CSR. The value of η_{fluid} is about 1 MPa·s for both tests, slightly higher than the values reached for clean sand (Leighton Buzzard) as shown in Figure 7.3a-b.

It is worth noting that the elbow of the curve is attained in correspondence of r_u equal to 0.90, while ε_{DA} of 5% occurs some cycle later.

Also for sand/laponite specimens $\Delta\eta/\eta$ versus N_{cyc} have been plotted in Figure 7.18 for both tests treated by means of nano-plastic suspensions. As for untreated specimens, a bell-shaped curve can be identified, whose maximum is attained closer to stress criterion (r_u=0.90).

Figure 7.17. Results of cyclic triaxial tests of sand treated with laponite in terms of η-N_{cyc}-r_u (a and c) and η-N_{cyc}-ε_a (b and d).

Figure 7.18. Results of cyclic triaxial tests in terms of Δη/η versus N_{cyc} for specimens treated with laponite.

In dense specimens, the difference in terms of N_{liq}, between the stress and strain criterion is much more evident. The results interpreted according to a viscous key are plotted in Figures 7.19 (Sant'Agostino sand) and 7.20 (Pieve di Cento, GSS).
It can be noted as, even for dense specimens, $r_u = 0.90$ is reached at the same number of cycles as the elbow of the apparent viscosity decay law, while $\varepsilon_{DA} = 5\%$ is attained after more cycles and then in correspondence of η_{fluid}. Also in this case, $\Delta\eta/\eta$ versus N_{cyc} have been plotted, to better identify the drop of the apparent viscosity and then pick out the number of cycles at which liquefaction occurs.
As for specimens treated with laponite, for dense sands the viscosity criterion seems to confirm the stress one. In other words, the pore water pressure based criterion is a stronger way to identify the attainment of liquefaction than the strain based criterion, which moreover, depends on the choice of the operator.

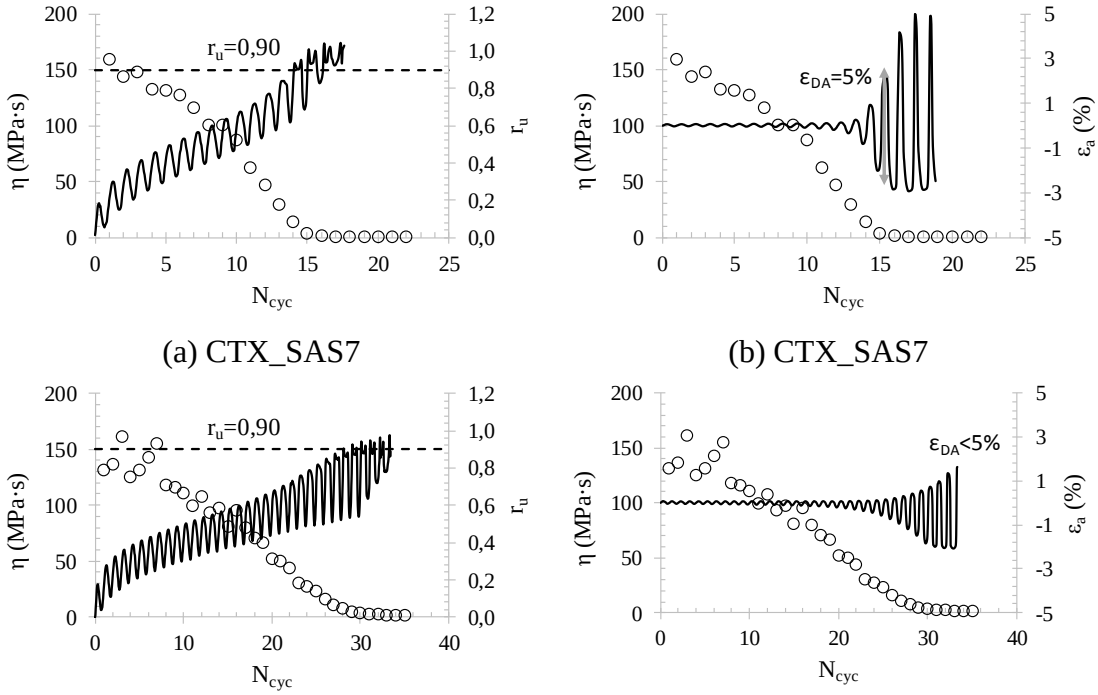

(a) CTX_SAS7 (b) CTX_SAS7

(c) CTX_SAS9 (d) CTX_SAS9

Figure 7.19. Results of cyclic triaxial tests on dense Sant'Agostino specimens in terms of η-N_{cyc}-r_u (a-c) and η-N_{cyc}-ε_a (b-d).

Figure 7.20. Results of cyclic triaxial tests on dense Pieve di Cento (GSS) specimens in terms of η-N_{cyc}-r_u (a-c-e) and η-N_{cyc}-ε_a (b-d-f).

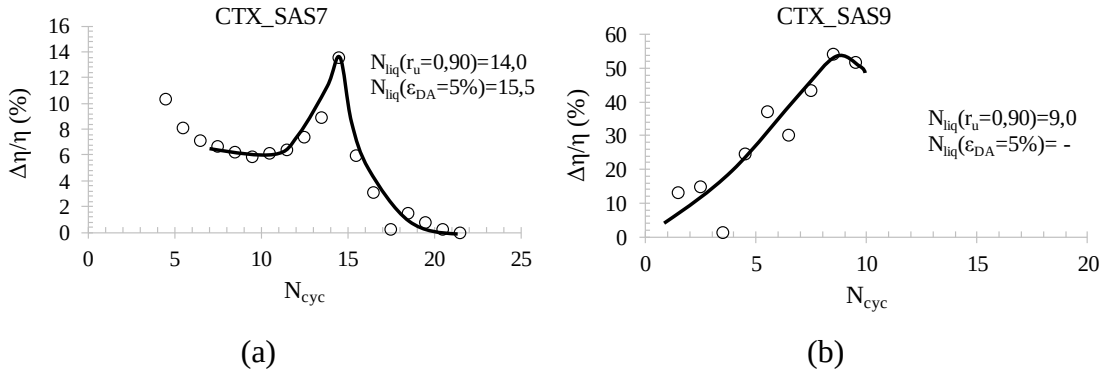

Figure 7.21. Results of cyclic triaxial tests in terms of Δη/η versus N_{cyc} for dense specimens of Sant'Agostino (a-b) and Pieve di Cento (GSS) (c-d-e) sands.

Finally, similar considerations have been done for non-saturated soils. In the planes η-N_{cyc}-r_u and η-N_{cyc}-ε_a the results from Sant'Agostino, Pieve di Cento (GSS) and silica (N°5) sands have been shown in Figures 7.22-23-24 respectively.
As mentioned in Chapter 6, the difference between N_{liq}, evaluated according to stress and strain criteria is much bigger for unsaturated soils than partially saturated ones. This is clear comparing the experimental results shown in Figures 7.22-23-24 for different sandy soils.
In particular, N_{liq} evaluated according to the strain criterion seem to correspond to the elbow of the apparent viscosity decay laws. See for instance, Figure 7.23a-b (UCTX_GSS5 test), where, even though excess pore pressure ratio does not reach the critical value (0.90), η_{fluid} is already attained. In other words, the liquefaction triggering occurs before the attainment of r_u equal to 0.90.
Such considerations can be emphasized by observing Figure 7.25, where $\Delta\eta/\eta$ versus N_{cyc} is plotted and the comparison between N_{liq} evaluated according to the two traditional criteria is reported as well.
Unlike dense specimens, for non-saturated specimens, the maximum of the gradient is attained in correspondence of N_{liq} achieved from strain criterion, regardless of the type of soil. This confirms that for non-saturated soils, strain criterion is preferred to that stress based because physically stronger than the other one.
A further confirmation that the strain criterion better represents the attainment of liquefaction, is provided by Mele et al. (2018). Taking into account the results of bauxite and Inagi sand, they highlighted as, regardless of the kind of soil, the value of apparent viscosity attained at ε_{DA}=5% assumes values in a very narrow range. Such interesting evidence is confirmed by the results reported in this thesis. In fact, an average value $\eta(\varepsilon_{DA5\%})$ equal to 400 kPa·s can be assumed. On the contrary, η_{ru} (lower than η ($\varepsilon_{DA5\%}$)) varies from soil to soil and also, for a given soil, depending on the degree of saturation. Even because of such subjectivity, the strain criterion should be preferred.

Figure 7.22. Results of cyclic triaxial tests on non-saturated Sant'Agostino specimens in terms of η-N_{cyc}-r_u (a-c-e) and η-N_{cyc}-ε_a (b-d-f).

Figure 7.23. Results of cyclic triaxial tests on non-saturated Pieve di Cento (GSS) specimens in terms of η-N_{cyc}-r_u (a-c-e) and η-N_{cyc}-ε_a (b-d-f).

Figure 7.24. Results of cyclic triaxial tests on non-saturated silica sand (N°5) specimens in terms of η-N_{cyc}-r_u (a) and η-N_{cyc}-ε_a (b).

Figure 7.25. Results of cyclic triaxial tests in terms of $\Delta\eta/\eta$ versus N_{cyc} for non-saturated specimens of Sant'Agostino (a-b-c), Pieve di Cento (GSS) (d-e-f) and silica (N°5) (g) sands.

To sum up, the results of cyclic triaxial tests carried out on untreated (Chapter 5) and treated (Chapter 6) soils have been analysed in terms of apparent viscosity decay law (η-N_{cyc}), highlighting the relevance of η as a physically based parameter for an appropriate identification of the liquefaction triggering, being able to represent the change of state from solid to liquid. Such trigger has been identified as the elbow of the apparent viscosity decay law, which represents a drop of η, and then the change of state. This sudden decrease of η has been plotted clearly in the plane $\Delta\eta/\eta$ - N_{cyc}, where the experimental points identify a bell-shaped curve, whose maximum allows to pick out the number of cycles at which liquefaction occurs. Interestingly, it has been noted that generally, the maximum corresponds to the attainment of r_u=0.90, except for non-saturated soils, where the bell-shaped curve exhibits its maximum in correspondence of ε_{DA}=5%.
In other words, to build the cyclic resistance curve of a saturated soil, the stress criterion should be preferred, regardless of its state conditions, such as relative density and confining stress; on the contrary, for non-saturated soils, the drop of apparent viscosity suggests using strain criterion to identify liquefaction triggering.

7.1.1.2 PORE WATER PRESSURE GENERATION FOR SATURATED SANDY SOILS

The results of tests performed on saturated sandy soils discussed in the previous paragraph, reveal a strong link between the decay law of the apparent viscosity η-N_{cyc} and the pore pressure ratio build up during the cyclic loading path: the value of η decreases as the pore water pressure r_u increases and the maximum gradient of the curvature (the elbow of the curve η-N_{cyc}) is attained at the pore pressure ratio threshold (r_u=0.90). This can be more clearly observed plotting the gradient of the curvature ($\Delta\eta/\eta$) versus r_u for untreated (Fig. 7.26) and treated (Fig. 7.27) specimens.
Also in this case, the relationship may be described by a bell-shaped curve, whose maximum is attained when r_u is 0.90, confirming once again that the pore water pressure based criteria is a stronger way to identify the attainment of liquefaction than the strain based criteria.

Figure 7.26. Results of cyclic triaxial tests in terms of $\Delta\eta/\eta$ versus N_{cyc} for untreated specimens of Leighton Buzzard (a-b-c), Ticino (d), Sant'Agostino (e-f) and Pieve di Cento (g-h-i) sands.

Figure 7.27. Results of cyclic triaxial tests in terms of $\Delta\eta/\eta$ versus N_{cyc} for treated specimens of Leighton Buzzard (a-b), Sant'Agostino (c-d) and Pieve di Cento (GSS) (e-f-g) sands.

As suggested by Lirer and Mele (2019), the results of saturated cyclic triaxial tests can be plotted in the plane η/η_0 versus r_u, identifying a unique average curve for each material. Such relationship is mathematically expressed as:

$$\frac{\eta}{\eta_0} = \frac{(1 - r_u)^a}{1 + b \cdot r_u^c} \quad (7.1)$$

Where a, b and c are parameters that should be calibrated to have the best fitting for the experimental results.

In Figure 7.28 the average curves, calibrated on the experimental results of saturated cyclic triaxial tests are shown.

Apart from Sant'Agostino sand, where all tests performed (loose and dense) seem to identify a unique curve, in all other cases, the generation pore water pressure model based on the concept of apparent viscosity seems to be dependent on the state of the soil. To better understand, the results of tests performed on Leighton Buzzard, clean and treated sand with laponite, can be compared (Fig. 7.27a-b). For clean sand, the ratio η/η_0 is maintained constant and equal to 1, till r_u of 0.50. It means that the difference between the maximum and minimum strain rate do not change so much, while the excess pore pressure ratio increases. For r_u higher than 0.50, the apparent viscosity drops shortly, till to reach r_u equal to 1. On the contrary, for sand treated with laponite (Fig. 7.27b) the transition phase (Fig. 7.2) starts in correspondence of lower r_u - about 0.30 – and then the

apparent viscosity drops smoothly. A similar trend can be observed for the other sandy soils. However, as already anticipated, it is worth noting as for Sant'Agostino sand, regardless of the relative density ($45<D_r(\%)<74$), the pore pressure-viscosity model seems to identify a unique curve, congruently with what reported by Lirer and Mele (2019). By contrast, for Pieve di Cento (GSS) sand, it has been needed to separate the tests based on the value of relative density as shown in Figure 7.27f-g respectively for loose and dense specimens. In particular, for dense specimens ($55<D_r(\%)<67$), the transition phase starts for r_u of 0.40, higher than that of loose specimens ($r_u \approx 0.30$).

Moreover, in all cases, it can be noted that the liquefaction is completely developed ($r_u=0.90$) when the viscosity is reduced by 95% compared to its initial value.
Eq. (7.1) may play an important role in the constitutive models of fluid mechanic to simulate the behaviour of liquefied soils. For a given soil the value of η_0 can be found through D_{50}, from the relationship plotted in Figure 7.5 and the relationship between η and r_u may be easily obtained via eq. (7.1). Last, but not least, for $r_u = 0.90$, the value of η_{fluid} can be quantified. Further tests on soils with different grading ($1 < D_{50}$ (mm) < 10) need to be carried out to confirm the relationship of Figure 7.5.

Figure 7.28. Relationship between η/η_0 and r_u for Leighton Buzzard: clean (a) and treated with laponite (b); Ticino (c); Sant'Agostino (d); Pieve di Cento, BSS (e) and GSS for loose (f) and dense specimens (g).

Table 7.1. Calibrated parameters of eq. (7.1).

	a	b	c
Leighton Buzzard			
Leighton Buzzard+Laponite			
Ticino			
Sant'Agostino			
Pieve di Cento (BSS)			
Pieve di Cento (GSS) - loose			
Pieve di Cento (GSS) - dense			

7.1.1.3 PSEUDO-PLASTIC BEHAVIOUR OF LIQUEFIED SOILS

As already discussed in §2.2.2.3, liquefaction is characterized by a state change from solid to liquid, posing a problem in modelling of liquefied soils. The framework of soil mechanics can be adopted up to the transition phase ($\eta<\eta_{trans}$, Fig. 7.2) because the soil persists in its original solid state. In the transition phase ($\eta_{trans}<\eta<\eta_{fluid}$) the change of state happens, and then the soil can be studied using a fluid mechanics approach. At the end of the transition phase, the liquefaction fully develops ($r_u=0.90$) and the complete change of state leads to a sudden collapse of the value of the apparent viscosity to a minimun value ($\eta=\eta_{fluid}$). In this phase ($\eta=\eta_{fluid}$), a rapid loss of the soil strength and stiffness occurs and the liquefied soil behaves as a pseudo-plastic fluid as concluded by Hamada and Wakamatsu (1998). Owing to that, the rheological behaviour of liquefied soils can be studied through eq. (2.18).

With the main aim to verify the pseudoplastic fluid model and eventually, calibrate the parameters k and n (fluid consistency coefficient and liquidity index, respectively). The values of the apparent viscosity have been plotted versus the corresponding maximun value of the shear strain rate $\dot{\gamma}$ measured in the cycles (Fig. 7.1) for all loose and dense specimens (Tabs. 5.3 and 6.6) as reported in Figure 7.29. The experimental results confirm that a power law function exists between the apparent viscosity (η) and the shear strain rate ($\dot{\gamma}$) (eq. (2.18)). In Figure 7.29 the average curve, which fits the experimental results is shown.

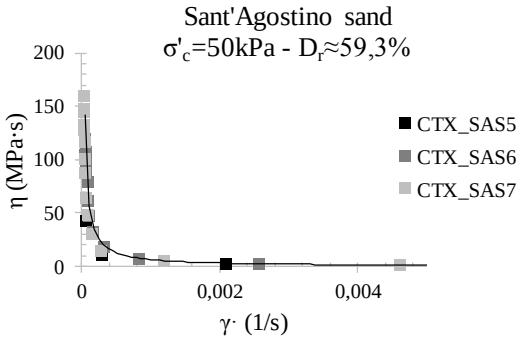
Sant'Agostino sand
σ'c=50kPa - Dr≈59,3%
η (MPa·s)
γ· (1/s)
CTX_SAS5
CTX_SAS6
CTX_SAS7
200
150
100
50
0
0
0,002
0,004

(g)

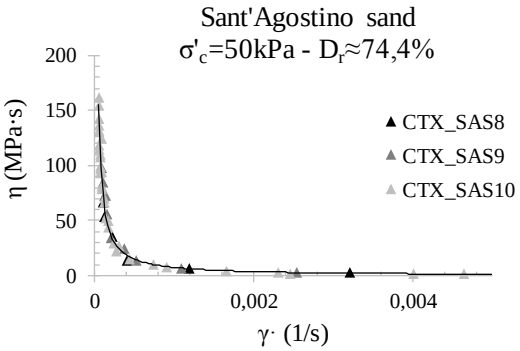
Sant'Agostino sand
σ'c=50kPa - Dr≈74,4%
η (MPa·s)
γ· (1/s)
CTX_SAS8
CTX_SAS9
CTX_SAS10
200
150
100
50
0
0
0,002
0,004

(h)

Figure 7.29. Apparent viscosity versus shear strain rate for cyclic triaxial tests on Leighton Buzzard (a-b-c, for effective stress of 25, 50 and 100 kPa, respectively), Leighton Buzzard treated with laponite (d), Ticino (e); Sant'Agostino (f-g-h, for D_r= 45.1, 59.3 and 74.4% respectively), Pieve di Cento, BSS (i) and GSS for σ'_c=50kPa (l-m-n, for D_r= 40.4, 57.0 and 64.3% respectively) and σ'_c=25kPa.

Although Zhou et al. (2014) stated that the effect of CSR is negligible as would seem looking at Figure 7.29, studying in depth the experimental results, a dependence on CSR seems to exist for k. In fact, the scale of such graphs does not allow to appreciate the difference in terms of k and n due to an effect of the applied CSR. This can be easily understood looking at Table 7.2, where the calibrated values of k and n for each test are shown. Moreover, it is much more evident plotting the results in the plane CSR-k (Fig. 7.30). Although a dispersion of the experimental data exists, it is evident as k increases with the applied CSR, according to a linear relationship.

Certainly, the consistent coefficient (k) is affected by soil grading, relative density and confining pressure, but the new findings shown in Figure 7.30a highlight a much more significant dependence on CSR.

Regarding the liquid index (n), it should reflect the nature of the fluid. However, it is always less than 1 (shear thinning flow) and seems to be mainly affected by the relative density (Tab. 7.2), even though a direct relationship n-D_r has not been found. Nevertheless, a direct dependence of n on k seems to be evident (Fig. 7.30b).

Interestingly, the two parameters of the rheological behaviour of sand subjected to liquefaction seems to be strongly connected, according to a linear relationship, with a regression coefficient (R^2) equal to 0.732. Such results, if confirmed by other tests performed on different sands in different conditions, would lead to important advantages in the calibration of pseudo-plastic models, able to simulate the behaviour of liquefied sands. In fact, a direct dependence between two parameters, allows to simplify the calibration procedures, implying the calibration of only one parameter (k).

Table 7.2. Calibrated parameters k and n of eq. (2.18).

Sand	Test	σ'_c (kPa)	D_r* (%)	CSR	N_{liq}	k	n
LB	CTX_LB1						
LB	CTX_LB3						
LB	CTX_LB4						
LB	CTX_LB7						
LB	CTX_LB8						
LB+Lap	T_CTX_LB1						
LB+Lap	T_CTX_LB2						
Ti	CTX_T1						
Ti	CTX_T2						
SAS	CTX_SAS1						
SAS	CTX_SAS2						
SAS	CTX_SAS3						
SAS	CTX_SAS6						
SAS	CTX_SAS7						
SAS	CTX_SAS8						
SAS	CTX_SAS9						
SAS	CTX_SAS10						
BSS	CTX_BSS1						
BSS	CTX_BSS2						
BSS	CTX_BSS3						
GSS	CTX_GSS3						
GSS	CTX_GSS4						
GSS	CTX_GSS5						
GSS	CTX_GSS6						
GSS	CTX_GSS8						
GSS	CTX_GSS9						
GSS	CTX_GSS11						
GSS	CTX_GSS12						
GSS	CTX_GSS13						
GSS	CTX_GSS14						

*at the end of consolidation phase

Figure 7.30. Consistent coefficient (k) versus CSR (a) and linear relationship between k and n (b).

7.2 POST LIQUEFACTION CYCLIC BEHAVIOUR

In the previous paragraph (§7.1) the behaviour of liquefied soils has been studied. However, another important aspect in the study of liquefaction phenomena is the post liquefaction behaviour. In this thesis, the cyclic behaviour of sands, that experienced liquefaction during a first cyclic loading has been analysed. Post liquefaction cyclic behaviour has been studied in cyclic triaxial (saturated and unsaturated specimens), re-consolidating the specimens after the occurrence of a first liquefaction, as explained in §4.2.1.1. Pieve di Cento (GSS) sand has been used to study post-liquefaction effects.
In the following paragraphs the main results will be shown and discussed in detail.

7.2.1 POST LIQUEFACTION IN CYCLIC TRIAXIAL TESTS

Post liquefaction behaviour has been investigated in cyclic triaxial tests on saturated and non-saturated specimens, whose cyclic behaviour has been already analysed in Chapter 5 and 6. The results will be shown in two different sections.

7.2.1.1 SATURATED SPECIMENS

In Table 7.3 the testing program of saturated tests, subjected to a second cyclic phase is shown, moreover, the values of void ratio – and then D_r – after the post liquefaction consolidation is reported. As expected, after the re-consolidation phase, the relative density of the specimens increases (see for instance Fig. 2.34), due to the dissipation of the excess pore pressure risen during the first liquefaction.

Table 7.3. Testing program of saturated CTX tests subjected to a second cyclic loading.

Test	σ'_c (kPa)	e_0*	D_{r0}*(%)	CSR^I	N_{liq}	e_0**	D_{r0}**(%)	CSR^{II}
CTX_GSS7								
CTX_GSS8								
CTX_GSS9								
CTX_GSS11								
CTX_GSS12								
CTX_GSS13								

*at the end of the first consolidation. **at the end of post-liquefaction consolidation.

As an example, for CTX_GSS9 test, the first consolidation and the post-liquefaction consolidation have been shown in the plane p' – e (Fig. 7.31). At the end of the first consolidation, the void ratio reaches a value of 0.642 (Tab. 7.3). During the cyclic loading, in undrained conditions, the void ratio is obviously constant and consequently the effective stresses tend to vanish (see the red arrow of Fig. 7.31). When liquefaction

occurs, the test is stopped and a re-consolidation phase is imposed opening the drainage to dissipate the induced excess pore pressure. During the re-consolidation, the void ratio decreases again, while the effective stresses increases until to reach the initial value (50 kPa in Fig. 7.31).

Figure 7.31. Pre and post liquefaction consolidation of CTX_GSS9 test.

As an example, the results of three tests CTX_GSS8, CTX_GSS11 and CTX_GSS13 on specimens subjected to a cyclic re-loading have been plotted in the planes: ε_a- q (a-e-i); p'-q (b-f-h); N_{cyc}-CSR (c-g-l); r_u- N_{cyc}-ε_a (d-h-m), as shown in Figure 7.32.

Figure 7.32. Results of cyclic triaxial tests subjected to cyclic re-consolidation, plotted in the planes: ε_a- q (a-e); p'-q (b-f); N_{cyc}-CSR (c-g); r_u- N_{cyc}-ε_a (d-h).

The results are similar to that already shown in Chapters 5 and 6 of this thesis, where "virgin" soils have been tested. However, it is worth doing two important observations. Firstly, in the plane p'-q, the stress-path is congruent with the critical state line achieved for virgin soil. It seems to suggest that the CSL does not change after liquefaction.

However, such experimental observation should be confirmed by carrying out monotonic tests after liquefaction. Secondly, regardless of the relative density, stress and strain criteria seems to provide results in terms of N_{liq}, completely different. While r_u attains to a value equal to 1, axial strains are still small (<5%). For example, for CTX_GSS8 test ε_{DA} does not overcome the value of 4% (Fig. 7.32a-d) and 3% in CTX_GSS11 test (Fig. 7.32e-h). In addition, for CTX_GSS13 test, although the fully liquefaction condition (r_u=1.0) is reached, ε_{DA} is only 2% (Fig. 7.32i-n). To better understand such behaviour, the apparent viscosity has been introduced and in particular, the ratio $\Delta\eta/\eta$ for each test has been plotted versus N_{cyc} and r_u, to identify the attainment of liquefaction according to a viscous concepts, as previously done for tests on specimens subjected to first liquefaction (§7.1.1.1 and 7.1.1.2).

Such new findings, if confirmed by further tests, could be useful to explain why soils which have already experienced liquefaction present a lower liquefaction resistance as demonstrated by several real cases (§2.2.3).

Figure 7.33. Results of cyclic triaxial tests in terms of $\Delta\eta/\eta$ versus N_{cyc} (a-c-e-g) and $\Delta\eta/\eta$ versus r_u (b-d-f-h).

Starting from such experimental evidences, liquefaction has been identified according to viscosity criterion. The value of N_{liq} for post liquefied soils have been reported in Table 7.4.

Table 7.4. Testing program and main information on saturated CTX tests subjected to a second cyclic loading.

Test	σ'_c (kPa)	e_0*	D_{r0}*(%)	CSR^I	N_{liq}	e_0**	D_{r0}**(%)	CSR^{II}	N_{liq}
CTX_GSS7									
CTX_GSS8									
CTX_GSS9									
CTX_GSS11									
CTX_GSS12									
CTX_GSS13									

*at the end of the first consolidation. **at the end of post-liquefaction consolidation.

It is evident a decreased liquefaction resistance of Pieve di Cento sand, which is also shown in Figure 7.34, where the results are plotted in the typical plane N_{liq}-CRR. These results highlight that specimens that have experienced liquefaction, regardless of their initial relative density, present a lower resistance, confirming once again what happened in several real cases, where re-liquefaction occurred much more frequently than it is thought, as already mentioned in §2.2.3.

The reason why these specimens exhibit a lower liquefaction resistance has been attributed to weaker zones on the top of the specimen after being liquefied (Finn t al. 1970; Toki et al., 1981) or to an effect induced by anisotropy (Ishihara and Okada, 1982; Suzuki and Suzuki, 1988), which was confirmed by Oda et al. (2001), who introduced a microstructural interpretation of re-liquefaction mechanism, stating that even though the overall void ratio does not change significantly, the fabric of the soil is completely modified (§2.2.3).

Figure 7.34. Data points and liquefaction resistance curves of virgin soil (first liquefaction) and data points from re-consolidated (second liquefaction) specimens.

In order to improve the basic understanding on the mechanics of post-cyclic undrained behaviour, comparisons between results from virgin and re-consolidated specimens are shown as follows.

First of all, the trend of the excess pore pressure with number of cycles has been investigated. In Figure 7.35a-c-e-g-i, r_u has been plotted with N_{cyc}, showing, as expected, a higher accumulation of pore pressure during the second liquefaction. Moreover, with the main aim to better compare pore pressure build-up, during the first and second liquefaction, the normalized N_{cyc} with N_{liq} – evaluated in fully liquefaction condition – has been plotted with r_u in Figure 7.35b-d-f-h-l. It is clear as the rate of generation pore pressure with N_{cyc} increases during the second cyclic loading.

Figure 7.35. Excess pore pressure (r_u) versus N_{cyc} (a-c-e-g-i) and r_u versus N_{cyc}/N_{liq} (b-d-f-h-l) for Pieve di Cento (GSS) sand during the first and second liquefaction.

Moreover, looking in detail at Figure 7.35, it can be noted as for CTX_GSS9 and CTX_GSS11 tests, during the second cyclic loading, the excess pore water pressure sharply raises in the first cycle, reaching r_u=0.60. On the contrary, for the other tests

(CTX_GSS7, CTX_GSS8 and CTX_GSS13) the pore water pressure response observed in the second cyclic loading is similar to that observed in the first cyclic loading. As suggested by Ishihara and Okada (1982), the reason can lie in the fact that the excess pore water pressure generation is very different according to whether "pre-shearing" is applied toward extension or compression side.

Such experimental evidences confirm that the induced anisotropy, which occurs after liquefaction is responsible of a different cyclic behaviour of the soil. A further confirmation is given by plotting the results of two tests (CTX_GSS8 and CTX_GSS11) in the plane η/η_0 versus r_u, as shown in Figure 7.37.

Figure 7.36. Stress-strain behaviour during the first liquefaction (a-c) and stress-path related to the second liquefaction (b-d).

As expected, for CTX_GSS8 test, the apparent viscosity decay law (η/η_0 - r_u) is similar during the first and second liquefaction, due to the fact that the pre-shearing is applied towards the compression side, as mentioned above. By contrast, the apparent viscosity decay law of CTX_GSS11 test, exhibited during the second liquefaction is completely different from that observed during the first one, as a matter of the fact that the pre-shearing is applied towards the extension side.

Figure 7.37. Comparisons between first and second liquefaction in terms of η/η_0 and r_u for CTX_GSS8 (a) and CTX_GSS11 (b).

Finally, a comparison between first and second liquefaction has been done in terms of η versus the shear strain rate ($\dot{\gamma}$) to investigate the pseudo-plastic behavior of liquefied soils.

In Figure 7.38, the rheological laws of the first and second liquefaction have been compared. The laws appear slightly different after the re-consolidation. The values of k and n of eq. (2.18) are reported in Table 7.5.

Figure 7.38. Comparisons between first and second liquefaction in terms of apparent viscosity versus shear strain rate for tests of Table 7.4.

The consistent coefficient (k) changes slightly passing from first to second cyclic loading, while the liquidity index (n) seems to assume a similar value for all re-consolidated tests (Tab. 7.5). Moreover, the linear relationship between k and n found in §7.1.1.3 (Fig. 7.30b) seems to be confirmed for re-consolidated specimens (Fig. 7.38).

Table 7.5. Calibrated parameters k and n of eq. (2.18) during the first and second liquefaction.

	First Liquefaction				Second Liquefaction			
Test	CSR^{I}	N_{liq}	k	n	CSR^{II}	N_{liq}	k	n
CTX_GSS7								
CTX_GSS8								
CTX_GSS9								
CTX_GSS11								
CTX_GSS12								
CTX_GSS13								

Figure 7.39. Linear relationship between k and n.

7.2.1.2 NON-SATURATED SPECIMENS

Post-liquefaction behaviour has been studied in depth mainly for saturated soils, while little or nothing has been done on non-saturated sandy soils, which have already experienced liquefaction. In order to improve the basic understanding of post-liquefaction on unsaturated soils, six tests, whose results related to first cyclic loading have been shown in Chapter 6, have been subjected to a cyclic re-loading after a re-consolidation phase (§ 4.2.3.1). The testing program is summarized in Table 7.6 together with the main information.

As previously shown for saturated specimens (§7.2.1.1), after the re-consolidation the relative density increases (Tab. 7.6). Obviously, for non-saturated soils, the increase of D_r is higher than that observed for saturated ones, due to a higher compressibility of fluid phase. Moreover, as a consequence of higher D_r, it can be noted an increase, even if small, of S_r (Tab. 7.6).

Table 7.6. Testing program and main information on post liquefaction tests on non-saturated specimens.

Test	σ'_{un} (kPa)	S_{r0}* (%)	e_0*	D_{r0}* (%)	CSR^I	N_{liq}	S_{r0}** (%)	e_0**	D_{r0}** (%)	CSR^{II}
UCTX_GSS6										
UCTX_GSS7										
UCTX_GSS8										
UCTX_GSS10										
UCTX_GSS11										
UCTX_GSS13										

*at the end of consolidation phase; **at the end of post-liquefaction consolidation.

To better understand what happens during tests on non-saturated specimens subjected to a second cyclic loading, following a re-consolidation, Figure 7.40 can be considered, where the path of a partially saturated soil (UCTX_GSS10, see Tab. 7.6) during the first and second liquefaction is plotted in the plane p'_{un}-e. At the end of first liquefaction, the confining stress is 50.0 kPa and the void ratio is 0.609. As known, in non-saturated specimens positive volumetric strains arise also during loading in undrained conditions, implying a decrease of void ratio (0.550). A further decrease of void ratio obviously occurs during the re-consolidation, which lead the void ratio to a lower value (0.513). At the end of re-consolidation, effective stress takes up its initial value of 50 kPa, since excess pore pressures induced by the first cyclic loading is completely dissipated. Finally, during the second cyclic loading void ratio decreases again, up to reach, in this case, the value of 0.450.

Figure 7.40. Path of non-saturated soils during the first and second liquefaction in the plane p'_{un}-e (UCTX_GSS10 test).

Additionally, it can be noted as the path of non-saturated soils during the first and second liquefaction are practically parallel, showing a similar compressibility of the fluid mixture since S_r during the first and second liquefaction are very similar (Tab. 7.6).
As an example, the typical results of UCTX_GSS10 test on a specimen, subjected to a second cyclic loading, are plotted in Figure 7.41, in four planes: q - ε_a; q - (p-u_w); u_w versus N_{cyc} and finally ε_a versus N_{cyc}.
To identify the attainment of liquefaction, the viscous criterion has been chosen, based on the experimental evidences reported in § 7.1.1.1.

Figure 7.41. Results of UCTX_GSS10 test, subjected to a second cyclic loading, in the planes: ε_a- q (a); q - (p-u_w) (b); u_w with N_{cyc} (c), and finally ε_a – ε_v - N_{cyc} (d).

In particular, in Figure 7.42, $\Delta\eta/\eta$ versus N_{cyc} is plotted for the tests reported in Table 7.6. For each test the number of cycles at liquefaction evaluated according to stress (r_u=0.90) and strain (ε_{DA}=5%) criteria is reported too. Once again, the viscosity approach to evaluate the attainment of liquefaction seems to give a N_{liq} closer than that evaluated according to strain criterion, even though the two traditional criteria give similar N_{liq} as noted in Figure 7.42. This is probably due to the fact that the degrees of saturation are high and then the two criteria tend to provide the same results in terms of N_{liq} as already shown in Chapter 6.

Figure 7.42. Results of cyclic triaxial tests in terms of $\Delta\eta/\eta$ versus N_{cyc} for non-saturated specimens of Pieve di Cento (GSS) sand.

As a matter of the fact that the viscosity approach is physically consistent with the definition of liquefaction, it has been used to evaluate the attainment of liquefaction. N_{liq} values are reported in Table 7.7 and the results of post-liquefaction tests are plotted in the semi-log plane N_{liq}-CRR (Fig. 7.43).

Table 7.7. Results of post liquefaction tests on non-saturated specimens.

Test	σ'_{un} (kPa)	S_{r0}* (%)	e_0*	D_{r0}* (%)	CSR^I	N_{liq}	S_{r0}** (%)	e_0**	D_{r0}** (%)	CSR^{II}	N_{liq}
UCTX_GSS6											
UCTX_GSS7											
UCTX_GSS8											
UCTX_GSS10											
UCTX_GSS11											
UCTX_GSS13											

*at the end of consolidation phase; **at the end of post-liquefaction consolidation.

Figure 7.43. Liquefaction resistance curves of virgin (first liquefaction) and re-consolidated (second liquefaction) non-saturated specimens.

Unlike saturated soils, where the cyclic resistance always decreases during the second liquefaction, it seems not to be a general rule in non-saturated soils. Figure 7.43a shows that re-consolidated specimens exhibit a cyclic resistance similar to that of virgin soil, despite a relevant difference in terms of relative density, which reaches value of 80-85%. On the contrary, Figure 7.43b seems to suggest that specimens re-consolidated at 50 kPa have a slightly higher liquefaction resistance while that re-consolidated at 25 kPa shows a lower resistance to liquefaction than that of the virgin specimen.

Obviously, as for saturated soils, a change of fabric effect occurs for non-saturated ones as can be easily understood by the fact that the change in terms of D_r does not influence the cyclic resistance. In other words, virgin and post-consolidated specimens cannot be compared as the same soil in different condition in terms of D_r, because in this case, a different cyclic resistance curve should have existed. By contrast, as a matter of the fact that the liquefaction resistance is the same, a change fabric must be assumed.

Furthermore, looking carefully at Table 7.7, it can be noted that UCTX_GSS13 test reaches a higher S_r after the re-consolidation (S_r=94.1%) than the other specimens and it could explain why it exhibits a lower liquefaction resistance.

In Chapter 6 (§ 6.3.1) it has been shown that ε_v increases during the cycles to a final value $\varepsilon_{v,fin}$ which depends on values of S_{r0}, D_r (or e) and confining pressure (σ'_{un}), and then a

unique final value of $\varepsilon_{v,fin}$ exists for each set of S_r, D_r (or e) and σ'_{un}. Moreover, it was also demonstrated than for high S_r $\varepsilon_{v,fin,}$ is coincident with $\varepsilon_{v,liq}$ ($\varepsilon_v(N_{liq})$ in Fig. 7.44).
In order to verify such evidences for post-liquefied specimens, ε_v has been plotted with N_{cyc} for virgin and re-consolidated specimens (Fig. 7.44a-c-e-g-i-m).
It can be noted that $\varepsilon_{v,liq}$, practically coincident with $\varepsilon_{v,fin,}$ for the virgin soil is roughly the same as that of re-consolidated specimens. In Figure 7.44a-c-e-g-i-m, the average value of $\varepsilon_{v,liq}$ is reported.
Additionally, further comparisons have been done in the plane ε_v - σ'_{un} as reported in Figure 7.44b-d-f-h-l-n. It is worth noting that the curves overlap each other except for UCTX_GSS6 and UCTX_GSS13. In both cases, the area subtended by the curve of the second cyclic loading (the grey one) is lower than that relative to the first cyclic loading. Such considerations will be extremely useful in the Chapter 8, where liquefaction resistance will be studied according to an energetic approach. Therefore, further considerations regarding these results will be discussed in the next Chapter.

Figure 7.44. Comparisons between virgin and re-consolidated specimens in the planes: N_{cyc}- ε_v (a-c-e-g-i-m) and ε_v-σ'_{un} (b-d-f-h-l-n).

REFERENCES

Finn, W. D., Bransby, P. L., and Pickering, D. J. (1970). Effect of strain history on liquefaction of sand. *Journal of Soil Mechanics & Foundations Div*, *96*(SM6).

Flora, A., S. Lirer, and F. Silvestri. Undrained cyclic resistance of undisturbed gravelly soils. *Soil Dynamics and Earthquake Engineering* 43 (2012): 366-379.

Hamada, M., and Wakamatsu, K. (1998). A study on ground displacement caused by soil liquefaction. *Proc. JpnSoc Civil Eng*, *1998*(596), 189-208.

Ishihara, K., and Okada, S. (1982). Effect of large preshearing on cyclic behavior of sand. *Soils and Found.*, Tokyo, 22(3): 109–125.

Lirer, S., and Mele, L. (2019). On the apparent viscosity of granular soils during liquefaction tests. *Bulletin of Earthquake Engineering*, DOI: 10.1007/s10518-019-00706-0.

Mele L., Tan Tian J., Lirer S., Flora A., Koseki J. (2018). Liquefaction resistance of unsaturated sands: experimental evidence and theoretical interpretation. *Géotechnique*. DOI: 10.1680/jgeot.18.p.042.

Oda, M., Kawamoto K., Suzuki K., Fujimori H., Sato M. (2001). Microstructural interpretation on reliquefaction of saturated granular soils under cyclic loading. *Journal of Geotechnical and Geoenvironmental Engineering ASCE*, 127 (5): 416-423.

Suzuki, T., and Suzuki, T. (1988). Effects of density and fabric change on reliquefaction resistance of saturated sand. *J. Japanese Geotech. Soc.*, Tokyo, 28(2): 187–195 (in Japanese).

Toki, S., Miura, S., and Tanizawa, F. (1981). A few remarks on the relationship between relative density and strength characteristics of sand. *Proc., Symp. on Relative Density and Engrg. Characteristics of Sand*, 78–86 (in Japanese).

Zhou, E. Q., Lv, C., Wang, Z. H., and Chen, G. X. (2014). Fluid Characteristic of Saturated Sands under Cyclic Loading. In *Advances in Soil Dynamics and Foundation Engineering* (pp. 178-186).

CHAPTER 8

8. ENERGETIC APPROACH APPLIED TO LIQUEFACTION TESTS

This Chapter is entirely dedicated to an innovative and promising approach to study liquefaction. It is an energetic approach based on the fact that a soil spends energy to liquefy. Such approach have been applied to saturated and non-saturated soils, although the most important findings have been obtained for non-saturated soils, for which the energetic approach can be used also for predicting the cyclic resistance curves and then used as a simple design tool in desaturation interventions as countermeasure against liquefaction.

8.1 THEORETICAL PRINCIPLES OF THE ENERGETIC MODEL

In recent years, energetic concepts are increasingly developing, with the main aim to determine the parameters that could better define liquefaction potential of a soil deposit, as shown in Chapter 2 (§2.3.3). In saturated soils, the energetic approaches seem to be very promising, due to the fact that the dissipated energy required for the onset of liquefaction is practically independent of the applied loading pattern (uniform or non-uniform) and type of test performed. However, very little has been done on the effect of energy on non-saturated sandy soils. With the main aim to generalize the energetic concepts for saturated and non-saturated soils, the results of laboratory tests performed on saturated and non-saturated soils (Chapters 5 and 6) have been interpreted according to the concept of total energy spent by the soil specimen during the pore pressure build-up process till liquefaction. A non-saturated soil can be considered as a three-phases thermodynamic system. In order to quantify the energy spent to reach liquefaction, four hypothesis will be introduced:

- the process is isothermal (i.e. no heat is generated or lost during the test);
- the mass of the system is constant (i.e. no increase or decrease of the mass of air, water or soil in the specimen during the test);
- the system is thermodynamically open (i.e. within the specimen the deformation process implies internal flows of air and water);
- the pore gas (air) can be treated as an ideal gas.

Under such hypothesis, the portion of the internal energy that is free for doing work at a constant temperature, represented by the gradient $d\psi$, where ψ is the Helmholtz function, can be formally written as (Li, 2007):

$$d\psi = [(\boldsymbol{\sigma} - u_a\boldsymbol{\delta}) + sS_r\boldsymbol{\delta}]: d\boldsymbol{\varepsilon} - \frac{e}{1+e}sdS_r + \frac{e_0}{1+e_0}(1 - S_{r,0})u_a d(\ln \rho_a) \qquad (8.1)$$

where the incremental dissipations are neglected. In Equation 8.1 the term ($\boldsymbol{\sigma}$-$u_a\boldsymbol{\delta}$) is the net stress, u_a is the pore air pressure, s is the suction, S_r is the degree of saturation, e is the void ratio of the soil and ρ_a is the mass density of the air.
Equation 8.1 can be formally rewritten by introducing the concept of total specific (i.e. referred to a unit reference volume, therefore to be measured in J/m^3 or Pa) energy of deformation E_{tot} needed to reach liquefaction, that can be seen as the sum of three components: the first one represents the work done by the deformation of the soil skeleton, the other two are related to the work caused by the flow of mass of water and air into the system of pores. E_{tot} can be expressed as (Mele et al., 2018):

$$E_{tot,liq} = E_{sk,liq} + E_{w,liq} + E_{air,liq} \quad (8.2)$$

where $E_{sk,liq}$, $E_{w,liq}$ and $E_{air,liq}$ are the energies of deformation of soil skeleton, water and air, respectively. The term $E_{sk,liq}$ (energy of the soil skeleton) is composed by two components: the volumetric and the deviatoric part. In the following, the volumetric part of soil skeleton will be called $E_{v,sk,liq}$ because it is connected to the change in volume, while the deviatoric one is $E_{s,sk,liq}$, connected with the distorsional strain ε_s:

$$E_{sk,liq} = E_{v,sk,,liq} + E_{s,sk,,liq} \quad (8.2)$$

Obviously, in undrained tests, the term $E_{v,liq}$ differs from zero only for non-saturated specimens. The role played by these two components within the liquefaction phenomenon will be discussed in the following. However, the volumetric specific energy ($E_{v,liq}$) can be seen as the sum of three components (Mele et al., 2018):

$$E_{v,liq} = E_{v,sk,liq} + E_{w,liq} + E_{air,liq} \quad (8.3)$$

$E_{v,sk,liq}$, $E_{w,liq}$ and $E_{air,liq}$ represent the specific work done respectively to cause the deformation of the soil skeleton, the flow of water and the flow of air into the pores network. They can be expressed as:

$$E_{v,sk,liq} = \int_0^{\varepsilon_{v,liq}} [(\sigma - u_a) + sS_r] \cdot d\varepsilon_v \quad (8.4)$$

$$E_{w,liq} = -\int_{Sr0}^{Sr,liq} \frac{e(S_r)}{1+e(S_r)} s(S_r) \cdot dS_r \quad (8.5)$$

$$E_{air,liq} = \frac{e_0}{1+e_0}(1 - S_{r,0}) u_{a,liq} \left(\ln \frac{V_{air,0}}{V_{air,liq}} \right) \quad (8.6)$$

$E_{v,sk,liq}$ depends on the stress state (σ'_{un}) and on the initial void ratio e_0 ($E_{v,sk,liq} = f(\sigma'_{un}(S_r), e_0)$), while it depends neither on CSR nor on N_{liq}. Obviously, $E_{v,sk,liq}=0$ for undrained tests

on saturated soils. In eq. (8.4) $d\varepsilon_v$ is the increment of volumetric strain during undrained cyclic loading. Furthermore, the integral of eq. (8.4) represents the area of the average curve σ'_{un}-ε_v (i.e. Fig. 6.31) for a specific soil state, till liquefaction.
The energy of deformation of water (eq. (8.5)) is due to the change of water content. Equation 8.5 can be seen as the energetic contribution of the water content change, being $E_{w,liq}$ proportional to the integral of the water retention curve starting from a given initial degree of saturation S_{r0}.
Finally, the energy of deformation of air (eq. (8.6)) describes the effect of pressure variation in the gas phase, where $V_{air,0}$ is the volume of air at the beginning of deviatoric phase, while $V_{air,liq}$ is that corresponding to liquefaction condition.
Since no distorsional strains are generated by the work input into the liquid and gas phases, the distorsional energetic contribution of eq. (8.2) is linked just to soil skeleton ($E_{s,sk,liq}$=$E_{s,liq}$). $E_{s,liq}$ has been already defined in §2.3.3 as the sum of the areas of all the cycles in the ε_s-q plane, for cyclic triaxial tests and γ-τ for cyclic simple shear tests, and formally written in eq. (2.12a) for triaxial tests and eq. (2.12b) for cyclic simple shear tests. Because of its definition, $E_{s,liq}$ is strictly related to soil damping, and it thus quantifies the amount of energy dissipated during the distorsional cyclic path. Therefore, it should depend on soil properties, soil state and cyclic stress amplitude CSR.
In conclusion, the total specific energy to reach liquefaction, can be easily written as the sum of a volumetric and a deviatoric part, as reported below:

$$E_{tot,liq} = E_{v,liq} + E_{s,liq} \quad (8.7)$$

Obviously, the first volumetric component is different from zero only for non-saturated soils. In other words, for saturated soils the specific total energy to reach liquefaction is given only by the deviatoric component.
The role of specific volumetric and deviatoric energies will be analysed in the following. According to what has already been said, the role of specific volumetric energy to liquefaction will be investigated only for non-saturated soils. By contrast, the role of the specific deviatoric energy to liquefaction will be investigated in depth for both saturated and non-saturated soils.

8.2 ENERGETIC APPROACH FOR SATURATED SOILS

As mentioned before, for saturated soils in undrained condition, being null the specific volumetric energy to liquefaction, eq. (8.7) can be re-written more easily as:

$$E_{tot,liq} = E_{s,liq} \quad (8.8)$$

It means that the specific total energy to reach liquefaction is given by the only deviatoric component.

The typical results of cyclic tests shown in Chapters 5 and 6, highlight that the area of cycles in the plane ε_a – q, in triaxial tests and γ-τ in simple shear tests increases until to reach liquefaction.
Defining the specific deviatoric energy as the sum of the areas of all the cycles in stress – strain planes, it can be easily understood that E_s increases with number of cycles until to attain liquefaction, where for $N_{cyc} = N_{liq}$, E_s is exactly $E_{s,liq}$. It is clearly shown in Figure 8.1, where, as an example, E_s is plotted with N_{cyc} (Fig. 8.1a) for three cyclic triaxial tests performed on Pieve di Cento (BSS) sand (Tab. 5.14), whose cyclic resistance curve is shown in Figure 8.1b.

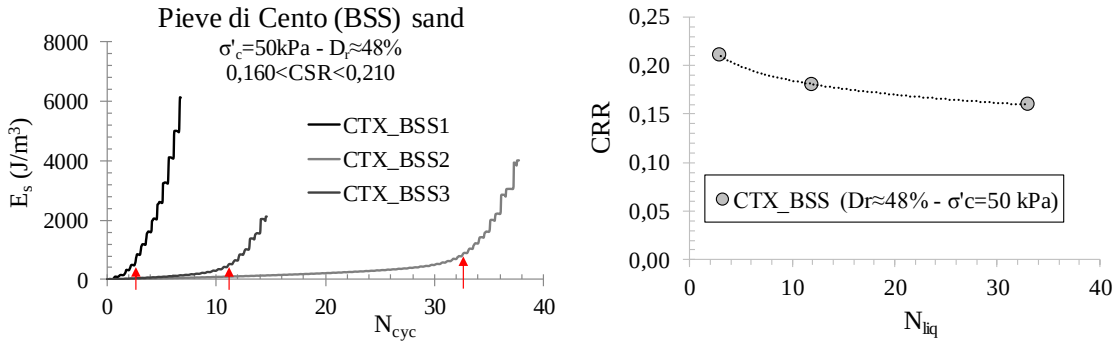

(a) (b)

Figure 8.1. E_s with N_{cyc} (a) for cyclic triaxial tests; cyclic resistance curve of Pieve di Cento (BSS) sand (b).

It can be noted that the curves E_s – N_{cyc} are almost linear in the first cycles and "at a certain point" E_s suddenly increases. Such a "point", indicated by red arrows in Figure 8.1a, corresponds to N_{liq}, and then with the attainment of liquefaction (see, for instance Figure 8.1b).
Generally speaking, it can be said that the highest gradient of the curve E_s-N_{cyc} may indicate when liquefaction occurs, allowing to identify $E_{s,liq}$.
An interesting insight has been done on this aspect of the specific deviatoric energy, with the main aim to better understand the role that it plays in the attainment of liquefaction.
In Figure 8.2 the results of some saturated cyclic triaxial tests on loose and dense sands have been plotted in the plane E_s-N_{cyc}-r_u and E_s-N_{cyc}-ε_a.
The results of cyclic triaxial tests reported in Figure 8.2 confirm that, when liquefaction occurs or close to its attainment, the curve E_s-N_{cyc} changes its slope, as a consequence of a higher increase of dissipated energy with number of cycles. Furthermore, it is worth noting that the maximum gradient of the curve E_s-N_{cyc} roughly corresponds to the stress and strain thresholds (r_u=0.90 and ε_{DA}=5%) for loose sands, while it is roughly coincident with r_u = 0.90 for dense sands (CTX_SAS7 and CTX_SAS8, in Fig. 8.2k-l-m-n; CTX_GSS8 in Fig. 8.2s-t), except for CTX_GSS13 (Fig. 8.2u-v) where the gradient of the dissipated energy with N_{cyc} occurs some cycle before than r_u=0.90. However, the correspondence of such gradient with the stress liquefaction triggering criterion seems to

be further confirmed for tests performed on sand/laponite specimens, as shown in Figure 8.2e.

Figure 8.2. Results of cyclic triaxial tests in terms of E_s-N_{cyc}-r_u and E_s-N_{cyc}-ε_a.

As a further confirmation of the reliability of specific deviatoric energy as a liquefaction triggering criterion, based on what has been said in Chapter 7, E_s has been plotted together with the apparent viscosity (η) and the gradient $\Delta\eta/\eta$ versus N_{cyc} (Fig. 8.3), for the same tests reported in Figure 8.2.

It is evident that the elbow of the apparent viscosity decay law (η-N_{cyc}) and that of the curve E_s – N_{cyc} are coincident. It is much clearer in the plane $\Delta\eta/\eta$ - N_{cyc}, where the maximum of the ratio $\Delta\eta/\eta$ matches the slope change of the deviatoric energy.

Figure 8.3. Results of cyclic triaxial tests in terms of E_s-N_{cyc}-η and E_s-N_{cyc}-$\Delta\eta/\eta$.

The experimental evidences seem to confirm the reliability of the specific deviatoric energy as liquefaction triggering criterion and that in correspondence of the elbow of the curve E_s-N_{cyc} liquefaction is attained and there $E_{s,liq}$ can be identified.
In order to verify such findings for cyclic simple shear tests, the specific deviatoric energy has been computed according to eq. (2.12b) and then plotted in the planes: E_s-N_{cyc}-r_u and E_s-N_{cyc}-γ, as reported for some tests in Figure 8.4.
As for cyclic triaxial tests, the maximum gradient of the relationship E_s-N_{cyc} roughly occurs in correspondence of r_u=0.90 and γ_{DA}=3.75%. Moreover, it is independent on the specimen preparation methods. In fact, in Figure 8.4 three tests on GSS specimens prepared by different techniques have been shown: CSS_GSS2F for 1D-compression (Fig. 8.4c-d); CSS_GSS1MT for moist tamping (Fig. 8.4e-f) and CSS_GSS1AP for air pluviation (Fig. 8.4g-h).

Figure 8.4. Results of cyclic simple shear tests in terms of E_s-N_{cyc}-r_u and E_s-N_{cyc}-γ.

Also for cyclic simple shear tests the relationship E_s-N_{cyc} has been compared with the apparent viscosity decay law and with $\Delta\eta/\eta$ versus N_{cyc} (Fig. 8.5) for the same tests already shown in Figure 8.4. Once again the apparent viscosity confirms that the elbow of the curve E_s-N_{cyc} identifies the liquefaction triggering, allowing to pick out $E_{s,liq}$.
The experimental evidences of tests performed on CTX and CSS tests show a similar trend of the dissipated energy with the number of cycles, which can be generalized in Figure 8.6, as reported by Mele et al. (2019a). Furthermore, as mentioned before the specific deviatoric energy to liquefaction ($E_{s,liq}$) can be identified roughly in correspondence of the maximum gradient of the relationship E_s-N_{cyc}.

Figure 8.5. Results of cyclic simple shear tests in terms of E_s-N_{cyc}-η and E_s-N_{cyc}-$\Delta\eta/\eta$.

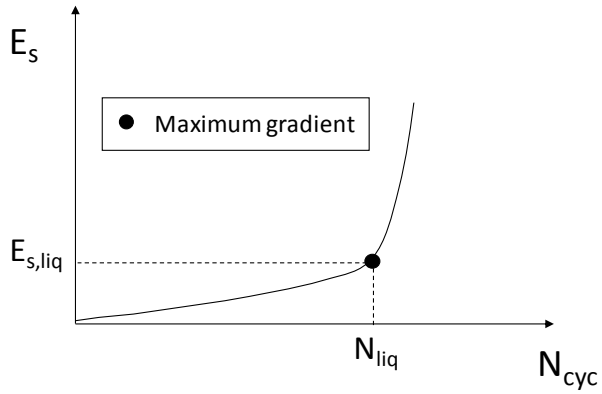

Figure 8.6. General relationship between E_s-N_{cyc} and identification of $E_{s,liq}$ (Mele et al., 2019a).

The results of Figures 8.2 and 8.4 seem to suggest a strong link between E_s and r_u or ε_a for CTX and γ for CSS tests. Owing to that, E_s has been plotted versus r_u and ε_a for some saturated cyclic triaxial tests in Figure 8.7, while in Figure 8.8 E_s has been depicted versus r_u and γ for cyclic simple shear tests.

Figure 8.7. Results of cyclic triaxial tests in the planes: r_u-E_s (a-c-e) and ε_a-E_s (b-d-f).

Figure 8.8. Results of cyclic simple shear tests in the planes: r_u-E_s (a-c-e) and γ-E_s (b-d-f).

As a matter of the fact that stress criterion can be considered the best way to identify liquefaction triggering for saturated soils since it is congruent with the attainment of liquefaction according to viscosity approach, as demonstrated in Chapter 7 and looking at Figures from 8.2 to 8.5, it is possible to evaluate $E_{s,liq}$, from the relationship r_u-E_s, identifying $E_{s,liq}$ which corresponds to r_u=0.90.

8.2.1 FACTORS AFFECTING $E_{S,LIQ}$ AND THE RELATIONSHIP r_u-E_s

In order to investigate the relevance of different state and intrinsic parameters on $E_{s,liq}$, further considerations will be done in the following, where $E_{s,liq}$ has been evaluated for r_u=0.90. Additionally, the strong relationship between E_s and r_u (energetic pore pressure generation law) will be discussed, as well.

8.2.1.1 CONFINING STRESS

First of all, the role that confining stress plays in the calculation of $E_{s,liq}$ has been investigated. To do that the results of cyclic triaxial and simple shear tests consolidated at different stresses have been considered.
Firstly, the CTX tests on Leighton Buzzard and Pieve di Cento (GSS) sands have been analysed (Tab. 5.14 and 6.7). $E_{s,liq}$ has been computed via eq. (2.12a) and plotted versus σ'_c in Figure 8.9a-b, for Leighton Buzzard and GSS sands, respectively.

Figure 8.9. Effect of confining stress on the specific deviatoric energy to liquefaction for cyclic triaxial tests on Leighton Buzzard (a) and Pieve di Cento (GSS) (b) sands.

The dependence of $E_{s,liq}$ on σ'_c results evident. As expected, when the confining stress increases the energy to reach liquefaction has to be higher than that at lower σ'_c.
Regarding the results of cyclic simple shear tests, a mean effective stress (σ'_m) has to be considered and defined as follows:

$$\sigma'_m = \frac{\sigma'_v \cdot (1 + 2 \cdot K_0)}{3} \quad (8.9)$$

Taking into account the effect of k_0, the earth pressure coefficient at-rest.
As for cyclic triaxial tests, the effective stress influences significantly $E_{s,liq}$, according to a linear relationship as shown in Figure 8.10 for Pieve di Cento (GSS) sand.

Figure 8.10. Effect of confining stress on the specific deviatoric energy to liquefaction for cyclic simple shear tests on Pieve di Cento (GSS) sand.

To take rid such dependence, the dimensionless ratio $E_{s,liq}/\sigma'_m$ can be considered, reminding that σ'_m is equal to σ'_c in cyclic triaxial tests, where an isotropic state occurs during the consolidation (k_0=1).
Thereafter, the following considerations will be done moistly on the normalized specific deviatoric energy to liquefaction ($E_{s,liq}/\sigma'_m$).

8.2.1.2 LABORATORY DEVICES

The first important aspect which was analysed is related to the influence of laboratory devices on the normalized specific deviatoric energy to liquefaction. This goal was pursued comparing the results of tests performed on the same sands in similar conditions but by means of different devices (cyclic triaxial and simple shear cells). As a matter of the fact that $E_{s,liq}/\sigma'_m$, is evaluated for r_u=0.90, the results of Pieve di Cento (BSS and GSS) sands carried out in CTX and CSS devices have been interpreted in the plane: E_s/σ'_m – r_u, as reported in Figure 8.11.

Figure 8.11. Normalized specific deviatoric energy versus r_u of CTX and CSS tests on Pieve di Cento, BSS (a) and GSS sands (b).

For both BSS and GSS, cyclic triaxial results have been represented by black lines while those of cyclic simple shear tests by grey lines. First of all, it should be noted that in both cases, regardless of the applied CSR, the curves r_u - E_s/σ'_m overlap each other for the same soil suggesting that roughly a unique relationship r_u - E_s/σ'_m may exist for a soil whatever the CSR is. Additionally, it can be observed that the kind of test (i.e. the stress path) seems to have a minor influence on the relationship between E_s/σ'_m and r_u, even though for GSS (Fig. 8.11b) the dissipated energy in triaxial tests is a little bit higher than that measured in simple shear conditions. However, the values of $E_{s,liq}/\sigma'_m$ (attained for r_u =0.90) are very similar, about 0.007 for CSS and 0.012 for CTX.
Further comparisons have been made on the results of cyclic simple shear tests, taking into account the effect of boundary conditions. The results of cyclic simple shear tests performed on Pieve di Cento (BSS) sand, by means of flexible and rigid boundary have been processed in terms of normalized specific deviatoric energy. It should be emphasised that the configuration with rings does not allow to know the value of k_0, that is why it has been assumed equal to 0.479, congruently with the results of tests achieved through a flexible boundary (Tab. 5.20).
In Figure 8.12 the tests carried out by means of confining rings have been plotted in black, while those performed with confining pressure in grey. Looking carefully at Figure 8.12, it can be noted that the energetic pore generation exhibits a different behaviour. For r_u

ranging from 0 to 0.80, tests with rigid boundary show lower E_s/σ'_m than that of tests performed with a flexible one but thereafter, the curves tend to meet each other attaining a similar value at liquefaction (about 0.006).

Figure 8.12. Comparison between normalized specific deviatoric energy versus r_u in cyclic simple shear tests with confining rings and confining pressure for BSS sand.

Generally speaking, it can be said that the kind of performed test could have an effect on the relationship E_s/σ'_m - r_u and consequently on the value of $E_{s,liq}/\sigma'_m$ but it can be considered negligible, since it ranges in a limited interval. This confirms the experimental evidences of other authors (Dief and Figueroa, 2007; Baziar and Jafarian, 2007).
The results presented in this paragraph highlight that there is no need to study separately the results of CTX and CSS tests, therefore in the following they will be treated together specifying the kind of test performed when needed.

8.2.1.3 SOIL GRADING AND FINES CONTENT

Soil grading may obviously have an effect on the normalized specific deviatoric energy to liquefaction. A simple way to estimate it is to separately analyse the effect of uniformity coefficient $U_c(=D_{60}/D_{10})$ or D_{50} and of fine content (FC). The first comparison can be done for the results obtained on Leighton Buzzard and Ticino sands (Fig. 4.1; Tab. 4.1), which are uniform and clean sands with FC=0 having shapes of the grading curves (U_c=1 and U_c=1.3, respectively) but different values of D_{50} (D_{50}=0.10 and 0.53, respectively).
Plotting together the results of some tests in the plane r_u- E_s/σ'_m, for Leighton Buzzard (Fig. 8.13a) and Ticino (Fig. 8.13b) sands, $E_{s,liq}/\sigma'_m$ can be easily identified for r_u=0.90.

Figure 8.13. Normalized specific deviatoric energy versus r_u for Leighton Buzzard (a) and Ticino (b) sands.

Once again, regardless of the applied CSR the curves r_u - E_s/σ'_m overlap each other for the same soil. It means that for the same soil in a known state, $E_{s,liq}/\sigma'_m$ should be very similar. This has been investigated plotting the values of $E_{s,liq}/\sigma'_m$ versus U_c and D_{50} in Figure 8.14a-b, respectively. As expected, a dependence of $E_{s,liq}/\sigma'_m$ exists on soil grading. In both cases a band can be identified where the upper and lower bounds result parallel.

Figure 8.14. Effect of soil gradings on the specific deviatoric energy to liquefaction (U_c, a and D_{50}, b).

Although a dependence on soil grading seems to exist, the normalized specific deviatoric energy to liquefaction ranges in a limited interval, that is why the effect of fines content (FC) can be evaluated putting together the results of all sandy soils presented in Figure 4.1, whose D_{50} ranges between 0.18 mm (BSS) and 0.30 mm (GSS). In particular, in Figure 8.15, the relationship $E_s/\sigma'_m - r_u$ has been evaluated comparing the results of three kinds of sand: Leighton Buzzard (FC=0%); BSS (FC=8%) and Sant'Agostino (FC=20%) sands.

Figure 8.15. Normalized specific deviatoric energy versus r_u on specimens with different fines content (0<FC(%)<20).

Interestingly, the effect of FC seems to be negligible, in fact not only the curves $E_s/\sigma'_m - r_u$ identify roughly a unique curve but additionally $E_{s,liq}/\sigma'_m$ ranges between a limited interval (0.005 and 0.012).

It is well-known that FC plays an important role in liquefaction resistance and then in pore pressure build-up; owing to that, such interesting aspect deserves to be studied in depth. In order to have a wider range of FC, further tests have been performed on finer bauxite (FC=80%, see Fig. 4.1c and Table 4.1), whose results have been summarized in Table 8.1 together with the values of $E_{s,liq}/\sigma'_m$. Such tests have been carried out in cyclic simple shear apparatus by means of rigid boundary, assuming a value of k_0 equal to 0.45 in computing σ'_m (eq. (8.9)).

Table 8.1. Cyclic simple shear tests on finer bauxite.

Test	Material	σ'_v (kPa)	e_0*	CSR	N_{liq}	$E_{s,liq}$ (J/m^3)	$E_{s,liq}/\sigma'_m$
CSS_BX1R	Finer bauxite	95.0	1.47	0.178	3.5	917.0	0.0152
CSS_BX2R	Finer bauxite	95.9	1.05	0.163	2.5	547.0	0.009
CSS_BX3R	Finer bauxite	296.8	1.13	0.170	3.7	2400.0	0.012
CSS_BX4R	Finer bauxite	94.6	0.921	0.167	2.5	550.0	0.0092
CSS_BX5R	Finer bauxite	97.1	1.16	0.155	3.0	762.0	0.012
CSS_BX6R	Finer bauxite	291.8	1.23	0.180	1.7	1430.0	0.0078

*at the end of consolidation phase.

Figure 8.16. Effect of fines content on the specific deviatoric energy to liquefaction.

Such findings confirm what has been reported by Kokusho (2013). Even though he performed tests in a more limited range of FC (0 – 20%), he concluded that FC does not influence the attainment of $E_{s,liq}/\sigma'_m$.
However, despite the high fines content of finer bauxite, $E_{s,liq}/\sigma'_m$ ranges in a limited interval but, as reported in Chapter 4, the fines content of finer bauxite presents a low plasticity. In order to evaluate the possible effect of plasticity index on $E_{s,liq}/\sigma'_m$, the tests of sand treated with laponite (Tab. 6.1) have been analysed according to an energetic key. The normalized specific deviatoric energy (E_s/σ'_m) from tests on specimens treated with laponite has been computed and plotted versus r_u in Figure 8.17, together with the results of clean sand. The trend of the normalized energetic pore pressure law of sand-laponite with r_u follows that of untreated specimens. Moreover, the value of $E_{s,liq}/\sigma'_m$ results about 0.006 (average value).

Figure 8.17. Relationship between r_u and E_s/σ'_m for treated and untreated specimens.

To sum up, as a matter of the fact that the fines content has a negligible effect on $E_{s,liq}/\sigma'_m$, the results of all sandy soils can be plotted together to confirm the role of U_c and D_{50}, already discussed in this paragraph (Fig. 8.14).
It seems that U_c has a negligible effect on the ratio $E_{s,liq}/\sigma'_m$, in fact such ratio is mostly constant with U_c (Fig. 8.18a), even though it should be confirmed by further tests covering a wider range of uniformity coefficient. On the contrary, the effect of D_{50} is confirmed once again (Fig. 8.18b) where, despite a natural scatter among the experimental data, a linear trend can be identified.

Figure 8.18. Effect of soil gradings on the specific deviatoric energy to liquefaction (U_c, a and D_{50}, b).

8.2.1.4 RELATIVE DENSITY

One of the most important state parameters in sandy soils is the relative density (D_r), whose role played in the normalized specific deviatoric energy will be investigated in this paragraph. The effect of D_r has been analysed by comparing the results of Sant'Agostino and Pieve di Cento (GSS) sands from CTX (Fig. 5.19a-b) tests and of Pieve di Cento (BSS and BSS) sands tested in CSS apparatus (Fig. 8.19c).

Figure 8.19. Normalized specific deviatoric energy versus r_u on specimens with different D_r in cyclic triaxial tests on Sant'Agostino (a) and Pieve di Cento (GSS) (b) sands and in cyclic simple shear tests on Pieve di Cento sands (c).

The results depicted in Figure 8.19 show that the curves E_s/σ'_m -r_u overlap each other, once again indicating that relative density has not measurable effect on the energetic pore pressure generation law. However, plotting the results in the plane: D_r-$E_{s,liq}/\sigma'_m$ makes possible to appreciate the differences in terms of $E_{s,liq}/\sigma'_m$, that exist when D_r changes. It is worth noting that in simple shear tests, such differences are much more relevant than those observed in cyclic triaxial tests.

However, although a dependence of $E_{s,liq}/\sigma'_m$ on D_r could exist, it is not possible to trace a trend. Moreover, the ratio $E_{s,liq}/\sigma'_m$, changes with D_r in a limited range, as shown for FC, too. Owing to that, the influence of D_r will be considered negligible in the following. Once again, such results confirm those that Kokusho (2013) reported in his research. He investigated the behavior of loose and dense specimens ($27<D_r(\%)<76$) in terms of $E_{s,liq}/\sigma'_m$, showing that the influence of D_r on the specific deviatoric energy to liquefaction can be assumed negligible.

Figure 8.20. Effect of relative density on the specific deviatoric energy to liquefaction.

8.2.1.5 SHAPE OF CYCLIC LOADING

The dependence of cyclic loading shape on the specific deviatoric energy required to trigger liquefaction has been examined by Polito et al. (2013), carrying out some cyclic triaxial tests using five different load shapes, including the irregular cyclic loading. They demonstrated that the normalized dissipated energy to cause liquefaction is independent on the shape of loading. In order to confirm such findings, further cyclic simple shear tests have been performed by using four different waveforms: sinusoidal, triangular, rectangular and sawtooth, whose results have been already shown in §5.1.5.4 to analyse their effect on the cyclic resistance curve.

In Figure 8.21, the energetic pore pressure laws of some tests performed with different waveforms are shown. It is evident how the relationships r_u-E_s/σ'_m for triangular and rectangular loading shapes exhibit a higher amplitude than that observed for sinusoidal or sawtooth waveforms, even though this effect could be due to higher CSR for triangular and rectangular waveforms. Furthermore, especially the tests performed by applying the rectangular loading shape show lower E_s/σ'_m till $r_u=0.7$; thereafter, the normalized specific deviatoric energy increases attending at liquefaction a similar value of those observed for different waveforms.

Figure 8.21. Effect of load shape on the relationship r_u-E_s/σ'_m.

To sum up, the value $E_{s,liq}/\sigma'_m$ seems to be independent on the used waveforms, confirming what has been observed by Polito et al. (2013). On the other hand, the trend of the energetic pore pressure law could be affected by the loading shape, especially for r_u lower than 0.70.

8.2.1.6 SPECIMEN PREPARATION METHOD AND UNDISTURBED SPECIMENS

One of the most important aspects which involve the experimental research is how the specimen is reconstituted in laboratory, as abundantly said in Chapter 2. However, the influence of the specimen preparation method on the energetic pore pressure law, has never been discussed. Owing to that, a further insight on the effect of specimen preparation methods has been done in terms of specific deviatoric energy.
Such interesting aspect has been analysed in cyclic simple shear tests, where the effect of three different specimen preparation methods (1D-compression, moist tamping and air pluviation) have been already evaluated in terms of liquefaction resistance (§5.1.5.3).

Figure 8.22. Effect of specimen preparation technique on the relationship r_u-E_s/σ'_m.

Surprisingly, specimens prepared by 1D-compression and moist tamping methods exhibit an evident difference (Fig. 8.22), despite a similar cyclic behaviour (§5.1.5.3). Also the value $E_{s,liq}/\sigma'_m$ is a bit different, it is higher for CSS_GSS2F test (0.0133) than that computed in tests reconstituted by moist tamping (about 0.007). On the other hand, despite a different liquefaction resistance, the energetic pore pressure laws of moist tamping and air pluviation specimens exhibit a similar trend, although $E_{s,liq}/\sigma'_m$ for air pluviation specimens is a bit lower than that observed for moist tamping ones.
In order to better understand the effect of soil fabric on the relationship r_u- E_s/σ'_m and in the value at liquefaction, E_s has been computed for undisturbed specimens too.

Figure 8.23. Effect of fabric effect on the relationship r_u-E_s/σ'_m.

8.2.1.7 POST-LIQUEFACTION

The last aspect which will be discussed is the effect of post liquefaction on the relationship r_u- E_s/σ'_m and on the value $E_{s,liq}/\sigma'_m$. In Chapter 7 it has been demonstrated as the specimens which have experienced liquefaction exhibit a lower liquefaction resistance. Furthermore, it has been also observed that the excess pore water pressure generation was affected by the side toward the "pre-shearing" is applied (triaxial extension or triaxial compression).
In particular, when pre-shearing is applied in extension side, higher pore water pressure is produced by a triaxial compression reloading because of the soil fabric change. It was

shown that in such case, the excess pore pressure model based on the apparent viscosity has been re-calibrated (Fig. 7.37).
To investigate the role that E_s/σ'_m plays in the pore pressure generation of re-consolidated specimens, the energetic pore pressure generation laws of virgin and re-consolidated specimens have been compared and depicted in Figure 8.24.

Figure 8.24. Comparisons between virgin and reconsolidated specimens in terms of r_u-E_s/σ'_m.

Interestingly, looking at Figure 8.24, it can be noted that the energetic pore pressure generation laws of virgin and re-consolidated specimens appear very similar without relevant differences, such as to be considered unique.
These findings demonstrate that even though the excess pore pressure generation is strongly affected by the magnitude of pre-shearing and the side towards the pre-shearing is applied, such influence "disappears" if the specific deviatoric energy is introduced. The traditional or more sophisticated pore pressure generation models need to be recalibrated

for a soil that experienced liquefaction, on the contrary, the energetic pore pressure law does not change for a virgin and a re-consolidated soil.
The experimental results of Figure 8.24, in addition to those shown in the previous paragraph (§8.2.1.6), can be seen as a further confirmation that the fabric effect plays a negligible effect in energetic pore generation law and then on the normalized specific deviatoric energy to liquefaction.

8.2.2 SOIL CAPACITY

The reliability of the obtained results can be proved comparing the values of $E_{s,liq}/\sigma'_m$ of this reasearch work with those reported in literature by other authors as clearly shown in Figure 8.25, where the results of this research are plotted together with the results of cyclic triaxial tests performed by Polito et al. (2013). Despite a scatter among the experimental data, $E_{s,liq}/\sigma'_m$ seems to increase with N_{liq} as indicated by Polito et al. (2013), who explained it with the increase of viscous effect of dissipation when N_{liq} increases.

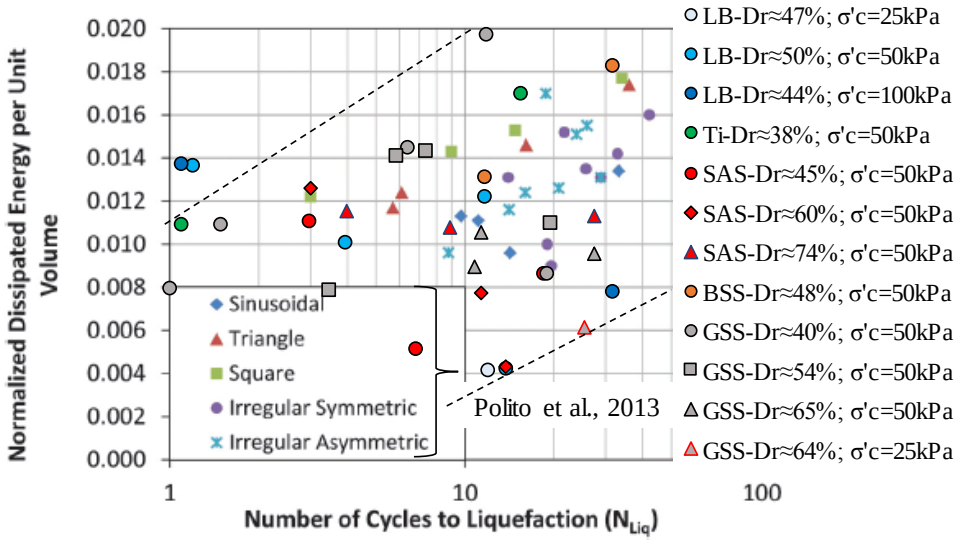

Figure 8.25. Normalized specific deviatoric energy to liquefaction versus the number of cycles at liquefaction of tests shown in this research and compared with those of Polito et at. (2013).

The experimental results of this research highlight that the normalized specific deviatoric energy to liquefaction seems to slightly depend on state and intrisic parameters, with the exception of D_{50}, although, even in such case, $E_{s,liq}/\sigma'_m$ ranges in a limited interval (Fig. 8.18b). All parameters which play an important role in liquefaction resistance, such as state parameters, methods to reconstitute specimens, CSR and the imposed waveforms seems to not have measurable effect on the ratio $E_{s,liq}/\sigma'_m$.
However, Baziar and Jafarian (2007) developed an artificial neural network (ANN) model correlating the state parameters of a soil to $E_{s,liq}$, which represents the energy required to

reach liquefaction and can be defined as the capacity of the soil. It was possible employing a set of data including the results of cyclic triaxial, torsional shear and simple shear tests performed on specimens subjected to different conditions. According to them, the dependence of $E_{s,liq}$ on σ'_m, D_r, FC, U_c and D_{50} can be expressed as (Baziar and Jafarian, 2007):

$$logE_{s,liq} = 2.1028 + 0.004566 \cdot \sigma'_m + 0.005685 \cdot D_r + 0.001821 \cdot FC - 0.02868 \cdot U_c + 2.0214 \cdot D_{50} \quad (8.10)$$

It is worth noting that the coefficients of eq. (8.10) are very low, except for that of D_{50} (2.0214), confirming the results shown in this research, where D_{50} is the only parameter to have a measurable effect on $E_{s,liq}$. Generally speaking, it can be said that the strongest influence of D_{50} on $E_{s,liq}/\sigma'_m$ does not allow to highlight the minor dependence of $E_{s,liq}/\sigma'_m$ on the other investigated parameters, however, a dependence of $E_{s,liq}/\sigma'_m$ on D_r, FC and U_c should exist.

In order to verify eq. (8.10), the experimental data (summarized in Tabs. 8.2 and 8.3) have been plotted in the plan Log(Estimated capacity) versus Log (Measured capacity) (Fig. 8.26a), where the estimated capacity has been evaluated from eq. (8.10), while the measured capacity are those obtained from the saturated tests. To evaluate the error, two bounds have also been plotted: the upper bound is given by measured=1.15·estimated, while the lower one is measured=0.85·estimated, as suggested by Baziar and Jafarian (2007).

It is evident that some experimental data, mainly those related to Ticino and Pieve di Cento (GSS) sands tend to overestimate the capacity of the soil. With the main aim to improve the correlation of Baziar and Jafarian (2007) a new correlation has been proposed in this research, whose expression is reported below:

$$logE_{s,liq} = 1.99 + 0.0080 \cdot \sigma'_m + 0.005685 \cdot D_r + 0.001821 \cdot FC - 0.02868 \cdot U_c + 0.830 \cdot D_{50} \quad (8.11)$$

Where some coefficients – related to confining stress and D_{50} - have been modified to have the best fitting for the experimental results.

In Figure 8.26b the estimated capacity, evaluated according to eq. (8.11), is plotted with the measured capacity highlighting a better agreement with the experimental results than that achieved by eq. (8.10).

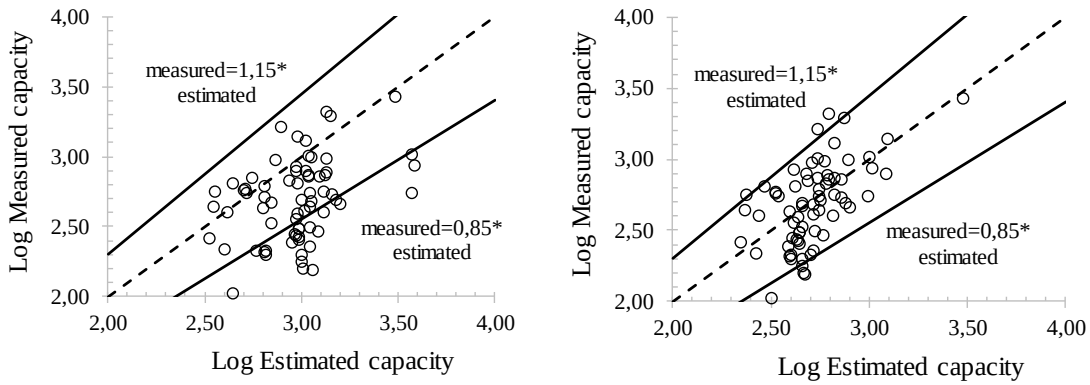

(a) (b)

Figure 8.26. Comparisons between the measured capacity of the experimental results with the estimated one from eq. (8.10, proposed by Baziar and Jafarian (2007) (a) and that estimated from eq. (8.11), proposed in this research (b).

Additionally, the error of the correlations reported in eqs. (8.10) and (8.11) has been computed and shown in Figure 8.27 versus Log (Measured capacity).

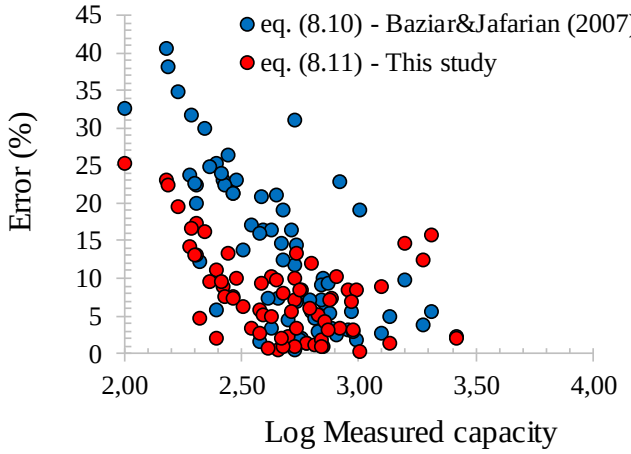

Figure 8.27. Comparison in terms of error between the correlation proposed by Baziar and Jafarian (2007) (eq. (8.10)) and that proposed in this research (eq. (8.11)).

The error by applying eq. (8.10) to the experimental data of this study, reach a value of 40% for lower $E_{s,liq}$, while eq. (8.11) never overcomes an error of 25%. In other words, the correlation proposed in this research seems to be a promising tool to estimate the capacity of the soils. Comparing such value with that of the demand the liquefaction potential of a site can be easily evaluated (§ 2.3.3).

Table 8.2. Results of cyclic triaxial tests in terms of $E_{s,liq}$ and $E_{s,liq}/\sigma'_c$.

Test	Material	σ'_c (kPa)	e_0*	D_{r0}* (%)	CSR	N_{liq}	$E_{s,liq}$ (J/m^3)	$E_{s,liq}/\sigma'_m$
CTX_LB1	LB							
CTX_LB2	LB							
CTX_LB3	LB							
CTX_LB4	LB							
CTX_LB7	LB							
CTX_LB8	LB							
CTX_LB9	LB							
CTX_T1	Ticino							
CTX_T2	Ticino							
CTX_T3	Ticino							
CTX_SAS1	SAS							
CTX_SAS2	SAS							
CTX_SAS3	SAS							
CTX_SAS5	SAS							
CTX_SAS6	SAS							
CTX_SAS7	SAS							
CTX_SAS8	SAS							
CTX_SAS9	SAS							
CTX_SAS10	SAS							
CTX_BSS1	BSS							
CTX_BSS2	BSS							
CTX_BSS2	BSS							
CTX_GSS1	GSS							
CTX_GSS2	GSS							
CTX_GSS3	GSS							
CTX_GSS4	GSS							
CTX_GSS5	GSS							
CTX_GSS6	GSS							
CTX_GSS7	GSS							
CTX_GSS8	GSS							
CTX_GSS9	GSS							
CTX_GSS11	GSS							
CTX_GSS12	GSS							
CTX_GSS13	GSS							
CTX_GSS14	GSS							

*at the end of consolidation phase.

Table 8.3. Results of cyclic simple shear tests in terms of $E_{s,liq}$ and $E_{s,liq}/\sigma'_c$.

Test	Prep. Tech	Boundary	σ'_m (kPa)	D_{r0}* (%)	Wave form	CSR	N_{liq}	$E_{s,liq}$ (J/m^3)	$E_{s,liq}/\sigma'_m$
CSS_BSS1F									
CSS_BSS2F									
CSS_BSS3F									
CSS_BSS1R									
CSS_BSS2R									
CSS_BSS3R									
CSS_BSS4F									
CSS_BSS5F									
CSS_BSS6F									
CSS_GSS1F									
CSS_GSS2F									
CSS_GSS1MT									
CSS_GSS3MT									
CSS_GSS4MT									
CSS_GSS5MT									
CSS_GSS1R									
CSS_GSS2R									
CSS_GSS3R									
CSS_GSS8MT									
CSS_GSS9MT									
CSS_GSS10MT									
CSS_GSS1AP									
CSS_GSS2AP									
CSS_GSS3AP									
CSS_GSS4AP									
CSS_GSS1tri									
CSS_GSS2tri									
CSS_GSS3tri									
CSS_GSS1rect									
CSS_GSS2rect									
CSS_GSS3rect									
CSS_GSS1st									
CSS_GSS2st									
CSS_GSS3st									

*at the end of consolidation phase.

8.2.3 ENERGETIC PORE PRESSURE GENERATION MODEL

The specific deviatoric energy to liquefaction can be used to predict the trend of pore pressure build up, as shown in Chapter 2 (§2.2.2.2), where the main energetic pore pressure generation models have been presented. It has been said that they are extremely promising since the earthquake motion has not to be converted to an equivalent number of uniform cycles and additionally, the relationship r_u-E_s is slightly affected by the intrinsic and state parameters, so that it can be considered independent on such variables. In fact as mentioned before, even though Baziar and Jafarian (2007) proposed a

correlation for $E_{s,liq}$ – and then modified in this research - to take into account the effects of σ'_m, D_r, FC, U_c and D_{50}, the coefficients of the correlation are extremely low (eq. (8.10) or eq. (8.11)). In other words, the specific deviatoric energy to reach liquefaction can be considered unique or at least variable in a limited range.

Based on the results presented in the previous paragraphs, the simple empirical formulation proposed by Berrill and Davis (1985) (eq. (2.13)) has been calibrated to simulate the trend of excess pore pressure ratio, r_u, considering the lower bound of the energetic pore pressure laws.

The parameters α and β of eq. (2.13) has been calibrated on all results of tests reported in Tables 8.2 and 8.3, but for sake of brevity in Figure 8.28a only the energetic pore pressure laws of tests performed on Pieve di Cento (BSS) sand are shown. The calibrated pore pressure model of Berrill and Davis (1985) are represented by a green curve, according to the calibrated values of α and β, equal to 2.00 and 0.18, respectively.

Figure 8.28. Comparison between the calibrated model of Berrill and Davis (1985) and the experimental results (a) and a zoom for lower ru (b).

Apparently, the model seems to fit well the experimental data. However, zooming the experimental curves and the energetic pore pressure generation model for lower r_u (Fig. 8.28b) it can be noted that the model is not able to reproduce the real behaviour of the soil for r_u lower than 0.80 but thereafter, it fits well the experimental data.
In other words, the model proposed by Berrill and Davis (1985) results probably too simple to predict correctly the pore pressure build-up from low to higher r_u, up to liquefaction.
Such limit could be overcome by introducing a new energetic pore pressure law, based on the experimental results of tests performed in this research.
Putting together the experimental relationships r_u- E_s/σ'_m the average curve, which fits better the experimental results is a polynomial function, whose mathematical formulation is:

$$\frac{E_s}{\sigma'_m} = \qquad (8.12)$$

It is worth noting that when r_u is 0.90 the normalized specific deviatoric energy is 0.006.
Eq. (8.12) is plotted in Figure 8.29 together with some experimental results and the model of Berrill and Davis (1985), previously calibrated (α=2.00; β=0.18).
The difference between the simple model of Berrill and Davis (1985) and that proposed in this research (eq. (8.12)) is extremely significant (Fig. 8.29b). Based on the experimental data of this study, eq. (8.12) allows to predict much more correctly the pore pressure build-up, known the specific deviatoric energy, especially for lower r_u.
Such model could result an important and powerful tool for predicting preliminarily the excess pore pressure induced by a seismic event and for assessing the liquefaction potential on site.
Owing to that, eq. (8.12) will be validated by simulating the excess pore pressure ratio measured in centrifuge tests and in real sites, comparing the results with those achieved from dynamic analyses (Chapter 9).

Figure 8.29. Comparison between the proposed energetic pore pressure model (eq. (8.12)) and that of Berrill and Davis (1985) together with the experimental results (a) and a zoom for lower r_u (b).

8.3 ENERGETIC APPROACH FOR NON-SATURATED SOILS

Unlike saturated soil, the total specific energy to reach liquefaction of non-saturated soils includes the volumetric component, as reported in eq. (8.7). In the following the role of $E_{v,liq}$ and $E_{s,liq}$ in non-saturated conditions will be discussed.

8.3.1 THE ROLE OF THE SPECIFIC VOLUMETRIC ENERGY TO LIQUEFACTION, $E_{V,LIQ}$

To better investigate the role of the specific volumetric energy to liquefaction ($E_{v,liq}$), such a variable has been computed for three tested materials (Sant'Agostino, Pieve di Cento (GSS) and silica sands) via eqs. (8.3 to 8.6).

It should be specified that the soil skeleton component ($E_{v,sk,liq}$) can be evaluate by solving the integral of eq. (8.4), whose integration extremes for the volumetric strains have to be assigned. These are 0 and $\varepsilon_{v,liq}$, respectively corresponding to the effective stresses (Bishop's notation) $\sigma'_{un,0}$ and $\sigma'_{un,liq.}$ The latter is the value of the effective stress at liquefaction and is not nil because of the conventional definition of liquefaction (ε_{DA}=5%). It can be calculated as a function of the initial degree of saturation S_{r0} using eq. (6.1a). Known the ratio $\sigma'_{un,0}/\sigma'_{un,liq}$, the ratio $\varepsilon_v/\varepsilon_{v,fin}$ can be evaluated from eq. (6.3) and then, known $\varepsilon_{v,fin}$, the value of ε_v corresponding to liquefaction (ε_{DA}=5%) can be easily computed. Known the integration extremes, the integral of eq. (8.4) can be easily computed as the area subtended to the average curve $\varepsilon_v - \sigma'_{un}$, shown in Figure 6.32b-d-f.

Regarding the water component ($E_{w,liq}$), it is due to the change of water content. Since the small cyclic variations of S_r along the deformation process would make the calculation

cumbersome, a simplification has been introduced in solving eq. (8.5), considering a constant (average) value of s. Such a simplification has no effect, since the variation of s along the tests was always very low.

$E_{air,liq}$ can be easily computed by solving eq. (8.6), reminding that $V_{air,liq}$ is given by the difference between $V_{air,0}$ and the volume change (ΔV), which is related to $\varepsilon_{v,liq}$.

Such three components have been computed for each non-saturated test (Chapter 6, see Tab. 6.14) and reported in Table 8.4 together with the results already published by Mele et al., (2018) on bauxite (coarser) and Inagi sand.

Table 8.4. State properties and energetic components calculated for each test.

Test	Material	σ'_{un} (kPa)	e_0*	S_{r0}* (%)	$E_{v,sk,liq}$ (J/m^3)	$E_{w,liq}$ (J/m^3)	$E_{air,liq}$ (J/m^3)	$E_{v,liq}$ (J/m^3)	$E_{v,liq,ave}$ (J/m^3)
UCTX_SAS1	SAS	49.5	0.71	53.0	1700	0	574	2274	
UCTX_SAS2	SAS	50.5	0.67	54.0	1700	-40.0	572	2232	2280
UCTX_SAS3	SAS	48.9	0.67	56.0	1700	-20.0	654	2334	
UCTX_SAS4	SAS	50.5	0.61	90.0	1095	0	106	1201	
UCTX_SAS5	SAS	49.8	0.60	81.5	1095	0	210	1305	
UCTX_SAS6	SAS	49.8	0.59	87.2	1095	0	54	1149	1192
UCTX_SAS7	SAS	49.9	0.58	86.7	1095	0	13	1232	
UCTX_SAS8	SAS	48.8	0.59	87.6	1095	0	49	1144	
UCTX_SAS9	SAS	50.4	0.61	88.5	1095	0	27	1122	
U_BA1	Bauxite	51.9	0.91	58.0	2347	-138	1070	3279	
U_BA2	Bauxite	56.3	0.92	56.0	2347	-167	991	3172	3087
U_BA3	Bauxite	51.8	0.94	56.0	2347	-109	572	2811	
U_BA4	Bauxite	47.4	0.76	84.0	933	106	145	1185	1200
U_BA5	Bauxite	48.4	0.75	85.0	933	127	156	1215	
U_IN1	Inagi	62.2	1.20	49.0	3452	-581	1141	4012	
U_IN2	Inagi	64.2	1.22	48.0	3452	-655	1323	4120	4035
U_IN3	Inagi	62.3	1.14	52.0	3452	-661	1182	3973	
UCTX_GSS1	PdC_GSS								
UCTX_GSS2	PdC_GSS								
UCTX_GSS3	PdC_GSS								
UCTX_GSS4	PdC_GSS								
UCTX_GSS5	PdC_GSS								
UCTX_GSS6	PdC_GSS								
UCTX_GSS7	PdC_GSS								
UCTX_GSS8	PdC_GSS								
UCTX_GSS9	PdC_GSS								
UCTX_GSS10	PdC_GSS								
UCTX_GSS11	PdC_GSS								
UCTX_GSS12	PdC_GSS								
UCTX_GSS13	PdC_GSS								
UCTX_GSS14	PdC_GSS								
UCTX_SS1	SS5								
UCTX_SS2	SS5								

*at the end of consolidation phase.

The volumetric specific energy $E_{v,liq}$ (from eq. (8.3) to (8.6)) is a function of the initial values of the effective confining stress (Bishop notation), of the void ratio and of the degree of saturation ($E_{v,liq}=E_{v,liq}(\sigma'_0, e_0, Sr_0)$), and increases - from zero for saturated soils- as S_r decreases. In this sense, $E_{v,liq}$ may be seen as a synthetic state variable ruling the increment of liquefaction resistance of sands (at low confining stresses) from CRR_s (S_r=100%) to CRR_{un} (S_r<100%).

In order to verify such a conclusion, the ratio of the average value of the specific volumetric energy ($E_{v,liq}$), reported in Table 8.4 and the atmospheric pressure (p_a), has been plotted versus the ΔCRR calculated at N_{liq}=15, as the difference between the CRR_{un} and CRR_s. In particular, such difference has been calculated for the experimental data of cyclic triaxial tests ($\Delta CRR^{ctx}=CRR_{un}{}^{ctx}-CRR_s{}^{ctx}$) and correcting them through Castro's correlation (eq.(2.7)) ($\Delta CRR^{css}=CRR_{un}{}^{css}-CRR_s{}^{css}$), because in design issues the liquefaction resistance in simple shear conditions (CRR^{css}) is needed. As well known, in eq. (2.8) k_0 is the coefficient of earth pressure at rest, that can be evaluated as $k_0=1-\sin\varphi_p$, where φ_p is the peak friction angle. Mele and Flora (2019) assumed a φ_p of 35° for Inagi sand and 36° for bauxite, estimated basing on their gradings and mineralogies. In this research the values of φ_p for Sant'Agostino and Pieve di Cento (GSS) sand were experimentally measured. It should be specified that variations of φ_p have a minor effect on the correction factor (c_r) proposed by Castro (1975), so this assumption does not have any significant quantitative effect, thus being acceptable.

In Figure 8.30a ΔCRR^{ctx} is plotted versus $E_{v,liq}/p_a$ for the tested sands, while in Figure 8.30b ΔCRR^{css} versus $E_{v,liq}/p_a$ is depicted. The atmospheric pressure p_a (98.1 kPa) has been introduced to make the relationship ΔCRR - $E_{v,liq}/p_a$ non-dimensional.

Figure 8.30. Ratio between unsaturated and saturated liquefaction resistance at N_{liq}=15 for $\Delta CRR_{,15}{}^{ctx}$ (a) and $\Delta CRR_{,15}{}^{css}$ (b) versus $E_{v,liq}/p_a$.

A clear relationship between ΔCRR^{ctx} (or ΔCRR^{css}) and $E_{v,liq}$ is observed for all the tested initial state conditions, confirming that an increase in the specific volumetric energy spent to liquefaction corresponds to an increase in liquefaction resistance with a rate that seems to reduce as $E_{v,liq}$ increases. Based on the experimental results reported in Figure 8.30, the relationships between $E_{v,liq}$ and $\Delta CRR_{,Nliq}{}^{ctx}$ and $\Delta CRR_{,Nliq}{}^{css}$ (for N_{liq}=15) can be expressed as:

$$\Delta CRR_{N_{liq}}^{ctx} = -94.67 \cdot \left(\frac{E_{v.liq}}{p_a}\right)^2 + 9.88 \cdot \frac{E_{v,liq}}{p_a} \qquad (8.13a)$$

$$\Delta CRR_{N_{liq}}^{css} = -73.47 \cdot \left(\frac{E_{v.liq}}{p_a}\right)^2 + 7.17 \cdot \frac{E_{v,liq}}{p_a} \qquad (8.13b)$$

The two correlation represent the best fit for the experimental results, and although an experimental point relative to Pieve di Cento (GSS) sand (Sr≈47%) is a bit far from the average curve, the regression coefficient is 0.83 and 0.80 for eqs. (8.13a) and (8.13b), respectively.

Figure 8.31a for triaxial tests, and Figure 8.31b for corrected experimental data in simple shear conditions, indicate that, in the range of N_{liq} of practical interest (N_{liq}≤20), the validity of eqs. (8.13a) – (8.13b) can be extended to all values of N_{liq}: ΔCRR^{ctx} does not depend on N_{liq} but only on $E_{v,liq}$. In other words, for N_{liq}≤20, ΔCRR can be univocally related to $E_{v,liq}$, and therefore desaturation leads to a simple translation towards higher values of CRR of the liquefaction resistance curve, without appreciable change in shape.

Figure 8.31. ΔCRR^{ctx} versus N_{liq} (a); ΔCRR^{css} versus N_{liq} (b).

8.3.1.1 THE SPECIFIC VOLUMETRIC ENERGY TO LIQUEFACTION IN RE-CONSOLIDATED SPECIMENS

In Chapter 7 the results of non-saturated tests on re-consolidated specimens subjected to a new cyclic loading have been shown. In Figure 7.44 σ'_{un} - ε_v plots of virgin and re-consolidated specimens have been compared. The curves overlap each other showing no remarkable differences between the specific volumetric energy to liquefaction of soil skeleton ($E_{v,sk,liq}$) of virgin and re-consolidated specimens.

In Table 8.5 the volumetric energy components of the first and second liquefaction have been summarized.

Table 8.5. Volumetric energy components of first and second liquefaction.

Test	σ'_{un} (kPa)	First Liq					Second Liq			
		S_{r0}* (%)	$E_{v,sk,liq}$ (J/m^3)	$E_{w,liq}$ (J/m^3)	$E_{air,liq}$ (J/m^3)	$E_{v,liq}$ (J/m^3)	$E_{v,sk,liq}$ (J/m^3)	$E_{w,liq}$ (J/m^3)	$E_{air,liq}$ (J/m^3)	$E_{v,liq}$ (J/m^3)
UCTX_GSS6										
UCTX_GSS7										
UCTX_GSS8										
UCTX_GSS10										
UCTX_GSS11										
UCTX_GSS13										

*at the end of consolidation phase.

As expected, the component $E_{v,sk,liq}$ of the specific volumetric energy to liquefaction remains approximately constant, such as $E_{air,liq}$ even though some differences have been noted, while $E_{w,liq}$ is nil because no suction has been measured. Overall, the specific volumetric energy to liquefaction ($E_{v,liq}$) relative to the second liquefaction is a bit lower than that computed for the first liquefaction. Furthermore, the post-liquefied tests consolidated at 50 kPa show similar value of $E_{v,liq}$, consequently such experimental points identify a unique cyclic resistance curve as depicted in Figure 8.32. On the other hand, the tests consolidated at 25 kPa exhibits a lower liquefaction resistance, to which corresponds a $E_{v,liq}$ of 353 J/m^3 (Tab. 8.5).

As shown in Table 7.7, the re-consolidated specimens with a σ'_{un} of 50 kPa present a similar state condition (σ'_{un}; e and S_r), and then, for that said above, $E_{v,liq}$ can only be the same for such tests. In other words, the same $E_{v,liq}$ relative to a similar state condition, also for re-consolidated soils, has to necessarily identify the same cyclic resistance curve achieved by incrementing the CRR of saturated tests of a fixed ΔCRR connected to $E_{v,liq}$ as shown for virgin soils in Figure 8.30a (eq. (8.13a)). However, being unknown the cyclic resistance curve of saturated soils at the same conditions of the non-saturated re-consolidated specimens, it has not been possible to verify eq. (8.13a), so that further tests will be performed to confirm the reliability of such equation for soils which have already experienced liquefaction.

Figure 8.32. Post-liquefaction cyclic resistance curve identified by $E_{v,liq}$.

8.3.2 THE ROLE OF THE SPECIFIC DEVIATORIC ENERGY TO LIQUEFACTION, $E_{S,LIQ}$

As mentioned above for saturated sandy soils, the specific deviatoric energy to liquefaction $E_{s,liq}$ can be evaluated from eq. (2.12a) for CTX tests and eq. (2.12b) for CSS tests. For some of the non-saturated cyclic triaxial tests, the current specific deviatoric energy E_s has been evaluated along the whole path to liquefaction and after (Fig. 8.33) to show its evolution.

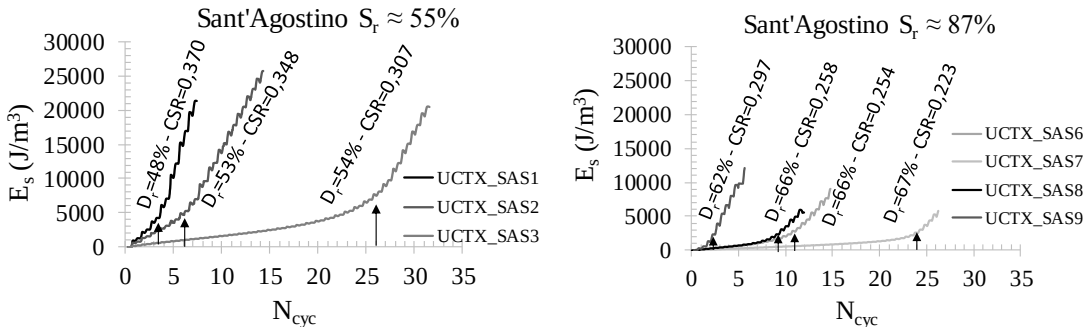

(a) σ'_{un}=50 kPa (b) σ'_{un}=50 kPa

Figure 8.33. E_s versus N_{cyc} along the cyclic undrained tests of non-saturated tests on Sant'Agostino sand (a-b); Pieve di Cento (GSS) sand (c-d-e) and silica sand N°5 (f). Liquefaction triggering is indicated by the vertical arrows.

As for saturated tests, the figures indicate that in the first cycles the relationship N_{cyc} - E_s is roughly linear with a slope which depends on the applied CSR and on soil state. This means that, for each test, the specific deviatoric energy spent in each of these first cycles

is roughly the same, i.e. no significant change in the shape of each of them is taking place. Approaching liquefaction, shear strains and damping sharply increase and so does E_s. The onset of liquefaction ($N_{cyc}=N_{liq}$, $E_s=E_{s,liq}$, as conventionally evaluated for $\varepsilon_{DA}=5\%$ and indicated with vertical arrows in Figure 8.33) corresponds to the highest gradient in the N_{cyc} - E_s plot for all tests. As for saturated tests, specific deviatoric energy results a valid liquefaction triggering criterion. It is confirmed by plotting E_s-N_{cyc}-η and E_s-N_{cyc}-$\Delta\eta/\eta$ in Figure 8.34. The maximum gradient of the relationship E_s – N_{cyc}, corresponds to the change state from solid to liquid, as clearly observed in the plane E_s-N_{cyc}-$\Delta\eta/\eta$, where the maximum of the ratio $\Delta\eta/\eta$ is attained in correspondence of the maximum gradient of N_{cyc} - E_s curve.

Generally speaking, as for saturated soils $E_{s,liq}$ can be evaluated in correspondence of the maximum gradient of the relationship E_s – $N_{cyc,}$ as shown in the scheme of Figure 8.6.

Figure 8.34. Results of cyclic triaxial tests in terms of E_s-N_{cyc}-η and E_s-N_{cyc}-$\Delta\eta/\eta$ for non-saturated specimens.

In Table 8.6 the specific deviatoric energy to liquefaction has been summarized for each non-saturated test together with the volumetric energetic components (§8.3.1).
Looking carefully at the value of $E_{s,liq}$ summarized in Table 8.6, and comparing such values with those of saturated soils in Table 8.2, it can be noted that the degree of saturation plays an important role in identifying the specific deviatoric energy to liquefaction. In §8.2.1 some factors have been analysed to better understand the parameters on which $E_{s,liq}$ depends for saturated soils. In this paragraph additionally, the role of S_r will be investigated.
In Figure 8.35a-c, E_s/σ'_{un} of Sant'Agostino and Pieve di Cento (GSS) sands, respectively has been plotted versus N_{cyc}/N_{liq}, where N_{liq} was evaluated according to strain criterion (Fig. 7.25). Such dependence has been quantified introducing S_r through a function $k(S_r)$, whose expression is reported below:

(8.14)

It is worth noting that in saturated conditions S_r is obviously 1, therefore $k(S_r)$ is equal to 1. In other words, by applying this scale function, the relationship between the normalized specific deviatoric energy and ratio N_{cyc}/N_{liq} can be generalized for saturated and non-saturated soils.

Table 8.6. State properties and energetic components calculated for each test.

Test	Material	σ'_{un} (kPa)	e_0*	S_{r0}* (%)	$E_{v,sk,liq}$ (J/m^3)	$E_{w,liq}$ (J/m^3)	$E_{air,liq}$ (J/m^3)	$E_{v,liq}$ (J/m^3)	$E_{v,liq,av}$ (J/m^3)	$E_{s,liq}$ (J/m^3)
UCTX_SAS1	SAS	49.5	0.71	53.0	1700	0	574	2274		4257
UCTX_SAS2	SAS	50.5	0.67	54.0	1700	-40.0	572	2232	2280	4721
UCTX_SAS3	SAS	48.9	0.67	56.0	1700	-20.0	654	2334		7534
UCTX_SAS4	SAS	50.5	0.61	90.0	1095	0	106	1201		3545
UCTX_SAS5	SAS	49.8	0.60	81.5	1095	0	210	1305		7042
UCTX_SAS6	SAS	49.8	0.59	87.2	1095	0	54	1149	1192	3267
UCTX_SAS7	SAS	49.9	0.58	86.7	1095	0	13	1232		3043
UCTX_SAS8	SAS	48.8	0.59	87.6	1095	0	49	1144		2486
UCTX_SAS9	SAS	50.4	0.61	88.5	1095	0	27	1122		1427
U_BA1	Bauxite	51.9	0.91	58.0	2347	-138	1070	3279		21638
U_BA2	Bauxite	56.3	0.92	56.0	2347	-167	991	3172	3087	13308
U_BA3	Bauxite	51.8	0.94	56.0	2347	-109	572	2811		7987
U_BA4	Bauxite	47.4	0.76	84.0	933	106	145	1185	1200	1417
U_BA5	Bauxite	48.4	0.75	85.0	933	127	156	1215		3622
U_IN1	Inagi	62.2	1.20	49.0	3452	-581	1141	4012		14492
U_IN2	Inagi	64.2	1.22	48.0	3452	-655	1323	4120	4035	15902
U_IN3	Inagi	62.3	1.14	52.0	3452	-661	1182	3973		10306
UCTX_GSS1	PdC_GSS									
UCTX_GSS2	PdC_GSS									
UCTX_GSS3	PdC_GSS									
UCTX_GSS4	PdC_GSS									
UCTX_GSS5	PdC_GSS									
UCTX_GSS6	PdC_GSS									
UCTX_GSS7	PdC_GSS									
UCTX_GSS8	PdC_GSS									
UCTX_GSS9	PdC_GSS									
UCTX_GSS10	PdC_GSS									
UCTX_GSS11	PdC_GSS									
UCTX_GSS12	PdC_GSS									
UCTX_GSS13	PdC_GSS									
UCTX_GSS14	PdC_GSS									
UCTX_SS1	SS5									
UCTX_SS2	SS5									

*at the end of consolidation phase.

It should be specified that, eq. (8.14) is not defined for two S_r values (0.319 and 1.02), therefore it can be assumed valid in the range $0.32 \leq S_r \leq 1.00$.

In Figure 8.35b-d the values of $E_s/\sigma'_{un} \cdot k(S_r)$ for Sant'Agostino and Pieve di Cento (GSS) sands, respectively are plotted versus N_{cyc}/N_{liq}. The value of normalized specific deviatoric energy to liquefaction corrected by $k(S_r)$ ranges between 0.004 and 0.009 for Sant'Agostino sand and 0.006 and 0.012 for Pieve di Cento (GSS) sand, confirming that the range of values at liquefaction is extremely small and independent on several state parameter that generally influence the resistance to liquefaction. This is an interesting aspect of the energetic methods. In fact, a critical value of $E_{s,liq} \cdot k(S_r)/\sigma'_{un}$ can be used in site response analysis, not only in saturated conditions but also in unsaturated ones, for

example for soils over the ground water table or to evaluate the susceptibility of a soil deposit after an intervention of desaturation to mitigate liquefaction risk.

Figure 8.35. Dissipated energy for saturated and unsaturated tests plotted in the plane N/N_{liq} versus E_s/σ'_m (a-c) and $E_s/\sigma'_m \cdot k(S_r)$ (b-d).

Apart from S_r, $E_{s,liq}$ depends on the applied cyclic stress (CSR) and on the number of cycles to liquefaction (N_{liq}), contrary to $E_{v,liq}$. In fact, Figure 8.35 also indicate that the values of $E_{s,liq}$ increase as the degree of saturation decreases and as the applied cyclic stress CSR decreases.

Figure 8.36a reports the same experimental results in the $E_{s,liq}$ - CRR^{ctx} plane, confirming that the value of CRR attained in each test, for each soil and initial state, is uniquely related to $E_{s,liq}$. Since state conditions of non-saturated soils during cycling tests are well represented by $E_{v,liq}$, a much more general interpretation can be obtained by plotting the experimental data in the normalized plot in Figure 8.36b, in which a unique, non-linear relationship links $E_{s,liq}$ to the term $(CRR^{ctx} \cdot (1\text{-}5 \cdot E_{v,liq}/p_a)^{10})$, where the exponent has been calibrated to obtain the best fitting for the experimental data with the equation (Mele and Flora, 2019):

$$E_{s,liq} = 0.297 \cdot p_a \cdot e^{-16.7 \cdot CRR^{ctx} \cdot \left(1-5 \cdot \frac{E_{v,liq}}{p_a}\right)^{10}} \qquad (8.15a)$$

Similarly, considering the cyclic resistance ratios in simple shear conditions (eq. (2.7)) the best fit relationship is found as (Mele and Flora, 2019):

$$E_{s,liq} = 0.300 \cdot p_a \cdot e^{-23.7 \cdot CRR^{css} \cdot \left(1 - 5 \cdot \frac{E_{v,liq}}{p_a}\right)^{10}} \qquad (8.15b)$$

Summing up all the experimental evidences, it may be concluded that - for a given soil - $E_{v,liq}$ represents the state variable defining the modification of position (increase of resistance) of the liquefaction curve due to unsaturation (Fig. 8.30), while $E_{s,liq}$ is the energetic variable that, given the value of $E_{v,liq}$, defines the cyclic resistance CRR (and therefore also the number of cycles to liquefaction N_{liq}).

Figure 8.36. CRR^{ctx} vs $E_{s,liq}$ (a); $CRR^{ctx}\cdot(1-5\cdot E_{v,liq})^{10}$ vs $E_{s,liq}$ (b); Cyclic triaxial and corrected triaxial data (Castro correlation) in the plane $CRR\cdot(1-5\cdot E_{v,liq})^{10}$ vs $E_{s,liq}$ (c).

8.3.2.1 ENERGETIC PORE PRESSURE BUILD-UP

As for saturated soils, the strong correlation between the pore pressure and specific deviatoric energy to liquefaction has been investigated for non-saturated soils, too.
In Figure 8.37a-c, some test results on saturated and non-saturated soils from Sant'Agostino and Pieve di Cento, respectively, are plotted in the plane r_u-E_s/σ'_m.
It can be observed that the relationship r_u-E_s/σ'_m is strongly dependent on S_r, confirming what has been said in §8.3.2 and depicted in Figure 8.35a-c.
With the main aim to find a general relationship r_u-E_s/σ'_m valid for saturated and non-saturated soils, the same tests reported in Figure 8.37a-c have been reported in the plane $r_u/r_{u,liq} - E_s/\sigma'_m\cdot k(S_r)$, where $r_{u,liq}$ is the value of r_u at liquefaction defined according to stress criterion, while $k(S_r)$ is defined in eq. (8.14).
The results are shown in Figure 8.37b-d. Regardless of the soil, the curves overlap each other so that it is possible to generalize the energetic pore pressure generation model for saturated and non-saturated soils according to such equation:

$$\frac{E_s}{\sigma'_m}\cdot k(S_r) = \qquad (8.16)$$

For saturated soils ($r_{u,liq}$=0.90 and $k(S_r)$=1) eq. (8.16) is equal to eq. (8.12).
Eq. (8.16) can be used as a general law to predict the trend of excess pore pressure ratio of saturated and non-saturated soils, known the normalized specific deviatoric energy.

Figure 8.37. Normalized specific deviatoric energy versus r_u in saturated and unsaturated tests for Sant'Agostino (a) and Pieve di Cento (b) sands.

8.3.2.2 THE SPECIFIC DEVIATORIC ENERGY TO LIQUEFACTION IN RE-CONSOLIDATED SPECIMENS

As for saturated soils, the energetic pore pressure build-up of virgin and re-consolidated non-saturated specimens have been compared.

For saturated soils the energetic pore pressure build-up of virgin and re-consolidated specimens have been compared in §8.2.1.7. It was demonstrated that, although the excess pore pressure generation of soils which have experienced liquefaction can be different, depending on the side of the applied "pre-shearing", the relationship $E_{s,liq}/\sigma'_m - r_u$ does not exhibit measurable differences from first to second liquefaction occurrence. In other words, contrarily to the other excess pore generation models, eq. (8.12) does not need to be re-calibrated, so that such model results extremely advantageous.

In order to confirm those new findings for non-saturated soils the results of some tests have been plotted in Figure 8.38, where the relationship $E_{s,liq}/\sigma'_m - r_u$ of virgin non-saturated specimens has been compared with that of re-consolidated ones.

Unlike saturated soils, the comment to Figure 8.38 cannot be unique. It is possible to notice that for some tests the curves relative to the first and second liquefaction are exactly overlapping (see, for instance Fig. 8.38a-d-e). On the contrary, some differences can be noted comparing UCTX_GSS10 and UCTX_GSS10_PL tests (Fig. 8.38c) and a significant discrepancy can be observed for UCTX_GSS8 and UCTX_GSS8_PL tests (Fig. 8.38b). In such case, the curves appear different from small r_u (about 0.30) to

r_u=0.90. This could be due to a difference in terms of $E_{v,liq}$ as shown in Table 8.5. Unlike the other tests, where $E_{v,liq}$ seems to be maintained roughly constant, for UCTX_GSS8 test $E_{v,liq}$ passes from 1518 J/m^3 to 1269 J/m^3 (UCTX_GSS8_PL test) and as well-known $E_{s,liq}$ is strongly dependent on the state of soil represented by $E_{v,liq}$ (see, for instance eq. (8.15) and Fig. 8.36b).

It is expected that the relationship $E_{s,liq}/\sigma'_m - r_u$ could be generalized for virgin and re-consolidated specimens by introducing the parameter $E_{v,liq}$ and thus further studies and considerations will be done to better clarify such aspect.

Figure 8.38. Comparisons between virgin and re-consolidated non-saturated specimens in the plane E_s/σ'_{un} versus r_u.

8.3.3 THE TOTAL SPECIFIC ENERGY TO LIQUEFACTION ($E_{TOT,LIQ}$) AND THE NORMALIZED CYCLIC RESISTANCE CURVE

In the attempt to find a relationship between the specific energy spent to liquefaction and the cyclic resistance ratio CRR, Mele et al. (2018) proposed a relationship between $CRR/(E_{v,liq})^{0.5}$ and N_{liq}. Later, based on the above reported evidences, the contribution of the specific deviatoric energy was also accounted for by Mele and Flora (2019), reporting the experimental results in the plane $CRR^{ctx}/(1+E_{tot,liq}/p_a)^6$ versus N_{liq} (Fig. 8.39a), where $E_{tot,liq}$ is the sum of the volumetric and the deviatoric energies spent to liquefaction (eq. (8.7)). In Figure 8.39a the experimental data of Pieve di Cento and silica (N°5) sands have been added, confirming the relationship proposed by Mele and Flora (2019).
In Figure 8.39b the normalized cyclic resistance curve of the triaxial data (CTX) are compared with those corrected (CSS) through Castro correlation (eq. (2.7)).

Figure 8.39. Normalized cyclic resistance curve for cyclic triaxial tests (a); Normalized cyclic resistance curves for cyclic triaxial and corrected data (Castro correlation) (b).

The best fitting for the experimental results in Figure 8.39a is (Mele and Flora, 2019):

$$\frac{CRR^{ctx}}{\left(1+\frac{E_{tot,liq}}{p_a}\right)^6} = -0.039 \cdot \ln\left(N_{liq}\right) + 0.285 \qquad (8.17a)$$

Which can be transformed for simple shear conditions (eq. (2.7)) as (Mele and Flora, 2019):

$$\frac{CRR^{css}}{\left(1+\frac{E_{tot,liq}}{p_a}\right)^6} = -0.028 \cdot \ln\left(N_{liq}\right) + 0.202 \qquad (8.17b)$$

Eqs. (8.17) assume that whole the considered experimental results may be analysed together, thus implicitly assuming that the only influent parameter to quantify the liquefaction resistance curve is the total energy. This is true only if there is no other relevant effect, like for instance for soil grading. Actually, the experimental results reported in Figure 8.39a seem to indicate that such a dependency may exist, as the finer soil results (Inagi) fall in the lower part of the graph, while Pieve di Cento sand (GSS) with a higher D_{50} seems to lie on the upper one. However, the quantity of the experimental results is not sufficient to introduce explicitly such a dependency. With this limitation, eqs. (8.17) may be seen as a synthetic way to express the cyclic resistance of non-saturated fine sands accounting for the specific total energy spent to liquefy ($E_{tot,liq}$). The use of the total specific energy allows to plot the CRR-N_{liq} curve of non-saturated soils without knowing the one in saturated conditions, while by using only the specific volumetric component of the energy (eqs. 8.13) the latter is needed.

Eq. (8.17a) has been calibrated on experimental data having a limited range of confining stresses (25 – 60 kPa). Other tests must be carried out to confirm the validity of eq. (8.17a) (and eq. (8.17b)) out of the tested ranges of state properties, and to check its possible dependency on grain size distribution within the broad family of fine sands. However, it has to be emphasized again that liquefaction occurs in loose sand (low D_r) and at shallow depths (low confining stresses). Therefore, even though the curve of Figure 8.39b (eq. 8.17b) cannot be intended as a general law for all possible soil states, it may be useful to predict the effects of induced partial saturation in the conditions of maximum practical interest on site.

In the following, the consistency of the two possible approaches will be tested on independent literature data.

8.3.4 PROCEDURES TO EVALUATE THE LIQUEFACTION RESISTANCE OF NON-SATURATED SOILS ON SITE

The experimental evidences of the role played by the energetic components $E_{v,liq}$ and $E_{s,liq}$ allow to propose two simple and straightforward approaches, defined approach 1 and approach 2, to plot the liquefaction resistance curve of non-saturated soil on site (in simple shear conditions) for a given material and initial state (σ'_{un0}, e_0, S_{r0}). Although the parameters of the equations proposed in this research work have been calibrated on low confining pressures, the models hereafter presented will aim to simulate the cyclic resistance curves of non-saturated soil under such and different conditions.
Approach 1 consists of scaling the saturated cyclic resistance curve of a soil in fixed conditions of a quantity (ΔCRR) defined by $E_{v,liq}$ (eq. (8.13b)).
Conversely, approach 2 is based on the total specific energy to reach liquefaction. According to it, the cyclic resistance curve of a non-saturated soil in a fixed state ($E_{v,liq}$) can be simulated through the eq. (8.17b).
In both the approaches, the energetic components have to be computed.
The steps to calculate the two components $E_{v,liq}$ and $E_{s,liq}$ are the following:

Calculation of the volumetric specific energy

1. Once the initial stress state, void ratio and saturation degree (σ'_{un0}, e_0, S_{r0}) are known, from eq. (6.2) the final volumetric deformation of the soil, $\varepsilon_{v,fin}$ can be calculated.

2. Known $\varepsilon_{v,fin}$, the regression curve reported in Figure 6.33 (eq. (6.3)) allows to obtain the analytical relationship σ'_{un} - ε_v along the cycling loading path for the specific considered case. In order to calculate the component of the specific volumetric energy related to soil skeleton deformation $E_{v,sk,liq}$ (eq. (8.4)), the integration extremes for the volumetric strains have to be known. As mentioned above, $\varepsilon_{v,liq}$ corresponds to $\sigma'_{un,liq}$, which can be found from eq. (6.1a) once $\sigma'_{un,0}$ and S_{r0} are known. The volumetric strain at liquefaction $\varepsilon_{v,liq}$ can be finally calculated using eq. (6.3).

3. Known the water retention curve (relationship between the degree of saturation S_r and suction s), eq. (8.5) allows to calculate $E_{w,liq}$. Again, the integration extremes have to be assigned. Based on the experimental evidences reported by Mele et al. (2018), the value of the degree of saturation at liquefaction $S_{r,liq}$ can be simply assigned as $S_{r,liq}=S_{r,0}+0.08$.

4. The volumetric specific energetic component of air flow to liquefaction ($E_{air,liq}$, eq. (8.6)) can be calculated using the regression curve of Figure 6.32: once the state at liquefaction is known in terms of effective stress $\sigma'_{un,liq}$ (Bishop's notation) as indicated at step 2, the corresponding value of air pressure can be calculated, from the eq. (8.18) because σ_{liq}, $S_{r,liq}$ and $s_{,liq}$ are known.

$$u_{a,liq} = \left(\sigma_{liq} - \sigma'_{un,liq}\right) + S_{r,liq} \cdot s_{liq} \quad (8.18)$$

Similarly, since $\varepsilon_{v,liq}$ is known, the value of $V_{air,liq}$ can be calculated.

5. The total volumetric component of the specific energy $E_{v,liq}$ can be then computed using eq. (8.3), based on what has been obtained in the steps from 1 to 4.

Calculation of the deviatoric and total specific energy

6. Since $E_{v,liq}$ is known, once the cyclic stress CSR (expected earthquake) is assigned, $E_{s,liq}$ can be calculated from eq. (8.15b) (Fig. 8.36c).
7. $E_{tot,liq}$ can be easily calculated as the sum of the two components ($E_{tot,liq}=E_{v,liq}+E_{s,liq}$).

To use approach 1 (based on only $E_{v,liq}$), it is necessary to know the cyclic resistance curve in saturated conditions (CRR_s^{css}-N_{liq}) and the soil water retention curve to calculate $E_{v,liq}$ (steps 1 to 5) and therefore ΔCRR^{css} (eq. 813b, Fig. 8.30b). Then, the cyclic resistance curve in non-saturated conditions can be obtained by adding ΔCRR^{css} to CRR_s^{css}:

$$CRR_{un}^{CSS}(N_{liq}) = CRR_s^{CSS}(N_{liq}) + \Delta CRR^{CSS} \quad (8.19)$$

To use approach 2 (based on $E_{tot,liq}$), the knowledge of the saturated liquefaction resistance curve is not needed, but the deviatoric specific energy has to be calculated and added to the volumetric one to obtain the total specific energy (steps 6 and 7). Using the correlation (eq. 8.17b) between $CRR^{css}/(1+E_{tot,liq}/p_a)^6$ and N_{liq}, assuming $CSR=CRR^{css}$, the corresponding value of N_{liq} is obtained. By repeating the procedure from step 1 to 8 for different values of CRR, the cyclic resistance curve for cyclic simple shear condition can be finally obtained with approach 2.

8.3.4.1 APPLICATION OF APPROACHES 1 AND 2 TO LITERATURE DATA

In order to check the consistency of the previously exposed procedures, the two approaches have been applied to estimate the cyclic resistance of non-saturated soils for which experimental results are available in literature. In particular, triaxial tests results from Wang et al. (2014) and from Okamura et al. (2010) have been used. The first ones have been obtained on the same Inagi sand presented in Chapter 4 (Fig. 4.1 and Tab. 4.1) (at different degrees of saturation) and on Toyoura sand, while the results reported by Okamura et al. (2010) have been obtained on a sand of a test site in the Kochi prefecture, Japan, hereafter simply called Kochi sand.
For completeness, some information on these soils are reported (soil gradings in Figure 8.40, and physical properties in Table 8.7). Okamura et al. (2010) do not provide the value of the specific gravity G_s for Kochi sand (see Tab. 8.7). In the calculations, the value

G_s=2.674 (as calculated for Sant'Agostino sand) was assumed. Considering the very little range of values of G_s for typical sands (see, for instance Tab. 4.1), this assumption is expected to have a minor influence on the results in terms of calculation of the specific volumetric and deviatoric components of the energy spent to liquefy.

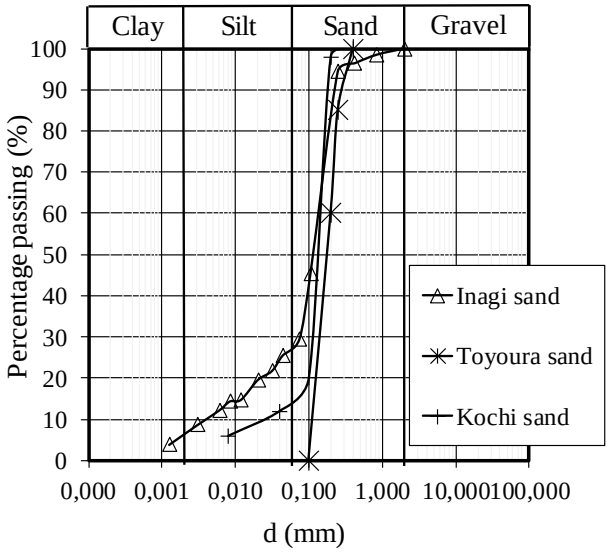

Figure 8.40. Grain size distributions of the soils tested by Wang et al. (2014) (Inagi and Toyoura) and Okamura et al. (2010) (Kochi).

Material properties	Toyoura sand*	Kochi sand**
FC (d<0.0075mm) (%)	-	15
Gs	2.656	-
D_{50} (mm)	0.20	0.15
e_{max}-e_{min}	0.898-0.611	-
U_c	1.90	5.0

*Wang et a. (2014); **Okamura et al. (2010)

Table 8.7. Material properties of the soils (literature data) on which the two approaches proposed in this study have been checked. Properties of Inagi sand can be found in Table 4.1.

APPROACH 1

The cyclic resistance curves already published by Wang et al., (2014) and Okamura et al., (2010), given the specific testing state conditions (represented by $E_{v,liq}$), have been obtained using approach 1 as described in §8.3.4 (Figs. 8.41-8.42). It is worth noting that the state conditions of the tests presented by Wang et al., (2014) and Okamura et al., (2010) are different from those studied in this research and on which the energetic model has been calibrated. Tests on Inagi sand have been performed with a D_r of 72%, while Toyoura specimens are extremely loose (D_r=-6%), and finally, non-saturated cyclic triaxial tests on Kochi sand have been consolidated at 88 kPa. Nevertheless, the curves interpret reasonably well the results obtained by Wang et al. (2014) (Fig. 8.41), with some overestimation of CRR_{un} for Inagi sand, and a slight underestimation for Toyoura sand.
For Kochi sand (Fig. 8.42), the curve well fits the experimental results pertaining to the lower values of CRR, while it largely underestimates the result for the highest value (corresponding to the lowest value of N_{liq}). This shows the major drawback of the use of

approach 1: being based on a simple translation of the cyclic resistance curve (ΔCRR does not depend on N_{liq}) it is not able to catch the possible change of curvature of the non-saturated cyclic resistance curve. Furthermore, it may fail in the prediction of non-saturated cyclic resistance if applied out of the range of values of N_{liq} on which the saturated resistance curve was obtained (as is the case for Kochi sand reported in Fig. 8.42).

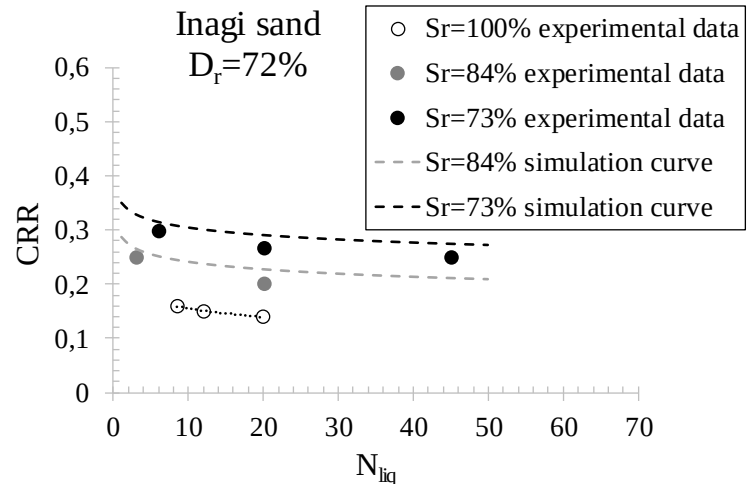

(a)

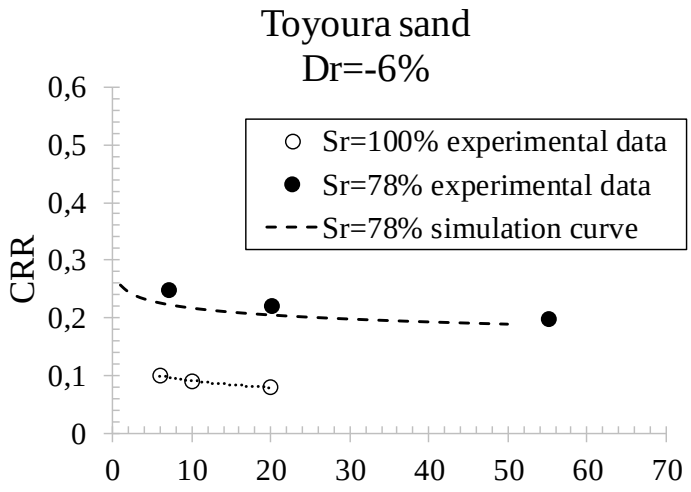

(b)

Figure 8.41. Cyclic resistance curves of Inagi and Toyoura sand obtained by approach 1 along with the experimental data reported by Wang et al. (2014) at different relative densities and at a confining stress of 60 kPa.

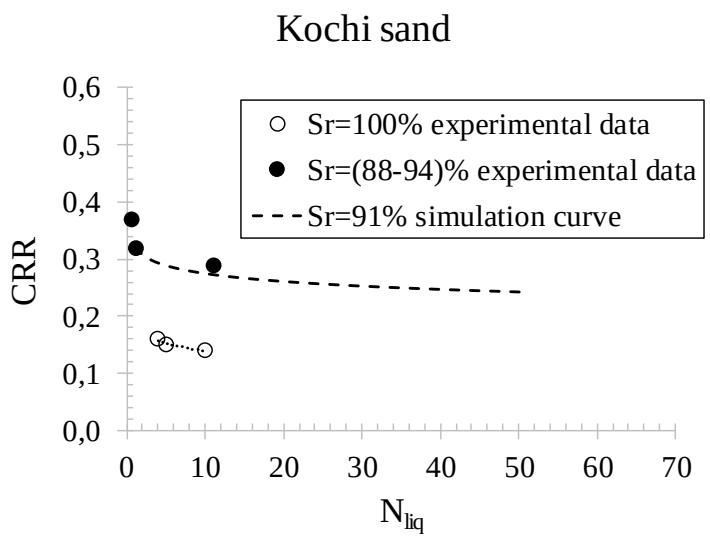

Figure 8.42. Cyclic resistance curves of Kochi sand obtained by approach 1 along with the experimental data reported by Okamura et al. (2010) at different relative densities and at a confining stress of 88 kPa.

The experimental values of ΔCRR_{15} for the tests reported by Wang et al. (2014) and from Okamura et al. (2010) have been plotted in Figure 8.43 along with the curve reported in Figure 8.30a (eq. (8.13a)), for triaxial tests. The good agreement of the literature data with the regression curve obtained from the results presented in this research confirms that this approach is consistent also for different soils subjected to different conditions.

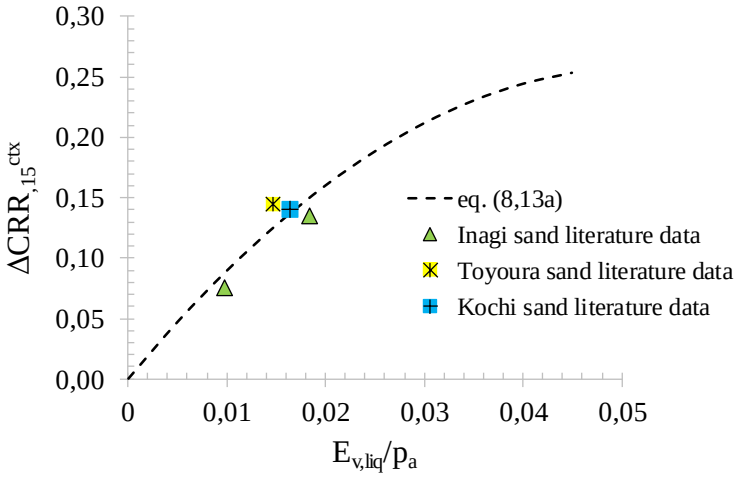

Figure 8.43. ΔCRR_{15} versus $E_{v,liq.}$ Comparison of the proposed relationship (eq. 8.13a, Fig. 8.30a) with the experimental results by Wang et al. (2014) and by Okamura et al. (2010).

APPROACH 2

Figures 8.41 and 8.42 show the cyclic resistance curves obtained using approach 2 to predict the experimental results by Wang et al. (2014) and by Okamura et al. (2010), respectively. Both figures show that this modelling approach well fits the experimental results in non-saturated conditions, with a higher accuracy than approach 1.
Once again, it should be emphasised that the simulated curves are relative to different conditions in terms of D_r and confining stress than those on which the energetic model has been calibrated, making more general and consistent such approaches.

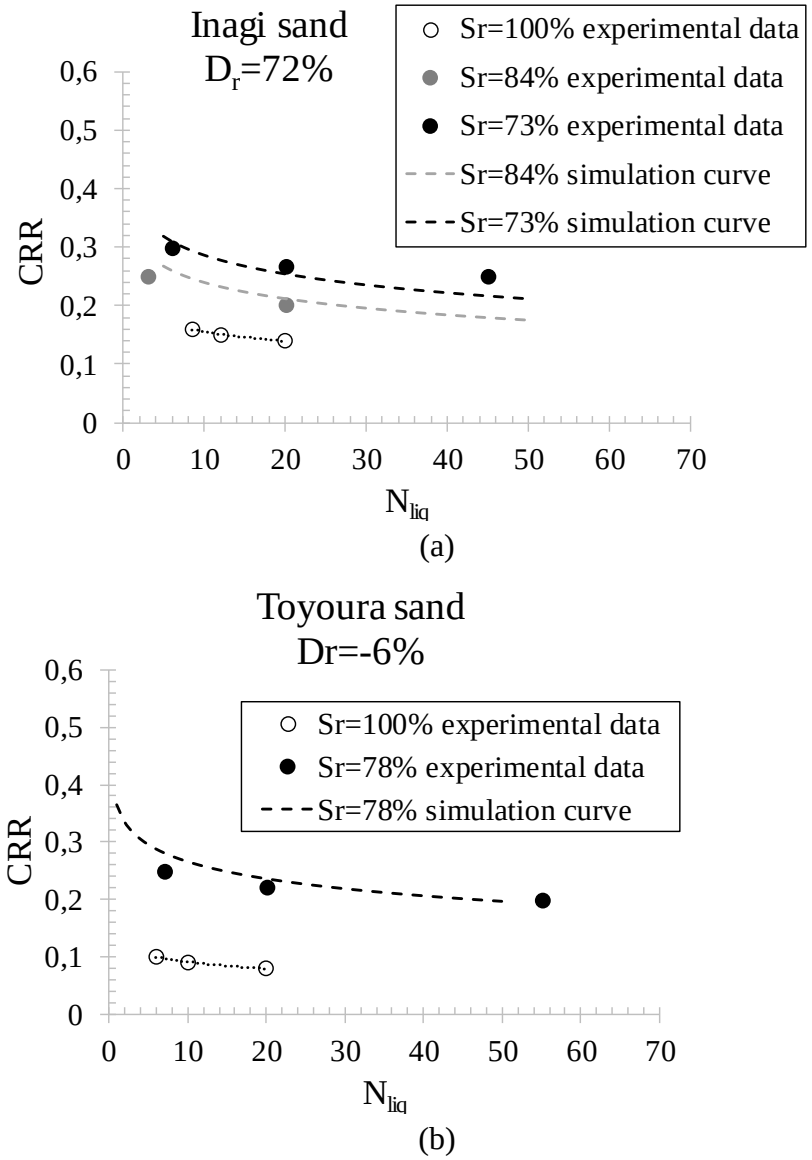

Figure 8.44. Cyclic resistance curves of Inagi and Toyoura sand obtained by approach 2 (eq. 8.15a) along with the experimental data reported by Wang et al. (2014) at different relative densities and at a confining stress of 60 kPa.

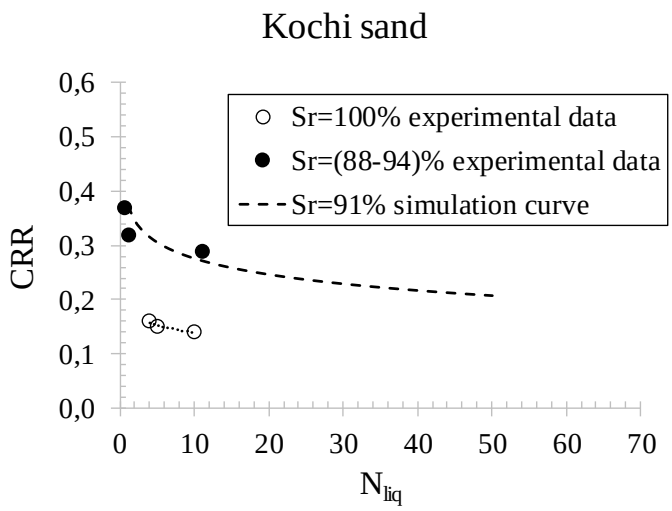

Figure 8.45. Cyclic resistance curves of Kochi sand obtained by approach 2 (eq. 8.17a) along with the experimental data reported by Okamura et al. (2010) at different relative densities and at a confining stress of 88 kPa.

8.3.4.2 APPROACHES 1 AND 2 AS DESATURATION DESIGN TOOLS

The two procedures previously described can be used to predict the cyclic resistance of non-saturated soil in simple shear conditions and may be seen as relatively simple design tools to calculate the necessary degree of saturation to be obtained via a desaturation treatment for a given soil to increase its resistance to liquefaction.

Approach 1 is simpler to adopt, as it assumes that the liquefaction resistance curve related to a given degree of saturation can be obtained as a simple upwards translation of the one in saturation conditions. As previously discussed, the assumption that CRR-N_{liq} curve does not change shape at different values of S_r is a strong simplification and must be adopted with extreme care. From all the experimental data provided by an extensive testing program performed in this research work, including the ones already published by Mele et al., (2018) (bauxite and Inagi sand), on which the approach has been calibrated, and the ones by Wang et al., (2014) and Okamura et al., (2010), however, the approach seems to hold, at least in the range of values of N_{liq} of engineering interest (say $N_{liq}<20$). Likely, it will lack in accuracy for very low saturation degrees and higher N_{liq}. But these conditions are of little practical interest.

Approach 2 needs a few calculation steps more than approach 1, being based on the calculation of the total specific energy and not only of its volumetric component. However, it has the advantage of not requiring the knowledge of the saturated liquefaction resistance curve to predict the behaviour of the non-saturated soil. The result is not a translation of the CRR-N_{liq} curve, and any shape may be obtained, depending on the combination of specific volumetric and deviatoric energies to liquefaction. Approach 2 needs just the knowledge of the state parameters and of the soil water retention curve.

Comparing the simulations of independent experimental data reported in Figures 8.41, 8.42, 8.44 and 8.45 for the two approaches, it can be noted that approach 2 better simulates

the cyclic resistance of the three different sands. This is not surprising: being based on the calculation of the total specific energy spent to liquefy, it takes into account both the initial state conditions via the volumetric component, and cyclic damping via the deviatoric one (not considered by approach 1).
In the design of a desaturation treatment (or IPS), the goal is to find what degree of saturation S_r is needed to guarantee for the structures to protect a satisfactory performance with reference to serviceability and limit conditions with the desired safety margins, with reference to any kind of mechanism related to liquefaction (Bray and Macedo, 2017). In particular, two scenarios may be foreseen: one in which the risk is linked to the attainment of liquefaction (i.e. a temporary but total loss of stiffness and strength of the liquefied soil), and one in which the pore pressure build up may trigger limit states in the structures (e.g. bearing capacity failure or excessive settlements) before liquefaction is reached. In the first case, an increase of CRR^{css} for the given value of N_{eq} (which is the number of cycles corresponding to the design seismic action) is needed. In the second case (which may refer to situations in which the safety margins against liquefaction may be sufficient in saturated conditions), it is simply asked to have lower pore pressures for $N=N_{eq}$. Formally, this may be seen as the need to increase, for the given value of CSR, the value of N_{liq} to a higher value N_{liq}*. Both scenarios ask for an increase of soil capacity via desaturation (or IPS) to cope with seismic demand, and the two procedures depicted in Figure 8.46 can be alternatively considered to this aim.

Increase CRR

The first procedure, on the left side of Figure 8.46, refers to the need of increasing the safety factor against liquefaction. This means that the original safety margins are known (i.e., the saturated CRR^{css}-N_{liq} curve is known). In this case, it is trivial to know what increment of liquefaction resistance (ΔCRR^{css}) is needed to reach an appropriate safety margin, and therefore the previously proposed approach 1 is best suited as design tool. In fact, by knowing ΔCRR^{css} it is possible to calculate $E_{v,liq}$ (eq. 8.13b). For high values of S_r (as will generally be the case for IPS), the contribution of $E_{w,liq}$ is negligible. Therefore, $E_{v,liq}$ can be considered as the sum of two components ($E_{v,sk,liq}$ and $E_{air,liq}$). Through an iterative procedure, the design value of S_r (S_{rd}) can be finally calculated. Notwithstanding the limitations of approach 1 previously discussed, it has to be highlighted that N_{liq} is usually lower than 20, and thus its use is confined to the range of values of N on which it has been experimentally tested.

Increase N_{liq}

In this case, the seismic action (CSR) leads for $N=N_{eq}$ to excessive pore pressures (but not to liquefaction). There is the need to reduce such pore pressures, regardless of the original safety margins against liquefaction. The saturated liquefaction resistance curve is not a necessary design tool in this case, being the design goal to increase N_{liq} till N_{liq}*. The quantification of N_{liq}* is out of the scope of this research and will be discussed elsewhere. Generally speaking, it may be obtained once the maximum tolerable pore pressure u_{max} at $N=N_{eq}$ has been evaluated with reference to the specific critical mechanism. In the case of bearing capacity failure triggered by pore pressure build up

during seismic shaking, for instance, there are bearing capacity analytical formulations (e.g. Karamitros et al. 2013) from which the value of $u_{max}(N_{eq})$ at failure can be calculated. Then, using an analytical expression for the pore pressure build up curve u=u(N) (e.g. Chiaradonna et al., 2018) calibrated on such a value, N_{liq}* is obtained.
In this case, approach 2 is best suited as design tool, as depicted on the right side of Figure 8.46: once N_{liq}* has been identified, eq. 8.17b allows to know the ratio $CRR^{css}/(1+E_{tot,liq}/p_a)^6$ (considering in this case $CRR^{css}=CSR$). The total specific energy to liquefaction $E_{tot,liq}$ is the sum of two components $E_{v,liq}$ and $E_{s,liq}$, where $E_{s,liq}$ can be computed as a function of CSR and $E_{v,liq}$ (see Fig. 8.36c, eq. 8.15b). $E_{tot,liq}$ is therefore given by:

$$E_{tot,liq} = E_{v,liq} + 0.300 \cdot p_a \cdot e^{-23.7 \cdot CRR^{css} \cdot \left(1-5 \cdot \frac{E_{v,liq}}{p_a}\right)^{10}} \qquad (8.19)$$

Using eq. (8.19), the design value $S_{r,d}$ can be calculated as done with approach 1 with a simple iterative procedure.

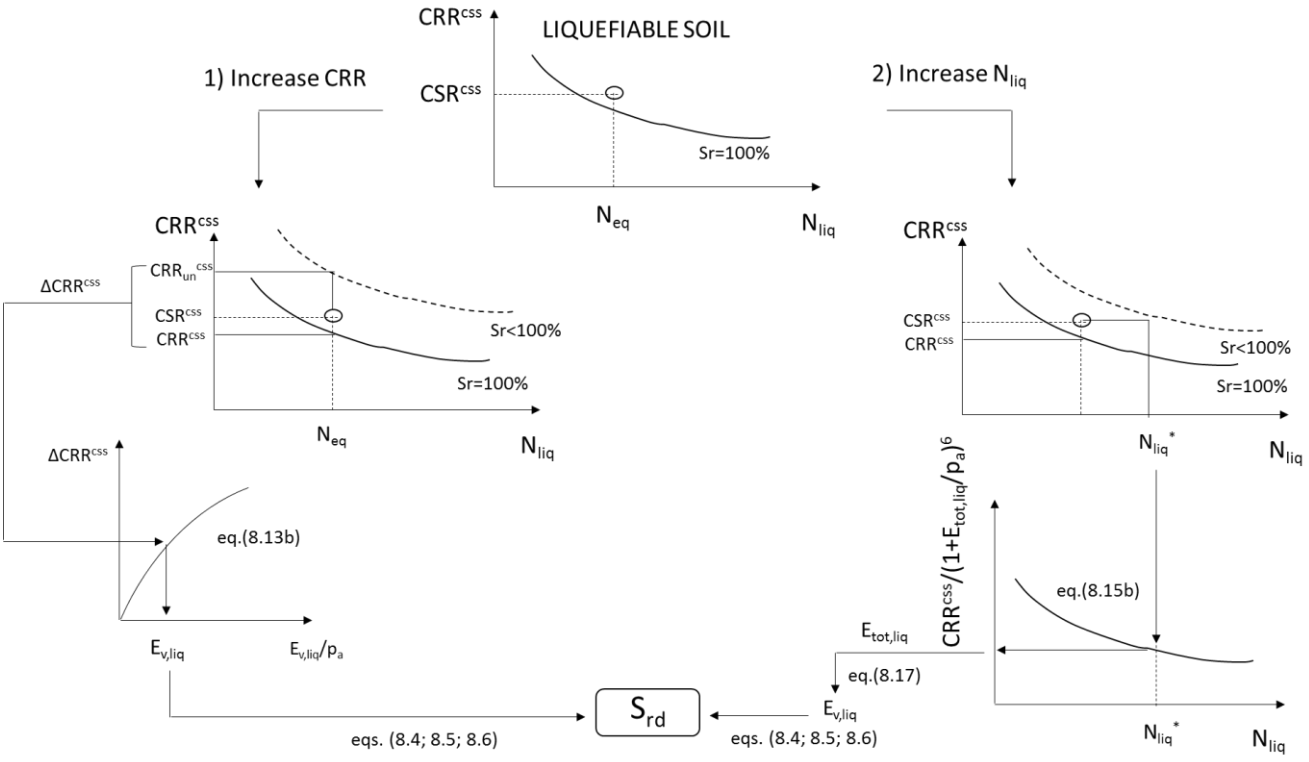

Figure 8.46. Possible procedures to calculate the degree of saturation needed to increase liquefaction resistance of sandy soils. The once on the left refers to Approach 1 (increase CRR); the one on the right to Approach 2 (increase N_{liq}).

8.3.4.3 IPS DESIGN CHARTS FOR PIEVE DI CENTO

The consistence of the two proposed energetic approaches has been widely demonstrated in the previous paragraphs simulating the cyclic resistance curves of different sandy soils in different conditions. Owing to that, desaturation design tools have been provided and well summarized in the flow chart of Figure 8.46. However, for a site susceptible to liquefaction an Induced Partial Saturation (IPS) design chart ($0.85<S_r<0.99$) can be easily built by using Approach 1 or 2. In the following the IPS design charts for Pieve di Cento ($D_r=47\%$) have been obtained by means of the two energetic approaches proposed in this Chapter.

According to Approach 1, known the cyclic resistance curve of saturated soil in simple shear condition, several curves relative to different S_r – and thus $E_{v,liq}$ - can be obtained as described in detail in §8.3.4. The IPS chart for Pieve di Cento is shown in Figure 8.47a. As mentioned several times, using approach 1 the non-saturated curves are translations of the experimental one obtained from cyclic simple shear tests.

In Figure 8.47b the IPS chart has been obtained by using approach 2, which has been applied as described in §8.3.4, computing the specific deviatoric energy to liquefaction and consequently the total one, on which the approach is based.

Comparing the results obtained from the proposed energetic approaches it is also possible to make further and useful considerations about them.

Firstly, it is evident a difference between the non-saturated curves obtained by means of the two approaches. In particular, the non-saturated cyclic resistance curves ($0.90<S_r<0.98$) simulated according to approach 2 (Fig. 8.47b) seems to collapse in a single curve because the differences in terms of CRR are insignificant. It is obviously due to the fact that for higher S_r and thus lower $E_{v,liq}$, the curve of Figure 8.36c (eq. (8.15b)) tends to reach an asymptote and, as a consequence, the differences in terms of $E_{s,liq}$ are negligible, so that $E_{tot,liq}$ is not affected by remarkable variations.

Additionally, in the range of N_{liq} of engineering interest ($N_{liq}<20$), approach 2 provides higher resistance than those of approach 1 (Fig. 8.47a) for $S_r > 95\%$, and thus resulting less precautionary than the first approach. On the contrary, for S_r lower than 95% the liquefaction resistance evaluated according to approach 2 is lower than that achieved according to the first one. In such case, the difference in terms of $E_{v,liq}$ tends to become more important and thus – far from the asymptote – the relationship of eq. (8.15b) should return more reliable results.

In conclusion, even though the approach 2 is considered better than the first one as already mentioned in § 8.3.4.2 and demonstrated by simulating the cyclic resistance curves of non-saturated sandy soils reported in literature, it should be emphasised that when a very high S_r has to be applied, approach 1 could return more realistic results. Obviously, it should be confirmed by performing tests on partially saturated soils ($S_r>90\%$), but in the meantime, approach 1 is recommended under such conditions.

Regardless of the chart chosen and used by the operator, it results a simple and a useful design tool in desaturation interventions. S_r can be easily achieved intersecting the correspondent curve according to the two procedures described in Figure 8.46: increasing CRR (left in Fig. 8.46) or N_{liq} (right in Fig. 8.46).

Figure 8.47. IPS design charts for Pieve di Cento achieved by means of energetic approaches 1 (a) and 2 (b).

8.3.4.4 CPT AND SPT BASED LIQUEFACTION TRIGGERING CURVES FOR IPS

From a technical point of view, charts, which link CRR with the parameters of in situ tests ($(N_1)_{60cs}$ and q_{c1Ncs} for SPT and CPT tests, respectively), may be extremely useful for design of IPS. Owing to that, SPT and CPT based liquefaction triggering curves of partially saturated soils can be easily achieved by using approach 1 of the energetic model. The curves of saturated soils, shown in Figure 8.48 (eqs. (2.26) – (2.27)), have been translated for each degree of saturation investigated (98; 95; 93; 90; 85 and 80%) and void ratio (D_r is linked to $(N_1)_{60cs}$ and q_{c1Ncs}, see for instance Idriss and Boulanger, 2008), calculating the specific volumetric energy to liquefaction (§8.3.4), which is correlated to ΔCRR (eq. (8.13b)). Unsaturated curves in the planes $(N_1)_{60cs}$ versus CRR and q_{c1Ncs}

versus CRR have been reported in Figure 8.48a and 8.48b, respectively. The upward translation of the saturated curves is possible because for high S_r, there is no mechanical effect of suction on soil skeleton, even though air and water pressure are slightly different, so $(N_1)_{60cs}$ and q_{c1Ncs} do not change passing from saturated to unsaturated conditions.
As already mentioned, the charts of Figure 8.48 can be a useful tool in IPS design.
If a soil results liquefiable from a liquefaction susceptibility analysis (CSR>CRR), the charts of Figure 8.48 can be used to identify the degree of saturation to apply in situ to have the increment of resistance desired.

Figure 8.48. SPT (a) and SPT (b) based liquefaction triggering curves for partially saturated soils.

8.4 ENERGETIC INTERPRETATION OF LIQUEFACTION PHENOMENA: A LIQUEFACTION SURFACE

In this Chapter the concept of energy spent to reach liquefaction has been used to interpret the liquefaction tests in saturated and non-saturated conditions. Additionally, considerations done on non-saturated tests have allowed to calibrate an energetic model, which is extremely promising as a design tool in desaturation or IPS interventions as mitigation technique against liquefaction.

To conclude, this paragraph has been developed with the main aim to process together the results of saturated and non-saturated tests, showing further considerations and deepening such aspects already presented in this Chapter. Finally, it will try to provide an energetic interpretation of liquefaction phenomena analyzing the main variables which play an important role in liquefaction induced by a seismic event.

As mentioned several times, the total specific energy to reach liquefaction is given by the sum of two components: volumetric and deviatoric energies.

It has been argued that $E_{v,liq}$ (which is nil in saturated soils) can be considered as a state variable to quantify the increase of cyclic resistance caused by a reduced degree of saturation, being thus constant along a given cyclic resistance curve. Conversely, $E_{s,liq}$ is related to a specific value of cyclic resistance ratio or number of cycles at liquefaction via the value of the volumetric component (Fig. 8.36; eq. (8.15)).

Mele et al. (2019a) investigated the behavior of E_s with N_{cyc} for saturated soils, and the most important result is that, regardless of the position of cyclic resistance curve, $E_{s,liq}$ reaches similar values for equal N_{liq}.

The results show that for the same N_{liq}, $E_{s,liq}$ for two kinds of sand in different conditions in terms of confining stress, are similar (N_{liq} = 12 and 33). In particular, the curves E_s–N_{cyc} intersect each other roughly in correspondence of the same number of cycles at liquefaction as the arrows show in Figure 8.49a. It suggests a strong connection between $E_{s,liq}$ and N_{liq} for saturated tests, confirming what has been reported by Polito et al. (2013) and shown in Figure 8.25.

In Figure 8.49b the cyclic resistance curves of Leighton Buzzard and Pieve di Cento (BSS) sands have been depicted and it can be observed that they are different, actually PdC sand has a higher cyclic resistance to liquefaction than Leighton Buzzard sand. Despite such difference, at a fixed N_{liq}, $E_{s,liq}$ is almost the same, consequently $E_{s,liq}$ seems to be independent on the applied CSR for saturated soils. However, in Figure 8.49a CTX_BSS1 (N_{liq}=3) and CTX_LB7 (N_{liq}=4) have been compared, too. In this case, $E_{s,liq}$ is not the same, the curves do not meet each other and the grey curve (CTX_BSS1) reach liquefaction before than the black one (CTX_LB7). The reason could be that when N_{liq} is low (i.e 3), the calculation of E_s (eq.(2.14a)) may be affected by a higher error than in case of high N_{liq}, because axial strains suddenly increase.

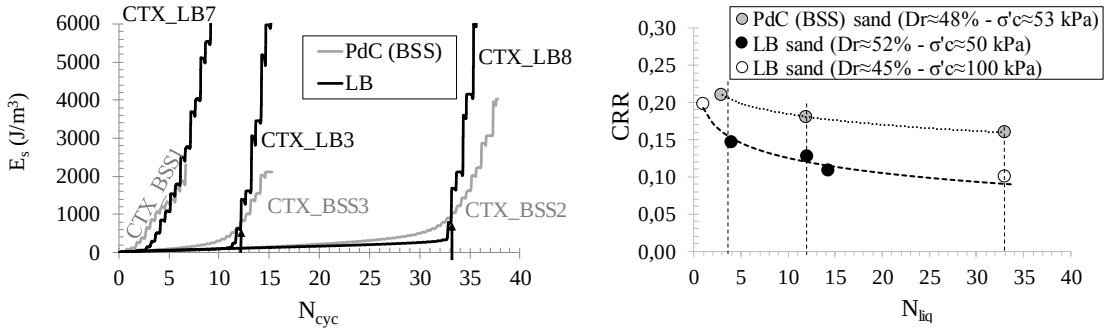

(a) (b)

Figure 8.49. E_s with N_{cyc} for tests on PdC (BSS) and LB sands (a); Cyclic resistance curves of PdC (BSS) and LB sands (b) (adapted from Mele et al., 2019a).

So, while from tests on non-saturated soils $E_{s,liq}$ is linked to CRR as demonstrated in Figure 8.36b (eq. (8.15)), from tests on saturated soils such dependence seems not to exist, while a slight influence of N_{liq} can be noted, although $E_{s,liq}$ varies in a small range as mentioned several times in §8.2.1.

In order to verify how N_{liq} affects $E_{s,liq}$ in non-saturated conditions, that is with $E_{v,liq}$ not null (and variable), Mele et al. (2019b) compared three tests, carried out by Mele et al. (2018) in terms of $E_s - N_{cyc}$ and shown in Figure 8.50 together with UCTX_GSS12 test on Pieve di Cento (GSS) sand. The tests have been chosen among the non-saturated tests of Mele et al. (2018) where liquefaction occurs at a very similar N_{liq}, as summarized in Table 8.8.

Table 8.8. State properties and energetic components of non-saturated tests (modified from Mele and Flora, 2019).

Test	Material	σ'_{un} (kPa)	e_0	S_{r0} (%)	CRR	N_{liq}*	$E_{v,liq,av}$ (J/m³)	$E_{s,liq}$ (J/m³)
U_SA8	SAS	48.8	0.59	87.6	0.258	9.6	1192	2486
U_BA5	Bauxite	48.4	0.75	85.0	0.279	8.3	1200	3622
U_IN3	Inagi	62.3	1.14	52.0	0.404	8.6	4035	10306
UCTX_GSS12	PdC_GSS							

*evaluated for ε_{DA}=5%

Even though N_{liq} is not exactly the same in these tests, it can be noted that unlike saturated tests, $E_{s,liq}$ is not constant for a fixed value of N_{liq} and it is much higher as $E_{v,liq}$ increases. This has a clear physical meaning: by reducing the degree of saturation, $E_{v,liq}$ increases and so the deviatoric energy needed to liquefy.

In Figure 8.51a the experimental tests of Mele et al. (2018) and those reported in this research work have been plotted in the plane N_{liq}- $E_{s,liq}$, where each curve relates to a value of $E_{v,liq}$.

$E_{v,liq}$=0 corresponds to saturated material; in this case regardless of the kind of sand, $E_{s,liq}$ is similar for a fixed value of N_{liq}. In this case, the straight line (obtained by considering the average values of saturated tests for different N_{liq}) seems to be horizontal because of the small range of $E_{s,liq}$. For higher values of $E_{v,liq}$ the line gradient is much more important and when $E_{v,liq}$ increases $E_{s,liq}$ increases at a fixed number of cycles. Considering N_{liq} equal to 15 (often considered in literature as a reference value), it can be noted that $E_{s,liq}$ increases with $E_{v,liq}$, according to a linear relationship, as shown in Figure 8.51b. It is worth noting that the regression coefficient is very high, about 0.9721.

Figure 8.50. E_s with N_{cyc} for different $E_{v,liq}$ (adapted from Mele et al., (2019b)).

(a)

Figure 8.51. $E_{s,liq}$ with N_{liq} for fixed values of $E_{v,liq}$ (a) and $E_{s,liq}$ with $E_{v,liq}$ for N_{liq} = 15 (b).

The experimental evidences shown in this paragraph on saturated and non-saturated tests have allowed to deduce that $E_{v,liq}$, $E_{s,liq}$ and N_{liq} are three variable strongly linked each other. Moreover, they play an important role in liquefaction.
To sum up:

- $E_{v,liq}$ is a synthetic state variables in liquefaction tests, able to summarize σ'_0, e_0 and S_{r0}, and consequently it can express the state of the soil.
- N_{liq} can be considered as the variable which describes the energy of the seismic action and is typically related to the earthquake magnitude (M) (e.g. Seed and Idriss, 1982).
- $E_{s,liq}$ is the energetic variable which describes the response of the soil in particular state conditions ($E_{v,liq}$) to a fixed seismic event (N_{liq}), allowing to quantify the resistance to liquefaction because of its dependence on CRR (Fig. 8.36b).

Generally speaking, it can be asserted that the liquefaction behaviour of sandy soils can be described by three variables: $E_{v,liq}$, $E_{s,liq}$ and N_{liq}, which are reduced to two ($E_{s,liq}$ and N_{liq}) in saturated soils. The results of the experimental tests may be reported in the space $E_{v,liq}$-N_{liq}-$E_{s,liq}$. Figure 8.52 shows a surface in such a plane connecting the experimental points reported in Figure 8.51a. Then, Figures 8.51a and 8.51b are just cross sections of this surface.
So, the three variables: $E_{v,liq}$, $E_{s,liq}$ and N_{liq} define a "liquefaction surface" describing the resistance to liquefaction of non-saturated soils.

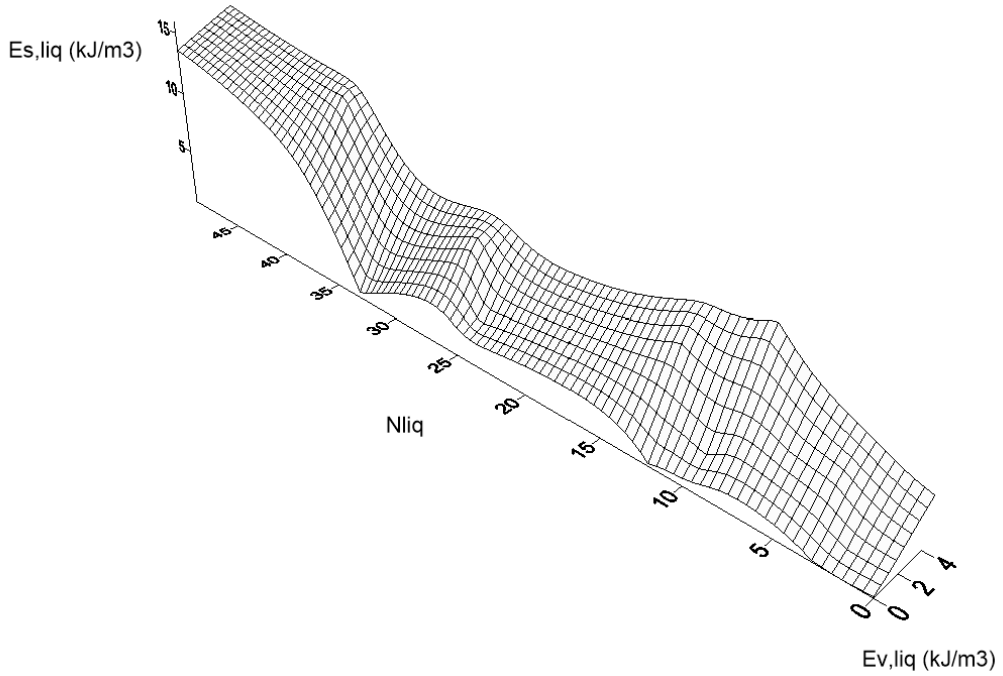

Figure 8.52. Liquefaction surface $E_{v,liq}$-N_{liq}-$E_{s,liq}$ (Mele et al., 2019b).

The surface reported in Figure 8.52 is not regular as it connects a limited number of experimental points. Assuming to have a more regular and known surface, interpolating a larger number of data, it would describe the behaviour of a sandy soil in particular conditions (described by $E_{v,liq}$) subjected to a seismic event (N_{liq}) in terms of the deviatoric energy $E_{s,liq}$ needed to liquefy. The latter is connected to CRR_{un} (Fig. 8.36b).
Such result is a preliminary study and therefore needs further data and considerations. However, such approach seems to be very promising and could be a useful tool to evaluate the liquefaction resistance of non-saturated soils not only at small (laboratory) scale but also on site.

REFERENCES

Baziar, M. H., and Jafarian, Y. (2007). Assessment of liquefaction triggering using strain energy concept and ANN model: capacity energy. *Soil Dynamics and Earthquake Engineering*, 27(12): 1056-1072.

Berrill, J. B., and Davis, R. O. (1985). Energy Dissipation and Seismic Liquefaction of Sands: Revised Model. *Soils and Foundations*, 25: 106-118.

Bray J. D. and Macedo J. (2017) Simplified procedure for estimating liquefaction-induced building settlement. *Proceedings of the 19th International Conference on Soil Mechanics and Geotechnical Engineering,* Seoul 2017.

Chiaradonna A., Tropeano G., d'Onofrio A., Silvestri F. (2018). Development of a simplified model for pore water pressure build-up induced by cyclic loading. *Bulletin of Earthquake Engineering, BEE*, 16(9): 3627-3652, https://doi.org/10.1007/s10518-018-0354-4.

Dief, H. M., and Figueroa, J. L. (2007). Liquefaction assessment by the unit energy concept through centrifuge and torsional shear tests. *Canadian Geotechnical Journal*, 44(11): 1286-1297.

Idriss, I. M., and Boulanger, R. W. (2008). Semi-empirical procedures for evaluating liquefaction potential during earthquakes, *in Proceedings, 11th International Conference on Soil Dynamics and 106 Earthquake Engineering, and 3rd International Conference on Earthquake Geotechnical Engineering, D. Doolin et al., eds., Stallion Press,* Vol. 1, pp. 32–56.

Karamitros D.K., Bouckovalas G.D., Chaloulos Y.K., Andrianopoulos K.I. (2013). Numerical analysis of liquefaction-induced bearing capacity degradation of shallow foundations on a two-layered soil profile. *Soil Dynamics and Earthquake Engineering*. Elsevier.

Kokusho, T. (2013). Liquefaction potential evaluations: energy-based method versus stress-based method. *Canadian Geotechnical Journal,* 50(10): 1088-1099.

Li X.S. (2007). Thermodynamics-based constitutive framework for unsaturated soils. 1: Theory. *Gèotechnique***.** 57(5): 411-422.

Mele, L., and Flora, A. (2019). On the prediction of liquefaction resistance of unsaturated sands. *Soil Dynamics and Earthquake Engineering*. DOI: 10.1016/j.soildyn.2019.05.028.

Mele, L., Lirer, S., Flora, A. (2019a). The specific deviatoric energy to liquefaction in saturated cyclic triaxial tests. *7th International Conference on Earthquake Geotechnical Engineering, 7ICEGE, Rome (Italy)*, 17-20 June 2019. ISBN: 978-0-367-14328-2 (Hbk), eISBN: 978-0-429-03127-4 (eBook).

Mele L., Lirer S., Flora A. (2019b). A liquefaction surface to describe liquefaction phenomena in unsaturated sandy soils. *7th International Conference on Earthquake*

Geotechnical Engineering, 7ICEGE, Rome (Italy), 17-20 June 2019. ISBN: 978-0-367-14328-2 (Hbk), eISBN: 978-0-429-03127-4 (eBook).

Mele L., Tan Tian J., Lirer S., Flora A., Koseki J. (2018). Liquefaction resistance of unsaturated sands: experimental evidence and theoretical interpretation. *Géotechnique*. DOI: 10.1680/jgeot.18.p.042.

Okamura M., Takebayashi M., Nishida K., Fujii N., Jinguji M., Imasato T., Yasuhara H., Nakagawa E. (2010). In-Situ desaturation test by air injection and its evaluation through field monitoring and multiphase flow simulation. *J. Geotech. Geoenviron. Engng ASCE*, 137(7): 643-652.

Polito, C., Green, R. A., Dillon, E., and Sohn, C. (2013). Effect of load shape on relationship between dissipated energy and residual excess pore pressure generation in cyclic triaxial tests. *Canadian Geotechnical Journal*, 50(11): 1118-1128.

Seed, H.B. and Idriss, I.M. (1971). Simplified Procedure for Evaluating Soil Liquefaction Potential. *Journal of the Soil Mechanics and Foundations Division ASCE* 97(SM9): 1249-1273.

Wang H., Koseki J., Sato T. (2014). Resistance against liquefaction of unsaturated Toyoura sand and Inagi sand. *Bulletin of ERS* No. 47, 2014.

CHAPTER 9

9. ENERGETIC APPROACH: FROM SMALL TO LARGE SCALE

In this Chapter two important topics, strongly linked, will be discussed: the assessment of liquefaction potential and the prediction of excess pore pressure induced by a seismic event according to an energetic approach.
The experimental results observed in Chapter 8 highlight that, in saturated soils the pore pressure build-up during cyclic loading is uniquely correlated to the normalized specific deviatoric energy (E_s/σ'_m). Since such relationship is demonstrated to be slightly dependent on intrinsic and state parameters of the soils, an average curve, passing from the lower bound of the energetic pore pressure laws (r_u - E_s/σ'_m) for different soils in different conditions, has been proposed in the previous Chapter (§8.2.3; eq. (8.12)). Moreover, for r_u=0.90, the normalized capacity of the soil ($E_{s,liq}/\sigma'_m$) is uniquely identified and equal to 0.006.
Starting from such interesting results of laboratory tests, processed according to an energetic interpretation (Chapter 8), it has been tried to extend such energetic considerations to a large scale, combining laboratory test results with in situ seismic energy evaluation methods to assess the liquefaction potential, and to predict the maximum excess pore pressure ratio induced by a seismic event. Furthermore, the results achieved by applying the energetic methods have been compared with those of a more traditional stress-based method.

9.1 LIQUEFACTION POTENTIAL ASSESSMENT AND EXCESS PORE PRESSURE PREDICTION

As already described in Chapter 2, the liquefaction potential of a site, in free field condition, is generally evaluated by means of simplified approaches, where the Factor Safety (FS) is computed at a given depth by the ratio between the "soil capacity" (CRR) to resist liquefaction and the "seismic demand" generated by the earthquake (CSR).
It is well known that the stress-based approach is very common because it is very easy to apply; the cyclic shear stress ratio required to attain liquefaction (CRR) is generally estimated through several empirical correlations developed from in situ tests (§2.3.1), while the earthquake induced cyclic shear stress (CSR) is computed by eq. (2.24). It should be noted that the coefficient 0.65 is a correction factor, which was introduced by Seed and Idriss (1971) to transform the irregular shear stress history in an equivalent uniform cyclic shear stress loading. However, Ishihara and Yasuda (1972) carrying out a series of liquefaction tests using various type of random time histories proposed a correction factor ranges from 0.41 to 0.72, depending on the amplitude of stress pulses. In other words, the choice of the correction factor appears totally arbitrary. This drawback can be overcome by introducing the energetic based approaches, because among several advantages, already counted in Chapter 2 (§2.3.3), there is the independence of the specific dissipated energy on the applied load pattern (random or harmonic), so that there

is no need to introduce a correction factor. In this kind of model, the safety factor is obviously defined according to an "energetic key" computed as the ratio between $E_{s,liq}$ (capacity) and E_s induced by a seismic event (demand):

$$FS = \frac{E_{s,liq}}{E_s} \qquad (9.1)$$

Regarding the soil capacity, it can be computed from laboratory test results, by means of eq. (8.11). However, with the main aim to provide a procedure to assess liquefaction potential which results as simple as possible, the soil capacity can be more easily assumed equal to $0.006 \cdot \sigma'_m$ (corresponding to r_u=0.90 in eq. (8.12)). In this Chapter, $E_{s,liq}$ will be considered equal to $0.006 \cdot \sigma'_m$ in order to validate eq. (8.12) on which the simple procedure of assessing liquefaction potential is based. In more sophisticated analyses $E_{s,liq}$ computed from eq. (8.11) should be used.

However, the key point in the energy-based approach is the properly computation of the energy demand. In this research it was computed via an equivalent site response analysis, performed by means of the 1D computer program EERA (Equivalent-linear Earthquake site Response Analysis) (Bardet et al., 2000).

In EERA a soil profile can be discretized, characterizing each layer by means some physical and mechanical properties (including soil density, V_s profile, and the decay and damping laws: γ-G/G_0 and γ-D). The input motion (acceleration time history) can be applied in every point of the model and, according to an iterative procedure, the response analysis is returned and the area of the cycles γ-τ with time for each depth (middle of the discretized layer) can be calculated, or in other words, the trend of E_s with time for each depth.

Known E_s (demand) and $E_{s,liq}$ (capacity), FS can be easily computed via eq. (9.1). Furthermore, known the profile of E_s with depth, the profile of the maximum r_u attained during the earthquake can be easily estimated from eq. (8.12). Such equation will be validated in the following by centrifuge tests, comparing the experimental measure of pore pressure with those estimated by eq. (8.12). Additionally, the assessment of liquefaction potential of real case histories will be studied together with the prediction of excess pore pressure ratio distribution with depth (eq. (8.12)). The obtained results will be finally compared with those already published and achieved by means of SCOSSA (Tropeano et al., 2016-2019), a 1D non-linear code, in which the soil column is modelled as a system of consistent lamped masses connected by viscous dampers and springs with hysteretic non-linear behaviour. The stiffness of the springs is a function of the current effective stress state, and consequently of the excess pore water pressure induced by seismic action, through the relationship proposed by Matasovic and Vucetic (1993). The proposed pore water pressure model implemented in SCOSSA is based on the endochronic theory that express the pore pressure build-up as a function of a single variable called "damage parameter", which can be computed from cyclic tests data and irregular loading paths (Chiaradonna et al., 2018).

9.2 VALIDATION OF ENERGETIC PORE PRESSURE MODEL BY CENTRIFUGE TESTS

The energetic pore pressure model proposed in Chapter 8 (eq. (8.12)) has been validated starting from the results of centrifuge tests.
In order to reproduce typical ground conditions where liquefaction occurs, a set of centrifuge tests has been carried out at ISMGEO (Italy) laboratory on models of a liquefiable soil, within the European project LIQUEFACT.
ISMGEO centrifuge has an arm of 3 m and a capacity of 240 g-tonnes (maximum payload 400 kg, max acceleration 600 g). In 2010 it was equipped with a 1 degree-of-freedom shaking table. Two hydraulic actuators fire input signals up to 1MHz at 100 g. The peak velocity of the shaking table is 0.9 m/s and the peak displacement 6.35 mm (Fasano et al., 2018).
The soil models were reconstituted by air pluviation of dry sand at a target void ratio. A latex membrane between the soil and the container guarantees water-tightness along the vertical sides. The membrane is fixed to the bottom and the top of the frame stack. A flexible aluminium mesh was inserted between the soil and the membrane along the short sides of the box. It was connected to the bottom of the stack to improve shear stress transmission at the side boundaries of the soil layer during shaking. During soil pluviation the models were instrumented with miniaturised accelerometers and with pore pressure transducers deployed at several depths. Displacement transducers (potentiometers) were located at the ground surface. After deposition, the soil layer was saturated with a pore fluid with scaled viscosity. A hydraulic gradient was imposed between the bottom and the top of the layer using a vacuum system. The achievement of complete saturation was controlled by measuring the volume of fluid accumulating in the box and comparing it with the volume of voids (Fasano et al., 2018).
To study the effect of the initial confining stress (σ'_c), dynamic centrifuge tests were conducted at scales of 50g, in free-field conditions. Finally, acceleration time histories were applied at the base of the model.
Three centrifuge tests have been analysed: two of them have been performed by ISMGEO on Pieve di Cento (BSS) (M1_S3_GM17 model) and Ticino (M1_S1_GM31) sands (database LIQUEFACT), while the third one was carried out on Hostun sand, whose results were published by Adamidis and Madabhushi (2016).

9.2.1 CENTRIFUGE TEST ON PIEVE DI CENTO (BSS) SAND: M1_S3_GM17 MODEL

In this section, the centrifuge test: M1_S3_GM17 on Pieve di Cento (BSS) sand is processed.
A sketch of the laminar box and instrumentation placed within the soil is illustrated in Figure 9.1.

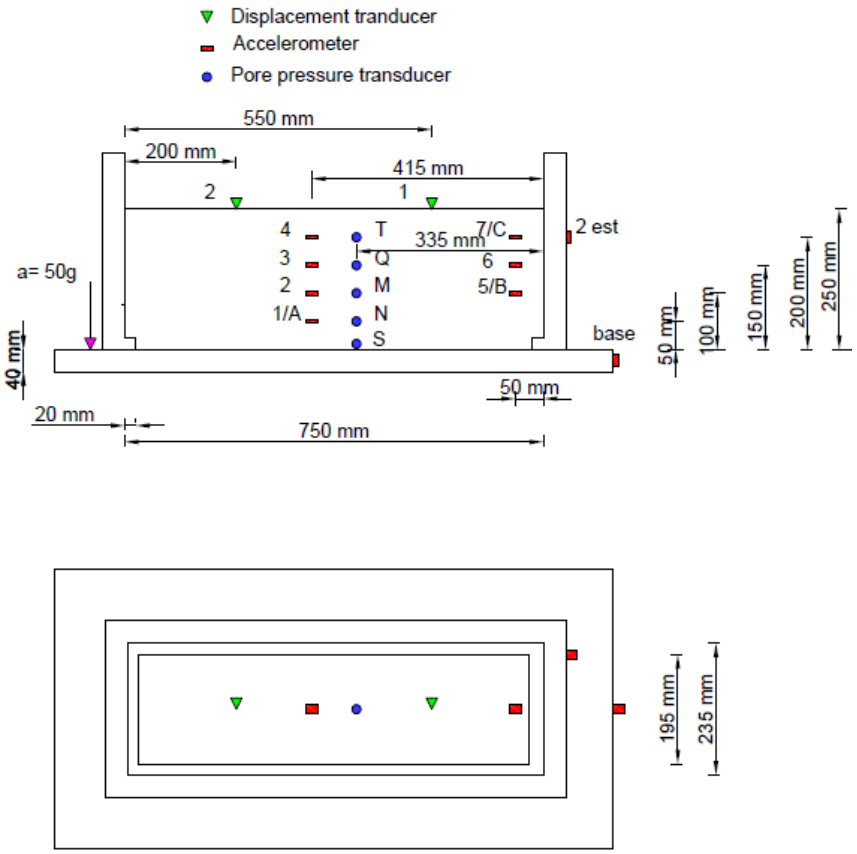

Figure 9.1. Laminar box and model configuration of M1_S3_GM17.

The acceleration time history for prototype is shown in Figure 9.2a. It is applied at the base of the model and is spectrum compatible with the 2012 Emilia Romagna (Italy) earthquake.

Figure 9.2b shows the excess pore pressure ratio with time at several depth. r_u was calculated from the recorded excess pore pressure by means of pore pressure transducers (Fig. 9.1). As clearly shown in Figure 9.2b, liquefaction never occurs since the maximum r_u is 0.40, recorded at the point T (Fig. 9.1).

In Figure 9.3a, the soil column at prototype scale has been represented together with the pore pressure measurements before and during the shock. Furthermore, in Figure 9.3b the excess pore pressure ratio has been reported with depth. Since r_u never reach the threshold of 0.90, the safety coefficient should be higher than 1. In order to confirm such assumption, the energy-based method has been used to evaluate the liquefaction potential. The capacity of the soil has been considered equal to $0.006 \cdot \sigma'_m$, while the demand has been computed by performing a dynamic response analysis by means of EERA, as explained in §9.1.

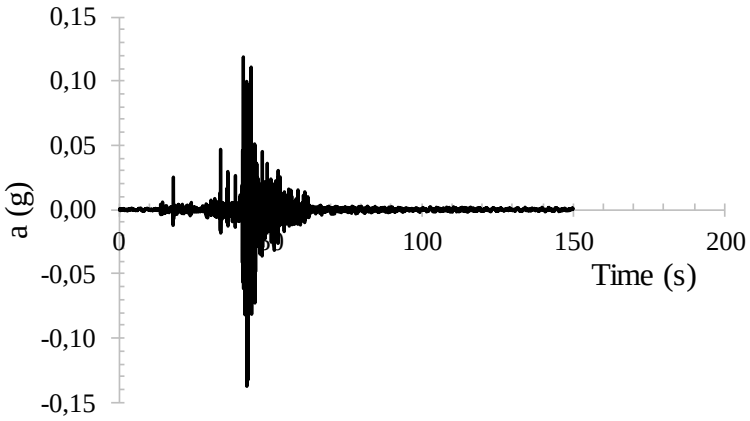

(a)

Figure 9.2. Horizontal base acceleration time history (a) and excess pore pressure ratio with time at different depth (b).

(a)

(b)

Figure 9.3. Soil model and pore pressure measurements before and during the shock (a) and excess pore pressure ratio with depth (b).

The soil column of 11.5 m has been discretized in layer of 0.5 m with a total unit weight of 19.0 kN/m^3 and attributing to it the decay and damping laws reported by Chiaradonna et al. (2019b). Finally, the input motion has been applied at the base of the model.
The cumulated value of the dissipated energy has been provided by EERA for each layer of Pieve di Cento soil profile. As an example, two depths have been considered (2.48 and 6.97 m from ground surface), whose cycles τ-γ have been reported in Figure 9.4a-c, while in Figure 9.4b-d the normalized dissipated energies with time have been plotted together with the value of capacity (E_s/σ'_m= 0.006, represented with the black dashed line). It is worth noting that the effective stress has been calculated via eq. (8.9), assuming a representative value of k_0= 0.50, congruently with the results achieved in laboratory tests (cyclic simple shear tests with confining pressure, see §5.1.5.1).

Moreover, the energetic pore pressure generation models presented in Chapter 8 have been used to simulate the experimental trend of the excess pore pressure ratio with depth, already shown in Figure 9.3. Starting from the values of E_s/σ'_m with depth, achieved from the dynamic response analysis performed by EERA, the values of r_u with depth have been computed by means of the simple and traditional model of Berrill and Davis (1985) (eq. (2.13)) and that proposed in this research (eq. (8.12)). In the latter case, it should be specified that r_u can be evaluated by solving eq. (8.12) according to an iterative procedure, known E_s/σ'_m at different depths. In Figure 9.5 the comparisons between the experimental r_u and those evaluated according to the model of Berrill and Davis (1985) (a) and those computed by means of the energetic model proposed in this research (eq. (8.12)) are plotted.

Figure 9.4. Cycles τ-γ induced by input motion (a; c) and normalized dissipated energy with time (b; d) at different depths.

The model of Berrill and Davis (1985) overestimates significantly the excess pore pressure ratio, predicting a r_u almost constant with depth and equal to 0.60 (Fig. 9.5a). On the other hand, the proposed method is in good agreement with the experimental results at a depth of 2.48 m from ground surface (Fig. 9.5b), while at deeper layers it tends to overestimate r_u as well.

Generally speaking, it can be said that the prevision of excess pore pressure ratio with depth should be more reliable as higher is r_u and thus closer to liquefaction.

Figure 9.5. Recorded and computed excess pore pressure ratio by means of the energetic model of Berrill and Davis (1985) (a) and the proposed eq. (8.12) (b) along the soil column.

In order to verify what has been asserted, eq. (8.12) has been used to predict the excess pore pressure profile for a centrifuge test where liquefaction occurs. The results will be shown in the following paragraph.

9.2.2 CENTRIFUGE TEST ON TICINO SAND: M1_S1_GM31 MODEL

In this section, the centrifuge test: M1_S1_GM31 on Ticino sand will be analysed. The laminar box and the relative instrumentation are illustrated in Figure 9.6.

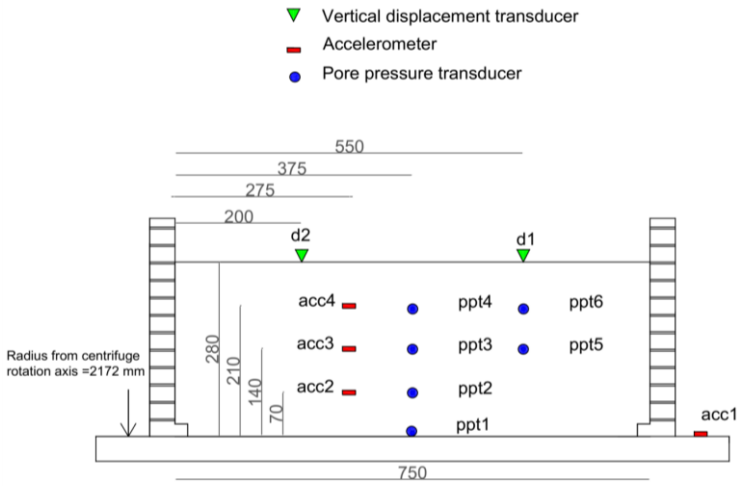

Figure 9.6. Laminar box and model configuration of M1_S1_GM31.

The acceleration time history is shown in Figure 9.7a and, as for the tests on Pieve di Cento sand, it is applied at the base of the model.

Figure 9.7b shows the excess pore pressure ratio with time at several depth. r_u was calculated from the recorded excess pore pressure by means of pore pressure transducers (Fig. 9.6). It can be noted that liquefaction occurs in the middle of the model (see, ppt2 and ppt3), while the shallowest pore pressure transducer, ppt4 reaches a pore pressure which correspond to r_u of 0.75, a bit higher than that computed from the measure of ppt1 transducer (0.68).

In Figure 9.8a, the soil column at prototype scale is represented together with the pore pressure measurements before and during the shock (maximum reached values), while in Figure 9.8b the excess pore pressure ratio has been reported with depth. As already anticipated looking at Figure 9.7b, liquefaction is attained between 6 and 10 m.

In order to confirm such experimental evidence, the liquefaction potential has been computed by means of the proposed energy-based approach. The specific deviatoric energy to reach liquefaction has been achieved by EERA carrying out a site response analysis of the uniform soil column by applying the accelerogram (Fig. 9.7a) at the base.

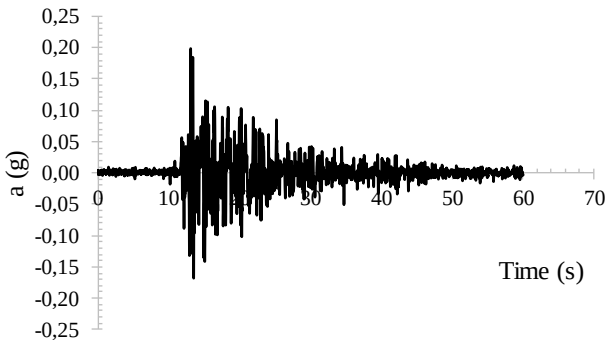

(a)

Figure 9.7. Horizontal base acceleration time history (a) and excess pore pressure ratio with time at different depth (b).

Figure 9.8. Soil model and pore pressure measurements before and during the shock (maximum value) (a) and excess pore pressure ratio with depth (b).

The soil column, with a thickness of 12.9 m has been discretized in layers of 0.5 m each, with a total unit weight of 19.5 kN/m^3. The decay and damping laws of Ticino sand has been kindly provided by ISMGEO.
As for Pieve di Cento sand, the cycles τ-γ have been reported in Figure 9.9a-c for two different depths (2.93 – 6.07 m), while in Figure 9.9b-d the soil capacity (E_s/σ'_m= 0.006) has been compared with the demand, assuming k_0 of 0.50.
It can be noted that at the depth of 2.93 m the demand is lower than capacity, on the contrary at the depth of 6.07 m, the demand comes very close to the black dashed line, which represents the capacity (Fig. 9.9d). It suggests that at the depth of 6.07 m FS results close to 1, congruently with the experimental evidences.

Figure 9.9. Cycles τ-γ induced by input motion (a; c) and normalized dissipated energy with time (b; d) at different depths.

In Figure 9.10a-b E_s/σ'_m and FS (defined by eq. (9.1)) have been plotted with the depth. Figure 9.10a explains more clearly at which depth the demand is higher than capacity and thus FS is close to 1 (Fig. 9.10b). The results achieved by performing liquefaction analysis

by using the energetic approach show that liquefaction occurs between 6 and 10 m, congruently with the experimental evidences.

In addition, the excess pore pressure ratio with depth has been simulated by means of Berrill and Davis (1985) model and that proposed in this research (eq. (8.12)). The results are shown in Figure 9.11, where the predictions are compared with the experimental measurements.

Unlike M1_S3_GM17 model, where it was possible to note a significant misprediction using Berrill and Davis (1985) model, for Ticino soil column its prediction fits well the experimental results, even though r_u is always slightly lower than 0.90 (Fig. 9.11a). This is because the model of Berrill and Davis (1985) has been calibrated in Chapter 8 to fit the experimental curve to have a good agreement with the results close to liquefaction (r_u>0.80) rather than far from it (low r_u values).

Figure 9.10. Comparison between capacity and demand (a) and factor safety (b) with depth in M1_S1_GM31 model.

Figure 9.11. Recorded and computed excess pore pressure ratio by means of the energetic model of Berrill and Davis (1985) (a) and the proposed eq. (8.12) (b) along the soil column.

9.2.3 CENTRIFUGE TEST ON HOSTUN SAND

In order to verify the energetic pore pressure model on centrifuge tests performed on different sands from those characterized in this thesis, the test of Adamidis and Madabhushi (2016) has been considered. A horizontal uniform layer of Hostun sand (G_s=2.65; e_{max}=1.041 – e_{min}=0.555) was created in a laminar box container, reproducing an ideal free-field condition. The model was prepared by air pluviation with a void ratio of 0.825 and spun up to a centrifuge acceleration of 50g. The horizontal time history acceleration, plotted in Figure 9.12, was applied at the base of the model. Four pore water pressure transducers at depths of 1.21, 5.47, 6.90 and 11.40 m were able to measure and record the pore pressures.

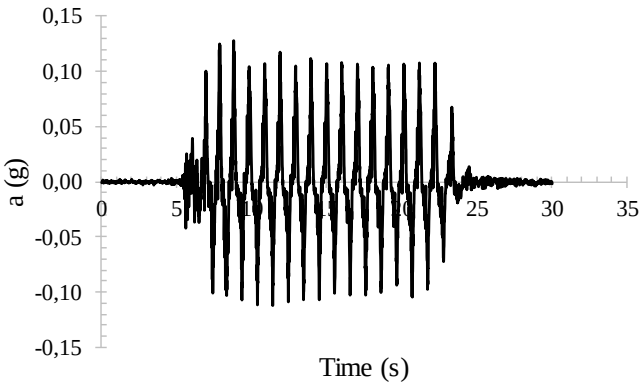

Figure 9.12. Input motion of centrifuge test on Hostun sand.

The results reported by Adamidis and Madabhushi (2016) show that r_u exceeds 0.90 along the whole column, except at a depth of 11.40m, where r_u reaches a value of about 0.70. In other words, liquefaction occurs almost along the whole column.
As previously shown for the other centrifuge tests, the energetic approach has been used to assess the liquefaction potential. In Figure 9.13a E_s/σ'_m has been plotted with depth. Apart from the shallowest layer, the demand is always higher than the capacity, suggesting that such layers are susceptible to liquefaction. It is much more evident plotting FS with depth. FS is obviously lower than 1 when demand overcomes the capacity, on the contrary it is higher than 1 at a depth of 1.60m.
Furthermore, the excess pore pressure ratio has been predicted by means of Berrill and Davis (1985) model and that proposed in this thesis (eq. (8.12)). The results have been plotted in Figure 9.14.
Both the energetic pore pressure models returned similar results, overestimating r_u at the bottom of the soil column and underestimating that in the shallow layer.
Such results confirm that Berrill and Davis (1985) model and the proposed one tend to give similar results when liquefaction occurs or when r_u are higher enough (r_u>0.70).
Despite such difference with the experimental data, the proposed model seems to work satisfactorily, taking into account the fact that it does not depend on the time histories acceleration (regular or irregular) and it no need to be calibrated on the results of laboratory tests. In fact, it should be emphasised that this centrifuge test has been performed on Hostun sand, which has not been tested in this research, so that it seems to suggest that eq. (8.12) can be used as a general rule for different kind of sandy soils in different state conditions.

Figure 9.13. Comparison between capacity and demand (a) and factor safety (b) with depth.

Figure 9.14. Recorded and computed excess pore pressure ratio by means of the energetic model of Berrill and Davis (1985) (a) and the proposed eq. (8.12) (b) along the soil column.

In conclusion, despite some limitations for extremely low r_u (<0.20) as shown in §9.2.1, the proposed model seems to be consistent returning better results than those achieved by means of the simpler model of Berrill and Davis (1985). In other words, eq. (8.12) results a useful tool to predict in simple way the excess pore pressure ratio, known the ratio E_s/σ'_m which can be easily computed by dynamic response analysis. Obviously, it has to be specified that it should be used as a preliminary analysis to get an idea of the excess pore pressure ratio profile and cannot replace more sophisticated models based on dynamic analyses, which take into account the non-linear behaviour of the soil.

9.3 CASE HISTORIES: ASSESSMENT LIQUEFACTION POTENTIAL AND PREDICTION OF EXCESS PORE PRESSURE

The same procedure described in §9.1 to assess liquefaction potential and predict the excess pore pressure, and applied for centrifuge tests has been used for two case histories, in free-field conditions related to the 1989 Loma Prieta earthquake (Marina district) and to the 2012 Emilia Romagna earthquake (Pieve di Cento).

9.3.1 MARINA DISTRICT (1989 LOMA PRIETA EARTHQUAKE)

Marina District is located on the north side of San Francisco, California, and experienced significant damage during the 1989 Loma Prieta earthquake (M_w=6.9) even though it was more than 100 km from the epicentre (Chiaradonna et al., 2019a). Most of damage was due to liquefaction phenomena.

Unfortunately, no accelerometer was located in the Marina District during the earthquake, even though the closest site recording main-shock accelerograms was located on the bedrock in Pacific Heights, approximately 1.5 km south of the Marina District (Boatwright et al. 1992). Further information about the geological profile of this site can be found in Bonilla (1992).

At the time of the earthquake, the depth to the ground water table ranged between 2.3 and 5.5 m within the Marina District. However, Bonilla (1992) considered the ground water table at 2.9 m, so that such depth has been considered in this study.

The geotechnical profile used in the analyses is reported in Figure 9.15 (Chiaradonna et al., 2019b), where the shear wave velocity profile is that reported by Rollins and Mc Hood (1991).

As reported by Chiaradonna et al. (2019b), since no recorded accelerograms were available, the E-W component of the acceleration record at Yerba Buena Island will be used as input motion at the base of the numerical model. Because of the uncertainties in the definition of the outcrop motion, Rollins and McHood (1991) suggested applying it scaling the recorded PGA to 0.15g (Figure 9.16).

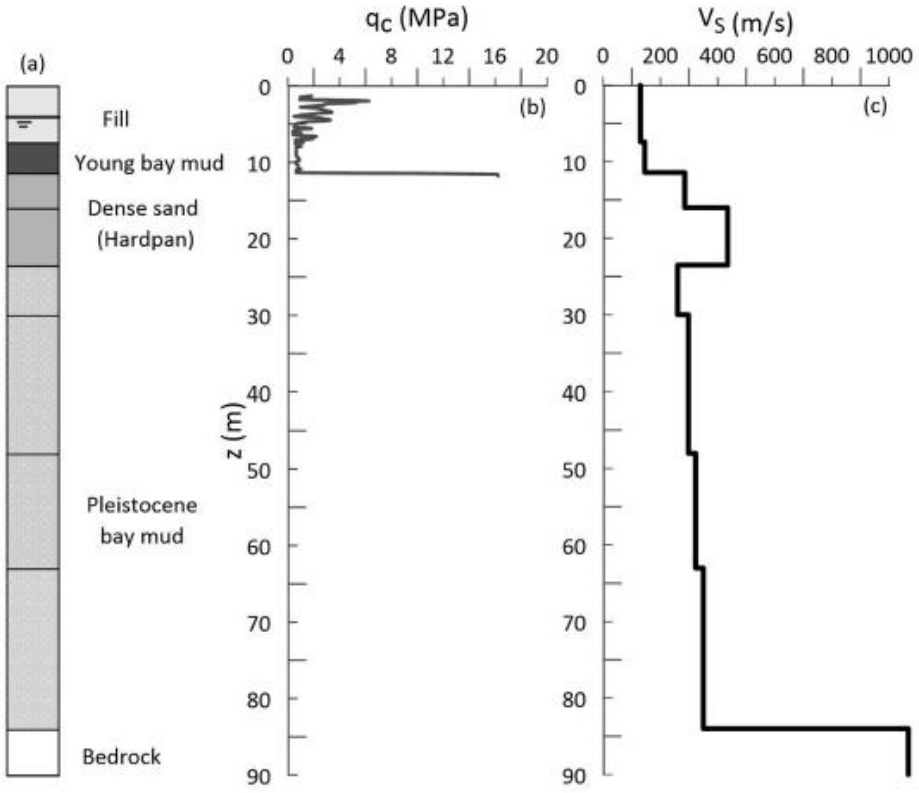

Figure 9.15. Soil profile (a); CPT (b) and vs profile (c) (Chiaradonna et al., 2019a).

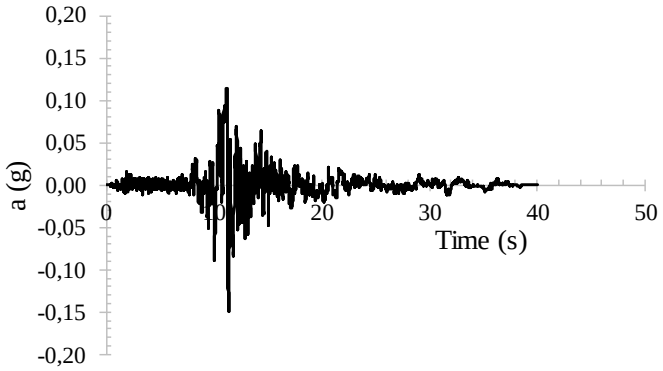

Figure 9.16. Input motion of Marina District.

The assessment of liquefaction potential has been performed by means of stress and energy-based approaches, as will be shown in the following sections.

9.3.1.1 STRESS BASED APPROACH

As described in §2.3.1 the stress-based approach is the most common way to assess liquefaction potential. In Figure 9.17a the vertical profile of CRR and CSR, computed via eqs. (2.27)-(2.24), respectively, has been plotted, where the a_{max} of eq. (2.24) is 0.15g. CSR results higher than CRR along the whole profile, so that the safety factor defined as the ratio between CRR and CSR is lower than 1 (Fig. 9.17b). In other words, the whole sandy layer is potentially liquefiable under the assigned input motion.
Furthermore, FS lower than 1 means that the excess pore pressure ratio is 1 along the profile (Chiaradonna and Flora, 2019).

Figure 9.17. Vertical profile of CRR and CSR (a) and FS (b).

9.3.1.2 ENERGY BASED APPROACH

The energy-based approach can be used performing a dynamic response analysis by means of EERA as described in §9.1. As reported by Chiaradonna et al. (2019a), the upper bound decay and damping curves proposed by Seed and Idriss (1970) were assumed for the sandy layers, while the curves obtained by laboratory tests on young bay mud samples by Sun et al. (1988) were assumed for the clayey formations (Fig. 9.18a-b).

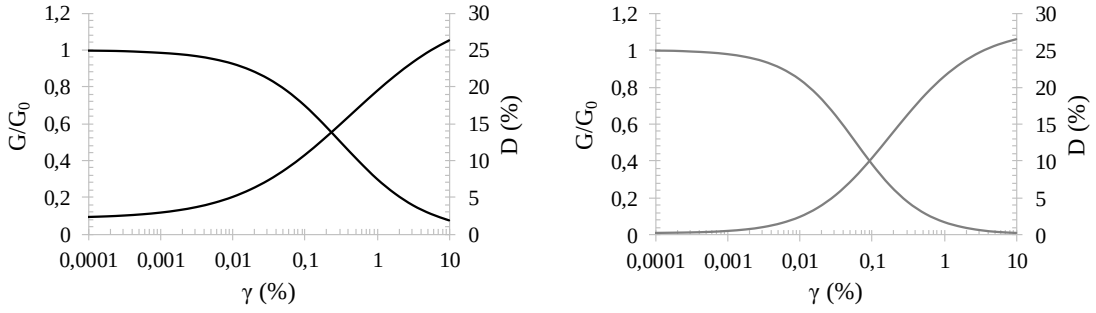

Figure 9.18. Normalized shear modulus and damping ratio versus shear strain for clayey (a) and sandy (b) deposits.

The input motion of Figure 9.16 has been applied at the base of the soil column. As an example, the cycles γ-τ at two different depths (3.73 and 5.28 m) have been plotted in Figure 9.19.

Figure 9.19. Cycles τ-γ induced by input motion (a; c) and normalized dissipated energy with time (b; d) at different depths.

At a depth of 3.73 m the capacity is higher than the demand, on the contrary at 5.28m the demand overcomes the threshold of 0.006, so that such layer can be assumed liquefiable. In Figure 9.20a-b the profile of E_s/σ'_m and FS can be observed, respectively.
For the layers between 5.0 and 8.5 m FS is lower than 1 and thus they result potentially liquefiable.

Figure 9.20. Comparison between capacity and demand (a) and factor safety (b) with depth for Marina District.

In order to predict the excess pore pressure, starting from the values of E_s/σ'_m, the model of Berrill and Davis (1985) and that proposed in this research (eq. (8.12)) and validated by centrifuge tests have been used.

The results have been compared with those achieved by Chiaradonna et al. (2019a) by means of SCOSSA. Figure 9.21a shows the comparison of r_u profile between SCOSSA and Berrill and Davis (1985), while Figure 9.21b compares the results of SCOSSA and the energetic model proposed in eq. (8.12). The two energetic pore pressure models return a similar trend of r_u with the depth. r_u computed according to the energetic models are lower than that evaluated through SCOSSA in the shallowest layers, between 3 and 4 m, while from 4.5 to 7 m, the energetic models and SCOSSA give the same result in terms of r_u profile (r_u=0.90) congruently with the susceptibility analysis shown in Figure 9.20.

Figure 9.21. Comparisons between the excess pore pressure ratio profile evaluated by SCOSSA that achieved by the energetic model of Berrill and Davis (1985) (a) and that proposed in eq. (8.12) (b) along the soil column of Marina District.

9.3.2 PIEVE DI CENTO (2012 EMILIA ROMAGNA EARTHQUAKE)

The second case history which has been studied is Pieve di Cento, affected by extensive liquefaction phenomena during the 2012 Emilia Romagna earthquake.
The subsoil profile has been shown in Figure 3.9. As already mentioned, the grey silty sand from a depth of 4.7 to 6 m is considered liquefiable, based on the observations after the earthquake.
As for Marina District case history the stress and energy-based approaches have been used to assess liquefaction potential. Then, the results achieved with two approaches have been compared.

9.3.2.1 STRESS BASED APPROACH

As well-known, CSR can be computed via eq. (2.24). The maximum acceleration a_{max} has been evaluated according to the recorded peak ground acceleration (PGA) in the MRN station of the Italian strong motion network, located in Mirandola town (a_{max}=0.273g) during the mainshock of the Emilia 2012 earthquake sequence occurred on May 20, (Chiaradonna et al., 2019c).
Regarding CRR, it should be specified that it can be achieved by eq. (2.27), based on the results of CPT tests, performed by TREVI (Chapter 3). Considering the ground water table at a depth of 1.80 m, the CRR and CSR profile is shown in Figure 9.22a. As a matter

of the fact that CSR is always higher than CRR, the safety coefficient (FS) is obviously lower than 1 and thus, according to stress-based approach all sandy layers from 1.80 to 6.00 m from ground surface should be liquefiable, in disagreement with the evidences emerged after the earthquake.

Figure 9.22. Vertical profile of CRR and CSR (a) and FS (b).

Such results have been compared with those obtained by performing a liquefaction susceptibility analysis according to the energetic approach.

9.3.2.2 ENERGY BASED APPROACH

In order to perform a susceptibility analysis to liquefaction according to the energy-based method, a site response analysis of Pieve di Cento has been carried out by means of EERA (§9.1).
The stratigraphy column has been modelled till 10 m, by using the decay and damping laws of Chiaradonna et al. (2019b) (Fig. 9.23a). Also the input motion – applied at a depth of 10 m from the ground surface - was provided by the same authors and reported below (Fig. 9.23b), with a PGA of 0.122g. As reported by Chiaradonna et al. (2019b), the input motion was adopted deconvolving outcrop motion until the bedrock (230m) and then propagating it up to 10m depth.

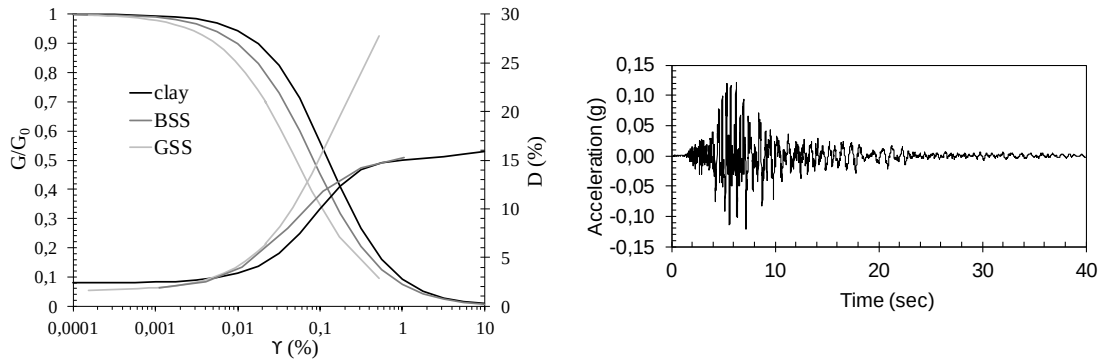

(a) (b)

Figure 9.23. Decay and damping laws of Pieve di Cento soils (a) and input motion applied at 10 m (b).

The cumulated value of the dissipated energy has provided by EERA for each layer of Pieve di Cento stratigraphy. As an example, two depths have been considered (2.25 and 5.20 m from ground surface), whose cycles τ-γ have been reported in Figure 9.24a-c while in Figure 9.24b-d the normalized dissipated energies with time have been plotted together with the value of capacity (E_s/σ'_m= 0.006, represented with the black dashed line). It is worth noting that the effective stress (σ'_m) has been calculated via eq. (8.9), assuming a representative value of k_0= 0.50, which was achieved in laboratory tests (cyclic simple shear tests with confining pressure, §5.1.6). At depth of 2.25 m the capacity is higher than demand suggesting that these layers are not susceptible to liquefaction, conversely, the layer at a depth of 5.20m has a higher demand which overcomes the critical value of 0.006 identified as the capacity of the soil. Therefore, according to energy-based method, this layer could be subjected to liquefy.

Figure 9.24. Cycles τ-γ induced by input motion (a; c) and normalized dissipated energy with time (b; d) at different depths.

In Figure 9.25a the demand has been plotted with depth for each sandy layer together with the capacity (Lirer et al., 2020). It can be noted that after 5 m from ground surface, sandy soils are potentially liquefiable confirming the experimental evidences of Lombardi and Bhattacharya (2014), according to which grey silty sand liquefied during the 2012 earthquake. Moreover, the safety factor FS has been plotted with depth in Figure 9.25b. As expected, it is lower than 1 (liquefiable layer) after 5m from ground surface.

Figure 9.25. Comparison between capacity and demand (a) and factor safety (b) with depth in Pieve di Cento site.

In order to confirm, once again, the effectiveness of the energetic-based models of Berrill and Davis (1985) and that proposed in eq. (8.12), the excess pore pressure ratio has been evaluated in each layer, known the value of the normalized specific deviatoric energy

(demand) given by EERA (Fig. 9.26). Those values have been compared with the ones given by the computer code SCOSSA.
The energetic model to predict the excess pore pressure in a sandy soil deposit, calibrated on the experimental results of tests on several sands in different conditions, gives results in very good agreement with those of a more complex dynamic analysis (Fig. 9.26b) (Lirer et al., 2020). On the contrary, the simple model proposed by Berrill and Davis (1985) overestimates the excess pore pressure ratio at shallow depth, where the normalized specific deviatoric energy is lower (Fig. 9.26a) and overestimates r_u at deeper layers, where liquefaction is attained. As already shown in the previous paragraph, the model of Berrill and Davis (1985) is not able to simulate the excess pore pressure lower than 0.70, while it seems to improve close to liquefaction (r_u=0.90). However, once again the model proposed in this thesis seems to give a better prevision of r_u profile than that of Berrill and Davis (1985).

Figure 9.26. Comparisons between the excess pore pressure ratio profile evaluated by SCOSSA that achieved by the energetic model of Berrill and Davis (1985) (a) and that proposed in eq. (8.12) (b) along the soil column of Pieve di Cento.

9.4 FINAL CONSIDERATIONS

To sum up, the potentiality of the energetic approach proposed in this study to evaluate the liquefaction potential seems to be confirmed by the results shown in this Chapter. Moreover, the energy-approach returns results congruent with the experimental evidences, as for Pieve di Cento, where the energetic analysis reveals that only grey silty sand is liquefiable, on the contrary the stress-based approach identifies all sandy soils potentially liquefiable. In other words, the stress-based approach returns results which

can be no-reliable resulting a bit rough, just think to the coefficient 0.65 of eq. (2.24), which could be questionable. On the contrary, the energy-based method is based on more consistent concept of energy which is demonstrated to be independent – or slightly dependent - on the shape of loading, state and intrinsic parameters of the soil.

Within the energy framework, the knowledge of the seismic demand E_s/σ'_m at each depth, allows the quantification of the corresponding induced excess pore pressure ratio r_u by means of the experimental relationship between $E_s/\sigma'_m - r_u$ reported in eq. (8.12). Such relationship has been applied to simulate the profile of r_u in centrifuge tests performed on three different soils: Pieve di Cento (BSS), Ticino and Hostun sands. Despite some differences, especially for r_u lower than 0.20 (see, for instance the results of centrifuge test on Pieve di Cento sand), the agreement between the results achieved from the eq. (8.12) and the experimental data can be considered satisfactorily. In fact, no need to calibrate any parameter because the eq. (8.12), obtained as an average curve of the relationship $E_s/\sigma'_m - r_u$ for different soils in different conditions, can be assumed as a general law.

Finally, the proposed energy model is in a very good agreement with the prevision given by the more accurate dynamic analysis (code SCOSSA), especially for the case history of Pieve di Cento.

In conclusion, the large potentiality of the energy-based approach to assess the liquefaction triggering and the induced excess pore pressure within the soil during the earthquake is confirmed and demonstrated. However, it is important to estimate adequately the seismic demand and to remind that the proposed model can be a useful tool to predict the profile of excess pore pressure when a preliminary analysis has to be performed, while in more complex case studies the dynamic analysis is strongly recommended.

REFERENCES

Adamidis O, and Madabhushi G.S.P. (2016). Post-liquefaction reconsolidation of sand. *Proc R Soc A472:20150745*. https ://doi.org/10.1098/rspa.2015.0745.

Bardet J.P., Ichii K. and Lin C.H. (2000). EERA – A computer program for Equivalent-Linear Earthquake site response analysis of layered soil deposits. *Department of Civil Engineering, University of Southern California,* USA.

Berrill, J. B., and Davis, R. O. (1985). Energy Dissipation and Seismic Liquefaction of Sands: Revised Model. *Soils and Foundations*, 25: 106-118.

Boatwright J., Seekins L.C., Fumal T.E., Liu H., Mueller C.S. (1992). Ground-motion amplification. *The Loma Prieta, California, Earthquake of October 17, 1989—Marina District*. USGS survey professional paper 1551-F.

Bonilla M.G. (1992). Geologic and historical factors affecting earthquake damage. *The Loma Prieta, California, Earthquake of October 17, 1989—Marina District.* USGS survey professional paper 1551-F.

Chiaradonna, A., d'Onofrio, A., and Bilotta, E. (2019a). Assessment of post-liquefaction consolidation settlement. *Bulletin of Earthquake Engineering*, *17*(11): 5825-5848.

Chiaradonna, A., Lirer, S., Flora, A. (2019b). A damage-based liquefaction potential index for microzonation studies. *Engineering Geology* (Under review).

Chiaradonna A. and Flora A. (2019). On the estimate of seismically-induced pore water pressure increments before liquefaction. *Geotechnique letters*. In print.

Chiaradonna A., Tropeano G., d'Onofrio A., Silvestri F. (2018). Development of a simplified model for pore water pressure build-up induced by cyclic loading. *Bulletin of Earthquake Engineering 16(9)*:3627–3652. https://doi.org/10.1007/s10518-018-0354-4.

Chiaradonna, A., Tropeano, G., d'Onofrio, A., Silvestri, F. (2019c). Interpreting the deformation phenomena of a levee damaged during the 2012 Emilia earthquake. *Soil Dynamics and Earthquake Engineering*, *124*: 389-398.

Fasano G., Bilotta E., Flora A., Fioravante V., Giretti D., Lai C.G. and Özcebe A.G. (2018). Dynamic centrifuge testing to assess liquefaction potential. *Physical Modelling in Geotechnics, Proc. 9th Int. Conf. on Physical Modelling in Geotechnics, ICPMG 2018,* July 17-20, London, United Kingdom, Volume 2, 955-960.

Ishihara, K., and Yasuda, S. (1972). Sand liquefaction due to irregular excitation. *Soils and foundations*, 12(4): 65-77.

Lirer, S., Chiaradonna, A., and Mele, L. (2020). Soil Liquefaction: from mechanisms to effects on the built environment. *RIG* (submitted).

Lombardi, D., and Bhattacharya, S. (2014). Liquefaction of soil in the Emilia-Romagna region after the 2012 Northern Italy earthquake sequence. *Natural hazards*, *73*(3): 1749-1770.

Matasovic N., and Vucetic M. (1993). Cyclic Characterization of Liquefiable sands. *J Geotech Eng 119(11)*:1805–1822.

Rollins K.M., McHood M.D. (1991). Comparison of computed and measured liquefaction-induced settlements in the Marina District, San Francisco. *The Loma Prieta, California, Earthquake of October 17, 1989-Liquefaction.* USGS survey professional paper 1551-B.

Seed H.B. and Idriss I.M. (1970). Soil moduli and damping factors for dynamic response analysis. *Report No EERC 70-10, University of California*, Berkeley, California.

Seed, H. B. and Idriss, I. M., (1971). Simplified procedure for evaluating soil liquefaction potential. *Journal of Soil Mechanics and Found. Division, ASCE, 107(SM9):* 1249 - 1274.

Sun J.I., Golesorkhi R., Seed H.B. (1988). Dynamic moduli and damping ratios for cohesive soils. *Report No UCB/EERC-88/15. University of California* at Berkeley.

Tropeano G., Chiaradonna A., d'Onofrio A. , Silvestri F. (2019). A numerical model for non-linear coupled analysis on seismic response of liquefiable soils. *Computers and Geotechnics* 105: 211-227.

Tropeano G., Chiaradonna A., d'Onofrio A., Silvestri F. (2016). An innovative computer code for 1D seismic response analysis including shear strength of soils. *Geotechnique*, 66(2):95–105. http://dx.doi.org/10.1680/jgeot.SIP.15.P.017.

CHAPTER 10

10. CONCLUDING REMARKS AND FUTURE WORK

Such Chapter concludes this research work, summarizing the main findings presented in this thesis and providing useful recommendations to carry on such work.

10.1 SUMMARY AND CONCLUDING REMARKS

Liquefaction is a phenomenon marked by a rapid loss of shear strength and stiffness which can be induced by a seismic event. The consequences may be catastrophic as demonstrated in several case histories. In this framework the European project LIQUEFACT has been developed, studying traditional and innovative mitigation techniques against liquefaction. In order to verify the effectiveness of some mitigation techniques (horizontal drainage and induced partially saturation) a site located in Pieve di Cento (Emilia Romagna Region, Italy), affected by extensive liquefaction phenomena during the 2012 earthquake in Northern Italy, was chosen as a test site.
Within the project LIQUEFACT an extensive testing program has been performed, representing one of the most important part of this research work. It is organized into three macro-parts: a contribution to site characterization of Pieve di Cento field trial, the study of mitigation techniques at small scale and further considerations on the basic mechanisms of liquefaction phenomena, which have allowed to pass from small to large scale.

10.1.1 CONTRIBUTION TO CHARACTERIZATION OF PIEVE DI CENTO FIELD TRIAL

The first part of this work has been completely dedicated to the characterization of Pieve di Cento field trial. With the main aim to contribute to the definition of a geotechnical model, grain size analyses and Atterberg's limit tests (on finer soils) were carried out on soil samples retrieved from boreholes sampling. This information, together with the results of CPTu carried out in this test-site, part of another research, have allowed to hypothesize the stratigraphic profile of Pieve di Cento test site till 10 m from ground surface. A wide laboratory and in-situ testing program have been performed mainly involving such work in laboratory tests, studying the behaviour of the sandy soils at small scale. Permeability, oedometric, monotonic and cyclic tests have been performed within this study on Pieve di Cento sands. Such sands have been distinguished in brown silty sand (BSS) retrieved by a backhoe in the first 2 meters, and grey silty sand (GSS) obtained as an "average sand" mixing sands retrieved from five boreholes sampling at a depth of 2.8 – 3.0 m from ground surface, where the mitigation interventions have been placed.
Monotonic triaxial tests have been performed on Pieve di Cento sands and compared with the results on sand from a site located at Sant'Agostino (Ferrara, Italy), in an area that was affected by extensive liquefaction phenomena during 2012 earthquake, as well. Such

tests have been performed by a Bishop & Wesley triaxial cell carrying out tests in strain-controlled mode. Considerations about the critical state condition have been made, extrapolating the results by means of a sigmoid function. The CSL has been achieved in the plane p'-q and logp'-e. Critical state friction angles (φ_{cs}) of 32.4° for Sant'Agostino and 32.9° for Pieve di Cento sands have been obtained.

In order to evaluate the effects of end conditions on the results of triaxial tests, further monotonic tests (drained and undrained) on GSS have been carried out by using MaTrix cell (§ 4.2.2).

The results of triaxial tests obtained with the Bishop & Wesley Triaxial cell and those of the MaTrix cell have been compared. The tested specimens have been prepared with similar relative densities, but two different preparation techniques have been adopted (frozen specimens for Bishop & Wesley and 1D compression for MaTrix cell).

Looking at the comparisons of the results between the two types of device, above mentioned, used in this research, the following observations can be done:

- the stiffness of the specimens is smaller in Bishop & Wesley than in MaTrix tests; this may be an effect of a greater uniformity of strains into the specimens that takes place in MaTrix apparatus;
- the peak of deviatoric stress which occurs in MaTrix tests is always higher than that achieved in the Bishop & Wesley apparatus. The reason can be twofold. Firstly, the two devices are different. Bishop & Wesley cell works through a pneumatic loading system, while the MaTrix cell is much more sophisticated, equipped with a mechanical loading system. Secondly, the specimens have been prepared with two different techniques. It surely influences the mechanical behaviour of soil, especially its peak strength;
- unlike the results of tests performed in the Bishop & Wesley triaxial cell, all specimens of MaTrix cell attain a steady condition. It can be considered as an effect of lubricated ends, enable to avoid localization phenomena of strains into the specimens;
- the CSL from MaTrix test results is above that obtained from tests performed by Bishop & Wesley cell, even though the difference is not so significant;
- the critical state friction angle (φ_{cs}), is 36.7° for tests performed in MaTrix cell and 32.9° in Bishop & Wesley apparatus. These results are in agreement with those reported in literature. In fact, even though a peak of strength should occur in tests performed with rough plates, it is followed by a softening (non-uniformity of strains), which is responsible of an underestimation of the φ_{cs}.

The results obtained from triaxial tests have been compared with those of simple shear tests. Undrained simple shear tests on Pieve di Cento (GSS) sand were performed with flexible boundary. In this case, the k_0-consolidation was performed by means of a sophisticated control system which allows to maintain a constant diameter - adjusting the vertical load - and thus to guarantee a simple shear stress condition. First of all, the truly simple shear condition has been verified. It can be easily understood that the control system introduces unavoidable oscillations of the diameter's measure around the target value. The radial strains have been quantified; they have an order of magnitude of 10^{-3}% that can be considered low enough to consider the deformations belong to the elastic field.

In other words, the diameter does not change permanently because plastic deformations are not induced.

The simple shear monotonic response of loose and dense GSS spacimens has been evaluated preparing specimens with two average relative density (D_r): 41 and 70%. As expected, the denser specimens exhibit a strain hardening type response. Even though the tests were conducted under different initial vertical stresses and void ratios, the stress path is similar.

It is well known that in simple shear tests continuous rotation of principal stress directions occurs, so the vertical and the horizontal stresses are not principal stress direction anymore. It makes complex the interpretation of such kind of tests. With the main aim to contribute to improve the interpretation of simple shear tests, further considerations have been done on the results of undrained simple shear tests. Performing tests with a flexible boundary makes possible to completely know the stress state of the specimen and thus build the Mohr's circles. From these tests, the friction angle in critical state condition (φ_{cv}) has been evaluated, resulting equal to 35.8°, consistent with the value achieved for triaxial tests in MaTrix cell (36.7°) and higher than that obtained from Bishop & Wesley cell (32.9°).

Additionally, the critical state line (CSL) in the plane logp' – e, from simple shear tests, has been compared with that obtained from triaxial tests. Consistently with Riemer and Seed (1997), the CSL of SS tests has been found below that of TX tests (Bishop & Wesley and MaTrix cell), even though the slope is the same and the scatter of the experimental data is much more evident.

Extensive testing has also been carried out under cyclic loading conditions. As for monotonic tests, for the cyclic ones, the results performed in triaxial and simple shear conditions has been compared. In particular, cyclic triaxial tests have been carried out also on standard sand, such as Leighton Buzzard, fraction E and Ticino sands. Such tests have been performed on loose specimens ($D_r \approx 45\%$) isotropically consolidated at 50 kPa, even though, for Leighton Buzzard sand one test at 25 kPa and two tests at 100 kPa have been performed. Despite the difference in terms of σ'_c, the cyclic resistance curve of specimens consolidated at 25, 50 and 100 kPa is unique. The reason could be explained by introducing the concept of state parameter (ψ), which is defined as the difference between the void ratio at the initial and at the critical state for the effective confining pressure of interest and that should synthetically identify a cyclic resistance curve, depending on both void ratio and confining stress.

The results of all cyclic tests have been interpreted according to the relationship of Booker et al. (1976) in the plane $N_{cyc}/N_{liq} - r_u$. The parameter β, which depends on the soil type and test conditions, influencing the shape of the curve, has been calibrated for all tests on different sands. The most important finding is that β seems to be strongly dependent on D_{60}. A power function $\beta = f(D_{60})$ fits well the experimental results, and if confirmed by further tests, it would be a useful tool to predict the excess pore pressure build-up of loose saturated sandy soils subjected to low confining stresses (from 25 to 100 kPa).

Cyclic simple shear tests have been performed on Pieve di Cento (BSS and GSS) sands and the results were compared with those of cyclic triaxial tests performed in similar

conditions, in terms of liquefaction resistance. To do that, Castro's correlation (Castro, 1975) has been used, evaluating k_0 according to two ways:

- by means of Jacky's formula (k_0=1-senφ), where the peak friction angle (φ_p) has been evaluated from monotonic tests performed in the same conditions as cyclic tests;
- from laboratory tests, such as cyclic simple shear tests performed with flexible boundary.

In both cases, in the plane N_{liq}-CRR, the CTX experimental points for BSS are slightly higher than those from CSS tests. For GSS the agreement of CTX and CSS results improve when k_0 is estimated according to cyclic simple shear tests. It can be said that k_0, deriving from the results of laboratory tests, seems to be more reliable than that computed via Jacky's formula. This is a further confirm of the reliability of the control system of CSS tests with flexible boundary.

Finally, undisturbed specimens have been tested. As well known, the results from reconstituted sandy specimens cannot perfectly reflect the natural fabric of a sand deposit and therefore it is extremely important to perform tests on undisturbed specimens. Oedometric and cyclic simple shear tests have been performed, contributing to define a geotechnical model of Pieve di Cento field trial, which was extremely useful also for other research works.

10.1.2 MITIGATION TECHNIQUES

Within the European project LIQUEFACT, three of the most promising and innovative liquefaction mitigation techniques have been studied: addition of fines, densification and desaturation. The main findings have been summarized in the following sections.

10.1.2.1 ADDITION OF FINES CONTENT

The effectiveness and applicability of adding fines content as a countermeasure against liquefaction has been studied by using laponite, so called "super-plastic nanoparticle".

Laponite appears like a white powder and when it is mixed with water hydrates and the mixture water laponite is liquid. Over time, such mixture becomes a gel. The time that the mixture takes to reach this physical state is called gelling time. This can be controlled by adding to the mixture an additive, such as sodium pyrophosphate (SPP).

The effectiveness of addition of fines content as a liquefaction countermeasure has been evaluated comparing the cyclic resistance of clean sand (Leighton Buzzard) with that of sand treated with laponite (1% of dry weight of sand). Although only two tests have been performed on sand/laponite specimens, the increase of liquefaction resistance is clear. Such effect can be attributed to the presence of laponite gel within the pores, which contributes to create bridge between the particles of sand, limiting the mobility of sand

and thus delays the triggering of the liquefaction process. Moreover, it seems more evident for higher N_{liq}.

Although the presence of laponite plays an important role in increasing soil liquefaction resistance, the evolution of pore pressure versus N_{cyc}/N_{liq} follows the same trend of untreated specimens. This is probably due to the fact that the concentration of laponite is high enough to increase resistance to liquefaction, but low enough not to alter the trend of excess pore pressure. Therefore, the excess pore pressure models proposed for clean sand can be used for sand treated with laponite when the concentrations are low (<5%).

Verified the effectiveness of such technique, it has been very important evaluate the rheological aspect, which may lead to problems regarding the applicability in situ. Owing to that, the injectability of mixture water-laponite has been studied in depth. The injectability of a mixture within the pores of a soil is related to the size of the suspended particles, the initial viscosity of the mixture (μ_0), and its gelling time (t_{gel}).

The results of viscosity tests, performed by a Marsh cone, for laponite concentration of 1.5% and 3%, show that the initial value of the viscosity (μ_0) of the tested mixtures is very low and similar to that of the water (μ_w=1cP). The results indicate that initial viscosity and the gelling time (t_{gel}) of the mixtures without additives are obviously a function of the concentration of laponite. As expected, the additive (SPP) ensures low viscosity of the mixture even in the presence of high concentration (ϕ_{lap}= 3%), and delays the gelification process of the mixture, favouring in situ mixture injection.

Regarding permeability tests, performed by a permeameter, it has been noted that there is no permeation into the specimen to the mixture water/laponite, regardless of concentration of nanoparticle in water (ϕ = 1.5 or 3.0%). The addition of SPP allows the mixture to permeate. It is worth noting that the presence of SPP not only improves the permeability into the specimen but contributes to make the permeability coefficient to the mixture (k_m) very similar to that of water.

In conclusion, the effectiveness of this technique at small scale has been verified, such as the possible applicability in situ, since it results injectable by adding SPP. Moreover, laponite is not so expensive and then, it should be used in little quantities, so that this countermeasure could be convenient also from an economic point of view. Despite these positive aspects, it is also important to consider the negative ones. Firstly, the environmental aspects. This technique, in fact consists of introducing a plastic material into the soil, that even if it is not polluting, it is a mixture which will become a gel and could obstruct the natural flow of groundwater. Another crucial point is the duration of this countermeasure and from a technical point of view, the treated volume is unknown. It is impossible to know which is the area that this intervention will recover. Moreover, a possible change in compressibility of soil as a result of the treatment need to be investigated.

10.1.2.2 DENSIFICATION

Densification is one of the most known technologies used against liquefaction in the world. It reduces the void space of the soil, thereby decreasing the potential for volumetric change that would lead to liquefaction. It is well known that, because of their dilatative

behaviour of dense sands have a higher resistance to liquefaction than loose sandy soils. The effectiveness of densification as liquefaction mitigation technique has been verified by performing cyclic triaxial and simple shear tests on Sant'Agostino and Pieve di Cento (BSS and GSS) sands.
Regardless of the tests performed, when D_r increases the liquefaction resistance increases as well. Moreover, it was observed that the value of D_r, in the investigated range (40-74%), does not influence significantly the shape of excess pore pressure law and thus β; on the contrary, the type of the soil and in particular D_{60} plays an important role in pore pressure generation, confirming the relationship found for untreated soils.
As for loose sands, the results of cyclic simple shear and triaxial tests have been compared by using Castro's correlation, where k_0 has been evaluated from the results of cyclic simple tests as the ratio between σ'_h and σ'_v. The average value of k_0 for tests on GSS is 0.521, obviously higher than that evaluated for loose sand (0.500). The results of cyclic triaxial and cyclic simple shear tests clearly identify a unique curve in the plane N_{liq}-CRR. This result confirms, once again, that Castro's correlation is fine to transform the data of cyclic triaxial tests in those of cyclic simple shear tests, showing additionally the reliability of the performed tests.
Regarding a possible in-situ application, it should be specified that densification is a simple technique and there are several ways to apply it (dynamic compaction, vibro compaction, the use of stone columns or compaction grouting), moreover it lasts over time. However, also this technique has negative aspects which have to be considered: it changes the stress state of the soil and it is not recommended close to existing buildings.

10.1.2.3 DESATURATION

Desaturation seems to be one of the most innovative and promising techniques against liquefaction. Its effectiveness has been tested in laboratory by means of non-saturated cyclic triaxial tests performed on three different kinds of sand: Sant'Agostino, Pieve di Cento (GSS) and Silica (N°5) sands. They have been tested in several conditions in terms of S_r, D_r and confining stress (σ'_{un}) where the confining stress has been evaluated according to Bishop notation, assuming the material parameter (χ) equal to S_r. Due to a difficulty to define the effective stress in non-saturated soils, liquefaction triggering has been identified according to the strain criterion (ε_{DA}=5%). However, comparing stress and strain criteria, it has been noted that they give different results in terms of N_{liq} and the difference tends to decrease as S_r increases. It means that, when ε_{DA}=5%, r_u will be lower than 0.90, and then the value of effective stress, at liquefaction (ε_{DA}=5%), or so called $\sigma'_{un,liq}$ will not be nil. Mele and Flora (2019) expressed a relationship between $\sigma'_{un,liq}/\sigma'_{un,0}$ as a function of S_{r0}, which has been confirmed by the experimental results presented in this thesis. It should be emphasized that such results are related to several grains distributions and state conditions in terms of D_r (from 29.4 to 67.2) and confining stresses (25-60 kPa). It is believed that, obviously, D_r influences the trend of r_u and then the value of $\sigma'_{un,liq}$; however, such dependence seems to be negligible if compared with the effect of S_r, which plays a most important role in liquefaction resistance of non-saturated soils.

Moreover, the proposed equation is extremely important for non-saturated soils, where the attained r_u at liquefaction (ε_{DA}=5%), lower than 0.90 for what has already been said, can be easily computed as ($1- \sigma'_{un,liq}/\sigma'_{un,0}$) and called $r_u(\varepsilon_{DA}=5\%)$.
Taking into account such important considerations, it was possible to build the cyclic resistance curve of non-saturated soils. As expected, when the degree of saturation decreases the resistance to liquefaction increases.
Based on the results of non-saturated tests, further considerations, which have been extremely useful in the proposed design methods, have been made. They are synthetically reported in the following:

- during the cycling loading, ε_v increases with a rate that resembles that of the pore pressure or the effective stress decrements. ε_v increases with the number of cycles due to the compressibility of air (because of the undrained condition), delaying the pore pressure build-up is at least one of the reasons of liquefaction resistance increase;
- ε_v increases to a final value $\varepsilon_{v,fin}$ which depends on values of S_{r0}, D_r (or e) and confining pressure (σ'_{un}). Therefore, a unique final value of $\varepsilon_{v,fin}$ exists for each set of S_r, D_r (or e) and σ'_{un}.
- defined $\varepsilon_{v,liq}$ as the value of ε_v attained at liquefaction evaluated according to strain approach, it was noted that especially for lower degree of saturation $\varepsilon_{v,fin}$ does not correspond with $\varepsilon_{v,liq}$;
- plotting the effective stress versus the volumetric strain, the results related to the same S_r overlap each other. Consequently, an average curve for a fixed S_r can be identified in the plane ε_v- σ'_{un};
- plotting all the average curve in a non-dimensional plane ($\sigma'_{un}/\sigma'_{un,0}$ - $\varepsilon_v/\varepsilon_{v,fin}$), it can be noted that all the results follow a unique trend. The relationship between $\sigma'_{un}/\sigma'_{un,0}$ and $\varepsilon_v/\varepsilon_{v,fin}$, already reported by Mele et al. (2018b), is independent on soil intrinsic and state properties and thus it can be considered as a general law.

In conclusion, even though such technique might be difficult for in situ application it does not have environmental problems. Further tests should be done to evaluate the duration of this countermeasure in-situ.

10.1.3 INSIGHT ON LIQUEFACTION MECHANISMS

In this research an insight on liquefaction mechanisms has been done. In particular, an energetic approach to interpret liquefaction phenomena from laboratory tests to the evaluation of liquefaction potential in situ has been shown, with particular attention to energetic pore pressure model for saturated and non-saturated soils. Additionally, the traditional "mechanisms", such as triggering, behaviour of liquefied soils and post-liquefaction behaviour have been analysed in depth.

10.1.3.1 ENERGETIC APPROACH: FROM EXPERIMENTAL EVIDENCES TO DESIGN TOOLS

One of the most innovative and promising part of this research is the energetic interpretation of liquefaction phenomena. It is based on the evidence that a soil spends energy to liquefy. The total specific energy is given by the sum of two components: the volumetric energy ($E_{v,liq}$) and the deviatoric one ($E_{s,liq}$). $E_{v,liq}$ represent the specific work done to cause the volumetric deformation and it can be seen as the sum of three components: the volumetric energy of soil skeleton ($E_{v,sk,liq}$), the volumetric energy of water ($E_{w,liq}$) and that of air ($E_{air,liq}$). It can be easily understood that it is nil for saturated soils, where the total specific energy to liquefaction is given only by the deviatoric component, which is defined as the sum of the areas of all the stress strain cycles. The role of these two components has been investigated.

The specific volumetric energy to liquefaction ($E_{v,liq}$) can be easily computed starting from the experimental evidences on non-saturated tests. It is a function of the initial values of the effective confining stress (Bishop notation), of the void ratio and of the degree of saturation ($E_{v,liq}=E_{v,liq}(\sigma'_0, e_0, Sr_0)$), and increases from zero (for saturated soils) as S_r decreases. It may be seen as a synthetic state variable ruling the increment of liquefaction resistance of sands (at low confining stresses) from CRR_s (S_r=100%) to CRR_{un} (S_r<100%). This is confirmed by plotting the ΔCRR calculated at N_{liq}=15, as the difference between the CRR_{un} and CRR_s versus $E_{v,liq}/p_a$ for different soils. A clear and unique relationship between ΔCRR^{ctx} (or ΔCRR^{css}) and $E_{v,liq}$ is observed for all the tested initial state conditions, confirming that an increase in the specific volumetric energy spent to liquefaction corresponds to an increase in liquefaction resistance with a rate that seems to reduce as $E_{v,liq}$ increases. A mathematical expression of this relationship has been presented in triaxial and simple shear conditions. Although such correlations has been achieved for N_{liq}=15, it was demonstrated that ΔCRR^{ctx} does not depend on N_{liq} but only on $E_{v,liq}$. In other words, for $N_{liq}\leq 20$ ΔCRR can be univocally related to $E_{v,liq}$, and therefore desaturation leads to a simple translation towards higher values of CRR of the liquefaction resistance curve, without appreciable change in shape.

The volumetric component of such an energy univocally identifies the position of the CRR-N_{liq} curve in non-saturated conditions, once the position of the saturated one is known, and may be seen as a synthetic state variable.

Additionally, the role of the specific deviatoric energy on liquefaction occurrence has been studied. Starting from laboratory tests performed on different soils in different conditions, the factors affecting $E_{s,liq}$ have been analysed and the results have been briefly summarized below:

- the *confining stress* influence $E_{s,liq}$ and in particular it increases linearly with σ'_m. To take rid such dependence, $E_{s,liq}/\sigma'_m$ has been considered;
- the *kind of test* (i.e. *the stress path*) seems to have a minor influence on the normalized specific deviatoric energy to liquefaction ($E_{s,liq}/\sigma'_m$), ranging between 0.007 and 0.012 as confirmed by other authors;
- as expected, *soil grading* has an effect on the normalized specific deviatoric energy to liquefaction. Such effect can be quantified through D_{50}: the ratio

$E_{s,liq}/\sigma'_m$ increases with D_{50}. On the other hand, the *uniformity coefficient* does not exhibit a clear influence on $E_{s,liq}/\sigma'_m$, even though it seems to be slightly affected by U_c;

- surprisingly, despite the fact that a wide range of *fines content* has been investigated (0<FC(%)<80), FC seems not to influence in a remarkable way the normalized specific deviatoric energy to liquefaction;
- tests performed on sand treated with laponite (PI=1100%) have allowed to investigate the effect of the *plasticity index*. Such effect results, once again, negligible;
- plotting $E_{s,liq}/\sigma'_m$ versus the *relative density* makes possible to appreciate the differences in terms of $E_{s,liq}/\sigma'_m$, that exist when D_r changes. However, although a dependence of $E_{s,liq}/\sigma'_m$ on D_r could exist, it is not possible to identify clearly a trend;
- the value $E_{s,liq}/\sigma'_m$ seems to be independent on the used *loading waveforms*, confirming what has been observed by Polito et al. (2013);
- $E_{s,liq}/\sigma'_m$ assumes a similar value, regardless of specimen preparation technique or if undisturbed specimens have been tested. In other words, also the *fabric effect* does not influence significantly the specific deviatoric energy to liquefaction;
- unlike the other state parameters presented in the previous points, the *degree of saturation* plays an important role in the specific deviatoric energy to liquefaction. Such dependency has been quantified according to the relationship reported in eq. (8.14);
- a clear dependence of $E_{s,liq}$ on the *number of cycles at liquefaction* (N_{liq}) has been observed especially for non-saturated soils;
- for N_{liq}=15, a linear correlation between $E_{s,liq}$ and the *specific volumetric energy to liquefaction* ($E_{v,liq}$) has been noted;
- for each non-saturated soil and initial state, $E_{s,liq}$ is uniquely related to CRR attained in each test. Since state conditions of non-saturated soils during cycling tests are well represented by $E_{v,liq}$, a much more general interpretation can be obtained by plotting the experimental data in the normalized plot, in which a unique, non-linear relationship links $E_{s,liq}$ to the term $(CRR^{ctx}\cdot(1-5\cdot E_{v,liq}/p_a)^{10})$;
- $E_{s,liq}/\sigma'_m$ has been also studied in reconsolidated specimens, which have already experienced liquefaction, distinguishing the case of saturated and non-saturated soils. For saturated soils $E_{s,liq}/\sigma'_m$ does not change from first to second liquefaction. On the contrary, some difference can exist in non-saturated soils especially when $E_{v,liq}$ changes.

Based on the experimental data for saturated soils, the expression of the soil capacity, which express the dependence on σ'_m, D_r, FC, U_c and D_{50} and introduced by Baziar and Jafarian (2007) (eq. (8.10)), has been modified in this research work providing a new equation, which fits better the experimental results (eq. (8.11)). Such equation can be used to have a good estimation of soil capacity ($E_{s,liq}$) in situ.

The energetic consideration made on non-saturated soils have allowed to suggest two possible approaches to predict the liquefaction resistance of non-saturated soils, that may

be seen as relatively simple design tools for desaturation interventions (or IPS), with reference to different design goals.

It has to be emphasized that the two approaches were calibrated on experimental results obtained in triaxial conditions on fine sands with a very limited range of confining stresses (25-60 kPa). However, they have been successfully tested on independent literature results also out of this range of state conditions: in fact, some of these results were obtained with a higher relative density (Dr=72%) (namely Inagi sand, Wang et al., 2014) or at higher confining stress (data from Okamura et al., 2010, σ'_c=88 kPa).

Approach 1 is simpler to adopt, as it assumes that the liquefaction resistance curve related to a given degree of saturation can be obtained as a simple upwards translation of the curve related to saturation conditions, based on the assumption that the CRR-N_{liq} curve does not change shape at different values of S_r, such as has been demonstrated in the range of N_{liq} of engineering interest (N_{liq}<20).

Approach 2 needs a few calculation steps more than approach 1, being based on the calculation of the total specific energy and not only of its volumetric component. However, it has the advantage of not needing the knowledge of the saturated liquefaction resistance curve to predict the behaviour of the non-saturated soil. The result is not a translation of the CRR-N_{liq} curve, and any shape may be obtained, depending on the combination of specific volumetric and deviatoric energies to liquefaction. Approach 2 needs just the knowledge of the state parameters and of the soil water retention curve.

Comparing the simulations of independent experimental data, it can be noted that approach 2 better simulates the cyclic resistance of the three different sands. This is not surprising: being based on the calculation of the total specific energy spent to liquefy, it takes into account both the initial state conditions via the volumetric component, and cyclic damping via the deviatoric one (not considered by approach 1).

In the design of desaturation (or IPS), the goal is to find what degree of saturation S_r is needed to guarantee for the structures to protect a satisfactory performance with reference to serviceability and limit conditions with the desired safety margins, with reference to any kind of mechanism related to liquefaction. Two scenarios may be foreseen: one in which the risk is linked to the attainment of liquefaction (i.e. a temporary but total loss of stiffness and strength of the liquefied soil), and one in which the pore pressure build up may trigger limit states in the structures (e.g. bearing capacity failure or excessive settlements) before liquefaction is reached. In the first case, an increase of CRR^{css} for the given value of N_{eq} is needed. In the second case, it is simply asked to have lower pore pressures for $N=N_{eq}$. Both scenarios ask for an increase of soil capacity via desaturation (or IPS) to cope with seismic demand, and the two procedures can be alternatively considered to this aim.

10.1.3.2 LIQUEFACTION MECHANISMS: FROM TRIGGER TO POST-LIQUEFACTION

In this research work an insight on liquefaction mechanisms has been done studying in depth the experimental results of cyclic triaxial and simple shear tests. Liquefaction phenomena has been widely studied starting from the trigger, passing from the parameters affecting liquefaction resistance, the behaviour of liquefied soils and concluding with the behaviour of re-consolidated soils, which experienced liquefaction. So, all the phases of a liquefied soils have been processed.

Firstly, the liquefaction trigger has been analysed. It is well known that liquefaction is traditionally defined according to stress and strain criteria. Stress criterion is based on the concept of excess pore pressure ratio (r_u), when r_u=0.90 liquefaction is attained. On the other hand, strain criterion is based on the axial strain in double amplitude (ε_{DA}) for triaxial tests and shear strain in double amplitude (γ_{DA}) for simple shear tests. The strain thresholds are 5% and 3.75 %, respectively.
The two criteria generally give the same results in loose sands, where the excess pore pressure is immediately accompanied by accumulation of large shear strains. Conversely, in denser sands or non-saturated soils the two criteria generally give different results in terms of N_{liq}. In other words, the cyclic resistance curve is strongly influenced on the choice of the liquefaction triggering criterion.
To overcome this drawback, two other triggering parameters, that involve both the cyclically induced stresses and strains, can be adopted: the *apparent viscosity* η (slope of the stress-strain rate hysteresis loop in a generic loading cycle) and *energy dissipated per unit volume* E_s (area bounded by the stress-strain hysteresis loop in a generic loading cycle).
The concept of apparent viscosity (η) is based on a state change of soil, that switches from that of a solid to that of a viscous fluid. So, unlike stress and strain criteria, the apparent viscosity (η) is a physically based parameter able to represent this change of state. Plotting the experimental results in the plane η-N_{cyc} an apparent decay law can be identified. The experimental evidences showed that N_{liq} (evaluated according to stress criterion) is attained exactly in correspondence of the elbow of the apparent viscosity decay law. It is clearly evident plotting $\Delta\eta/\eta$ versus N_{cyc}. The result is a bell-shape curve, whose maximum corresponds to N_{liq} evaluated according to stress criterion for saturated soils and strain criterion for non-saturated ones.
Owing to that, it is recommended to use:

- stress criterion (r_u=0.90) for saturated soils;
- strain criterion (ε_{DA}=5% or γ_{DA}=3.75%) for non-saturated soils.

Regarding the specific deviatoric energy (E_s) it can be used as a liquefaction triggering criterion as well. Plotting E_s with N_{cyc} it can be noted that the shape of the curve is almost linear and when liquefaction occurs, it sharply increases. The maximum gradient of the relationship E_s-N_{cyc} identifies N_{liq} evaluated according to the apparent viscosity approach and thus according to stress criterion for saturated soils and the strain one for non-saturated sandy soils.

The second aspect which will be discussed is related to the factors affecting the liquefaction resistance. All of them have been studied under simple shear conditions.
First of all, the *effect of confinement* has been investigated by performing tests by means of flexible and rigid boundaries. The most important considerations can be drawn up as follows:

- the configuration with rigid boundary ensures nil radial strains, guaranteeing a perfect simple shear stress state. On the contrary, flexible boundary for maintaining a constant diameter introduces unavoidable oscillations of the diameter's measure around the target value. Such a value has been computed and considered low enough to assume a simple shear stress state;
- flexible boundary has the advantage to completely know the stress state of the specimens, allowing to plot Mohr's circles;
- liquefaction occurs when $\alpha=\beta=45°$, because under these conditions the alignment of the plane of maximum shear stress with the bedding plane occurs;
- even though the cyclic resistance curve seems to be roughly unique, the stress-strain response of the soil is different. A slightly lower cyclic resistance of tests carried out with rigid boundary could be due to a more uniform deformations than those obtained in the other configuration;
- normalizing N_{cyc} with N_{liq}, r_u follows the same trend for tests performed with different boundary conditions.

In order to evaluate the *effect of waveforms* on liquefaction resistance, nine tests have been carried out by applying non-sinusoidal waveforms on GSS. In particular, three different shape of loading have been used: triangular, rectangular and sawtooth. The effect of different waveforms on the cyclic resistance curve is clear. Triangular and rectangular load shapes require higher amplitudes of loading at a fixed N_{liq} than those subjected to sinusoidal loading. The higher liquefaction resistance of triangular load shape than that of rectangular or sinusoidal load can be attributed to an effect of the instantaneous change of velocity.

As well known the *effect of the preparation techniques* on the liquefaction resistance can be extremely relevant, owing to that such aspect has been studied by preparing specimens by three different preparation techniques: 1D-Compression (1D-C), moist tamping (MT) and air pluviation (AP). The main conclusions are reported below:

- 1D-C and MT give the same resistance curve. It is surely due to the fact that these two methods are very similar. Also the cyclic behaviour in the plane τ-γ seems not to be affected on the preparations;
- the cyclic resistance curve achieved for air pluviated specimens lies below that of moist tamping and 1D-compression. It is probably due to a lower distribution of contacts created during the air pluviation preparation method;
- regardless of specimen preparation, the slopes of the cyclic resistance curves are the same;

- interpreting the results in terms of excess pore pressure (r_u) versus N_{cyc}/N_{liq}, it can be observed that despite different cyclic resistance curves, the value of β, calibrated to have the best fitting with the experimental results is 1.0 for MT specimens and 1.1 for 1D-C and AP ones.

To better understand the best method able to reflect the *natural fabric* of a soil deposit, the results of tests prepared by different methods have been compared with those of undisturbed specimens, retrieved by means of Osterberg and Gel-Pusher samplers. The experimental points relative to Gel-Pusher samplers exhibit lower liquefaction resistance than those from Osterberg sampler and it is certainly due to the effect of sampling. In addition to the void ratios, the grain distribution plays an important role, as well. The scatter of the experimental dots can be obviously explained by an effect of variability, due to the fact that natural soils have been tested.
The results of undisturbed samples confirm the cyclic resistance curve obtained by 1D-compression and moist tamping method.

From a practical point of view, the presence of a static shear stress can influence significantly the liquefaction resistance of sands. Owing to that, the *effect of a static shear stress* and thus, of a non-symmetrical cyclic loading, a τ_{st} has been applied, and thus $\alpha \neq 0$, where α is defined as the ratio between τ_{st} and σ'_{v0}.
A different cyclic behaviour has been highlighted comparing symmetrical and non-symmetrical tests.
In symmetrical tests ($\tau_{st}=0$), shear stresses cycle around 0 symmetrically, while shear strains accumulate slowly in the beginning and then increase, always cycling around 0. A different behaviour is observed in non-symmetrical tests. Such response depends on whether the cyclic stress (τ_{cyc}) is higher or not than the static one (τ_{st}).

- When $\tau_{cyc} \leq \tau_{st}$ *non-reversal condition* is observed. In this case, failure results from the accumulation of excessive permanent shear strains (drift).
- in *shear stress reversal* ($\tau_{cyc} > \tau_{st}$) the shear strains accumulate in the direction of the driving shear force. It is commonly called "ratcheting".

In the examined tests, small static shear stresses (positive or negative) have been imposed, with a value of α ranging between -0.02 and 0.12, they are not such as to affect the liquefaction resistance significantly. On the other hand, the excess pore pressure build-up is influenced on the presence of a static shear stress. In particular, combining the effects of non-symmetrical cyclic loading and preparation techniques it can be noted that the presence of a static shear stress for moist tamping specimens seems not to be significant in pore pressure generation models. A possible explanation could be the fact that the moist tamping preparation is the method which guarantees more uniform specimens. The effect of a static shear stress could be redistributed among sand grains more uniformly in such specimens. On the contrary, for 1D-compression and AP specimens the excess pore pressure generation is much more sensitive to an applied static shear stress, albeit small.

The third aspect, which has been analyzed is the behavior of liquefied soils. Once again, the concept of the apparent viscosity has been used. The liquefied soils behave as shear thinning non-Newtonian fluid (pseudo-plastic fluid) and the useful relationships between

η and $\dot{\gamma}$ (shear strain rate) have also provided for different tested materials in different state conditions, giving original data in terms of flow parameters k and n (*consistency coefficient* and *liquidity index*, respectively*)* needed to calibrate flow constitutive models. The most important findings are summarized as follows:

- a correlation between k and CSR has been observed, contrary to what has been reported by Zhou et al. (2014);
- k and n seem to be strongly linked (linear relationship). Such results, if confirmed by other tests performed on different sands in different conditions, would lead to important advantages in the calibration of pseudo-plastic models, simplifying the calibration procedures.

One of the most important and interesting aspect linked to liquefaction is the behaviour of sandy soils that have already experienced liquefaction. Post- liquefaction behaviour has been investigated on saturated and non-saturated soils by means of cyclic triaxial tests.

Despite an increase of relative density after the re-consolidation, saturated soils exhibit a lower liquefaction resistance, which has been attributed to weaker zones on the top of the specimen after being liquefied or to an effect induced by anisotropy. Comparing virgin and re-consolidated specimens, it can be noted that:

- a higher accumulation of pore pressure during the second liquefaction occurs;
- when the pre-shearing is applied in compression direction, higher pore pressure in the extension side;
- when the pre-shearing is applied in extension direction, higher pore pressure in the compression side.

Generally speaking, the excess pore water pressure generation is very different according to whether "pre-shearing" is applied on the side of triaxial extension or triaxial compression. It was justified through the concept of the induced anisotropy. During the first cyclic loading, when liquefaction occurs, because of a very low confining stress, the contacts of individual particles of the specimens are released and new structures are formed. They are oriented predominantly in the vertical direction if pre-shearing is applied in compression side, while the normals of grain-to-grain are oriented mainly horizontally if pre-shearing is applied in extension side.

Finally, a comparison between first and second liquefaction has been done in terms of η versus the shear strain rate ($\dot{\gamma}$) to investigate the pseudo-plastic behavior of liquefied soils. The apparent viscosity decay laws appear slightly different after the re-consolidation.

The consistent coefficient (k) changes slightly passing from first to second cyclic loading, while the liquidity index (n) seems to assume a similar value for all re-consolidated tests. Moreover, the linear relationship between k and n found for virgin soils seems to be confirmed for re-consolidated specimens. It is extremely important because no need to re-calibrated the parameters k and n for re-consolidated soils.

As for saturated soils, for non-saturated ones, after the re-consolidation the relative density increases and consequently an increase of S_r occurs, as well.

Unlike saturated soils, where the cyclic resistance always decreases during the second liquefaction, it seems not to be a general rule in non-saturated soils. Some tests exhibit a

cyclic resistance similar to that of virgin soil, despite a relevant difference in terms of relative density. On the contrary, other tests show lower liquefaction resistance. Obviously, as for saturated soils, for non-saturated ones a change of fabric effect occurs as can be easily understood by the fact that the change in terms of D_r does not influence the cyclic resistance. In other words, virgin and post-consolidated specimens cannot be compared as the same soil in different condition in terms of D_r, because in this case, a different cyclic resistance curve should have existed. By contrast, as a matter of the fact that the liquefaction resistance is the same, a change fabric must be assumed.
Further considerations have been made plotting ε_v with N_{cyc} for virgin and re-consolidated specimens. It can be noted that $\varepsilon_{v,liq}$, practically coincident with $\varepsilon_{v,fin,}$ for the virgin soil, is roughly the same as that of re-consolidated specimens. Additionally, comparing the curves of virgin and re-consolidated specimens in the plane ε_v - $\sigma'_{un,}$ it can be noted that they overlap each other except for two tests. In both cases, the area subtended by the curve of the second cyclic loading ($E_{v,sk,liq}$) is lower than that relative to the first cyclic loading. Such difference in terms of $E_{v,sk,liq}$ and consequently of $E_{v,liq}$ is responsible of a different $E_{s,liq}$.
The study on post-liquefied behaviour has been only preliminary, especially for non-saturated soils, therefore further tests are extremely necessary to improve the basic understanding on this interesting topic.

10.1.3.3 EXCESS PORE PRESSURE GENERATION MODELS

One of the most important part of this research work has been dedicated to study of excess pore pressure generation models of saturated and non-saturated soils.
In this work three excess pore pressure generation models have been introduced and discussed, all of them calibrated on the experimental results presented in this thesis. The models are summarized below:

- viscosity based model for saturated soils;
- energy based model for saturated and non-saturated soils;
- stress based model for non-saturated soils.

The proposed *viscosity-based model* for saturated soils has been developed starting from the experimental observations, according to which a strong link between the apparent viscosity (η) and the excess pore pressure ratio (r_u) can be noted. The value of η decreases as the pore water pressure r_u increases and the maximum gradient of the curvature (the elbow of the curve η-N_{cyc}) is attained exactly at the pore pressure ratio threshold (r_u=0.90).
The results of saturated cyclic triaxial tests can be plotted in the plane η/η_0 versus r_u, identifying a unique average curve for each material. Such relationship is mathematically expressed via eq. (7.1), where three parameters (a, b and c) should be calibrated on the experimental results. Such parameters have been calibrated for all studied sands and apart from Sant'Agostino sand, where all tests performed (loose and dense) seem to identify a unique curve, in all other cases, the generation pore water pressure model based on the

concept of apparent viscosity seems to be dependent on the state of the soil. In other words, the parameters of the relationship η/η_0 - r_u are affected by soil grading and state of the soil. However, it can be said that:

- the parameters a and c govern the trigger of the transition phase, moving forward and backward the curve;
- the parameter b regulates the slope of the curve η/η_0 - r_u.

The relationship η/η_0 versus r_u may play an important role in the constitutive models of fluid mechanic to simulate the behaviour of liquefied soils.

The *energy-based model for saturated soils* has been introduced aiming to propose a general law to predict the excess pore pressure ratio (r_u), known the normalized specific deviatoric energy (E_s/σ'_m). As for the apparent viscosity, a strong link between E_s/σ'_m and r_u has been observed. As already mentioned, at liquefaction the ratio E_s/σ'_m (equal to $E_{s,liq}/\sigma'_m$) is slightly influenced by intrinsic and state parameters, and thus ranging in a small interval. However, the trend of the relationship E_s/σ'_m - r_u can be affected by some parameters. In particular the waveforms or the fabric effect seem to play an important role in the energetic-pore pressure law. Generally speaking, it can be said that although for lower r_u the trend of the relationship E_s/σ'_m - r_u can be influenced by some factors, for higher r_u, regardless of soils, state and devices, the curves tend to converge towards $E_{s,liq}/\sigma'_m$ (about 0.006), which can be assumed roughly unique, as reported by several authors. With this limitation an energetic pore generation model has been proposed (eq. (8.12)) as a general rule for different fine sands in different conditions, reminding that for very low value of E_s/σ'_m, r_u can be mispredicted.

Such equation has been validated by centrifuge tests, where excess pore pressure ratio can be computed by the physical measures of pore pressure transducers, while the predicted r_u can be achieved from E_s/σ'_m, evaluated by performing a 1D dynamic analysis, for example by EERA. The latter one is able to provide the specific dissipated energy with time at the middle of each discretized layer. The maximum value of E_s/σ'_m has been used to estimate r_u via eq. (8.12) through an iterative procedure.

Three centrifuge tests on three different sandy soils (Pieve di Cento, Ticino and Hostun sand) have been considered. In all cases, the soil columns have been modelled in EERA and the input motion has been applied at the base of stratigraphy profile. The results can be summarized as follows:

- centrifuge test on Pieve di Cento (BSS) sand: the experimental results show very low r_u (<0.10) in the deepest layers, while at a depth of 2.48m r_u is 0.40. The proposed model is in good agreement with the experimental result in the shallowest layer (2.48m), where the predicted value is 0.33. However, it overestimates r_u, returning values of 0.30 against 0.10, which are those measured. It confirms that for lower r_u the results of the proposed method should be used with extreme care;
- centrifuge test on Ticino sand: the proposed energetic pore generation model (eq. (8.12)) shows a very good agreement with the experimental results. Apart from the depth of 12.9 m, where the proposed model overestimates the excess pore

pressure (0.82 against 0.70, which is that measured), eq. (8.12) seems to perfectly fit the experimental data demonstrating the reliability of the calibrated model to predict the excess pore pressure ratio known E_s/σ'_m, especially when r_u are high (>0.60).

- centrifuge test on Hostun sand: as for tests carried out on Ticino sand, the model seems to be in agreement with the experimental results despite such difference with the experimental data in the shallowest and deepest layers.

Despite such difference with the experimental data, the proposed model seems to work satisfactorily, taking into account the fact that it does not depend on the time histories acceleration (regular or irregular) and it no need to be calibrated on the results of laboratory tests.

Once the model has been validated, it has been used to predict r_u profile of two case histories: Marina District (Loma Prieta earthquake, 1989) and Pieve di Cento (Emilia Romagna earthquake, 2012), where the estimated values of r_u have been compared with those achieved by a 1D numerical code (SCOSSA). As for centrifuge tests, the stratigraphy columns have been modelled in EERA, which returns the sum of the areas of stress-strain cycles, applying the input motion at the base of the model.

- For Marina District, apart from some differences at depth of 2.5 - 4.0 m, where the proposed model returns lower r_u than SCOSSA, eq. (8.12) seems to be congruent with the r_u profile achieved by the more complex dynamic analysis.
- For Pieve di Cento, the results of SCOSSA and those of the proposed model of eq. (8.12) are congruent, no significant differences can be highlighted.

In conclusion, despite some limitations for extremely low r_u (<0.20), the proposed model seems to be consistent returning better results than those achieved by means of the simpler model of Berrill and Davis (1985). In other words, eq. (8.12) results a useful tool to predict, in simple way, the excess pore pressure ratio, known the ratio E_s/σ'_m which can be easily computed by dynamic response analysis. Obviously, it has to be specified that it should be used as a preliminary analysis to get an idea of the excess pore pressure ratio profile and cannot replace more sophisticated models based on dynamic analyses, which take into account the non-linear behaviour of the soil.

However, it can be used as a simple tool to preliminarily predict the r_u profile, and consequently to assess liquefaction potential. The factor safety (FS) can be defined as the ratio between the capacity ($E_{s,liq}$), easily assumed equal to $0.006 \cdot \sigma'_m$ (from eq. (8.12)) and the demand, computed by EERA (E_s).

The energy approach for the assessment of liquefaction potential of the two case histories has been compared with the stress based approach.

The energy-approach returns results congruent with the experimental evidences, as for Pieve di Cento, where the energetic analysis reveals that only grey silty sand is liquefiable, on the contrary the stress-based approach identifies all sandy soils potentially liquefiable. In other words, the stress-based approach returns results which can be no-reliable. On the contrary, the energy-based method is based on more consistent concept of energy which is demonstrated to be independent – or slightly dependent - on the shape of loading, state and intrinsic parameters of the soil.

The large potentiality of the energy-based approach to assess the liquefaction triggering and the induced excess pore pressure within the soil during the earthquake is confirmed and demonstrated. However, it is important to estimate adequately the seismic demand and to remind that the proposed model can be a useful tool to predict the profile of excess pore pressure when a preliminary analysis has to be performed, while in more complex case studies the dynamic analysis is strongly recommended.
The *energetic model* proposed in eq. (8.12) for saturated soils has been modified *for non-saturated soils*. It has been observed that the relationship r_u-E_s/σ'_m is extremely dependent on S_r. The results of saturated and non-saturated sandy soils can identify a unique relationship in the plane $r_u/r_{u,liq} - E_s/\sigma'_m \cdot k(S_r)$, where $r_{u,liq}$ is r_u in correspondence of liquefaction defined according to stress criterion, while $k(S_r)$ depends on the initial degree of saturation.

Finally, a *stress-based model for non-saturated soils* has been developed. One of the biggest problems in the prediction of pore pressure build-up of non-saturated soils is due to the fact that the attainment of liquefaction is traditionally defined according to a strain criterion (ε_{DA}=5%) and thus, at N_{liq} does not correspond r_u=0.90. The proposed model has been developed starting from the model of Booker et al. (1976), whose reliability has already been proved for saturated tests. The challenge has been to generalize the expression of Booker et al. (1976) for saturated and non-saturated soils, taking into account the fact that for non-saturated soils, liquefaction occurs when ε_{DA} reaches the threshold of 5%. The accumulation of pore pressure for non-saturated soils can be achieved easily scaling the curve of saturated soils, generally expressed according to the formula of Booker et al., (1976). Such model has been verified simulating the accumulation of excess pore pressure of non-saturated soils (Sant'Agostino, Pieve di Cento (GSS) and silica (N°5) sands).
The prediction of excess pore pressure build-up for non-saturated soils seems to satisfactorily agree with the experimental data to which has been compared. Some differences between the experimental and simulated accumulation of r_u with N_{cyc} is mainly found when liquefaction occurs at a small N_{liq} (N_{liq}<5). In these cases, as for saturated soils, the shape of the curve is not well defined due to the fact that liquefaction is attained in few cycles. However, such approach appears very promising, and therefore, it deserves further insights.

10.2 FUTURE WORK

In this paragraph, recommendations for further study are made. For future work, the following items are recommended to be considered in conducting the research.

First of all, an insight on the *monotonic behavior of sands* should be done aiming at better understanding the effect of smooth plates. Tests in MaTrix cell should be performed replacing the smooth ends with rough ones, to take rid of a possible effect due to the used device and the specimen preparation methods. Additionally, further monotonic tests

should be performed in a simple shear apparatus to further investigate the effect of different stress paths on the critical state line, which results extremely important to describe the behaviour of sands and study the liquefaction susceptibility.

Cyclic triaxial tests on saturated silica sand (N°5) would result extremely useful to better investigate the effect of soil grading on the two components of the total specific energy to liquefaction. Additionally, several tests on saturated and non-saturated specimens of the same sand should be performed by changing the fines content and the plasticity index to evaluate the effect on $E_{v,liq}$ and $E_{s,liq}$. Further tests are extremely useful to confirm the energetic approach proposed for non-saturated soils, on which the design tools of desaturation (or IPS) interventions are based.

Post-liquefaction behaviour should be studied in cyclic simple shear conditions too. Moreover, the residual strength of liquefied soils should be studied in depth.

As mentioned several times in this thesis, *energetic approach in the assessment of liquefaction potential* seems to be very promising. Therefore, to improve the basic understanding on such topic, it could be useful to perform further analyses on case histories, where a lot of data are available in literature.

APPENDIX A

A.1 EXTRAPOLATION PROCEDURES TO EVALUATE THE CRITICAL STATE OF SANDS

In this section the assessment of critical state in undrained and drained tests is discussed.

A.1.1 UNDRAINED TESTS

In undrained tests, the best fitting of sigmoidal function on the curve of $\partial p'/\partial \varepsilon_a$ versus ε_a with the experimental results can allow to find the critical state of sandy soils as proposed by Murthy et al. (2007). The mathematical expression of the sigmoidal function is reported below:

$$\frac{\partial p'}{\partial \varepsilon_a} = \left(\frac{\partial p'}{\partial \varepsilon_a}\right)_0 \cdot exp\left(-\left\{\left[\left(\frac{\varepsilon_a}{\alpha_s}\right)^{\gamma_s} - \left(\frac{\varepsilon_{1,0}}{\alpha_s}\right)^{\gamma_s}\right]^{\beta_s}\right\}\right) \qquad (A.1)$$

Where α_s, β_s and γ_s are fitting parameters, while $\varepsilon_{1,0}$ and $\left(\frac{\partial p\prime}{\partial \varepsilon_a}\right)_0$ are the axial strain and the value of the first derivative of the p' – ε_a curve respectively, at the point of inflexion, which corresponds to a stationary point in the plane ε_a - $\frac{\partial p\prime}{\partial \varepsilon_a}$. From eq. (A.1) it can be easily understood that the inclination of the p' – ε_a curve decreases with strain and approaches zero asymptotically. The fitted response in terms of p' versus ε_a can be achieved by integrating eq. (A.1).
As an example, the results of some tests have been plotted in Figures A.1, A.2 and A.3 for Sant'Agostino, Pieve di Cento (BSS and GSS) sands, respectively.
Similar considerations can be done for undrained simple shear tests. In this case, p'$_{in}$ critical state condition can be evaluated from the extrapolation of the experimental data by means of eq. A.1, replacing ε_a with γ.

For greater clarity, the sigmoidal function for simple shear tests has been reported as follows:

$$\frac{\partial p'}{\partial \gamma} = \left(\frac{\partial p'}{\partial \gamma}\right)_0 \cdot exp\left(-\left\{\left[\left(\frac{\gamma}{\alpha_s}\right)^{\gamma_s} - \left(\frac{\gamma_{1,0}}{\alpha_s}\right)^{\gamma_s}\right]^{\beta_s}\right\}\right) \qquad (A.2)$$

As an example, the extrapolation procedure applied for SS_GSS3 has been depicted in Figure A.4.

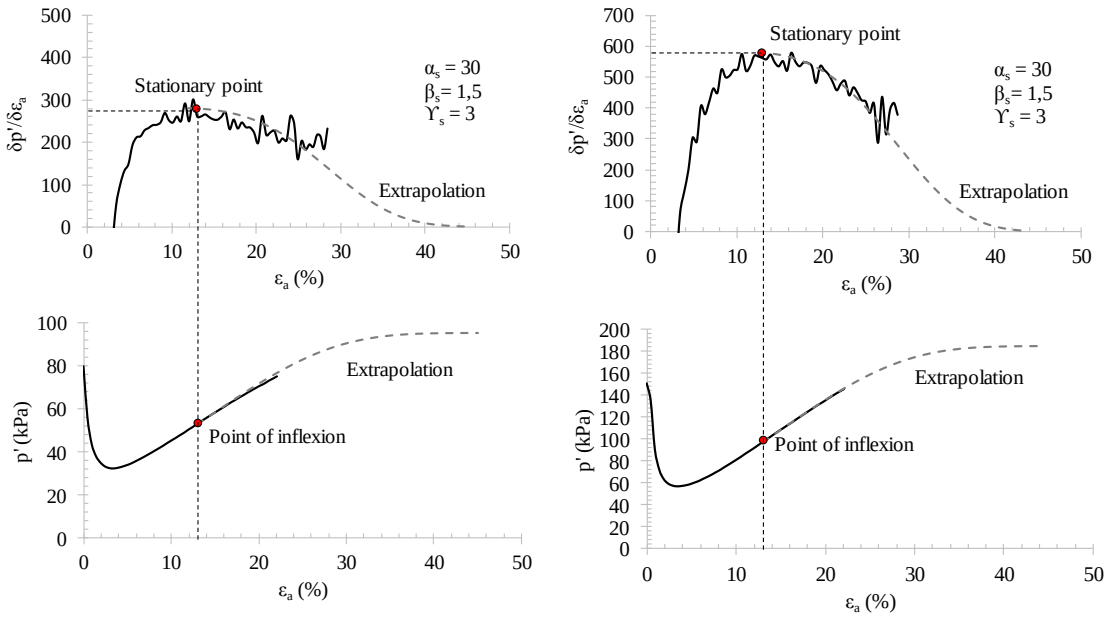

(a) (b)

Figure A.1. Extrapolation procedure to find the critical state for Sant'Agostino sand: TX_SAS2 (a) and TX_SAS3 (b).

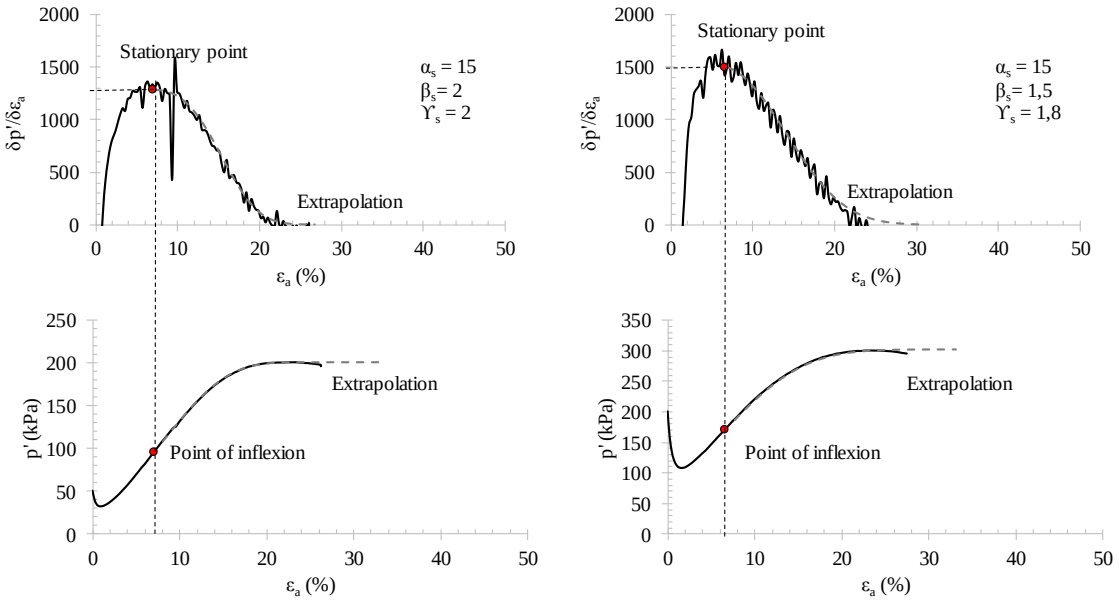

(a) (b)

Figure A.2. Extrapolation procedure to find the critical state for Pieve di Cento (BSS) sand: TX_BSS1 (a) and TX_BSS3 (b).

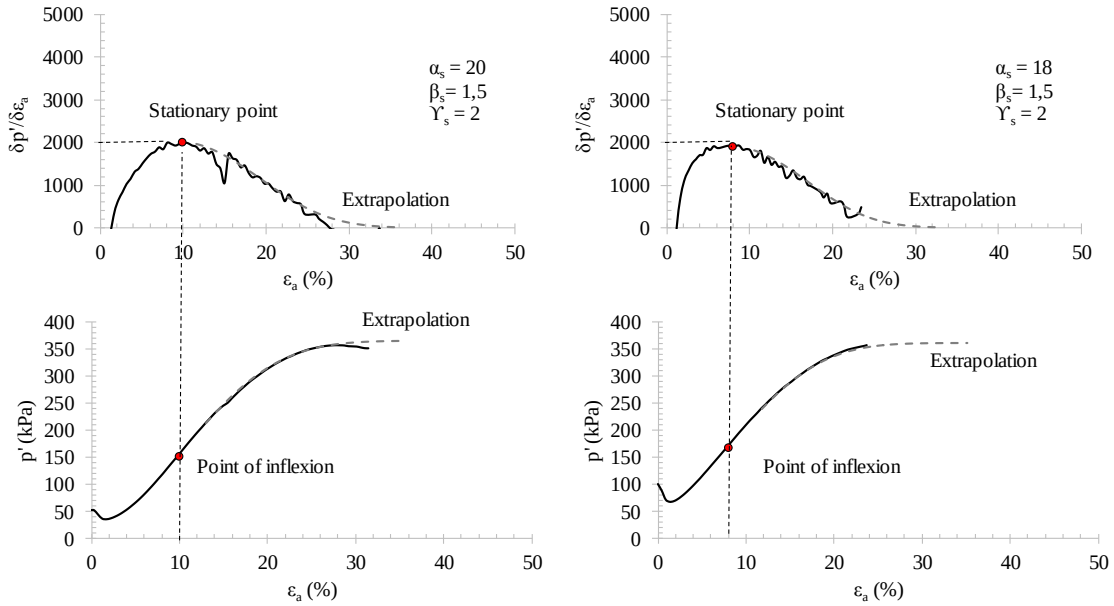

Figure A.3. Extrapolation procedure to find the critical state for Pieve di Cento (GSS) sand: TX_GSS1 (a) and TX_GSS2 (b).

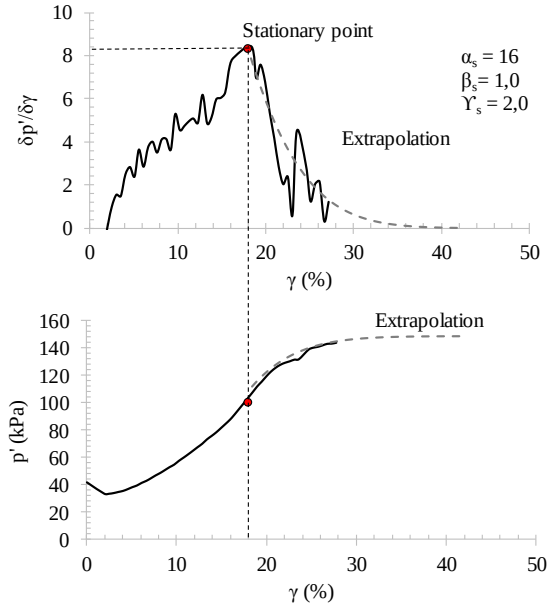

Figure A.4. Extrapolation procedure to find the critical state for Pieve di Cento (GSS) sand: SS_GSS3.

A.1.2 DRAINED TESTS

In drained tests, the volume of the specimen changes and the extrapolation procedure can be done introducing the concept of dilatancy ($\frac{\partial \varepsilon_v}{\partial \varepsilon_a}$). The critical state void ratio (e_{cs}) can be evaluated by applying the eq. (A.1), replacing p' with the volumetric strain (ε_v), as reported below:

$$\frac{\partial \varepsilon_v}{\partial \varepsilon_a} = \left(\frac{\partial \varepsilon_v}{\partial \varepsilon_a}\right)_0 \cdot exp\left(-\left\{\left[\left(\frac{\varepsilon_a}{\alpha_s}\right)^{\gamma_s} - \left(\frac{\varepsilon_{1,0}}{\alpha_s}\right)^{\gamma_s}\right]^{\beta_s}\right\}\right) \qquad (A.3)$$

Where $\frac{\partial \varepsilon_v}{\partial \varepsilon_a}$ is the dilatancy, while $\left(\frac{\partial \varepsilon_v}{\partial \varepsilon_a}\right)_0$ is the value of the first derivative of the $\varepsilon_v - \varepsilon_a$ curve at the point of inflexion, which corresponds to a stationary point in the plane ε_a - $\frac{\partial \varepsilon_v}{\partial \varepsilon_a}$. After the calibration of the parameters α_s, β_s and γ_s, the integration of eq. (A.3) allows to extrapolate the last part of the curve $\varepsilon_v - \varepsilon_a$. As an example, the results of some tests for the tested sands have been plotted in Figures A.5, A.6 and A.7.

It should be noted that when the dilatancy tends to zero, the volumetric strain tends to zero as well.

Moreover, the value of mean effective stress in critical state conditions (p'_{cs}) in drained tests, can also be evaluated: plotting p' versus ε_a it can be noted that its value is constant after an axial strain up to 15 – 20%, so that p'_{cs} can be easily determined. As an example, p' versus ε_a has been plotted in Figure A.8 for some tests.

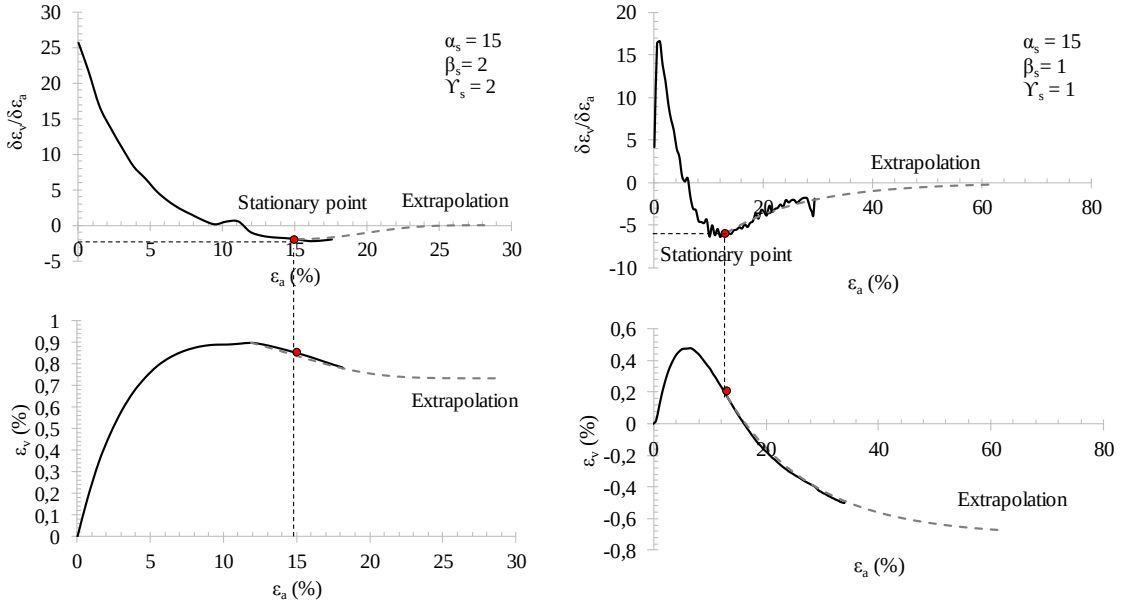

(a) (b)

Figure A.5. Extrapolation procedure to find the critical state for Sant'Agostino sand: TX_SAS5 (a) and TX_SAS7 (b).

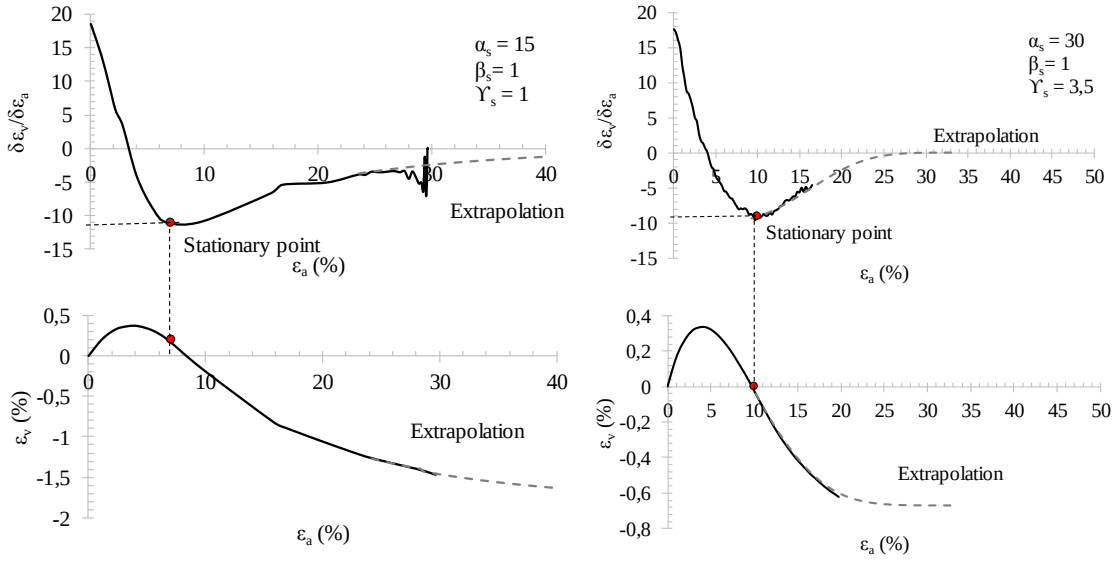

(a) (b)

Figure A.6. Extrapolation procedure to find the critical state for Pieve di Cento (BSS) sand: TX_BSS6 (a) and TX_BSS7 (b).

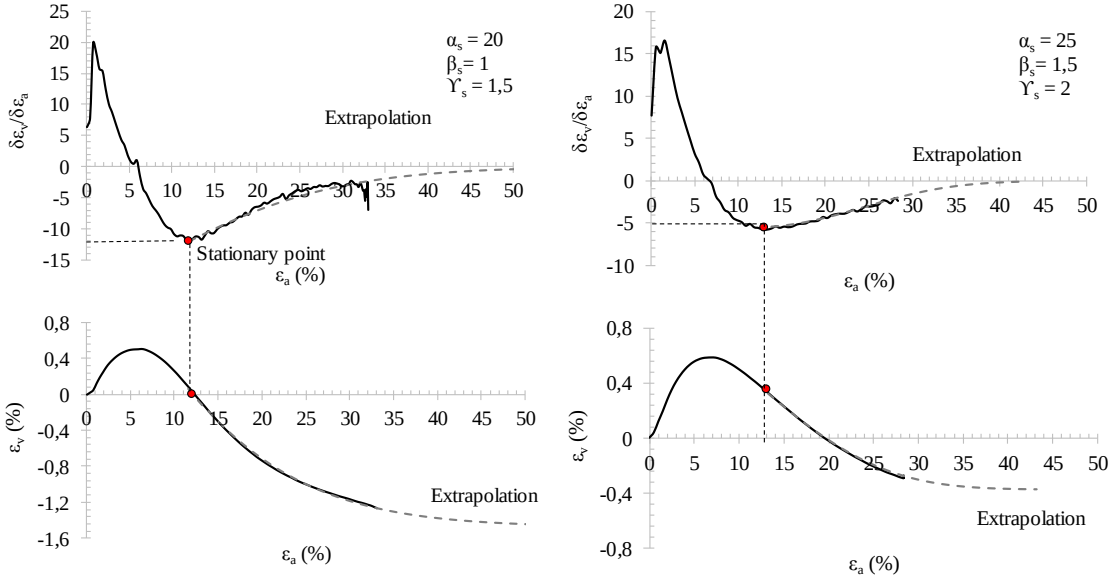

(a) (b)

Figure A.7. Extrapolation procedure to find the critical state for Pieve di Cento (GSS) sand: TX_GSS4 (a) and TX_GSS7 (b).

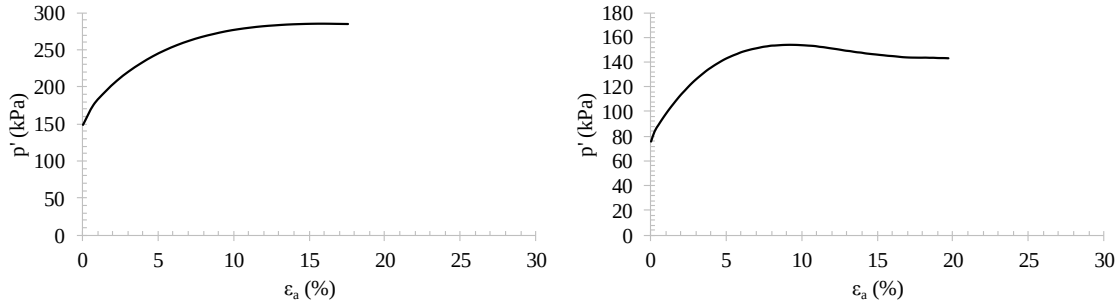

(a) (b)

Figure A.8. p' versus ε_a in drained tests: TX_SAS5 (a) and TX_BSS7(b).

ACKNOWLEDGEMENTS

At the end of this wonderful journey, it is necessary to thank my companions in this journey. First of all, I would like to thank my family and in particular my parents, to whom I owe everything and dedicate such work, because even though they did not contribute materially to my research, they have been always patient, caring and loving with me. Their support has been essential for the success of my thesis.

Regarding people who contributed in some way to my PhD research, first and foremost, I would like to thank my supervisors, Professors Alessandro Flora and Stefania Lirer, for their tremendous support, valuable suggestions and fruitful discussions on tests results and interpretation. It is my privilege to be under their guidance in both my Master and PhD. Additionally, I would like to thank them for giving me the opportunity to take part in LIQUEFACT project. It was a stimulating environment, where I had the opportunity to interact with the most important experts in geotechnical field, improving my academic and communication skills.

Such work could not have been completed without the technical assistance of Alfredo Ponzo and Antonio Cammarota. They always have brilliant ideas to help me in performing tests in the best way.
Additionally, I would like to thank Prof. Augusto Penna for his encouragement when my test results were not good and for providing useful discussions on my tests results.

Furthermore, I would like to acknowledge Professor Junichi Koseki, because I had the privilege and honor to be under his guidance during my study trip in University of Tokyo. I was glad to work in his laboratory and with his research team.
I would like to thank Sato san, the brilliant technician of Japanese laboratory. My unsaturated tests could not have been completed without his work.
I spent two wonderful months in Japan where I was able to know and taste a new culture, it was possible thanks to outstanding laboratory mates.
First of all, I want to thank Jay, not only because he taught me how to use the unsaturated Japanese triaxial cell, but especially because he has been a good friend, sympathizing and encouraging me during my research. Additionally, he helped me to improve my English and I am grateful to him for this. He was a perfect guide in Ueno zoo, Yokohama and Akihabara, even though, in my opinion, the most enjoyable moment was our badminton match. He was also a perfect Japanese Professor, thanks to him I was able to learn several Japanese sentences. For everything, arigatou gozaimasu (ありがとう ございます).
I would like to thank also Tokio, from Japan, because he was always available and with whom I spent a wonderful day in Nikko; Zhao san, from China, because he was always very nice and we laughed a lot in laboratory, he taught me that research is first of all enjoyment; Lin san, from China too, because she always helped me, especially when I was not able to speak to Sato san. She patiently translated my sentences in Japanese; Anthuan, from Vietnam, has been always friendly and I cannot forget when he left sweets and cakes on my desk.

In Japan, I was lucky to know the Catholic community of Sant'Alphonsus Church in Tokyo. I met a lot of outstanding people, and even though it is impossible to remind all of them, I cannot forget Sachiko san (Mrs Maria), who has prayed for me and for the success of my research. I am looking forward to seeing her again.

I would also like to express a special acknowledgement to Erminio Salvatore. He taught me how to use the Bishop & Wesley apparatus at University of Cassino. He was very patient in explaining things to me when I could not understand.

To Sara, with whom I shared these academic years and in particular, my master thesis, which "deserves a Senese award". She has been able to make these past years much more enjoyable.
To my friend Maria Pia, always present in my life and available to give me the best tips.
To Elisa, my favourite "uagliotta" for her true friendship and spontaneity. I shared with her the funniest moments in these years.

Last but not the least, I would like to thank the "angels" of my life, such as the two Antonietta, who always pray for me and for the success of my research.
I would like to thank the students, who worked with me and helped me during these years.

Finally, I want to say a word for me. Although these three years were beautiful, bad moments have not been missed, but they contributed to make me stronger and to learn that if you really want something you can achieve it and "if people are doubting how far you can go, go so far that you can't hear them anymore" (M. Ruiz).